THE TECTONOTHERMAL EVOLUTION OF THE HIGH HIMALAYAS IN THE SURU VALLEY, NW ZANSKAR, WITH CONSTRAINTS FROM METAMORPHIC MODELLING

Thesis submitted for the degree of Doctor of Philosophy
to the University of Oxford

by

Christian Bryan Walker M.A. (Cantab)

Trinity Term 1999

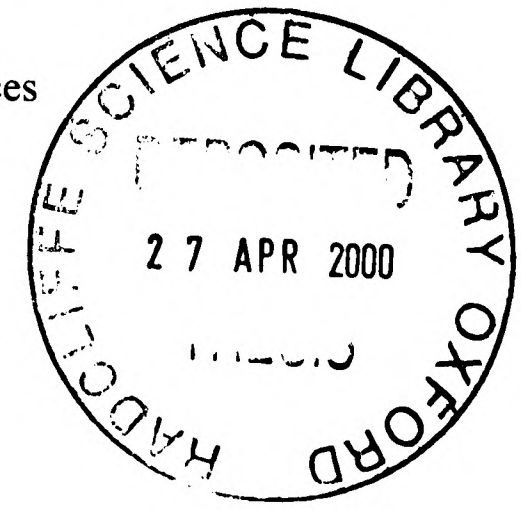


Worcester College

and

Department of Earth Sciences

University of Oxford





The mountains of Kun (7037 m) and Nun (7135 m) above the Kangri glacier, Suru valley.

ACKNOWLEDGEMENTS

When looking back over the best part of four years it took my to complete this thesis, it seems impossible to remember every individual who has in some way contributed either to the thesis itself, or my time spent attempting to avoid it. However, there are certain people who deserve a special mention for their contributions to my academic and social well-being.

Firstly I should like to thank my supervisors; Dave Waters for showing patience and opening many cans of worms as I became an apprentice in the sorcerer's art of metamorphic petrology, and Mike Searle for his unflagging optimism ("It never rains in Zanskar") and energy, be it while arguing with Suru valley porters or trying to distract me from my research with offers of beers in the Rose & Crown.

Equally as important was the support I have received from my family throughout this thesis, and indeed my entire student career. Without their moral, social and financial encouragement none of this would have been possible. I promise to get a job now, Dad, so it's *my* round this time.

The two months spent in India on field work were of great importance to me, because I feel it developed my character as well as my geological knowledge and ability. Thanks must go to Johan Bradley and Wak for being not only extremely able field assistants but good companions as well. Big Steve must have rued the day he agreed to come on "holiday" with Wak, but his presence was much appreciated. The people of Kashmir and Ladakh are among the most hospitable and friendly anywhere in the world, and further gratitude is extended towards Ali Hussein Shillichkey of Kargil, Fida Hussein of Leh, Muslim the cook from Namsuru (and his cloth of doom) and the chowkidar and cook of the Tourist Banglow (sic.), Panikhar.

My time spent in Oxford would have been infinitely poorer but for the friends and colleagues who shared in my experiences over the years. These include my fellow Himalayan wallahs B.J., Pete; Rich, for many mountain trips and office sanity; Wak again for an inimitable sense of humour and the same name; James-thanks for the holiday; Simon; £25! and Rob. Lunacy and gin was assured with the arrival of Dan & Nick. Credit indeed must go to Chris, Keith and Kate who deigned to live with me and who gave new perspectives on vegetables. Sarah is thanked for the state of my liver. Others too numerous to mention , but just as important, include Ali & Jude, Paul, Lesley, Jane, Andy, Anna, Jim, Natalie, Stu, Rose & Hannah.

Thanks must also go to the many administrative and technical staff at the department, without whom the place would cease to exist. These include: Norman Charnley, who taught me how to break the probe, Steve Baker, Phil Jackson, Jeremy Hyde, Richard McAvoy, Steve Usher, Sally Thompson, Diana Relton, Roy Goodwin and John O'Sullivan. Tim Holland, Roger Powell and Frank Spear are thanked for their advice and assistance with THERMOCALC and GIBBS respectively.

NERC studentship GT4/95/249/E is gratefully acknowledged, as is additional support from Worcester College, NERC, the Burdett-Coutts fund and the Irvine Fund

THE TECTONOTHERMAL EVOLUTION OF THE HIGH HIMALAYAS IN THE SURU VALLEY, NW ZANSKAR, WITH CONSTRAINTS FROM METAMORPHIC MODELLING

Thesis submitted for the degree of Doctor of Philosophy to the University of Oxford
by
Christian Bryan Walker M.A. (Cantab)
Department of Earth Sciences
&
Worcester College

Trinity Term 1999

ABSTRACT

This thesis attempts to construct an integrated model for the tectonothermal evolution of the Suru valley region of the High Himalayan Crystalline unit of north-west India, and combines detailed field mapping, petrographic and microstructural analysis, thermobarometric techniques and metamorphic modelling.

This work confirms that the metasedimentary lithologies of the Suru valley correspond to the Palaeozoic-Mesozoic Tethyan shelf sediments found in Kashmir and Zanskar and that the meta-igneous bodies correlate with Permian rift-related igneous units. This demonstrates that all the metamorphism in the Suru valley is Himalayan in age. Subsequent to India-Asia collision at ~54 Ma the units of the Suru valley underwent a polyphase deformational and metamorphic history. The large scale structure of the area is that of kilometre-scale, SW-vergent recumbent folds that are domed by a later structure, the Suru Dome. Barrovian metamorphism resulting from collision and burial reached a maximum of kyanite grade, and is believed to be syn- to post-kinematic with respect to the formation of the large folds. Thermobarometric analysis indicates that peak conditions relating to this Barrovian event were of the order of 9.5-10.5 kbar and 620-650 ^{0}C. A later metamorphic event associated with doming throughout the Zanskar Himalaya and crustal anatexis in the core of the High Himalaya caused re-equilibration of deeper Suru Dome rocks to conditions of 8.7-9.7 kbar and 630-640 ^{0}C.

Metamorphic modelling, involving phase diagram construction and P-T path determination using Gibbs method calculations, suggests that metamorphic garnets grew under conditions of burial and heating. Rapid exhumation of the High Himalayan Crystallines on the Main Central Thrust and the Zanskar Shear Zone occurred shortly after peak metamorphism. The results suggest that phase diagram construction and P-T path calculation should be used in conjunction in order to confidently model metamorphic rocks.

THE TECTONOTHERMAL EVOLUTION OF THE HIGH HIMALAYAS IN THE SURU VALLEY, NW ZANSKAR, WITH CONSTRAINTS FROM METAMORPHIC MODELLING

Thesis submitted for the degree of Doctor of Philosophy to the University of Oxford
by
Christian Bryan Walker M.A. (Cantab)
Department of Earth Sciences
&
Worcester College

Trinity Term 1999

EXTENDED ABSTRACT

The metamorphic evolution of mountain belts in space and time is crucial to our understanding of the tectonic processes involved in continental collision. Metamorphic rocks are found in the cores of most large mountain belts, and as such the information they provide is directly related to the orogenic processes which formed these mountains. The Himalayas are the premier example of such an orogenic belt and provide an excellent opportunity in which to study the thermal and mechanical effects of orogenesis. The metamorphic core of the Himalayas, or the High Himalayan Crystalline unit (HHC) is a continuous wedge of greenschist-to amphibolite grade metamorphic rocks, migmatites and granitoids, running for approximately 2500 km along the length of the chain, that exposes up to 25 kilometres thickness of middle and deep crustal rocks. These rocks were metamorphosed due to crustal thickening and burial subsequent to India-Asia collision some 54 Ma ago before being exhumed along the crustal-scale fault systems of the Main Central Thrust (MCT) and the South Tibetan Detachment (STD). This thesis focusses on the Suru valley region of NW Zanskar, which is an excellent location to study the early part of the Eo-Himalayan Barrovian (M1) metamorphic event that has not been overprinted by the later Neo-Himalayan Buchan-style process (M2) that affects large parts of the rest of the High Himalayan Crystallines.

The study sets out to combine detailed field mapping, petrographic and microstructural analysis, thermobarometric techniques and metamorphic modelling in an attempt to elucidate the prograde metamorphic history of the area and construct an integrated model for the thermal and structural evolution of the Suru valley. This is the first time such an integrated study has been performed in this area.

The lithologies mapped in the Suru valley comprise pelites/semi-pelites/calc-pelites, psammites, marbles, amphibolites and granitoids which are correlated with the Upper-Palaeozoic-Mesozoic sediments of the north Indian continental margin in Kashmir and

Zanskar, and Permian igneous bodies related to rifting. A marble unit 170-500 m thick can be correlated with Triassic limestones, and surrounding amphibolite units correspond to the metamorphosed equivalents of the Permian Panjal Trap volcanics. The granitoid bodies at Sankoo and Parkatchik are strongly deformed and infolded with the surrounding metasedimentary and metabasic lithologies. The Sankoo nappe is particularly distinctive, as it comprises layered basic and acid sills on a decimetre to metre scale that are folded into a kilometre-scale recumbent fold. The Sankoo granite gives a U-Pb monazite age of 268 ± 5 Ma for crystallisation. Field evidence suggests that the intrusion of the granite preceded the intrusion of the subordinate basic units. Because all the units of the Suru valley are believed to be Palaeozoic-Mesozoic in age this determines that all the metamorphism and deformation observed must be Himalayan in age.

Subsequent to India-Asia collision some 54 Ma ago the rocks of the Suru valley underwent burial and Barrovian regional metamorphism that reached a maximum of kyanite grade. Crustal thickening is believed to have been achieved by tight to isoclinal folding and thrusting verging towards the SW. Evidence for this early D_1 phase of deformation can be seen in the deformed sediments of the Zanskar shelf and in overturned bedding-cleavage (S_0/S_1) relationships at low grades near Sankoo. At higher grades D_1 is preserved as intrafolial isoclinal folds, and as folded inclusion trails within garnets. The dominant structural features of the Suru valley are kilometre-scale, SW-verging D_2 recumbent folds, or nappes, principally the Donara, Tapshah and Sankoo nappes that are domed by the underlying D_3 Suru Dome. These nappes formed in a ductile fashion as a result of non-coaxial deformation, and interlock in a complex three-dimensional pattern. The folds are separated by parasitic NE-verging folds, or ductile shear zones. In the Suru Dome a new S_3 foliation is developed, that is manifest by S-C shear planes cutting the earlier S_2 foliation. Further away from the Suru Dome in the overlying nappes this D3 event is sometimes represented by a crenulation of the S_2 fabric. The HHC of the Suru valley is bounded to the north by the ZSZ and to the south-west by a late-stage backthrust that cuts out the MCT.

Metamorphic grade as defined by the first appearance of index minerals increases from biotite grade at the ZSZ southwards to a maximum of kyanite grade, before decreasing westwards and south-westwards. Isograds appear to cross-cut certain lithological boundaries but are folded to an extent by the nappes and the Suru Dome, although the isograds are not folded entirely around the folds. Microstructural and petrographic analysis suggests that this M1 metamorphic event was syn -to post-kinematic with respect to the formation of the nappes. Associated with doming of the Suru Dome, and throughout Zanskar, is an M2

metamorphic event that is characterised by sillimanite K-feldspar grade conditions and crustal anatexis in the core of the HHC, and garnet resorption and new mica growth in the Suru Dome.

Thermobarometric analysis was performed using the self-consistent dataset of Holland & Powell (1998), and conventional thermobarometry. Peak M1 conditions are typically 9.5-10.5 kbar and 620-650 ^{0}C for rocks of the Donara and Tapshah nappes, and around 5 kbar and 400-500 ^{0}C for Sankoo nappe rocks. Rocks from the Suru Dome record conditions of 8.7-9.7 kbar and 630-640 ^{0}C even though they are structurally deeper than the Donara and Tapshah rocks. This is interpreted as an M2 re-equilibration along an uplift path related to doming and movement on the MCT and ZSZ. Certain samples from the Donara nappe re-equilibrate to conditions of 7.2-8.4 kbar and 570-600 ^{0}C. If we assume a lithostatic gradient of 0.285 kbar/km then peak metamorphic conditions preserved in the Donara nappe imply that burial to depths of greater than 35 km took place.

Metamorphic modelling was performed in order to elucidate the prograde P-T path followed by samples from the Suru valley. Compositional changes of growth-zoned garnets should ideally preserve information pertaining to the equilibrium thermodynamic conditions at all stages of garnet growth, from core to rim. Two methods were employed in an attempt to model the evolution of garnet growth, namely phase diagram construction using the program THERMOCALC, and Gibbs method modelling using the program GIBBS. Both programs use a self-consistent thermodynamic database. The principal difference between the two approaches is that THERMOCALC performs calculations that solve for the integrated forms of the thermodynamic equations whereas GIBBS solves the differentiated forms. The integrated approach is best suited to predicting phase relations of rocks and permits comparisons of calculated and observed phase relations, whilst the differential approach is best suited to calculations of changes in thermodynamic variables. Furthermore, it can accommodate the fractionation of garnet from the system. The two methods are used in conjunction with one another, where THERMOCALC is used to construct a framework in which to compute GIBBS P-T paths. It also allows prediction of both a start (garnet core) and end (garnet rim) point to the P-T path calculations.

The results of the metamorphic modelling calculations described above show that growth-zoned garnets from the Donara and Tapshah nappes grew while heating and burial of 50-130 ^{0}C and 2.3-5 kbar (8-17 km) were taking place. The P-T paths have moderate slopes in P-T space, unlike paths calculated by other workers for overthrust terranes that predict initial

near-isothermal burial followed by near-isobaric heating. This is believed to result from the fact that garnets were growing as the large nappes were forming, which could be considered at the largest scale to represent homogenous thickening. This would lead to pressure increasing more slowly relative to temperature than purely simple overthrusting. The observation that the concentration of heat-producing isotopes in the HHC is three times that of average crustal levels may also have some bearing on the P-T trajectories of Suru valley samples.

Temperature-time models calculated using U-Pb monazite ages, $^{40}Ar/^{39}Ar$ mica cooling ages, and apatite and zircon fission track data from the Shafat area of the Suru valley imply that rapid exhumation of the HHC on the MCT and ZSZ took place between 21 and 18.5 Ma, followed by slower erosion-controlled uplift from 18.5 Ma to the present day. Doming of the Suru Dome was probably related to movement on the MCT, and may have preceded movement on the ZSZ by some 1-2 Ma.

This thesis concludes that in order to obtain reliable and consistent P-T paths from metamorphic rocks, both integrative and differential calculation techniques should be used. This allows checks on the consistency of each method, and exploits the features that each method performs best. Furthermore, if these techniques are used to constrain the tectonic evolution of an area, then as much knowledge as possible must be obtained on the area in order to evaluate the validity of calculated P-T paths. This includes the correlation of regional deformation with microstructures, the introduction of structural time-markers into the evolution of mineral assemblages, and the absolute pressure-temperature conditions recorded by the mineral assemblages.

Contents

1. INTRODUCTION

1.1. Metamorphism as a tectonic process 1
1.1.1. Limitations of absolute thermobarometry 1
1.2. Obtaining P-T paths from metamorphic rocks 2
1.2.1. Introduction and previous work 2
1.2.1.1. Petrogenetic grids and reaction textures 3
1.2.1.2. Estimation of post-peak metamorphic conditions 3
1.2.1.3. Fluid inclusion constraints 4
1.2.1.4. Amphibole zoning 4
1.2.1.5. Inclusion thermobarometry 5
1.2.1.6. Gibbs method thermobarometry 5
1.2.1.7. Phase diagram calculations 6
1.3. The Himalayas as a natural laboratory 7
1.3.1. General introduction 7
1.3.2. Regional geology of the Himalayas 8
1.3.2.1. The Transhimalayan batholith 8
1.3.2.2. The Indus-Tsangpo suture zone (ITSZ 8
1.3.2.3. The Tibetan Tethys zone 8
1.3.2.4. The High Himalayan Crystalline unit (HHC) 9
1.3.2.5. The Lesser Himalaya 10
1.3.2.6. The Sub-Himalaya (Siwaliks) 10
1.3.3. Models for inverted metamorphism in the HHC 10
1.3.3.1. "Hot -over-cold" thrusting and folding of isotherms 11
1.3.3.2. Shear heating (dissipative heating) 11
1.3.3.3. Polymetamorphism and heat focussing 12
1.3.3.4. Folding and thrusting of isograds 12
1.3.3.5. Other mechanisms 13
1.4. The Suru valley 14
1.4.1. Previous work in the Suru Valley 14
1.4.1.1. Structure and lithology 14
1.4.1.2. Metamorphism and dating 15
1.5. Aims of this study 16

2. STRUCTURE AND LITHOLOGIES OF THE SURU VALLEY

2.1. Geographical location and nature of the area 19
2.2. Structure and deformation 19
2.2.1. Introduction 19
2.2.2. Structure 20
2.2.2.1. Major structures 20
2.2.2.2. Mineral lineations and minor folds 23
2.3. Rock types and metamorphism 24
2.3.1. Introduction 24
2.3.2. Description of rock types 26
2.3.2.1. Pelites, semi-pelites and psammites 26
2.3.2.2. Calc-pelites 27
2.3.2.3. Marbles 27
2.3.2.4. Amphibolites 27
2.3.2.5. Granitoids 27
2.3.3. Suru Dome rocks 30

2.4. Conclusions 31

3. PETROGRAPHY AND MINERAL CHEMISTRY
3.1. Introduction 33
3.2. Petrographic descriptions 33
3.2.1. Pelites and semi-pelites 33
3.2.2. Calc-pelites 35
3.2.3. Psammites. 35
3.2.4. Marbles and siliceous carbonates 36
3.2.5. Amphibolites 36
3.2.6. Granitoids 37
3.2.7. Suru Dome rocks 37
3.2.8. Fe-Ti minerals 39
3.3. Microstructure and porphyroblast growth 40
3.3.1. Donara and Tapshah nappes 40
3.3.2. Sankoo nappe and Jildo section 43
3.3.3. Suru Dome 43
3.4. Mineral chemistry 44
3.4.1. Introduction 44
3.4.2. Garnet 44
3.4.2.1. Models for the development of growth zoning 44
3.4.2.2. Results 45
3.4.3. Biotite 47
3.4.4. Muscovite 48
3.4.5. Chlorite 49
3.4.6. Staurolite 49
3.4.7. Hornblende 49
3.4.8. Feldspars 50
3.5. Conclusions 51

4. THERMOBAROMETRY AND P-T RESULTS
4.1. Principles and techniques 52
4.1.1. Conventional thermobarometry 52
4.1.2. THERMOCALC 53
4.2. Rationale 54
4.2.1. Garnet 54
4.2.2. Biotite 55
4.2.3. Muscovite 55
4.2.4. Plagioclase 56
4.2.5. Results 56
4.3. Suru Valley P-T results 58
4.3.1. THERMOCALC results 58
4.3.2. Conventional thermobarometry results. 64
4.4. Comparison with other studies 67
4.4.1 Suru Valley 67
4.4.2 Central Zanskar 68
4.4.3 The rest of the Himalaya 69
4.5. Conclusions 70

5. METAMORPHIC MODELLING
5.1. Introduction 72
5.1.1. THERMOCALC vs. GIBBS 73
5.2. Phase diagram calculations 74
5.2.1. Introduction 74
5.2.1.1. The Gibbs phase rule, variance and Duhem's theorem 75
5.2.2. Setting up the problem 76
5.2.2.1. KFMASH 78
5.2.2.2. MnKFMASH 79
5.2.2.3. CNMnKFMASH 79
5.3. P-T pseudosections for Suru Valley rocks 80
5.3.1. Sample selection 80
5.3.2. Pseudosections 81
5.3.2.1. THERMOCALC "modes" 81
5.3.2.2. Agreements between the calculated and the observed 82
5.3.2.3. The effect of aH_2O 83
5.3.2.4. Discrepancies between the calculated and the observed 84
5.3.2.5. Errors on phase boundaries 85
5.3.3. Isopleths of garnet composition and mode 86
5.3.4. Garnet core calculation 88
5.3.5. Discussion 89
5.3.6. "Garnet fractionation" pseudosections 91
5.4. Gibbs method modelling 93
5.4.1. Introduction 93
5.4.2. Rationale and results 94
5.4.2.1. Discrepancies between Gibbs modelling and THERMOCALC modelling 104
5.5. Conclusions 105

6. SYNTHESIS
6.1. Introduction 108
6.2. Tectonometamorphic evolution of the HHC in the Suru valley area 108
6.2.1. Pre-collisional history (>54 Ma) 108
6.2.2. Post-collisional history and burial (40-35 Ma) 109
6.2.3. Post-collisional history and burial (35-25 Ma) 110
6.2.4. Doming and rapid extrusion (25-18.5 Ma) 111
6.2.5. Continued uplift and erosion (18.5-0 Ma) 114
6.3. Tectonic implications 115
6.4. The validity of metamorphic modelling 117
6.5. Further work 118

REFERENCES 119

APPENDICES

A. ACTIVITY MODELS USED IN THERMODYNAMIC CALCULATIONS
A.1.Mixing models used in THERMOCALC 132
A.1.1. Mixing models for solutions used in phase diagram calculations 132
A.1.2. Mixing models used in AX 138
A.1.3. Sample datafile used for THERMOCALC phase diagram construction 140
A.2. Mixing models used with program GIBBS 146

B. METHODOLOGY AND ERRORS IN THERMODYNAMIC CALCULATIONS
B.1. Basic thermodynamic principles 147
B.1.1. Applications to thermobarometry 148
B.1.2. Uncertainties in thermobarometry 149
B.2. Calculations using THERMOCALC 150
B.2.1. Uncertainties in calculations 151
B.2.2. Calculating average P-T's using THERMOCALC 153
B.2.2.1. Diagnostics 154
B.2.3. Calculating P-T projections and pseudosections using THERMOCALC 155
B.3. Calculations using GIBBS 157

C. MODAL ANALYSES 160

D. ELECTRON MICROPROBE RESULTS 161

Ab	albite	Fact	Fe-actinolite	Mnst	Mn-staurolite
Afchl	Al-free chlorite	Fcel	ferroceladonite	Naph	Na-phlogopite
Alm	almandine	Fcld	Fe-chloritoid	Parg	pargasite
Ames	amesite	Fep	Fe-epidote	Pg	paragonite
Ann	annite	Fst	Fe-staurolite	Phl	phlogopite
An	anorthite	Gl	glaucophane	Pl	plagioclase
Andr	andradite	Gph	graphite	Pist	pistacite
Bt	biotite	Grs	grossular	Prp	pyrope
Cal	calcite	Grt	garnet	Qtz	quartz
Cel	celadonite	Hbl	hornblende	Rt	rutile
Chl	chlorite	Ilm	ilmenite	Sil	sillimanite
Cld	chloritoid	Kfs	K-feldspar	Sps	spessartine
Clin	chlinochlore	Ky	kyanite	Spn	sphene
Czo	clinozoisite	Mrg	margarite	St	staurolite
Daph	daphnite	Ms	muscovite	Tr	tremolite
Dol	dolomite	Mnbt	Mn-biotite	Ts	tschermakite
East	eastonite	Mnchl	Mn-chlorite	Tur	tourmaline
Ed	edenite	Mncld	Mn-chloritoid	Zo	zoisite
Ep	epidote				

Table of mineral abbreviations used in the text, after Kretz (1973) and Holland & Powell (1998)

H = enthalpy	$X_{C,M}$ = mole fraction of cation C in site M
$\underline{H}$ = molar enthalpy	n_j = moles of component j
G = Gibbs free energy	M^k = moles of phase k in the system
$\underline{G}$ = molar Gibbs free energy	μ_j = chemical potential of component j
S = entropy	a_j = activity of component j
$\underline{S}$ = molar entropy	γ_j = activity coefficient for component j
V = volume	ν_i = stoichiometric coefficient of component or phase I in a reaction
$\underline{V}$ = molar volume	
P = pressure	K_{eq} = equilibrium constant
T = temperature	K_D = distribution coefficient
R = gas constant	W = Margules parameter
C_p = constant pressure heat capacity	npct = number of phase components in total
α = thermal expansivity	npc^k = number of phase components in phase k
β = isothermal compressibility	nph = number of phases in the system
p_i = proportion of phase component i in phase	nsc = number of system components in the system
X_j = mole fraction of component j	nrx = number of linearly independent reactions

Table listing the major thermodynamic symbols used in the text

Chapter 1



Indian motoring etiquette

1. Introduction

1.1. Metamorphism as a tectonic process

Metamorphic rocks are found in the cores of mountain belts the world over, and their formation is directly related to the processes which form the mountain belts themselves. As such, metamorphic rocks and the information they record provide valuable insights into the understanding of orogenesis and ultimately crustal evolution. The work of Barrow (1893, 1912) recognised zones of progressive metamorphism, as index minerals and textures changed with increasing pressure (P) and temperature (T) conditions, and this was elaborated on by Eskola (1914, 1915) to assign specific mineral *assemblages* to a particular P-T condition, or *facies*. For a long time it was believed that the Barrovian sequence of minerals was typical of every orogenic belt, until Miyashiro (1961) proposed the concept of *facies series* in mountain belts, these being the sequence of metamorphic facies that are observed in a transect across a metamorphic belt. This recognised that the observed metamorphic facies series is a function of the tectonic environment in which it was formed, such as a low P-high T environment as opposed to a high P-high T one. The three major types of metamorphic facies series are illustrated in Figure 1.1.A. The discovery of plate tectonics provided a new framework within which to view these facies series, and the work of Ernst (1973, 1976) illustrated the relationship between metamorphic facies types and plate boundaries, such as the association of blueschist facies rocks with subduction zones.

England & Richardson (1977) and England & Thompson (1984) showed that metamorphism should be viewed as a dynamic process, whereby rocks undergoing metamorphism are subject to constant changes in pressure and temperature through time, and that factors such as rate of exhumation are as important in the preservation of mineral assemblages as the maximum metamorphic grades reached, which has fundamental consequences for the interpretation of the metamorphic evolution of orogenic belts.

1.1.1. Limitations of absolute thermobarometry

Great advances have been made in the last twenty years in developing and refining new methods of calculating absolute pressures and temperatures of final equilibration of metamorphic rocks; the rationale and the associated errors are discussed in Chapter 4 and Appendix B. The fundamental tenet of thermobarometry is the application of basic

thermodynamic arguments to coexisting minerals in a rock that are assumed to be *in equilibrium* with each other. These minerals are also assumed to have compositions representative of conditions at or near the peak of metamorphism. The application of these principles has contributed greatly to our ability to calculate peak metamorphic pressures and temperatures and thus understand more fully the tectonic implications of orogenesis. However, as with the classification of facies series, it is essentially a static view of metamorphism, allowing only a "snapshot" of metamorphic conditions over an extremely small timescale. From the work of England & Richardson (1977) and others, we know metamorphism not to be an instantaneous event, but an evolutionary process that occurs over millions of years. The array of P-T conditions outcropping across a metamorphic terrane, such as Barrow's zones (or the *metamorphic field gradient* of Turner, 1981) may be entirely different from the path followed through P-T-t space by a particular rock. Their thermal model for an overthrust terrane predicted a clockwise P-T loop that intersects the metamorphic geotherm at quite a high angle, and only coincides with it on the final parts of the retrograde path (Fig. 1.1.B). It is also worth pointing out that the *metamorphic geotherm* of England & Richardson (1977) is not quite the same thing as the metamorphic field gradient due to the one-dimensional nature of the model used. Because the locus of maximum temperatures reached by different rocks reach the surface at different times (Figure 1.1.B.), the collection of rocks could never be exposed at the surface at the same time and thus could never represent a real metamorphic terrane. P-T paths from certain igneous intrusions, continental extension terranes or even subduction zones may exhibit anti-clockwise P-T paths e.g. Harley (1989). If we are able to calculate P-T loops for a number of samples across an orogenic belt, it should provide valuable insights into the tectonic process responsible for the orogenesis and subsequent metamorphism.

1.2. Obtaining P-T paths from metamorphic rocks.

1.2.1. Introduction and previous work

Although the thermal models proposed by authors such as England & Richardson (1977) have greatly increased the understanding of the processes that control the development of metamorphism in orogenic belts, the simplifying assumptions needed to obtain numerical solutions to the models mean that it is difficult to apply them to specific examples. Natural deviations include significant advection or convection by fluid flow, heat advection by magma emplacement, and lateral heat transport (St-Onge, 1987). Therefore, the ability to calculate P-

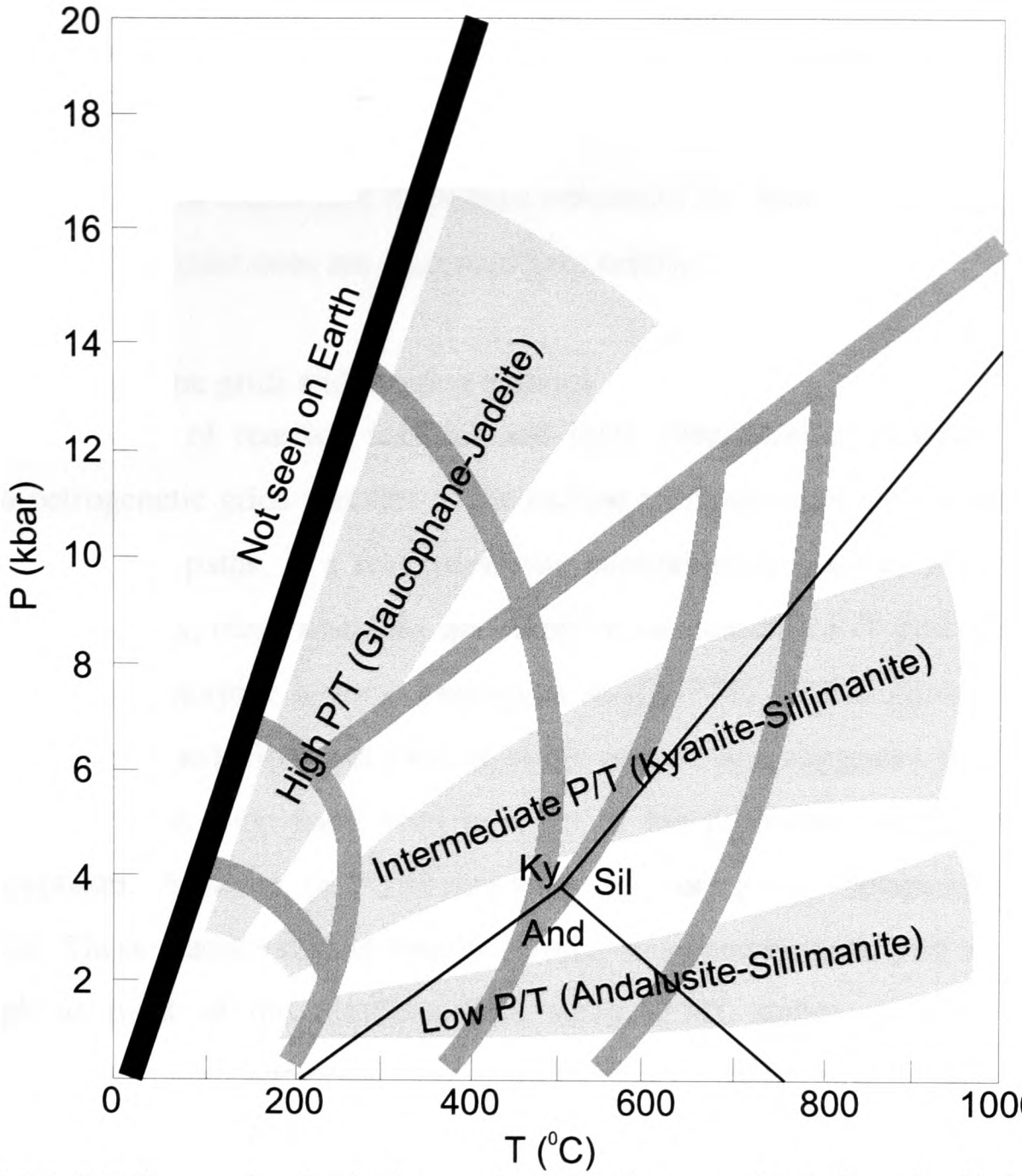


Figure 1.1.A. P-T diagram showing the three major types of metamorphic facies series. Each facies series represents a different type of tectonic environment. High P/T metamorphism is characteristic of subduction zones; intermediate P/T is characteristic of continental collisions and low P/T is characteristic of island arcs and ocean ridge metamorphism. The dark grey lines delimit specific metamorphic facies. After Spear (1993).

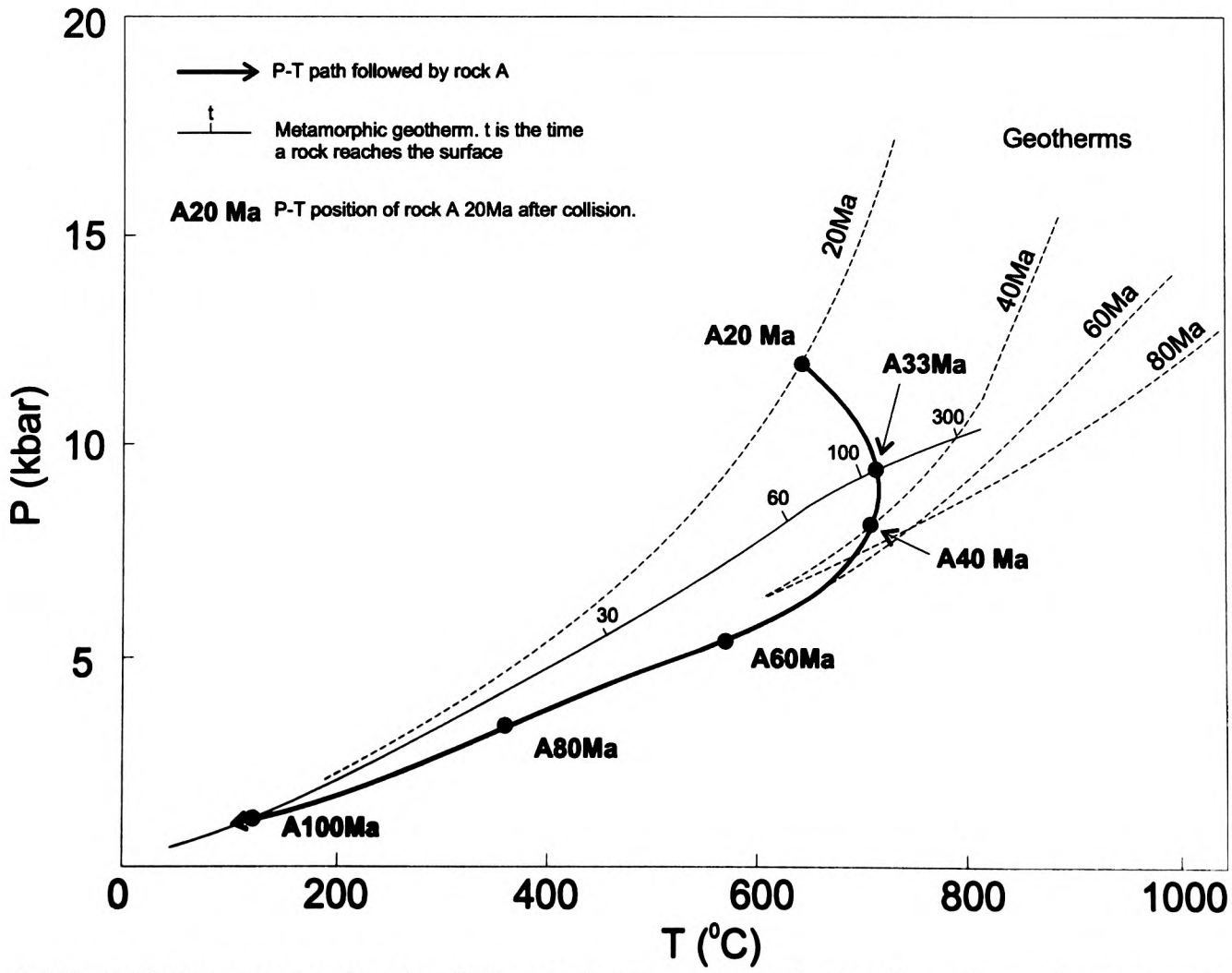


Figure 1.1.B. P-T diagram showing the difference between the P-T path of a rock, geothermal gradients over time and the "metamorphic geotherm" (see text). After England & Richardson (1977).

T paths for specific examples, which can be compared and contrasted with numerical models, should prove an invaluable tool.

A number of techniques have been employed for determining segments of P-T paths, and the most important ones are discussed here briefly.

1.2.1.1. Petrogenetic grids and reaction textures

The study of reaction textures and their interpretation in terms of experimentally derived petrogenetic grids was one of the earliest methods employed in attempts to construct metamorphic P-T paths. If a rock preserves mineralogical textures that can be ascribed to particular reactions, these reactions may then be located on a P-T grid and linked through a progressive metamorphic history. Thompson et al (1976) studied growth-zoned garnets that preserve mineral inclusions not present in the matrix, and suggested that these phases must therefore (in some way) have been used up in the production of garnet during prograde metamorphism. A series of AFM reactions for increasing metamorphic grade are then proposed. These reactions could then be located on an petrogenetic grid to deduce a P-T path, although as most of the reactions have steep dP/dT slopes, pressure would be poorly constrained. A similar approach, also using thermobarometry to calculate peak conditions, is employed by Droop & Bucher-Nurminen (1984). In this case, granulites preserve many matrix textural features such as pseudomorphs, symplectites and reaction coronas, in addition to garnet inclusions, allowing a retrograde PT path to be deduced, as well as a partial prograde loop.

Hodges & Royden (1984) adopted the more quantitative approach of using textural evidence to identify progressively more retrogressed samples from a co-metamorphic set of rocks, and apply thermobarometric techniques to calculate final pressures and temperatures of equilibration. This leads to a P-T array defining part of a retrograde P-T path during uplift (Figure 1.2.A.).

1.2.1.2. Estimation of post-peak metamorphic conditions.

The rationale behind this approach is similar to that of Hodges & Royden (1984), in that samples may undergo chemical re-equilibration from peak metamorphic conditions. Dempster (1985) and Indares & Martignole (1984) examined chemical zonation in Fe-Mg minerals that represents post-metamorphic diffusional equilibration. In the case of Indares and Martignole they were able to calculate peak metamorphic temperatures from the *cores* of isolated grains using garnet-biotite and garnet-clinopyroxene thermometry, and pressures

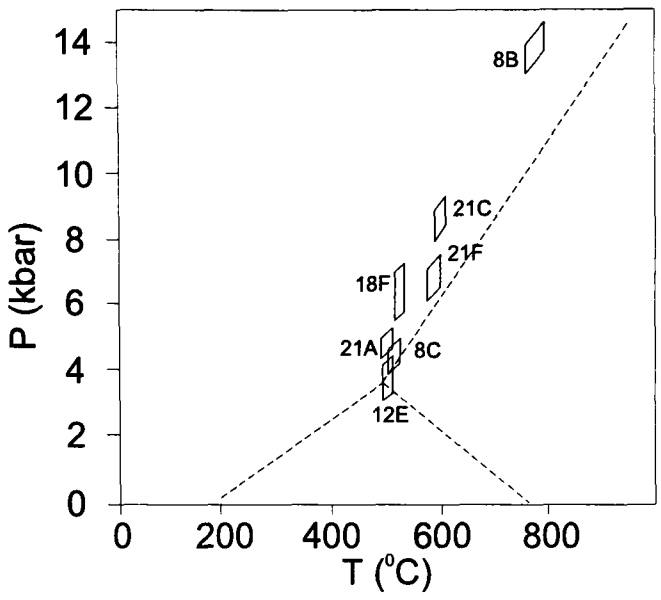


Figure 1.2.A. Synoptic P-T diagram showing the results of P-T calculations on samples from the Efjord area, Norway. The least retrogressed samples preserve the highest pressures and temperatures, and the array of results defines a trend that is interpreted as part of an uplift trajectory. After Hodges & Royden (1984).

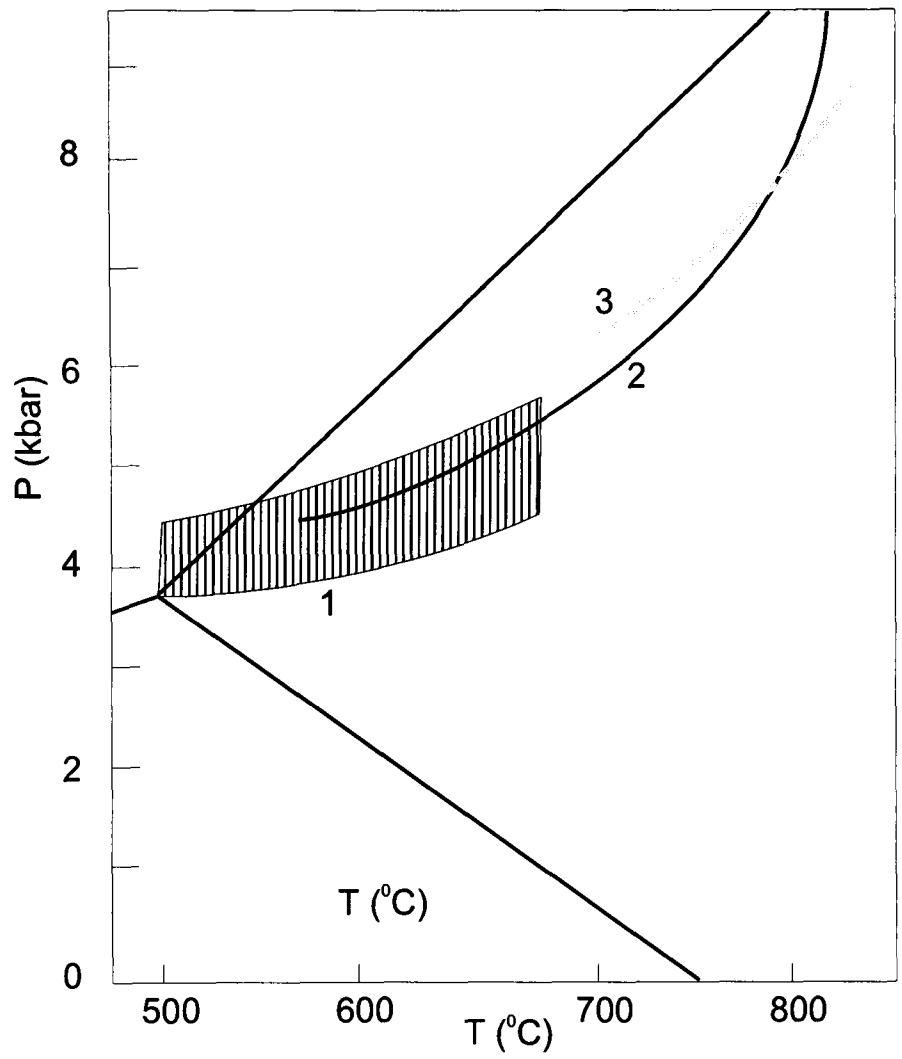


Figure 1.2.B. P-T path for rocks from the Maniwaki area, Canada, recorded by the Crd -Grt-Sil-Qtz (1), Bt-Grt-Pl-Sil-Qtz (2), and Px-Grt-Pl-Qtz assemblages respectively. After Indares & Martignole (1984).

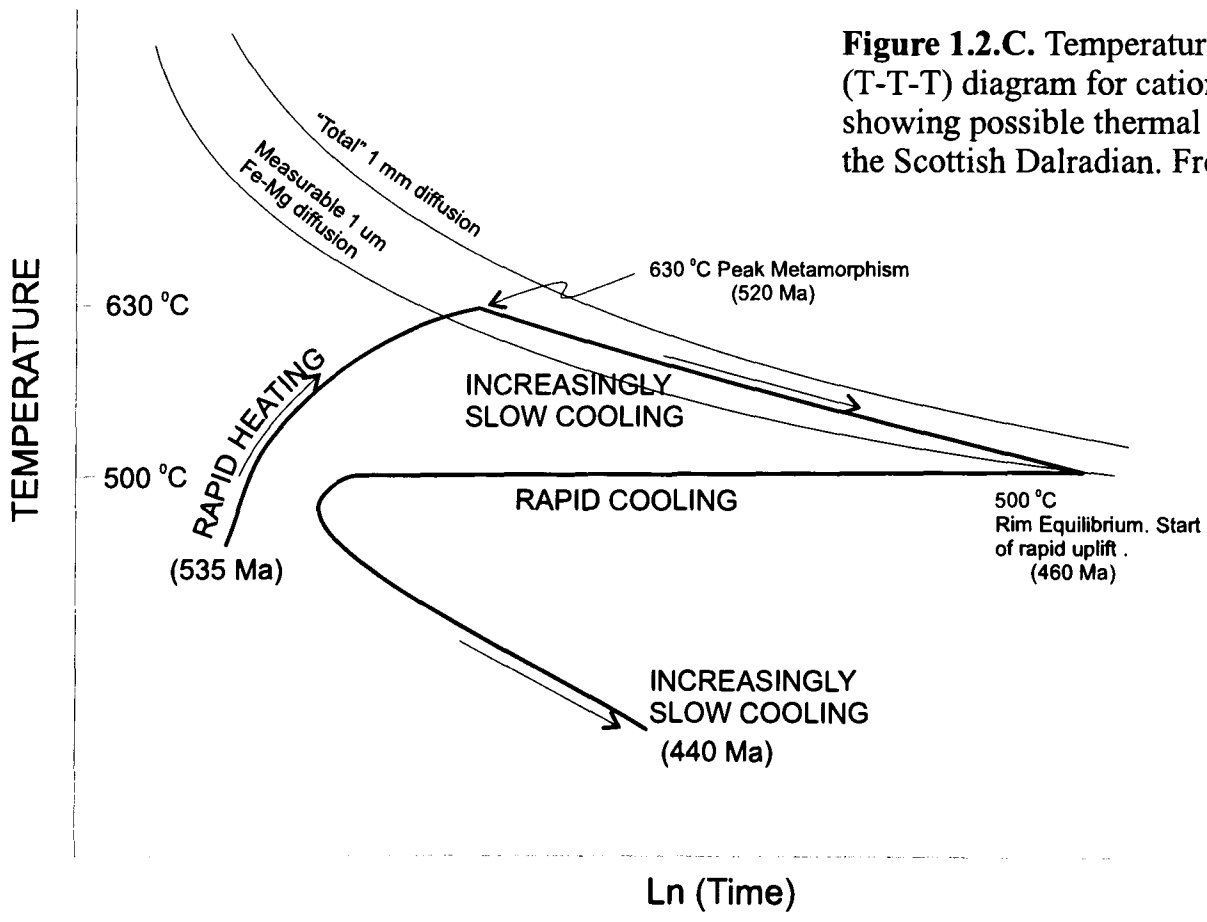


Figure 1.2.C. Temperature-Time-Transformation (T-T-T) diagram for cation diffusion in garnet, showing possible thermal evolution of a rock from the Scottish Dalradian. From Dempster (1985).

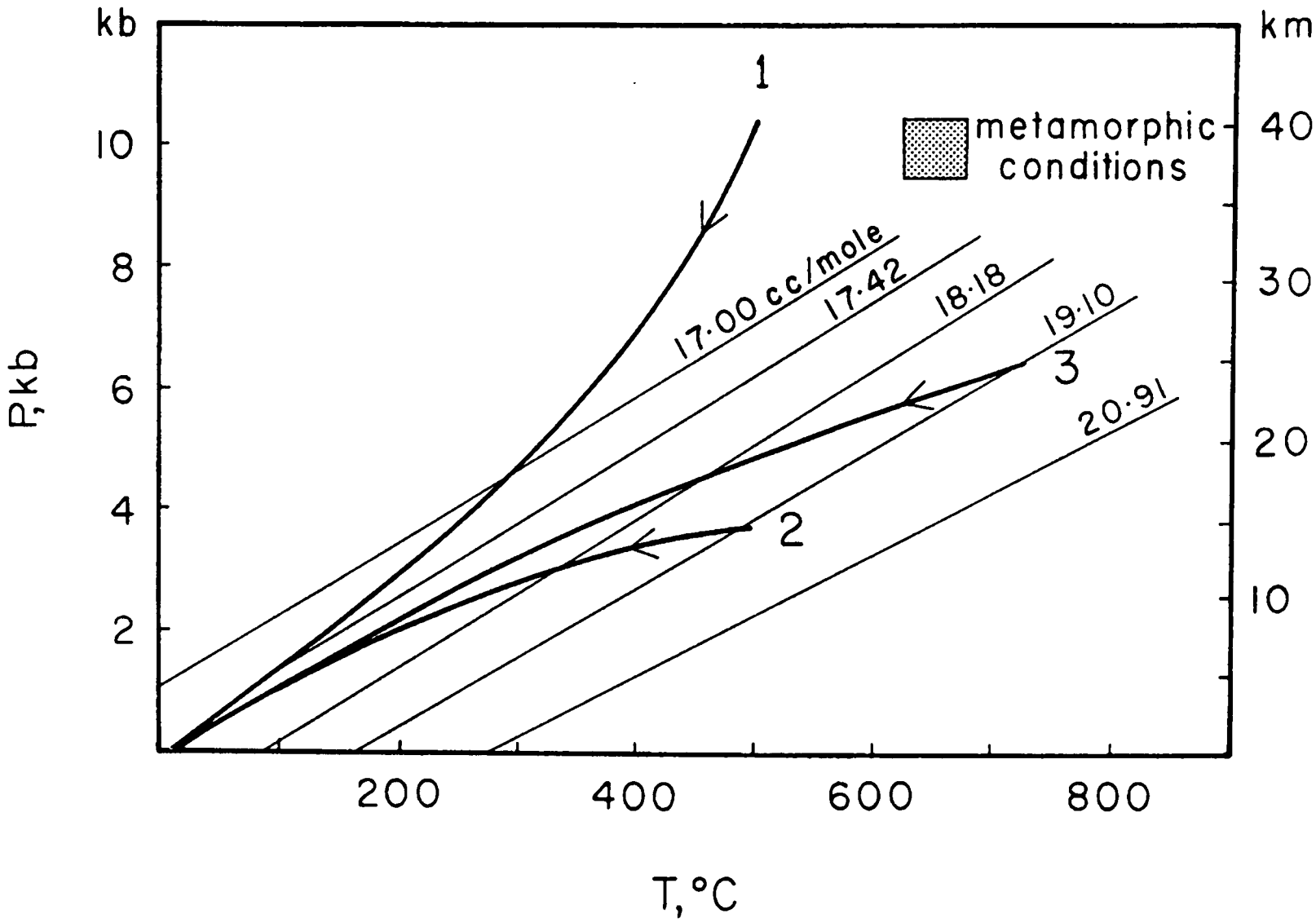


Figure 1.3.A. Uplift paths calculated for the Alps (1&2) and for the southern Appalachians (3), obtained using isochores of a metamorphic fluid. Isochores are for 25 wt% NaCl brines, values are cc/mole. From Crawford *et al* (1979).

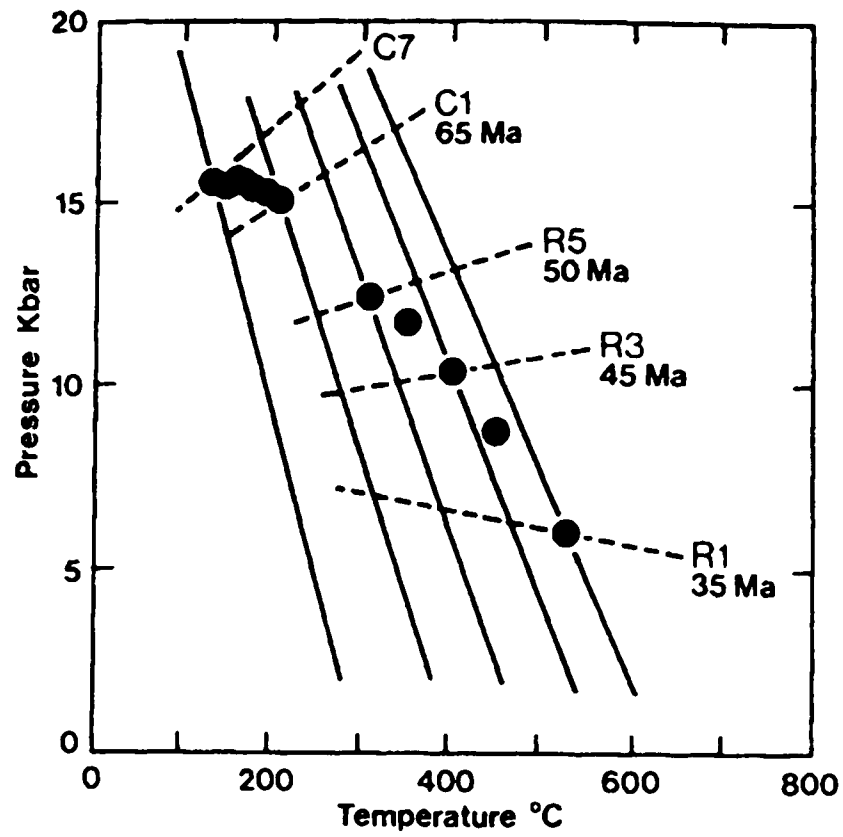


Figure 1.3.B. Calculated P-T conditions for amphiboles from the Tauern Window, Austria. Cores of zoned grains give high-P, low-T solutions and rims lower-P, higher-T solutions. The zonation is interpreted as a growth feature reflecting changing P-T conditions during the ~30 Ma after overthrusting. Approximate times at which four of the amphibole spots are calculated to have equilibrated along the P-T path are indicated. After Holland & Richardson (1979).

using garnet-plagioclase-sillimanite-quartz and clinopyroxene-garnet-plagioclase-quartz barometers. Retrograde conditions were recorded by the *rims* of zoned minerals, and retrograde phases such as cordierite. Compilation of the P-T results allows a P-T curve to be constructed (Figure 1.2.B.). Frost & Chacko (1989), however, illustrated how the differing effects of retrogressive processes on thermobarometers (usually net-transfer reactions) and thermometers (cation exchange reactions) may lead to spurious P-T path estimation.

Dempster (1985) also focussed on the importance of diffusional re-equilibration of phases, in Barrovian pelites, but interprets the results in terms of garnet diffusion timescales and Temperature-Time-Transformation diagrams with a view to interpreting the thermal evolution of the rocks (Figure 1.2.C.); an absolute P-T path as such is not presented.

1.2.1.3. Fluid inclusion constraints

Fluid inclusions trapped in minerals may preserve evidence of the composition and density of the fluid in equilibrium with the solid phases at peak metamorphic conditions. Typically, the nature and properties of the fluid phase are inferred from experiments and thermodynamic data. Crawford *et al.* (1979) examined fluid inclusions in calc-silicate rocks from British Columbia and compared the measured compositions and densities of the fluid with those predicted by experiment. The discrepancy between measured and predicted densities was interpreted as the inclusions forming at post-peak metamorphic conditions. This allowed predictions of uplift history for the measured samples (Fig.1.3.A.).

Hollister (1982) combined fluid inclusion data with petrological and age data to fit samples to a model uplift curve, which constrained the predictions of Crawford et al (1979) further.

1.2.1.4. Amphibole zoning

Holland & Richardson (1979) analysed zoned blue-green amphiboles in metabasites from the Eastern Alps in an attempt to understand the metamorphic conditions that lead to the zonation. For each amphibole composition from core to rim a pressure and temperature was obtained from six intersecting equilibria involving the amphibole components glaucophane, tremolite, edenite and tschermakite. This lead to an array of P-T points defining a curve in P-T space that implied amphibole growth during heating with uplift (Fig.1.3.B.). This was interpreted as a prograde growth feature, and not retrograde re-equilibration. While the absolute values of pressure and temperature calculated are uncertain, as pointed out by the authors, the trend of the P-T trajectory is more accurately constrained, as the isopleths of

equilibrium constant intersect at a high angle. The principle behind this approach is similar to that used subsequently in THERMOCALC (e.g. Powell & Holland, 1988)).

1.2.1.5. Inclusion thermobarometry

St-Onge (1987) presented a technique for P-T path determination based on microprobe analyses from core to rim of zoned garnet crystals that contain abundant inclusions. These inclusions included biotite, plagioclase, quartz and kyanite, which allow use of appropriate thermometers and barometers; namely garnet-biotite thermometry and the grossular-Al_2SiO_5.-anorthite-quartz (GASP). The rationale was that if the garnets preserved growth zoning, and the inclusions of plagioclase and biotite were in equilibrium with the adjacent garnet and preserved their composition at the time of inclusion, multipoint independent P-T estimates may be obtained from a single garnet poikiloblast (Fig.1.4.A.). St-Onge calculated P-T points that defined distinct segments of P-T-t paths which are then used to interpret the tectonic evolution of metamorphism in the Proterozoic Wopmay Orogen in northern Canada (Fig.1.4.B.).

The calculated P-T paths of St-Onge for individual samples are compatible with those of England & Richardson (1977), but the group of samples do not match the patterns obtained from thermal models of tectonically thickened crust undergoing thermal relaxation, uplift and erosion (e.g. England & Thompson, 1984), as they are not "nested" (St-Onge, 1987). This is used as further evidence that thermal modelling of orogenesis is often too simple to explain the real features observed.

1.2.1.6. Gibbs method thermobarometry

The Gibbs method approach (Spear *et al,* 1982; Spear & Selverstone, 1983; Selverstone *et al.*, 1984; Spear, 1988) to the analysis of zoning in minerals is a rigorous, analytical treatment of fundamental thermodynamic relationships. The process simultaneously calculates all linearly independent reactions that may be operating between phases in a given assemblage. The method allows evaluation of the relationships among all intensive thermodynamic variables of a heterogeneous system in equilibrium (Spear, 1988). If mass balance constraints are included, both intensive and extensive variables can be simultaneously evaluated, allowing monitoring of both phase chemistry and modal proportions. Duhem's Theorem specifies that if a system exhibits closed behaviour, for a known composition only two thermodynamic variables are necessary to describe the equilibrium state of the system (Prigogine & Defay, 1954). In other words, if for example the pressure and temperature of final equilibration are known, it is possible to calculate the compositions of all the phases

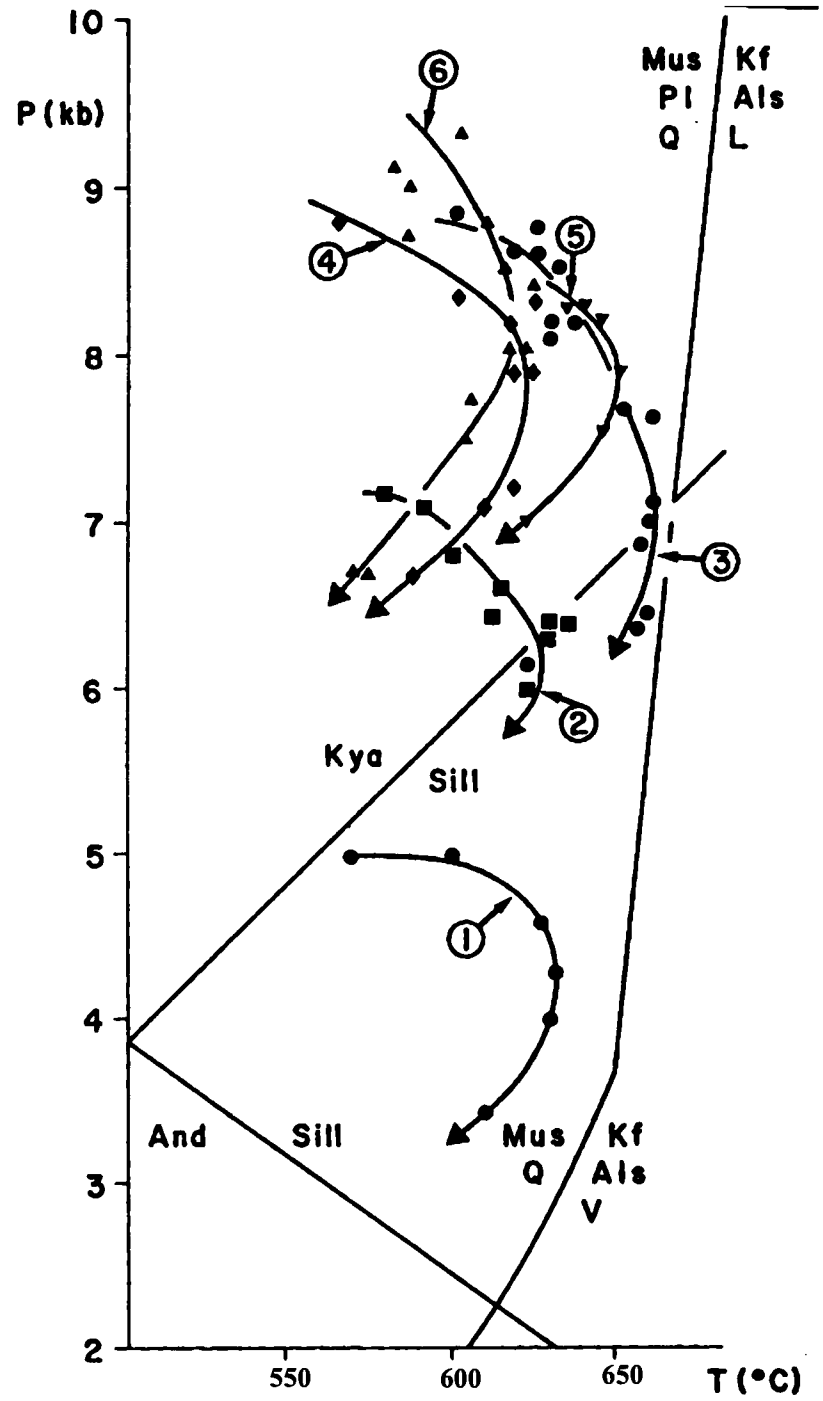


Figure 1.4.A. P-T diagram with P-T trajectories calculated from core to rim analyses of zoned poikiloblastic garnets 1 to 6. Individual point-symbols represent independent P-T determinations obtained from host-garnet/ entrapped mineral analyses. From St-Onge (1987).

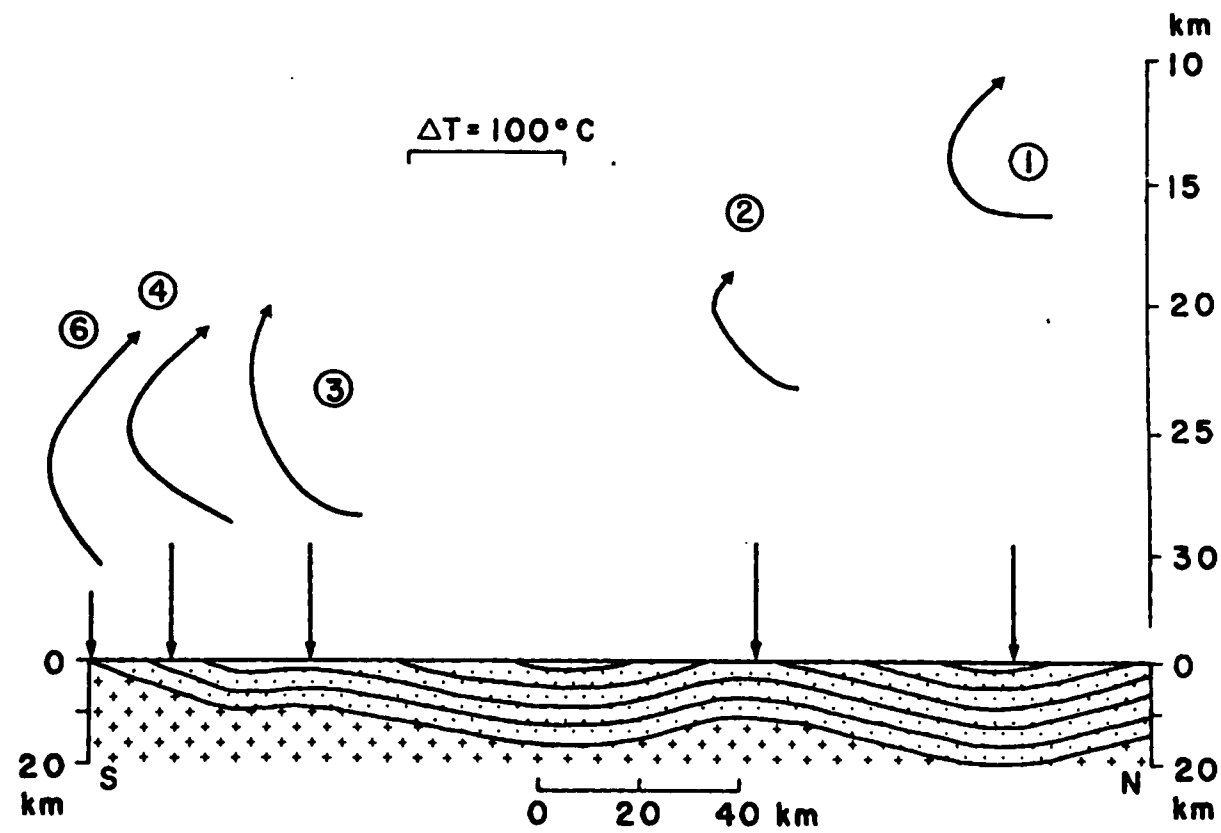


Figure 1.4.B. Section showing the internal zone of the Wopmay Orogen, Canada, with the P-T trajectories shown above projected to show their relative positions. From St-Onge (1987).

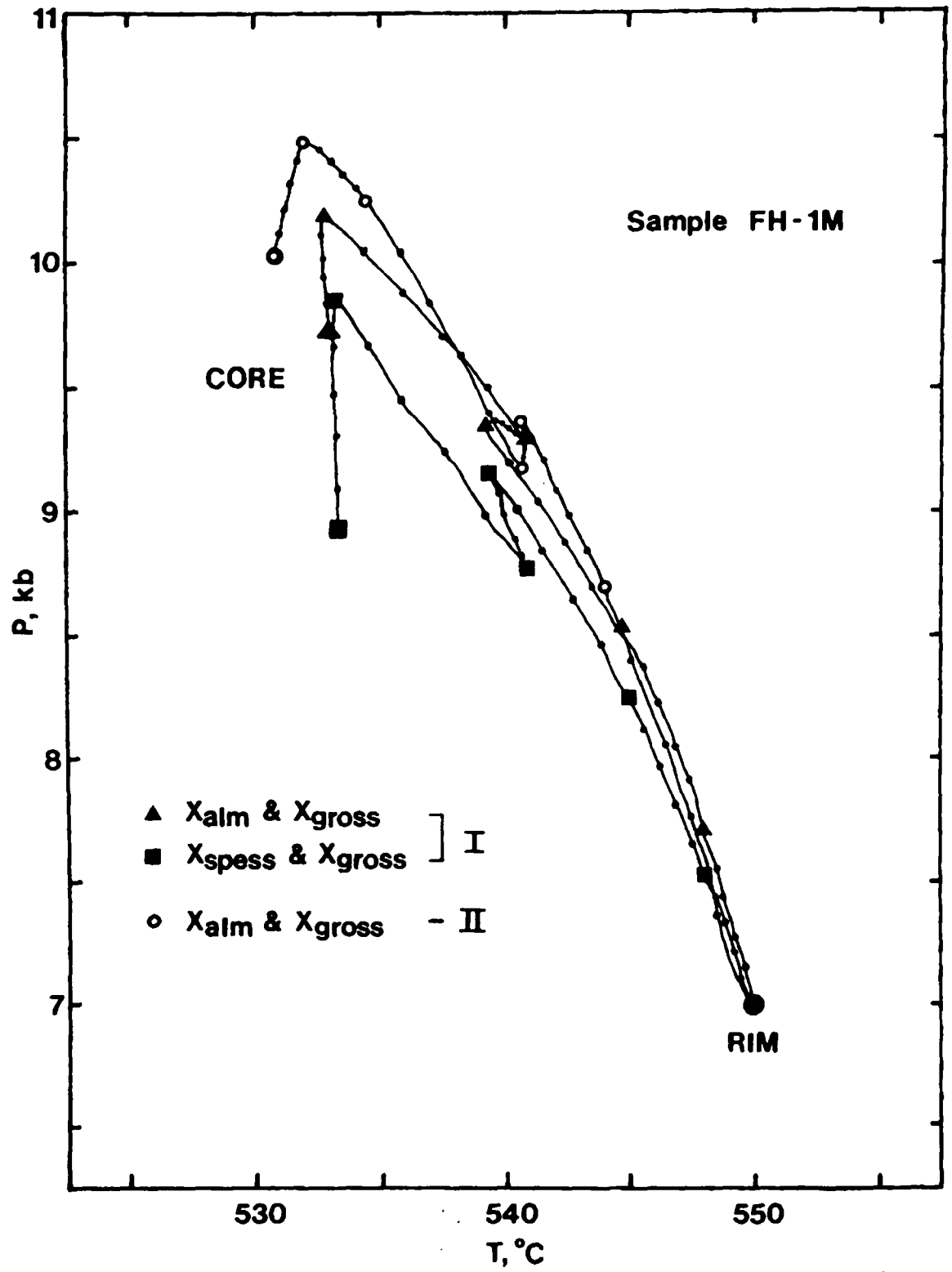


Figure 1.5.A. P-T diagram showing the P-T trajectories calculated from quantitative modelling of zoned garnets from hornblende-staurolite-kyanite schists from the Tauern Window in Austria. From Selverstone *et al* (1984).

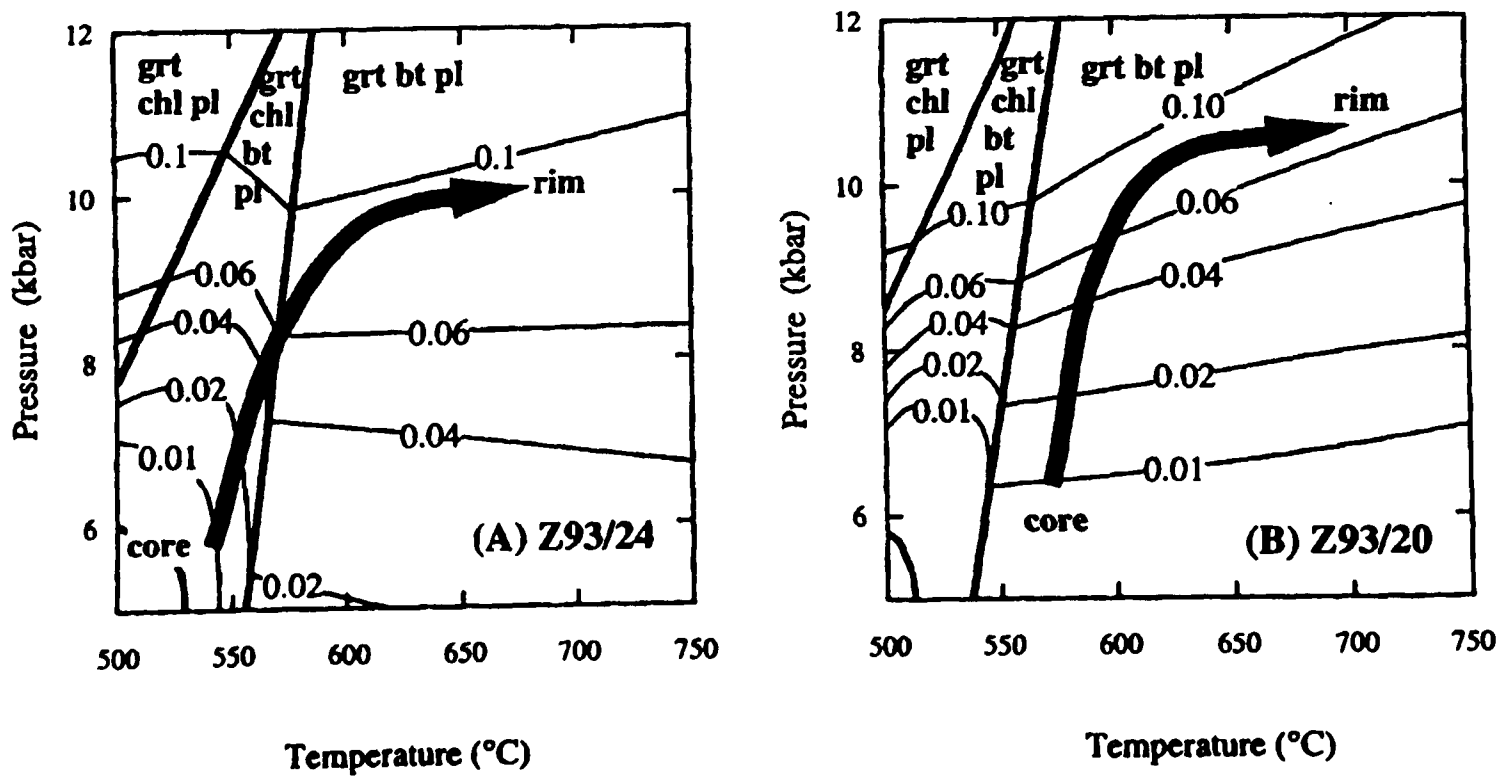


Figure 1.5.B. P-T paths during garnet growth as calculated from pseudosections and inclusion thermobarometry for rocks from the Zanskar Himalaya. The diagrams show the stability fields of mineral assemblages and are contoured for modal amount of garnet grown. From Vance & Harris (1999).

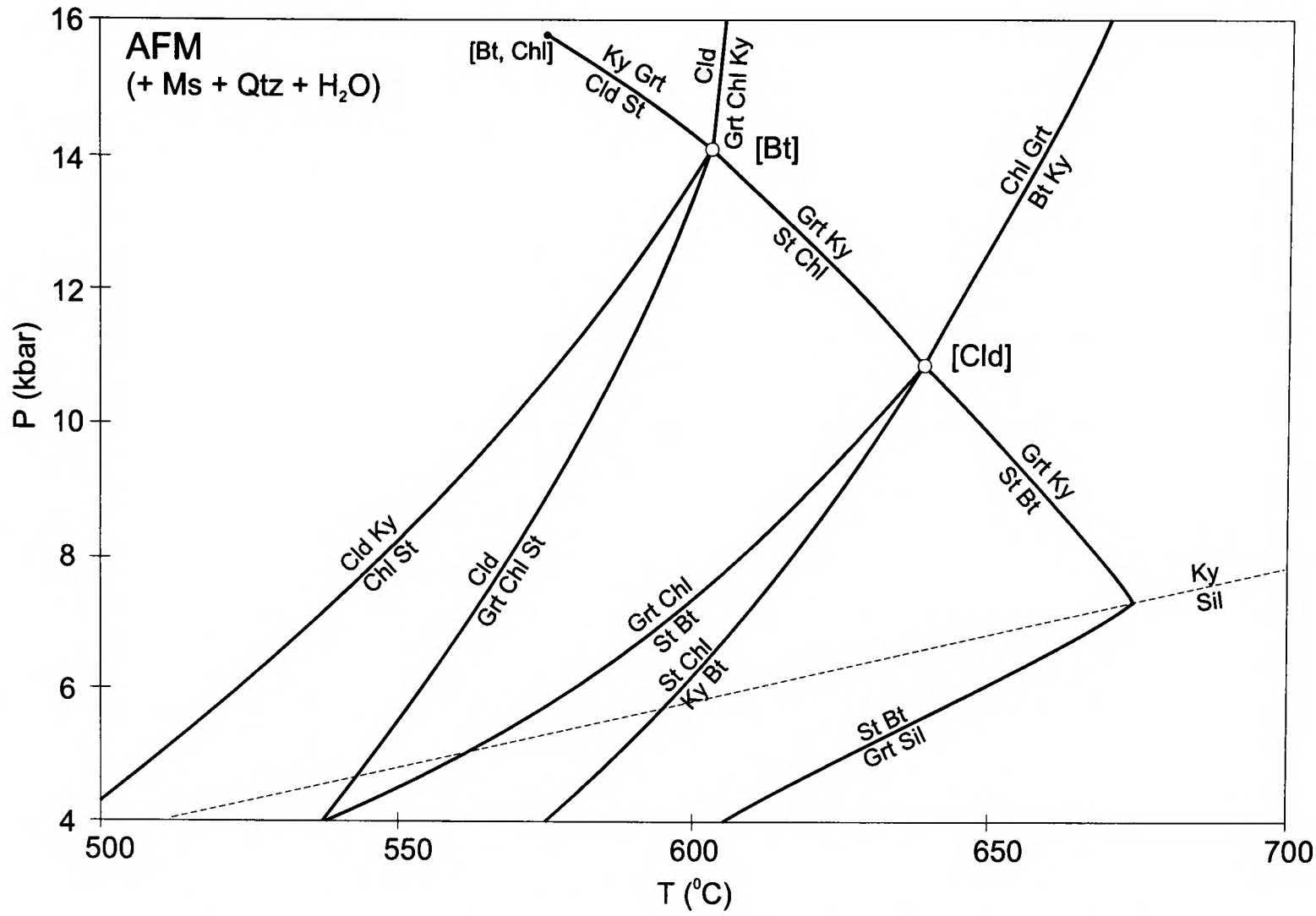


Figure 1.6.A P-T projection for the system KFMASH (+ Ms + Qtz + H_2O) calculated using THERMOCALC v2.7 and the dataset of Holland & Powell (1998). Phases in excess are not labelled.

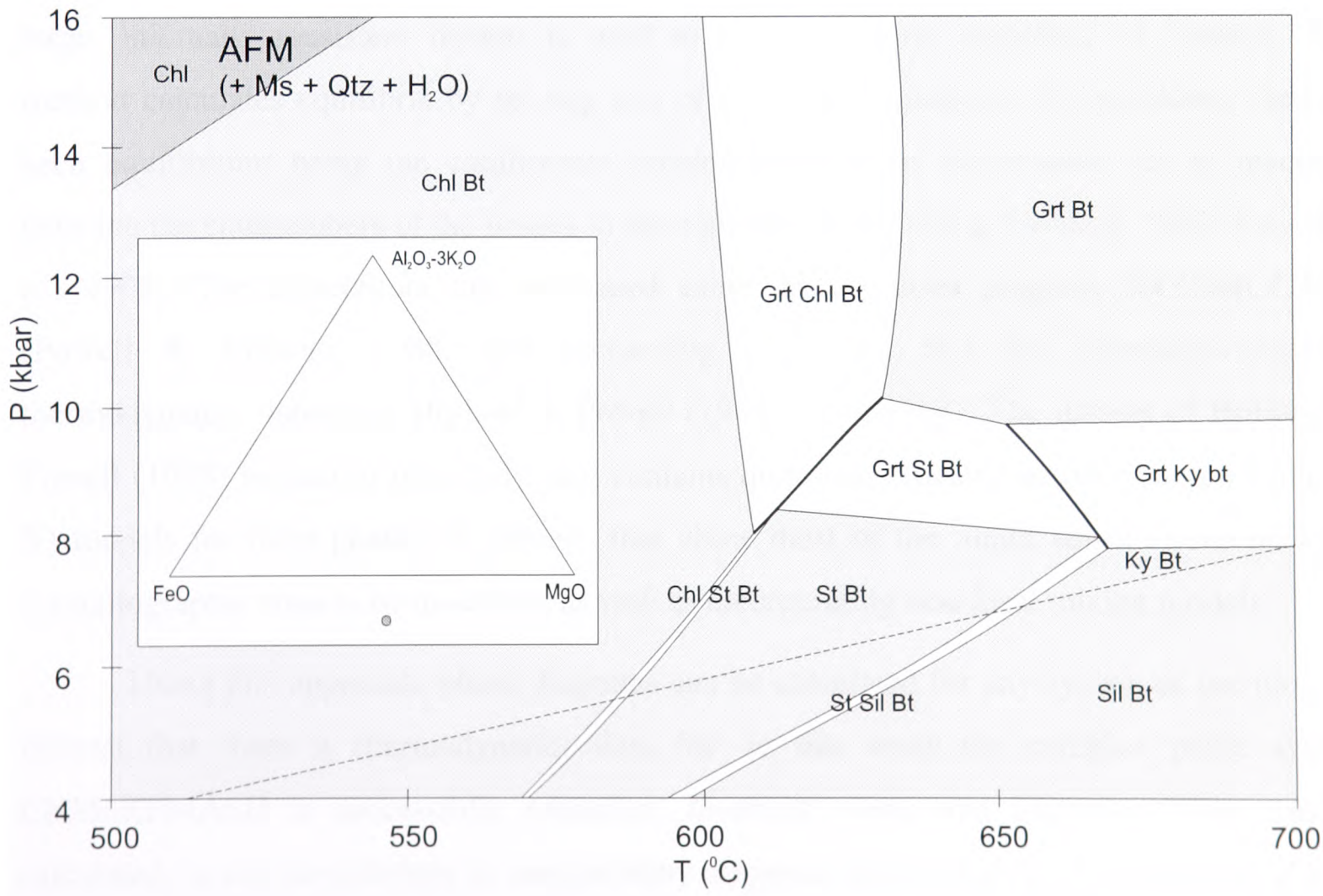


Figure 1.6.B P-T pseudosection in KFMASH (+ Ms + Qtz + H_2O) for a sub-aluminous pelite (Z47) with bulk composition Al_2O_3 = 0.5877, FeO = 0.537, MgO = 0.6029, K_2O = 0.244, as indicated on the AFM projection. The bulk composition is given in **moles**, and the Al_2O_3 content has been corrected for plagioclase.

present. Alternatively, to interpret mineral zoning, temperature and pressure can be determined by monitoring two independent composition parameters.

Applications of the method include contouring P-T space for mineral composition, modal changes and reaction progress; contouring reaction space with pressure, temperature and mineral composition; and calculation of compositional and modal changes of phases for set changes in pressure and temperature. Obviously, this method has extremely important implications for the interpretation of zoned minerals and theoretical modelling of rocks of a particular bulk composition, which may be compared with real samples (Spear *et al.*,1991). Furthermore, as the equations involve the *differentials* of the thermodynamic variables, it is best suited to the calculation of *changes* in thermodynamic variables, or in this case P-T paths (Figure 1.5.A.). By removing the need to include enthalpy in the calculations, the errors on these *relative* P-T paths should be much smaller than those calculated using *absolute* thermobarometry. An extremely useful feature of this method as applied using the computer program GIBBS (Spear & Menard, 1989) is the ability to account for the fractionation of growth-zoned garnet from the rock. The Gibbs method is employed in Chapter 5.

1.2.1.7. Phase diagram calculations

The phase diagram approach is similar to that taken by the Gibbs method in that a large, internally-consistent dataset is used to calculate phase equilibria of interest. This method calculates equilibria by solving sets of non-linear equations, the equations used for each equilibrium being the equilibrium relationships for an independent set of reactions between the endmembers of the phases in the equilibrium (Powell & Holland, 1990; Powell *et al.,* 1998). The calculations are performed using the computer program THERMOCALC (Powell & Holland, 1988, and succeeding upgrades), and the internally-consistent thermodynamic dataset of Holland & Powell (1985, 1990, 1998). The dataset of Holland & Powell (1998) is used in this study, and contains quite sophisticated activity-composition (a-X) models for most phases of interest, that allow most of the major substitutions between crystallographic sites to be modelled, as well as incorporating non-ideal mixing models.

Using this approach, phase diagrams can be calculated for any system of petrological interest that there is thermodynamic data for; in this study the complex pelite system CNMnKFMASH is successfully modelled. Invariant points and univariant lines can be calculated, as can co-ordinates in compatibility diagrams (Figure 1.6.A.). Furthermore, if bulk composition constraints are applied, then "pseudosections" for individual samples may be calculated, that is a petrogenetic grid that shows only the equilibria that that sample "sees"

(Figure 1.6.B.). Obviously, this is extremely useful in the interpretation of natural assemblages, as the bulk composition of a rock is crucial in determining the assemblages that it could encounter through P-T space. In a similar fashion to the Gibbs approach, P-T space can be contoured for isopleths of mineral composition and mode, which, as is shown in Chapter 5, can be used to interpret the evolution of zoned metamorphic minerals and therefore determine growth P-T paths (Figure 1.5.B.).

1.3. The Himalayas as a natural laboratory

The Himalayan chain of mountains is often cited as a premier example of a continental collision zone, and an excellent natural laboratory in which to study the thermal processes of orogenesis (e.g. Hodges *et al.*, 1988). This is because a) there is a large (over 100 000 km^2) exposure of metamorphic rocks in the core of the range; b) this metamorphic core contains many assemblages suitable for P-T analysis; and c) the extreme relief combined with the moderate dip of the metamorphic core allows up to ~20 km of mid-crustal sections to be studied. The following sections provide a brief overview of the major features of the Himalayan chain.

1.3.1. General introduction

The Himalayas, and Tibet, formed as a result of the collision of the Indian plate with Asia at approximately 54-50 Ma. (see Searle *et al.*, 1987, 1997; Dewey *et al.*, 1989). Following the break-up of Gondwanaland, India drifted northwards until it collided with the Asian plate along the southern margin of Tibet, preserving fragments of Tethyan ocean as ophiolites within the zone of collision, known as the Indus-Tsangpo suture zone. Subsequent to continental collision, northward drift of India continued, albeit at a slower rate, resulting in 2600 ± 900 km of crustal shortening (Patriat & Achache, 1984). Dewey *et al.*, (1989) calculated that India has undergone ~15-20 ^{0}C anticlockwise rotation since collision. Molnar & Tapponnier (1975) accounted for at least 1500 km of this shortening entirely within continental lithosphere. Geophysical evidence (e.g. Hirn *et al.*, 1984; Lyon-Caen & Molnar, 1985; Hirn, 1988) suggests that the thickness of the crust beneath the Himalayas and Tibet is of the order of 70 km, which is attributed to thickening as a result of the India-Asia collision (Molnar, 1988).

Continued convergence within the north Indian continental crust resulted in homogenous thickening and stacking on a series of S/SW directed, N-dipping thrusts which were ultimately responsible for the formation of the Himalayan topographic high. These

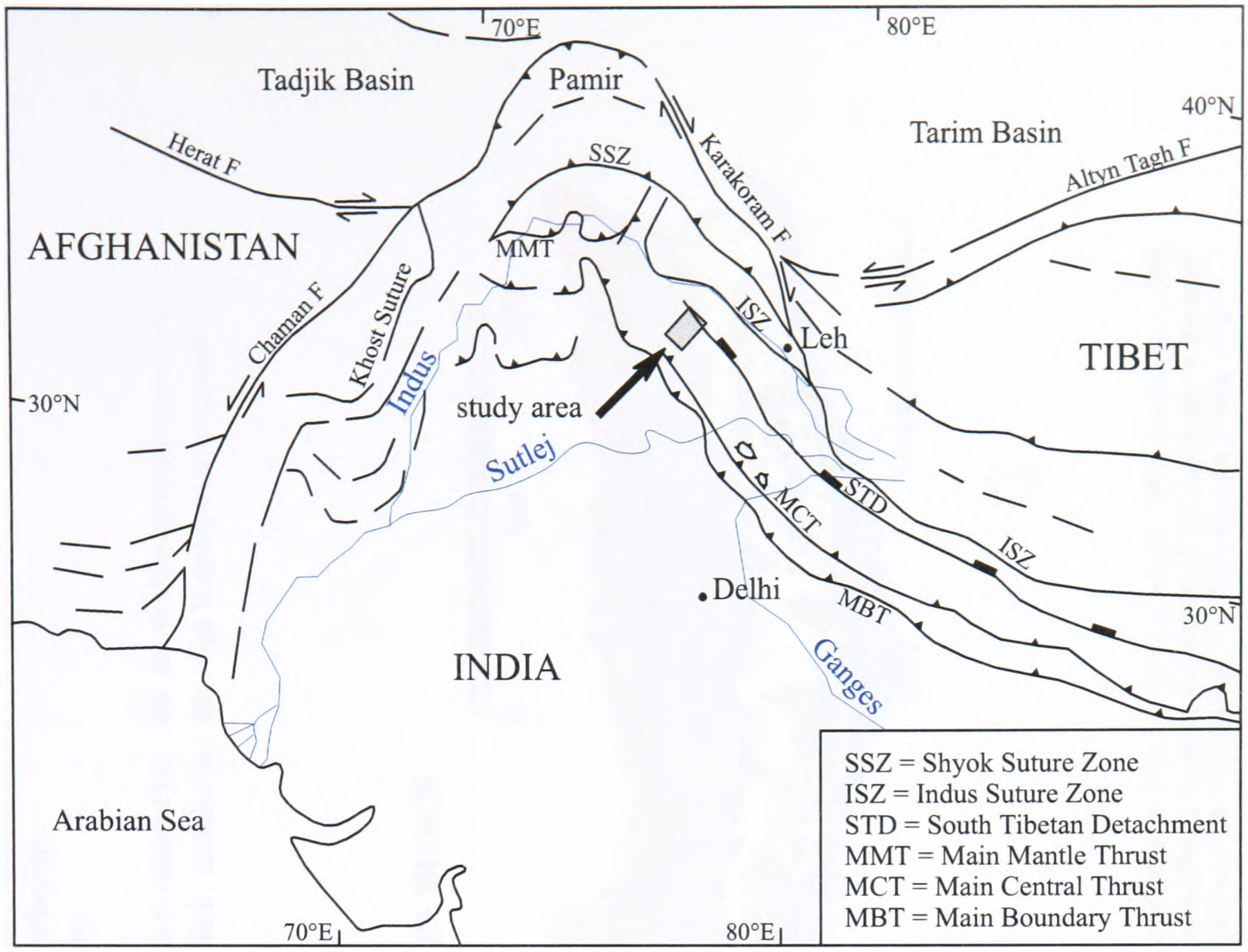
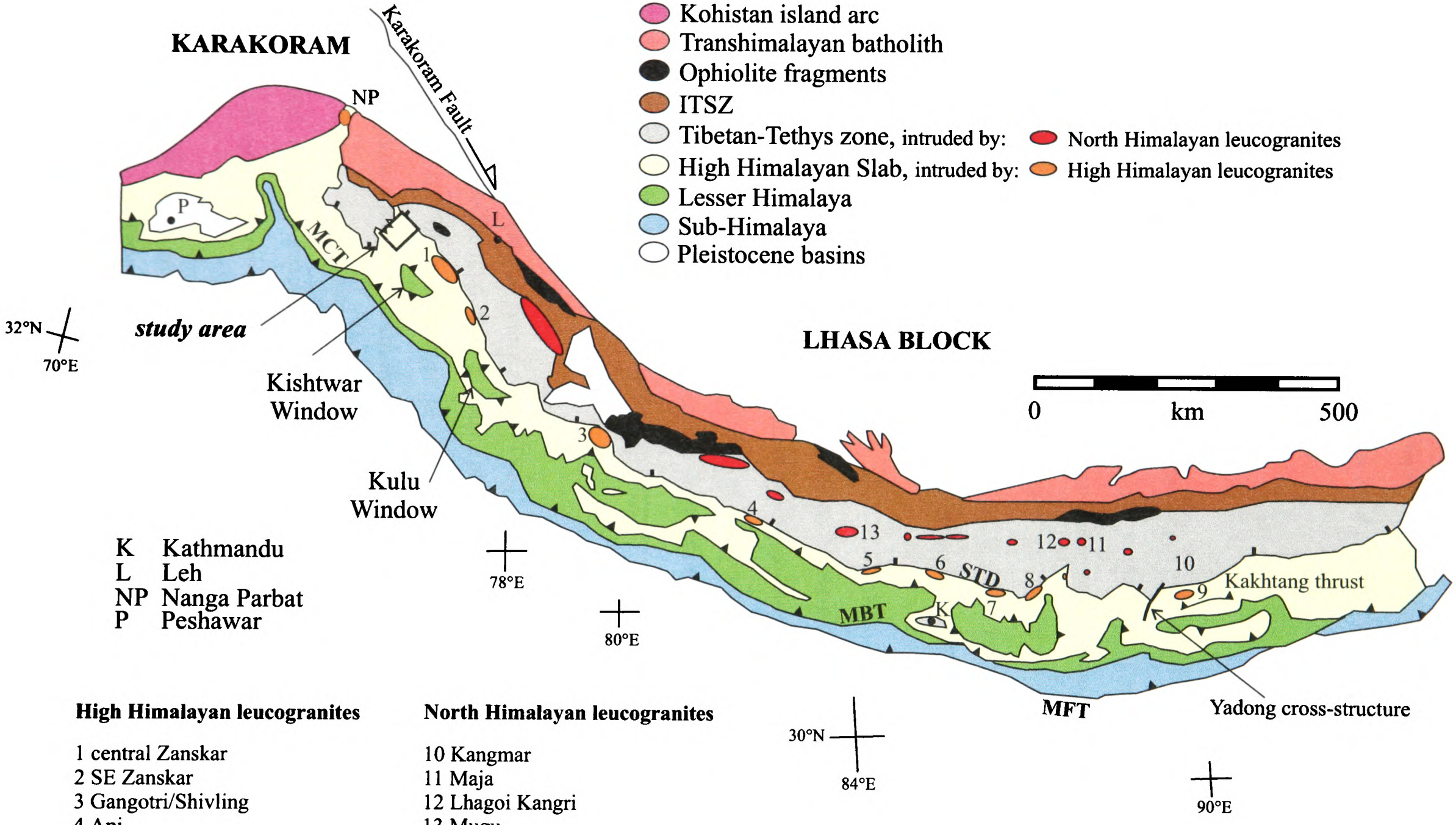


Figure 1.7. Tectonic framework of southern Asia illustrating the location of major crustal blocks, which are separated by suture zones, and the general geographical location of the study area. Modified after Searle (1991).



High Himalayan leucogranites

1 central Zanskar
2 SE Zanskar
3 Gangotri/Shivling
4 Api
5 Manaslu
6 Shishapangma
7 Nyalam
8 Rongbuk/Makalu/Everest
9 Kula Kangri

North Himalayan leucogranites

10 Kangmar
11 Maja
12 Lhagoi Kangri
13 Mugu

Figure 1.8. Tectonic framework of the Himalaya (modified after Gansser, 1964; Le Fort, 1988, Searle *et al.* 1988, Walker, 1998), showing the location of the study area in relation to the main structural and magmatic features of the orogen. MFT = Main Frontal Thrust, MBT = Main Boundary Thrust, MCT = Main Central Thrust, STD = South Tibetan Detachment.

thrusts generally propagated from the hinterland to the foreland, the Main Central Thrust (MCT) being the oldest and first to move, then the Main Boundary Thrust (MBT), and finally the presently active Main Frontal Thrust (MFT), which carried the older thrust stacks piggy-back style. The MCT is believed to have been active in Late Eocene-Oligocene times, with a reactivation in the Late Miocene (Harrison *et al.*, 1997), the MBT from ~11-1 Ma and the MFT from 1 Ma to the present.

1.3.2. Regional geology of the Himalayas

The present-day structure of the Himalayas is that of an arc 2500 km long, stretching from Pakistan in the west to Arunachal Pradesh in the east. The tectonic framework of the Himalayas is usually subdivided into six main lithotectonic units (Figures 1.7. & 1.8.), after Gansser (1964). One of the remarkable features of the orogen is that these units are continuous for 2500 km along strike, from the Nanga Parbat syntaxis in the west to the Namche Barwa syntaxis in the east. These lithotectonic units are introduced briefly here.

1.3.2.1. The Transhimalayan batholith

This consists of a chain of granite plutons forming a semi-continuous chain along the southern margin of the Asian plate, north of the India-Asia collision zone. It is a calc-alkaline series, formed by subduction-related melting of the upper mantle (Petterson, 1984) as Tethyan oceanic lithosphere was subducted beneath Asia. Isotopic ages from the granites using U-Pb on zircon span from around 100 Ma (e.g. Honegger *et al.*, 1982) to around 40 Ma (e.g. Schärer *et al.*, 1984).

1.3.2.2. The Indus-Tsangpo suture zone (ITSZ)

The Indus-Tsangpo suture zone lies south of the Transhimalayan batholith and represents the site of final closure of the Tethyan ocean (e.g. Gansser, 1964). The zone separates Indian plate rocks from those of the Asian plate, and comprises Mesozoic and early Tertiary marine sediments, Cretaceous island arc volcanics, ophiolitic melanges and continental molasse deposits (Searle, 1983). These molasse deposits are mid-Eocene to Miocene in age, and post-date India-Asia collision.

1.3.2.3.The Tibetan Tethys zone

The Tibetan Tethys zone is a sequence of essentially conformable marine sediments of Palaeozoic-Mesozoic and early Tertiary age that were deposited on the passive Indian continental margin prior to collision (Gansser, 1964; Fuchs, 1979). It is bounded to the north

by the ITSZ and to the south by the South Tibetan Detachment (STD) system of normal faults (Figure 1.9.), (Burg *et al.*, 1984; Searle, 1986; Herren, 1987). The Carboniferous-Permian Panjal Trap volcanics are related to rifting and opening of the Neo-Tethys ocean, in which the Permian-Eocene sediments were deposited. The entire sequence has been strongly deformed during the Himalayan orogenesis, and at the highest structural levels a fragment of Tethyan oceanic floor is preserved in the Spontang ophiolite klippe (Searle, 1986; Corfield, 1998).

1.3.2.4.The High Himalayan Crystalline unit (HHC)

The High Himalayan Crystallines , or High Himalayan Slab is a wedge of greenschist to amphibolite grade metamorphic rocks that form the metamorphic core of the Himalaya. It is thickest in Bhutan and Zanskar, where up to 25 km of crustal thickness is exposed, and thinnest in the Annapurna region of Nepal, where it is only 5 km thick (Pêcher, 1989). The unit comprises pelites/semi-pelites and calc-pelites, marbles, amphibolites, migmatites and granites and represents the metamorphosed Indian plate basement and sediment cover. In western Zanskar it has been demonstrated that large parts of the HHC represent the metamorphosed equivalent of the Tibetan Tethys cover (Honegger *et al.*, 1982; Searle, 1986; Walker, 1998; this study). The HHC can be viewed as a northward-tapering and dipping wedge of mid-crustal rocks, bounded to the north by the South Tibetan Detachment system, and to the south by the Main Central Thrust (MCT) (Figure 1.9.). It is believed that the HHC was ejected from mid-crustal depths in the Miocene, by simultaneous movement on the MCT and SDT as means of moderating the topographic gradient at the edge of the Tibetan plateau caused by the extreme crustal thickening of the India-Asia collision (Hodges *et al.*, 1993; Hodges, 1998).

Two main phases of Himalayan metamorphism have been identified in the HHC, as well as a Cambrian magmatic-metamorphic event (Le Fort *et al.*, 1986; Pognante *et al.*, 1990; Walker, 1998). The earliest Himalayan event, M1, is a high pressure, intermediate-temperature Barrovian episode resulting from crustal thickening subsequent to India-Asia collision. This was overprinted to varying degrees by a later, lower-pressure, higher-temperature M2 event which is associated with anatexis and leucogranite generation. This M2 event is believed to be contemporaneous with migmatisation and crustal melting. U-Pb dating of accessory phases in the leucogranites imply a Miocene age (24-12 Ma, with the greatest number of ages around 23-20 Ma) for leucogranite generation (e.g. Searle & Fryer, 1986; Noble & Searle, 1995; Hodges *et al.*, 1996). The M2 event overprints most evidence for M1 in the central and eastern Himalaya, but is less severe in western regions such as Zanskar,

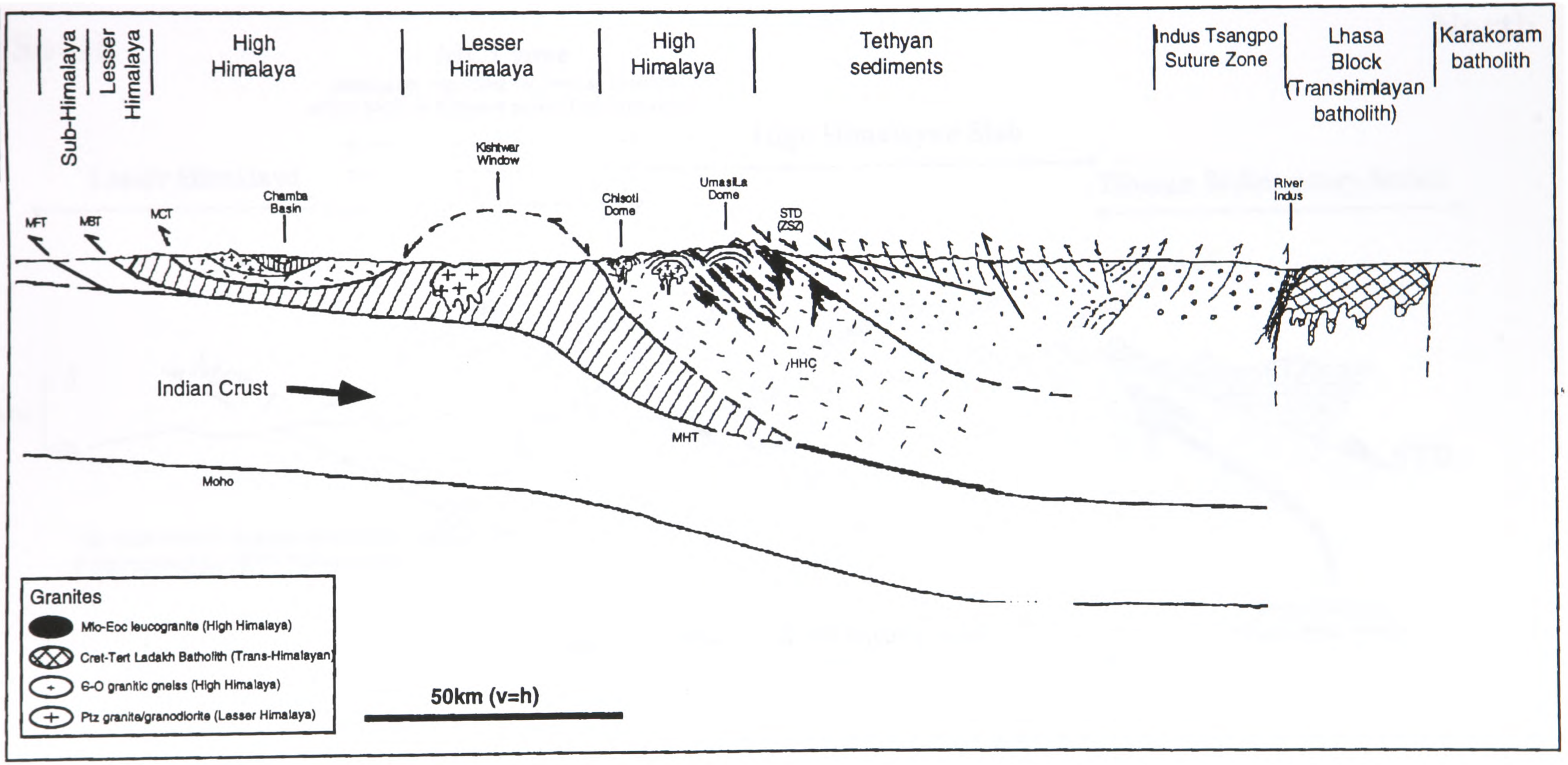


Figure 1.9. Schematic cross-section of the northwest Indian Himalaya (from Stephenson, 1997). MHT = Main Himalayan Thrust, MFT = Main Frontal Thrust, MBT = Main Boundary Thrust, MCT = Main Central Thrust, HHC = High Himalayan Crystalline unit, STD = South Tibetan Detachment, ZSZ = Zanskar Shear Zone.

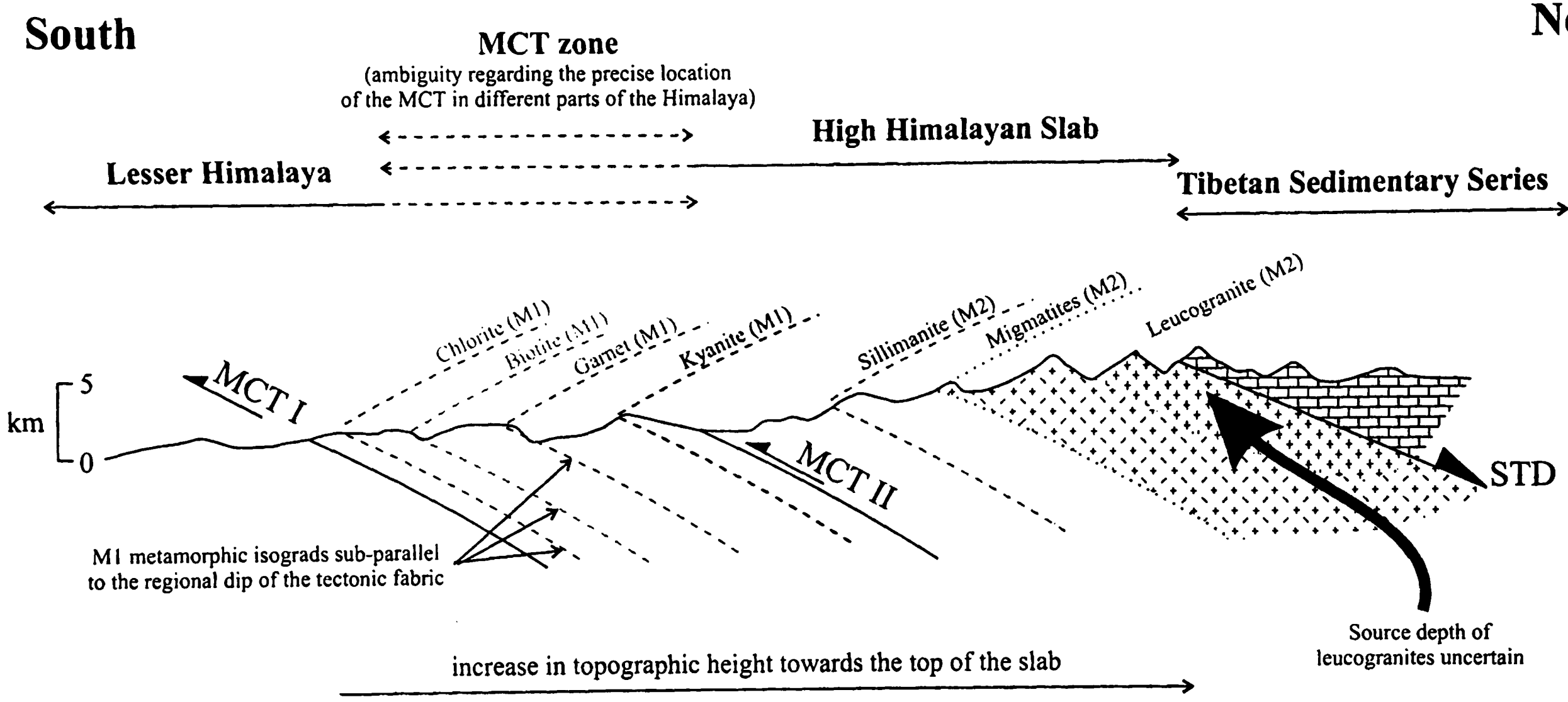


Figure 1.10. Schematic cross-section through the High Himalayan Crystallines illustrating the main features that are common to all parts of the slab. This shows the inverted metamorphic sequence through the MCT zone, with the M2 migmatites and leucogranites at the top of the slab. From Walker (1998).

which is the reason for the location of this study. Here, U-Pb and Sm-Nd geochronology demonstrate Early Oligocene (35-30 Ma) ages for the M1 metamorphism (Walker, 1998; Vance & Harris, 1999).

One of the most distinguishing features of the High Himalayan Crystalline unit is the occurrence of inverted metamorphic gradients at the base of the slab, preserved in both index mineral isograds, and often P-T gradients. Models for the inverted metamorphism are discussed in section 1.3.3.

1.3.2.5. The Lesser Himalaya.

The Lesser Himalaya form the footwall of the Main Central Thrust and are bounded at their base by another crustal-scale detachment, the Main Boundary Thrust (MBT). Rocks in the Lesser Himalaya comprise Upper Proterozoic to Palaeozoic sediments and Cambrian granites metamorphosed to greenschist facies (e.g. Le Fort, 1975; Pêcher, 1989).

1.3.2.6. The Sub-Himalaya (Siwaliks)

The Sub-Himalayan unit is bounded to the north by the MBT and to the south by the Main Frontal Thrust (MFT), and delimits the southern extent of Himalayan deformation. It comprises a ~5 km thick basin of molasse deposits derived from the erosion of the Himalaya since late Eocene times (e.g. Copeland, 1987; Najman *et al.*, 1997). Metamorphic detritus in the Siwaliks records the unroofing of the HHC, with the lowest-grade minerals being deposited first and the highest-grade last. This suggests that either the metamorphic inversion in the HHC occurred after the deposition of the Siwaliks, or that the source of the sediments was a right way-up metamorphic sequence, such as is found in Zanskar.

1.3.3. Models for inverted metamorphism in the HHC

The extent of the inverted metamorphic sequence preserved in the HHC (along the entire ~2500 km length of the chain) is such that the search for causal mechanisms has been at the forefront of research into the metamorphic evolution of the Himalaya. The inverted sequence is associated with the MCT zone, and is usually characterised by a progression from chlorite grade somewhere in the footwall (the Lesser Himalaya) to sillimanite grade in the hanging wall (Figure 1.10). Thermobarometric profiles also often reflect inverted thermal gradients (e.g. Hubbard, 1989; Stephenson, 1997).

The models proposed for inverted Himalayan metamorphism can be broadly grouped into those that invoke thermal perturbations or heat sources and those that view the inversion

as the product of mechanical processes that invert a previously right way-up sequence. The main differences between the models are described briefly below.

1.3.3.1. "Hot -over-cold" thrusting and folding of isotherms

This model, proposed by Le Fort (1975) advocated that the thrusting, along the MCT zone, of a hot HHC over a cold Lesser Himalaya will cause heating of the footwall and cooling of the hangingwall, leading to the observed pattern of inverted isograds (Figure 1.11.A). Furthermore, the release of volatiles from the underthrust Lesser Himalaya provide a source for vapour-present anatectic melting in the HHC. This model has largely been discounted in recent years for two main reasons. Firstly, the model requires that the inversion of the isograds be mainly a syn-metamorphic process, whereas a considerable number of studies show that movement on the MCT is essentially post-metamorphic (with respect to M1) (e.g. Hubbard, 1996; Inger & Harris, 1992; Metcalfe, 1993; Stephenson, 1997). In parts of the Himalaya, such as the Annapurna region (e.g. Vannay & Hodges, 1996) and the Everest region (Hubbard, 1989), the MCT has been shown to be syn-metamorphic, and the Le Fort model may be able to explain the inverted sequence *below* the MCT. It is important to emphasise here that all these hypotheses depend strongly on the exact definition and location of the MCT itself, which is often unclear. Secondly, numerical modelling (e.g. England & Molnar, 1993a) shows that the thermal effects of simple hot-over-cold thrusting are too transient to produce the widespread inversion.

1.3.3.2. Shear heating (dissipative heating)

Numerical modelling (e.g. England *et al.*, 1992; England & Molnar, 1993a) predicts that simple hot-over-cold thrusting as proposed by Le Fort (1975) is not sufficient to generate inverted metamorphic sequences as observed in the Himalaya (and other mountain belts), unless the rate of thrusting is significantly faster than the rate of heat diffusion, which does not seem to be the case. They propose instead that frictional shear heating (or dissipative heating) on the MCT created by shear stresses in the order of up to 100 MPa can generate and maintain temperatures at the base of the HHC that are sufficient to generate the inverted metamorphic profiles observed. Objections to this model include the observations that 1) as mentioned above, most of the movement on the MCT appears to be post-metamorphic whilst this model requires syn-metamorphic deformation; 2) this model suggested that the heating of the footwall by dissipative heating could release fluid into the overlying HHC, causing melting. Although these anatectic melts could rise through the crust to their present high structural levels, in Zanskar at least much of the leucogranites are believed to result from *in situ* anatexis

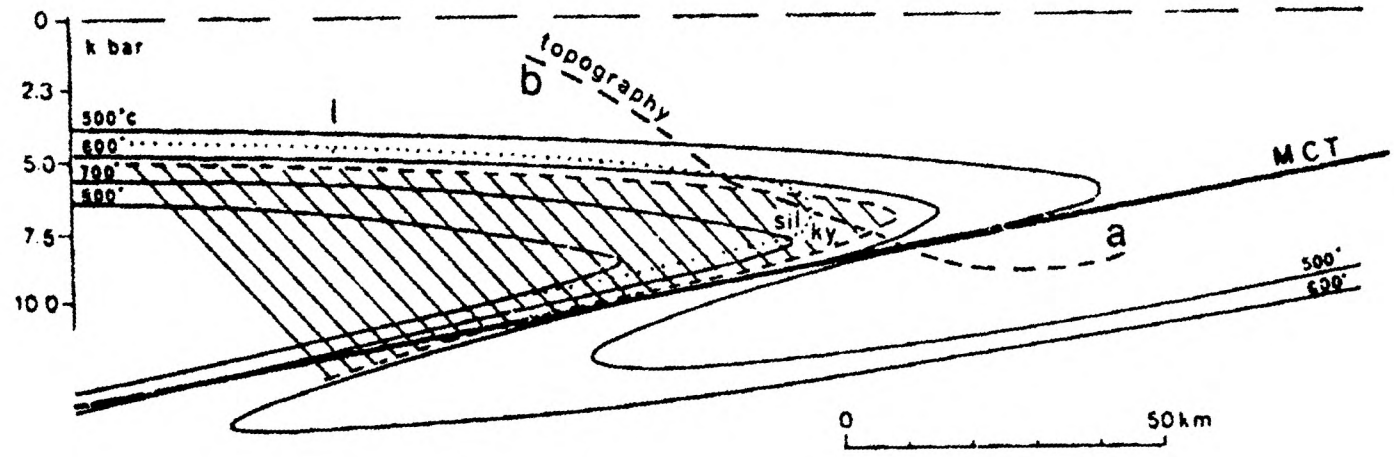


Figure 1.11.A. Diagram illustrating the main features of the hot-over-cold thrusting model. Note the downbuckling of the isotherms as a result of heat advection, creating a temporary inverted metamorphic sequence.. From Le Fort (1975).

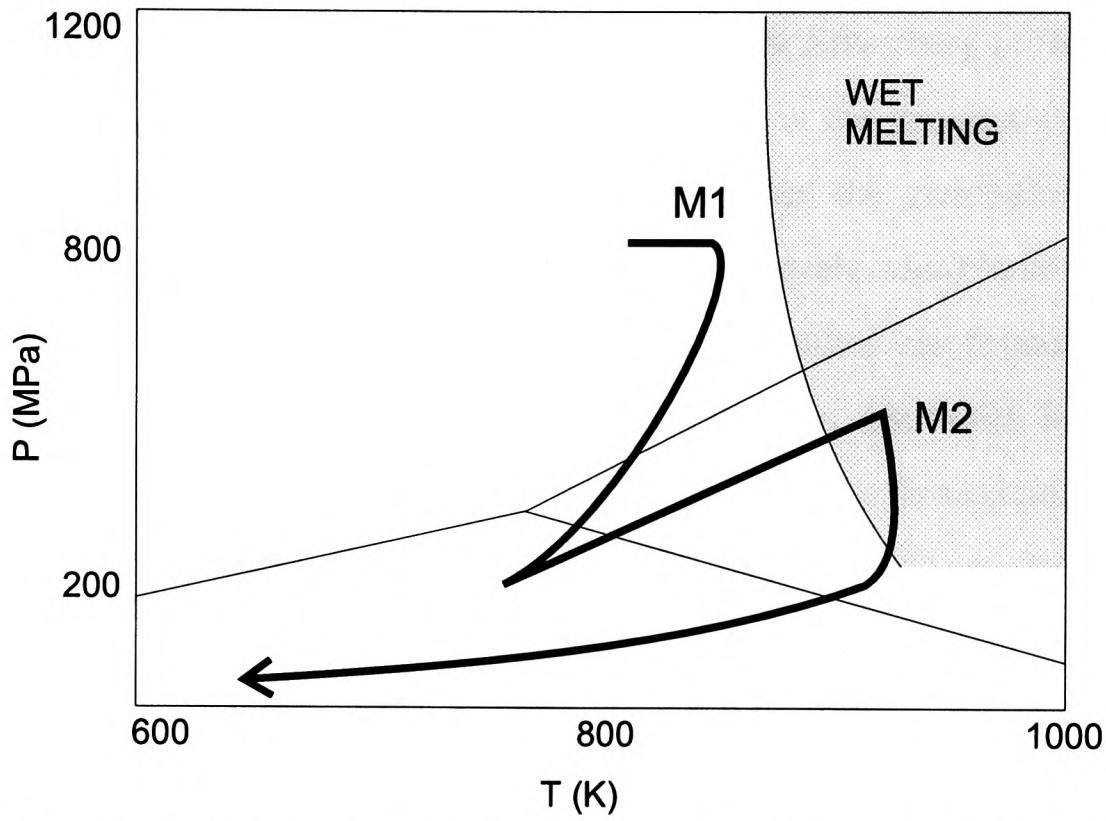


Figure 1.11.B. Model for the P-T evolution of the HHC in Garhwal. M1 Barrovian metamorphism is followed by "erosion-controlled" uplift. Subsequent thrusting and burial in the Late Oligocene-Miovene leads to M2 metamorphism and anatectic melting. After Hodges & Silverberg (1988).

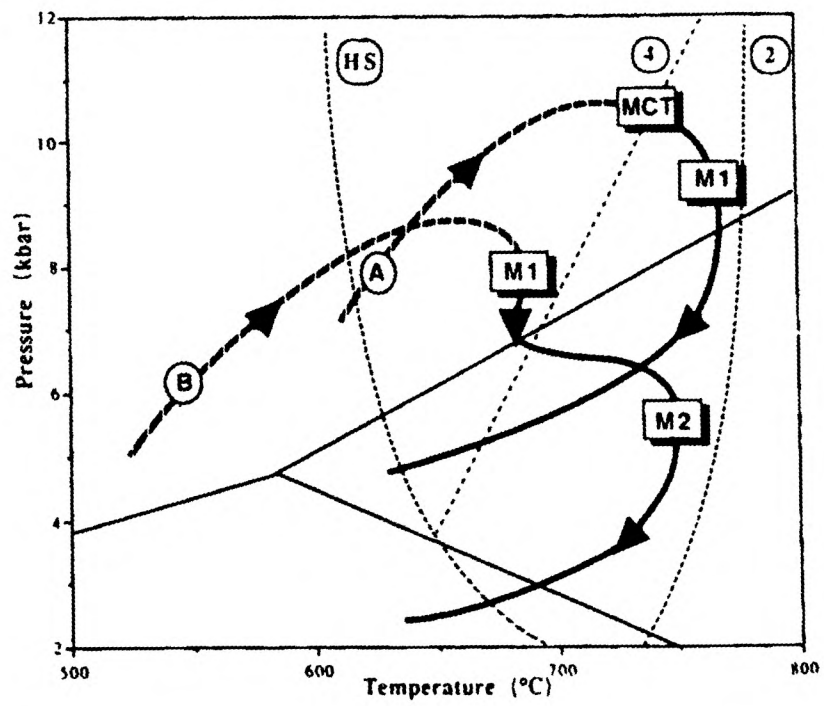


Figure 1.11.C. Schematic P-T array for (A) rocks near the base of the HHC and (B) rocks near the top. MCT indicates time of major thrusting along the Main Central thrust. This model predicts that M2 metamorphism and decompression melting will occur as the rocks pass through the pelite dry melting curve (4) during uplift. From Inger & Harris (1992).

some distance from the MCT zone; 3) Many thermal profiles obtained from thermobarometry show that the maximum temperatures attained in the HHC lie several kilometres up-section from the MCT zone (e.g. MacFarlane, 1995; Stephenson, 1997).

1.3.3.3. Polymetamorphism and heat focussing

Two main metamorphic events relating to Himalayan orogenesis have been widely observed in the HHC (e.g. Hodges & Silverberg, 1988; Stäubli, 1989; Searle & Rex, 1989; Inger & Harris, 1992; MacFarlane, 1995). The earliest event, M1, was a Barrovian high pressure, medium temperature event related to crustal thickening and underthrusting of the Indian plate (HHC). A later, high temperature, lower pressure Buchan M2 event is believed to be related to movement on the MCT and the ZSZ. Hodges & Silverberg (1988) argued that the inverted metamorphic gradient in the Garhwal Himalaya is the product of the two distinct metamorphic episodes (Figure 1.11.B.). They proposed that the generation and subsequent injection of leucogranites during M2 into higher structural levels could have provided some of the heat source for the M2 metamorphism. As the leucogranites are found at the top of the slab, this may explain why M2 assemblages are also found here. However, leucogranites often intrude rocks of lower than sillimanite grade, suggesting that the leucogranites did not cause M2 metamorphism everywhere. Conversely, Noble & Searle (1995) suggest instead that the leucogranites are the product of in situ melting as a result of M2 metamorphism. Inger & Harris (1992) propose decompression melting during M2 (Figure 1.11.C.) as a cause for leucogranite formation, and subsequent selective heating at the top of the slab due to heat focussing beneath thermally poorly conducting Tethyan sediments (Jaupart & Provost, 1985).

1.3.3.4. Folding and thrusting of isograds

In contrast to the above models which invoke largely thermal effects, many models rely on post-metamorphic mechanical disruption of a right-way-up metamorphic sequence, and the differences between these models depends largely on where in the Himalayas the model was proposed.

Brunel & Kienast (1986) invoke a model of entirely post-metamorphic movement along the MCT and within the HHC to account for the apparent inverted sequence. Their data, however, do not appear to take into account the effects of the M2 metamorphic event on the HHC. In many parts of the Himalaya, there is a continuous sequence of isograds across the MCT zone (e.g. in Zanskar, see Searle & Rex, 1989; Stäubli, 1989), and therefore syn-metamorphic disruption has been proposed. Furthermore, Zanskar is the only part of the Himalayan Crystallines where a right way-up sequence of isograds is observed at the top of

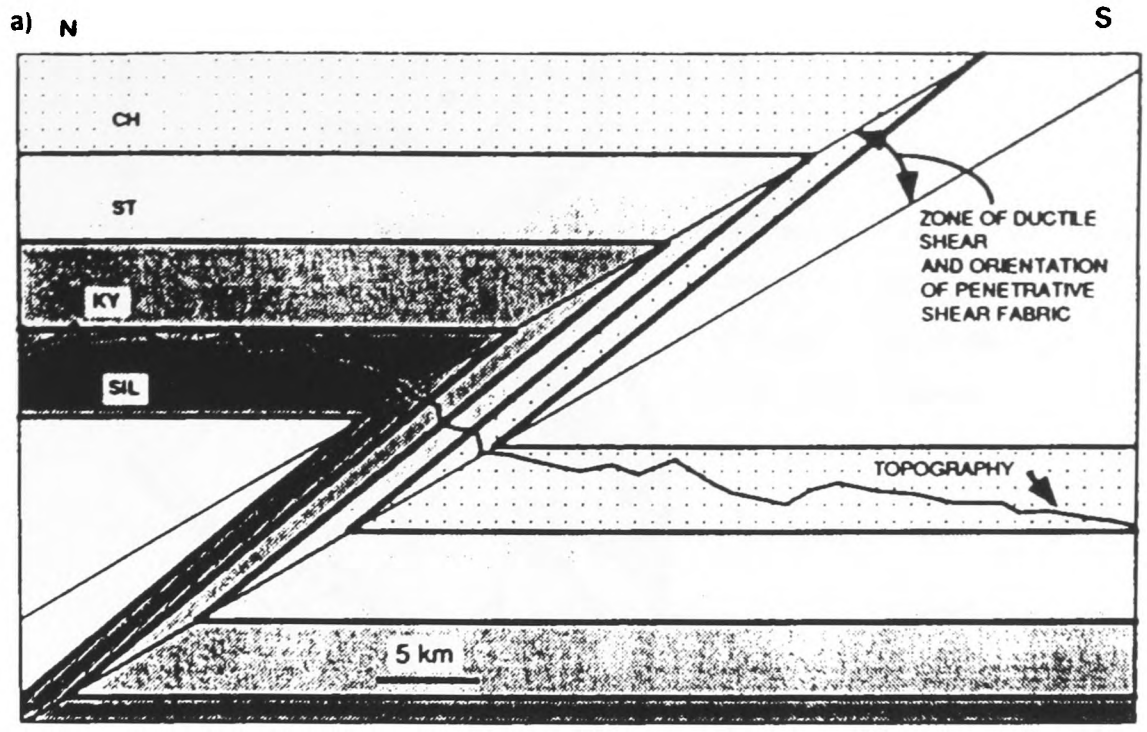


Figure 1.12.A. Hubbard (1996) model for inversion of metamorphic isograds by progressive simple shear along the MCT. The different metamorphic zones have been sheared in a ductile manner until they are sub-parallel to the edges of the shear zone.

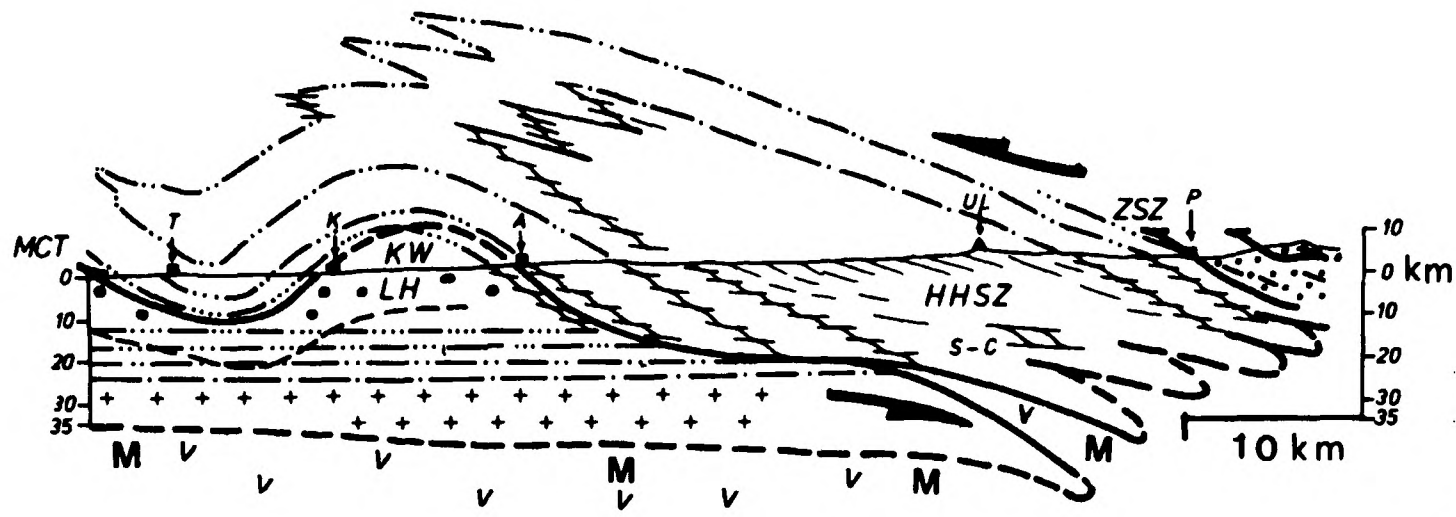


Figure 1.12.B. Jain & Manickavsagam (1993) model for inversion of isograds in the HHC. They propose ductile shear along closely spaced S-C shear planes throughout the entire HHC as a means of inverting the metamorphic sequence. This leads to an isograd geometry resembling a large recumbent fold.

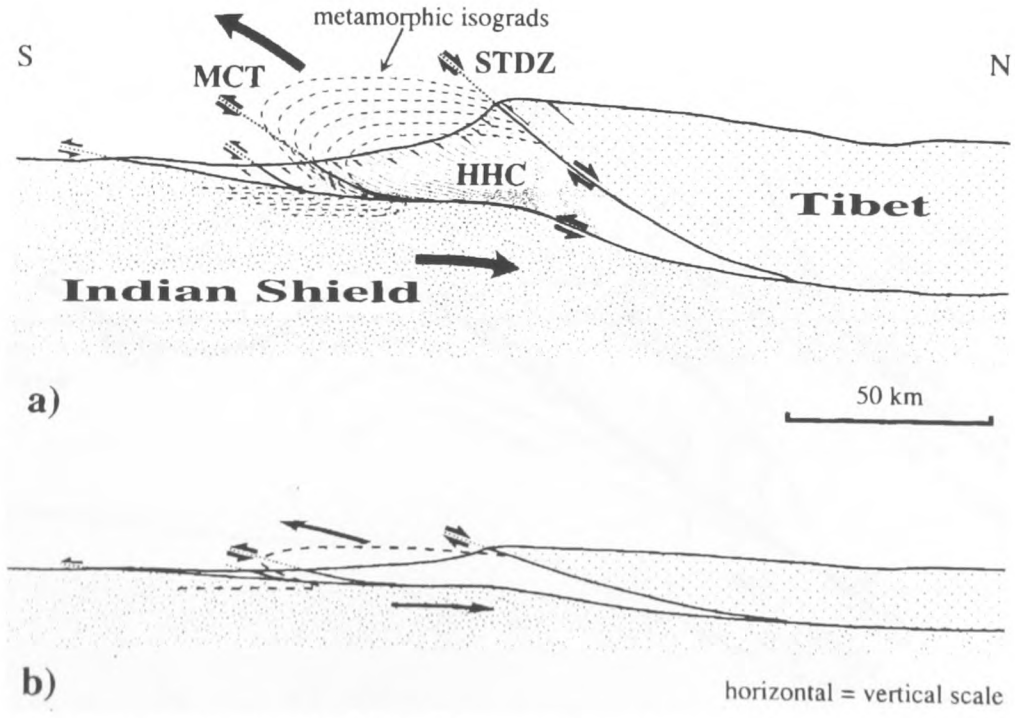


Figure 1.12.C. Model of Grujic *et al.* (1996). They envisage the ductile extrusion of the HHC, which is pervasively deformed throughout, with deformation being concentrated on the MCT and STDZ. The penetrative deformation and maximal finite displacement in the core of the HHC result in the metamorphic isograds being passively deformed.

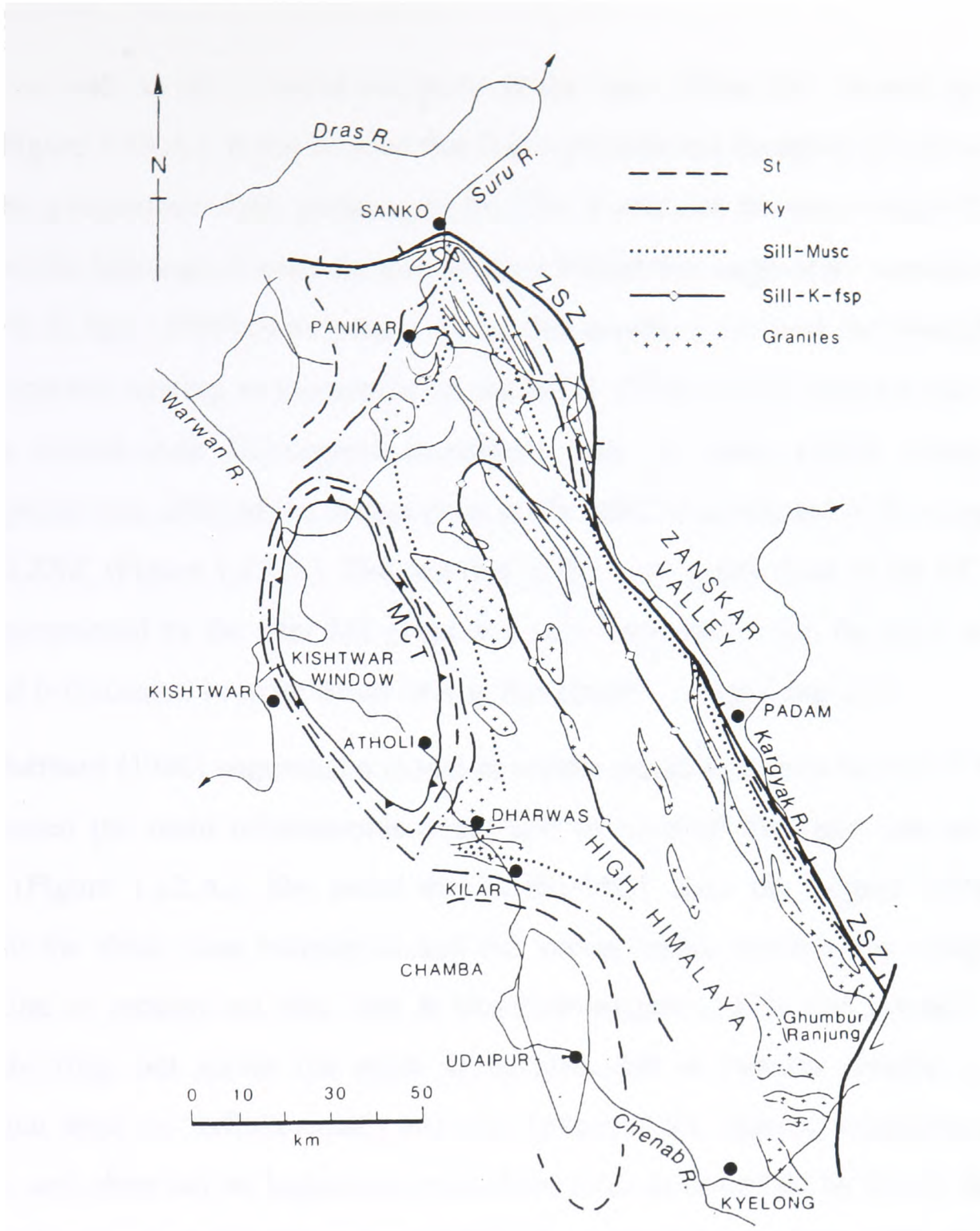


Figure 1.13.A. Sketch map of the Zanskar region of the HHC showing the approximate distribution of metamorphic isograds. Note how they are observed to close to the NW in the Panikhar region (see Chapter 2 and Enclosure 1 for more details). From Searle & Rex (1989).

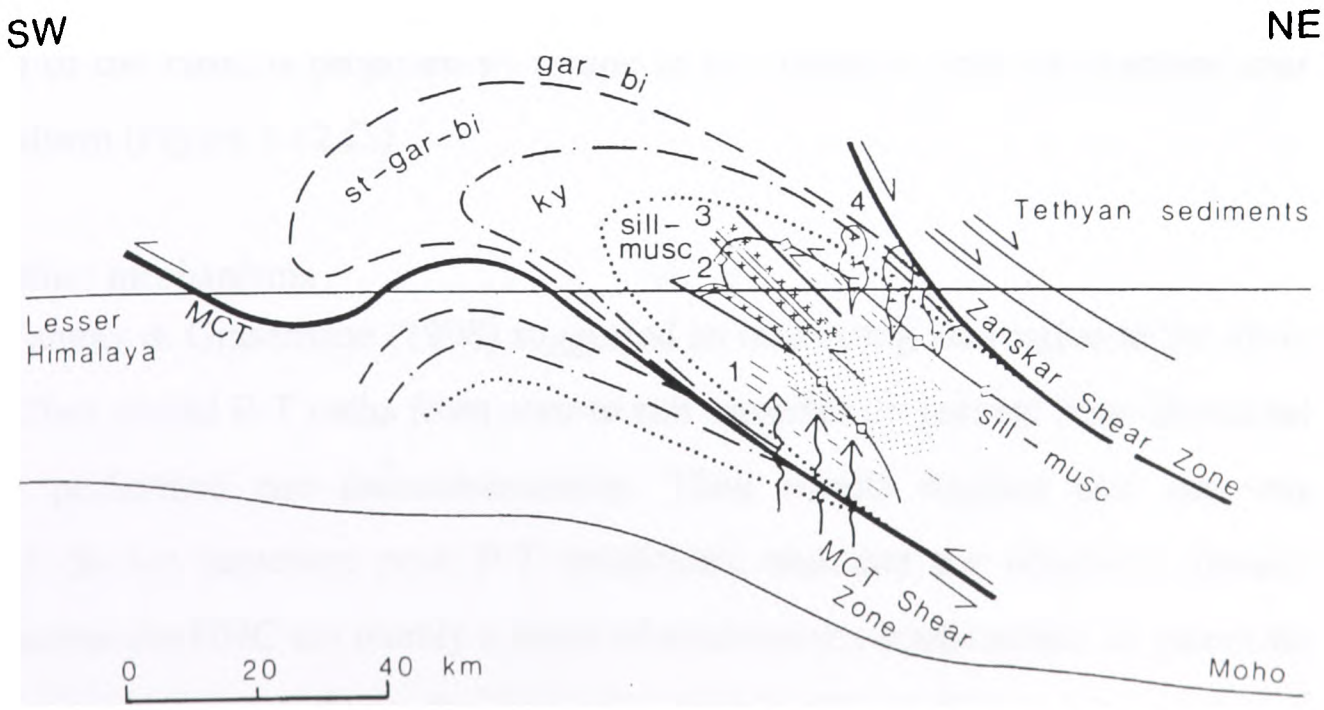


Figure 1.13.B. Searle & Rex (1989) model for the inversion of metamorphic isograds in Zanskar that invokes syn- to post-metamorphic recumbent folding of M1 isograds. M2 sillimanite-K feldspar metamorphism was synchronous with movement on the MCT.

the slab, as well as the inverted sequence at the base. From the mapped isograd outcrop pattern (Figure 1.13.A.), it can be seen that it is a geometrical necessity for the isograd pattern to describe a recumbent fold, plunging to the NW. It can also be seen around the Suru valley region that the *lithological units* are also strongly folded into large-scale recumbent folds. This lead Searle & Rex (1989) to propose a model that involved syn-post metamorphic folding of the M1 isograds relating to movement on the MCT. Their model stressed that this need not invoke a crustal-scale lithological recumbent fold, as many critics imagine. The M2 metamorphism that affected the deeper parts of the HHC is associated with movements on the MCT and ZSZ. (Figure 1.13.B.). The fact that in the Suru valley most of the M1 assemblages are not overprinted by the later M2 event is a very important point, the main reason for this study, and is discussed in more detail later in this chapter, and in Chapter 4.

Hubbard (1996) suggested a model of ductile thrusting across the MCT zone in Nepal that outlasted the main metamorphic event and so inverted the right way-up sequence of isograds (Figure 1.12.A.). She noted that in the MCT zone the isograd surfaces are sub-parallel to the shear zone boundaries and that metamorphic textures are overprinted by the deformation to substantiate this. Jain & Manickavasagam (1993) also invoked a process of ductile shearing, but across the entire Himalayan slab in Zanskar (Figure 1.12.B.). They suggest that shear on "infinitesimally and closely spaced S-C fabrics" could invert the isograd sequence, and observed no large-scale recumbent folds as described by Searle & Rex (1989). However, large-scale folds are present in NW Zanskar (Searle & Rex, 1989; this study), and S-C microstructures are not pervasive throughout the slab (Stephenson, 1997; this study). Where they are observed, such as around domal structures such as the Suru Dome (see Chapter 2), they are extensional in nature, not compressional. A similar model of ductile extrusion of the HHC is proposed by Grujic *et al.* (1996) to fold the isograds into a crustal scale antiform (Figure 1.12.C.)

1.3.3.5.Other mechanisms

Vannay & Grasemann (1998) suggested an interesting alternative to the above thermal models. They model P-T paths from core-to rim traverses on garnets from Himachal Pradesh, and also performed rim thermobarometry. Their results implied that rim temperatures calculated do not represent peak P-T conditions, and that the observed inverted thermal profiles across the HHC are merely a result of diachronous equilibration of garnet-biotite pairs at different temperatures. Thus, the inverted metamorphic profiles can be explained in terms of the limitations of the garnet biotite thermometer. An objection to this theory is that P-T

profiles calculated using self-consistent datasets (Stephenson, 1997; Searle *et al.* 1992, 1999; this study) and the program THERMOCALC still imply an inverted sequence. Due to the large number of reactions involved in calculating average P-T conditions by this process, the effect of localised re-equilibration of the garnet-biotite thermometer is minimised (see Chapter 4).

A further problem to interpreting the inverted metamorphism in the HHC is the likelihood that movement along the MCT may have been diachronous. Harrison *et al.* (1997) used $^{208}Pb/^{232}Th$ methods to date monazite inclusions in garnets from immediately below the MCT in central Nepal and found that the monazites (and therefore the garnets) grew as recently as 6-8 Ma. This suggests that the MCT may have been active as an out-of-sequence thrust, and the subsequent juxtaposition of higher-over lower-grade rocks may explain the inverted metamorphic sequence seen there. Searle *et al.* (1992, 1999) suggested that the MCT may have been reactivated by late Miocene brittle out-of-sequence thrusting.

1.4. The Suru Valley

The Suru Valley lies in the furthermost NW corner of the High Himalayan Crystallines in eastern Kashmir/western Zanskar. It comprises a metamorphic sequence from kyanite grade at the deepest structural levels to biotite grade at the contact with the ZSZ, where both right-way-up metamorphic isograds are preserved along the top of the slab, and inverted isograds are preserved along the bottom (Figure 1.13.A). The Suru Valley is an ideal area to study the metamorphic evolution of the HHC because 1) It lies at the periphery of the Himalayan Slab and contains assemblages that preserve the early M1 Barrovian metamorphic event and are not overprinted by M2 (except at the deepest structural levels), as are most deep parts of the HHC; 2) The structure of the area, and the pattern of isograds, make it an ideal place to study the relative timing of metamorphism with respect to deformation and thus evaluate models for the thermal evolution of the HHC.

1.4.1. Previous work in the Suru valley

1.4.1.1. Structure and lithology

The first major studies on the Suru valley region were carried out by Honegger (1983), and Honegger *et al.* (1982). He identified the series of large flat-lying folds that dominate the structure of the area, underlain by a domal structure, and correlated the marble-amphibolite units that are so prominent with Mesozoic rocks of the Tethyan shelf sediments and the

Permian Panjal Trap volcanics. His models for the structure involved a complex infolding of the Mesozoic sediments with Precambrian gneisses, and subsequent metamorphism, which along with his cross-sections, is a little difficult to envisage (Figure 1.14.A.). These large scale folds were also described by Searle & Fryer (1986), Searle & Rex (1989), Searle *et al.* (1992) (Figure 1.14.B) and Kündig (1989), who also described domal structures from the deepest levels of other parts of Zanskar. Granitic bodies have also been described in the area, mainly those at Sankoo and Parkatchik, which were ascribed Precambrian ages (Honegger, 1983) or described as leucogranites (Searle *et al.*, 1992), neither of which is correct (this study, Noble *et al.* in prep.). The occurrence of the ZSZ at the top of the HHC at Sankoo, separating the HHC from the Dras volcanics, was first described by Searle (1986), who traced the fault through Zanskar, and later by Herren (1987). The MCT is not exposed south-west of the Suru Valley; instead the HHC lies in contact with the Tethyan Kashmir sediments. This contact is interpreted as a late-stage fault (the Suru-Warwan cross fault) by Honegger (1983), and as a late-stage backthrust by Searle *et al.* (1992).

Gapais *et al.* (1992) presented structural data from the Suru valley and surrounding areas which imply flattening and stretching in an ENE-WNW-E-W direction, relating to extension of the HHC at the Oligocene-Miocene boundary (Figure 1.14.C). Stretching lineations and kinematic indicators of this kind are measured in this study, all relating to doming of the Suru Dome and extension on the ZSZ, but they are late features, and not related to earlier nappe formation.

1.4.1.2. Metamorphism and dating

Again, the work of Honegger (1983) and Honegger *et al.* (1982) provided the first real insight into the metamorphic conditions that occurred in the Suru valley. A metamorphic sequence progressing from garnet-biotite grade at the top of the slab to sillimanite-K-feldspar grade south east of the Suru valley was identified. The metamorphic isograds were mapped as being parallel to structures along the top of the slab, but discordant in the western parts (around the Donara nappe), essentially the same as has been mapped in this study. Porphyroblast growth was found to be pre-to-post kinematic in the deepest parts of the slab, and post-kinematic at tectonically higher levels. However, this interpretation does not take into account the two distinct metamorphic episodes M1 and M2 that are generally accepted to occur throughout the HHC. Rb-Sr dating on micas from Suru valley granites gives cooling ages of around 20 Ma, which are interpreted to represent cooling-uplift ages.

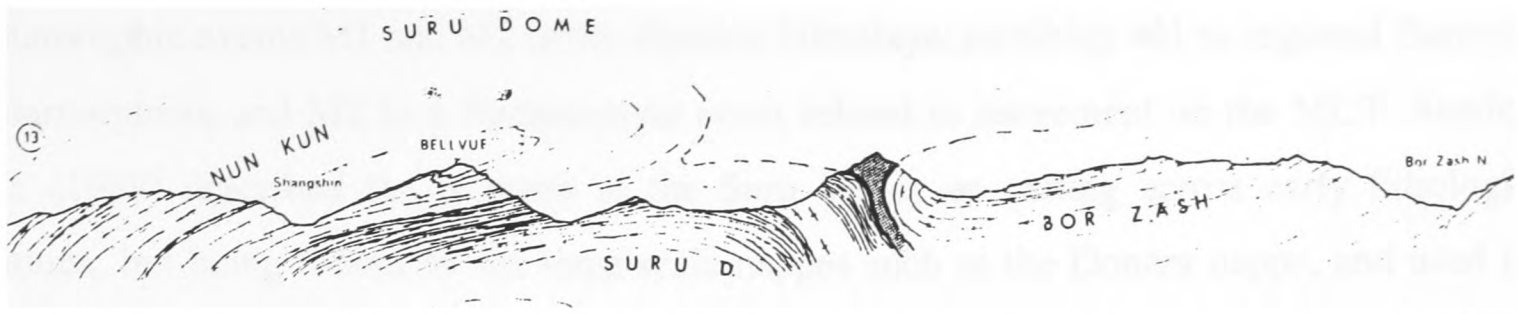


Figure 1.14.A. Cross-section from Honegger (1982) through part of the Suru valley, showing the SW and NE vergent recumbent folds seen in the area. This cross-section passes through a similar line to that of section B-B' on Enclosure 2. "Bellevue" is Panikhar Peak, 4879 m. The dark shaded units are the marbles seen in the Donara nappe.

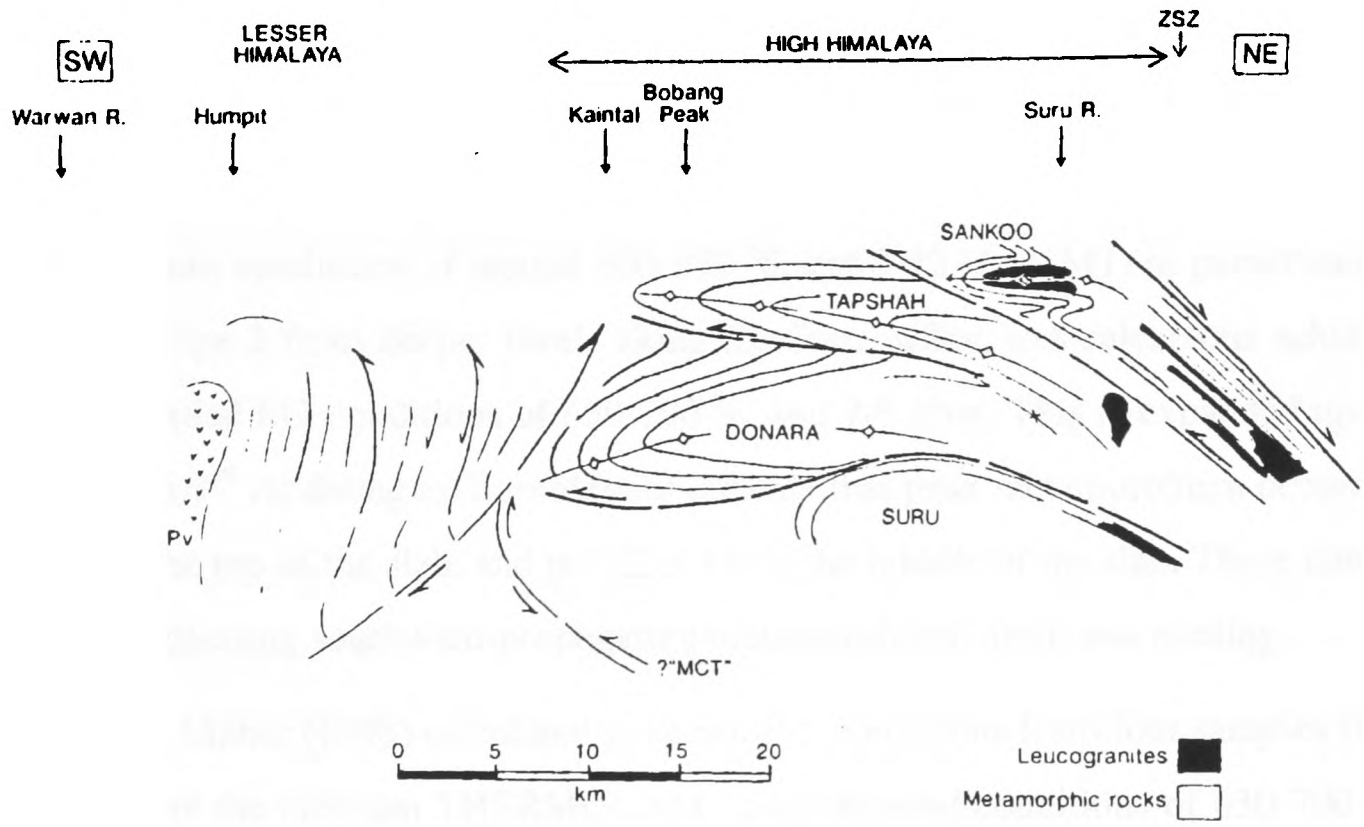


Figure 1.14.B. True-scale cross-section through the Kashmir-Zanskar HHC, taken from Searle *et al.* (1992), illustrating the major nappes and thrust units. In this model, the nappes are all thrust-bounded, unlike the evidence from this study. The MCT is truncated by a NE-vergent backthrust, and is postulated to be at depth beneath the Donara nappe. The ZSZ marks the top of the slab.

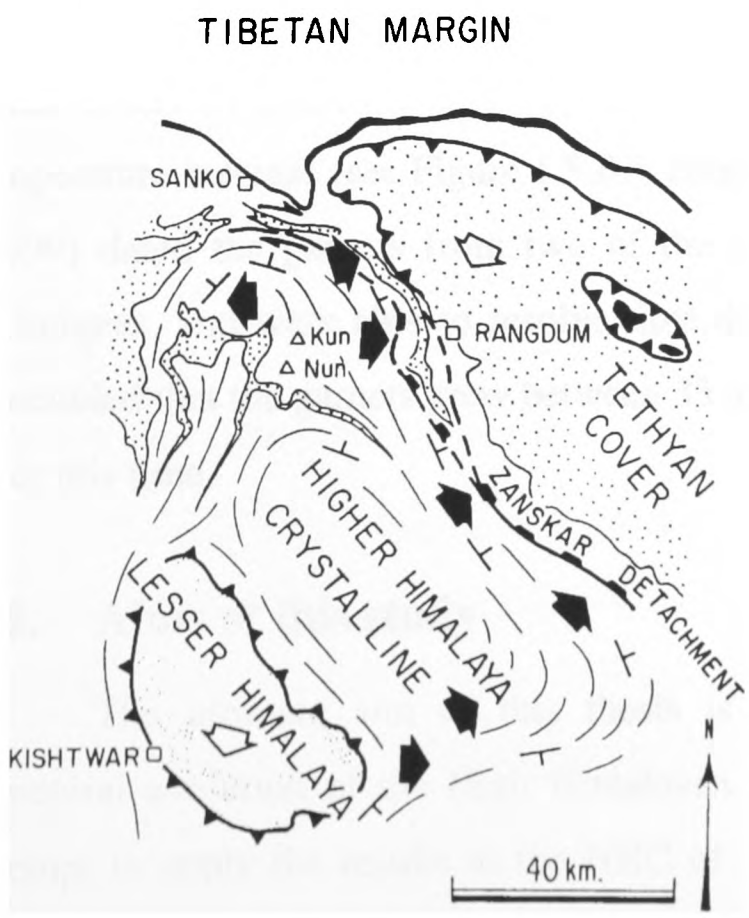


Figure 1.14.C. Sketch map from Gapais *et al.* (1992) illustrating their kinematic model for southwest Ladakh. Top-to-SW thrusting (white arrows) is overprinted bt EW to NE-SW extension (solid arrows), leading to dome formation.

Searle & Rex (1989), Kündig (1989) and Stäubli (1989) all recognised two metamorphic events M1 and M2 in the Zanskar Himalaya, ascribing M1 to regional Barrovian metamorphism and M2 to a Buchan-style event related to movement on the MCT. Searle & Rex (1989) described the isograds in the Suru Valley as cutting across early lithological features, but being folded by the large-scale nappes such as the Donara nappe, and used this observation to propose their folded isograd model to explain the inverted metamorphism in the HHC. Searle *et al.* (1992) were the first to provide quantitative P-T-t data on rocks from the Suru valley. They identified two main types of pelitic rock, those from the Suru Dome and deeper levels (Type 2), and those from the overlying nappes (Type 1). Whilst most nappe rocks preserved early deformation textures and M1 assemblages, Type 2 rocks displayed a later foliation that corresponds to doming and an M2 metamorphic event. Type 1 samples recorded maximum conditions of around 600-650 ^{0}C and 9-12 kbar (M1) in garnet-muscovite schists, whilst Type 2 from deeper levels along the Suru valley, and calcareous schists from the nappes, recorded M2 conditions of 650-700 ^{0}C and 7-8 kbar. This is expanded upon here in Chapter 4. $^{40}Ar/^{39}$ Ar dating on hornblendes indicate that peak metamorphism occurred pre-30.7 ± 2 Ma at the top of the slab, and pre-22 ± 1.0 in the middle of the slab. These dates were interpreted as indicating southward-propagating metamorphism, uplift and cooling.

Vance & Mahar (1998) calculated peak rim P-T conditions from four samples from the Suru Valley using the program THERMOCALC, and obtained conditions of 630-700 ^{0}C and 7-11 kbar. They do not, however, provide any regional framework as to the location of these samples and do not distinguish whether the conditions record M1 or M2. They combined these peak P-T conditions with P-T paths estimated from phase diagram calculations, again using THERMOCALC (see Chapter 5 for details of the technique), and concluded that the rocks followed paths of burial with little heating, followed by an essentially isobaric temperature increase (see Figure 1.5.B.), consistent with continental collision. Vance & Harris (1999) dated the garnets from two of the samples used in the above study using Sm-Nd techniques, and were able to resolve time differences between garnet cores and rims. They concluded that the garnets grew between 33 and 28 Ma, so exhumation must have taken place after this time.

1.5. Aims of this study

The ultimate aim of this thesis is to determine the prograde metamorphic and structural evolution of the High Himalayan Crystalline unit in the Suru valley region, and attempt to apply the results to the HHC of the rest of Zanskar. As stated above, the Suru

valley is an ideal area to study the early, prograde history of the HHC, as the metamorphic assemblages largely preserve the M1 Barrovian event, and the M2 overprint is not pervasive, as is the case in many parts of the HHC.

The thesis sets out to provide a detailed, integrated metamorphic and structural synthesis of the area and uses this to resolve important questions such as the relative timing of metamorphism and deformation in the Zanskar Himalaya, and the absolute conditions reached by this metamorphism. Furthermore, knowledge of the prograde thermal evolution of the HHC can provide important information on the rates and conditions of metamorphism in orogenic belts, whilst detailed structural observations allow us to understand the styles of deformation at these conditions.

The general objectives and layout of this thesis are summarised below:

Chapter 1 introduces the concepts of metamorphism as a record of tectonic processes and the problems associated with it. The general tectonics of the Himalayan study area are introduced, as are the specific aims of this project.

Chapter 2 describes the macro and mesostructure of the Suru valley, with reference to the styles of deformation at different depths, and the pattern of metamorphic isograds in the area. It also relates the metamorphic units of the HHC to the Palaeozoic-Mesozoic sediments of the Indian shelf, and Permian magmatism.

Chapter 3 provides detailed petrographic, microstructural and chemical descriptions of Suru valley rocks. Metamorphic mineral growth is related to three distinguishable phases of deformation that are in turn correlated with the regional structure. Mineral chemistry is related to growth of porphyroblasts and grade of metamorphism where possible.

Chapter 4 describes the principles, rationale and results of both conventional thermobarometry and those obtained using a self-consistent thermodynamic dataset. The results compare the two different techniques, and emphasise the variation of metamorphic grade across the entire slab, as well as individual structures such as the Donara nappe. The results are also correlated with those from other parts of the Himalaya.

Chapter 5 discusses the results of metamorphic modelling of six samples from various parts of the Suru valley. The principles and rationale of both phase diagram modelling using pseudosections and Gibbs modelling are introduced, and the reasons for utilising each of them. The results of both techniques are discussed with a view to assessing the strengths and

weaknesses of each technique, and their applicability to "real" rocks, as well as estimating the P-T paths followed by Suru valley rocks.

Chapter 6 attempts to summarise the conclusions of the previous chapters and synthesise a model for the evolution of the Suru valley, with regards to models for inverted metamorphism in the HHC, and movement on the MCT and ZSZ. The limitations of metamorphic modelling as a tool for analysing tectonic evolution are discussed.

Chapter 2



The view north over the Suru Dome from an altitude of 4800 m, south of Tongul.

2. Structure and lithologies of the Suru Valley.

2.1 Geographical location and nature of the area.

The study area comprises part of the Suru Valley, and the surrounding regions in NW Ladakh/Eastern Kashmir, NW India (Figure 2.1.). The principal area of interest is centred on the village of Panikhar, and runs along the Suru River valley for around 40 km south of the village of Sankoo, and up minor valleys to the west and south. A geological map covering of roughly 400 km^2 of this area was produced during a two-month field season from July to September 1996. Samples were also collected up-section for 12 km from the ZSZ at Rangdum, mainly for P-T work.

The area lies in the Greater Himalayan Range and is characterised by steep sided peaks of up to 7000m in height, dissected by deep valleys containing glaciers at altitudes above around 4500m and fast flowing rivers down to around 3000m. The region is semi-arid in the summer months and completely snow-covered in winter. Vegetation and agriculture, fed mainly by glacier meltwater and occasional rains from the monsoon spilling over the divide of the Himalaya, occur only on the lower slopes and valley floors.

Such variations in topography, combined with the general lack of vegetation cover, provide an excellent degree of exposure allowing the three-dimensional geology of the area to be studied.

2.2 Structure and deformation

2.2.1 Introduction

The High Himalayan Slab, or High Himalayan Crystallines (HHC), is a coherent unit of crystalline rocks running the length of the Himalayan chain (Figure 2.2.). It is separated from the lower-grade Lesser Himalaya to the south by the Main Central Thrust (MCT), and from the deformed Zanskar shelf sediments to the north by the Zanskar Shear Zone (ZSZ) (Searle, 1986; Herren, 1987), or South Tibetan Detachment (STD). From geophysical observations it can be seen that both the MCT and ZSZ are crustal-scale detachments.

The slab itself has an overall dip to the north-east; in the Suru Valley region, a 20 km right way-up crustal section is exposed in three dimensions (3-D), allowing the structure of the crust and its relationship to metamorphism to be studied at depths of 12-35 km. The aim

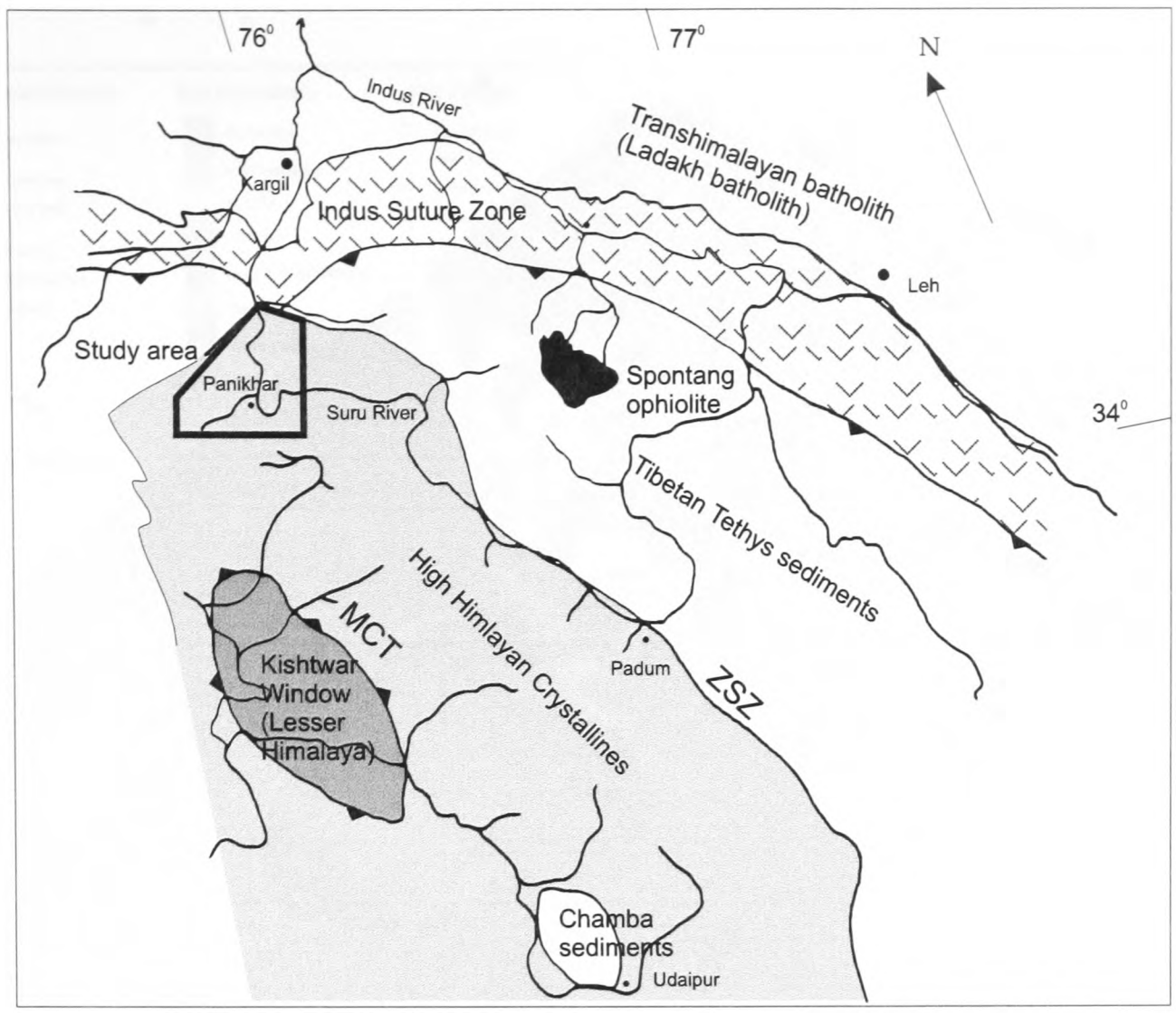


Figure 2.1. Sketch map of the Ladakh-Zanskar Himalaya, after Searle *et al.* (1992) illustrating the location of the study area and the main geological divisions and structures. MCT = Main Central Thrust, ZSZ = Zanskar Shear Zone.

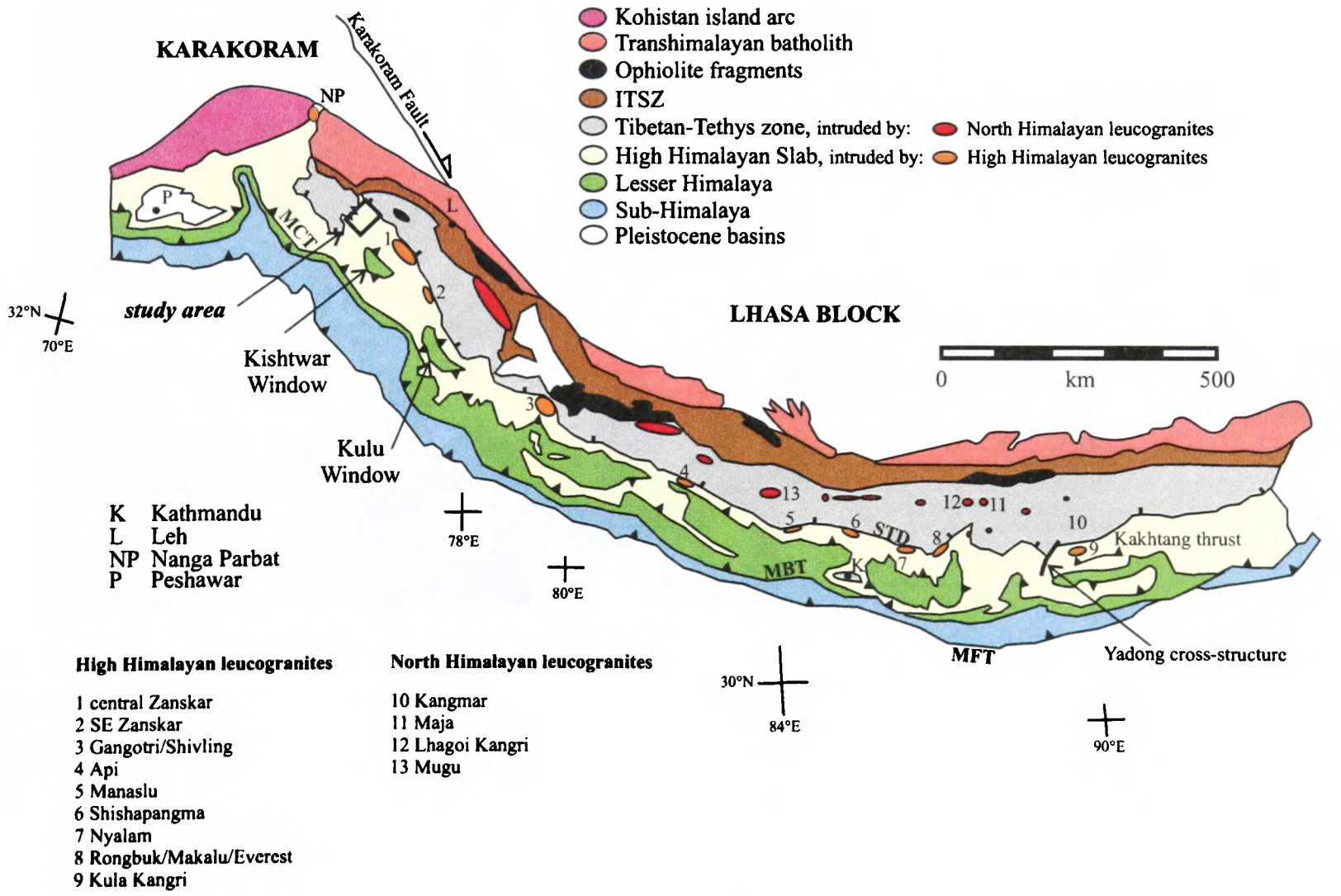


Figure 2.2. Tectonic framework of the Himalaya (from Walker, 1998) showing the location of the study area in relation to the main structural and magmatic features of the orogen. MFT = Main Frontal Thrust, MBT = Main Boundary Thrust, other abbreviations as for Figure 2.1.

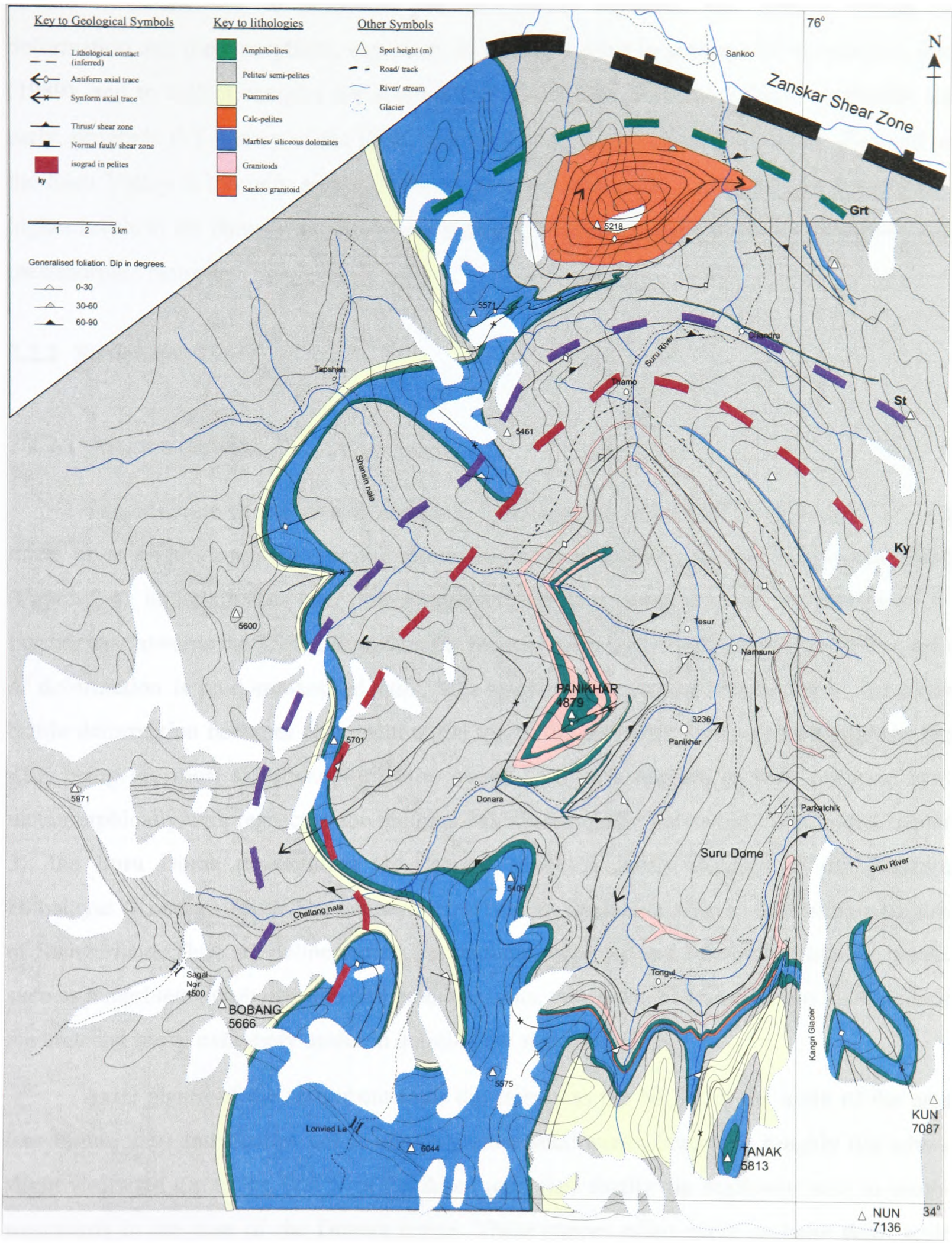


Figure 2.3. Geological map of the Suru Valley around Panikhar. All main lithological units and metamorphic isograds are shown. Scale is approximately 1: 176 000.

of the fieldwork was to determine the relationship between, and relative timing of, deformation and metamorphism, especially to test the folded isograd model of Searle & Rex (1989), and to collect samples for detailed P-T work. The ultimate aim is to determine the early, prograde P-T history of the HHC, and relate it to deformation, if possible. This part of the Suru Valley is the only area in Western Zanskar where this is possible, as it represents higher levels in the Himalayan slab where high-grade metamorphism does not obliterate early metamorphic histories.

2.2.2 Structure

2.2.2.1 Major structures

The structure of the area is complex, consisting of a series of large-scale (~2-3 km thick, up to 10 km long) SW-verging recumbent folds, or nappes, such as the Donara nappe (Figure 2.4), underlain by a later domal structure, the Suru Dome (Figure 2.6., Enclosure 2). Further east towards the ZSZ at Rangdum the foliation dips fairly consistently E/NE. The style of deformation is predominantly ductile, as a result of non-coaxial simple shear, but more brittle deformation becomes prominent at the top of the slab near Sankoo and Rangdum, the ZSZ being the most significant structure. Nappe formation appears to have occurred syn-metamorphically with respect to the regional M1 kyanite-grade Barrovian event, (see Chapter 3), the Suru Dome representing the deepest structural levels exposed in the Western Himalayas (Kündig, 1989). The nappes themselves are similar in style to the Pennine nappes of Switzerland. They are delineated by the regional foliation, and by obvious marker bands, such as a marble/amphibolite unit and granitoid units, which can be traced across the length of the area and prove extremely useful in defining the structure.

Axial planes of the recumbent folds dip steeply to the N/ NE in the north of the area (see Figure 2.7.) and shallow out as one progresses southwards, becoming roughly flat with a slight westward dip to the W/SW of Panikhar, until they finally dip shallowly west to south-westwards in the case of the Donara nappe. These nappes often occur as large (km) scale sheath folds, such as the nappe to the south of Tongul, and the Sankoo nappe (Figures 2.8., 2.9.). The overall structure dips away from the Suru Dome on all sides, which can be seen from the outcrop pattern of the marble/amphibolite unit (Figure 2.3 and Enclosure 1). This is a result of folding of the axial planes by a later, lower domal event centred on the Suru Dome. The nappe composed of granites and amphibolites which forms Panikhar Peak, structurally



Figure 2.4. Photo showing the closure of the Donara nappe, taken from above the Chellong nala, looking NW. Note internal isoclinal folding within the beige-brown marble band, which is approximately 400-500m thick. Cliff approximately 2km in height.



Figure 2.5. Photo taken at the confluence of the Chellong nala and Lonvied glacier river, looking N-NE. This is roughly perpendicular to the strike of the Donara nappe, and shows extreme folding and boudinaging within the marbles. The dark rocks above and below the marbles are the amphibolite bands.



Figure 2.6. View looking N over the Suru Dome (foreground) to the Sankoo nappe in the far distance. The tectonic structure of the dome is reflected in its topographic expression.



Figure 2.7. View looking SW from the road near Chandra to the Tapshah nappe. The axial plane of the fold can be seen from the changing dips of the beds in the cliffs, and from minor folding. The lighter rocks at the top of the cliffs are the marbles seen so clearly in the Donara nappe. Relief is in the order of 2500m.

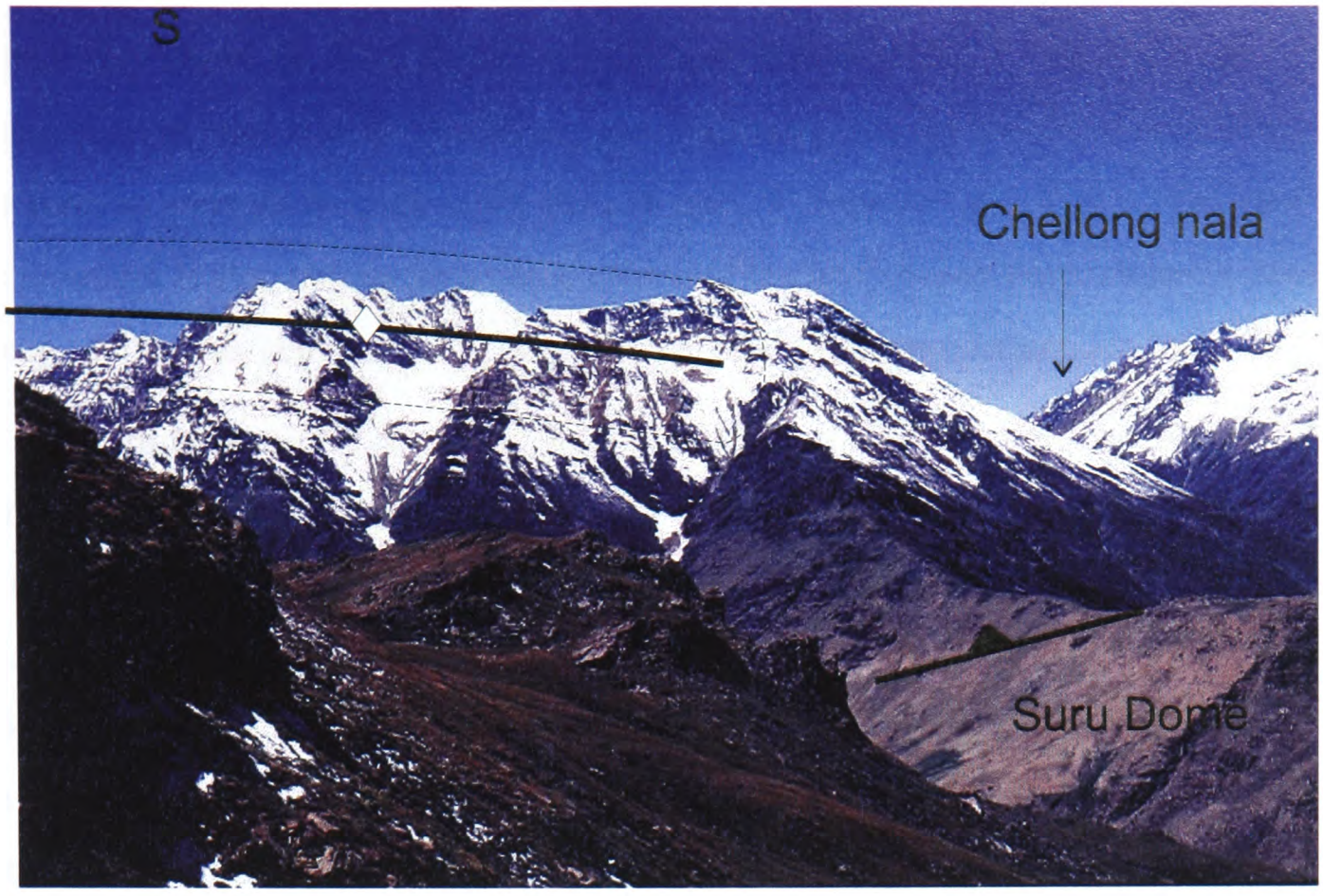


Figure 2.8. View S from the centre of the Suru Dome illustrating NE-vergent recumbent fold to the south of Tongul, occurring here as a sheath fold. Cliff approximately 5 km wide.



Figure 2.9. View from south of Tongul looking W-WNW end-on at the NE-vergent recumbent fold described above. Photo clearly illustrates the difference between the marble (beige-brown), amphibolite (dark grey/black) and pelitic layers (brown). Approximately 2 km or relief shown.

immediately above the Suru Dome is particularly flattened and elongate (Figure 2.10.), which is probably in part due to stretching and flattening caused by the downgliding of nappe structures as a result of uplift of the Suru Dome (cf. Gapais *et al.*, 1992). The domal nature of this structure is also emphasised in the course of the Suru River which forms a large loop, the course of the river being determined by the regional foliation (Figure 2.3., Enclosure 1).

In three dimensions, the detailed structure of the area, especially around the Suru Dome, is quite complex (Figures 2.11., 2.12., 2.13., Enclosure 2). The nappes all have sub-horizontal axial planes, except in the north of the area, and in places the erosion level allows a sheath fold geometry to be recognised, where the axial planes are curved. The isoclinal fold picked out predominantly in granites and amphibolites above Panikhar appears to be separated from the overlying nappes by a ductile shear zone, although field evidence for this is often far from clear. All the nappe structures are domed by the underlying Suru Dome.

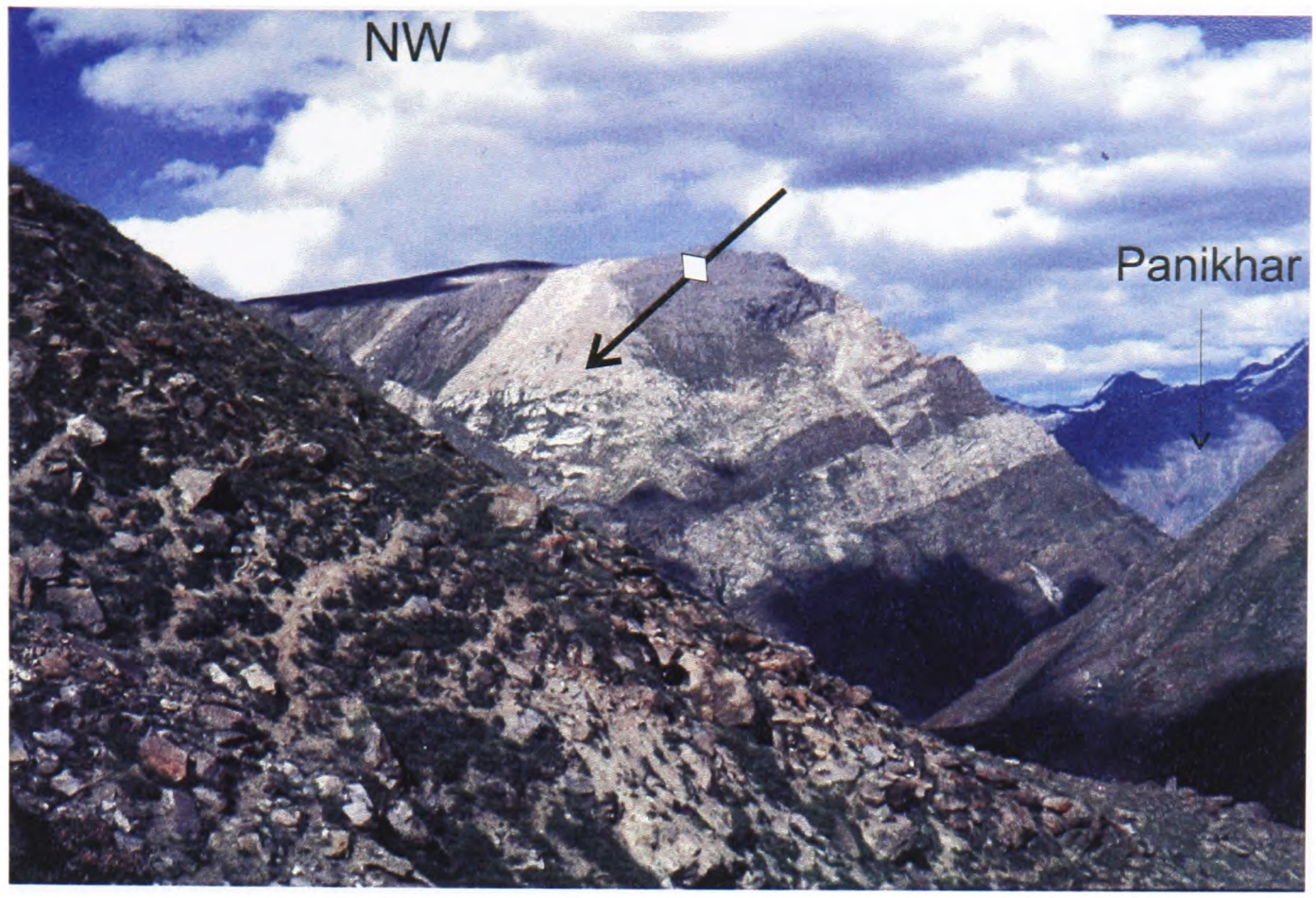
The imposition of fairly flat-lying axial planes on a rather extreme topography results in a complex axial planar outcrop pattern, which at first may appear confusing (Figure 2.3, Enclosure 1). The distinction between anticlines and synclines as mapped is simply that the dominant, SW-verging structures such as the Donara, Tapshah and Sankoo nappes are designated anticlines, whilst the NE-verging nappes separating them are termed synclines. As these folds are roughly flat-lying, the distinction is essentially an academic one, but useful in emphasising that the synclines are merely parasitic to the major anticlines that indicate SW direction of transport, and not separate structures showing NE transport as implied by Honegger (1983)

At least three phases of deformation can be distinguished from both microstructural and field evidence. Detailed petrographic descriptions of microstructures will be given in the next chapter, but the correlation between large-and small-scale structures is summarised here.

D_1 is preserved mainly as crenulated inclusion trials in garnets (S_0 and S_1 deformed by $D_{1\text{-}2}$), although intrafolial isoclinal folding is often seen in the field, especially in marble units and amphibolites. In the closures of the both Donara nappe and the nappe south of Tongul, sheath folds, re-folded folds, and extreme boudinaging can be seen in the marble units, which have obviously undergone highly ductile deformation. (Figure 2.5.). Similar isoclinal folds can be seen elsewhere, such as in Figures 2.14. and 2.15., and near Sankoo, albeit on a much smaller scale. It is worth emphasising the range of scales of isoclinal deformation encountered, from centimetres to hundreds of metres. As the nappes cannot solely have been responsible for crustal thickening leading to metamorphism, as evidenced by



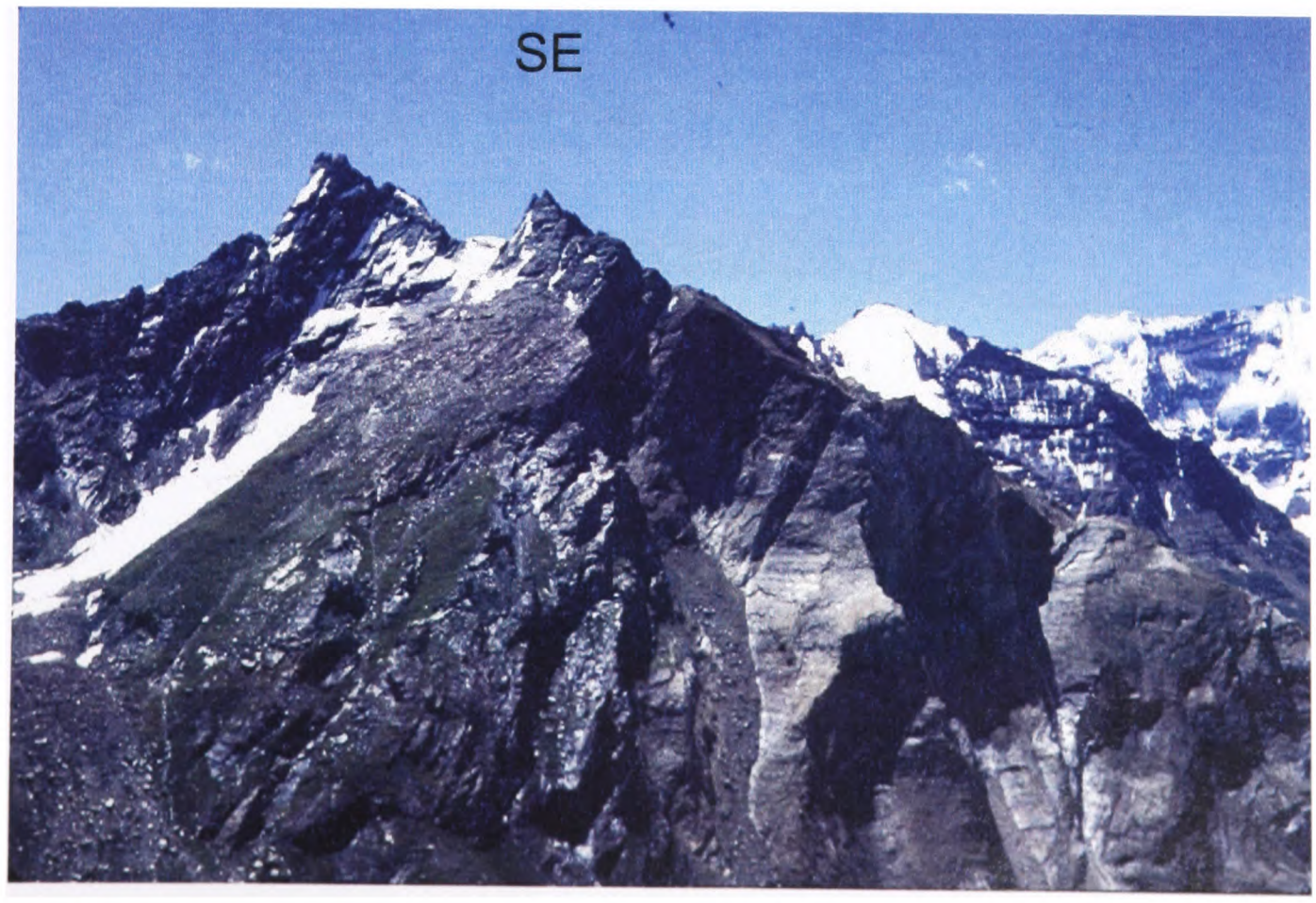
Figure 2.10. Photo montage from the centre of the Suru Dome looking W and N, illustrating major structures. The Donara and Tapshah nappes are highlighted by the marble/amphibolite bands (dashed lines).



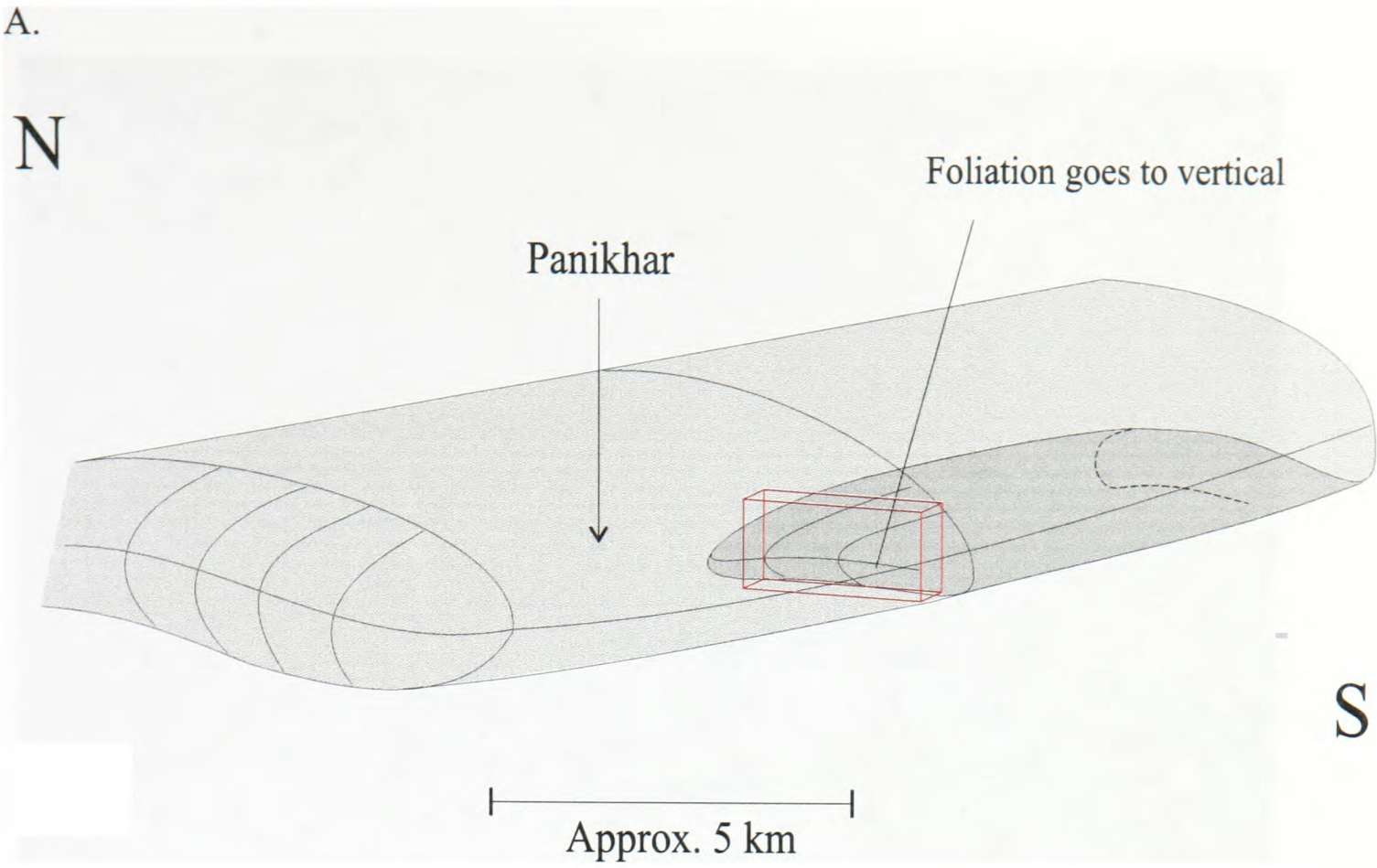
Figures 2.11. and 2.12. Two views, taken from roughly the same spot, illustrating the structure along the Chellong nala, around the Donara nappe.

Figure 2.11.,above, shows the tight recumbent fold in Panikhar Peak, picked out in granites (light) and amphibolites (dark).

Figure 2.12. below, shows steeply dipping amphibolites (dark) and marbles (light) across the valley from the closure of the SW-vergent Donara nappe (Figure 2.4). This illustrates well the three-dimensional structure of the interlocking recumbent folds; this near-vertical part of the structure can be thought of as the "edges" of a sheath fold if viewed end-on (figure 2.13). Over the top of the sharp peak at the left of the photo lies the NE-vergent fold above Tongul (Figures 2.8. and 2.9.).



A.



B.

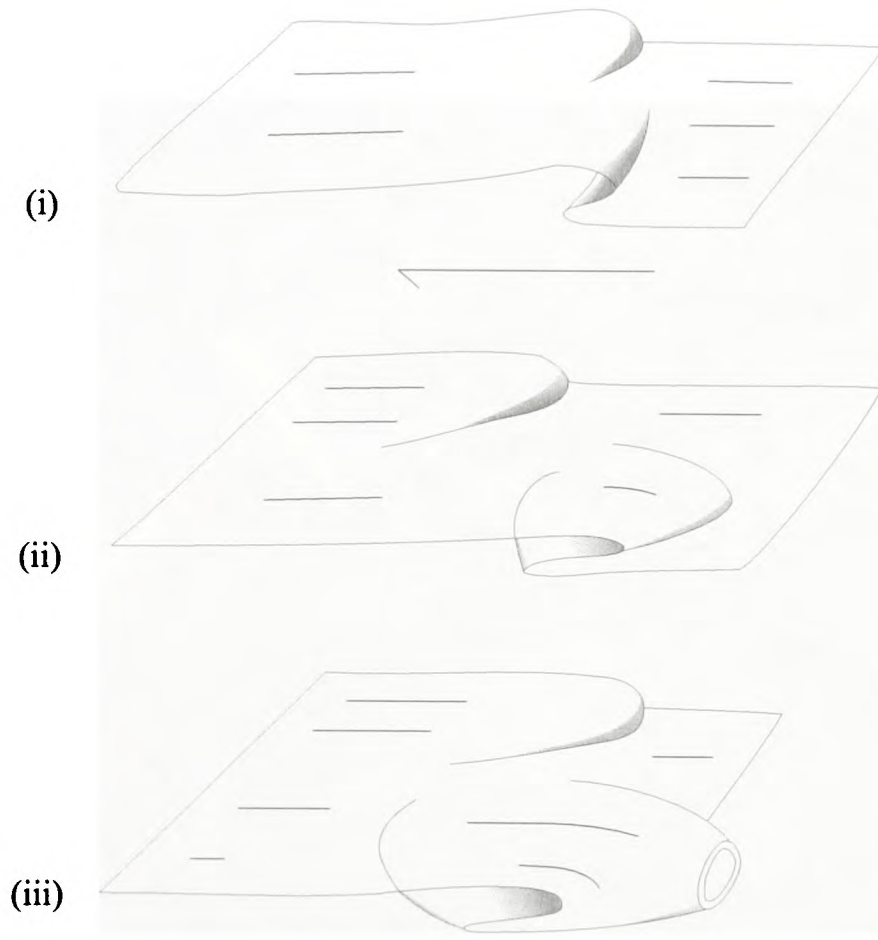


Figure 2.13. A) Diagrammatic 3-D section through the Donara nappe illustrating the geometry of the field relations described in Figure 2.12. Box size is roughly proportional to the field of view in the photograph. B) Geometry of sheath folds showing how erosion can produce an "eye" structure, and the development of the structure described in Figures 2.12. and 2.13.A. (After Price and Cosgrove, 1990 Chapter 10).



Figure 2.14. Photo showing an isoclinal fold in an amphibolite layer within the pelites/ semi-pelites of the Donara nappe. Hammer is approximately 30cm in length.



Figure 2.15. Photo illustrating tight-to-isoclinal folding within a marble unit to the south of Tongul.

syn-tectonic porphyroblasts in places (Chapter 3), early isoclinal folding would appear to be a plausible method for crustal thickening. Sense-of-shear indicators, such as quartz blebs and veins, and minor folds (Figure 2.18.) indicate top to the south-west sense of shear.

D_2 is the most obvious deformational event, forming the dominant S_2 matrix foliation that defines the large-scale nappes. It is generally syn-post peak M1 metamorphism i.e. the Barrovian event producing the mapped isograd sequence (Stäubli 1989). D_3 is related to the formation of the Suru Dome and is responsible for the dominant S_3 Suru Dome foliation, and (probably) D_3 crenulation of the S2 fabric in the overlying nappe rocks. In sample Z-47, a pelite from near the closure of the Donara nappe, garnet porphyroblasts overgrow an S_1 fabric that is discordant with the matrix S_2 foliation. This S_2 fabric is subsequently crenulated by a later D_3 event. Some kyanite porphyroblasts are aligned with the matrix foliation, implying that they are pre-syn deformation. Sample Z-4, a garnet-hornblende calcareous pelite from south of Tongul contains very pronounced spiral inclusion trails in garnets, with, apparently post-tectonic hornblende crystals. Some samples, however, such as Z-10, from south of Tongul, show trails of ilmenite inclusions that are continuous from the outer part of garnets into the matrix, which has itself undergone extensive recrystallization without a dominant foliation being imposed. This, and other more ambiguous samples (i.e. those in which it is not as easy to distinguish separate pre/post porphyroblast fabrics) suggest that the metamorphic/deformational history is that of a continuously evolving event which is differentially preserved in rocks of different bulk composition (more pelitic samples generally show more pronounced foliation/ crenulation than psammitic ones) and in which the relationships probably vary with structural height above the Suru Dome. This is discussed in more depth in chapters 3 and 4.

In biotite-chlorite grade pelites and semi-pelites a few hundred metres from the ZSZ itself, original bedding (S_0) can be determined. From bedding-cleavage (S_1) relationships (Figure 2.16.) which indicate way-up, it can be seen that the structure near the shear zone consists of a series of upright tight-to-isoclinal folds, that have subsequently been crenulated (Figure 2.17.). This low-grade deformation is possibly an insight into the early phases of deformation that have not been obliterated by higher temperatures and recrystallization (see above).

A few kilometres south of Sankoo, field evidence for more than one cleavage in garnet-grade rocks can be seen, as the dominant S_2 schistosity overprints an earlier (S_1?) foliation. Although one cannot trace the change in foliation continuously across the area, it



Figure 2.16. Photo illustrating S_0/S_1 bedding/cleavage intersection in biotite-grade semi-pelites near Sankoo. Bedding dips more steeply than cleavage, which suggests that the unit is structurally overturned, if this is a first cleavage. Note prominent quartz vein parallel to S_1. Clinometer approximately 10 cm long.

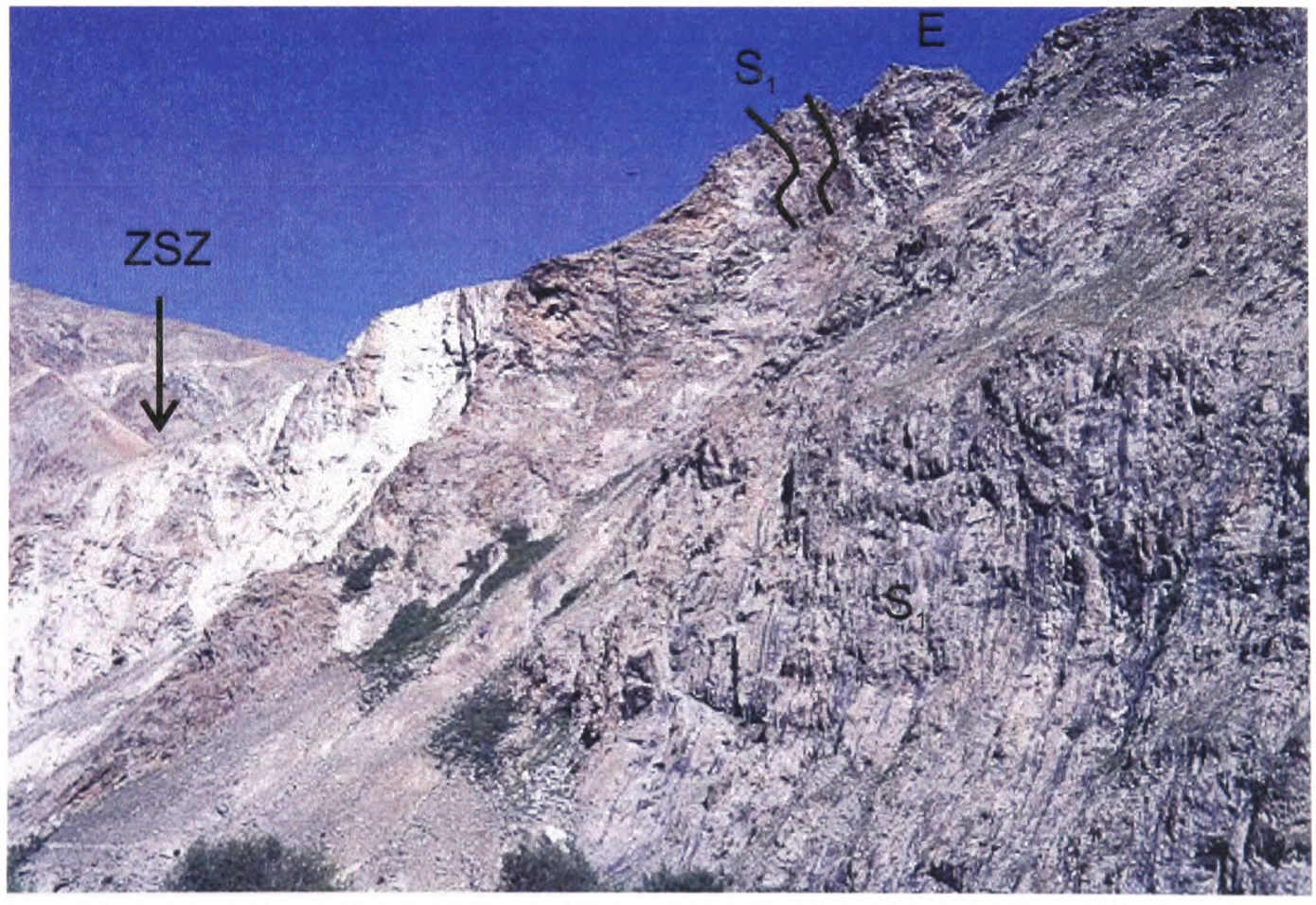


Figure 2.17. Photo looking E towards the ZSZ and the top of the HHC at Sankoo illustrating crenulations in S_1/S_0 which are generally upright and probably related to movement on the ZSZ. Field of view approximately 500 m.

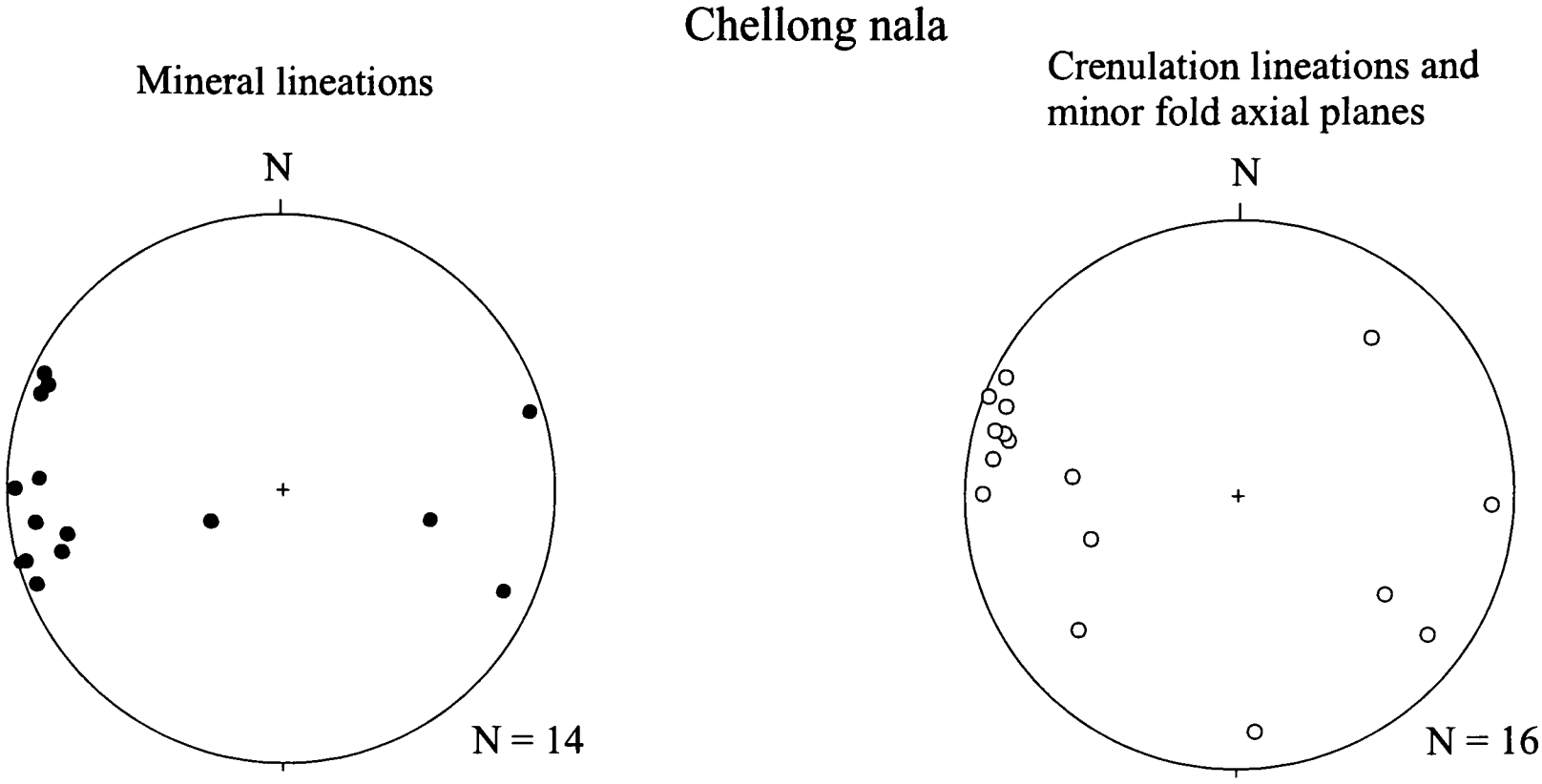


Figure 2.18. Stereoplots illustrating mineral stretching lineations and crenulation lineations / fold axial planes from south of Tongul and along the Chellong nala. Mineral lineations along the edge of the Suru Dome suggest extension due to doming, whilst crenulations and minor folds further along the Chellong nala imply WNW-ESE shortening.

seems that the lowest grade rocks preserve the earlier fabrics in the field, whilst these are only occasionally visible as inclusion trails in garnets in higher grade rocks such as those of kyanite grade in the Donara and Tapshah nappes.

Suru Dome rocks are generally coarser-grained and appear to contain a later S_3 foliation associated with a kyanite-grade M2 metamorphism and D_3 domal event.(Stäubli 1989; Searle *et al.,* 1992) on a microstructural level. This M2, and associated D_3 event, does not appear to greatly affect the overlying nappes. In the field, this is probably represented by S-C shear fabrics, such as those seen near Parkatchik, on the eastern flank of the dome, and near Panikhar on the western side. (Gapais *et al.,* 1992). These shear fabrics cut across an earlier foliation, and define the structure of the dome, dipping away from the centre. Crenulation of the nappe S_2 fabric may be related to this doming event.

2.2.2.2 Mineral lineations and minor folds

In addition to the major structures, minor kinematic indicators can be used to interpret the tectonic evolution of the area. Where possible, mineral lineations, crenulation/intersection lineations and minor fold axial planes were measured and used to corroborate inferences made from the large-scale structures.

Mineral stretching lineations appear to occur in greatest abundance in the nappes around the flanks of the Suru Dome, and in the Sankoo nappe near the ZSZ. (Figure 2.18.) Around the Suru Dome the lineations plunge at shallow angles of up to around 20^0 away from the centre of the dome, as does the main foliation trend. SW of Panikhar, and along the Chellong nala, the lineations plunge fairly consistently SW. South of Tongul they plunge in a more easterly direction. The most likely explanation for this is stretching due to the doming event and subsequent sliding of the nappes off the top (Figure 2.19.). Lineations near the closure of the Donara nappe generally show a SW trend, although the dip of the foliation is not as constant as that around the Suru Dome due to minor folding.

Near the ZSZ at the top of the slab, mineral lineations plunge much more steeply (40-50^0), as does the foliation, in an ENE direction. These lineations are most pronounced in the Sankoo granitoid body, where biotite, quartz and plagioclase show strong alignment. Although flexural slip during folding is a possibility, the activity of a major detachment on the scale of the ZSZ in such close proximity would almost certainly cause such a lineation. The azimuth of these lineations with respect to the strike of the ZSZ immediately to the north implies a possible dextral strike-slip component of movement on the fault in addition to the

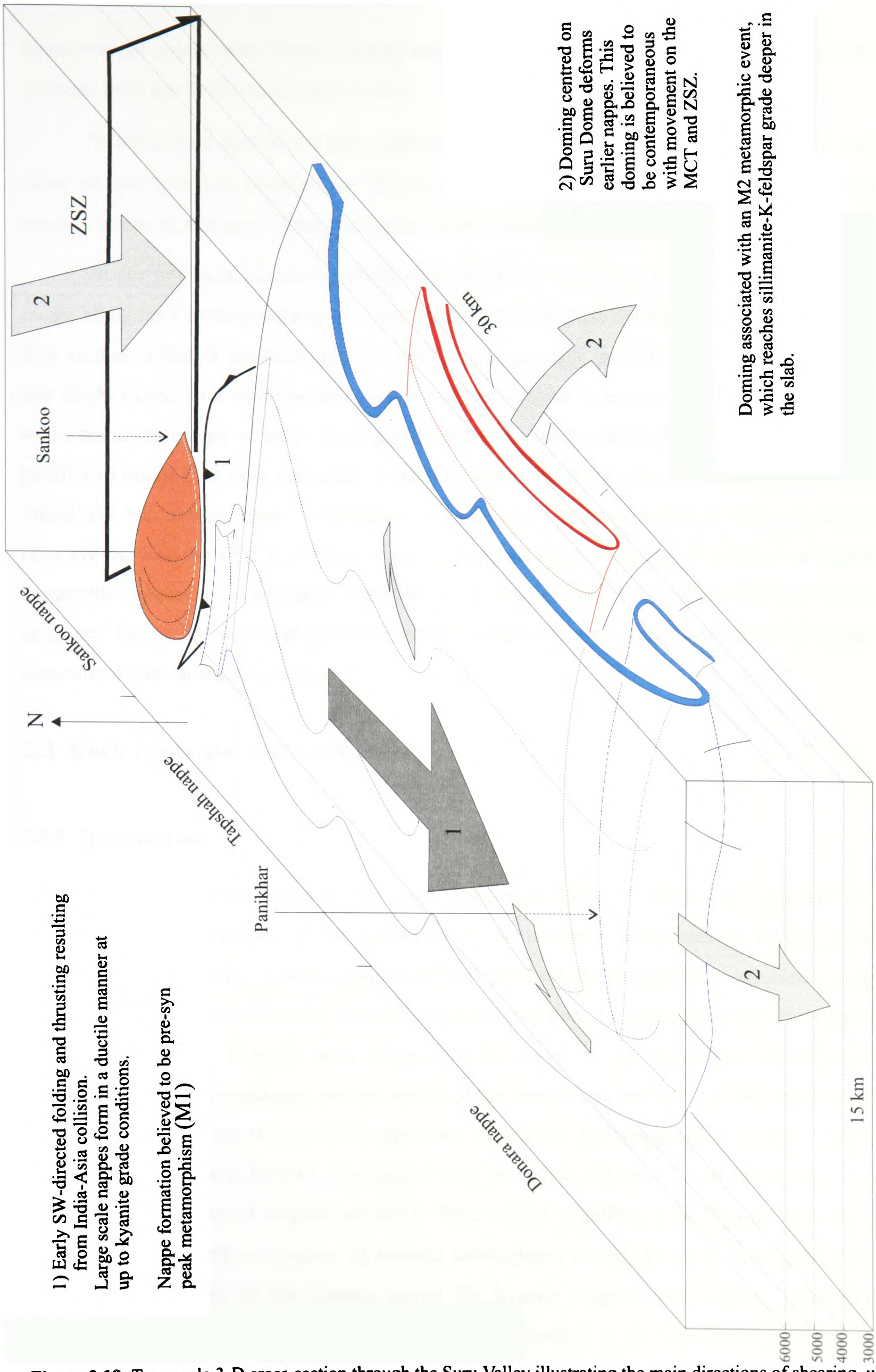


Figure 2.19. True-scale 3-D cross-section through the Suru Valley illustrating the main directions of shearing, with respect to the small-scale structures described in the text and in Figure 2.18.

major normal component. Walker (1998) also suggested such a component from migmatitic gneisses from the Temasa nala near Padum.

In the central part of the slab, such as in the Tapshah nappe, lineations are rare and show no real trends or correlations. This is possibly due to lower strain away from major tectonic contacts, and later folding of lineations on minor folds.

Minor fold axial planes and crenulation lineations occur most frequently in the Donara nappe along the Chellong nala, and around the Suru Dome. Fold axial planes have strikes and dips similar to that of the main foliation, and appear generally parasitic to the major folds, as one might expect in a highly-strained terrain. Sense of shear indicators generally indicate top to the south-west sense of shear. Crenulation lineations plunge almost always along strike, and parallel to minor fold axes, and most of this minor fold evidence appears to be related to the initial SW-NE striking nappe axial planes that have since been deformed by the later domal (D_3) event. Near the ZSZ at Sankoo, metre-scale crenulations in the biotite and garnet-grade metapelites appear to be related to extension on the ZSZ (Figure 2.17.). Shear indicators such as quartz bands and quartz-plagioclase enclaves indicate a top to the E-NE sense of shear, concordant with mineral lineations.

2.3 Rock types and metamorphism

2.3.1 Introduction

The metamorphic rocks of the High Himalayan Slab are thought to represent the metamorphosed equivalents of the sediments of the northern Indian margin to the north (Searle, 1986; this study). Kyanite grade conditions persist in the centre of the area, decreasing to the north, west, and south-west and defining a roughly domal isograd structure (Honegger, 1983; Searle, 1989). Isograds were mapped on the basis of the appearance of indicator minerals in pelitic assemblages, but the nature of the terrain and the fact that the majority of the rock types were not of suitable composition means that the mapping of isograds across large areas is extremely difficult. The isograd map produced (Figure 2.3. and Enclosures 1 & 2) relies on the outcrop of isograd surfaces in three valleys (Chellong nala, Shansin nala, Suru valley) and the general occurrence of mineral assemblages across the area. In the Chellong nala near the closure of the Donara nappe the kyanite isograd was mapped using the occurrences of kyanite through kyanite + staurolite to staurolite. In the Suru valley to the north the staurolite isograd was less clear and based mainly on the occurrence of staurolite without

kyanite in one unit of suitable composition. The garnet isograd south of Sankoo can be defined by the first occurrence of garnet, which although also dependent on composition, is stable in a much wider range of compositions.

From the isograd outcrop pattern, isograds can be seen to cross-cut earlier structures such as the marble/amphibolite unit in places, but are generally folded around the nappes. This is corroborated in some thin section samples, where kyanites and staurolites can be seen to be at least pre-to syn-tectonic (D_{2-3}). However, porphyroblasts are also seen to overgrow the main matrix foliation in some samples. The same is true for garnet porphyroblasts; in both the Donara nappe, and from the section south of Tongul, garnets can be seen to be wrapped by the foliation in some lithologies, but overgrowing it in others. This suggests a more complex relationship between deformation, metamorphism and bulk composition, which will be more fully discussed in following chapters.

The most common rock types are semi-pelitic to pelitic in composition, often slightly calcareous, with associated calc-pelites and psammites. A marble unit varying between 170 and 500 m in thickness, associated with smaller amphibolite bands above and below, is the most distinctive unit, and is extremely useful for mapping out the large-scale structure of the area. Granitoid bodies interbanded with both pelitic and amphibolitic rock types are also important, notably the Sankoo granite/amphibolite body which defines a large domal structure at the top of the slab. Two logs through the marble/amphibolite units and associated lithologies were made, one south of Tongul, on a metre scale, and the other through the closure of the Donara nappe, on a 10 metre scale. Schematic diagrams of these logs are shown in Figure 2.20. in comparison with the Permo-Mesozoic sequence shelf sequence from Kashmir/Zanskar (after Honegger, 1983; Gaetani & Garzanti, 1991). The similarities between both the logs from the Suru Valley, and the unmetamorphosed shelf sediments is striking; the juxtaposition of amphibolites, calc-pelites and marbles from Tongul and Donara shows a strong correlation with the Panjal Trap volcanics, sandy limestones and massive limestones of the Upper Permian-Lower Triassic of Zanskar. Geochemical studies by Honegger *et al.* (1982) suggest a common origin for the Panjal Traps and the amphibolites of the Suru Valley. It is therefore proposed that the metasediments of the Suru Valley are the metamorphosed equivalents of the Zanskar Palaeozoic/ Lower Mesozoic shelf sediments. Although Honegger (1983) recognised the marble/amphibolite units as being Mesozoic in origin, he ascribed Precambrian ages to all the surrounding pelitic and semipelitic lithologies and granitoids. This seems unnecessary for two reasons; 1) There is no break, tectonic or otherwise, between the "Mesozoic" bands and the under-and-overlying lithologies; 2) Noble *et al.* (in prep.) have

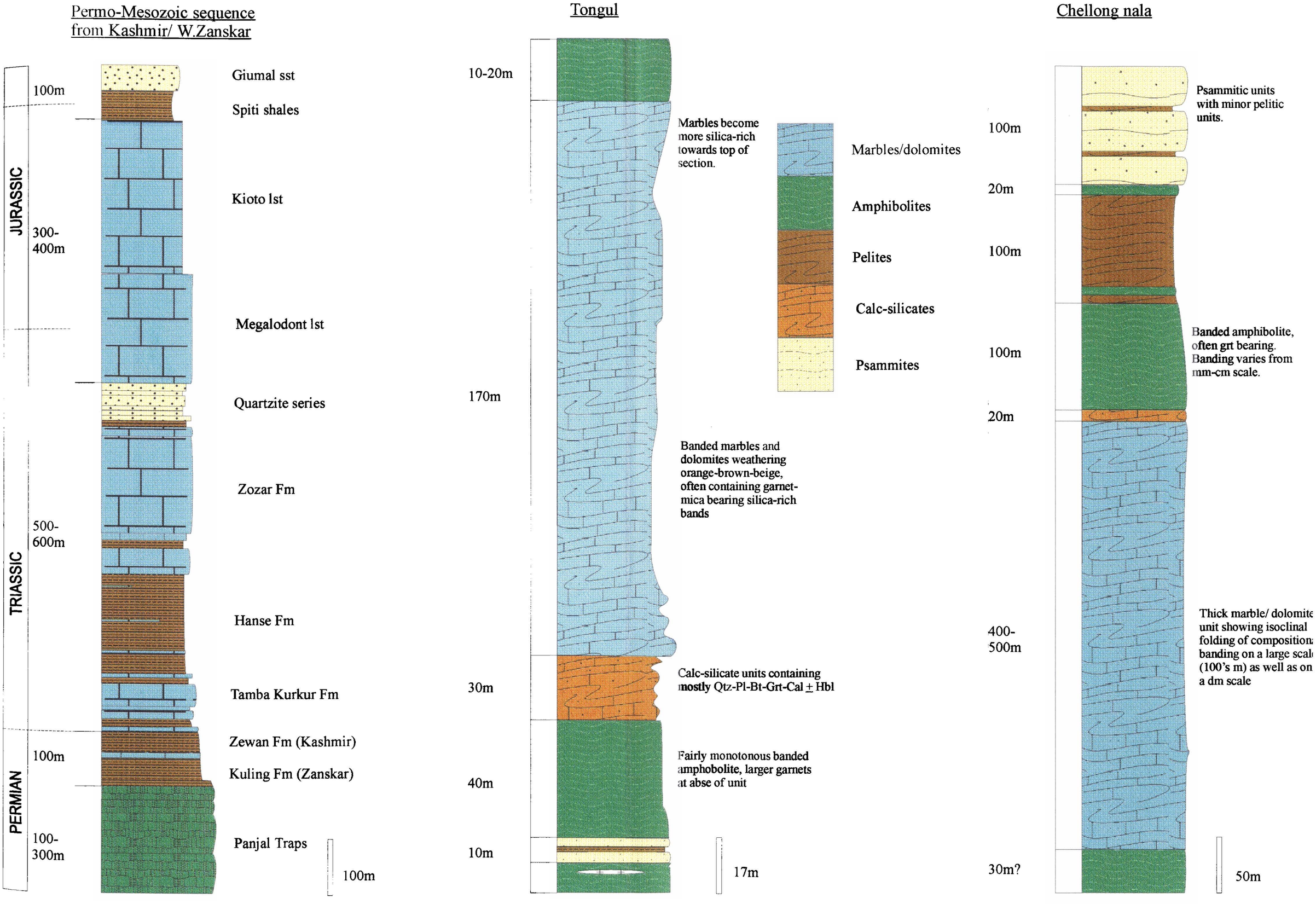


Figure 2.20. Lithological correlation between Suru valley units and Permo-Mesozoic sedimentary sequence.

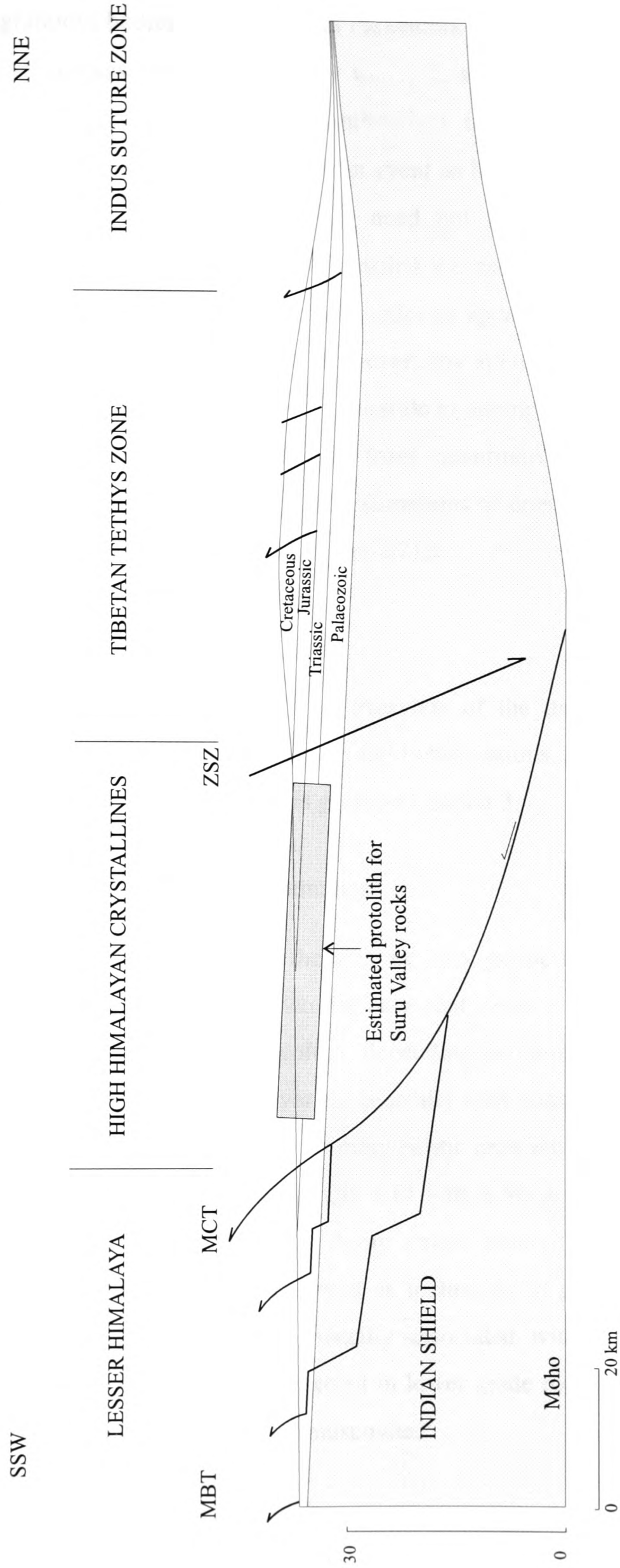


Figure 2.21. Palinspastic reconstruction of the northern continental margin of the Indian plate and the Tethyan oceanic margin in the late Cretaceous, prior to collision and metamorphism of the High Himalaya. The rocks of the Suru Valley are interpreted as the metamorphosed equivalents of the Palaeozoic-Mesozoic rocks of the Tethyan shelf sediments of the Zanskar Himalaya. Restoration of the Suru Valley section, and approximating depth of burial from P-T calculations implies at least 150-200km of shortening. Modified after Searle (1986).

dated the granitoid bodies at Sankoo and Parkatchik as being Permian in age, roughly coeval with the Panjal traps. This is extremely useful in a number of ways; a young age for the protoliths, demonstrates that the metamorphism in the Suru Valley area is definitely Himalayan in age, and an earlier Cambrian event as has been suggested in other parts of the Himalaya. (e.g. Pognante *et al.*, 1990), need not be invoked. Furthermore, with such stratigraphic constraints (and using P-T results) we can attempt to partially reconstruct the HHC prior to deformation and subsequently infer an approximate amount of shortening. In an area of such high ductile deformation, however, any attempts at line balancing and restoring cross-sections become meaningless. It is possible to attempt area balancing by estimating the maximum depth these rocks attained, from quantitative thermobarometry and rough reconstruction of the "unfolded" nappes. Estimations of crustal shortening using this method are on or of the order of 150-200km. (Figure 2.21.).

2.3.2 Description of rock types .

The following section offers an overview of the major compositional differences between the different rock types, based on field observations. A more detailed analysis of the petrography of the collected samples is given in Chapter 3.

2.3.2.1 Pelites , semi-pelites and psammites.

The majority of the units in the area are semi-pelitic to pelitic in composition, often with minor bands of more pelitic material on a centimetre to metre scale. In the field these rock types appear a brownish-grey colour, depending on composition and the attitude of the foliation. The intensity of foliation varies, generally with composition; more psammitic units tend to be more well-bedded, whilst the more pelitic beds are often highly crenulated. These rocks typically contain the parageneses Qtz + Pl + Bt ± Ms ± Grt, with staurolite and kyanite depending on grade and Al content. More calcic units can contain minor calcite and zoisite/clinozoisite, usually only preserved as inclusions in garnet. Rutile and ilmenite are common accessory phases. Chlorite, usually associated with ferromagnesian minerals, is generally thought to be retrogressive except in lower grade rocks such as those near Sankoo, where it defines a foliation along with muscovite.

2.3.2.2 Calc-pelites

Calc-pelitic units, such as those seen below the marble unit at Tongul and in the Donara nappe closure, generally contain the above parageneses, but with more calcite preserved in the matrix, and they commonly contain hornblende and sphene. They tend to weather a more orange colour, and are coarser grained than most pelites.

2.3.2.3 Marbles

The most distinctive unit consists of massive beige-yellow-brown-orange marbles and calc-silicates which can be seen to outcrop virtually continuously from south of Tongul to the Sankoo nappe. These are highly deformed, and contain much intrafolial isoclinal folding, which possibly preserves evidence of an earlier phase of deformation prior to nappe formation; this best seen in the closure of the spectacular Donara nappe in the SW of the area, and south of Tongul (Figure 2.4.). The mineral assemblage depends on the purity of the marble but is generally Cal ± Dol ± W.mica ± Qtz ± Phl ± Rt and occasionally zoisite (Sample Z-65). The thickness of this marble unit varies from around 170m south of Tongul to up to 500m in the closure of the Donara nappe (Figure 2.20).

2.3.2.4 Amphibolites

The marble unit is everywhere over and underlain by amphibolite units, which vary in thickness from around 20m south of Tongul, where the whole sequence appears condensed, to 100m in the Donara nappe closure. The amphibolites do not always occur as continuous units, but are often interbanded with the surrounding metapelitic units on a scale of a few tens of metres. Amphibolitic units of similar appearance occur interbanded within the pelitic/semipelitic units throughout the area, and not only associated with the marble bands, such as those at Chandra, and above the Chellong nala. They can vary in thickness from tens of centimetres to tens of metres. Although similar in appearance in the field, they appear to vary in composition on petrographic examination. All contain Hbl + Pl + Bt + Qtz ± Grt ± Spn ± Ep, but some also contain Cal, Zo/Czo in the matrix .

2.3.2.5 Granitoids

The final major rock types encountered in the Suru Valley are granitoid bodies, which fall into two main categories; Himalayan leucogranites, and pre-Himalayan granites (Searle & Fryer, 1986; Kündig, 1989). Leucogranites are not found in the area mapped, but are

important in the tectono-metamorphic evolution of the HHC, and so are described in reasonable detail here.

Leucogranite bodies are found throughout the HHC, generally associated with high-grade metamorphic rocks and migmatites (Le Fort, 1981; Dietrich & Gansser, 1981; Searle, 1983), and make up to possibly 30% of the map area of the HHC in Zanskar, Kulu, Lahoul and Kishtwar-Kashmir (Searle & Fryer, 1986). At deeper levels in the crust ultrametamorphism results in *in situ* anatexis, migmitization and *lit-par-lit* intrusions or stromatic layering within high-grade metasedimentary rocks. In Zanskar and Kashmir, at higher crustal levels, leucogranites tend to form relatively small sized intrusions in the form of dykes and sills, with rarer large stocks and sills (Burton, 1995). Migmatites and leucogranites are not found in the MCT region, suggesting that frictional heating along a fault zone is not responsible for their formation (Searle *et al.*, 1992). U-Pb data from leucogranites in Zanskar give a date of 21-19.5 Ma for crustal melting, and show that anatexis occurred along the Himalayan chain from Kashmir-Zanskar to eastern Nepal at ~ 24-19.5 Ma. (Noble & Searle, 1995). The leucogranite bodies occurring in the Suru Valley are most abundant around Shafat, to the east of the study area, and are dated at 20.8 ± 0.3 Ma. (Noble & Searle, 1995). The descriptions given here are taken mainly from Burton (1995). Leucogranites are peraluminous (Le Fort, 1975), and typically contain the paragenesis Qtz + Pl + Kfs + Ms + Grt + Tur ± Bt. They generally show good igneous textures and are rarely strongly deformed, cross-cutting the foliations in the sillimanite grade metasediments and older granites that make up the country rock. However, quartz also displays undulose extinction, and in some samples a coarse foliation, defined by the alignment of white micas and quartz recrystallization, is apparent.

Pre- Himalayan, megacrystic granites, unlike the Himalayan leucogranites, occur in the mapped study area, as well as being described from other parts of the HHC, (Kündig, 1989), where they usually form the cores of large gneiss domes at deeper structural levels in the Himalayan slab. They display deformational fabrics, and are folded along with the surrounding metamorphic rocks, implying that they underwent Himalayan deformation and metamorphism. Burton (1995) comments on two further mineralogical features of the megacrystic granites, from the Shafat region, that indicate a pre-Himalayan age. Antiperthitic plagioclase is common, suggesting temperatures greater than 800 ^{0}C (Deer *et al.*, 1982), which are in excess of those proposed for the Himalayan metamorphic events (~750 ^{0}C, Searle *et al.*, 1992). Furthermore, the presence of small oriented white micas and clinozoisite in plagioclase crystals (a *gefüllte* texture) is characteristic of metamorphism of pre-existing

granitoids at a lower temperature than magmatic crystallisation. Both of the above features are present in the pre-Himalayan granite samples from the mapped study area.

The megacrystic granites mapped in the Suru Valley typically contain the paragenesis Qtz + Pl + Kfs + Bt +Grt ± Ms, with a coarse foliation being defined by alignment of biotite flakes and preferential orientation of quartz. K- feldspar crystals often form megacrysts of up to 8 mm in length, sometimes displaying shear fabrics, such as those seen above Thamo (Burton (1995) reports megacrysts of 6cm from Shafat). Burton (1995), describes increasing modal proportion of garnet with increasing amount of deformation in the megacrystic granite, and a decrease in the amount of biotite.

There are three main granitic bodies mapped in the area of the Suru Valley that appear similar to the pre-Himalayan type; the Sankoo granite, Parkatchik granite, and a sill-like body between 20->120 m thick, interbanded with metapelites and amphibolites, that defines a nappe structure tectonically immediately above the Suru Dome, the mineralogy of which is described above. The Sankoo and Parkatchik bodies are more unusual and warrant further description.

The Parkatchik granitoid is interfolded with pelite/marble units in the nappe to the south of Tongul (Figures 2.22., 2.23.), and contains Qtz + Pl + Bt + Grt ± Ms. It shows a clear foliation, defined by alignment of biotite flakes and preferential alignment of quartz and plagioclase. Garnet tends to be fairly abundant.

The Sankoo nappe is a body unlike any other seen in the Western Himalayas, comprising a large (~2 km thick) domal nappe structure in interbanded granites and metabasites. From the south it appears as a huge sheath fold (Figure 2.24.). The metabasic units are thinner than the granitic sheets (~1.5m max), and are folded with the granite sheets, defining the structure (Figure 2.25.). They can sometimes be seen to be isoclinally folded within the granitic sheets. The granite as sampled south of Sankoo contains the paragenesis Qtz + Pl + Kfs + Bt + Ms + Grt + Ilm ± Ep, and shows mineralogical features such as gefüllte plagioclase as described above. The interbanded metabasite contains Ep + Bt + Kfs ± Pl + Qtz + Spn + Rt. The detailed petrography of these rocks, along with the other lithologies, is described more fully in the next chapter.

What makes the Sankoo nappe unusual is not the composition of the granite and metabasic units, which do not appear to be significantly different from other pre-Himalayan bodies, but the intimate fine-scale (dm-m scale) interbanding of the two rock types. Tectonic processes such as isoclinal folding related to early deformation must account for this in some

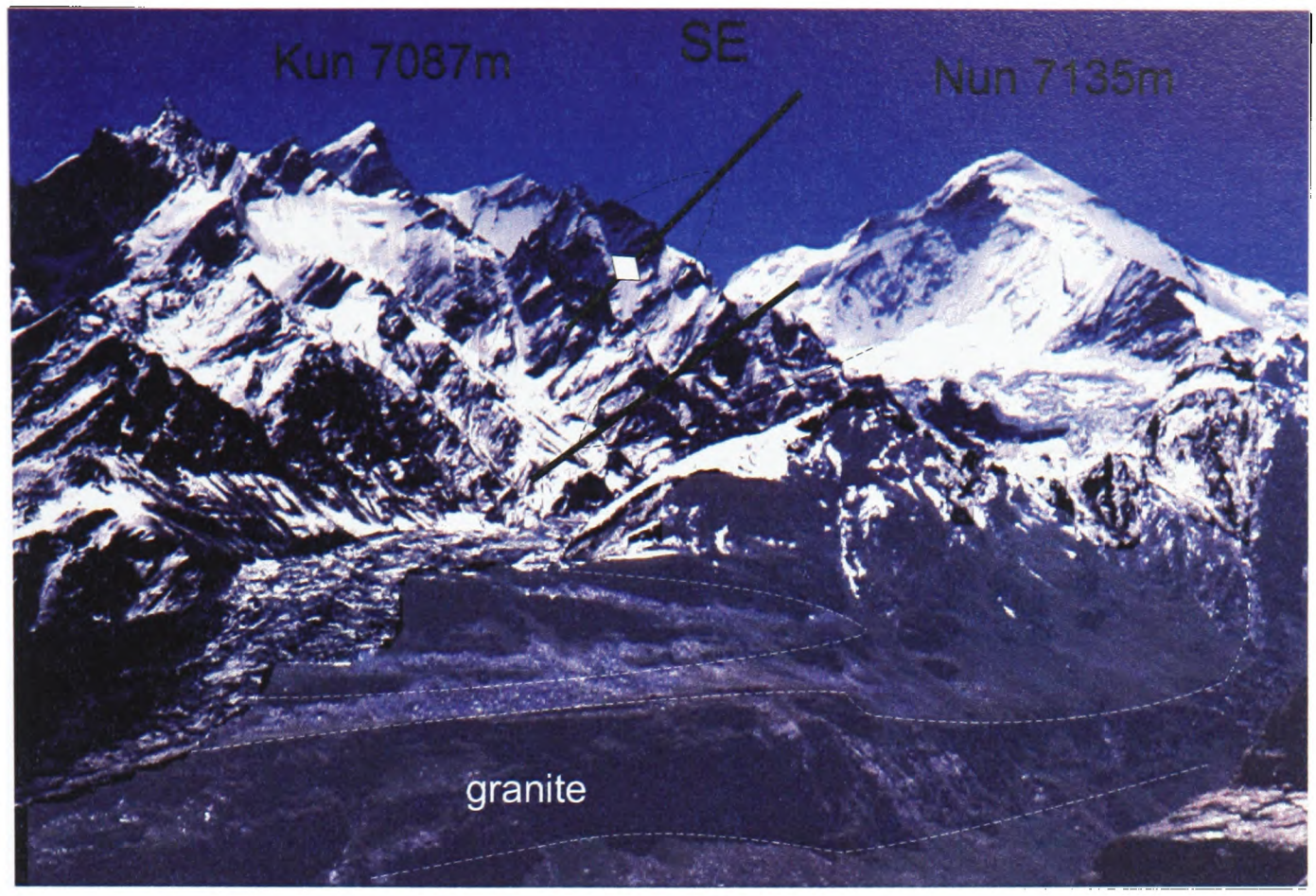


Figure 2.22. View SW from the top of the Suru Dome over the Parkatchik granite (foreground) and the Nun-Kun massif (background). The Parkatchik granite, which is highlighted, is folded with the nappes around the Suru Dome. Tight folding can be seen in the 3 km high face of Kun.

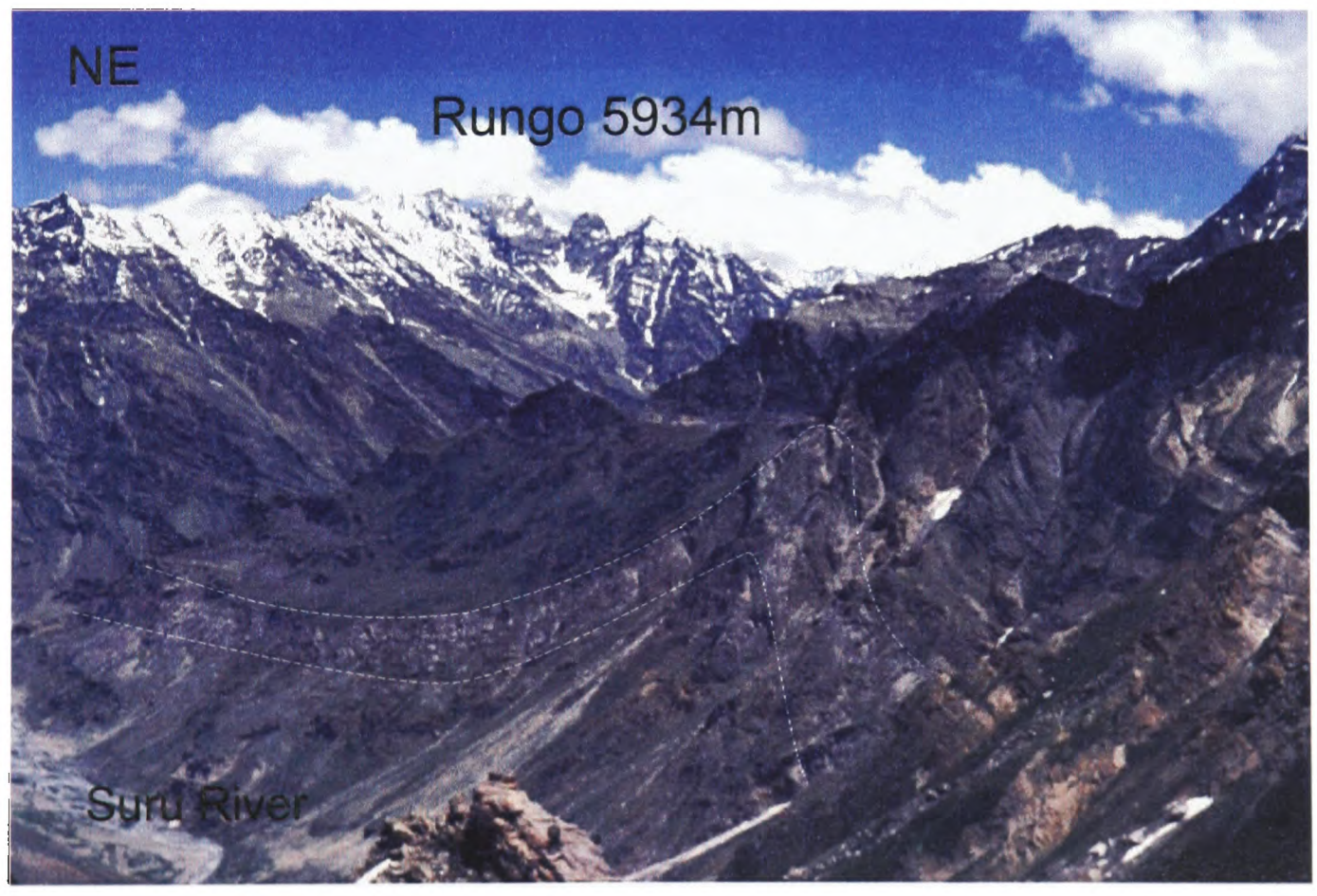


Figure 2.23. View looking NE to the Parkatchik granite from around 4800m altitude to the south of Tongul. This photo illustrates the folding of the granite around the NE-vergent fold more clearly. The Suru Dome is just out of picture to the left, Kun is to the right.



Figure 2.24. View looking N to the Sankoo nappe, which folds granite and amphibolite sheets, seen here as a large sheath fold (highlighted). Vertical relief approximately 2 km. The brown rocks in the foreground are pelites, semi-pelites and calc-pelites of kyanite and staurolite grade.

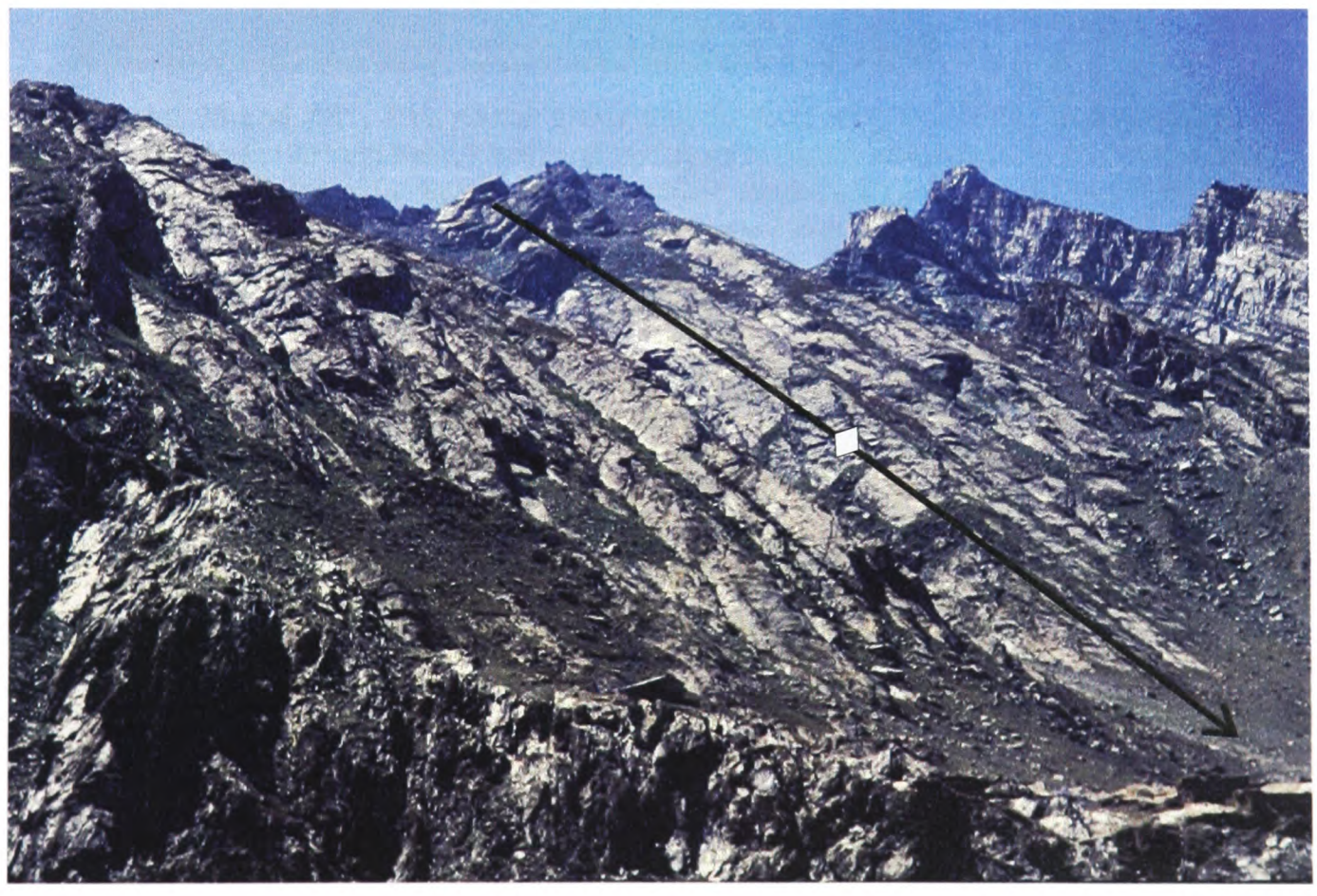
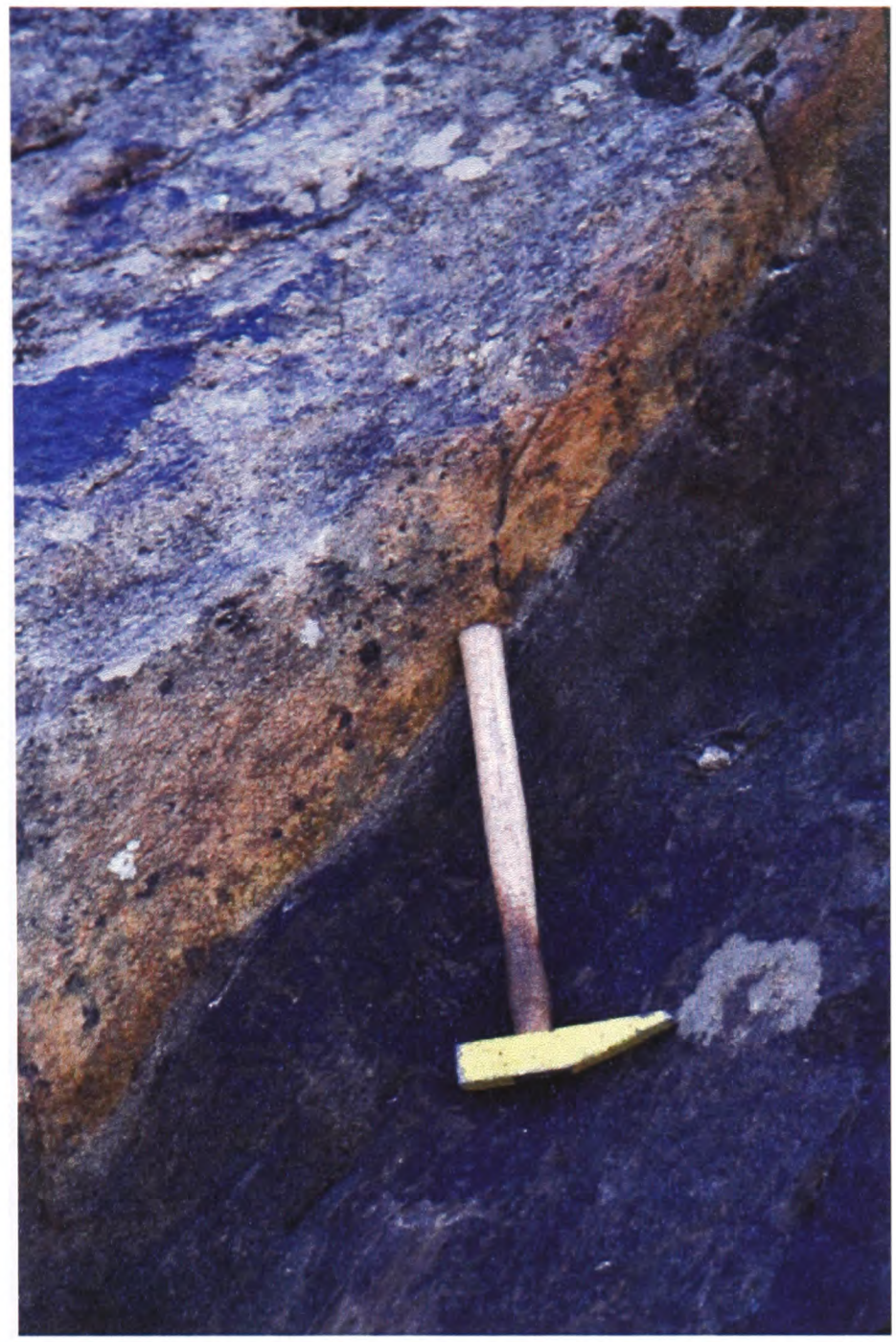
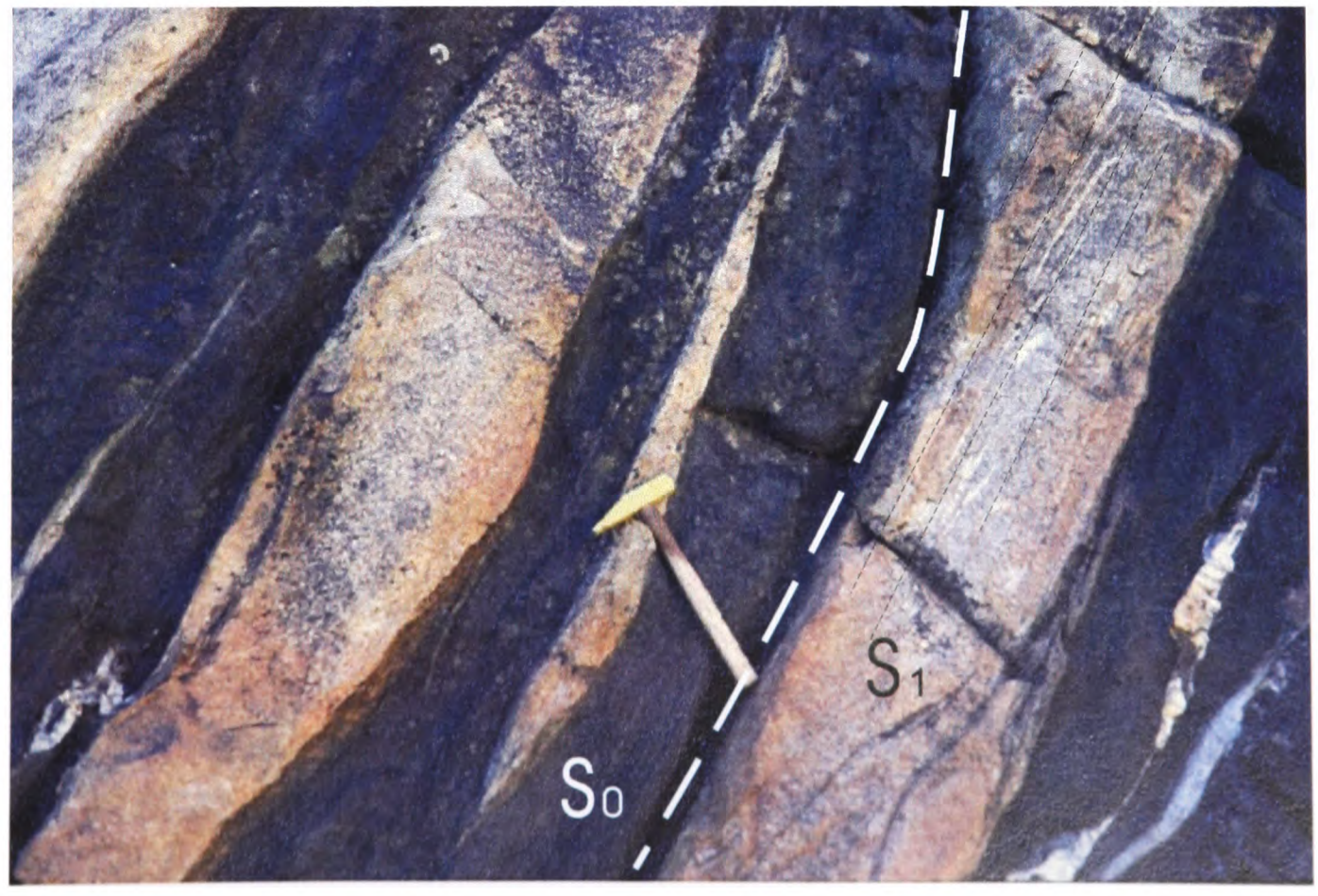


Figure 2.25. View W along the axial plane of the Sankoo nappe from near the bridge at Sankoo. The cliff on the right shows the dark bands of metabasite intruding, and deformed with, the granite.



Figures 2.26 and 2.27. Two photos illustrating the field relations of the Sankoo granitoid body. The contact between the metabasic (dark) and metagranite (light) units can be seen to be slightly oblique to the metamorphic foliation, suggesting a discordant emplacement before deformation. The inclusion of granite stringers within the metabasic layers (below) also implies that the basic dykes intruded the granite.



part, but field relations suggest that that granite body was intruded by basaltic sills; firstly, the subordinate amounts of basic rock; and secondly, the slight discordance between granitic foliation and the granite/basalt contact in places (Figures 2.26., 2.27.).

Spring *et al.* (1993) describe an alkali granite of Permian age (284 ± 1 Ma) from SE Zanskar/ Lahoul, the Yunam granite, which they ascribe to an anorogenic, rifting event which precedes by approximately 10 Ma the Panjal Trap extrusions. This granite is closely associated with parallel microgabbroic dykes, both rock types being on a scale of 2-15 m. Dates of 268 ± 5 Ma have been proposed for both the Sankoo and Parkatchik granites by Noble *et al.*, (in prep.). Although the dates of the Sankoo and Parkatchik granites differ from those of the Yunam granite by some 20 Ma, the similarity of the structure and basaltic dyke/granite association between them suggests that their mode of formation must have been similar. It is likely that all the Zanskar alkali granitoids are related to an anorogenic rifting event that occurred over a significant period of time.

The megacrystic granites described by Kündig (1989); Burton (1995), and others are generally believed to be at least Cambrian in age (e.g. Pognante *et al.*, 1990), and so would appear to be a different type of granite to the major units found in the study area. Furthermore, the package of rocks that comprises the HHC in the study area is believed to derive from an Upper Palaeozoic-Lower Mesozoic protolith (see above), which would be unlikely if the granites intruded were of Cambrian age.

2.3.3 Suru Dome rocks

The rocks of the structurally lowest part of the area, the Suru Dome, are generally quite distinct from those of the overlying nappes in the field. The Suru Dome is comparable to the deeper level granite gneiss domes described by Kündig (1989) from around the Kishtwar Window and central parts of the HHC. The domal event leading to the formation of these structures is thought to be synchronous with an M2 metamorphic event related to simultaneous movement on the MCT and ZSZ and involving pressure-decrease/temperature increase (Stäubli, 1989; Kündig, 1989). Thermobarometry suggests this M2 event preserved pressures and temperatures of around 8 kb and 700-750 ^{0}C (Searle *et al.*, 1992).

Although the tectonic contact between the dome and the nappes is indistinct in places, Suru Dome rocks can usually be recognised by their Al -rich, kyanite bearing schists. These schists weather a distinctive brown colour, and have anastomosing foliation surfaces. They contain typically Qtz + Pl + Ms + Bt + Grt + Ky ± St , and are generally coarser-grained than

most of the nappe rocks. Muscovite and biotite flakes are abundant and wrap large garnet porphyroblasts. Kyanite crystals grow up to 2 cm and appear randomly oriented on foliation surfaces, such as those seen above the village of Panikhar.

However, some lithologies found within the tectonic boundaries of the Suru Dome are much more felsic, as seen along the ridge to the SW of Panikhar and near the village of Mehta, and are essentially indistinguishable from the semi-pelitic rocks found in the overlying nappes with few indicator minerals. This, along with their structural position with respect to the overlying nappes, implies that there is no need to invoke an entirely separate origin for the rocks of the Suru Dome (Honegger, 1983), in that their protoliths are probably Lower-Upper Palaeozoic sedimentary rocks of the Indian shelf margin.

2.4 Conclusions

The structure of the Suru valley comprises a series of kilometre scale, SW-verging recumbent folds, underlain by a lower, later domal structure, the Suru Dome. These folds have mostly flat-lying axial planes, but steepen towards the ZSZ to the north. The major SW-vergent folds are often separated by NE-vergent folds that are parasitic to the main folds, and occasionally by ductile shear zones. The recumbent folds interlock in a complex three-dimensional pattern, and the axial planes are all domed by the Suru Dome

Three phases of deformation may be recognised in the field, and correlated with microstructural observations (Chapter 3). D_1 is preserved at the lowest grades near Sankoo, where original bedding/cleavage intersections are observed, although intrafolial isoclinal folds at higher grades may represent this earliest phase of deformation. D_2 forms the dominant S_2 foliation, which defines the structure of the area. D_3 is related to the formation of the Suru Dome, and manifests itself as an S-C fabric in the Dome, and at its edges, and also as a crenulation to the S_2 fabric in the overlying nappes.

Around the edges of the Suru Dome, mineral stretching lineations plunge away from the Dome on all sides, implying a sliding of the overlying nappes off the top. Mineral lineations near the ZSZ trend ENE and are related to movement on the ZSZ, which may imply a component of dextral strike-slip on the fault as well as a dominant normal sense of shear. Crenulation lineations and minor fold axial planes are generally parasitic to the major fold axes, especially in the Chellong nala, and are believed to be related to NE-SW compression. Metre-scale crenulations at Sankoo are related to movement on the ZSZ.

Isograd surfaces, although not always clear, appear to cross-cut early structures but are folded to an extent around the major folds. This, along with microstructural evidence, suggests syn-metamorphic deformation of the isograds.

Lithologies encountered in the Suru valley include pelites, semi-pelites, psammites, calc-pelites, marbles, amphibolites and granitoids. The metamorphic units are correlated with the Palaeozoic-Mesozoic sediments of the Tethyan shelf margin, and the granitoids are found to be of Permian age, and related to the Panjal traps. This confirms a Himalayan age for metamorphism and deformation of the Suru valley. Estimates of crustal shortening are in the region of 150-200 km.

Chapter 3



Afternoon sunlight highlights the limestones of the Zanskar Shelf from the village of Mulbeck on the Leh-Kargil road.

3. Petrography and mineral chemistry

3.1 Introduction

Figure 3.1. illustrates the distribution and location of samples collected in the Suru Valley area. Most of the samples are garnet bearing, these being of greatest practical use for thermobarometry and microstructural studies. They were collected across as wide an area as possible in an attempt to compare P-T data in a range of different rock compositions at varying tectonic levels in the HHC. The majority of the samples were collected along the Suru Valley between Sankoo and Parkatchik and along the adjoining side valleys, but 11 samples were collected during a traverse from the ZSZ at Rangdum to about 12km downstream of Jildo for P-T work.

3.2 Petrographic descriptions

3.2.1 Pelites and semi-pelites

Pelitic and semi-pelitic rocks collected from the Suru Valley traverse are diverse in their textural and microstructural properties, but share a broadly similar mineral assemblage. The most common equilibrium assemblage consists of Qtz + Ms + Bt + Pl + Grt in varying proportions, with Ky, St, Zo/Czo and graphite depending on grade and bulk composition. Most rocks also contain Fe-Ti minerals, which are discussed in a later section. One rock, sample Z9, is extremely Fe-rich and Al-poor, and as such does not contain muscovite, and has K-feldspar-albite instead of plagioclase.

Garnets range in size from less than 0.5mm to up to 2cm in diameter, and occur as euhedral, subhedral and anhedral crystals. Typically, garnet cores contain inclusion trails preserving an earlier fabric than the main matrix foliation; these inclusions comprise quartz, occasional white mica and clinozoisite, and also graphite. Ilmenite and rutile also occur, defining an inclusion fabric. Some garnets are embayed and show textures associated with breakdown, usually to Pl + Ms ± Bt, such as in sample Z10 (Figure 3.2.B), where in places large garnets are rimmed by a fine-grained intergrowth of Pl + Ms + Bt. Chlorite can occur at garnet rims and filling cracks, most likely as a retrogressive phase.

The matrix of most pelitic and semi-pelitic samples generally consists of a composite fabric that has segregated into felsic and mica-rich regions, although quartz and feldspar occur in micaceous layers and vice-versa.

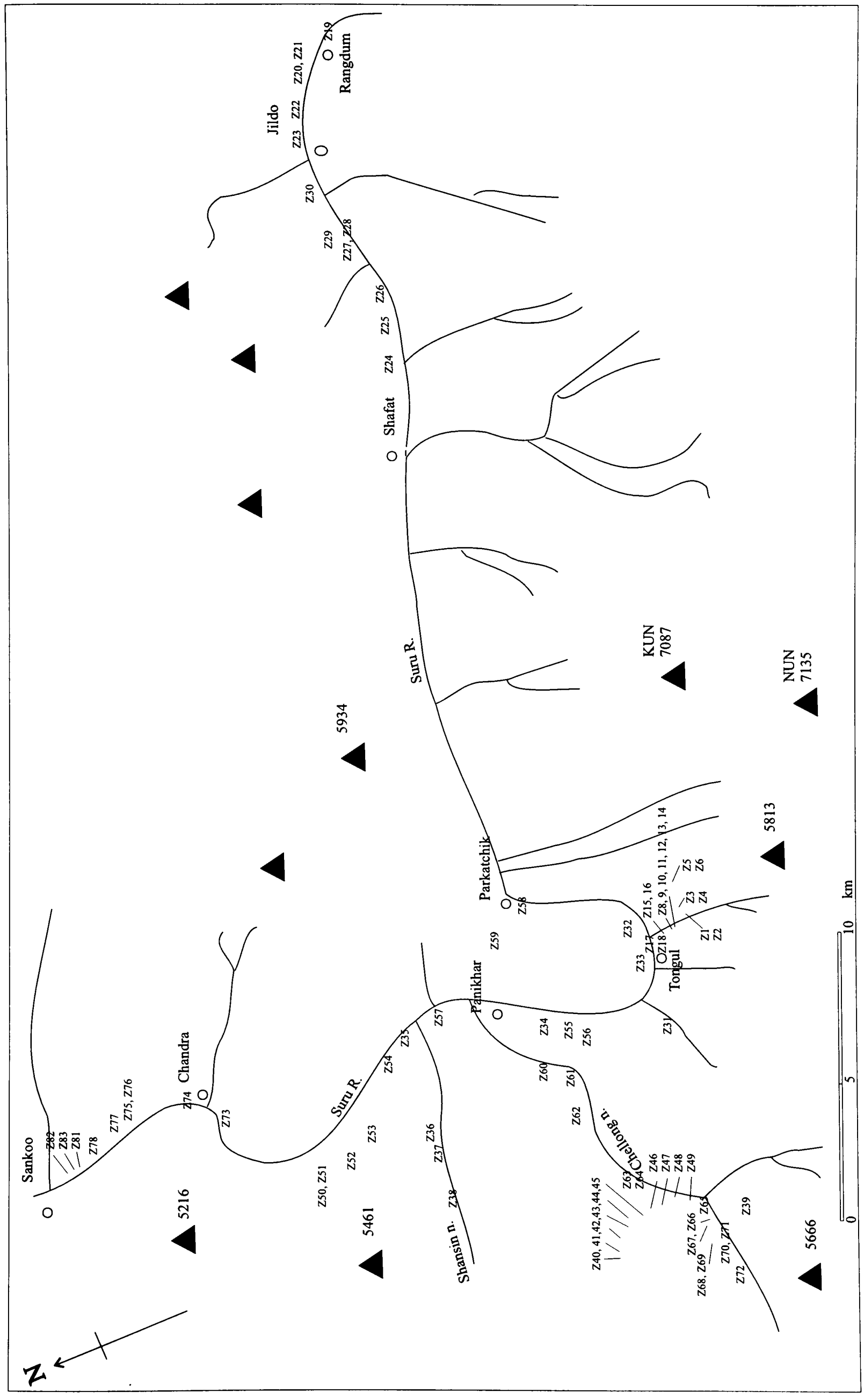


Figure 3.1. Map of the Suru Valley illustrating distribution and location of samples

Muscovite and biotite occur in sheaves or as more isolated crystals, usually depending on the Al content of the rock, with pelitic rocks containing a greater proportion of muscovite than semi-pelitic ones; for instance, the pelite Z70 from the Donara nappe contains nearly 40% modal muscovite compared to 12% in Z47. Texturally, there are two main types of pelite. In the first, muscovite and biotite crystals generally define a foliation, which is often crenulated and wraps garnet porphyroblasts in many samples (Figures 3.3.A & B) A second generation of muscovite crystals is sometimes associated with this crenulation, appearing to grow in an axial planar orientation, such as in sample Z43. Similarly, in some samples a second generation of coarser biotite crystals can be observed to overgrow the earlier fabric; this later growth could possibly be associated with the KFMASH univariant reaction

$$Grt + Ms + Chl = St + Bt + Qtz + H2O$$

In the second type, matrix muscovite and biotite appear to have crystallised more statically and do not define such an obvious foliation. There is also not as much discordance between the matrix fabric and garnet inclusion fabrics. In certain graphitic rocks, the matrix muscovites can be seen to overgrow graphitic trails which presumably represent an earlier foliation. Sample Z69 (Figures 3.4. A &B) is an example of this, and to a certain extent Z10, although not much matrix graphite is preserved. Sample Z70 shows good decussate muscovite textures (Figure 3.5.A). These rocks are analogous to the Type 1a pelites of Searle *et al.* (1992).

Plagioclase occurs in varying quantities in pelitic and semi-pelitic rocks, depending on grade and bulk composition. Ca-poor schists such as Z70 have little or no discernible plagioclase, whilst most contain around 1-2 modal %. Crystals tend to be small and aligned with the foliation, or occurring at garnet rims, often as symplectites, as in sample Z56. In recrystallised schists such as samples Z10 and Z69, plagioclase overgrows biotite and muscovite in the matrix, and also in low grade schists from near Sankoo, such as sample Z81. Here, albite crystals overgrow a spaced fabric defined by muscovite and chlorite and often preserve fine inclusion trails at an angle to the matrix foliation (Figures 3.6.A & B). The decreasing proportion of plagioclase with metamorphic grade implies that it is used up during prograde metamorphism after garnet grade.

The occurrence of staurolite and kyanite is a function of metamorphic grade and bulk composition. Many rocks from the staurolite and kyanite metamorphic zones do not contain these minerals because they are generally too Al-poor. Where they do occur, they appear as both syn-and post-tectonic phases with respect to the main foliation. Sample Z71 from near

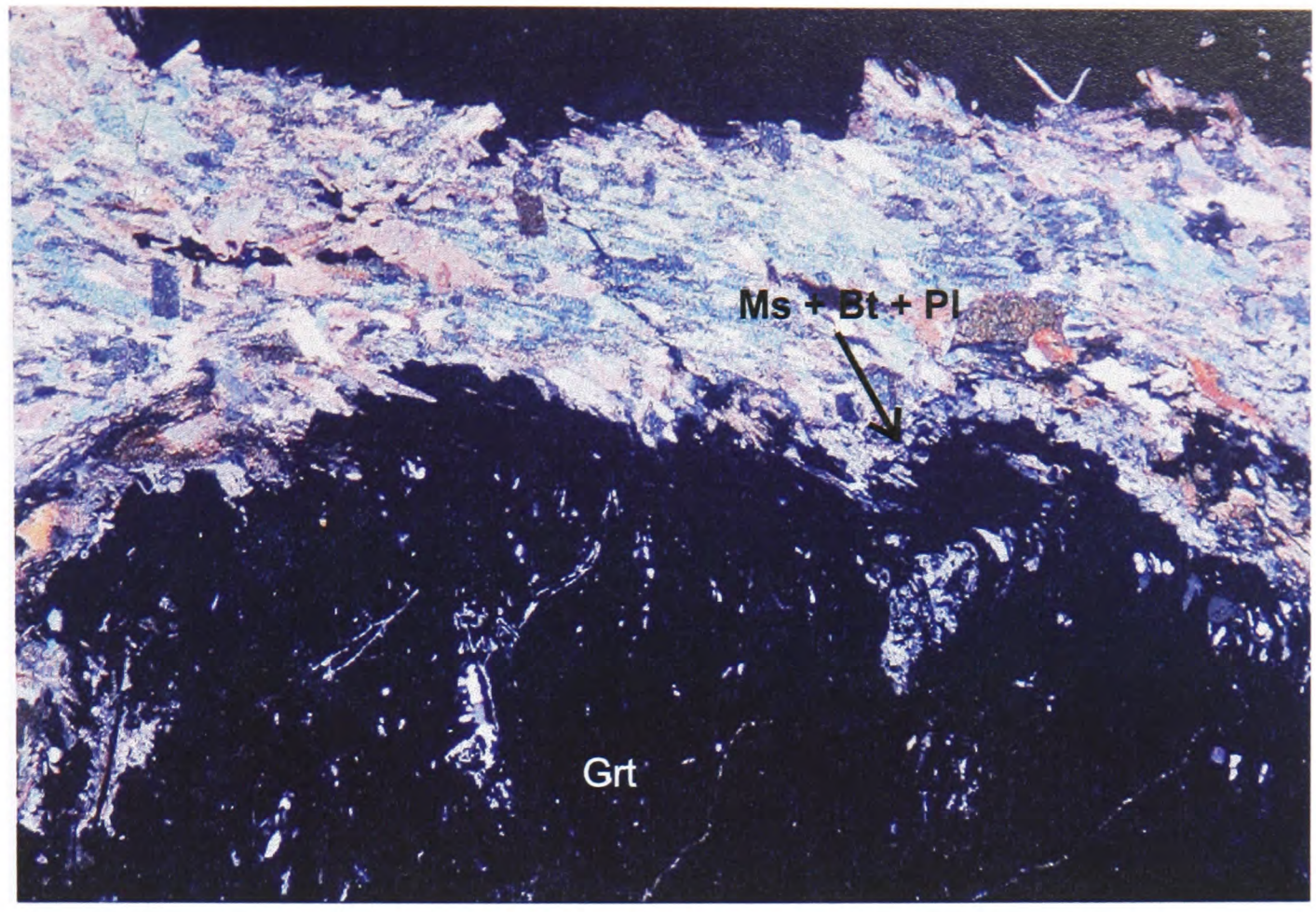


Figure 3.2.A. Photomicrograph of sample Z10 in XPL showing large garnet, which is embayed in places, and rimmed by a fine-grained intergrowth of Ms + Bt + Pl. The matrix is composed of more coarsely recrystallised Ms, Bt and Pl. Field of view is approximately 5mm.

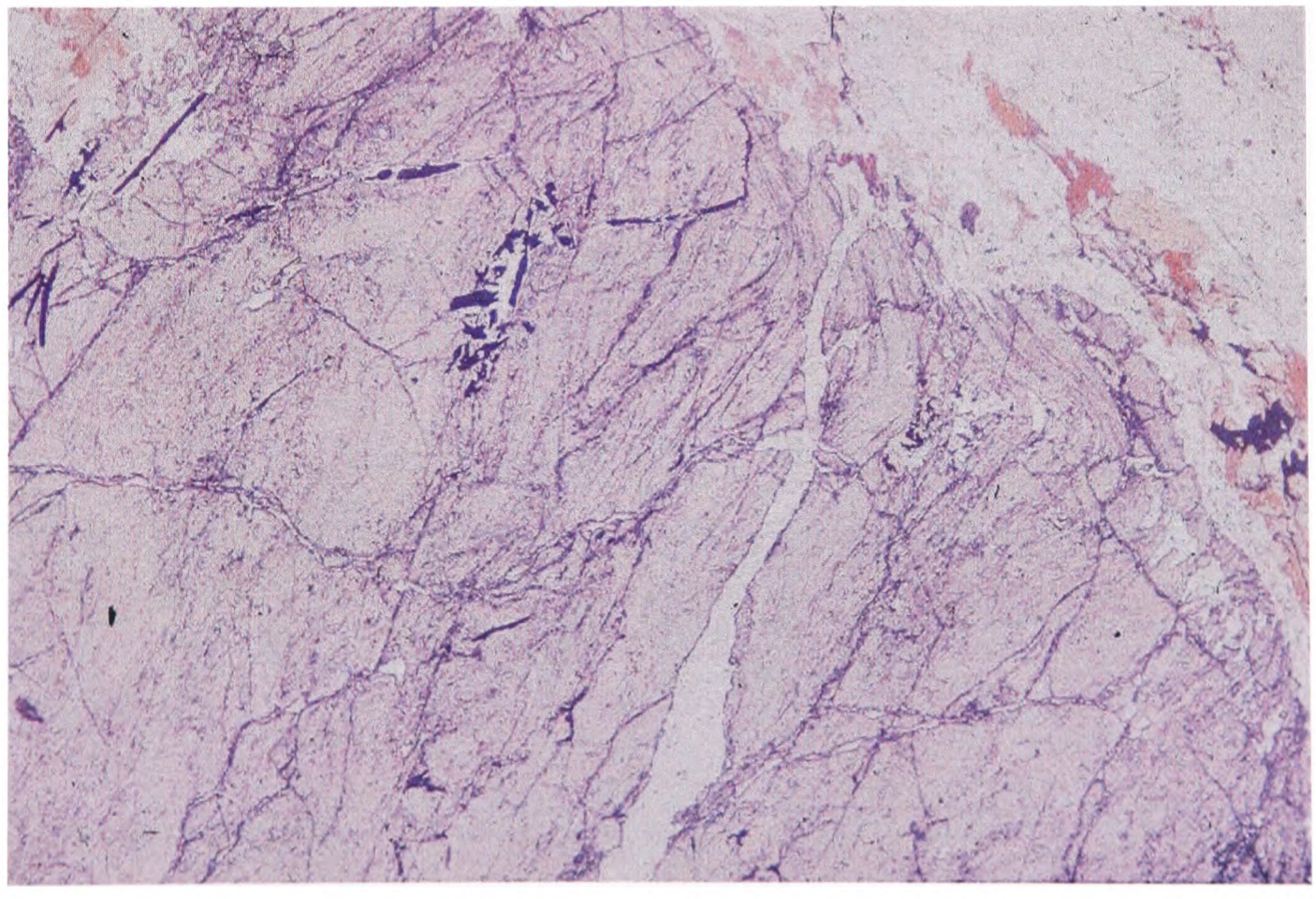


Figure 3.2.B. Photomicrograph of the same garnet from Z10 as above, in PPL, showing graphitic trails in garnet that are isoclinally folded near the rim region, before becoming concordant with trails in the matrix. Rim is embayed in places as above. Field of view approximately 5mm.



Figure 3.3.A. Photmicrograph of sample Z43 illustrating the gross composition and microstructure. A composite foliation of Ms + Bt rich, and Qtz + Pl rich domains is overgrown syn-tectonically by garnet porphyroblasts. This matrix fabric is subsequently coarsened and crenulated. Field of view approximately 1.4 cm.



Figure 3.3.B. Detailed view of the crenulated micas that define the foliation in 3.3.A. Muscovite sheaves display undulose extinction as a result of crenulation. Field of view approximately 5mm.

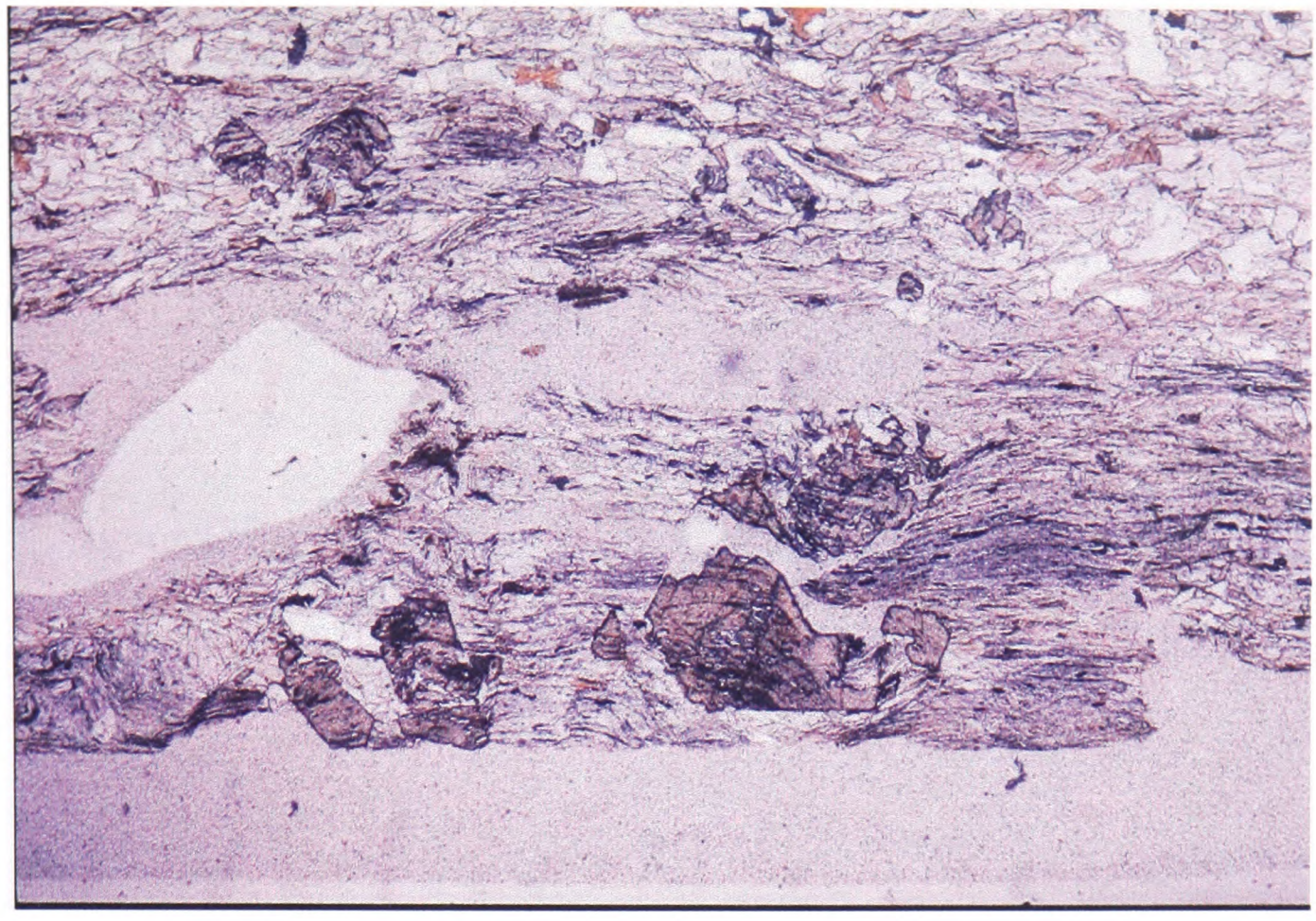


Figure 3.4.A. Photomicrograph of sample Z69 in PPL, showing staurolite crystals (bottom, yellow) that display good crystal faces, statically overgrowing graphite trails in the matrix. Field of view approximately 8mm.



Figure 3.4.B. XPL view of 3.4.A. In this photomicrograph, plagioclase porphyroblasts can be seen to overgrow the graphite trails, and a fine-grained foliation in muscovite and biotite. Some later muscovite and biotite appears to overgrow this earlier fabric.

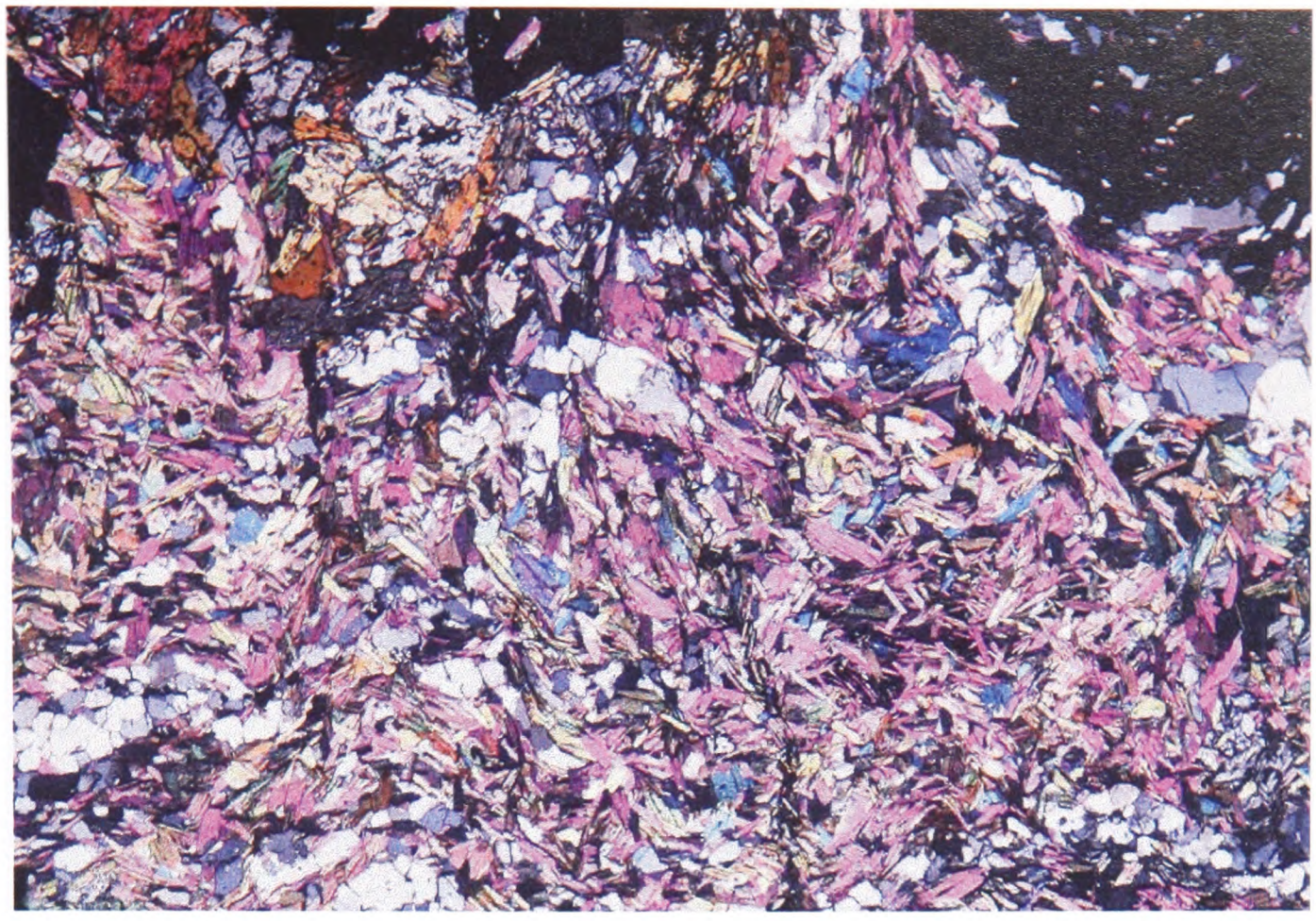


Figure 3.5.A. Photomicrograph of sample Z70 in XPL, showing decussate texture in recrystallised matrix muscovites. Kyanite and staurolite crystals are visible at the top of the picture at the garnet rim. Field of view approximately 5mm.

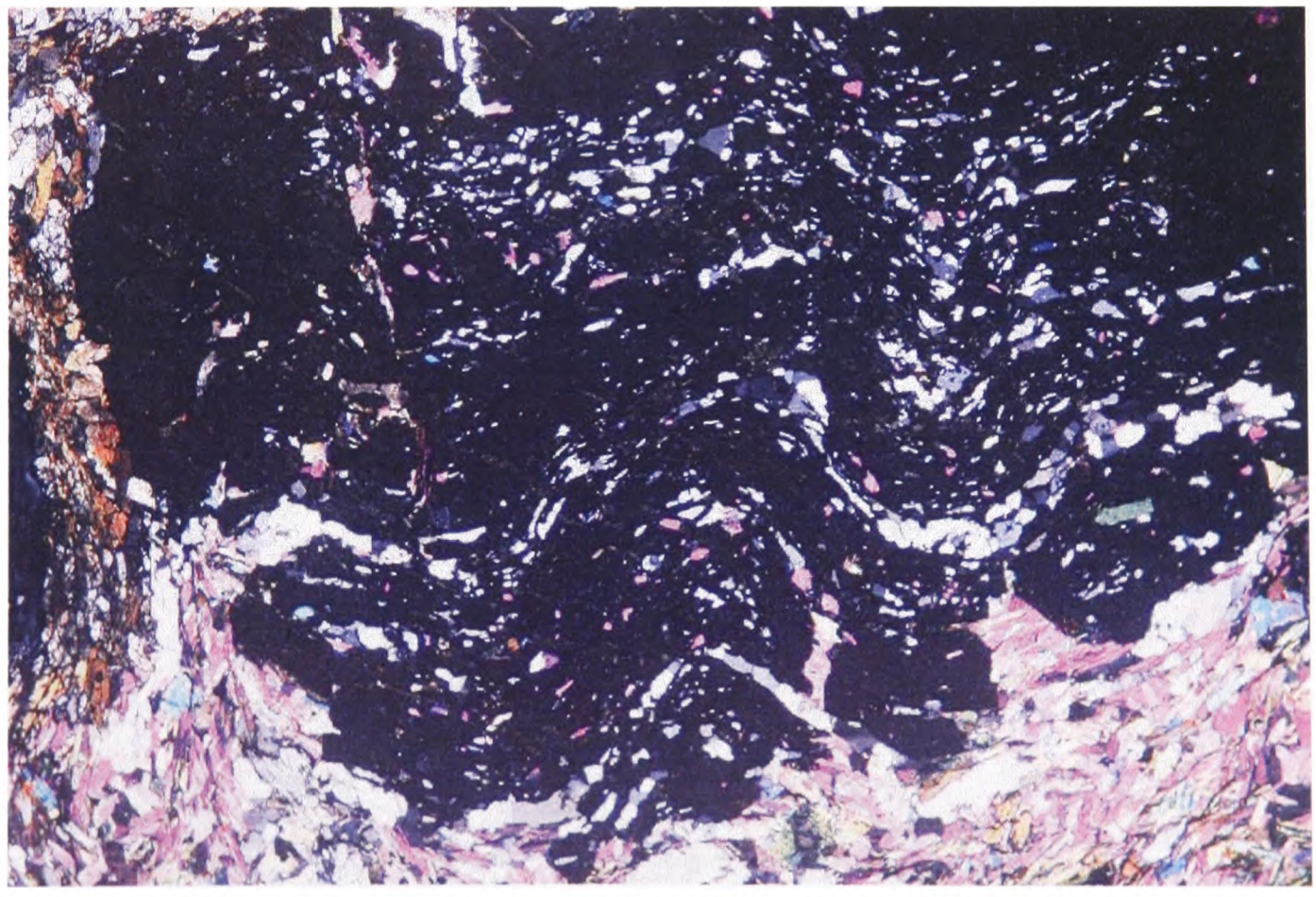


Figure 3.5.B. Photomicrograph of sample Z70 in XPL illustrating garnet porphyroblast apparently statically overgrowing a crenulated inclusion fabric of quartz and muscovite. Scale as above.

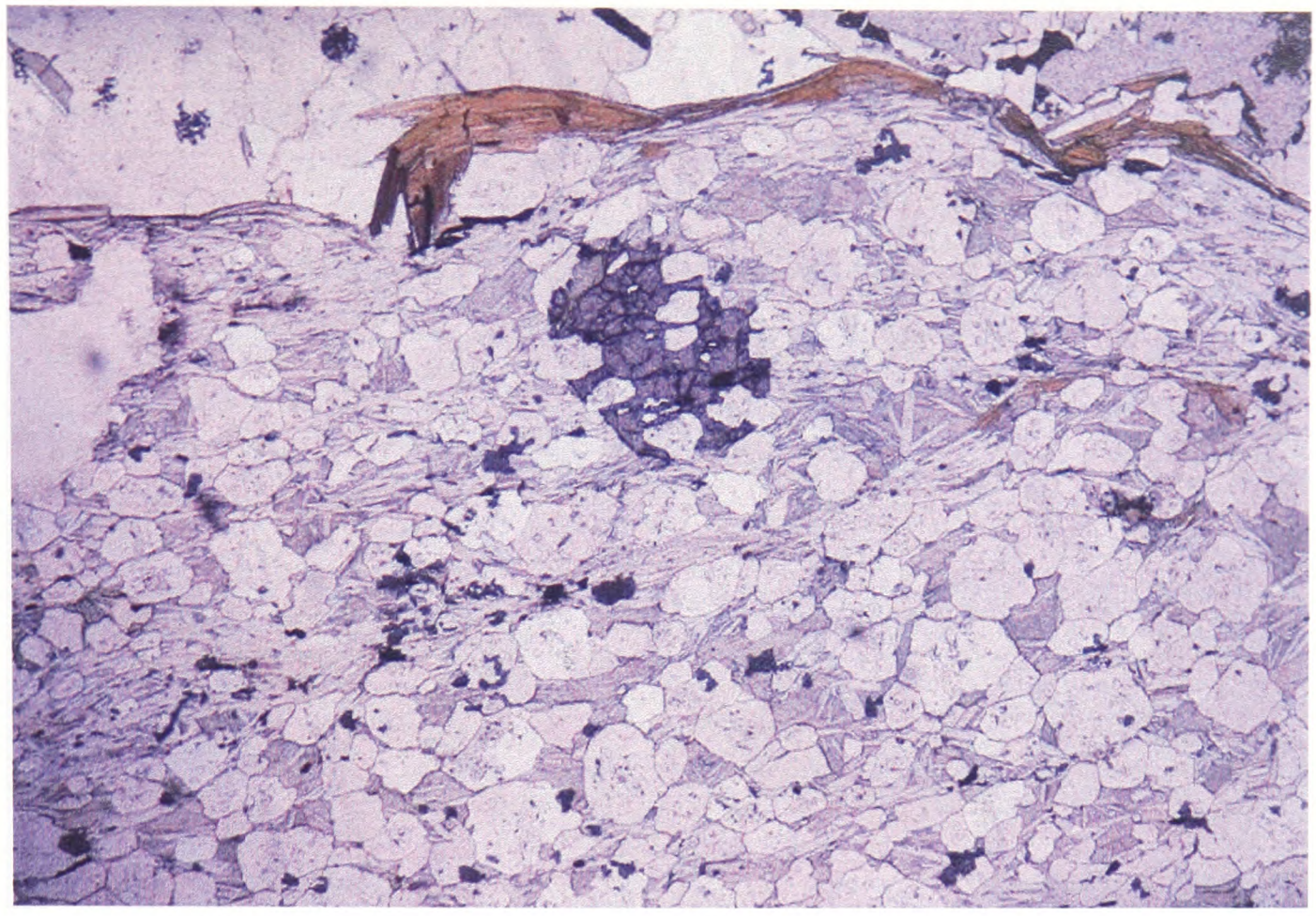


Figure 3.6.A. Photomicrograph in PPL of sample Z81 from the Sankoo nappe. A foliation defined by chlorite and muscovite (with some biotite at the top of the picture) is overgrown by albite porphyroblast, which preserve fine inclusion trails at an angle to the main foliation. Small, skeletal garnet crystals overgrow these albites and appear to be post-tectonic. Field of view approximately 5 mm.

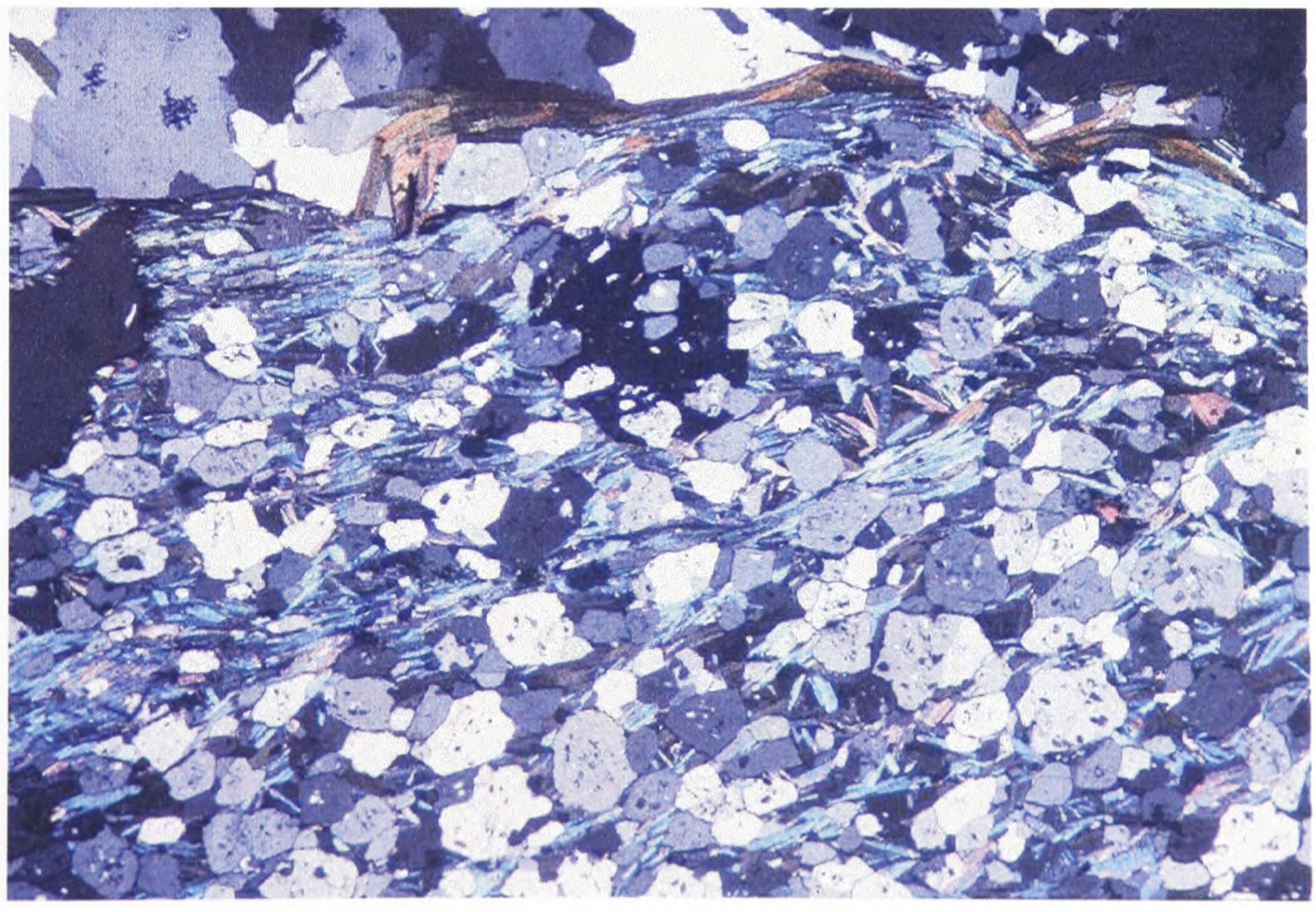


Figure 3.6.B. XPL view of 3.6.A.

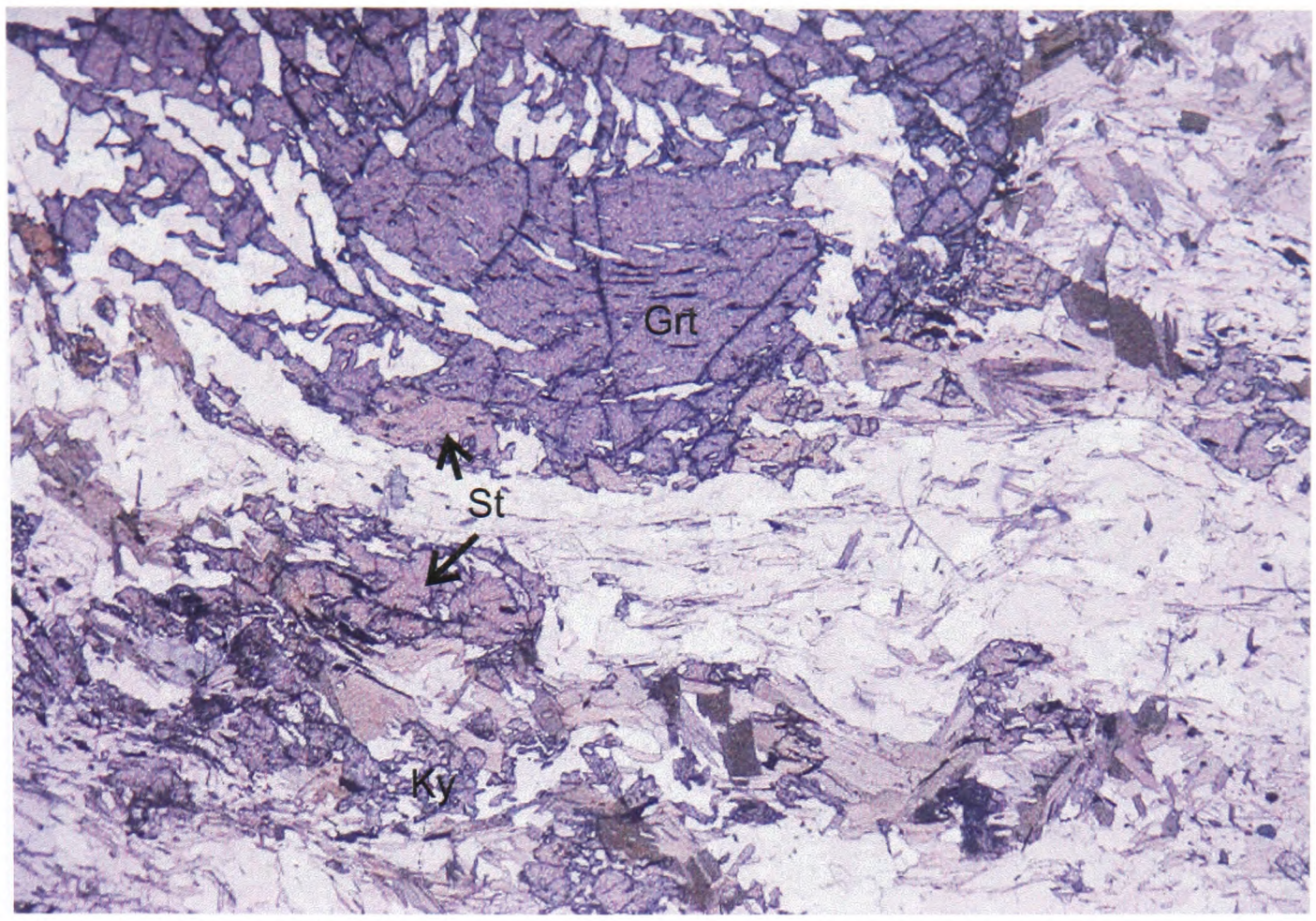


Figure 3.7.A. Photomicrograph in PPL of sample Z71 illustrating mineral growth with respect to deformation. Large garnet porphyroblasts overgrow a fabric of Qtz, Czo, Ms + Ilm that has already segregated into a composite foliation (S_1), that is tightly folded in places. This fabric has a similar orientation to the coarser matrix S_2 fabric near garnet rims, where both garnet and staurolite can be seen to be growing syn-tectonically. Some kyanites appear to align with S_2 in the matrix, although others appear to overgrow it. Field of view approximately 5 mm.



Figure 3.7.B. XPL view of 3.7.A.

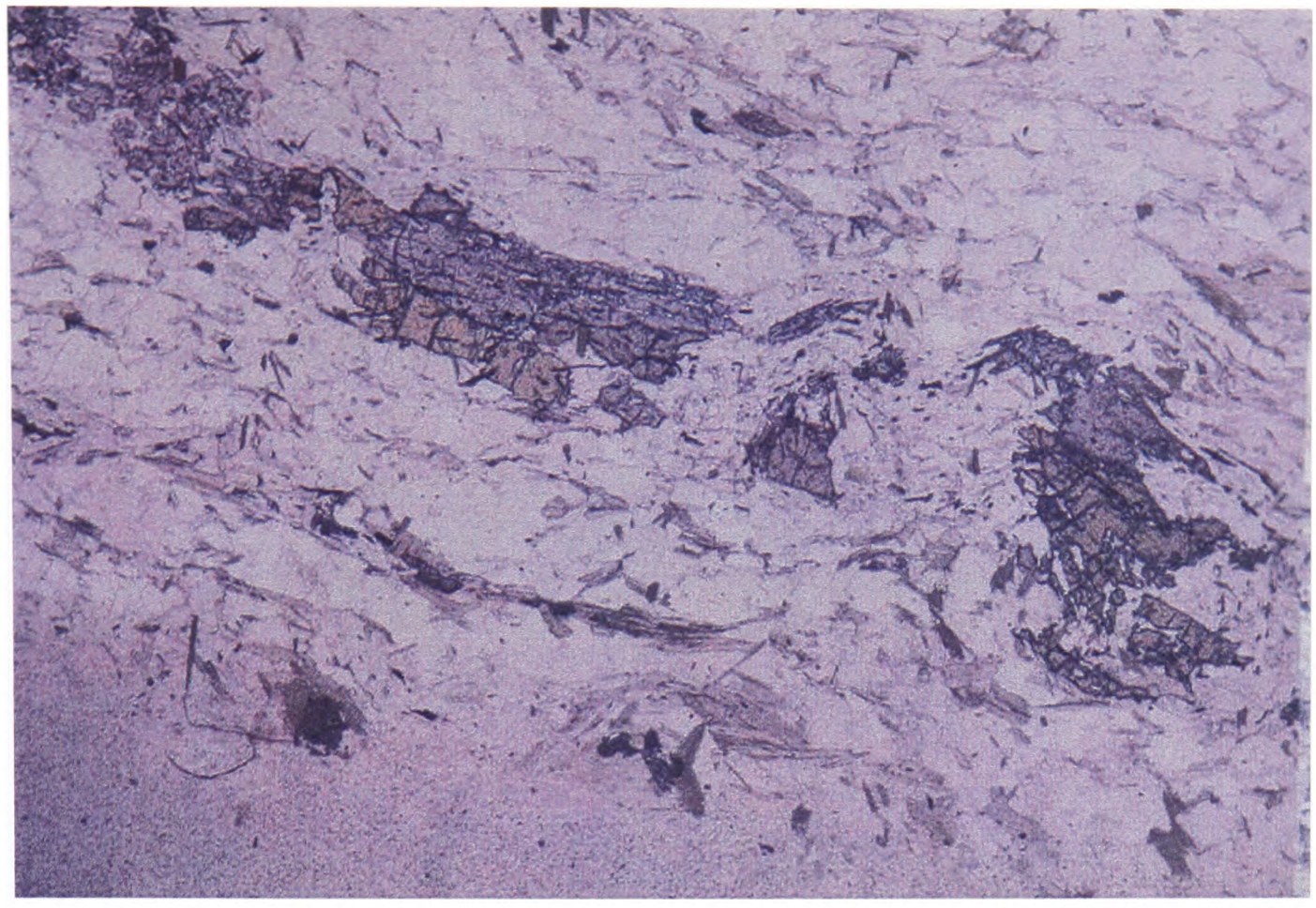


Figure 3.8.A. Photomicrograph of sample Z70 in PPL, illustrating staurolite and kyanite crystals that appear to be aligned with the S_2 matrix fabric. Some slight D_3 crenulation of S2 is visible. Field of view approximately 5 mm.

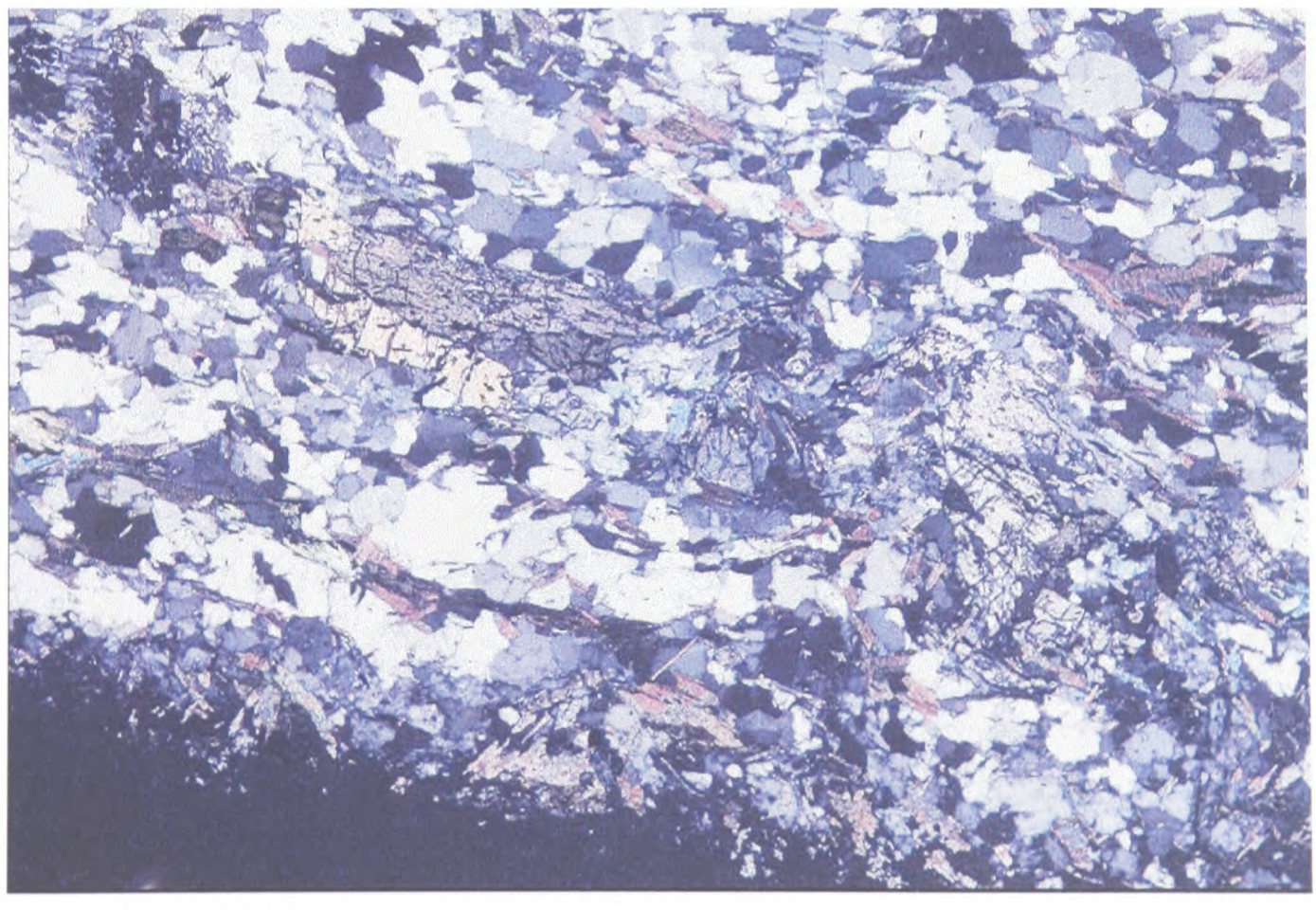


Figure 3.8.B. XPL view of 3.8.A.

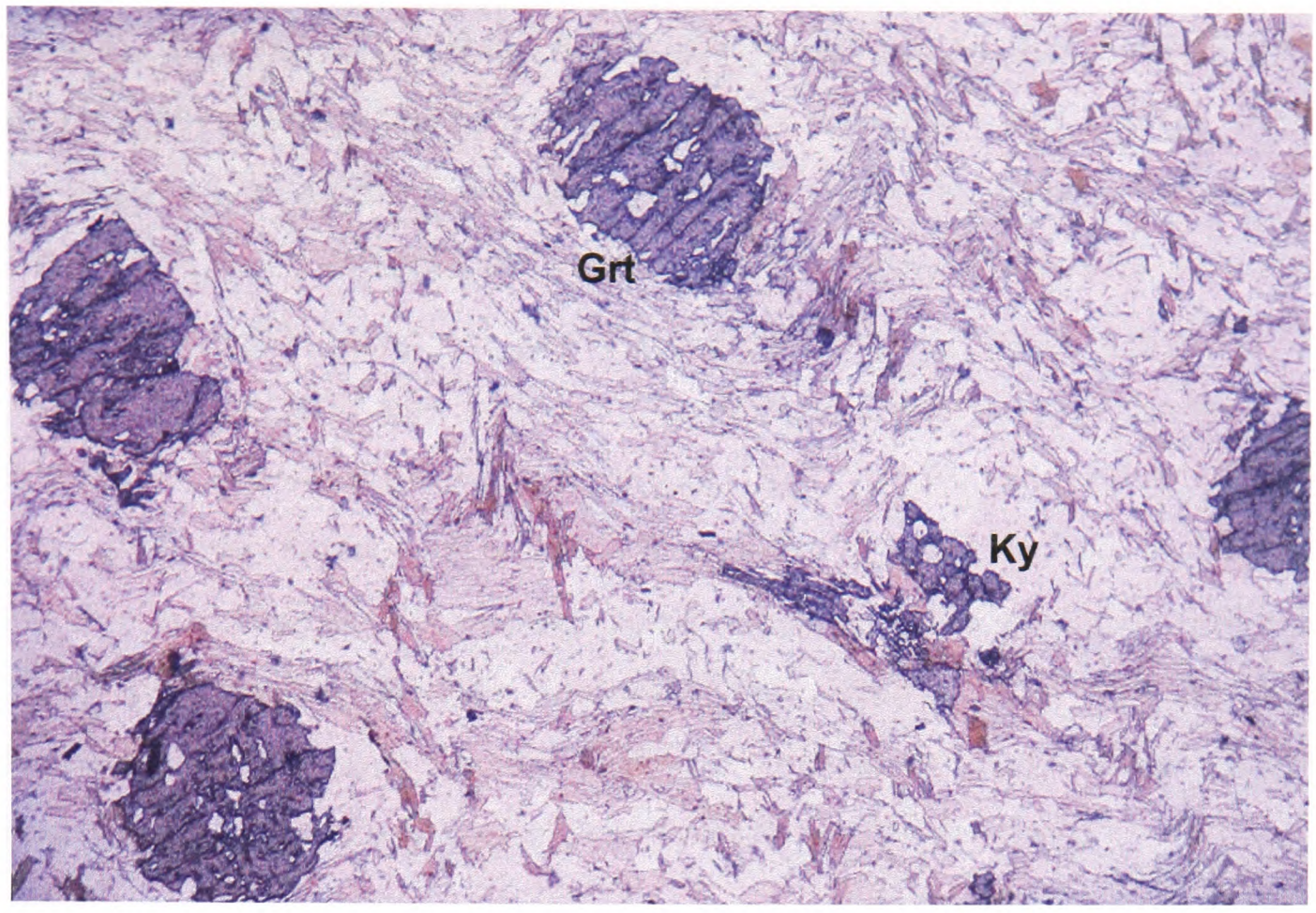


Figure 3.9.A. Photomicrograph of sample Z47 in PPL. Garnet porphyroblasts containing a fabric at an angle to the matrix foliation are wrapped by this foliation, defined by muscovite and biotite flakes. Kyanite crystals are wrapped in places by this foliation but appear to grow along foliation planes in others.

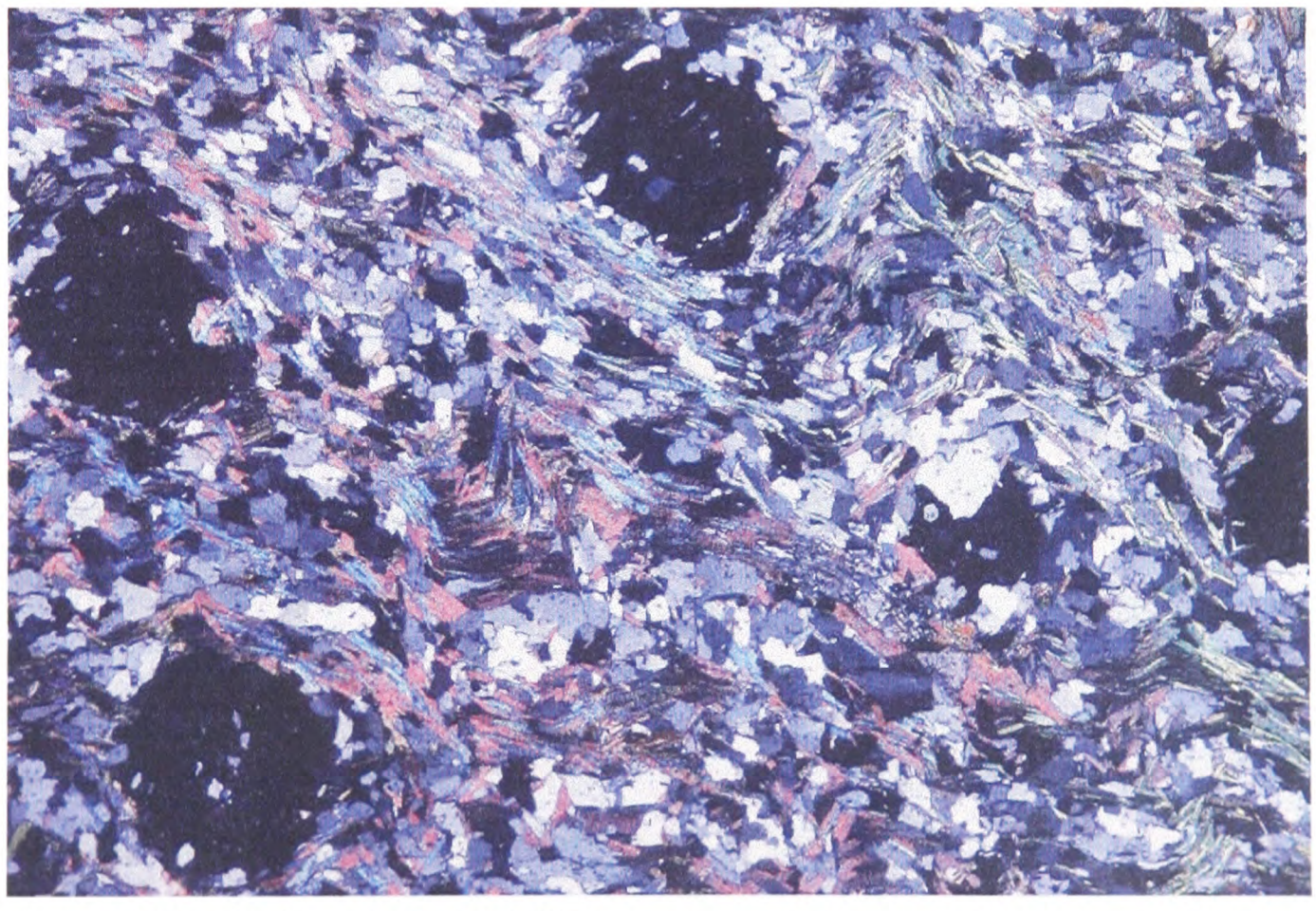


Figure 3.9.B. XPL view of 3.9.A. This illustrates the crenulations in the S_2 foliation.

the closure of the Donara nappe contains both staurolite and kyanite, along with garnet and hornblende as porphyroblast phases. Staurolite crystals occur in the matrix and also included at garnet rims, and shows a fairly strong alignment with the matrix foliation. Kyanite occurs mostly in the matrix, but is occasionally slightly included at large garnet rims. It is seen to mostly overgrow the matrix fabric, but occasionally shows slight alignment (Figures 3.7.A & B, 3.8.A & B). Sample Z47, also from the Donara nappe closure shows similar kyanite porphyroblasts that are wrapped by micas defining the main foliation, but show some signs of rotation into alignment (Figures 3.9.A & B). This is discussed later in the microstructure section, but implies at least some syn-tectonic porphyroblast growth. Conversely, sample Z69, less than 100m away, contains abundant staurolite crystals, some of which show good crystal faces, which statically overgrow graphitic trails in the matrix. In some samples, kyanite is partly breaking down to fine-grained aggregates of muscovite ± plagioclase (?).

3.2.2 Calc-pelites

Calc-pelites as defined here, as opposed to pelites that are slightly calcareous, generally contain Cal + Zo/Czo ± Hbl as matrix phases, as well as Qtz + Ms + Bt + Pl + Grt ± Ky. Commonly, these rocks contain three Ti minerals, sphene occurring along with rutile and ilmenite. Some samples are also graphitic, such as sample Z73 from the Tapshah nappe. This contains Qtz + Cal + Bt + Ms + Grt + Pl + Czo + Gph +Spn/Ilm/Rt + (Chl) as an equilibrium assemblage, with Czo + Qtz + Cal + Ms + Fe-Ti oxides preserving inclusion trails in garnet (Figures 3.10.A & B). The microstructure is similar to the recrystallised schists Z10 and Z69 described above and will not be discussed in detail. Sample Z50 from the Tapshah nappe contains fairly euhedral garnets of up to 6mm in diameter and large poikiloblasts of plagioclase (Figure 3.11), whilst sample Z51 immediately adjacent contains poikiloblastic hornblende (Figure 3.12). In general, calc-pelites contain a greater modal proportion of plagioclase than pelites, and tend to show less well-developed matrix foliation due to a lower abundance of micaceous material.

3.2.3 Psammites

Psammites are less common than pelites and semi-pelites in the Suru Valley, and due to their rather uninteresting mineralogy were scarcely sampled. They generally contain Qtz + Bt + Pl ± Grt ± Ms ± Zo/Czo, and sometimes Fe-Ti oxides. Garnets tend to be very small and interstitial, and foliation is not well developed due to the small amount of micaceous material present.

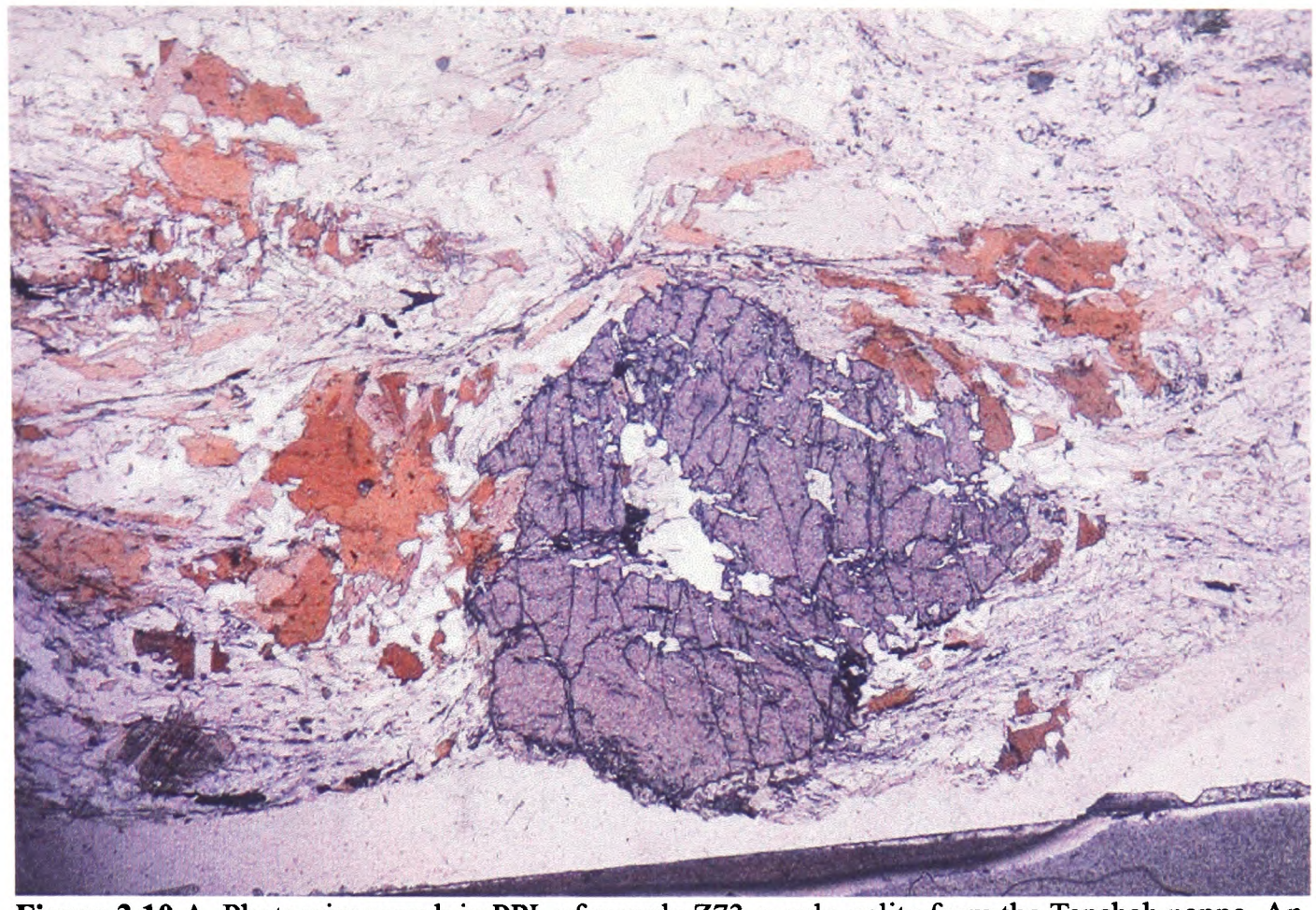


Figure 3.10.A. Photomicrograph in PPL of sample Z73, a calc-pelite from the Tapshah nappe. An early fabric defined by graphite trails and ilmenite is overgrown by Ms + Cal + Bt + Pl + Grt. Matrix appears to have recrystallised fairly statically. Field of view approximately 8 mm.

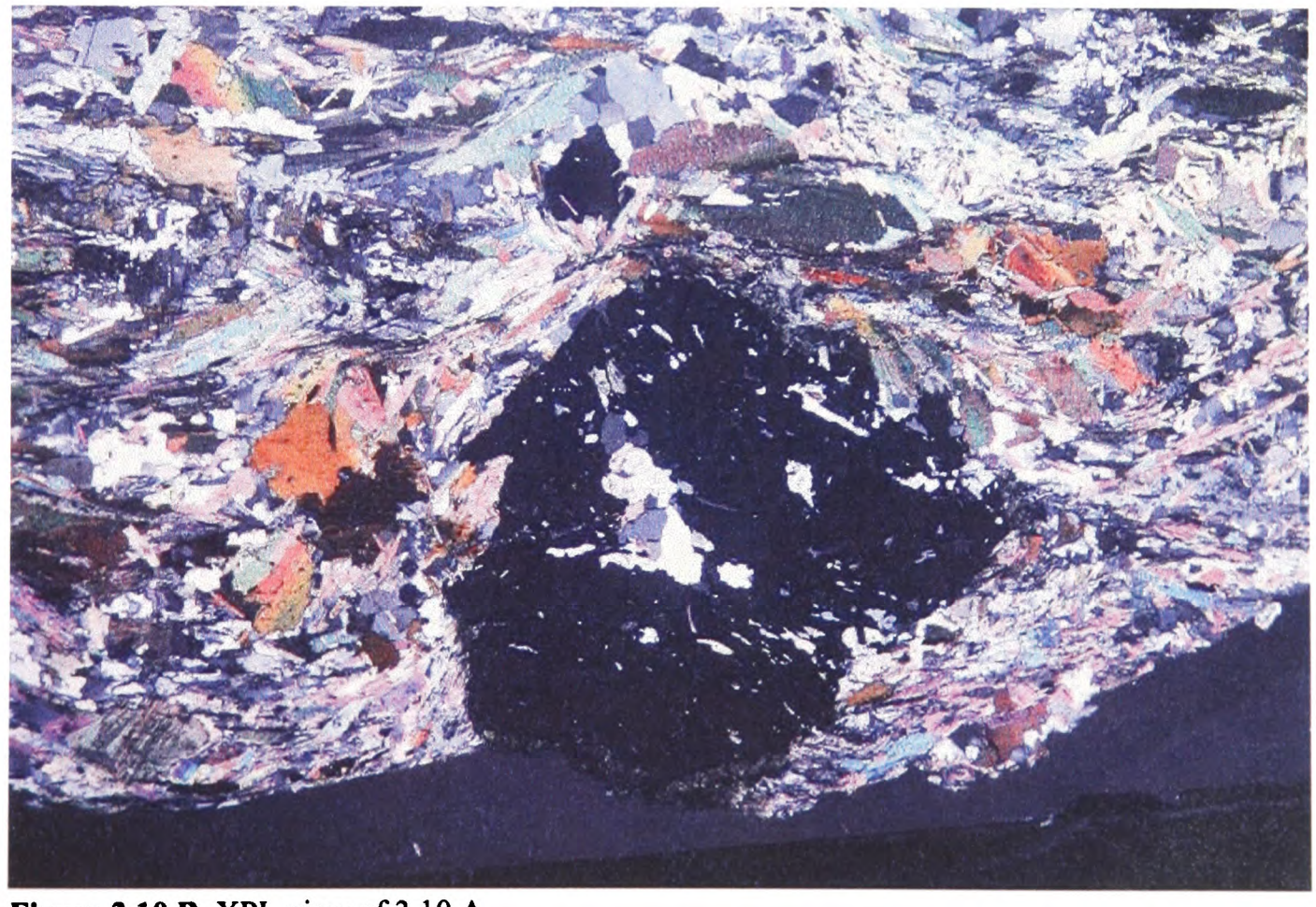


Figure 3.10.B. XPL view of 3.10.A.

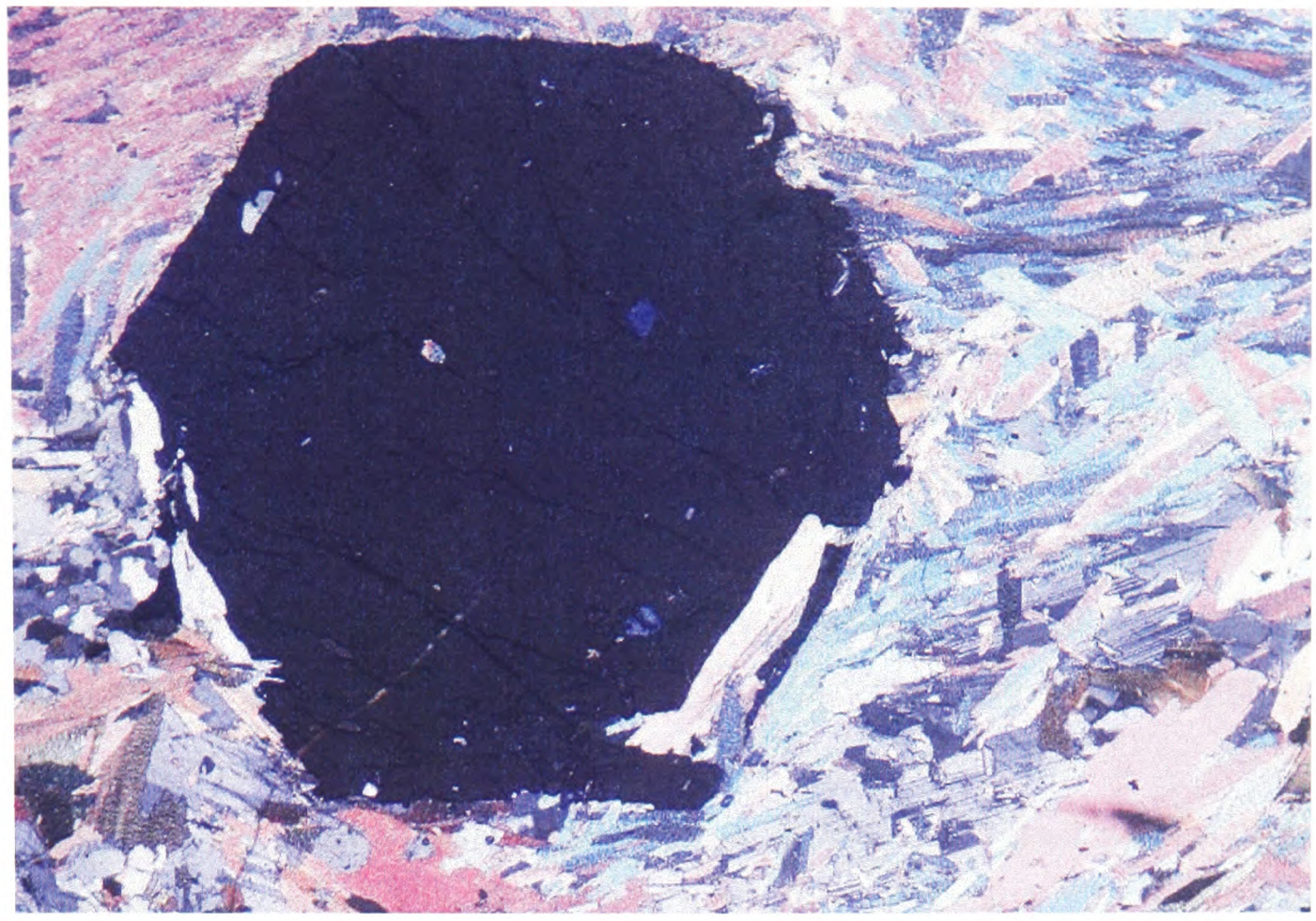


Figure 3.11. Photomicrograph in XPL of sample Z50. Euhedral garnet approximately 6 mm in diameter overgrows a fairly coarsely recrystallised matrix of Ms + Pl + Bt.

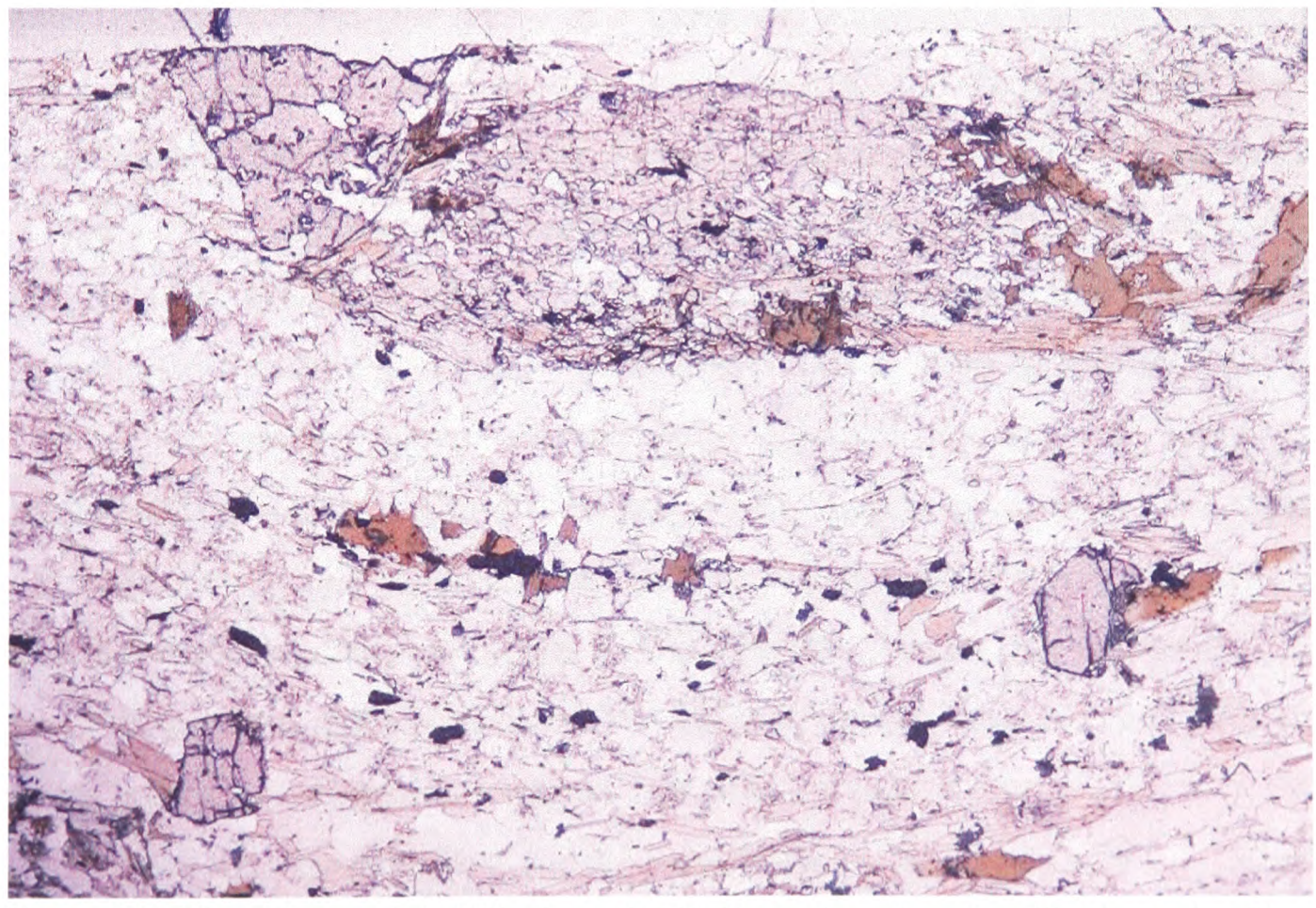


Figure 3.12. Photomicrograph in PPL of sample Z51 illustrating a large hornblende porphyroblast (top) in a matrix dominated by quartz and plagioclase. Small garnet crystals overgrow the matrix fabric. Field of view approximately 5 mm.

3.2.4 Marbles and siliceous dolomites

Only two samples of the marble units were sectioned, due to their unsuitability for thermobarometric calculations. Sample Z13 from south of Tongul consists of recrystallised calcite and dolomite crystals of up to nearly 3mm in diameter, with minor quartz and white mica. The quartz grains are fairly small and well-rounded, and resemble detrital grains in a sediment. The white mica appears to be muscovite and there are very minor amounts of clinochlore; the crystals are small and have a slight preferential orientation. Sample Z65, from the large marble band in the closure of the Donara nappe has a slightly more diverse mineralogy. The bulk of the rock consists of calcite and dolomite, but there is up to 5% of silicate materials, mainly muscovite and clinochlore, defining a faint fabric. Tiny phlogopite crystals align within carbonate-rich areas. Blocks of zoisite, generally associated with white mica and quartz are also present, up to around 1.5 mm in length, and show a faint alignment with the sheet silicates.

3.2.5 Amphibolites

Metabasic rocks in the Suru Valley occur at all metamorphic grades, and their mineral assemblages are to an extent dependent on this. The majority of the Suru Valley is in kyanite, or amphibolite, grade, so the metabasic rocks are described under this sub-heading. Amphibolites typically contain Hbl + Pl + Bt + Qtz ± Grt ± Zo/Czo ± Chl ± Cal ± Ep, with Ilm + Spn as Fe-Ti accessory phases. Garnet occurs in most, but not all amphibolites, growing up to 4mm in diameter. Many contain inclusion trails, often very fine grained, of Qtz ± Czo ± Pl ± Cal ± Spn ± Ilm. Sample Z4 from south of Tongul is fairly typical of the amphibolites sampled (Figure 3.13). Garnets of up to 3-4 mm diameter contain spectacular spiral inclusion trails of fine clinozoisite and sphene that imply rotation of the order of 360 degrees. Large flakes of biotite, and smaller sphene crystals define a matrix foliation that wraps garnet porphyroblasts and is crenulated . Hornblende poikiloblasts appear to overgrow this foliation, and contain inclusions of quartz, plagioclase, sphene and epidote. Epidote is present as a matrix phase, but in much smaller quantities than hornblende. Ilmenite and sphene are present as both matrix phases and garnet inclusions, but ilmenite appears to occur only near garnet rims, whereas sphene is present throughout. Chlorite is locally intergrown with biotite crystals, probably as a retrograde phase. In some amphibolites, such as sample Z2, chlorite is quite abundant.

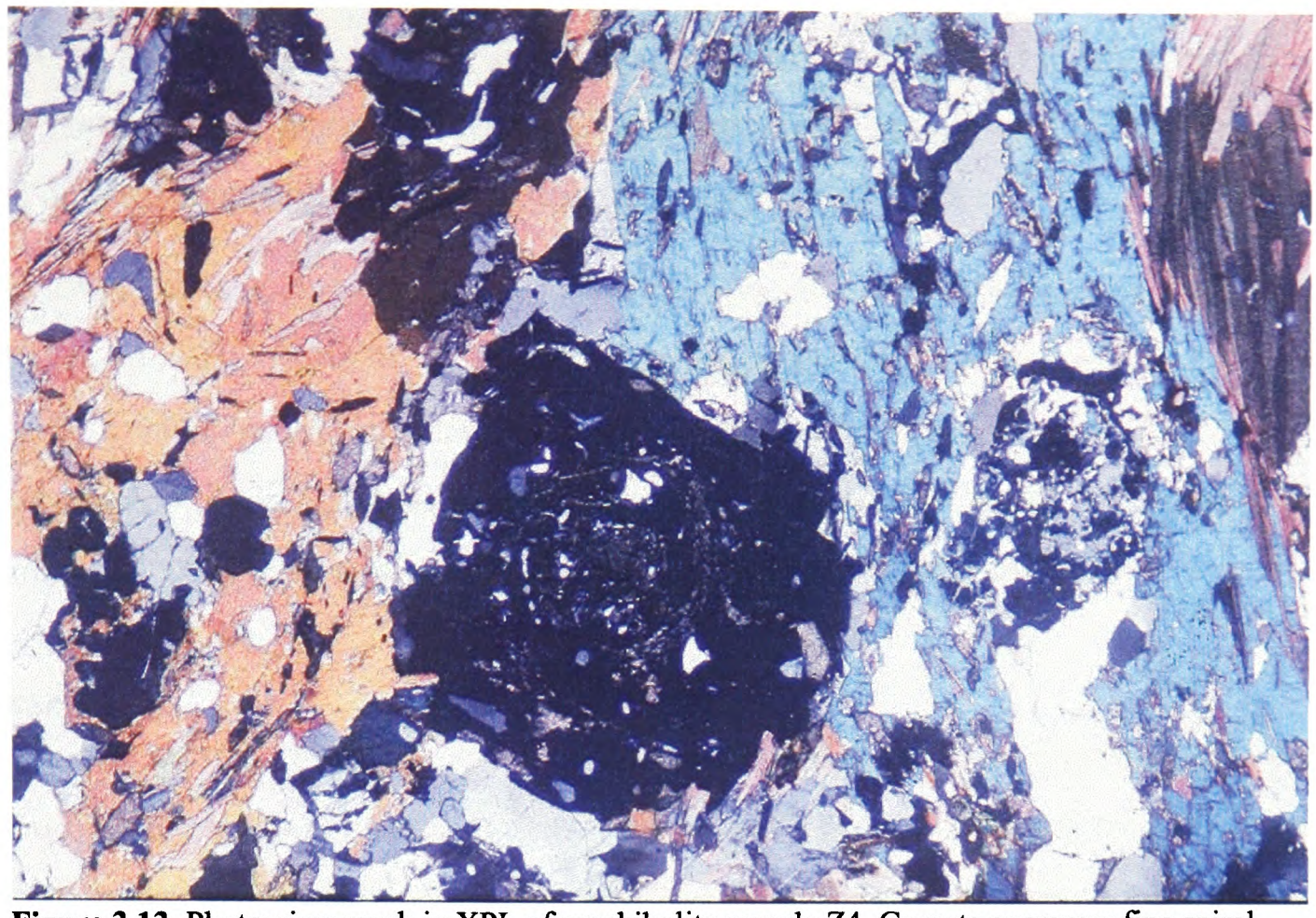


Figure 3.13. Photomicrograph in XPL of amphibolite sample Z4. Garnets overgrow fine spiral inclusion trails of clinozoisite and sphene that imply garnet rotation of up to 360°. Flakes of biotite and sphene crystals define a matrix fabric that wraps garnet porphyroblasts, and is crenulated. This is overgrown by large hornblende poikiloblasts. Field of view approximately 5 mm.

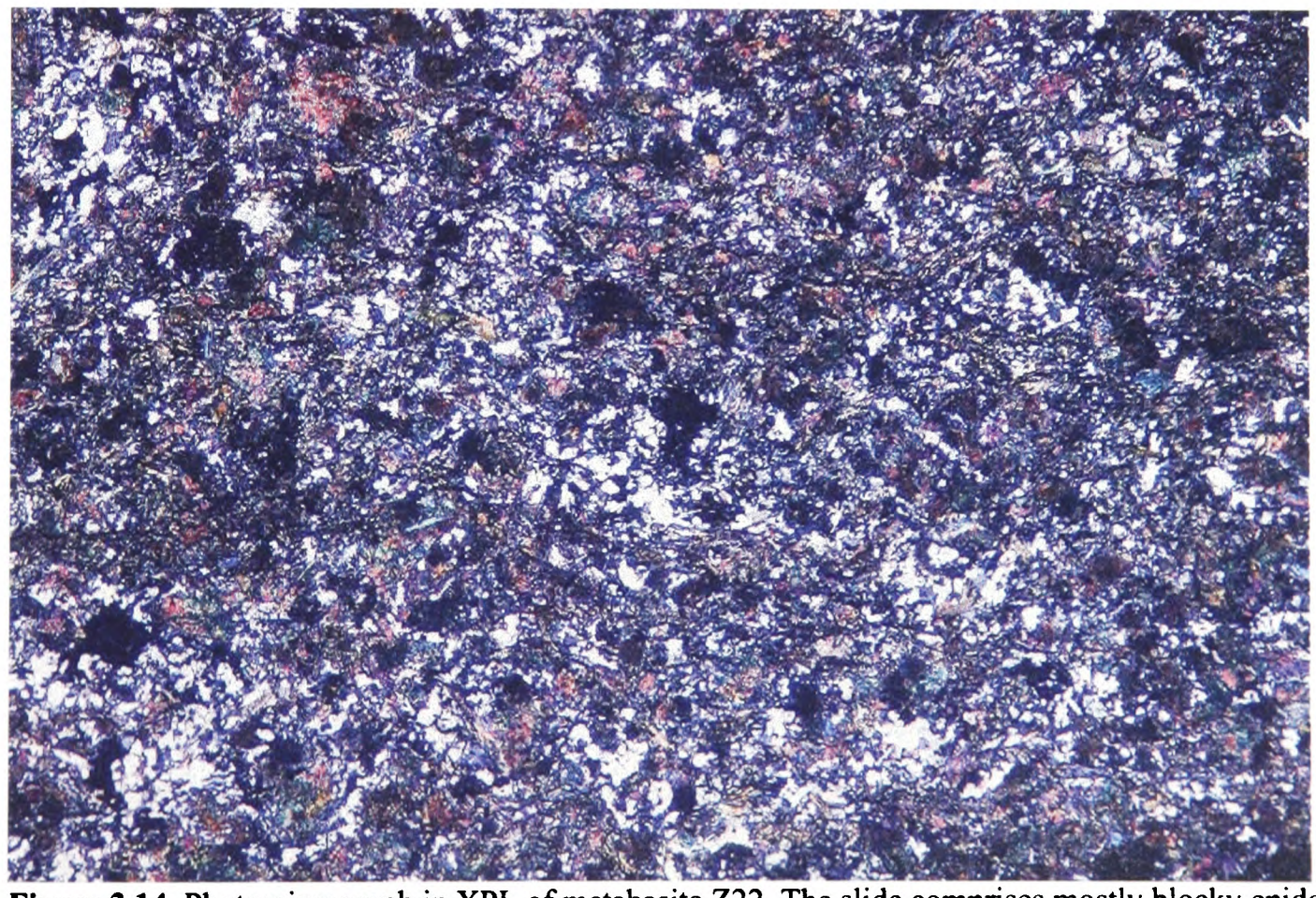


Figure 3.14. Photomicrograph in XPL of metabasite Z22. The slide comprises mostly blocky epidote crystals and albite. Fine needle-like actinolites, and scruffy chlorites are also present. The texture is mostly relict igneous, but the beginnings of a fabric may be discerned in places. Field of view is approximately 5 mm.

Not all amphibolites display an obvious foliation as described above, and many possess a more spaced fabric, being segregated into felsic and mafic bands that appear unfoliated on a microscopic scale, but show strong banding in the field.

At low grades, such as at the ZSZ at Rangdum, metabasic rocks contain Chl + Ep + Act + Qtz + Ab + Bt. There is no dominant foliation and the samples appear to preserve something of a relict igneous texture. As metamorphic grade increases away from the ZSZ, epidote appears to become more abundant whilst chlorite and actinolite decrease modally, and the beginnings of a foliation appear, as is observed in sample Z22 (Figure 3.14).

3.2.6 Granitoids

Metamorphosed granitoid units in the Suru Valley occur at metamorphic grades ranging from garnet grade at Sankoo to nearly sillimanite grade near Parkatchik, but all show a similar mineralogy. Typically they contain Qtz + Ab + Kfs + Bt + Ms ± Grt, and some epidote is present in sample Z78 from the Sankoo nappe (Figures 3.15.A & B). The samples generally have a coarse, reasonably well-annealed texture, with a faint foliation defined by flakes of biotite and muscovite, which make up less than 5% modal of the rock, and alignment of quartz and feldspar crystals. K-feldspars often preserve igneous perthitic textures, but no antiperthitic textures as described by Burton (1995) are seen. In samples Z78 and Z38, from the Shansin nala, gefüllte plagioclase crystals are observed, where small muscovite crystals occur within a plagioclase grain. This is suggests metamorphism of preexisting granitoids at a lower temperature than that of igneous crystallisation, as Al is released from anorthite to form white mica or clinozoisite (Burton 1995).

Biotite crystals in sample Z78 often occur in clots, and are dark green-black in colour, suggesting a low TiO_2 content with respect to Fe_2O_3/FeO ratio (Guidotti 1984).

3.2.7 Suru Dome rocks

Rocks from the tectonic unit of the Suru Dome are generally petrographically and microstructurally distinct from those of the overlying nappe units. Typically, they contain the paragenesis Qtz + Pl + Bt + Ms + Grt + Ky ± St ± Chl. Tourmaline and Fe-Ti oxide minerals also occur. Graphitic trails such as those observed in some rocks from the Donara and Tapshah nappes are never observed. Texturally they appear slightly coarser than samples from the overlying nappes, with sheaves of biotite and muscovite defining a foliation that separates more felsic domains.

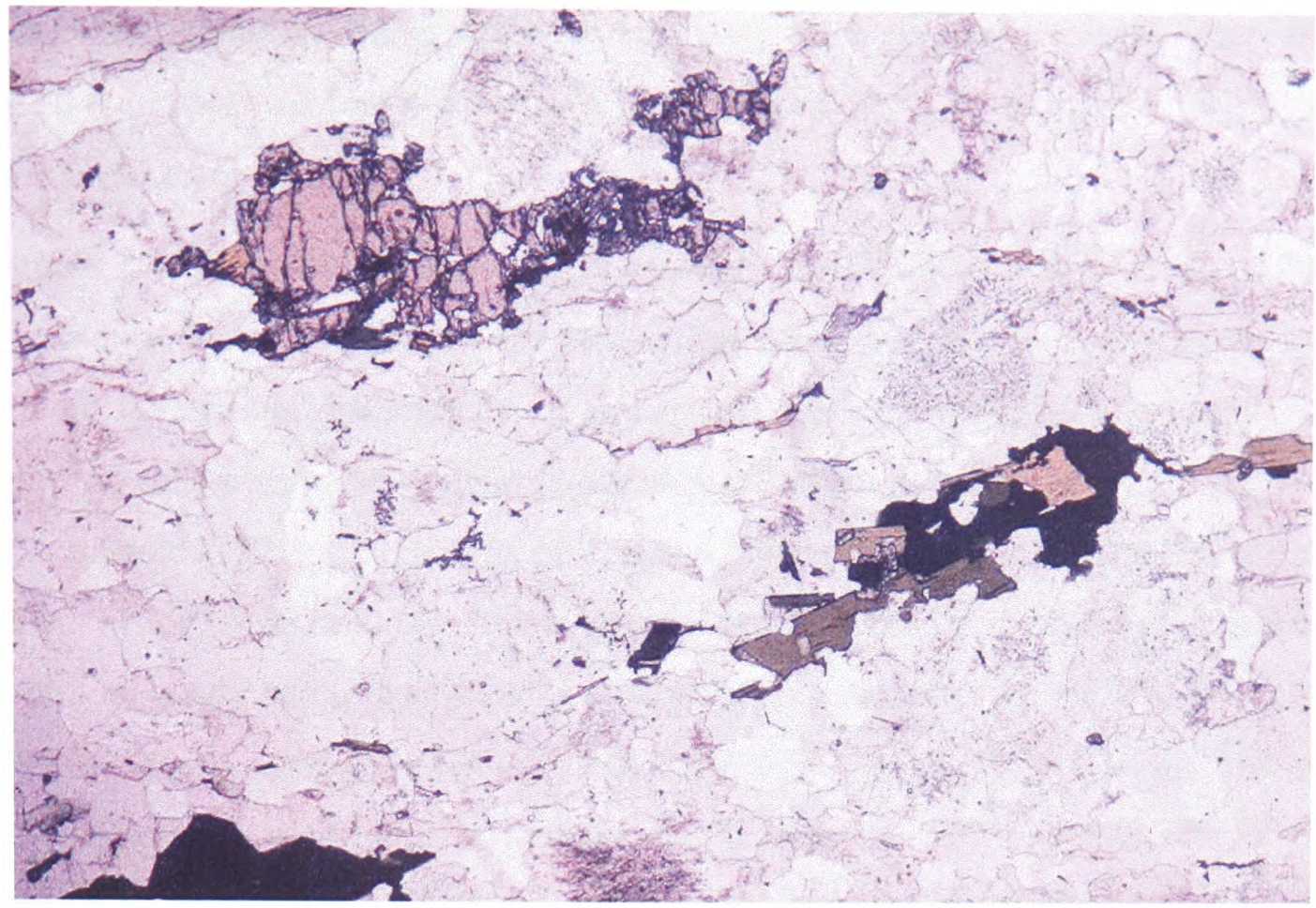


Figure 3.15.A. Photomicrograph in PPL of sample Z78, from the Sankoo granitoid body. Note dark-green-black biotite clots defining a coarse foliation, and the pinkish garnet near the top of the slide. Field of view approximately 5 mm.

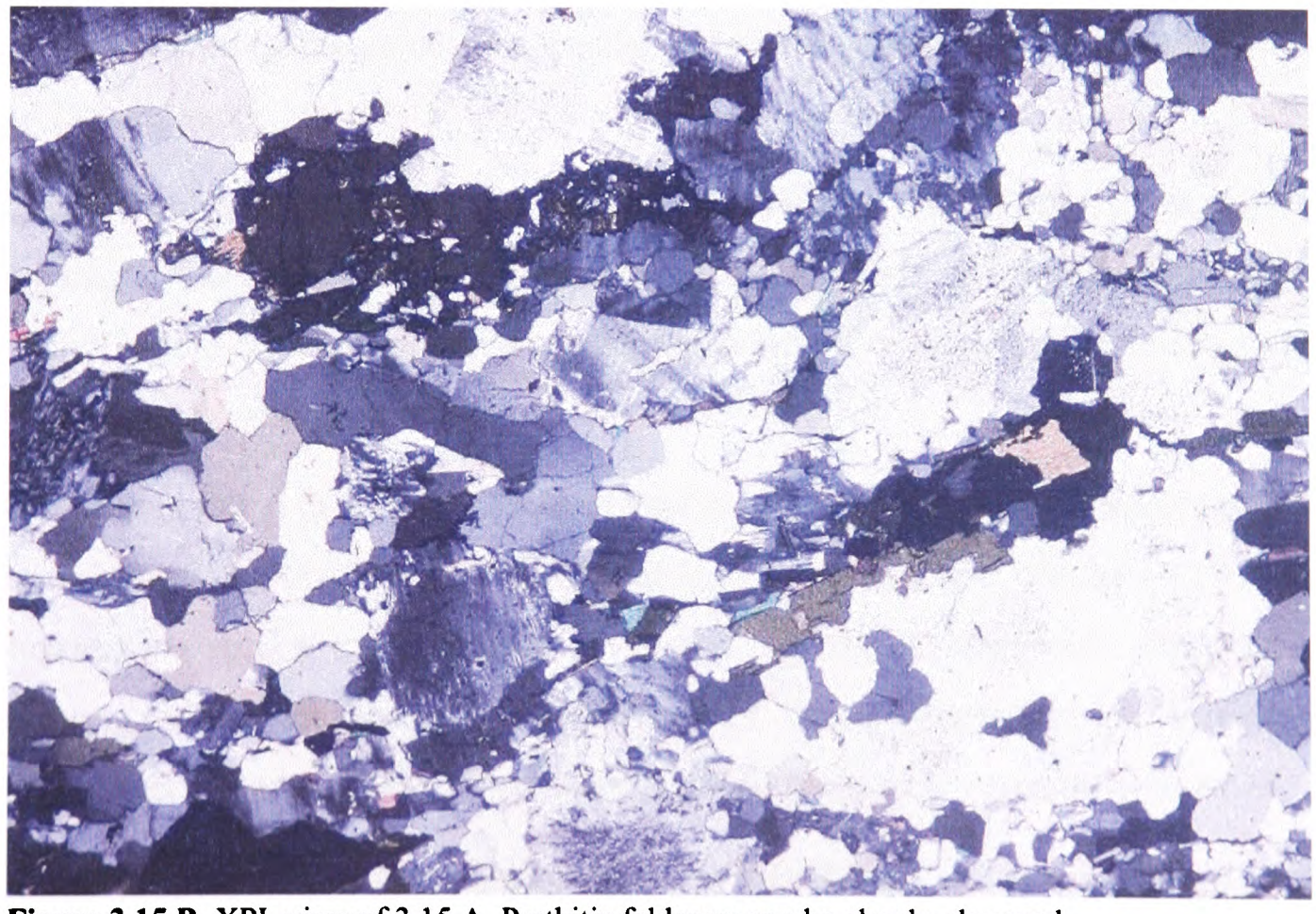


Figure 3.15.B. XPL view of 3.15.A. Perthitic feldspars can be clearly observed.

Plagioclase grains are fairly abundant, and grow up to 1-2mm in length. They often contain small muscovite and biotite inclusions. Some crystals are quite dusty with alteration to sericitic/white micaceous material.

Sample Z-18 from near Tongul is fairly representative of Suru Dome rocks as a whole; here coarse biotite flakes with lesser muscovite define a foliation that in places wraps small garnets around 1.5-2mm in diameter. These garnets are generally subhedral-euhedral in form and preserve an earlier inclusion trail in quartz that is slightly curved and discordant to the main fabric. Sample Z-59 from the centre of the Suru Dome structure shows a particularly fine garnet growth history. (Figure 3.16). One large garnet of around 1cm in diameter contains an inclusion trail of quartz and minor amounts of tourmaline and oxides in the core region, but contains a rim region approximately 0.8-1mm thick with no quartz inclusions. The core inclusions can be seen at the top and bottom of the garnet to curve sharply into the rim regions, where a dusty trail can be picked out, with tourmaline and oxides, running at right angles to the core trails. At the sides of the garnet, the core and rim trails are parallel, although no quartz is present in the rim. Parallel to the garnet rims are muscovite crystals which abut the garnet in areas which appear embayed, which suggest possible garnet breakdown to muscovite. In sample Z-33, a garnet of roughly 6mm diameter appears to form an atoll structure whilst breaking down to chlorite, muscovite and plagioclase (Figure 3.17). In general, however, Suru Dome garnets are smaller and do not preserve as many microstructural features as Donara nappe rocks.

Kyanite is almost ubiquitous in samples from the Suru Dome, apart from some very felsic samples. Crystals up to almost a centimetre in length occur, and overgrow the foliation in a generally random orientation. Many crystals are corroded at their rims to what appears to be a fine muscovite breakdown product.

Staurolite is found in sample Z58 from Parkatchik, forming porphyroblasts up to 3mm across that overgrow the biotite-muscovite foliation and small garnets (Figures 3.18.A & B). In the photomicrograph, a garnet crystal of around 0.7 mm is completely enclosed by a staurolite porphyroblast, with associated biotite crystals. This may represent garnet reacting to form staurolite and biotite, possibly by the same KFMASH reaction as mentioned above.

Chlorite is present in some samples from the Suru Dome, but is texturally associated with garnet and biotite and would appear to be a retrogressive phase, especially given the high-grade nature of these rocks.

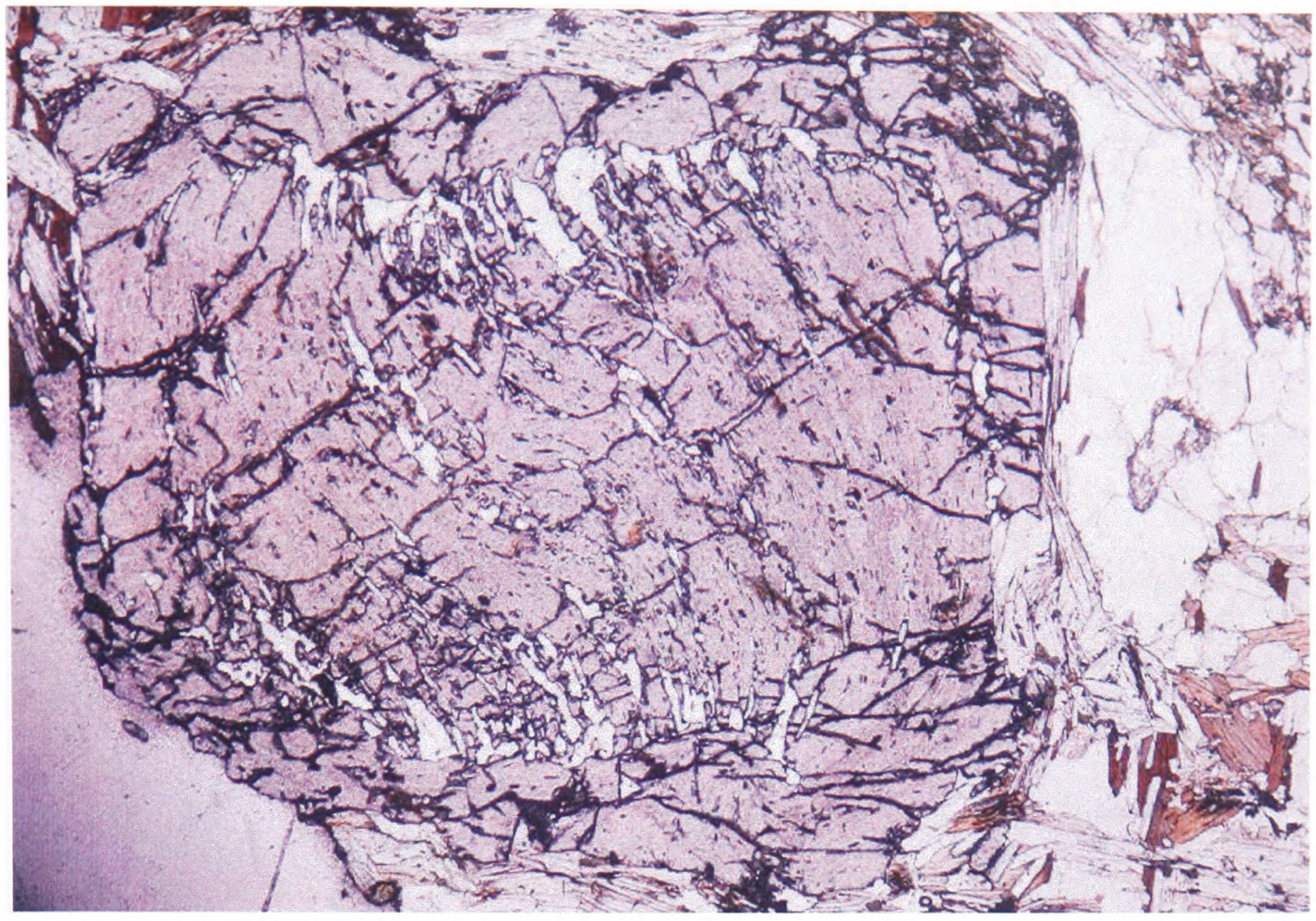


Figure 3.16.A. Photomicrograph in PPL of large garnet from sample Z59 from the Suru Dome. Features to note are the curved inclusion trails picked out in (mainly) quartz that are not present in the garnet rim region, although dusty trails can be seen in places to curve tightly from the core region into the rim. The rim appears to be embayed by micas in places (see below). Garnet approximately 1 cm in diameter.

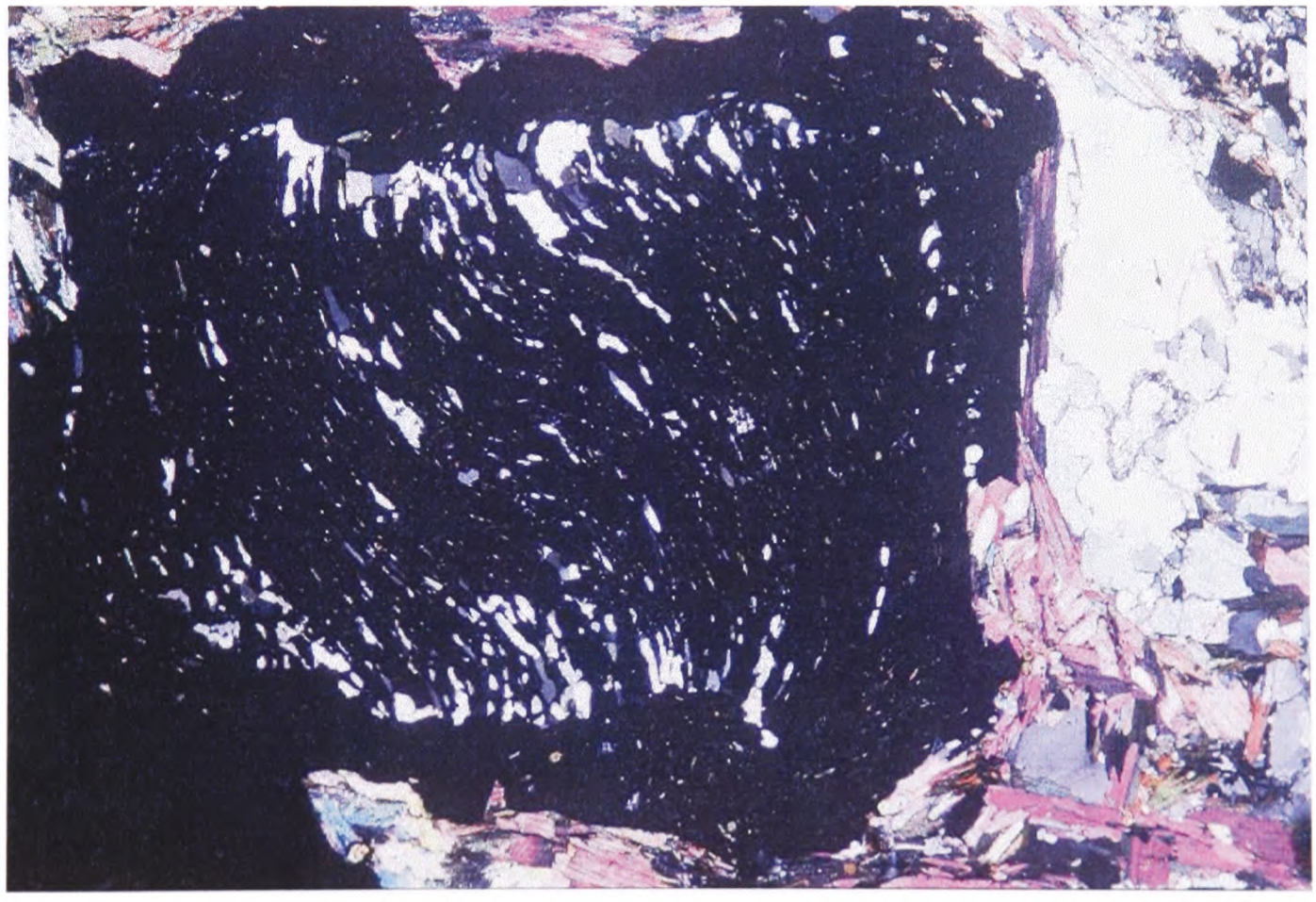


Figure 3.16.B. XPL view of Figure 3.16.A., which highlights the core and rim regions of the garnet.

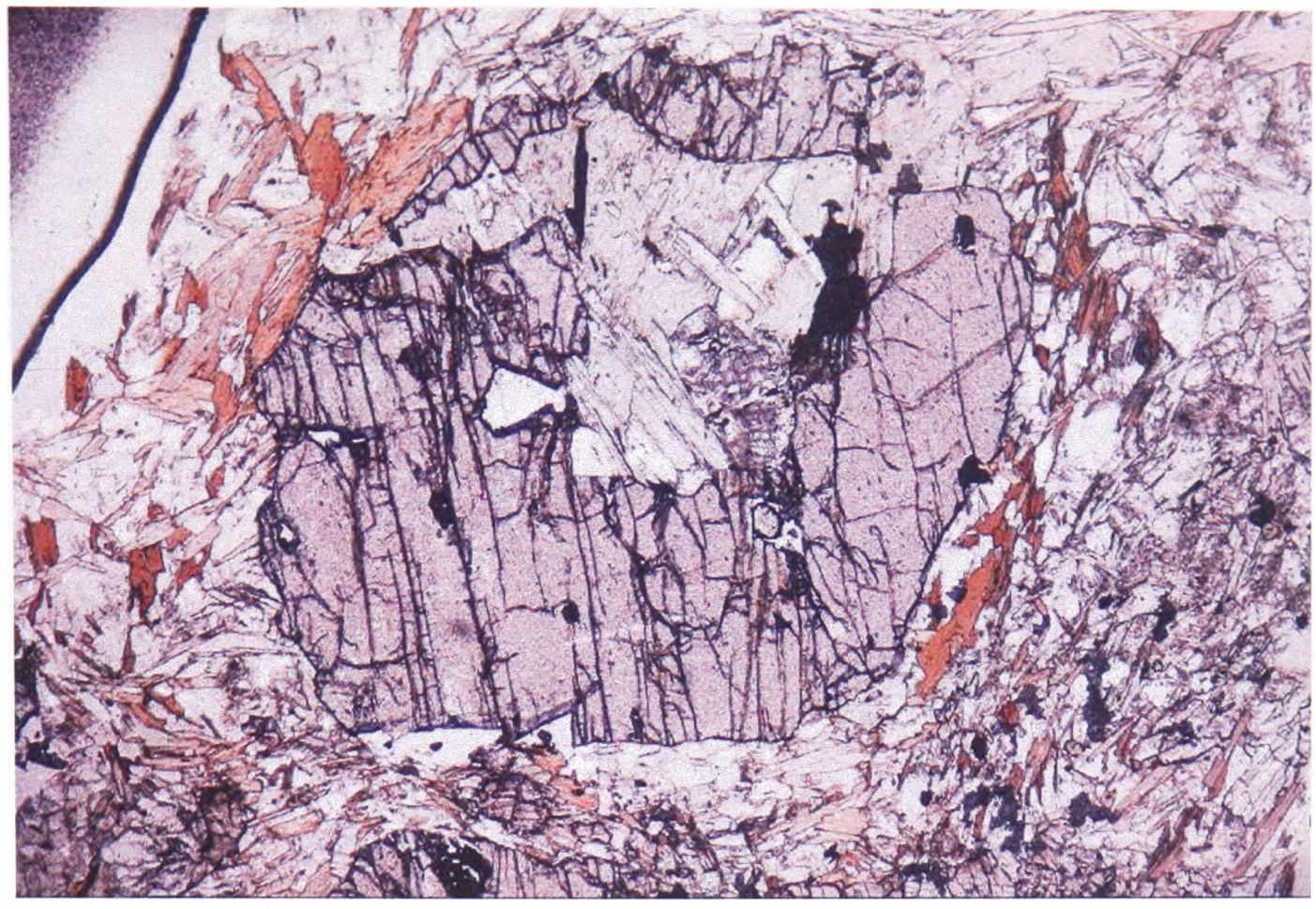


Figure 3.17.A. Photomicrograph in PPL of sample Z33 from the Suru Dome, illustrating a garnet approximately 6 mm in diameter that appears to breaking down to Chl + Ms + Pl and forming an atoll structure.

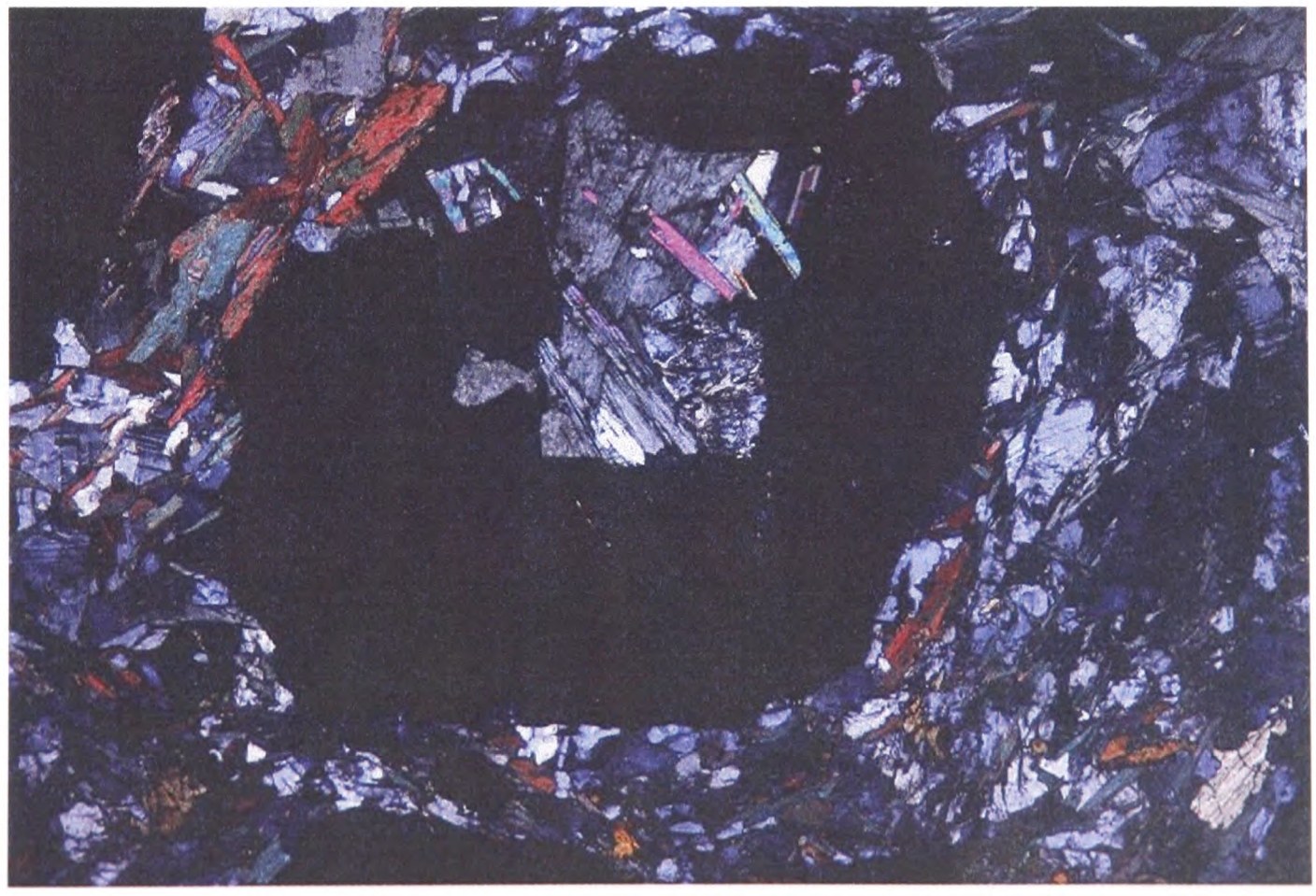


Figure 3.17.B. XPL view of Figure 3.17.A.

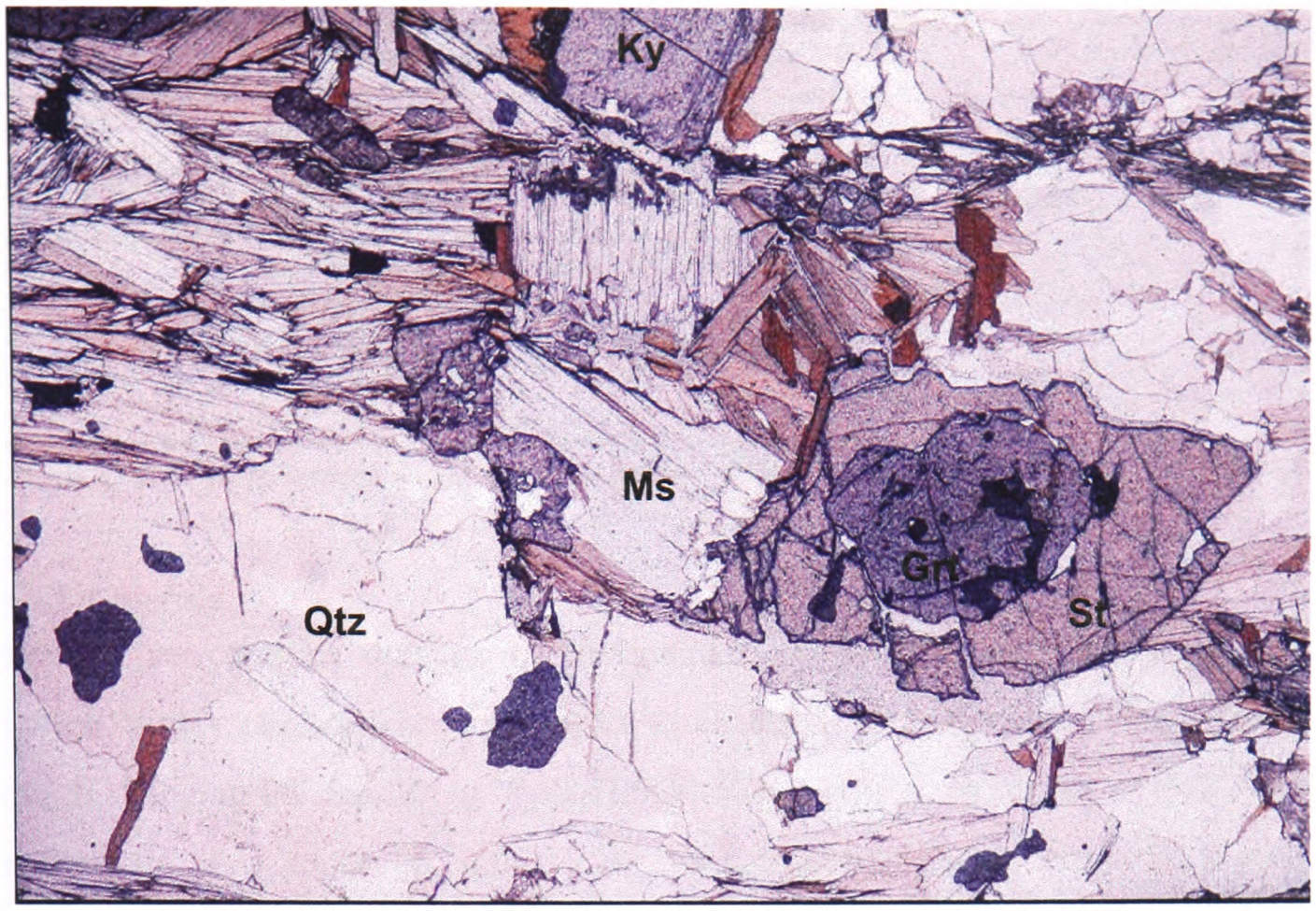


Figure 3.18.A. Photomicrograph in PPL of sample Z58 from the Suru Dome. This illustrates coarse micaceous and felsic regions defining the main S_3 foliation that are overgrown by Grt, St and Ky porphyroblasts. A small (0.7mm) garnet is completely rimmed by a staurolite crystal. Kyanite blades overgrow the foliation in a random orientation. Field of view approximately 5 mm.

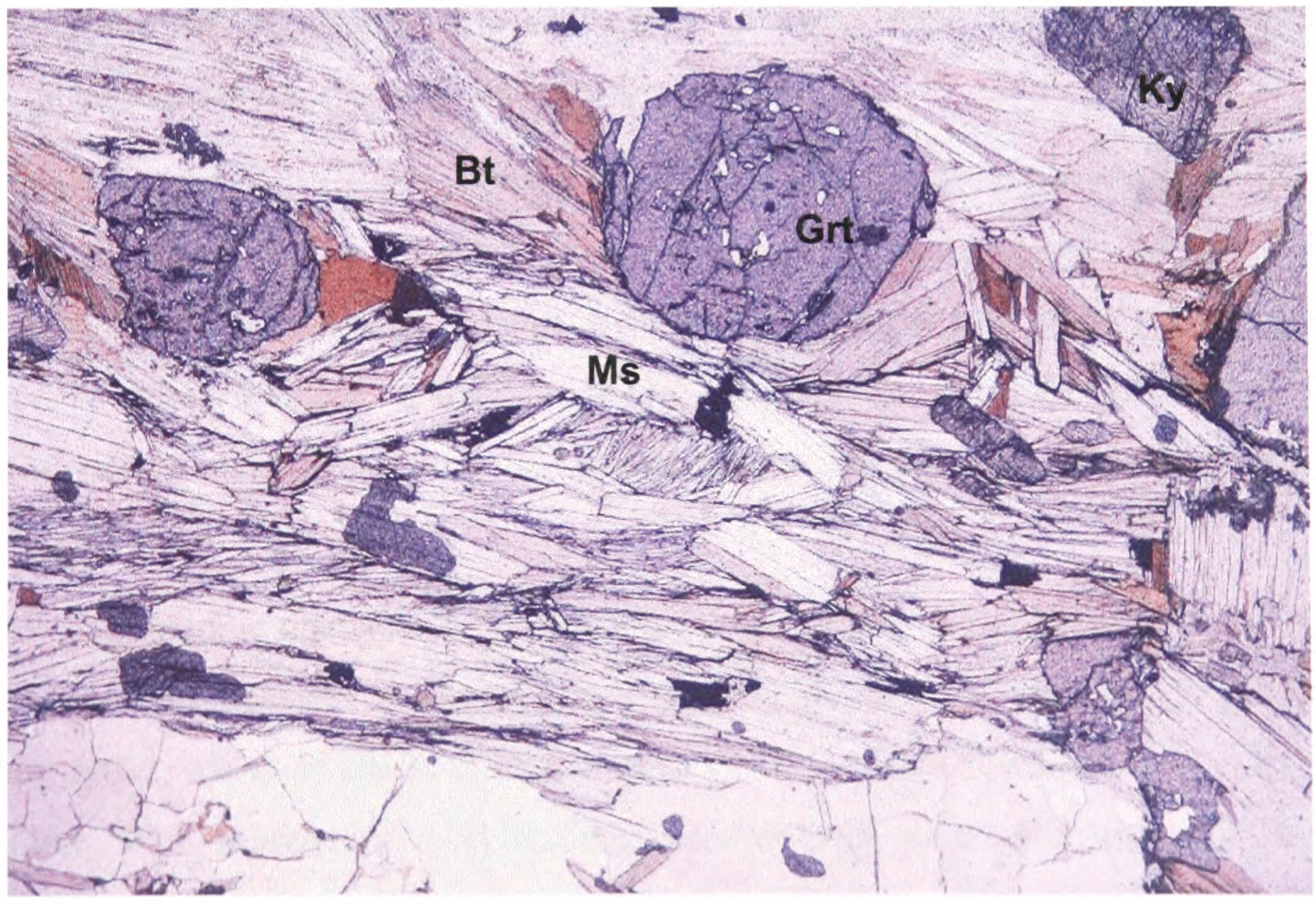


Figure 3.18.B. Another PPl view of sample Z58 illustrating the same textural features as described above and in the text.

Rock type	Typical assemblage	Rock type	Typical assemblage
Pelite/ semi-pelite	Qtz + Ms + Bt + Pl + Grt ± St ± Ky ± Chl ± Czo/Zo ± Gph ± Rt/Ilm	Amphibolite	Qtz + Bt + Pl + Hbl ± Grt ± Ep ± Chl ± Czo/Zo ± Cc/Dol ± Ilm ± Spn
Calc-pelite	as for pelite, and also Cal/Dol ± Hbl ± Spn	Marble	Cal + Dol ± Qtz ± Phl ± Clin ± Zo
Psammite	Qtz + Bt + Pl ± Grt ± Ms ± Zo/Czo ± Rt/Ilm	Granitoid	Qtz + Kfs + Ab + Bt + Ms ± Grt ± Ep

Table 3.1. Typical metamorphic assemblages observed in Suru Valley rock types. Abbreviations after Kretz (1983).

3.2.8 Fe-Ti minerals

Detailed petrographic analysis of metapelites, amphibolites and calcareous pelites from the Suru Valley reveals what appears to be a pattern of systematic changes in Fe-Ti minerals with changing PT conditions. Suru Dome rocks tend to contain fewer Fe-Ti oxides, but where they do, they appear to follow a similar pattern to those of the overlying nappe rocks.

In garnet bearing samples, collected mostly from the kyanite zone, ilmenite is the common Fe-Ti oxide in garnet cores, while rutile is seen towards the garnet rim, commonly replacing ilmenite. Rutile is common in the matrix, often pseudomorphing ilmenite plates, along with ilmenite that is apparently unaltered. In some samples ilmenite rims crystals of rutile, or appear as aggregated blocks, which is interpreted as ilmenite that has pseudomorphed to rutile transforming back to ilmenite.

Sample Z-10 from south of Tongul illustrates this history clearly. Large garnets overgrow a foliation defined by graphite trails and ilmenite plates aligned with this foliation in the core. As one proceeds towards the garnet rim the plates become blockier and change to rutile pseudomorphing ilmenite, sometimes rimmed by ilmenite, and usually surrounded by quartz. Most of the matrix Fe-Ti phase is ilmenite either rimming rutile or pseudomorphing blockier rutile crystals.

This petrographic observation is interpreted as being due to increasing PT conditions and subsequent retrogression; as pressure and temperature increase, ilmenite is gradually replaced by rutile, which is stable at higher pressures and temperatures, having a smaller molar volume. With subsequent uplift and erosion after peak metamorphism, rutile reverts back to ilmenite which is the most common phase. The reaction between rutile and ilmenite appears to involve a siliceous phase, as evidenced by the quartz surrounding the crystals that are undergoing the transformation.

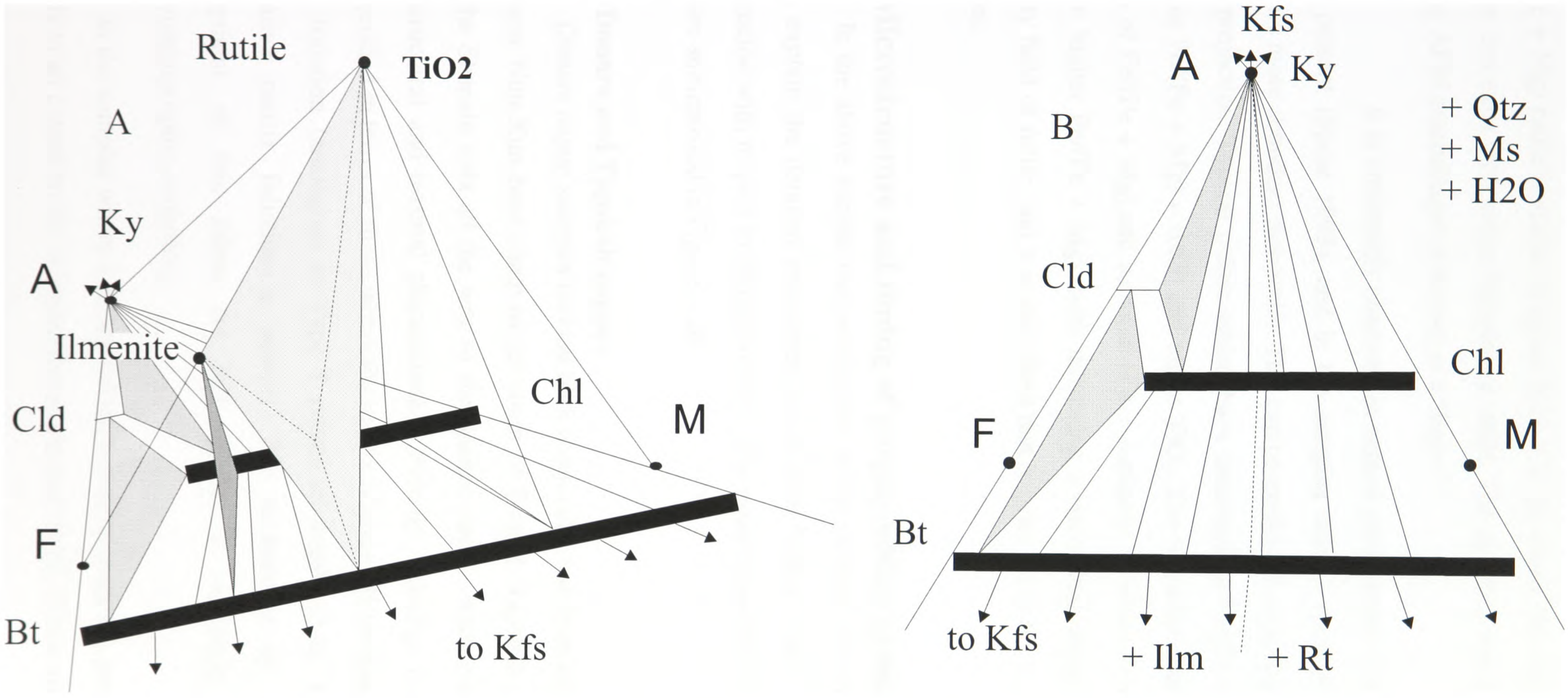


Figure 3.19. Phase diagrams in the system KFMASH + TiO2. A) shows the AFM + TiO2 tetrahedron. Note that Fe-rich assemblages must coexist with ilmenite whereas Mg-rich assemblages coexist with rutile. B) shows the ilmenite-rutile "fence" (dotted line), which separates ilmenite-bearing AFM assemblages from rutile-bearing ones. After Spear (1993).

Pressure and temperature are not the only controls on the relative stabilities of Fe-Ti oxides; bulk composition also determines whether rutile or ilmenite is stabilised by TiO_2 (Spear 1993). In rocks with high Fe/(Fe + Mg), ilmenite is stable, whereas in rocks with low Fe/ (Fe + Mg) rutile is stable. (Figures 3.19.A & B) shows the assemblages where biotite and chlorite can exist with either ilmenite or rutile. The dividing line between ilmenite and rutile bearing AFM assemblages is known as a "fence".

It is commonly observed in natural parageneses that ilmenite is the only Fe-Ti oxide present (Spear 1993), and in the samples studied from the Suru Valley ilmenite is certainly more abundant than rutile. This can be explained relatively simply by considering the AFM projection. Typical pelitic schists have intermediate Fe/(Fe + Mg) ratios of 0.8-0.5 (cf. Z47 has Fe/(Fe + Mg) = 0.65) and minor TiO_2. The ilmenite/ rutile fence is usually at lower values of Fe/(Fe + Mg),and so rutile is not common; however, the position of the fence will shift to higher Fe/(Fe + Mg), with increasing pressure and temperature, thus increasing the stability field of rutile, and it is this effect that is believed to be recorded in these Suru Valley samples.

3.3 Microstructure and timing of porphyroblast growth

In the above section the petrography of the samples was described. This section sets out to explain the detailed microstructure of Suru Valley rocks, and the relative timing of deformation with respect to metamorphism. The main microstructural features of Suru Valley rocks are summarised in Figure 3.26.

3.3.1 Donara and Tapshah nappes

Donara nappe samples include both those collected from along the Chellong nala, and from near Nun-Kun base camp to the south of Tongul. Tapshah nappe rocks include those from the Shansin nala all the way to the Sankoo nappe. Both exhibit a variety of different microstructural and textural characteristics. Broadly speaking, however, two types can be distinguished in terms of those where the matrix is generally recrystallised and does not have a strong foliation (analogous to Type 1 pelites of Searle *et al.* 1992), and those where a penetrative matrix foliation is present. The relationship of porphyroblast growth to development of this fabric (or lack of it) is obviously crucial to interpreting tectonometamorphic evolution.

In the samples where a strong foliation is developed, the precise nature of the foliation depends to an extent on the composition of the rock itself. Pelitic rocks with a high proportion

of micas develop a spaced foliation, defined by aligned muscovite and biotite crystals that separate domains of quartz and plagioclase crystals. This foliation is often crenulated, sometimes quite strongly, by later folding, and appears to wrap around garnet porphyroblasts. In more semi-pelitic to psammitic rocks, as there is less micaceous material, a more continuous foliation develops, again defined by alignment of quartz, plagioclase and micas. This does not preserve as much evidence for later crenulation or wrapping of porphyroblasts.

At least three phases of deformation can be recognised in pelitic samples from the Donara nappe, as outlined in Chapter 2. $\mathbf{D_1/S_1}$ is generally only preserved as inclusion trails in garnet porphyroblasts, and is defined by fine trails of graphite, quartz, muscovite and clinozoisite, although quartz is the only ubiquitous phase. These trails are varyingly spiral or crenulated depending on sample. $\mathbf{D_2/S_2}$ is the dominant matrix fabric described above and defines the large scale nappes themselves. $\mathbf{D_3/S_3}$ only forms a dominant fabric in Suru Dome rocks, but deforms the S_2 fabric to varying degrees in the overlying nappe rocks, such as crenulation of S_2. The following section illustrates these features in detail from a number of samples that all differ slightly in their petrography.

Sample Z10 (Figure 3.2.A.) displays fine-grained graphitic trails, with aligned clinozoisite crystals, in a garnet of around 1.2 cm diameter. These trails define an S_1 foliation, which is crenulated by D_2 near the garnet rims, and rotates into parallelism with the rather poorly-defined matrix foliation. The garnet porphyroblast appears to have overgrown this foliation fairly statically except at the rim region, and has undergone some resorption, presumably at the same time as matrix recrystallisation. Muscovite, biotite and plagioclase appear to have overgrown a preexisting matrix foliation which is still discernible despite the fairly random orientation of the crystals. This sample contrasts with others, such as Z43 from near the closure of the Donara nappe (Figures 3.20 A & B). Here, S_1 is preserved in garnet cores as spiral inclusion trails in fine quartz, muscovite and clinozoisite, with ilmenite also present. The inclusion density is greatest in the garnet core, suggesting that garnet grew fastest in the core region ,and the spiral nature of the inclusion trails suggest that the garnets grew syn-tectonically with respect to D_2 crenulation of S_1. The main S_2 matrix foliation is a spaced foliation, as described above, in coarse muscovite and biotite, which is itself tightly crenulated by a later D_3 event (Figure 3.3.B.). This foliation wraps around garnet porphyroblasts, but in a manner which suggests that the crenulation of the S_2 foliation and not the formation of it is the cause; no quartz pressure shadows are observed, and the overall orientation of the S_2 fabric is quite close to that of the S_1 fabric at garnet rims, which does not imply high strain after garnet growth. Associated with the hinges of these D_3 crenulations are smaller muscovites that

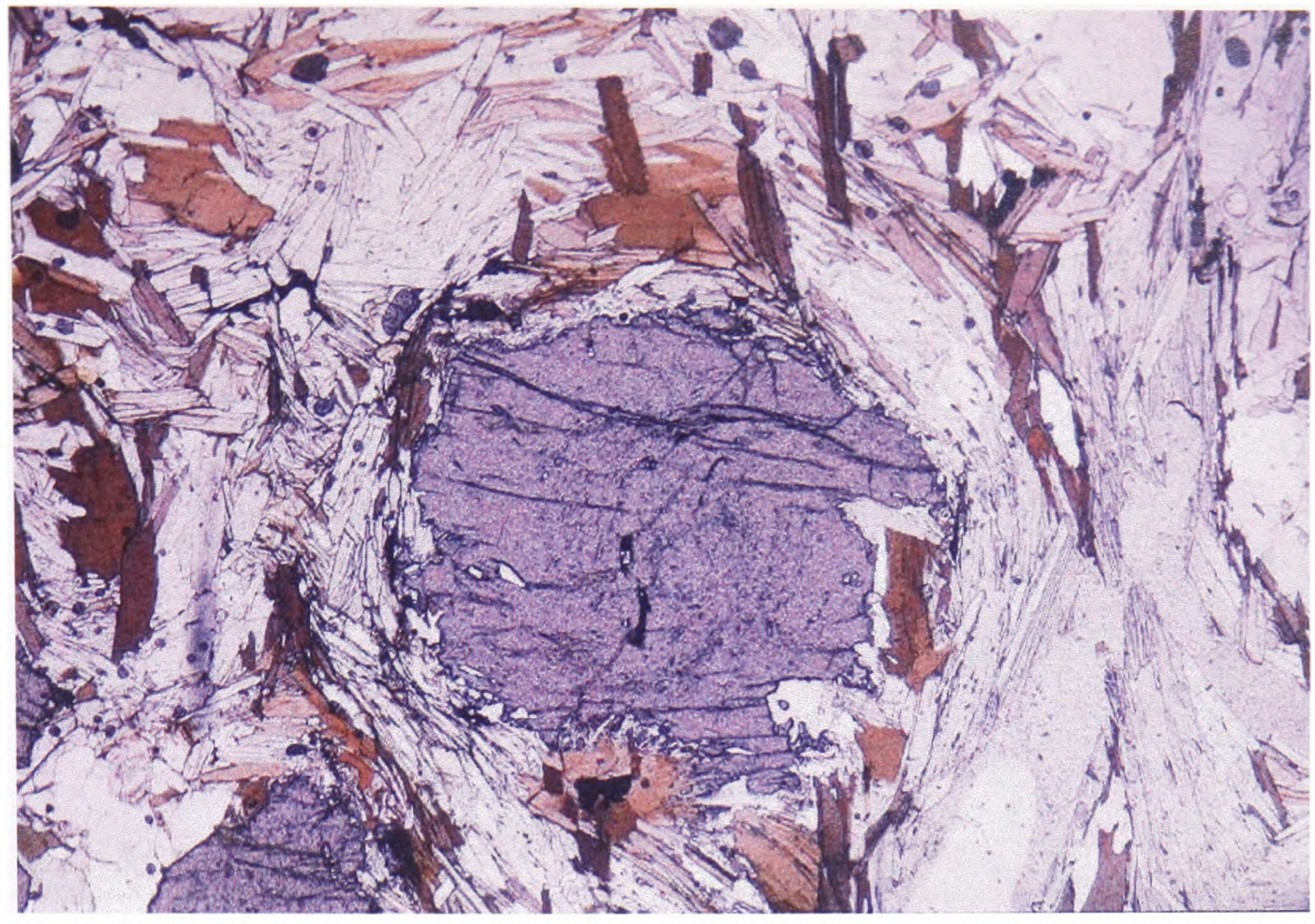


Figure 3.20.A. Photomicrograph in PPL of sample Z43 (cf. Figure 3.3) illustrating details of one garnet. In the core of the garnet, fine spiral inclusion trails of Qtz + Ms + Czo + Ilm suggest syn-tectonic garnet growth with respect to crenulation of S_1. The coarse flakes of Ms + Bt in the matrix define the S_2 foliation, which is itself crenulated by D_3

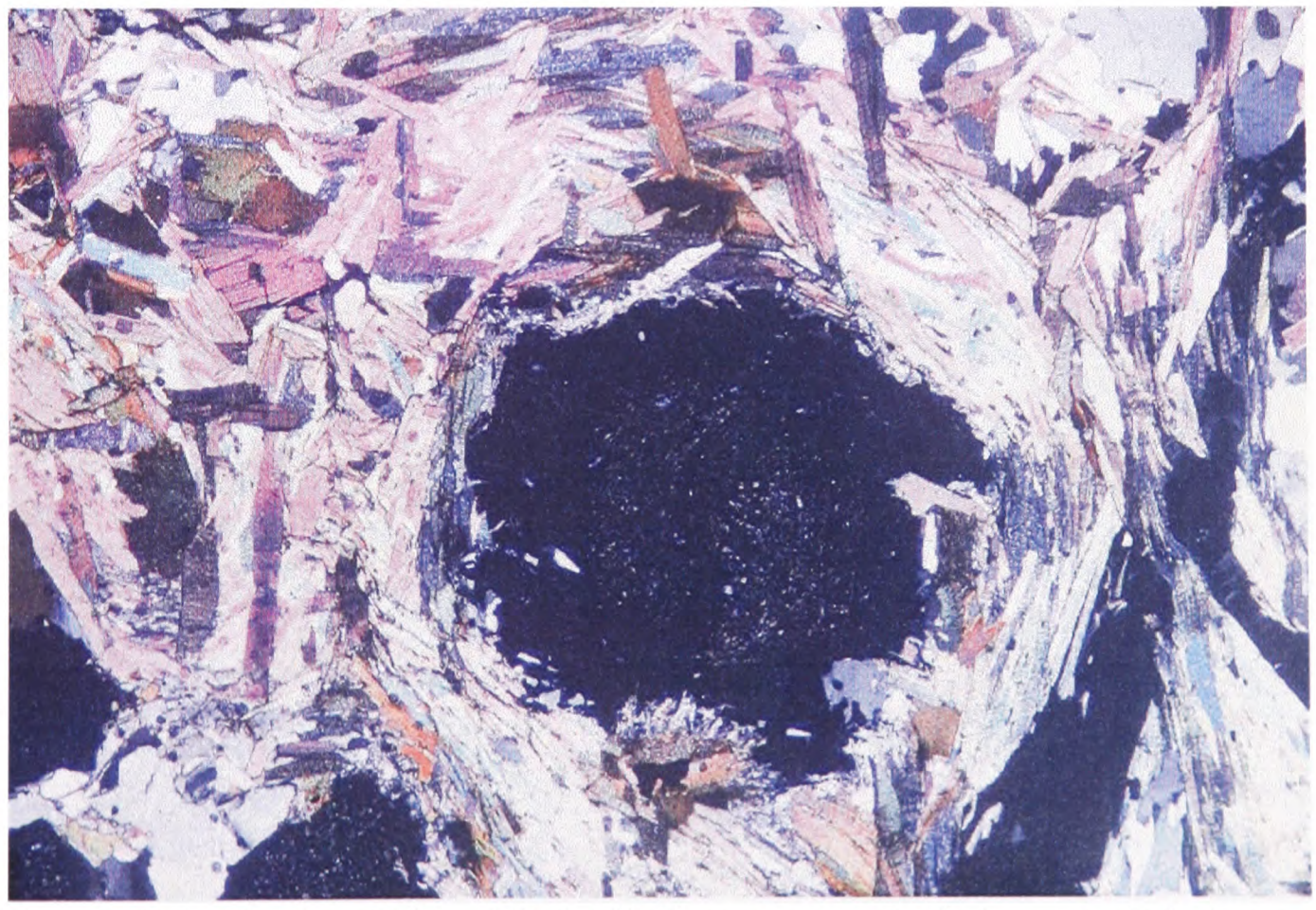
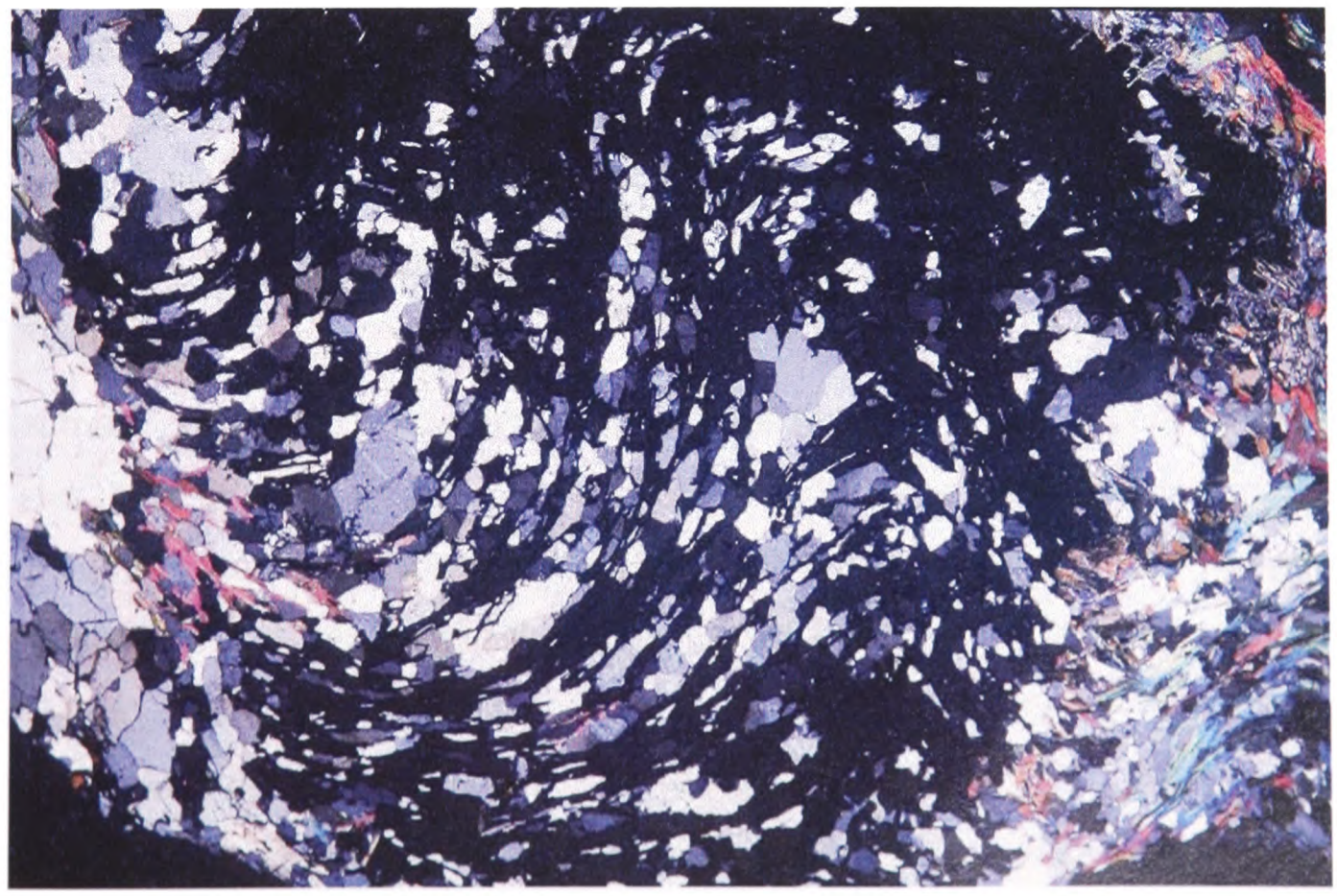


Figure 3.20.B. XPL view of Figure 3.20.A. This illustrates more clearly the greater inclusion density in the core region of the garnet. Field of view approximately 5 mm.





Figures 3.21 (above) and 3.22 (below). Photomicrographs in XPL of samples Z37 (above) and Z56 (below) illustrating large porphyblastic garnets that have overgrown a fabric (presumably S_1) that has already segragated into a composite foliation of felsic and micaceous regions. Field of view in both slides approximately 1.4 cm.

appear to be growing in an axial planar orientation, and could represent the beginnings of an axial planar cleavage.

Similar, but more common, are the relationships seen in Z71, from around 2-3km to the SW of Z43 (Figures 3.7.A & B). Here, garnets of nearly 1cm in diameter overgrow a fabric in quartz, clinozoisite, muscovite and ilmenite that has already segregated into a composite foliation of felsic and micaceous domains, and contains tight folding of the S_1.fabric. Towards the garnet rims, this fabric has a fairly similar orientation with the coarser matrix S_2 fabric, and the garnet can be seen to be growing syn-tectonically along foliation planes, along with staurolite crystals sometimes included at garnet rims. In the matrix, staurolite crystals appear to align with the foliation planes, as does kyanite to an extent, although some are found in a random orientation (Figures 3.8.A & B). There is a slight D_3 crenulation to the S_2 fabric.

Figures 3.21 and 3.22 show samples Z56 and Z37, which further illustrate garnet inclusion trails that had already segregated into a composite fabric by the time garnet overgrew them. Figures 3.23 A & B are of sample Z68, where muscovite, plagioclase and zoisite overgrow graphitic trails, defining the S_2 foliation which is subsequently tightly crenulated. Some plagioclase crystals appear to display deformation twinning.

Z69, a calcareous pelite from a nearby locality again displays syn-tectonic garnets, but contains well-formed staurolite crystals statically overgrowing graphitic trails (Figures 3.4.A & B), which are also overgrown by aligned micas.

Amphibolites often contain early inclusion trails in garnets, most notably in Z4 from south of Tongul, where inclusions of carbonate, sphene, quartz and zoisite imply garnet rotation of up to 360^0. Here, hornblende poikiloblasts overgrow garnet porphyroblasts and an earlier foliation in biotite (Figure 3.13). The foliation observed is on a coarser scale, where a spaced schistosity segregates plagioclase-rich and mafic bands, more easily visible on a hand-specimen scale.

In summary, rocks from the Donara and Tapshah nappes, which covers the majority of the study area, have three recognizable deformation episodes. S_1 is generally preserved in the cores of garnets as inclusion trails, where it is often folded by D_2; the main matrix foliation S_2 is often continuous with S_1 near garnet rims, and is defined by a spaced foliation in micas and quartz/plagioclase. Main porphyroblast growth, especially that of garnet rims (at least), appears to be contemporaneous with the development of this fabric. This fabric was then deformed by a later D_3 event which crenulated the S_2 foliation and caused some wrapping of

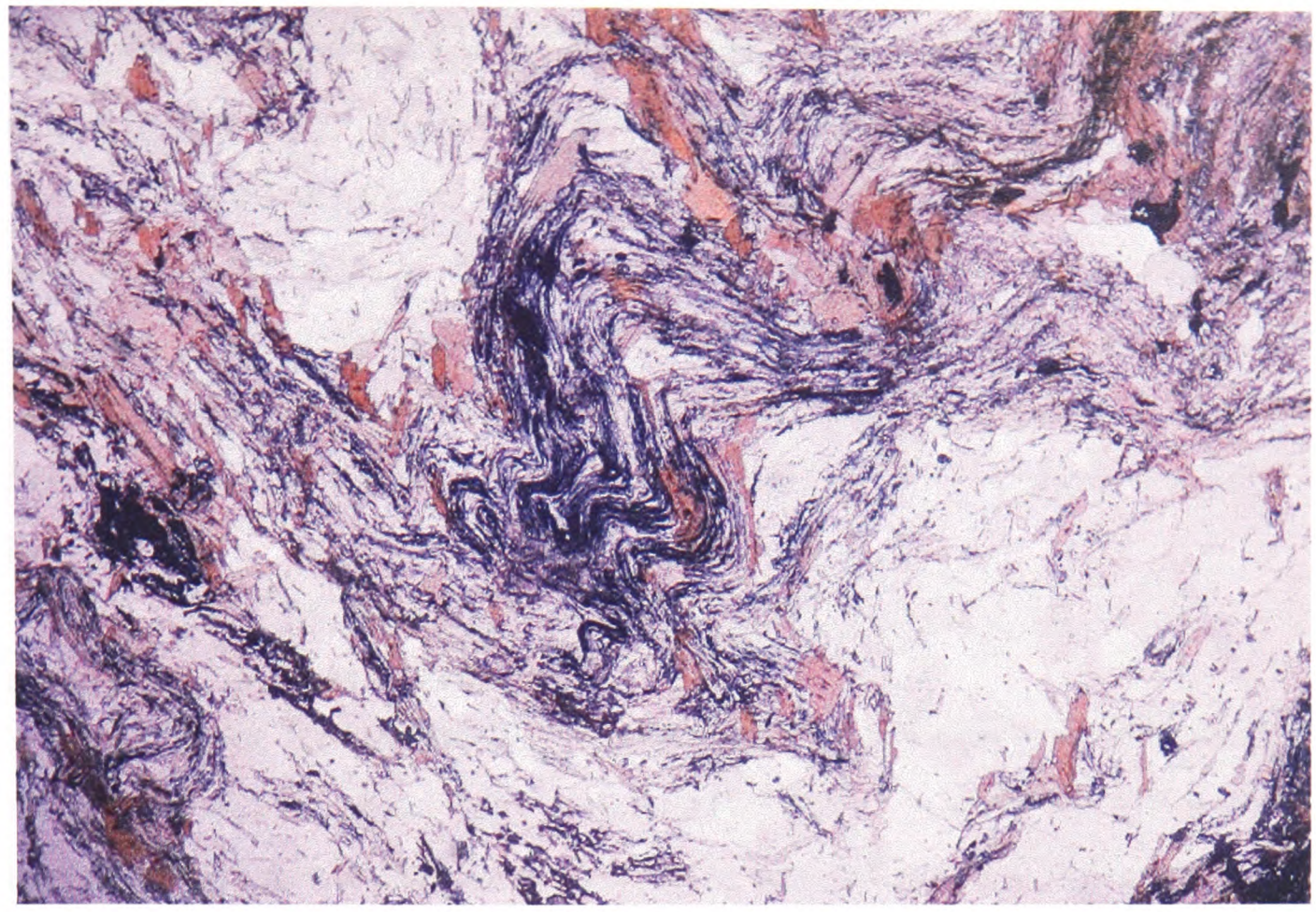


Figure 3.23.A. Photomicrograph of sample Z68 in PPL showing details of the matrix. Graphitic trails are overgrown by Ms + Bt + Pl + Zo, defining the S_2 foliation, which is subsequently tightly crenulated by D_3. Field of view approximately 5 mm.

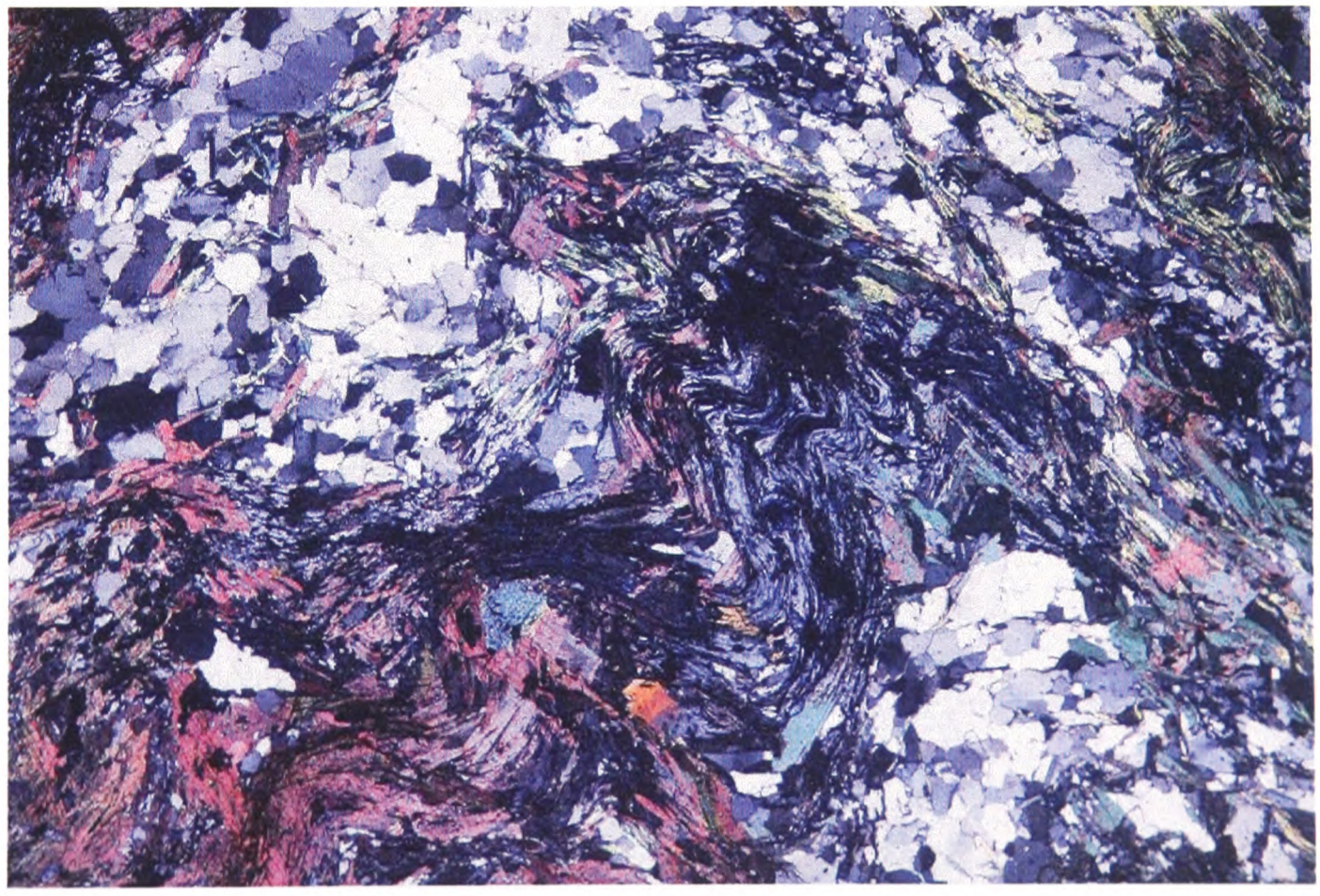


Figure 3.23.B. XPL view of 3.23.A. Some plagioclase crystals exhibit deformatiion twinning in the hinges of crenulations.

garnet porphyroblasts. Staurolite and kyanite growth is more strongly bulk composition dependent, but appears to be syn-post D_2. Even those samples without a pervasive matrix foliation show some evidence for crenulations related to D_3. It is quite possible, although by no means certain, that the D_3 event observed in Donara and Tapshah nappe samples is related to the D_3 event attributed to doming of the Suru Dome and formation of the main Suru Dome foliation, as described in Chapter 2. The beginnings of a crenulation cleavage as observed in sample Z43 may represent a less-well developed relation of the S-C fabrics described at Parkatchik.

3.3.2 Sankoo nappe and Jildo section

Samples from the Sankoo and Jildo sections are described separately from those from the Donara and Tapshah nappes, as they occur at lower grades near the top of the slab, and should therefore display microstructures that may have been obliterated at higher grades.

Z81 from around 2km south of the ZSZ at Sankoo displays features fairly characteristic of pelites from the traverse (Figures 3.6.A & B). A well-defined foliation in muscovite and chlorite is overgrown by porphyroblasts of albite, which preserve fine inclusion trails of quartz at a high angle to the main foliation. These albite crystals are abundant and in some places almost obscure the main foliation. Small, skeletal garnet crystals overgrow these albites, and appear to be post-tectonic. Z83, from slightly closer to the ZSZ, displays similar microstructures, but here the garnets grow along the foliation. From the locality of Z82, closest to the ZSZ, it can be observed in the field that the main fabric is an S_1 foliation overprinting S_0 bedding (Figure 2.16); it would seem appropriate that the main foliation observed in all these samples is an S_1 fabric, with possible remnant S_0 preserved as inclusion trails.

Z23 from just east of Jildo is a phyllite displaying a crenulation cleavage (Figure 3.24). The foliation is defined by cleavage domains, which are the limbs of microfolds, and microlithons, in the fold hinge areas. A later fabric is developing at a low angle to this crenulation cleavage, which may be related to shear on the nearby ZSZ.

3.3.3 Suru Dome

Although Suru Dome rocks, like Donara and Tapshah nappe rocks, display a number of different textural and microstructural styles, the "typical" Suru Dome rock (as described by Searle *et al.*, 1992) is distinct from those from the overlying nappes. Generally, they are coarser-grained, with large sheaves of biotite and muscovite defining a lenticular foliation that

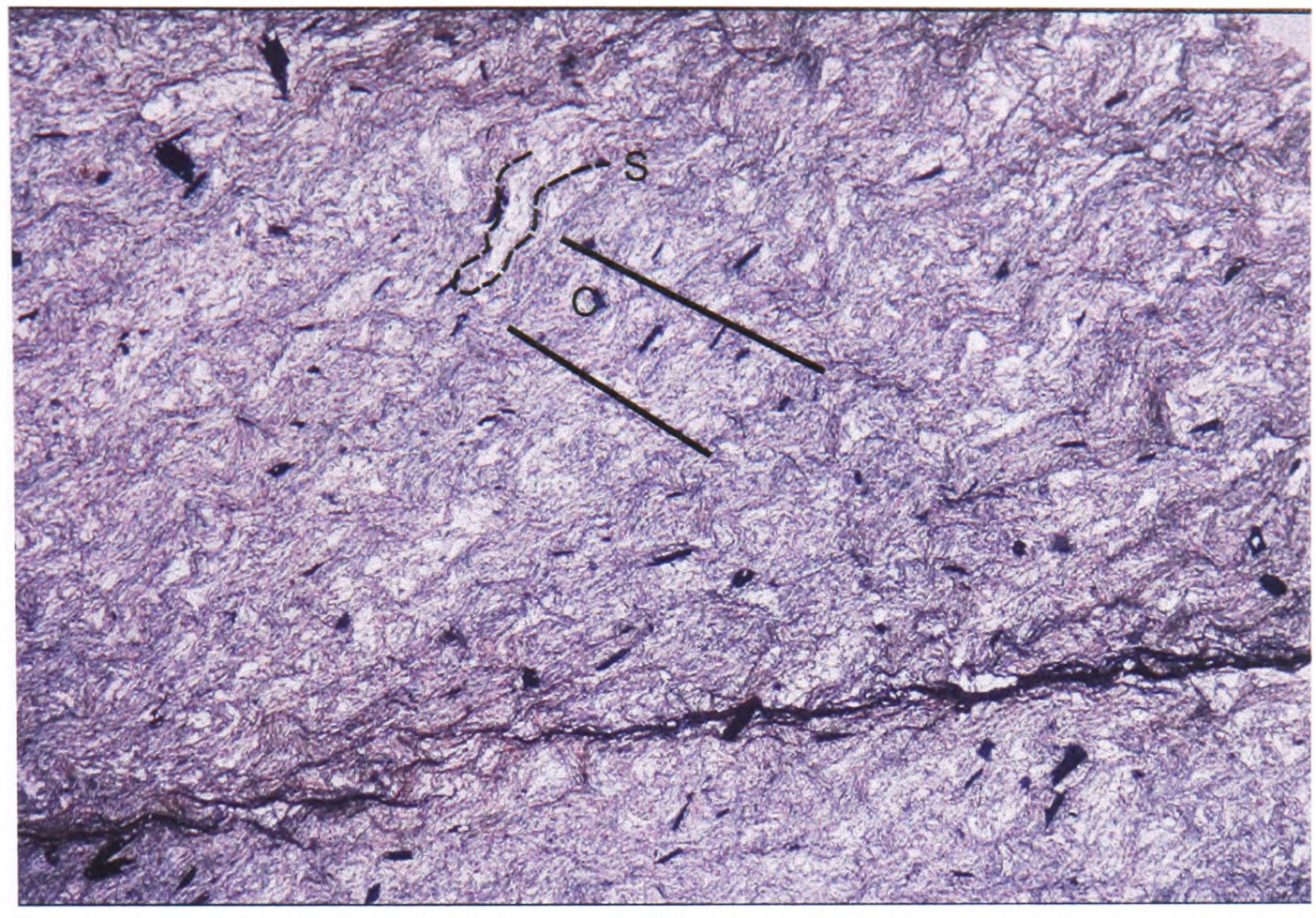


Figure 3.24.A. Photomicrograph of sample Z23 from near Jildo illustrating an early foliation (S) defined by cleavage domains (limbs of microfolds) and microlithons (fold hinge areas). A later C fabric is developing at an angle to this.

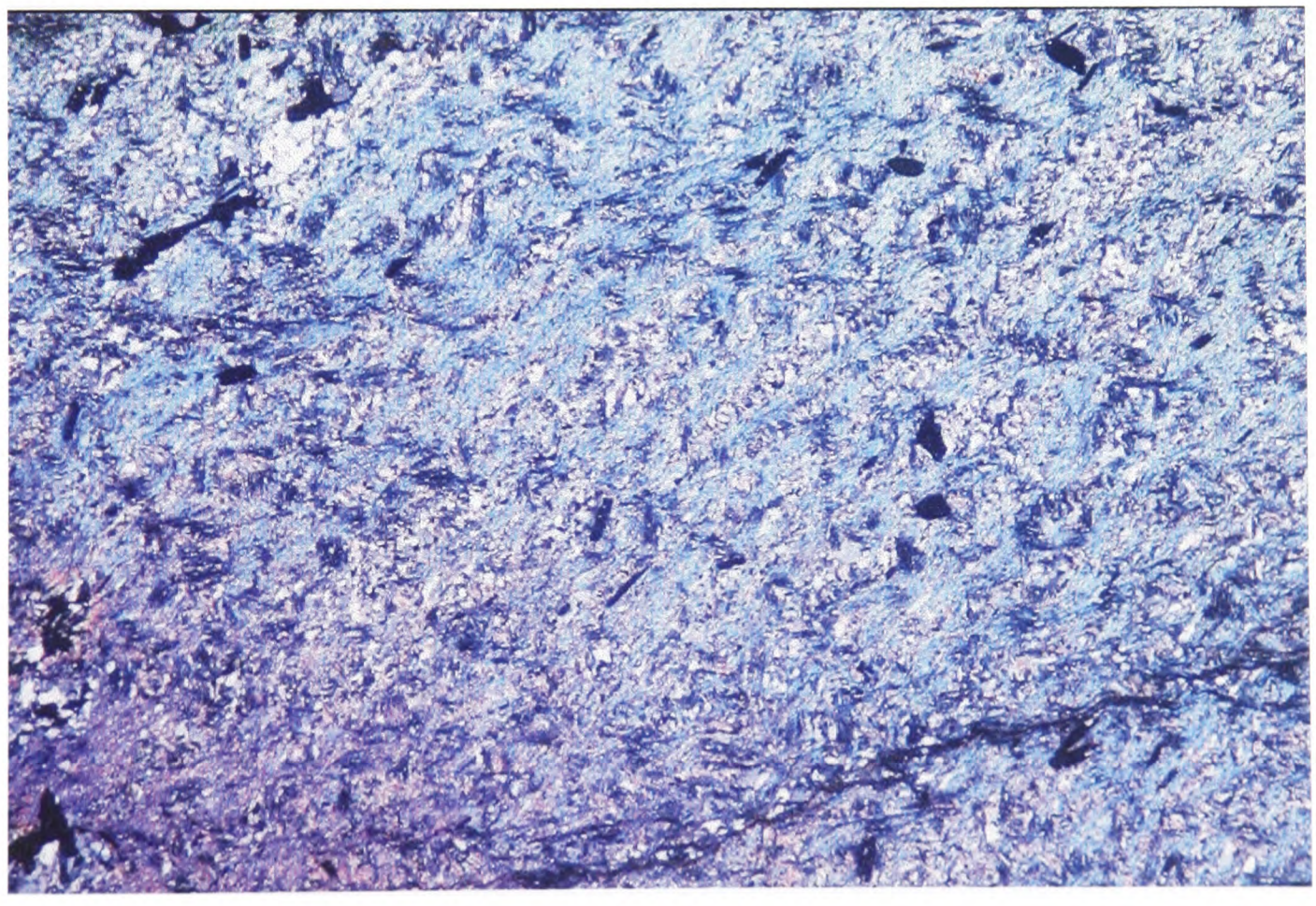


Figure 3.24.B. XPL view of Figure 3.24.A.

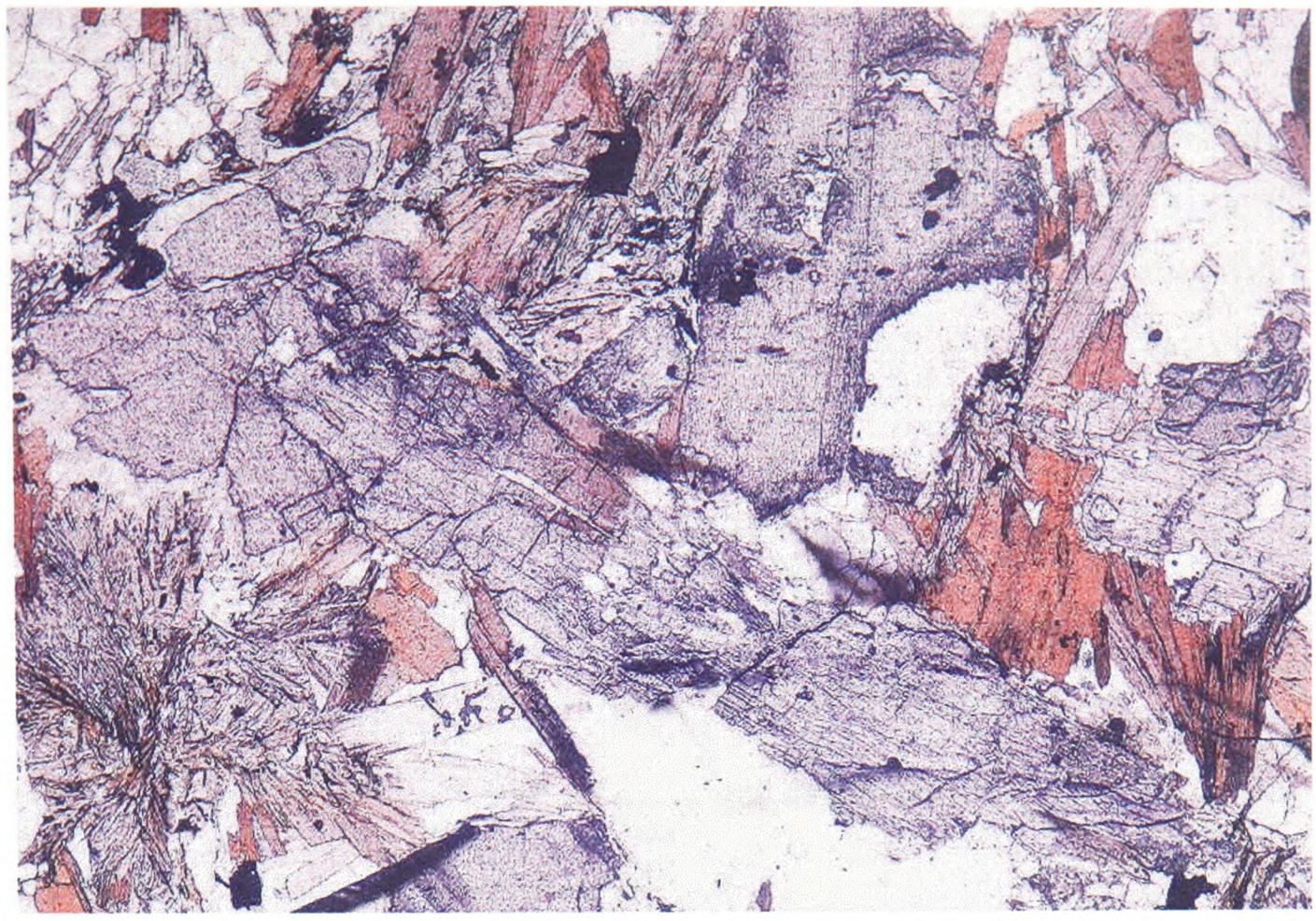


Figure 3.25. Photomicrograph in PPL of sample Z18 from the Suru Dome. Large kyanite blades up to 4 mm long grow in a random orientation, and here completely overprint the matrix fabric. Field of view approximately 5 mm.

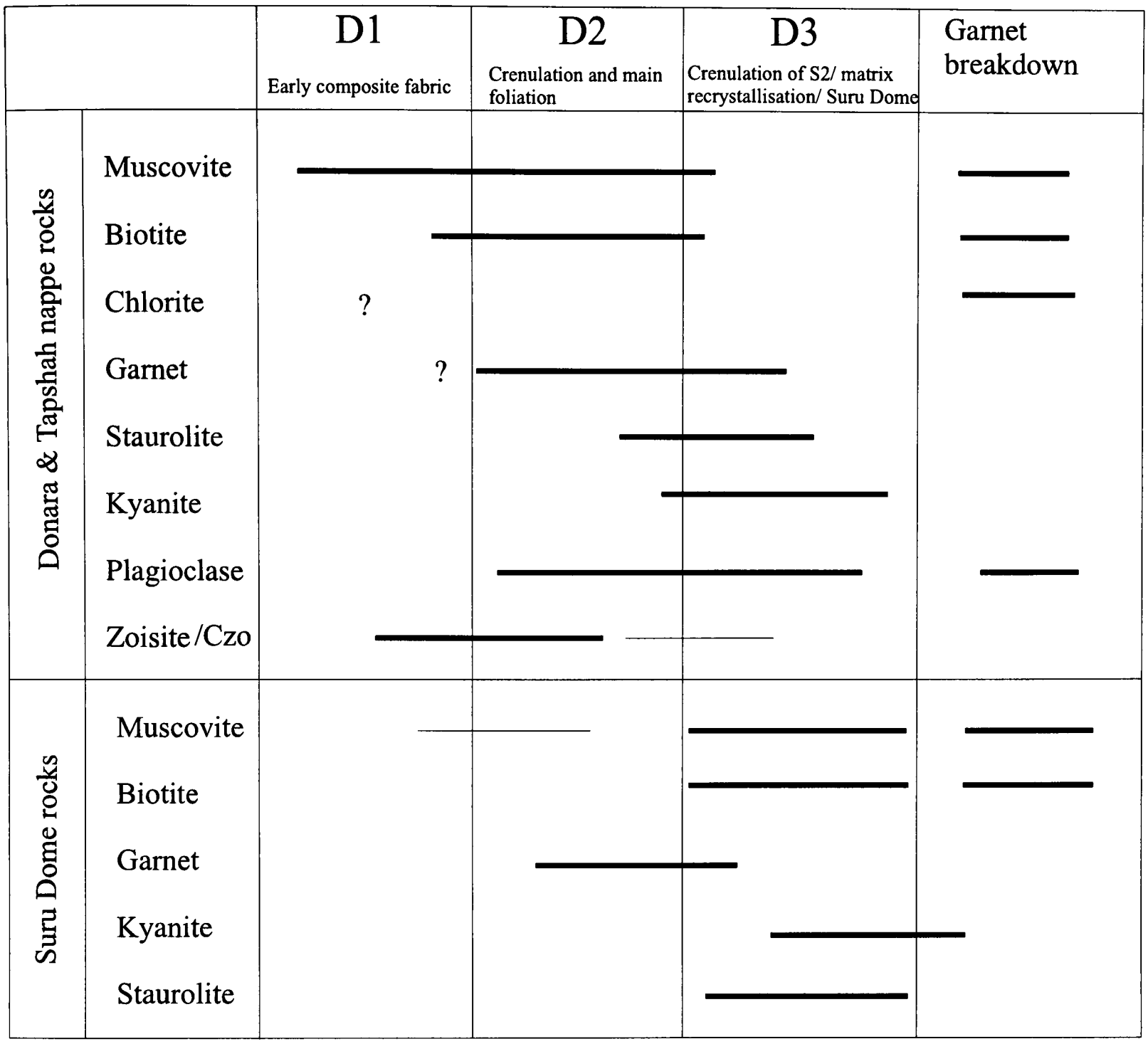


Figure 3.26. Summary of the main microstructural features of Suru Valley samples.

in places wraps garnet porphyroblasts, although in some samples the garnets appear to overgrow the foliation. Kyanite and staurolite overgrow this fabric, and occasionally align along it, but in some samples such as Z18 (Figure 3.25), appear to take on a random orientation. As described in an earlier section, some garnets preserve an earlier S_1 inclusion fabric, crenulated by a D_2 event, that lies at a high angle to the matrix foliation. Searle *et al.* (1992) described this matrix foliation as an S_3 fabric relating to Suru Dome formation, but this can be difficult to distinguish in thin section; only on an outcrop scale can a later S_3 shear fabric be seen to cut the main S_2 foliation, such as described at Parkatchik.

The main microstructural features of Suru Valley rocks are summarised in Figure 3.26

3.4 Mineral chemistry

3.4.1 Introduction.

A total of 30 samples from the area were analysed using a Cambridge Instruments Microscan 9 electron microprobe. Samples were mounted on 30 μm thick polished sections and analysed with an electron beam current with a diameter of 0.5 μm, a current of 40 nA and an accelerating potential of 20 kV. This results in an excitation volume on the sample with a maximum diameter of 3 μm, although this varies from element to element. Once elements were measured, a ZAF correction was applied to the apparent weight percents to correct for differences between the matrix of the unknown and the standards used to calibrate the microprobe. Samples were analysed with a view to determining relevant mineral compositions for use in thermobarometric calculations and to identifying zoned garnets for use in estimating the prograde metamorphic evolution of the samples.

3.4.2 Garnet

3.4.2.1 Models for the development of growth zoning

With the advent of the electron microprobe in the early 1960s and with it quantitative information on garnet composition, studies have attempted to explain the observed zoning in garnets. The earliest workers (Chinner, 1965; Harte and Henley, 1966) explained the bell-shaped Mn profile in sub-sillimanite grade rocks in terms of the preferential fractionation of Mn into garnet, and the subsequent depletion of the matrix Mn concentration with respect to garnet. If the interior of the garnet remained isolated from the matrix i.e. not modified by diffusional equilibration, then later layers of garnet would have a depleted reservoir of Mn to draw upon and thus be less manganiferous than earlier layers. This suggestion was quantified

by Hollister (1966) and Atherton (1968), who modelled the depletion of Mn in the rock as a Rayleigh fractionation process. The simple Rayleigh model requires that the partition coefficient K_D for Mn remains constant throughout garnet growth; however, as K_D is temperature dependent, and most garnets do not necessarily grow isothermally, this may not be a valid approximation. Furthermore, K_D is also dependent upon mineralogical compositions and proportions, especially those in direct contact with the garnet, which is a further complicating factor.

An alternative to the simple Rayleigh model, called the *reaction partitioning model*, was proposed by Kretz (1973) and Trczienski (1977). This proposed that zoned minerals grow while their surface composition is controlled by multivariant equilibria with one or more reactant minerals. If the material crystallised as garnet during these reactions loses communication with the matrix, then the effective bulk composition of the rock will shift away from the composition of the material in the garnet interior. Thus, each subsequent layer of garnet will sample material from a different bulk composition. The composition of this added material depends on K_D for the multivariant equilibria responsible for garnet formation.

Essentially, both the above models described the same process, that being the fractionation of certain elements preferentially into the garnet, but it is generally held that the reaction partitioning model is closer to the actual behaviour of the system (Tracy, 1982).

The models above assume heterogeneous equilibrium between reactive mineral compositions, and this appears to hold true for Fe, Mg and Mn in garnets. However, Chernoff and Carlson (1997) suggest that Ca does not equilibrate on a hand-specimen scale during garnet growth due to its relatively sluggish diffusion rate, and this has important implications for interpretation of Ca zoning profiles in garnet, and geobarometry.

3.4.2.2 Results

Garnets of a suitable size and shape (generally those greater than 1mm in diameter and not overly skeletal) were probed to determine the degree to which they were zoned. Point spacing was usually 100μm or 200μm, depending on the size of the garnet, smaller garnets requiring a smaller sample interval to illustrate zoning effects. Illustrative sample zoning profiles are presented in Figure 3.27. Zoning profiles vary from unmodified "normal" growth zoning through unzoned, to reverse zoned in one or two cases. The majority of garnets from the Donara and Tapshah nappes, however, display growth zoning profiles that appear essentially unmodified by diffusion. "Typical" growth zoning profiles such as sample L429

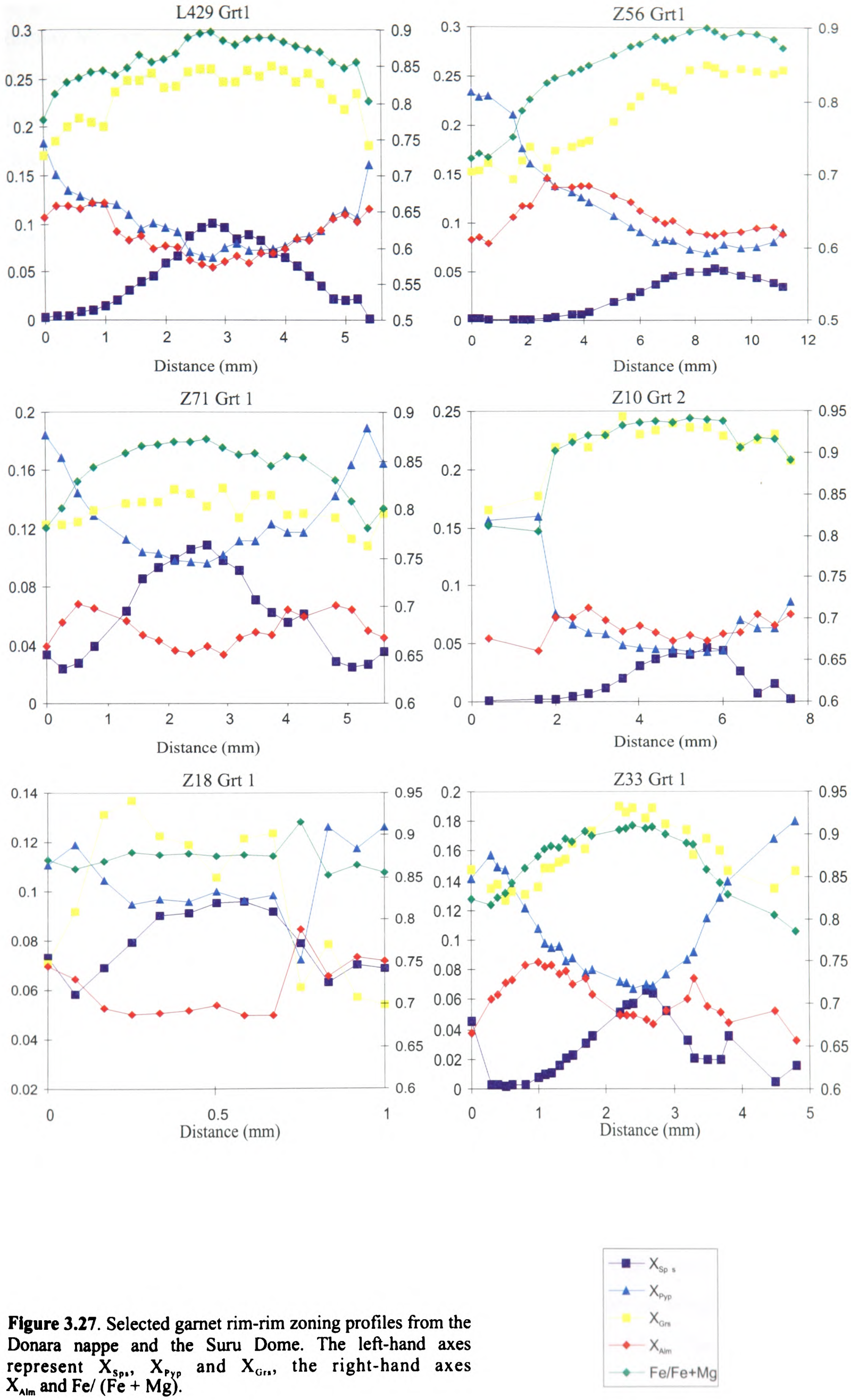


Figure 3.27. Selected garnet rim-rim zoning profiles from the Donara nappe and the Suru Dome. The left-hand axes represent X_{Sps}, X_{Pyp} and X_{Grs}, the right-hand axes X_{Alm} and Fe/ (Fe + Mg).

display Mn concentrations decreasing from core to rim, Ca fairly constant in garnet cores but decreasing more towards the rims, and Mg increasing from core to rim. These are the criteria used to distinguish growth-zoned garnets from those that have undergone significant diffusional re-equilibration. Fe concentrations tend to make up the difference between these components and do not follow such constant trends; however, the Fe/ (Fe + Mg) ratio is almost always constant in the core region before decreasing towards the rim. Such consistent behaviour should therefore be indicative of changes in P-T-X relations.

The plots of garnet zoning display the mole fraction of relevant phase components against the diameter of the garnets, either in millimetres or points counted across the garnet. Thus, X_{Sps} represents the mole fraction of spessartine component in garnet, being Mn/ (Mn + Fe + Mg + Ca), expressed as cations per formula unit. X_{Grs} represents the mole fraction of grossular, and so on. Typically, garnets from the Donara and Tapshah nappes have X_{Sps} core values of around 0.06-0.12, decreasing to virtually zero at the rims, although Z9, a manganese and calcium rich garnet has X_{Sps} values of around 0.2 in the core.

The mole fraction of pyrope, X_{Pyp}, increases fairly steadily from core to rim, and is usually antithetic to X_{Grs}. Typical core values of X_{Pyp} vary, and are dependent on the Ca content of the garnet, a low-Ca garnet such as sample Z70 has core X_{Pyp} of around 0.11 increasing to 0.17 at the rim, whilst sample Z9 contains virtually no Mg, which exists in smaller quantities than Mn even at the rims.

Grossular content, as with pyrope, tends to depend on the bulk composition of the rock, varying from core values of nearly 0.4 in sample Z9 to around 0.04 in sample Z58 from the Suru Dome. Generally, X_{Grs} decreases from core to rim, but the exact shape of the profile differs between samples, and this is probably a reflection on the P-T-X relations of the sample. In samples L429 and Z56 from the Donara nappe, X_{Grs} is fairly constant in the core regions (of differing width), but decrease rapidly in the rim regions. In contrast, sample Z71, from a similar locality to L429 displays an X_{Grs} profile that remains fairly constant throughout. A possible explanation for this may be gleaned from small clinozoisite inclusions preserved in all three garnets; in samples L429 and Z56 clinozoisite is present in the cores but not the rims, and is not present in the matrix. Sample Z71 contains clinozoisite throughout the garnet, and preserves clinozoisite and epidote in the matrix, albeit in very small quantities. The presence of a Ca-bearing mineral that reacts to form grossular, such as clinozoisite (in addition to plagioclase), may buffer the amount of Ca present in the garnet cores; when this is used up, X_{Grs} will fall as the remaining plagioclase is used up to form grossular. The irregular spikes

seen in many of the garnet X_{Grs} profiles may reflect local disequilibrium, as suggested by Chernoff and Carlson (1997).

Fe/(Fe + Mg) is typically around 0.85-0.9 in the cores of garnets, decreasing to around 0.7-0.8 at garnet rims. A decrease in Fe/(Fe + Mg) is a good indicator of increasing temperature during garnet growth (Spear, 1991, 1993), and this is discussed further in Chapter 5.

Some garnets exhibit zoning profiles that appear normally growth zoned in the core, but can be seen to have been diffusionally modified after growth ceased, such as in sample Z10 (Figure 3.27). X_{Sps} remains at almost zero towards the rim, but the X_{Pyp} and X_{Grs} profiles reverse slightly. There is textural evidence for garnet resorption and breakdown to muscovite + biotite + plagioclase at the rims (Figure 3.2.B), so this seems the most likely explanation for the modification of the zoning profiles. Sample Z71, at the left-hand edge of the profile, shows an upturn in X_{Sps} at the rim with no change in the X_{Pyp} or X_{Grs} profiles, and no textural evidence for resorption. Kretz (1973) suggested that slow volume diffusion in, for example, chlorite could result in the cores of chlorite becoming more Mn-rich as well as garnet during a reaction in which chlorite reacts to form garnet. Continued chlorite consumption would eventually lead to breakdown of the Mn-rich cores, which would be reflected by an increase in Mn at garnet rims. As X_{Sps} does not decrease to virtually zero near the rims, and chlorite is still present as a matrix phase in Z71, this may be a reasonable explanation for the zoning profile seen. Ilmenite has also been suggested as a source for Mn during prograde metamorphism.

Suru Dome garnets all show evidence for some sort of diffusional re-equilibration after garnet growth, i.e. an upturn in X_{Sps}, X_{Grs} and Fe/(Fe + Mg), and a downturn in X_{Pyp}. This occurs even when the garnet rim is not immediately adjacent to a biotite or other ferromagnesian grain, suggesting that a part of their *recorded* P-T history differs from that of the overlying nappe rocks.

3.4.3 Biotite

The variations in biotite chemistry from Suru Dome rocks are illustrated in Figure 3.28. The plots attempt to display the major cation substitutions in biotite crystal chemistry. Figure 3.28.A plots Si cations per formula unit (22 O) against Fe, Ti, Al_{vi} (octahedral aluminium) cations and X_{Mg}. Most biotites contain between 5.3-5.7 cations Si per formula unit (p.f.u.) which reflects the Tschermak's Si(Fe,Mg) = AlAl substitution away from the ideal phlogopite-annite endmembers, of Si 6 Al 2 in the tetrahedral site, towards eastonite (Si

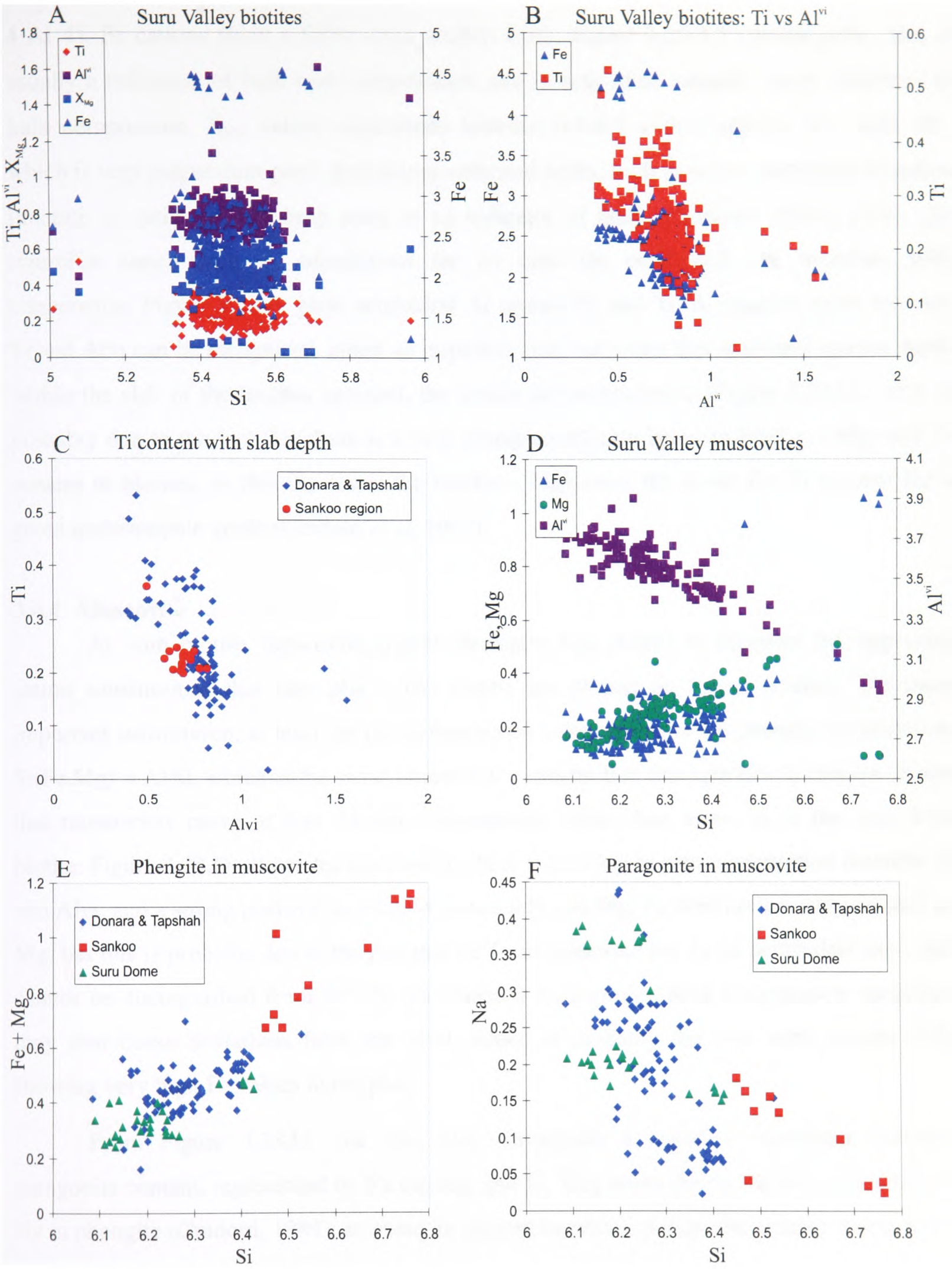


Figure 3.28. Suru Valley mica crystal chemistry. A) Biotites; B) Ti vs octahedral Al in biotite; C) Ti in biotite vs metamorphic grade; D) Muscovites; E) Phengite content in muscovite vs metamorphic grade; F) Paragonite content in muscovites vs metamorphic grade.

4 Al 4). Fe cations show a fairly large scatter, from around 1.25-4.5 cations p.f.u.; this is usually a reflection of bulk rock composition, and in individual samples, local variations in bulk composition. X_{Mg} values concentrate between 0.4-0.6 with exception of sample Z9, which is very magnesium-poor. In titanium-saturated rocks, such as those containing abundant ilmenite or rutile, Ti has been used as an indicator of grade (Guidotti, 1984); above the staurolite zone, since Ti substitution for Al onto the octahedral site increases with temperature. Figure 3.28.B. plots octahedral Al against Fe and Ti. A negative trend between Ti and Alvi can be recognised, albeit an imperfect one, but when this is plotted against depth within the slab of the biotites sampled, the results are inconclusive (Figure 3.28.C.). This is probably due to the fact that there is a very strong correlation between Fe/(Fe + Mg) and Ti content in biotites, in that the lower the Fe/(Fe + Mg) ratio, the lower the Ti content for a given metamorphic grade (Guidotti *et al*, 1977).

3.4.4 Muscovite

As with biotite, muscovite crystal chemistry was plotted to illustrate the important cation substitutions that take place. The results are plotted on Figure 3.28.D. The most important substitution, at least for thermobarometry calculations, is the phengite substitution, Si(Fe,Mg) = AlAl, which is the same Tschermak's substitution that operates in biotites except that muscovites move to less Al-rich compositions rather than more, as is the case with biotite. Figure 3.28.D. illustrates this clearly; there is a strong negative correlation between Si and Alvi, and a strong positive correlation between Si and Mg. Fe does not correlate as well as Mg, but this is probably due to the fact that Fe^{3+} can substitute for Al on octahedral sites, and cannot be distinguished from Fe^{2+} by the electron microprobe. Bulk composition variations may also cause deviations from the ideal, which is probably the case with sample Z78, showing very high Fe values in the plot.

From Figure 3.28.D. one may also distinguish a negative correlation between paragonite content, represented by Na cations, and Si. This arises due to the incompatibility of Na in phengite (Guidotti, 1984); as phengite content increases, paragonite content decreases.

The above substitutions are dependent on metamorphic grade. Various studies have shown that the phengite content of muscovite increases with increasing pressure, and decreases with increasing temperature (Guidotti and Sassi, 1976a). Figure 3.28.E. plots phengite content (Mg + Fe) with respect to depth in the HHC across the Suru Valley. Although there is some overlap, the low grade rocks at the top of the slab near Sankoo are higher in phengite content than those of the Donara and Tapshah nappes, and those from the

Suru Dome are amongst the lowest. The fact that Suru Dome rocks preserve higher temperatures than Sankoo nappe rocks (see Chapter 4) would seem to support the above observations.

Furthermore, the paragonite content of muscovites is also temperature dependent; as temperature increases, the muscovite-paragonite solvus closes, and a greater degree of solid solution is possible (Guidotti, 1984). Conversely, increasing pressure decreases the solubility of paragonite in muscovite. Figure 3.28.F. plots paragonite content with respect to depth within the HHC, as for Figure 3.28.E. There is a general trend of increasing paragonite content with recorded metamorphic temperatures, but there is a reasonable degree of scatter. One possible reason for this could be the presence of Al-silicates in many of the Donara, Tapshah and Suru Dome samples; in the AKNa system the reaction

$$\text{Na-Ms} + \text{Qtz} = \text{Al-Sil} + \text{Ab} + \text{K-richer Ms} + \text{H2O}$$

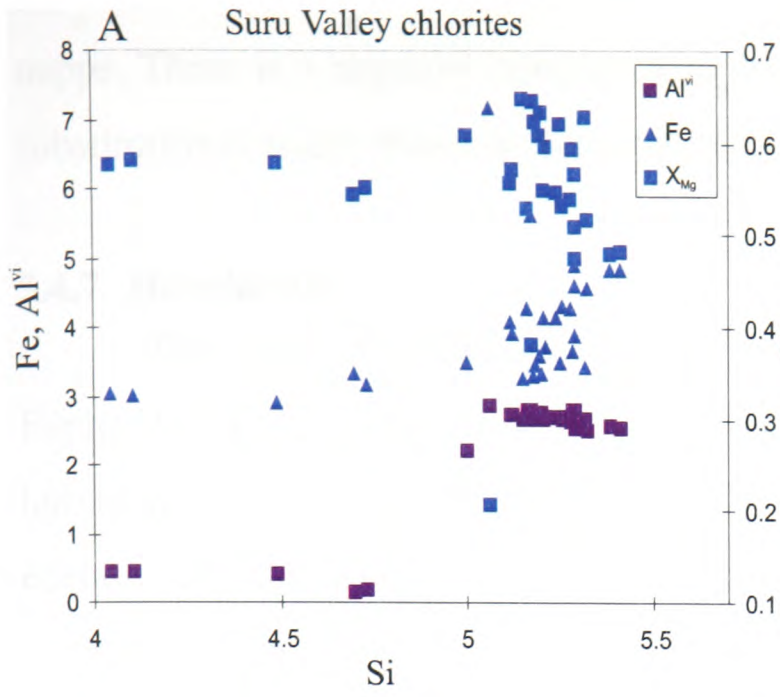
(Guidotti, 1984); that is, with the incoming of an Al-silicate phase such as kyanite, muscovite will start to become poorer in paragonite again. For the above reaction to be relevant, of course, the rock must be saturated in Na so that it contains sodic plagioclase and paragonite.

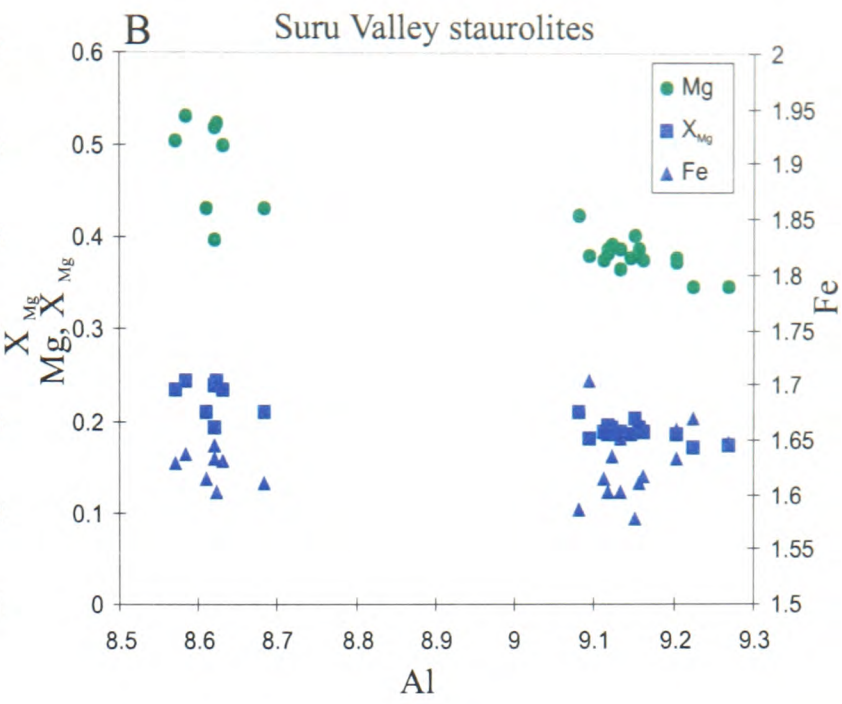
3.4.5 Chlorite

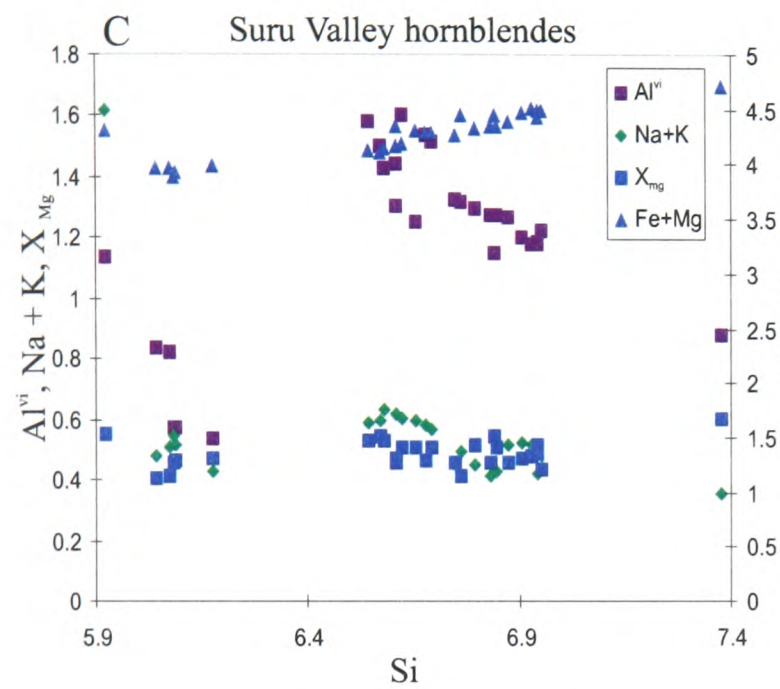
The range of chlorite compositions are plotted in Figure 3.29.A. Most chlorites analysed in rocks from the Suru Valley are interpreted as being retrograde, apart from samples from the Sankoo nappe and one or two examples from the Donara nappe. Si cations p.f.u. vary from 4-5.5., although the majority plot at around 5.2-5.5. Octahedral Al cations mostly have values of 2.6-3 and show a slight negative correlation with Si, apart from a few which are very poor in Al. These chlorites occur as intergrowths with biotite as a retrogressive phase. X_{Mg} values cluster mostly between 0.45-0.65, with one or two Fe-rich crystals. There does not appear to be a systematic difference in composition between prograde and retrograde chlorites.

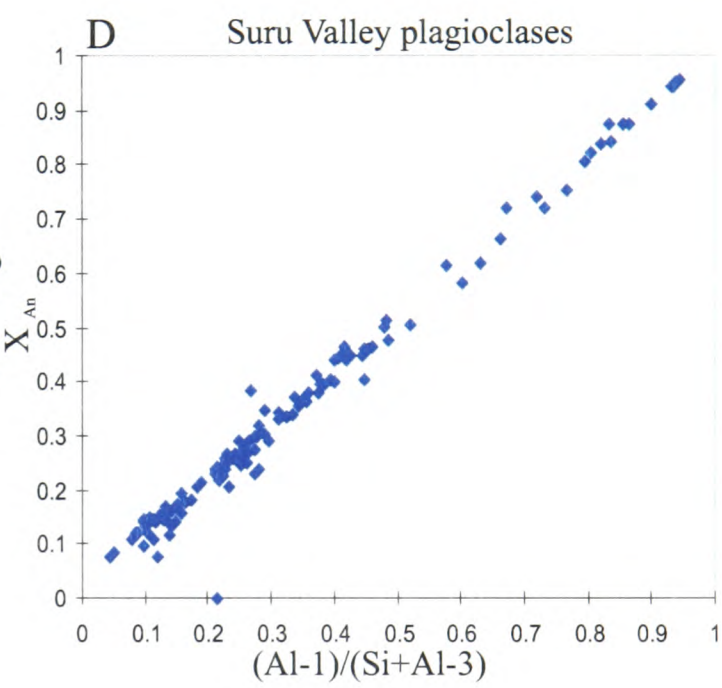
3.4.6 Staurolite

Staurolite compositions are plotted in Figure 3.29.B. The analyses fall into two main populations; those from sample Z71 with Al cations p.f.u. 8.56-8.68 and slightly higher Mg content, and the rest of the samples with Al 9.09-9.26. These differences most likely reflect differences in bulk composition, as Z71 is within 200m of both Z69 and Z70 in the Donara









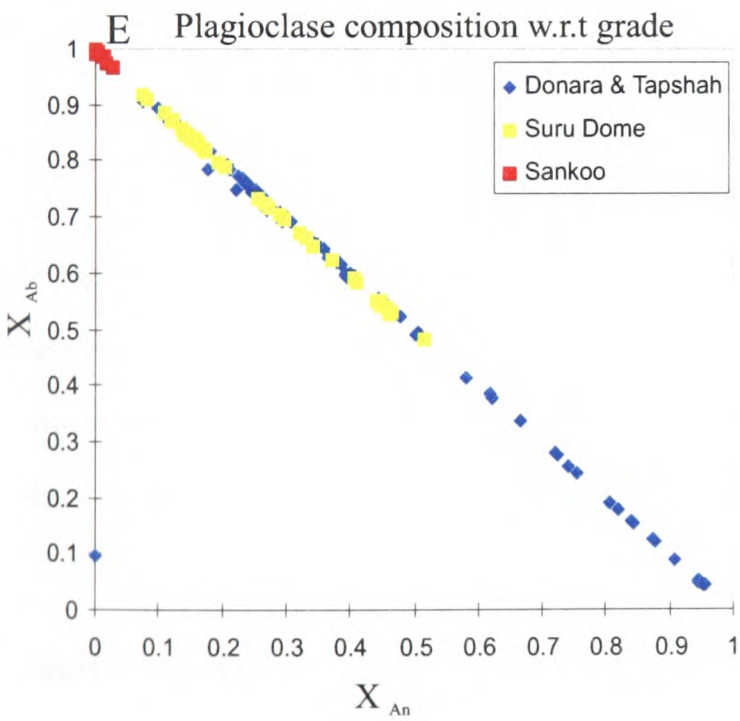


Figure 3.29. Suru Valley mineral chemistry. A) Chlorites; B) Staurolites; C) Hornblendes; D) Plagioclases; E) Plagioclase composition with respect to metamorphic grade as defined by depth within the HHC.

nappe. There is a negative correlation between Al and Mg cations which may suggest some substitution between these on the octahedral sites.

3.4.7 Hornblende

The range of hornblende compositions analysed from the Suru Valley are plotted in Figure 3.29.C. in such a way as to attempt to illustrate the main substitutions important in hornblende crystal chemistry; those being Tschermak's substitution Si(Fe,Mg) = AlAl, the edenite substitution AlNa = Si_ , and a combination of the two.

The majority of hornblendes have compositions with Si 6.5-6.94 and (Na + K) 0.4-0.6. In terms of just these substitutions, they can be classified as hornblende-edenite (Deer, Howie and Zussman, 1992). (Fe + Mg) cations show a good positive correlation with Si, illustrating the Tschermak's substitution, with values of 4-4.5 cations p.f.u. Octahedral Al cations show a negative trend with Si, although not as clearly defined; this scatter may be a result of Fe^{3+} and Ti substituting for Al on octahedral sites.

A group of analyses plot at lower Si values of around 6-6.2; these are from samples Z71 and Z42 from the Donara nappe. However, they also exhibit lower octahedral Al values, a deviation from the ideal Tschermak's substitution, which suggests that they may contain a higher proportion of ferric iron than the others.

3.4.8 Feldspars

Feldspar analyses from Suru Valley rocks are shown in Figure 3.29.D. to illustrate the NaSi = CaAl substitution active in plagioclase solid solution. The majority of the feldspars analysed are plagioclase feldspars and fall in the range An10 - An50, making them oligoclase-andesines, although compositions up to around An95 are measured. Sample Z78, a metagranitoid from the Sankoo nappe contains K-feldspar of composition Or75 - Or97, but this is the only principal K-feldspar bearing sample.

Plagioclase composition in metamorphic rocks is a function of metamorphic grade as well as bulk rock composition (Deer, Howie and Zussman, 1992); thus plagioclases from the low-grade samples from the Sankoo nappe are albitic in composition (average An0.09), while plagioclases from the Donara and Tapshah nappes and the Suru Dome have an average composition of An35 (Figure 3.29.E.). Amphibolites tend to contain plagioclase that is more calcic than pelites from similar grade.

In individual samples, some larger plagioclase crystals exhibit chemical zoning, such as is discussed briefly in Chapter 4. Plagioclase crystals will change composition as they grow

depending on the bulk composition of the rock, pressure and temperature changes, and other reacting phases (Spear *et al.*, 1991; Menard & Spear, 1993). If plagioclase is the only calcic mineral reacting to produce grossular in garnet, X_{An} will be expected to decrease with increasing garnet growth. If another calcic phase such as epidote or clinozoisite is present, X_{An} is predicted to increase. Where good plagioclase zoning was observed, these predictions appeared to hold true e.g. sample Z33 shows a decrease in X_{An} from core to rim, and plagioclase is the only calcic phase present. Z4, an amphibolite containing epidote exhibits an increase in X_{An} from core to rim.

3.5 Conclusions

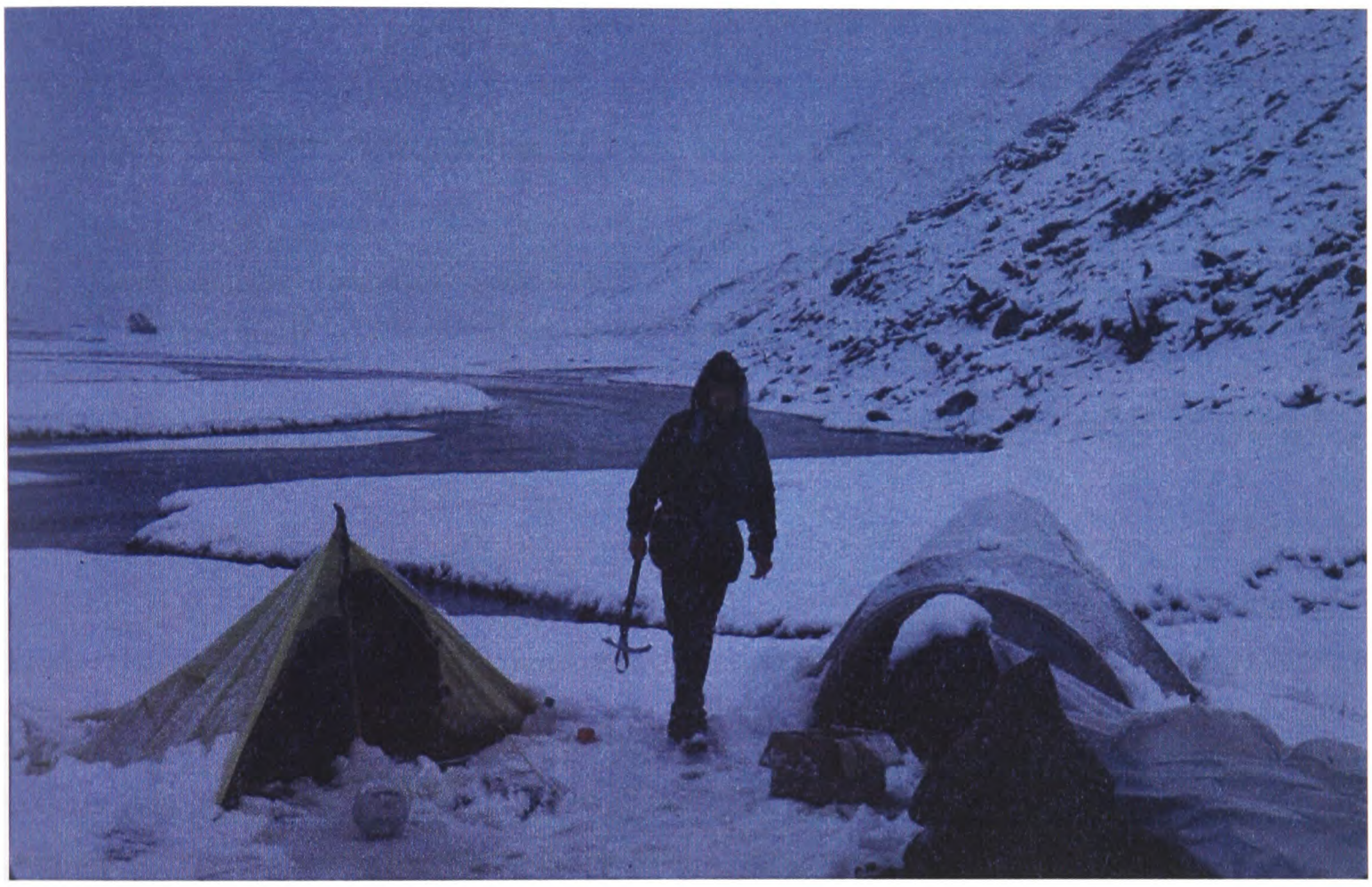
Pelitic rocks from the Suru Valley generally contain the assemblage Qtz + Ms + Bt + Pl + Grt ± Ky ± St ± Czo ± Chl ± Gph, depending on grade and bulk composition. Calc-pelites may contain the above phases, in addition to Cal/Dol + Zo + Hbl, whilst psammitic rocks tend to contain only Qtz + Bt + Grt + Pl ± Ms ± Czo. Amphibolite mineralogy is strongly grade-dependent, but in the main comprise Qtz + Pl + Bt + Hbl ± Grt ± Ep ± Cal/Dol ± Chl. Fe-Ti minerals are ubiquitous in most samples apart from Suru Dome rocks, where they are less abundant.

Three main deformation events can be recognised in samples from the Donara and Tapshah nappes. D_1 is generally preserved as S_1 inclusion trails in garnet, often crenulated by D_2. The main S_2 matrix foliation is often continuous with S_1 at garnet rims, and is defined by a spaced fabric defined by aligned micas and quartz/plagioclase domains. Porphyroblast growth in the overlying nappes is generally syn-post D_2 (nappe formation). In many samples S_2 is crenulated by a D_3 event. This D_3 event is probably related to Suru Dome formation, but is not as intense as the fabrics developed in the dome itself. Samples from the Suru Dome preserve a D_1 fabric crenulated by D_2, but the matrix foliation is a coarser spaced foliation, S_3, attributed to D_3 Suru Dome formation. At the top of the slab near Sankoo, S_0 and S_1 fabrics may be distinguished in both thin section and in the field.

Garnets from the Donara and Tapshah nappes show varying growth zoning profiles, but most are characterised by "normal" growth zoning profiles displaying a decrease in X_{Sps}, X_{Grs} and Fe/ (Fe + Mg), and an increase in X_{Pyp}, consistent with an increase in temperature during garnet growth. They do not show much evidence for retrograde re-equilibration. Suru Dome garnets all show some evidence for growth zoning, but exhibit "reverse" zoning at their rims implying some degree of resorption or diffusion.

Muscovite crystal chemistry, and to a certain extent plagioclase chemistry, reflect changes in P-T conditions across the HHC in the Suru Valley.

Chapter 4



"It never rains in Zanskar...." I was promised. It was therefore with great delight that we awoke to find our camp buried under a foot of snow.

4. Thermobarometry and P-T results

4.1 Principles and techniques

In order to determine the peak metamorphic pressures and temperatures of samples from the Suru Valley region, thermobarometric calculations were performed on suitable samples using both conventional techniques and the average PT approach of THERMOCALC (Powell & Holland, 1988, 1994). The following sections describe how particular mineral analyses were chosen and applied in order to obtain optimal pressures and temperatures at peak metamorphic conditions i.e. how errors were minimised in the calculations and the assumptions that were made in doing so.

4.1.1 Conventional thermobarometry

The condition for chemical equilibrium of a balanced reaction is:

$$\Delta G = 0 = \Delta H(298,1) + {}_{289}^{T}\!\int \Delta C_p \, dT + {}_{1}^{P}\!\int \Delta V \, dP - T\left(\Delta S(298,1) + {}_{298}^{T}\!\int \Delta C_p/T \, dT\right) + RT\ln K_{eq} \qquad (4.1)$$

(Spear, 1993) which is the fundamental equation describing the formal thermodynamic relationship among pressure, temperature and mineral composition. The terms ΔG, ΔH, ΔS, ΔV and ΔC_p are known as the free energy, enthalpy, entropy, volume and heat capacity of reaction respectively. The subscripts (298,1) indicate that the enthalpy, entropy and heat capacity terms are taken at standard state conditions of 298K and 1 bar, because they are a function of pressure and temperature. Equation (4.1) can be simplified to:

$$\Delta G = 0 = \Delta H^0 - T\Delta S^0 + \int \Delta V dP + RT\ln K_{eq} \qquad (4.2)$$

(see Appendix B for more details), where now ΔH and ΔS are computed at the P and T of interest. If we take the temperature and pressure derivatives of the free energy, and rearrange:

$$(\partial P/\partial T)_{\ln Keq} = (-R\ln K_{eq} + \Delta S)/\Delta V = \Delta H/T\Delta V \qquad (4.3)$$

which is a modified form of the Clapyron equation.

Essentially, this is a plot of a line in PT space, with axes T and P and slope

$$(-R\ln K_{eq} + \Delta S)/\Delta V.$$

The principle behind thermobarometry is to infer the conditions at which a sample equilibrated by measuring the value of the equilibrium constant K_{eq} and using that value to calculate T at a particular P or P at a particular T, or both P and T by solving two or more such equations simultaneously. From Equation (4.3), it can be seen that geothermometers (those measuring T) have a high temperature sensitivity (large ΔS and/or ΔH, small ΔV), whilst geobarometers have a good pressure sensitivity (large ΔV). From coexisting mineral composition data obtained from the microprobe, a line of constant K_{eq} can be drawn on a PT diagram, and the sample can be inferred to have equilibrated somewhere along that line. If two different equilibria can be evaluated, two intersecting lines can be plotted that should intersect at a unique pressure and temperature.

The geothermometer utilised in this study is the garnet-biotite Fe-Mg exchange thermometer, using the Bhattacharya *et al.* (1992) calibration for the reaction

almandine + phlogopite = pyrope + annite

Geobarometry was undertaken with two different equilibria applicable to medium-grade pelites, namely the GASP barometer:

anorthite = grossular + kyanite/sillimanite + quartz

and the GPMB-Mg and -Fe barometers:

grossular + pyrope + muscovite = anorthite + phlogopite, and:

grossular + almandine + muscovite = anorthite + annite

using the Holland & Powell (1995) dataset calibrations.

The results of the conventional thermobarometry are tabulated in Table 4.4.

4.1.2 THERMOCALC

THERMOCALC is a computer program that utilises a self-consistent thermodynamic dataset to calculate an independent set of reactions from a given set of mineral endmembers (Holland & Powell, 1985; Powell & Holland, 1988, 1994, 1998). The procedure involves the same thermodynamic principles as described above and in Appendix B, but differs from conventional thermobarometry in that instead of using two, or maybe three equilibria to calculate a PT point it calculates all possible independent reactions between the mineral endmembers that have been chosen for inclusion in the PT calculations. It then employs a least-squares method to obtain the optimal PT from those independent reactions, including uncertainties and correlations on the activities and enthalpies of formation of the endmembers. Essentially this process varies the positions of the reactions in PT space, in proportion to their

uncertainties and correlations (see Appendix B), so that they intersect at one point; the average PT. These displacements in any one reaction cannot be made independently of the other reactions because they are all correlated through shared endmembers. In this way the program attempts to obtain a more accurate estimate for pressures and temperatures by utilising a greater range of thermodynamic data than conventional thermobarometry.

4.2 Rationale

The principles of thermobarometry outlined above hold for phases that are in chemical equilibrium with each other, and in order to obtain meaningful PT estimates and minimise errors, mineral analyses must be chosen in such a way as to represent those phases as close to equilibrium as possible. In real rocks, chemical equilibrium is often not completely attained; the presence of zoned minerals such as garnet is testament to this. Furthermore, equilibrium may be attained on a local scale but not throughout the whole sample. The purpose of this section is to demonstrate how errors may be minimised by choosing the most suitable mineral analyses for equilibrium thermobarometry.

We will focus on one sample used for thermobarometry and discuss the analyses chosen.

Sample Z49 is a pelitic schist from near the closure of the Donara nappe containing the assemblage Qtz-Ms-Bt-Grt-Pl-Ky-Chl-Tur-Rt-Ilm. Rutile is found in the matrix replacing ilmenite, but is not observed in garnets. The garnets preserve inclusion trails aligned at an angle to the matrix foliation, of quartz, white mica, clinozoisite and ilmenite. In more quartz-rich layers, garnet porphyroblasts are elongated along the main foliation and appear to have grown syn-tectonically. The main foliation is defined by sheaves of muscovite and biotite, and was crenulated after the growth of garnet and kyanite porphyroblasts. Chlorite is reasonably abundant as a matrix phase but is probably retrogressive, occurring in cracks in garnet crystals and overgrowing biotite .

The above assemblage contains minerals which are eminently suitable for thermobarometry, in that both thermometer and barometer reactions are applicable.

4.2.1 Garnet

Figures 4.1.A & B illustrate rim-rim traverses across two garnets from the sample Z49, and display the variation in molar percentage of the main substituting components, namely Fe, Mg, Ca and Mn. Although data are missing from part of garnet 1 it can be seen that there is a fairly strong zoning from core to rim. The "bell-shaped" profile of the spessartine component is strongly suggestive of growth zoning of garnet (Tracy 1982). The fact that the spessartine

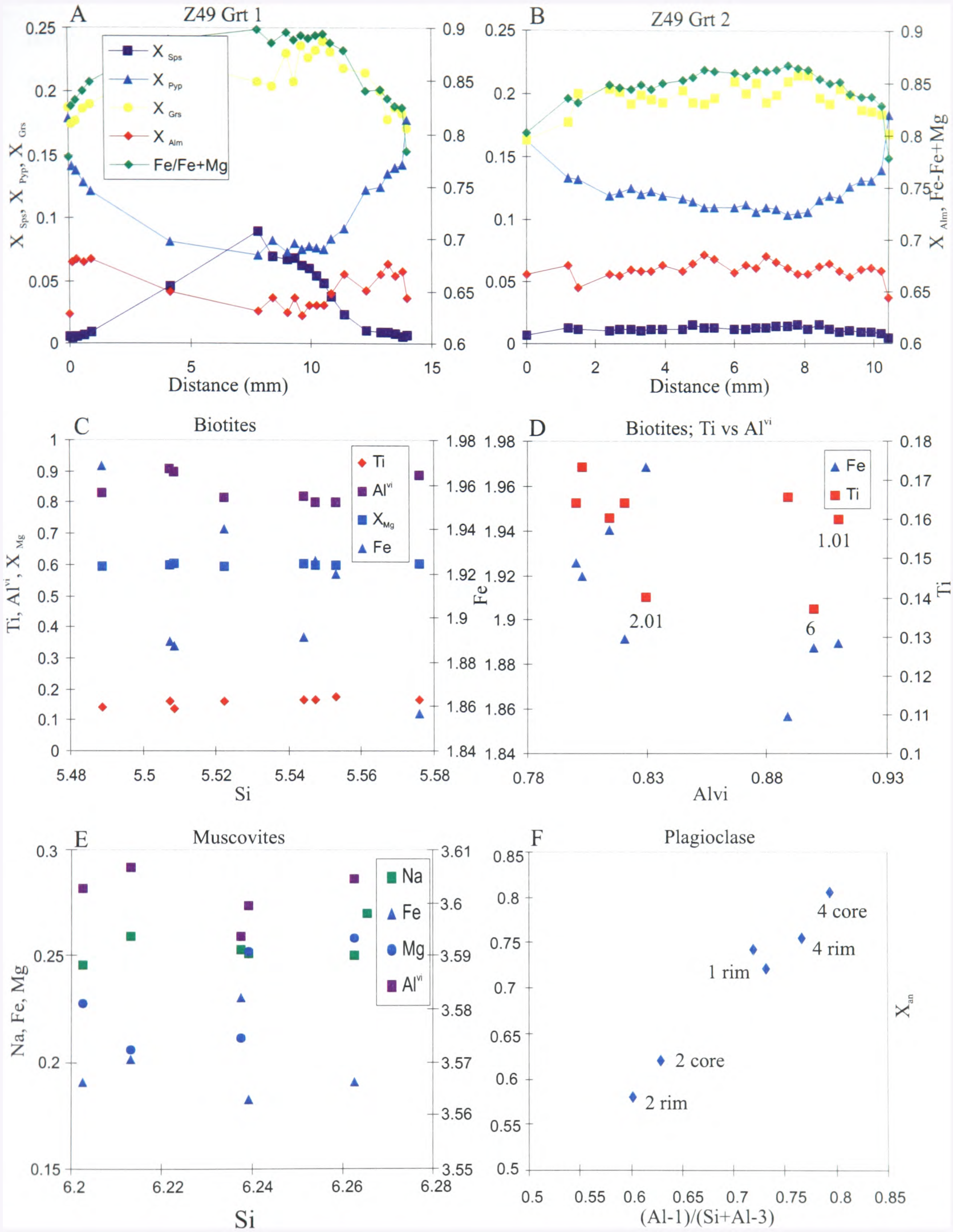


Figure 4.1. Z 49 mineral chemistry; A) Garnet 1 rim-rim profile; B) Garnet 2 rim-rim profile; C) Biotites; D) Ti & Fe vs octahedral Al in biotites; E) Muscovites; F) Plagioclase.

component decreases to nearly zero suggests that the garnet rim represents the final equilibrium composition i.e. at the peak of metamorphism. The Mn content, however, is flat for a short distance near the rims, so some post-peak diffusion may have taken place. The pyrope component increases from core to rim, consistent with a general shift to higher X_{Mg} values for reacting AFM phases, and also does not appear to show subsequent post-growth re-equilibration. Grossular is more irregular in the garnet core, possibly related to clinozoisite preserved as inclusions in the core reacting to produce garnet, but shows an overall decrease from core to rim. Garnet 2 does not display such a marked zoning profile despite the similar size, but this is probably due to the traverse not passing through the core. Rim compositions are similar to those of garnet 1. For thermobarometric calculations using the average PT mode of THERMOCALC, an average of the garnet rims of garnet 1 was used; these points also being close to adjacent biotite crystals.

4.2.2 Biotites

Eight biotite analyses were chosen from various domains of the sample, and plotted on Figures 4.1.C & D. In biotite, the substitutions Fe = Mg and MgSi = AlAl tend to reflect local bulk compositions rather than grade. In Ti-saturated rocks, such as those containing rutile or ilmenite (which Z49 does), workers have noticed an increase in Ti with metamorphic grade, at least above the staurolite zone (Guidotti, 1984). The analyses above appear to group into two populations distinguished by their octahedral Al content. However, the variations in Ti content from core to rim and between individual grains do not appear to correlate systematically with crystal location in the sample, so for use in THERMOCALC an average of the analyses was used. For conventional Grt-Bt thermometry, biotites 1 & 2 at garnet rims were used.

4.2.3 Muscovites

Various cations are plotted against Si, to monitor the extent of the celadonite (phengite) substitution MgSi = AlAl (Figure 4.1.E). This substitution can be an indicator of grade; higher Si and Mg content indicates higher pressures and lower temperatures (see Chapter 3 for more details). Likewise, the paragonite content is also a useful indicator, higher temperatures extending the range of Na = K substitution as the paragonite-muscovite miscibility gap narrows. From the plot of the analyses, it can be seen that there is a positive correlation between Si and Mg, and a slight negative one between Na and Si; however, the differences are fairly small, indicating good equilibration. As no strong trends in phengite and paragonite content are observed, the results are averaged.

4.2.4 Plagioclase

Plagioclase grains from various domains were analysed and plotted in Figure 4.1.F to display the variation in Ca and Al content. Grain 2 is close to garnet 1, and has the lowest An content, whilst grain 4 is distant from garnet. However, the grain closest to garnet (grain1) has An content closer to those grains which are more distant. The only real correlation appears to be a decrease in An content from core to rim, which may be indicative of plagioclase becoming more Na-rich as it is consumed to produce garnet (Menard & Spear, 1993); however, as clinozoisite is present as an inclusion, X_{An} would be expected to decrease by their calculations. This illustrates the potential difficulty in choosing the correct "equilibrium" analyses. Calculations were performed using both grain 1, adjacent to the garnet rim analyses, and an average of the plagioclase values, and the difference in pressures and temperatures obtained were trivial, although the results tabulated below were obtained using the average population.

4.2.5 Results

The results of the average PT calculations for sample Z49 performed using THERMOCALC and the mineral analyses described above are plotted in Figure 4.2., and in table 4.1. for various fluid compositions assuming a H2O-CO2 fluid.

XH2O	T (C)	sd (T)	P (kb)	sd (P)	corr	fit
1.0	**600**	11	**8.4**	0.7	0.585	1.12
0.9	**589**	11	**8.3**	0.7	0.583	1.15
0.7	**571**	12	**8.0**	0.8	0.584	1.22
0.5	**553**	12	**7.8**	0.8	0.586	1.3

Table 4.1. THERMOCALC average P-T results for Z49 at varying X_{H2O}.

The calculated average temperatures span a range of over 50 ^{0}C, with little deterioration in the quality of the least squares fit at lower X_{H2O}, and one cannot improve on this accuracy unless one has an independent estimate of either temperature or fluid composition. This situation arises because all the H2O-absent equilibria used in THERMOCALC for this pelite have similar PT slopes. In this situation it is easiest to gain an independent estimate of temperature, and the garnet-biotite thermometer is applied to 2 different garnet biotite pairs from the sample using a number of different calibrations, at a reference pressure of 8 kb.

Calibration	Gt1 Bt2 T	Gt2 Bt1 T
Bhattacharya *et al.* 1992, Hackler & Wood Grt model	636	638
Bhattacharya *et al.* 1992, Ganguly & Saxena Grt model	656	654
Dasgupta *et al.* 1991	647	659
Ferry & Spear 1978	616	613
Holdaway & Lee 1977	607	605

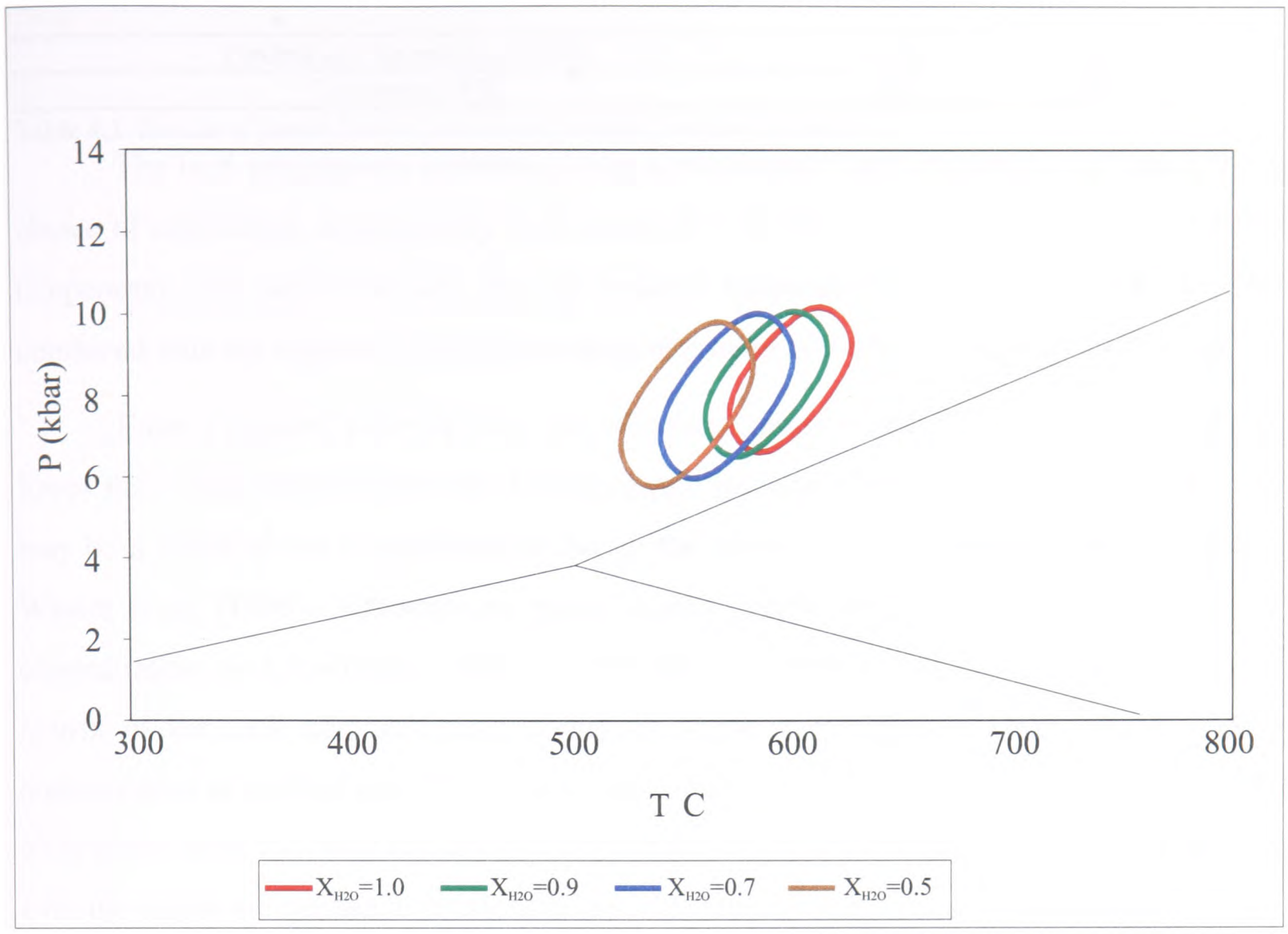


Figure 4.2. THERMOCALC average P-T results for sample Z49 illustrating the effect of varying water activity. Fluid is assumed to be an H2O-CO2 binary solution. Al-silicate triple point from Holdaway and Mukhopadhyay (1993). The error "ellipses" plotted are not actually true ellipses due to the plotting technique used, but they still serve to illustrate the calculated errors on P-T results.

Perchuk and Lavrent'eva (1983)	606	604
Thompson 1976	640	638

Table 4.2. Results of garnet-biotite thermometry utilising various calibrations.

The best temperature estimates using conventional thermometers are affected by the choice of calibration, and typically have errors of ± 25-50 ^{0}C, and so do not really constrain temperature that well; however, they all indicate temperatures in excess of 600 ^{0}C. This, combined with the regional temperature range of around 600-650 ^{0}C, suggests an X_{H2O} of 1.0.

From a regional point of view, the calculated result of 600 ^{0}C and 8.4 kbar is slightly lower than other samples from the Donara nappe (average 620-650 ^{0}C, 9.5-10.5 kbar). This may be a result of the re-equilibration due to the effects of M2 metamorphism described in Waters *et al.* (1995). Although the garnet zoning profile does not show an upturn in Mn concentration, or a downturn in Mg as is often the case with diffusionally altered garnets, the matrix of the rock may still have undergone slight re-equilibration, and indeed a biotite analysis next to another part of the rim gives a slightly lower pressure and temperature. Thus an apparent peak P-T may actually be a post-peak feature, and a large number of P-T analyses over the region are needed to confidently describe the regional P-T conditions.

The results from the complete set of samples employed for thermobarometry are tabulated in Tables 4.3. and 4.4. Unless otherwise stated, all activities were calculated using the program AX and the Holland & Powell (1998) thermodynamic dataset. Details of the activity-composition models used can be found in Appendix A.

4.3 Suru Valley P-T results

4.3.1 THERMOCALC results

Table 4.3 Complete list of THERMOCALC average PT results. See Appendix D for mineral analyses

Sample P-T stage	**Z2** peak	**Z10** post-peak?	**Z37** peak	**Z42** peak	**Z43** peak
Activities	at 600C	at 600 C	at 650 C	at 650 C	at 650 C
Garnet	rim	rim	rim	rim	rim
py	0.0054	0.00116	0.0091	0.00177	0.00064
gr	0.020	0.0106	0.00037	0.020	0.015
alm	0.21	0.32	0.37	0.23	0.31
sps	-		-	0.000006	-
andr	-		-	-	-
Biotite	adj grt	adj grt	adj grt	adj grt	adj grt
phl	0.061	0.032	0.069	0.046	0.035
ann	0.045	0.067	0.029	0.054	0.053
east	0.039	0.033	0.061	0.033	0.037
naph	-	-	-	-	-
Muscovite		adj grt	adj grt		adj grt
mu	-	0.77	0.65	-	0.62
pa	-	0.568	0.87	-	0.190
cel	-	0.019	0.024	-	0.035
Plagioclase	adj grt	adj musc	adj grt	av	-
an	0.59	0.76	0.20	0.45	0.493
ab	0.60	0.41	0.85	0.69	0.599
Chlorite	intergrowth				
clin	0.038	-	-	-	-
daph	0.015	-	-	-	-
ames	0.0199	-	-	-	-
Clinozoisite					
cz	-	-	-	-	-
ep	-	-	-	-	-
fep	-	-	-	-	-
Hornblende	av nr grt			adj grt	
tr	0.0511	-	-	0.00019	-
fact	0.01389	-	-	-	-
ts	0.005	-	-	0.01174	-
parg	0.0054	-	-	0.00787	-
gl	0.000981	-	-	0.00001	-
Others	qtz H2O CO2 spn	qtz H2O	qtz ky H2O	q H2O	q H2O
Results					
aH2O	1.0	1.0	0.7	0.8	0.1	0.3
T ^{0}C	**601**	**573**	**639**	**650**	**605**	**642**
s.d. (T)	16	27	19	19	69	52
P kbar	**7.8**	**7.4**	**10.2**	**10.3**	**10.1**	**9.7**
s.d.(P)	1.0	0.9	1.3	1.3	1.6	1.6
correl.	0.156	0.822	0.872	0.873	0.556	0.829
fit	1.08	0.67	0.52	0.48	0.59	1.44
Nr	6	5	5	5	5	5
end members eliminated	ames, fact, parg, gl	-	-	-	-	-

Sample P-T stage	**Z46** peak	**Z47** peak		**Z49** peak	**Z50** **peak**	**Z51** peak
Activities	at 600C	at 650 C		at 600 C	at 600 C	at 600 C
Garnet	av rim	rim		rim	rim	rim
py	0.00125	0.0058		0.0096	0.0062	0.0092
gr	0.013	0.0091		0.0083	0.0130	0.0079
alm	0.28	0.26		0.23	0.21	0.24
sps	0.000079	-		-	-	0.0000011
andr	-	-		-	-	-
Biotite	av adjgrt	adj grt		av	av	av
phl	0.0199	0.079		0.094	0.086	0.088
ann	0.079	0.023		0.024	0.030	0.027
east	0.021	0.074		0.069	0.067	0.063
naph	-	-		-	-	-
Muscovite	av adjgrt	adj grt		av	av	av
mu	0.61	0.63		0.65	0.67	0.68
pa	0.286	0.790		0.765	0.898	0.91
cel	0.039	0.039		0.029	0.034	0.032
fcel	-	-		-	-	-
Plagioclase	av	av		av	adj grt	av
an	0.39	0.34		0.76	0.60	0.36
ab	0.72	0.76		0.47	0.59	0.75
Chlorite				av		
clin	-	-		0.077	-	-
daph	-	-		0.0051	-	-
ames	-	-		0.079	-	-
Clinozoisite						
cz	-	-		-	-	-
ep	-	-		-	-	-
fep	-	-		-	-	-
Hornblende						rim
tr	-	-		-	-	0.01903
fact	-	-		-	-	0.004666
ts	-	-		-	-	0.012
parg	-	-		-	-	0.0032
gl	-	-		-	-	0.00413
Others	qtz H2O	qtz ky H2O		qtz ky H2O	qtz cz H2O	q ky H2O
Results						
aH2O	0.4	0.5	0.6	1.0	1.0	1.0
T ^{0}C	**645**	**629**	**643**	**600**	**597**	**635**
s.d. (T)	40	17	18	11	44	27
P kbar	**10.5**	**11.4**	**11.6**	**8.4**	**9.9**	**10.9**
s.d.(P)	1.3	1.1	1.1	0.7	1.5	1.1
correl.	0.814	0.807	0.811	0.585	0.984	0.827
fit	1.2	1.1	1.13	1.12	1.33	0.66
Nr	5	6	6	8	5	7
end members eliminated	-	-	-	-	-	parg, gl, fact

Sample P-T stage	**Z56** peak	**Z64** peak	**Z66** peak	**Z71** peak	**Z73** peak
Activities	at 650 C	at 600 C	at 600 C	at 600 C	at 600 C
Garnet	rim	rim	rim	rim	rim
py	0.018	0.0078	0.00069	0.0063	0.0043
gr	0.0065	0.020	0.014	0.0036	0.015
alm	0.20	0.15	0.31	0.27	0.22
sps	-	0.000002	-	0.000043	0.0000011
andr	-	-	-	-	-
Biotite	av	av	av		adj grt
phl	0.094	0.080	0.027	0.087	0.059
ann	0.018	0.029	0.070	0.033	0.051
east	0.074	0.056	0.029	0.061	0.047
naph	-	-	-	-	-
Muscovite	av	av	av		adj grt
mu	0.70	0.65	0.65	0.59	0.65
pa	0.745	0.445	0.212	0.653	0.727
cel	0.034	0.051	0.0114	0.037	0.047
fcel	-	-	-	-	-
Plagioclase	adj grt	av high An	av		adj grt
an	0.55	0.65	0.69	0.68	0.55
ab	0.61	0.56	0.53	0.54	0.63
Chlorite					av
clin	-	-	-	-	0.036
daph	-	-	-	-	0.016
ames	-	-	-	-	0.042
Staurolite					
fst	-	-	-	0.34	-
mst	-	-	-	0.0031	-
Clinozoisite		av			
cz	-	0.96	-	-	0.57
ep	-	0.040	-	-	0.36
fep	-	-	-	-	0.0101
Hornblende					
tr	-	-	-	0.006614	-
fact	-	-	-	0.01563	-
ts	-	-	-	0.007	-
parg	-	-	-	0.0010	-
gl	-	-	-	0.001589	-
Others	qtz ky H2O	qtz H2O	qtz cal H2OCO2	qtz ky H2O rt ilm	qtz cal H2OCO2
Results					
aH2O	1.0	0.5	0.5	1.0	0.5
T ^{0}C	**648**	**634**	**596**	**611**	**572**
s.d. (T)	16	27	34	21	22
P kbar	**10.1**	**10.8**	**8.2**	**7.2**	**8.9**
s.d.(P)	0.9	1.2	1.2	1.1	1.0
correl.	0.815	0.925	0.956	0.801	0.927
fit	0.95	1.48	1.28	0.69	1.33
Nr	5	7	6	9	7
end members eliminated	-	-	-	parg, fact, fst, alm, cel	ep, fep, clin, ames, daph

Sample P-T stage		***Z81** peak	****Z18** near peak	****Z33** near peak	****Z58** near peak	****Z59** near peak
Activities		at 500C	at 650C	at 650C	at 650C	at 650C
Garnet		rim	near rim	rim	near rim	rim
	py	0.000549	0.0063	0.0103	0.0091	0.00077
	gr	0.009866	0.00023	0.0048	0.000138	0.0022
	alm	0.252983	0.41	0.26	0.42	0.32
	sps	-	0.000013	0.0000036	0.000003	0.0012
	andr	0.000002	-	-	-	-
Biotite		adj grt	av	av	av	adj grt
	phl	0.054488	0.043	0.054	0.033	0.0244
	ann	0.056962	0.054	0.037	0.026	0.081
	east	0.032841	0.042	0.056	0.059	0.026
	naph	0.001201	-	-	-	-
Muscovite		adj grt	av loPh	loPh adj grt	av loPh	adj grt
	mu	0.512204	0.71	0.73	0.68	0.74
	pa	0.382139	0.97	0.612	0.7	0.718
	cel	0.075308	0.015	0.022	0.023	0.014
	fcel	0.061564	-	-	-	-
Plagioclase		adj grt	av hi An	av	av	rims nr grt
	an	0.018968	0.22	0.67	0.17	0.22
	ab	0.982324	0.84	0.52	0.87	0.84
Chlorite		adj grt				
	clin	0.027778	-	-	-	-
	daph	0.01556	-	-	-	-
	ames	0.013431	-	-	-	-
Staurolite						
	fst	-	-	-	0.42	-
	mst	-	-	-	0.0014	-
Clinozoisite						
	cz	-	-	-	-	-
	ep	-	-	-	-	-
	fep	-	-	-	-	-
Hornblende						
	tr	-	-	-	-	-
	fact	-	-	-	-	-
	ts	-	-	-	-	-
	parg	-	-	-	-	-
	gl	-	-	-	-	-
Others		qtz H2O	qtz ky ilm H2O	qtz ky ilm H2O	qtz ky H2O	qtz ilm H2O
Results						
	aH2O	0.3	1.0	1.0	1.0	1.0
	T ^{0}C	**498**	**638**	**638**	**637**	**623**
	s.d. (T)	17	23	22	23	30
	P kbar	**5**	**8.8**	**8.7**	**9.6**	**9.7**
	s.d.(P)	1.5	1.3	1.0	1.0	1.2
	correl.	0.398	0.803	0.749	0.051	0.752
	fit	1.14	0.43	0.82	0.97	0.53
	Nr	7	6	6	7	5
	end members eliminated	daph, cel, an, andr	-	-	pa	-

*Sankoo nappe rock. Calculated with WAX and THERMO 2.4 dataset

** Suru Dome rock.

"Correl." represents the correlation between the standard deviations on pressure and temperature. "Fit" is a measure of the goodness of fit of averaging Nr equilibria. (From Powell and Holland, 1988). See Appendix B for more details. "Av" = average; "adj" = adjacent.

The tabulated THERMOCALC average P-T results are plotted in Figure 4.3. in such a way as to distinguish samples from different parts of the study area. Although the error ellipses on some samples are quite large- up to ± 50 ^{0}C and ± 1.5 kbar, on average Donara and Tapshah nappe samples are fairly well-constrained, and record conditions of around 9.5-10.5 kbar and 620-640 ^{0}C, although Z47 from the core of the Donara nappe records a pressure of around 11.5 kbar. This is a record of the M1 Barrovian metamorphism affecting the entire Himalayan chain (Searle and Rex, 1989; Stäubli, 1989; Searle *et al.*, 1992). Samples Z2 and Z10, from south of Tongul, record slightly lower pressures than typical Donara and Tapshah nappe samples, which may reflect actual tectonic conditions. They lie immediately above the Suru Dome, and may be affected by the later M2 metamorphism attributed to dome formation throughout the High Himalayas, recording slightly lower pressures than the deeper Suru Dome rocks.

Suru Dome rocks themselves record closely spaced P-T conditions with good "fits" (i.e. the results have a low value for the fit parameter), which implies that they are perhaps better equilibrated than nappe rocks in general. As most garnet rims display evidence for retrograde re-equilibration, analyses were chosen which best represented peak garnet growth conditions, after the method of Indares and Martignole (1984). These gave results that record slightly lower temperatures and higher pressures than those calculated for much of the M2 sillimanite-grade metamorphism in the Suru Valley (Searle *et al.*, 1992); this is most likely due to the fact that they have not been as strongly affected by this event as rocks from further east in the slab, further evidenced by their lack of sillimanite. Samples Z58 and Z59, from approximately 5km to the north-east of Z18 and Z33, and therefore deeper in the slab, record pressures of almost exactly 1 kbar more than Z18 and Z33. THERMOCALC results for retrogressed garnet rims and adjacent mineral populations tend to give lower pressures, but not significantly lower temperature estimates, compared to conventional thermobarometry results. This is most likely a result of the way in which THERMOCALC averages equilibria, especially temperature-sensitive ones, which smooths out the effects of slightly out-of-equilibrium phases, but worsens the fit.

The only THERMOCALC result from the Sankoo nappe, Z81, records a temperature of 498 ± 17 ^{0}C, which is in agreement with garnet-biotite thermometry from nearby samples, and a rather poorly constrained pressure of 5 ± 1.5 kbar. One reason for the large errors on the pressure estimate may be due to the nature of the net transfer reactions used as barometers by THERMOCALC for this sample. Plagioclase-bearing equilibria are generally the most important in constraining pressure in metamorphic rocks as they generally have a large ΔV,

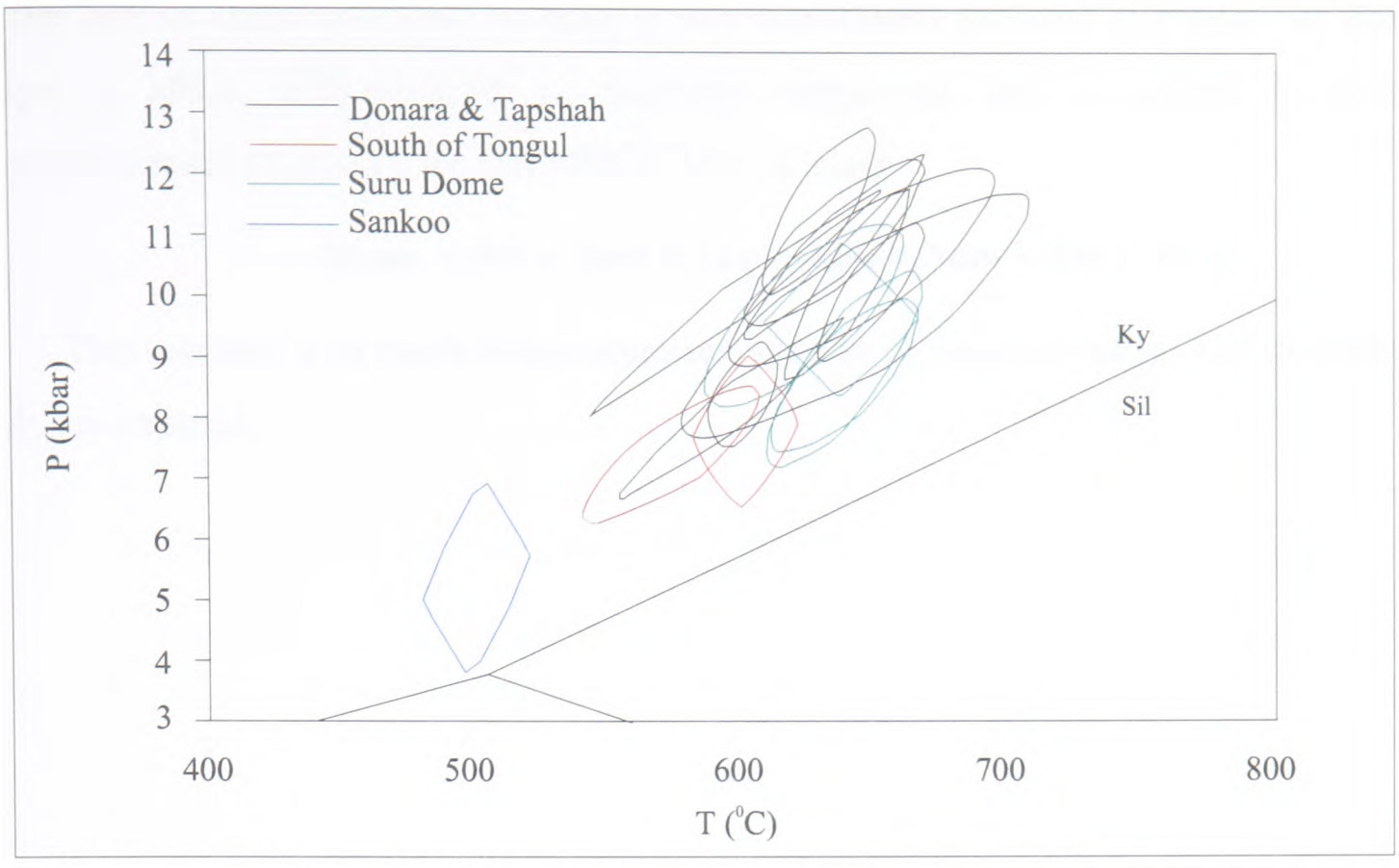


Figure 4.3. THERMOCALC average P-T results, as tabulated in Table 4.3. Error ellipses are constructed from the calculated standard deviations on pressure and temperature, and the correlation between these. Al-silicate triple point from Holdaway and Mukhopadhyay (1993).

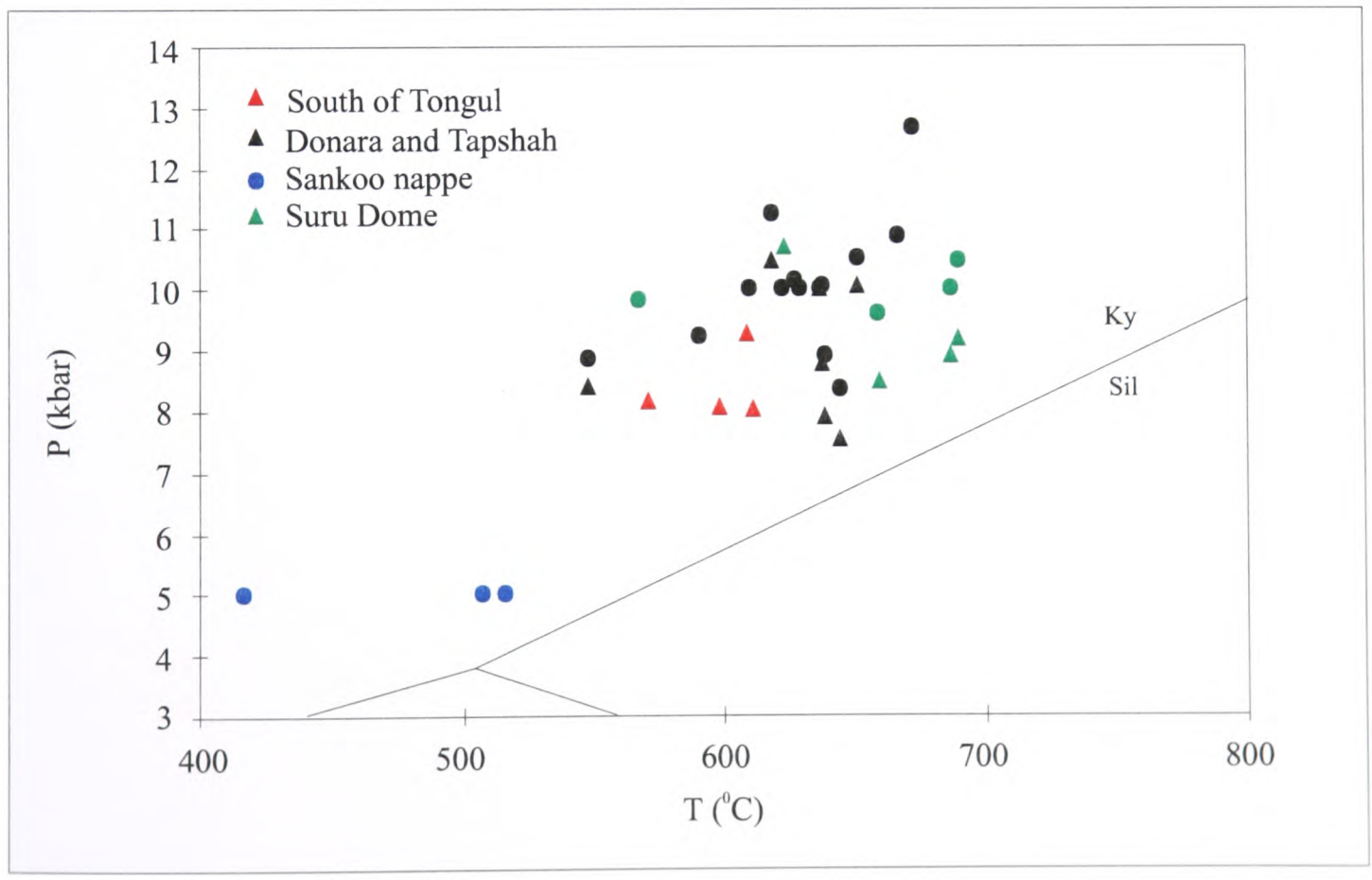


Figure 4.4. Results of garnet-biotite thermometry, and garnet-aluminium silicate-silica-plagioclase (GASP, triangles) and garnet-plagioclase-muscovite-biotite (GPMB-Mg, circles) barometry. All temperatures and pressures were calculated using the Hackler and Wood (1989) garnet non-ideal mixing parameters. Where GASP and GPMB-Mg equilibria were inappropriate, such as in samples lacking muscovite, temperature was calculated at a reference pressure appropriate to the area, such as 5kb for Sankoo samples.

and the lack of these will lead to more poorly-constrained pressure estimates. In Z81, the feldspar is albite, with virtually no anorthite component, and is present in only one independent reaction utilised by THERMOCALC, namely

$$5ames + 4ab + 3ann + 11q = 4clin + 2alm + 4pa + 3fcel$$

This reaction is as much temperature sensitive as pressure sensitive, and so pressure is poorly constrained.

4.3.2 Conventional thermobarometry results.

Table 4.4. Complete list of results of conventional thermobarometry

Sample		**Z2**	**Z4**	**Z9**	**Z10**	**Z25**	**Z28**
Mineral pairs		Gt1 rim Bt2	Grt 1 rim Bt1 Grt2 rim Bt7	Gt1 rim Bt 1	Gt2 rim Bt2 Ms1 Pl 2	Grt1 rim Bt1 av Ms1 av Pl	Grt1 rim Bt1 Ms2 av Pl1
T^0C Gt-Bt (Bhattacharya 1992 mixing parameters)	HW	599	571 568	618	605	582	635
	GS	602	599 597	529	600	593	638
P kbar	GASP HW	-	-	-	-	_	-
	GASP GS						
	GPMB-Mg HW	-	-	-	9.12	8.01	9.68
	GPMB-Mg GS				9.71	8.68	10.12
	GPMB-Fe HW	-	-	-	7.25	6.5	7.89
	GPMB-Fe GS				7.11	6.54	7.84

Sample		**Z37**	**Z42**	**Z43**	**Z46**	**Z47**	**Z49**
Mineral pairs		Gt1 rim Bt1 Ms1 Pl 1 rim	Gt1 rim Bt1 Gt3 rim Bt4	Gt2 rim Av pop	Av Gt rim Av Bt at rim Av lo Ph Mean	Gt1 rim Bt 2 Ms1 Pl	Gt 1 rim Bt 2 Ms 5 Pl 3
T^0C Gt-Bt (Bhattacharya 1992 mixing parameters)	HW	638	605 615	636	672	618	639
	GS	651	603 617	630	651	635	654
P kbar	GASP HW	8.77	-	-	-	10.49	7.9
	GASP GS	8.73				10.67	7.95
	GPMB-Mg HW	10.07	-	10.78	12.68	11.24	8.89
	GPMB-Mg GS	10.42		11.26	13.02	11.74	9.2
	GPMB-Fe HW	8.55	-	8.74	10.06	9.82	7.55
	GPMB-Fe GS	8.64		8.6	9.61	10.07	7.71

Sample			Z50	Z51	Z56	Z64	Z66	Z69
Mineral pairs			Gt1 rim Bt 2 Ms 1 Pl 1	Gt1 rim av Bt rim av Ms Pl rim	Gt2 rim Bt1 av Ms Pl sympl	Gt1 rim Bt1 av Ms hi An Pl	Gt1 rim Bt 2 Ms1 av Pl	Gt1 rim Bt1 Gt2 rim Bt2
T^0C Gt-Bt (Bhattacharya 1992 mixing parameters)		HW	622	627	667	651	590	622 639
		GS	637	643	684	667	550	635 652
P kbar	GASP	HW	-	-	-	10.05	-	-
		GS				10.21		
	GPMB-Mg	HW	10.01	10.16	10.89	10.52	9.25	-
		GS	10.47	10.59	11.24	10.93	9.78	
	GPMB-Fe	HW	8.62	8.79	9.32	9.01	6.9	-
		GS	8.84	9.02	9.57	9.25	6.27	

Sample			Z70	Z71	Z73	*Z78	*Z81	*Z83
Mineral pairs			Gt1 rim Bt 1 *(Gt1 adj Bt inclusion Bt inclusion)*	Gt1 rim Bt1 Ms1 Pl 3	Gt1 rim Bt1 Gt 2 rim Bt 6 Ms1&2 Pl1	Av Gt Av Bt	Gt1 rim Bt 2 Ms1 Pl 1	Av Gt rim Av Bt Av lo Ph Ms Pl 4
T^0C Gt-Bt (Bhattacharya 1992 mixing parameters)		HW	637 *(564)*	644	651 618	416	516	507
		GS	649 *(573)*	656	659 626	411	501	471
P kbar	GASP	HW	-	7.53	-	-	-	-
		GS		7.52				
	GPMB-Mg	HW	-	8.35	10.71	-	-	-
		GS		8.65	11.16			
	GPMB-Fe	HW	-	6.93	8.92	-	-	-
		GS		7.03	9			

Sample		**Z18	**Z33	**Z34	**Z58	**Z59
Mineral pairs		Gtnr rim Bt matrix Ms loPh Pl HiAn *(rim pop)*	Grt rim Bt1 adj grt Ms adj grt Pl adj grt	Av Grt rim Bt av hi XMg Pl adj grt	Grt maxPy Bt avmatrix Ms av loPh Av pop *(rim pop)*	Grt1 rim Bt adj grt Ms adj grt Pl rim
T^0C Gt-Bt (Bhattacharya 1992 mixing parameters)	HW	659 *(594)*	687	623	690*(586)*	567
	GS	667 *(596)*	698	630	697 *(586)*	541
P kbar	GASP HW	8.37 *(6.96)*	8.93	10.72	9.19 *(6.55)*	-
	GASP GS	8.25 *(6.78)*	8.91	10.74	9.05 *(6.34)*	
	GPMB-Mg HW	9.58 *(7.96)*	10.00	-	10.47 *(7.71)*	9.85
	GPMB-Mg GS	10.01 (8.46)	10.32		10.8 *(8.26)*	10.17
	GPMB-Fe HW	7.69 *(6.4)*	8.17	-	8.43 *(6.12)*	7.98
	GPMB-Fe GS	7.68 *(6.31)*	8.2		8.42 *(5.99)*	7.42

Abbreviations: HW = Hackler and Wood (1989) garnet model; GS = Ganguly and Saxena (1984) garnet model. GASP = Grt-Ky-Qtz-Pl barometer. GPMB-Mg/Fe = Grt-Pl-Ms-Bt (Mg or Fe endmembers) barometer.
* denotes Sankoo nappe rock
** denotes Suru Dome rock

The tabulated conventional thermobarometry results are plotted in Figure 4.4., and are again divided into separate regions from the Suru Valley. For the calculations, the Hackler and Wood (1989) garnet mixing model (HW) was used rather than the Ganguly and Saxena (1984) (GS), as the values of the garnet interaction parameters are closer to those of Newton and Haselton (1981), and those utilised by THERMOCALC. Furthermore, the Ganguly and Saxena (1984) mixing parameters are not effective at high Ca/(Ca+Mg) ratios (Ganguly and Saxena, 1984), as is evidenced in sample Z9, where there is a discrepancy of nearly 100 ^{0}C between the HW temperature of 618 ^{0}C and the GS value of 529 ^{0}C. Both HW and GS garnet-biotite temperatures from nearby samples are around 600 ^{0}C, highlighting the spurious nature of the GS temperature. Z9 garnets are very Ca and Mn rich, and other Ca-rich samples such as Z66 and Z51 also show greater discrepancies between the HW and GS temperatures. Figure 4.5.A. plots Ca/(Ca+Mg) against ΔT, GS-HW, for Suru Valley samples. Average ΔT is positive and between 10-20 ^{0}C, and although a good linear trend is not observed, above about Ca/(Ca+Mg) = 0.7, ΔT values tend to become negative and progressively larger. This increasing discrepancy between calculated temperatures with increasing Ca/(Ca+Mg) appears to agree with the results of Ganguly and Saxena (1984). A similar plot for XGrs against ΔT (Figure 4.5.B.) shows no such systematic relationship, suggesting that Ca content of garnet alone is not the most important factor.

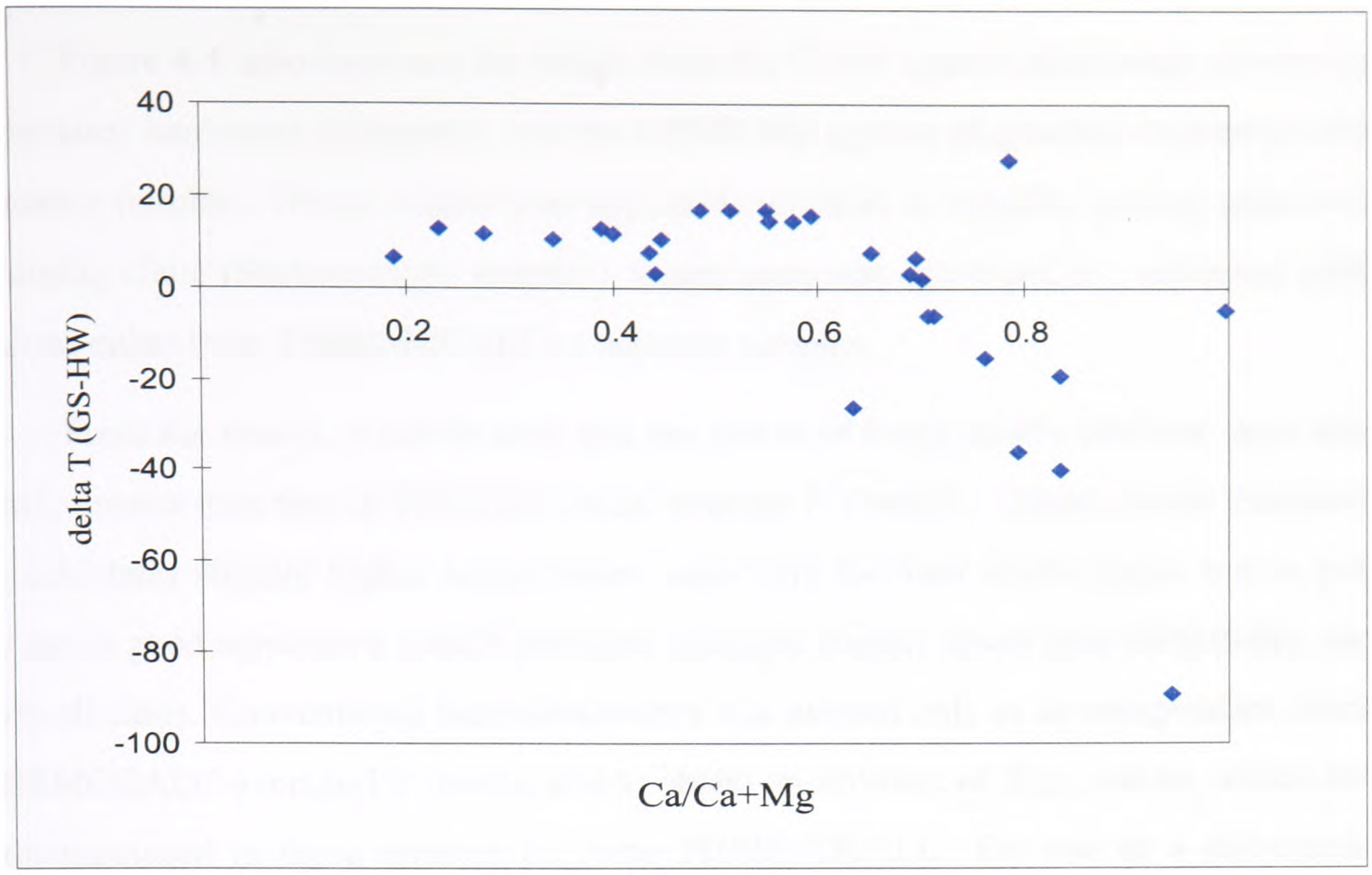


Figure 4.5.A. Plot of Ca/ Ca+Mg of garnet rim compositions used in garnet-biotite thermometry against the difference in calculated temperatures using the Ganguly & Saxena (GS) and Hackler & Wood (HW) calibrations for garnet mixing. For most values of Ca/ Ca+Mg delta T (GS-HW) is positive and generally has a value between 10-20 ^{0}C. However, at Ca/Ca+Mg values above about 0.7, delta T values appear to become negative and gradually larger. This would appear to agree with the findings of Ganguly and Saxena (1984).

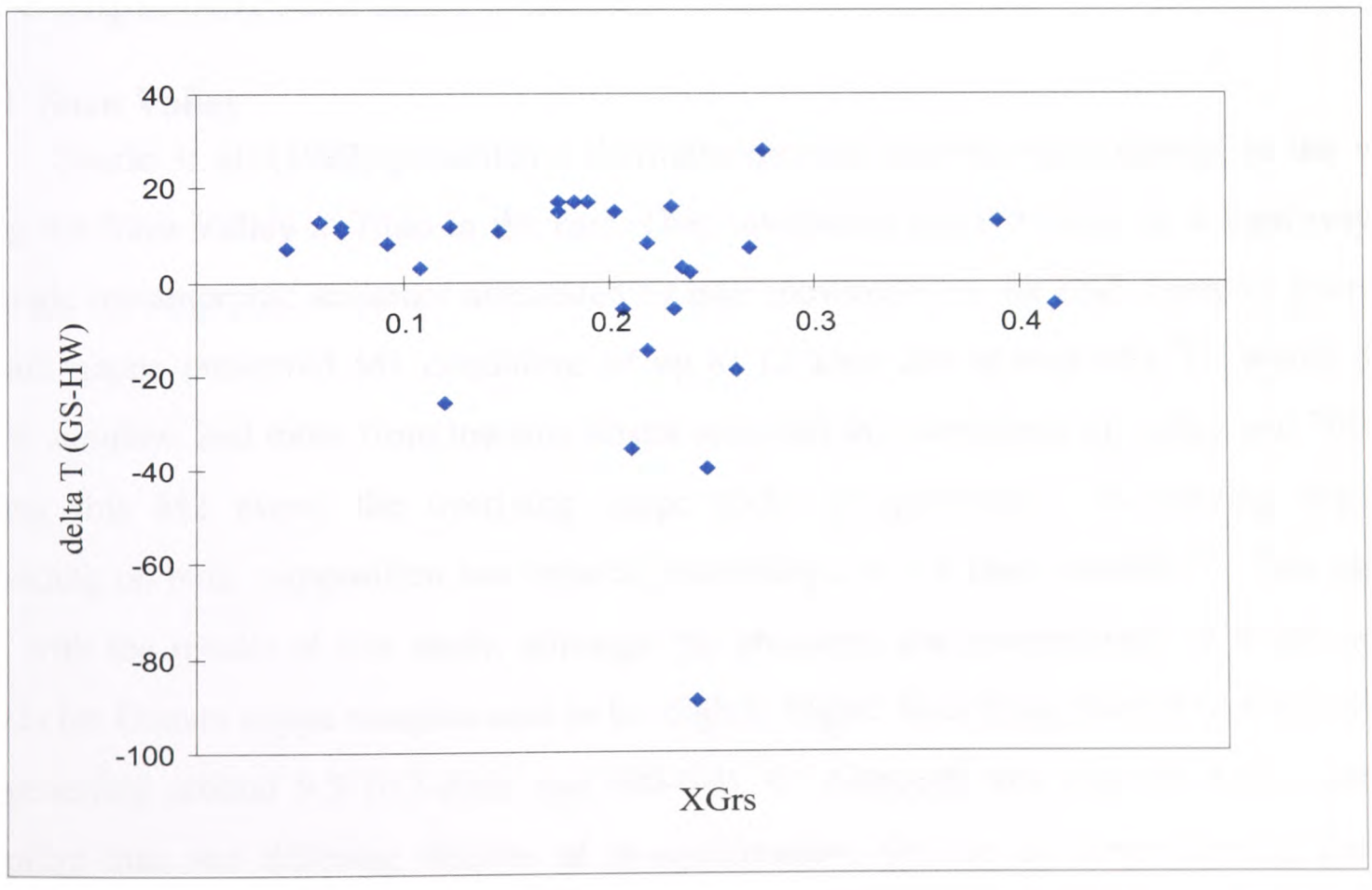


Figure 4.5.B. Plot of XGrs against delta T, as described above. This comparitive diagram illustrates that Ca content of garnet alone is not the most important factor in determining the degree of discrepancy between the GS and HW garnet calibrations; there appears to be no real systematic correlation between XGrs and delta T.

Figure 4.4. also separates the results from the GASP (garnet-aluminium silicate-silica-plagioclase) barometer (triangles), and the GPMB-Mg (garnet-plagioclase-muscovite-biotite) barometer (circles). Where neither was applicable, such as in samples lacking muscovite or containing albite (Sankoo nappe samples), temperature was calculated at a reference pressure obtained either from THERMOCALC or adjacent samples.

From the results, it can be seen that the spread of temperatures (without error bars) is slightly greater than that of THERMOCALC average P-T results. Garnet-biotite thermometry also calculates slightly higher temperatures, especially for Suru Dome rocks, but in general they are in good agreement. GASP pressures calculate slightly lower than GPMB-Mg ones in nearly all cases. Conventional thermobarometry was utilised only as an independent check on THERMOCALC average PT results, and to obtain an estimate of X_{H2O} values, which cannot be distinguished in these samples by using THERMOCALC. The use of a self-consistent thermodynamic dataset utilising a number of different equilibria should give more consistent estimates of pressure and temperature, as well as providing an evaluation of the degree to which measured phases are in equilibrium (Berman, 1988, 1990; Holland and Powell, 1990; Powell and Holland,1994).

4.4 Comparison with other studies

4.4.1 Suru Valley

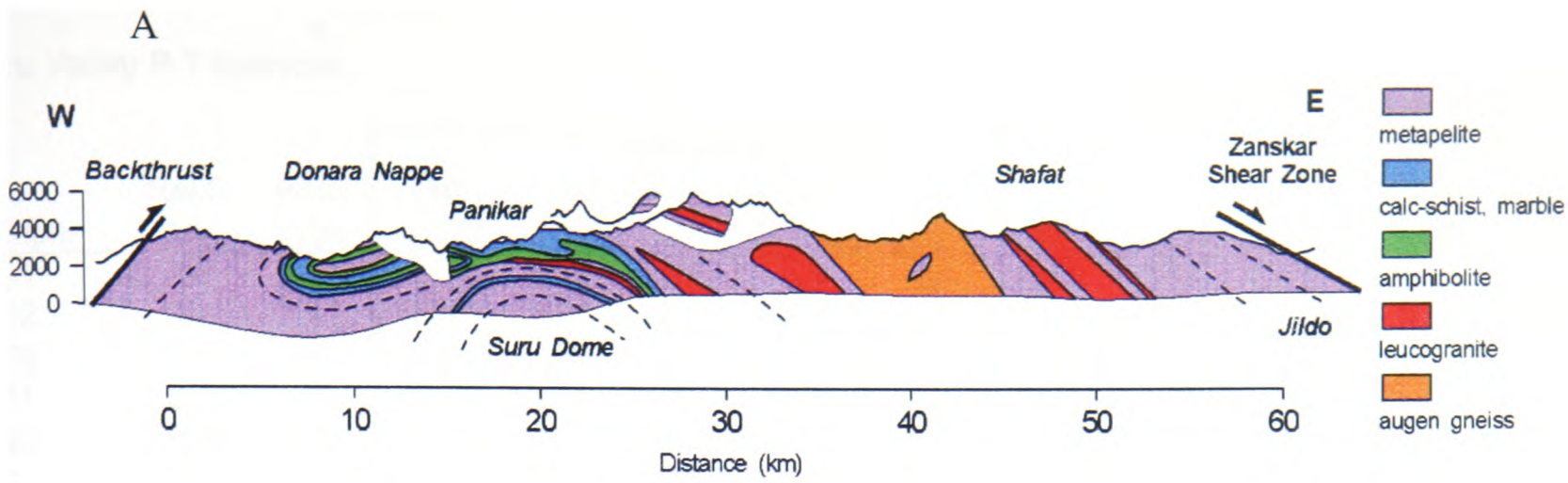
Searle *et al.* (1992) presented a thermobarometric traverse from Kaintal in the west along the Suru Valley to Jildo in the east. They interpreted the P-T array as a right-way up prograde metamorphic sequence attenuated by later movement on the ZSZ. Samples from the Donara nappe preserved M1 conditions of up to 12 kbar and around 650 ^{0}C, whilst Suru Dome samples, and those from towards Shafat recorded M2 conditions of 7 kbar and 700 ^{0}C. During this M2 event, the overlying nappe rocks re-equilibrated to varying degrees, depending on bulk composition and mineral assemblage, to 7-8 kbar and 600 ^{0}C. This agrees well with the results of this study, although the pressures and temperatures of Searle *et al.* (1992) for Donara nappe samples tend to be slightly higher than those from this study, which are generally around 9.5-10.5 kbar and 620-640 ^{0}C. Although this may be due in part to sampling bias and differing degrees of re-equilibration, the use of newer activity models (Holland and Powell, 1998) in calculating mineral activities (using the program AX) appears to show a systematic difference between the two studies. For example, muscovite non-ideal mixing models in the latest version of AX calculate a lower celadonite activity than the older WAX program; this will have the effect of slightly lowering the pressure estimate in

THERMOCALC. As these newer activity models take into account further site interactions and more recent experimental constraints, it seems reasonable to assume that they are more accurate, and should therefore give more realistic estimates of pressure and temperature.

Waters (pers. comm.) recalculated the P-T data from the Suru Valley traverse of Searle *et al.* (1992) (Figure 4.5.A.) using the latest activity models used in this study, and recent calibrations of various conventional thermometers. The method employed was to calculate peak temperatures using conventional thermometers, which were then "smoothed" using a simple polynomial function, These temperatures are plotted against distance in Figure 4.6.B. These temperatures were then used to calculate the average pressure of final equilibration using THERMOCALC, plotted in Figure 4.6.C. The advantage of this technique is that it enables independent temperatures and pressures to be compared, and to estimate water activities for samples, as these are all interdependent and correlated in THERMOCALC in average P-T mode, as described above. The results of conventional thermometry and THERMOCALC average P-T calculations are presented in Table 4.5. Calculated temperatures display a similar variation to those calculated in Searle *et al.* (1992) and Waters *et al.* (1996), while the calculated pressures appear slightly better constrained and average about 9 kbar throughout the width of the slab. Pressures of up to ~11 kbar are still recorded in the Donara nappe and towards the ZSZ in the Shafat-Jildo area. Furthermore, predicted values of X_{H2O} for a particular temperature appear to correlate well with rock type; graphitic schists (Type 1b of Searle *et al.*, 1992) tend to have X_{H2O} between 0.5-0.8, whilst non-graphitic schists commonly exhibit values of 1.0. This is a useful independent check on calculated THERMOCALC average P-T results.

4.4.2 Central Zanskar

This section will attempt to summarise the results of other thermobarometric studies across the Zanskar HHC, by way of comparison with the Suru Valley. To the southeast of the study area, in central Zanskar, sillimanite is the dominant aluminium silicate phase across most of the width of the slab, and the deepest levels correspond to the sillimanite + K-feldspar zone, with widespread migmatisation present (Searle and Fryer, 1986). Along the Kishtwar Window - Umasi-la traverse across central Zanskar, temperatures increase sharply across the MCT zone from 525-650 ^{0}C in only 0.5 km (Stephenson, 1997; Searle *et al.*, 1999). This sudden temperature increase across a narrow mylonitic zone further supports field evidence that post-metamorphic shearing has affected the early M1 isograds. Temperatures increase towards the middle of the slab, where maximum temperatures of 700-750 ^{0}C are recorded (Figure 4.6.A.), corresponding to the sillimanite + K-feldspar M2 metamorphism. These high



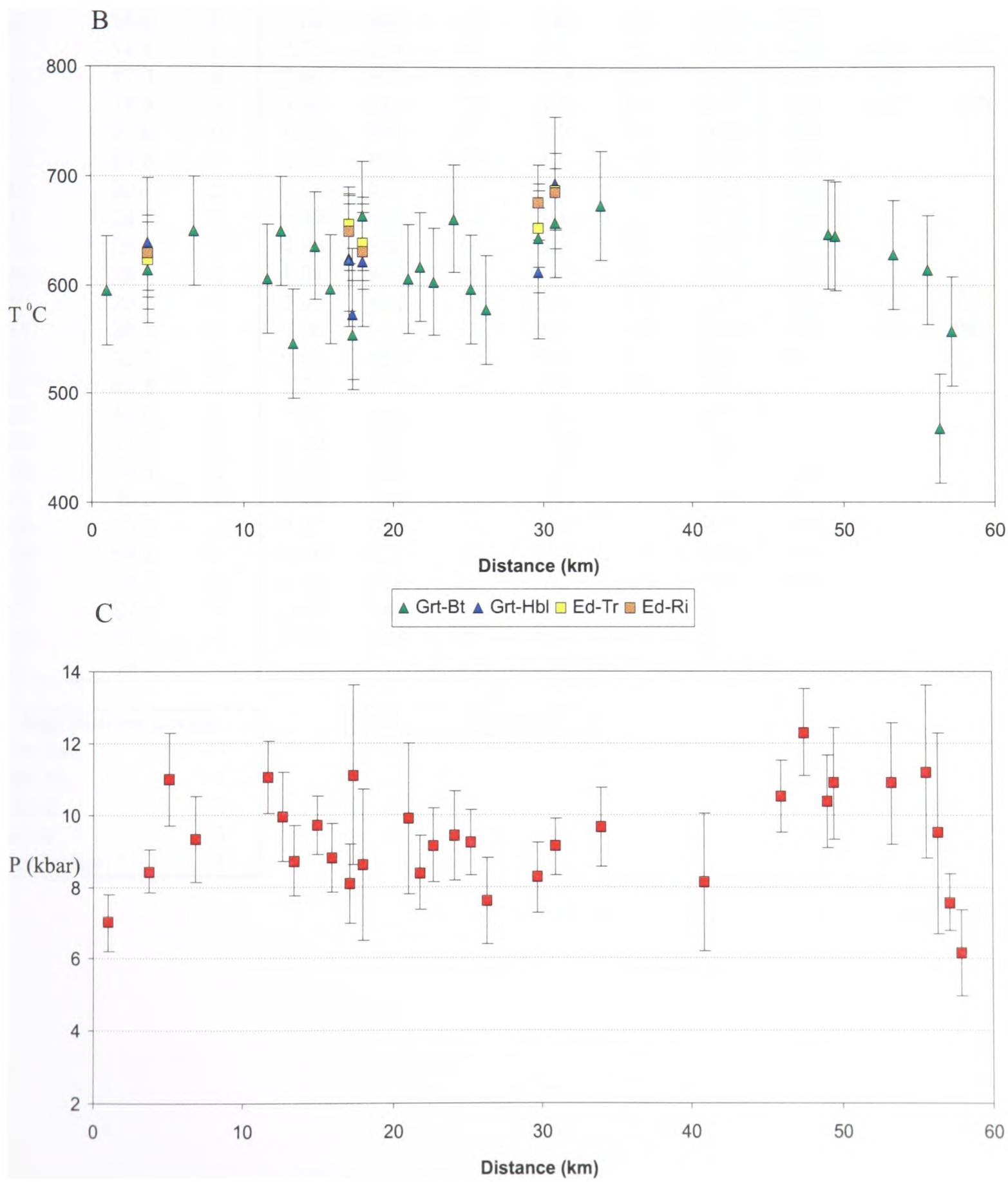


Figure 4.6. A) Schematic cross-section through the Suru Valley, after Waters *et al.* (1995); B) Plot of the results of various conventional thermometers against distance, corresponding to the cross-section in A); C) Plot of the results of THERMOCALC average P calculations against distance, as for B).

Suru Valley P-T traverse

			Holland & Powell						Conventional Thermometry			
				Ave T		Ave P					Hbl-Pl Temps	
Sample	Rel.D km	Rock Type	Ref XH2O	T°C	sd(T)	P(kbar)	sd(P)	Corrl	B92 T(C)	Gt-Hb T(C)	Ed-Tr T(C)	Ed-Ri T(C)
L401	1.0	0	1.00	537	22	7.0	0.8	0.70	594			
L402	3.7	4	0.61	601	16	8.4	0.6	0.86	614	638	623	629
L409	5.0	0	1.00	573	30	11.0	1.3	0.05				
L411	6.8	0	0.68	614	15	9.3	1.2	0.80	650			
L420	11.6	1	0.48	622	28	11.0	1.0	0.94	605			
L421	12.5	1	0.73	623	43	9.9	1.2	0.88	649			
L425	13.3	1	0.86	623	31	8.7	1.0	0.84	546			
L429	14.8	0	0.66	624	15	9.7	0.8	0.80	636			
L430	15.8	0	0.79	624	16	8.8	1.0	0.83	596			
L431	17.1	4	0.77	624	47	8.1	1.1	0.65	625	622	655	649
L432	17.3	4	0.50	613	28	11.1	2.5	0.52	554	573		
L433	17.9	4	0.30	643	72	8.6	2.1	0.58	663	621	639	631
L434	21.0	0	1.00	614	27	9.9	2.1	-0.50	605			
L439	21.8	1	0.56	626	32	8.4	1.0	0.80	617			
L440	22.7	2	0.83	627	17	9.1	1.0	0.57	603			
L441	24.1	2	0.68	629	23	9.4	1.2	0.78	661			
L442	25.2	0	0.69	630	24	9.2	0.9	0.75	596			
L445	26.2	2	1.01	632	24	7.6	1.2	0.80	577			
L449	29.7	4	0.90	640	50	8.2	1.0	0.81	643	611	652	676
L451	30.8	4	0.00	643	46	9.1	0.8	0.54	657	694	687	686
L462	33.9	2	0.96	652	18	9.6	1.1	0.86	673			
L463	40.8	3	0.70	670	42	8.1	1.9	0.77				
L465	46.0	3	1.00	526	60	10.5	1.0	0.31				
L466	47.5	3	1.00	538	56	12.3	1.2	0.25				
ZD24	49.1	2	0.85	656	32	10.4	1.3	0.75	646			
L473	49.5	0	1.00	654	0	10.9	1.6	0.00	645			
ZD26	53.3	2	0.21	615	35	10.9	1.7	0.71	627			
ZD28	55.6	0	0.50	620	70	11.2	2.4	0.98	613			
ZD29	56.4	0	0.50	552	80	9.5	2.8	0.98	468			
L477	57.2	1	0.47	546	13	7.6	0.8	0.58	557			
ZD33	57.9	4	0.73	528	30	6.2	1.2	0.97				
Jildo	58.7											

Key to rock codes	
Pelite 1a	0
Pelite 1b	1
Pelite 2	2
Granite	3
Amphibolite	4

Date:	5-Jan-99

Table 4.5. Recalculated P-T-XH2O results for Searle *et al.*(1992) dataset from the Kashmir-Jildo traverse. Abbreviations as follows: B92 = Bhattacharya *et al.* (1992) calibration of the garnet-biotite thermometer. Gt-Hb = garnet-hornblende thermometer. Ed-Tr = edenite-tremolite endmembers in the plagioclase-hornblende thermometer. Ed-Ri = edenite-richterite endmembers in the plagioclase-hornblende thermometer.

temperatures are maintained across 55 km of the slab (Stephenson, 1997, Searle *et al.*, 1999), before dropping off at the top of the slab at the ZSZ, where isograds are again condensed, but right way-up (Searle, 1986; Herren, 1987; Dransfield, 1994).

Stäubli (1989) carried out thermometry on samples from the Kishtwar-Zanskar MCT zone and concluded that isothermal results of 500-600 ^{0}C were a consequence of post-MCT retrograde metamorphism associated with exhumation of the Kishtwar Window.

Maximum pressures occur in the MCT zone, which represent the remnants of the kyanite-grade M1 metamorphism. Pressures increase again over a narrow 0.5 km wide zone from 6-8.5 kbar, then decrease gradually towards the middle of the slab to values of 4-7 kbar (Stephenson, 1997; Searle *et al.*, 1999) (Figure 4.6.B.), which records the lower pressure M2 metamorphic event.

The thermobarometric data from central Zanskar records much more of the later M2 metamorphic event than this study of the Suru Valley, which preserves a large area recording the early M1 Barrovian event that remains relatively unaffected by the overprinting M2 decompression event.

4.4.3 The rest of the Himalaya

The results of several thermobarometric studies across various parts of the Himalaya are presented in Table 4.6., after Walker (1998). It is not the purpose of this chapter to review in detail the thermotectonic evolution of the entire High Himalayan Crystallines, and so the results are tabulated for the purpose of comparing pressure-temperature estimates.

Table 4.6 Summary of various thermobarometric profiles across the High Himalaya

Area	M1 (regional Barrovian)		M2 (sillimanite overprint)		Reference
	P (kbar)	T (^{0}C)	P (kbar)	T (^{0}C)	
Central/western Zanskar	9.5-12	550-680	4.5-7	650 770	Searle et al (1998)
	9.5-10.5	620-650	8.7-9.7	630-640	This study
SE Zanskar & NW Lahoul	6-8	550-650	4-7	650-700	Walker (1998)
Western Garhwal	6-12	550-640	6-8	550-700	Metcalfe (1993)
Eastern Garhwal	8.6-9.1	580-650	3-5	500-700	Hodges & Silverberg (1988)
Western-central Nepal	7-8.5	600-690	7	650-710	Pêcher (1978)
Eastern-central Nepal	9-12	425-525	4-12	490-660	MacFarlane (1995)
	9$\pm$1	710$\pm$30	5.8$\pm$0.4	760$\pm$30	Harris & Inger (1992)
Eastern Nepal	8-10	550-680	4-7	650-750	Pognante & Benna (1993)
Bhutan	~7	480-500	4-6	650-700	Swapp & Hollister (1991)

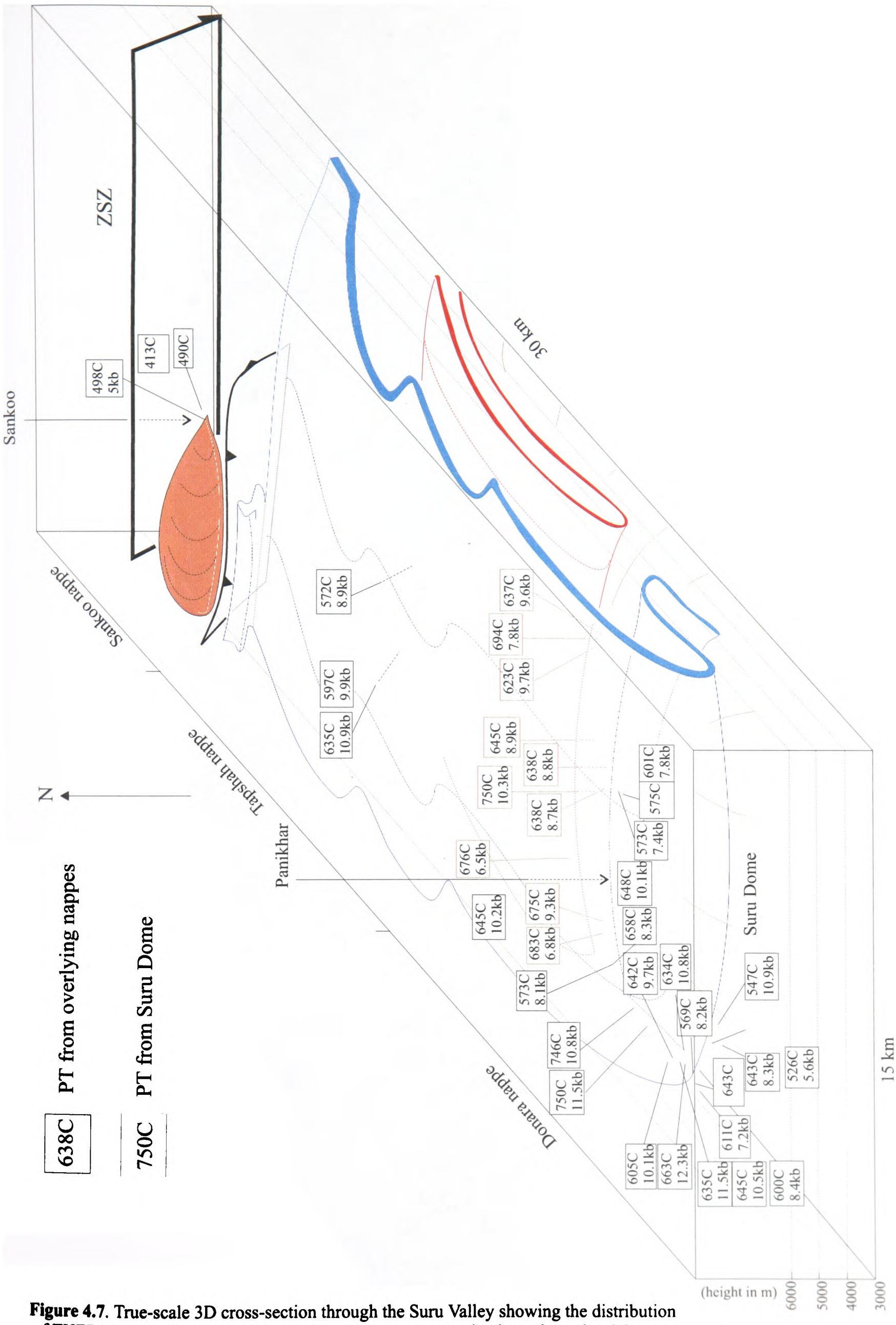
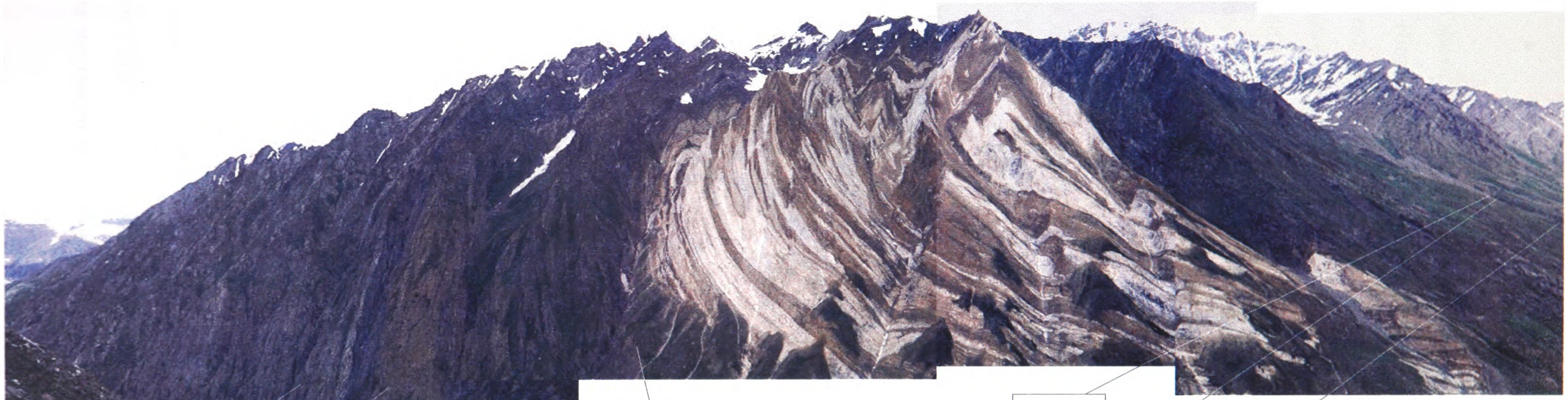


Figure 4.7. True-scale 3D cross-section through the Suru Valley showing the distribution of THERMOCALC average P-T and gt-bt thermometer results throughout the slab.



re 4.8. Photomontage looking westwards towards the closure of the Donara nappe showing THERMOCALC average P-T results for various rock types collected, and one garnet-biotite mometry result. The diagram attempts to demonstrate that there is no demonstrable systematic difference in P-T conditions across the Donara nappe, as one might expect if deformation had entirely post-metamorphic with respect to M1. The errors on P estimates, however, make this very difficult to demonstrate; a typical error of ± 1.5 kbar corresponds to nearly 5 km if al crustal densities are used.

From the above results, it can be seen that there is a striking similarity in P-T estimates along the entire Himalayan orogen, in that a high pressure-high temperature Barrovian M1 metamorphic event, and a later low-medium pressure-high temperature M2 event can be recognised in various regions. This implies that the entire High Himalayan Crystalline unit underwent a similar tectonometamorphic history subsequent to India-Asia collision 50 Ma ago. Whilst there is a wealth of data indicating a Himalayan age for both M1 and M2 metamorphism, as discussed in Chapter 1, it is worth pointing out that there is U-Pb monazite evidence for 500Ma magmatism and metamorphism in Lahoul-Zanskar (Pognante *et al.*, 1990; Walker, 1998), and that it is extremely difficult in many cases to texturally distinguish these monazites from supposed Himalayan ones. Care should then be taken when ascribing metamorphic P-T conditions to particular tectonic events.

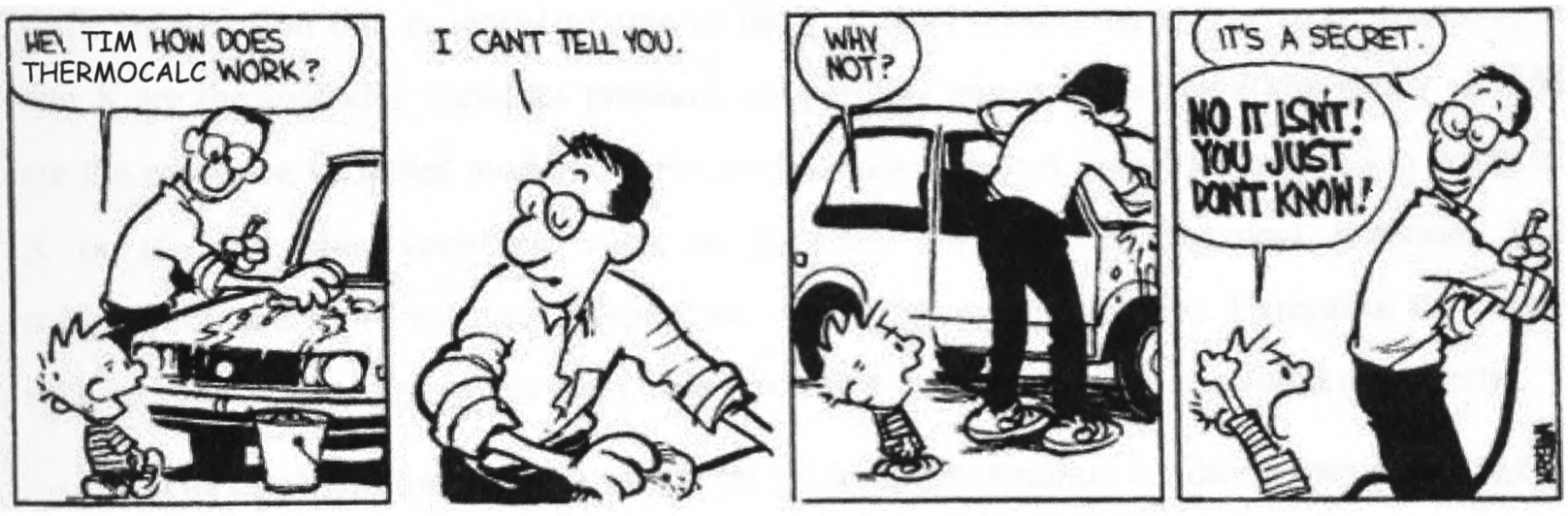
4.5 Conclusions

Thermobarometric calculations using the average P-T method of the program THERMOCALC, and using the activity models of Holland and Powell (1998), on samples from the Suru Valley predict peak M1 metamorphic conditions of 620-650 ^{0}C and 9.5-10.5 kbar, preserved in the Donara and Tapshah nappes. Rocks from the structurally lower Suru Dome record temperatures and pressures of 630-640 ^{0}C and 8.7-9.7 kbar. These are believed to represent part of a later M2 metamorphism, as they record generally lower pressures at greater structural depths, which implies later re-equilibration on an uplift trajectory. In the Suru Dome this M2 metamorphism is not as strongly developed as in those samples from further to the east (Searle *et al.*, 1992, 1999). Some samples from the Donara nappe record pressures and temperatures of 7.2-8.4 kbar and 570-600 ^{0}C, lower than peak conditions recorded in other nappe samples. This, combined with textural observations, suggest a degree of re-equilibration related to Suru Dome formation and M2 metamorphism. Peak recorded conditions decrease northwards towards the ZSZ at Sankoo, where pressures and temperatures of around 5 kbar and 411-516 ^{0}C are preserved in rocks near the garnet isograd. Figure 4.7 is a true-scale cross-section through the Suru Valley, with the thermobarometric results of this study and some of those of Searle *et al* (1992) superimposed. This illustrates how pressures and temperatures vary as described above, but cannot be distinguished across structures such as the Donara nappe (Figure 4.8).

The Suru Valley P-T array correlates well with thermobarometric data from other parts of Zanskar, and the rest of the Himalaya. The advantage of studying this part of the Suru

Valley is that it comprises a large area that preserves the early M1 Barrovian prograde metamorphism and is not overprinted by the sillimanite grade M2 decompressional event that obscures the early part of the Himalayan metamorphic evolution in the greater part of the High Himalayan Crystallines.

Chapter 5


HEY, TIM HOW DOES THERMOCALC WORK?
I CAN'T TELL YOU.
WHY NOT?
IT'S A SECRET.
NO IT ISN'T! YOU JUST DON'T KNOW!

5. Metamorphic modelling

5.1. Introduction

The previous chapter described the results of conventional and internally consistent thermobarometry used to calculate the conditions of peak metamorphism of Suru Valley rocks. Whilst this is useful in estimating the absolute temperatures and pressures that samples have been subject to, it does not provide us with any information on their prograde metamorphic history, i.e. how they came to be at those conditions. This chapter details attempts to model the prograde reaction histories of certain suitable samples and determine the prograde P-T paths of these samples.

In order to be able to model pre-peak metamorphic conditions it is necessary to have some information that is representative of the P-T-X-M conditions at that time, where P, T and X are the *intensive* variables pressure, temperature and composition respectively, and M are the *extensive* variables mode or moles of the phases present (usually described in terms of X or μ). Intensive variables, such as pressure, temperature, chemical potential and composition are those that are independent of the amount of material. Extensive variables, such as volume, entropy, moles and Gibbs free energy do depend on the amount of material.

The most common way in which pre-peak thermodynamic conditions are preserved is in zoned metamorphic minerals that maintain *disequilibrium* between the cores of these minerals and the matrix, such as garnet. Mechanisms of garnet zoning are described in Chapter 3, and are not reiterated here. The rationale applied is simply that, if we know the composition of the garnet from core to rim, and a set of thermodynamic data for all phases of interest, then if the reacting garnet rim is in equilibrium with the matrix phases it should be possible to calculate the P-T-X-M relations for all garnet compositions from core to rim. Two such methods are employed here; phase diagram calculations using the program THERMOCALC, described in Chapter 4, and Gibbs method differential thermodynamics (Spear *et al.*, 1982; Spear & Selverstone, 1983; Spear, 1988) using program GIBBS (Spear & Menard, 1989). The main differences between the two approaches, and their relative merits, are discussed briefly here.

5.1.1. THERMOCALC vs. GIBBS

The principal reason behind taking two different approaches to the modelling of phase equilibria in these samples is that the two programs employ different calculation method in determining the equilibrium relations between phases. The main difference is that THERMOCALC takes an integrative approach to calculations whilst the Gibbs method employs differential thermodynamics. Essentially, this means that the integrated approach solves the *integrated* forms of the thermodynamic equations e.g. (from Chapter 4)

$$\Delta G = 0 = \Delta H^0 - T\Delta S^0 + \int \Delta V dP + RT\ln K_{eq} \qquad 5.1$$

whilst the *differential* approach solves the differentiated forms:

$$\Delta G = 0 = (-\Delta S + R\ln_{Keq})dT + \Delta V dP \qquad 5.2$$

The integrated approach is best suited to predicting phase relations of rocks, and permits comparisons of calculated and observed phase relations, as it calculates *absolute* values of P, T, X and M. This can also be used to evaluate the degree to which the natural assemblage is equilibrated. This method requires accurate thermodynamic data and activity models for all phases. Conversely, the differential approach calculates *changes* in P, T, X and M, such as the change in P-T conditions associated with the changes in composition of a zoned garnet. Furthermore, from equation 5.2. above, it can be seen that the term for enthalpy has been lost, thus removing the thermodynamic variable associated with the largest errors.

The approach taken in modelling the evolution of Suru valley rocks is to combine the advantages of both methods. Phase diagrams are calculated using THERMOCALC in order to construct a petrogenetic framework within which to apply the differential techniques of Gibbs modelling; therefore it should be possible to predict the sequence of assemblages present from the garnet core through to the final equilibrium assemblage, and model the P-T evolution of the sample using garnet compositional zoning appropriately. THERMOCALC is used to calculate conditions at the start of garnet growth, the subsequent assemblages garnet should exist in, and the conditions of final rim equilibration. This is important, as Gibbs modelling, being a differential approach cannot do this; it can only calculate the *changes* in P, T, X or M. These starting conditions are then used as a basis for the calculations in program GIBBS.

An important consideration when dealing with the modelling of metamorphic rocks is that of disequilibrium and fractionation of materials. For the above methods to work, and indeed most thermodynamic calculations, equilibrium conditions must be assumed. However, as zoned minerals are our primary source of information for the earlier metamorphic history of

the samples, disequilibrium processes must be in operation, providing a neat contradiction. THERMOCALC does not have the ability to incorporate fractionation into its calculations as yet, as it would be a complex approach for integrative calculations. It is simpler to build fractionation into differential calculations, and program GIBBS does have this facility, by resetting the volume of garnet after each increment of calculation. The effects of garnet fractionation are crudely modelled using THERMOCALC in section 5.3.6., but other than this all THERMOCALC modelling assumes complete equilibrium growth, whilst all Gibbs modelling assumes fractional crystallisation.

In summary, both integrative and differential thermodynamic calculations are employed to best model the samples as close to "reality" as possible. The two methods are used in conjunction with one another, but are also compared and contrasted.

5.2. Phase diagram calculations

5.2.1. Introduction

A starting point for modelling the prograde evolution of metamorphic rocks is the construction of phase diagrams that model as closely as possible the "real" phase relations that occur in natural rocks. The approach taken here is to use an internally consistent dataset of thermodynamic data and use it to calculate the mineral equilibria involving solid solutions for all phases of petrological interest. The computer program THERMOCALC (Holland & Powell, 1985; Powell & Holland, 1988; Holland & Powell, 1990) calculates these equilibria using a series of non-linear equations that describe the equilibrium relations between the independent set of reactions between the endmembers of the phases in the equilibrium. The methodology of calculating phase diagrams using THERMOCALC is described in Appendix B, and in detail in Powell *et al.* (1998); it is worth pointing out that the calculation method differs from that where average P-T calculations are performed, although the same thermodynamic dataset is used. In this study the dataset of Holland & Powell (1998) is used in conjunction with THERMOCALC v2.7. The modelling uses many new activity-composition (a-X) models, combined with a version of the dataset in which data for many minerals (especially micas and chlorite) were refined according to the new models. The new dataset produces a better match to certain experimental and natural observations (e.g. the chlorite activity models are formulated around the results of Baker & Holland, 1996), and so should model phase equilibria more accurately than earlier versions.

The following sections introduce the petrogenetic grids that can be calculated for various chemical systems of choice, and the subsequent *pseudosections* that may be calculated. A pseudosection (Powell & Holland, 1990) is essentially a petrogenetic grid calculated with bulk compositional constraints, enabling us to model the phase relations of particular rock compositions. This is very important, as will be shown later. Firstly, it is worth introducing the concepts of thermodynamic variance and how the addition of mass balance constraints allows the construction of pseudosections. The following treatment is taken from Spear (1993).

5.2.1.1.The Gibbs phase rule, variance and Duhem's theorem

The phase rule is a statement of the number of thermodynamic degrees of freedom of a heterogeneous system at equilibrium. For a system such as this, the thermodynamic variables are pressure (P), temperature (T) and the composition (mole fraction, X) of each phase component of each phase in the assemblage. If npc^k is the number of phase components in each phase k and there are nph total phases in the system, then there are

$$\mathbf{npct = {}^{nph}\sum_{k=1} npc^k}$$

phase components in the system (npct). There are then npct + 2 variables in the system.

The number of linearly independent reactions that can be written among a set of phase components in an assemblage can be thought of as

number of independent reactions = total number of phase components - number of system components, or as

$$\mathbf{nrx = npct - nsc}$$

Each one of these nrx reactions acts as a constraint on the phase equilibria of a heterogeneous system. Furthermore, there is a stoichiometric constraint for each phase:

$$\mathbf{1 = {}^{npc}\sum_{j=1} X_j}$$

There is one such equation for each phase in the assemblage, leading to a total number of constraints of

$$\mathbf{nrx + nph = npct - nsc + nph}$$

The number of degrees of freedom of the system is calculated as the difference between the number of variables and the number of constraints:

$$\mathbf{Variance = npct + 2 - (npct\text{-}nsc + nph) = nsc - 2\text{-}nph}$$

This is known as the *Gibbs phase rule*, also written as P + F = C + 2

The phase rule only pertains to the intensive variables T, P and X. As shall be seen in later sections, the bulk composition of a rock is also an important factor when considering its metamorphic evolution. In order to incorporate bulk composition data into the analysis of phase equilibria, mass balance equations need to be incorporated. The new variables in the system are M^k, the moles of phase k in the rock of which there are nph (one for each phase), and m_i, the moles of system component i in the rock, of which there are nsc (one for each phase component). There are now nsc new equations with nph unknowns (the m_i's are known if bulk composition is fixed), and the variance can be calculated by adding the variables and subtracting the constraints:

$$\begin{aligned}\textbf{Variance} &= \textbf{2 + npct + nph - (nrx + nph + nsc)}\\ &= \textbf{2 + npct + nph - (npct - nsc + nph + nsc)}\\ &= \textbf{2}\end{aligned}$$

This states that the number of degrees of freedom in a system for which the bulk composition is fixed is 2, which is known as *Duhem's theorem*. Therefore, specification of any two independent variables completely determines the state of the system including the composition of all minerals and their modal abundance. This is used in both THERMOCALC, and GIBBS, and is very important when considering large chemical systems with many variables.

5.2.2. Setting up the problem

In order to obtain the best results from calculating pseudosections, the problem must be set up in such a way as to reflect as closely as possible "real" rock compositions. The different chemical systems are described in the sub-sections below, but a brief consideration of some of the more important compositional variants is given here.

The first consideration is which chemical system to consider. Too simple a system will not consider sufficient important phases and will not reflect important aspects of the compositional variations in minerals, as shown below. On the other hand, too complex a system will become unwieldy and make formulation of mixing models etc. a rather difficult process. The system CaO-NaO-MnO-K_2O-FeO-MgO-Al_2O_3-SiO_2-H_2O (CNMnKFMASH) is chosen, as it models most important pelite chemical substitutions (section 5.2.2.2.). Ti and Fe^{3+} are also present in minor quantities in pelites, but are not modelled here, mainly because of the reasons of maintaining a manageable level of complexity, but also because electron microprobe data does not distinguish between Fe^{2+} and Fe^{3+}, so all Fe is treated as Fe^{2+}. This makes little apparent difference to most of the calculations, with the possible exception of

those involving clinozoisite (section 5.3.3.2.). ZnO is known to have an effect on the stability of staurolite, but again this oxide was not measured by the electron microprobe, and staurolite is a minor phase in the samples modelled.

The way in which bulk composition is calculated (see Appendix C; section 5.3.1) also means that the estimates for bulk molar MnO need to be given special consideration, not least because of the important effect MnO has on mineral stability despite its very small concentrations (e.g. Mahar *et al.*, 1997) Essentially, bulk composition calculation involves combining microprobe analyses with modal proportions of minerals. MnO cannot be estimated in the usual way, as it concentrates in garnet cores, and decreases to almost zero at garnet rims. As garnet fractionates MnO so strongly, the concentration of MnO in the cores of garnets is realistically the most sensitive indicator of bulk rock MnO. The procedure taken was to assume that the garnet core comprised approximately 10% by volume of the total garnet, and this modal proportion was combined with the measured value of amount of Mn in the garnet. This value was converted into molar proportions of Mn (Appendix C), and then "tweaked" by calculating the garnet = 0 isopleth using THERMOCALC until the calculated value for X_{Sps} in garnet was as close as possible to the actual value. Although this may appear a rather circular route, it provides results similar to those calculated from bulk compositions obtained by XRF data (see section 5.3.4).

A final point to raise is the issue of aH_2O. Water activity was shown in Chapter 4 to have an important effect on calculated average P-T conditions, and therefore it should affect the calculation of phase equilibria in pseudosection calculations. Section 5.3.2.1. illustrates that this is indeed the case; however, it is in reality very difficult to model the effects of fluid composition accurately using the phase diagram approach. The approach taken is to use aH_2O values estimated from the average P-T approach described in Chapter 4, and model the phase equilibria for the relevant samples using this uniform value throughout. This approach provides no insights into the evolution of aH_2O, either through external or internal factors, and must be viewed as an oversimplification (although unavoidable).

The following sections describe how the phase diagram model has been developed, starting with simpler chemical systems and progressing to more complicated ones, and how the addition of successive system components affects the variance of phase equilibria of a particular number of phases.

garnet	Grt	$(Fe,Mg,Mn,Ca)_3Al_2Si_3O_{12}$
chloritoid	Cld	$(Fe,Mg,Mn)Al_2SiO_5(OH)_2$
chlorite	Chl	$(Fe,Mg,Mn)_4(Fe,Mg,Mn,Al)_2Si_2(Si,Al)_2O_{10}(OH)_8$
muscovite	Ms	$(K,Ca,Na)_(Fe,Mg,Al)_2Si_2(Si,Al)_2O_{10}(OH)_2$
paragonite	Pg	$(K,Ca,Na)_Al_2Si_2(Si,Al)_2O_{10}(OH)_2$
margarite	Mrg	$(Ca,Na)_Al_2Si_2(Si,Al)_2O_{10}(OH)_2$
clinozoisite	Czo	$Ca_2Al_2O.AlOH(Si_2O_7)(SiO_4)$
biotite	Bt	$K(Fe,Mg,Mn)(Fe,Mg,Mn,Al)_2Si2(Si,Al)_2O_{10}(OH)_2$
staurolite	St	$(Fe,Mg,Mn)_4Al_{18}Si_{7.5}O_{48}H_4$
kyanite	Ky	Al_2SiO_5
sillimanite	Sil	Al_2SiO_5
plagioclase	Pl	$(Ca,Na)Si_2(Al,Si)_2O_8$
quartz	Qtz	SiO_2

Table 5.1 Mineral abbreviations as in Kretz (1983) and formulae. The activity models used are included in Appendix A.

5.2.2.1.KFMASH

The model system K_2O-FeO-MgO-Al_2O_3-SiO_2-H_2O (KFMASH) is usually used when modelling pelites e.g. Thompson (1957), Spear & Cheney (1989), Powell & Holland (1990), as it allows the main Fe = Mg and (Fe,Mg)Si = AlAl substitutions to be modelled. Figure 5.1.A. is P-T projection for KFMASH in the P-T range of interest for Suru Valley rocks calculated using the latest version of THERMOCALC for DOS (v2.7) and the Holland & Powell (1998) dataset. This predicts two invariant points, [Bt] and [Cld], at 14.1 kbar, 603 ^{0}C and 10.9 kbar, 639 ^{0}C respectively. The (Bt, Chl) univariant curve ends at the [Bt, Chl] KFASH endmember invariant point at 15.8 kbar, 575 ^{0}C. This plot illustrates all possible univariant equilibria possible in the KFMASH system; however, natural assemblages rarely experience every reaction predicted by the grid.

Figure 5.1.B. is a P-T pseudosection calculated for the bulk composition of sample Z47, a sub-aluminous pelite from the Donara nappe. What is immediately apparent from the projection is the restriction in the extent of KFMASH univariant equilibria seen, and the extent of higher-variance equilibria. The incoming of garnet into the assemblage is also predicted to occur at quite high temperatures and pressures.

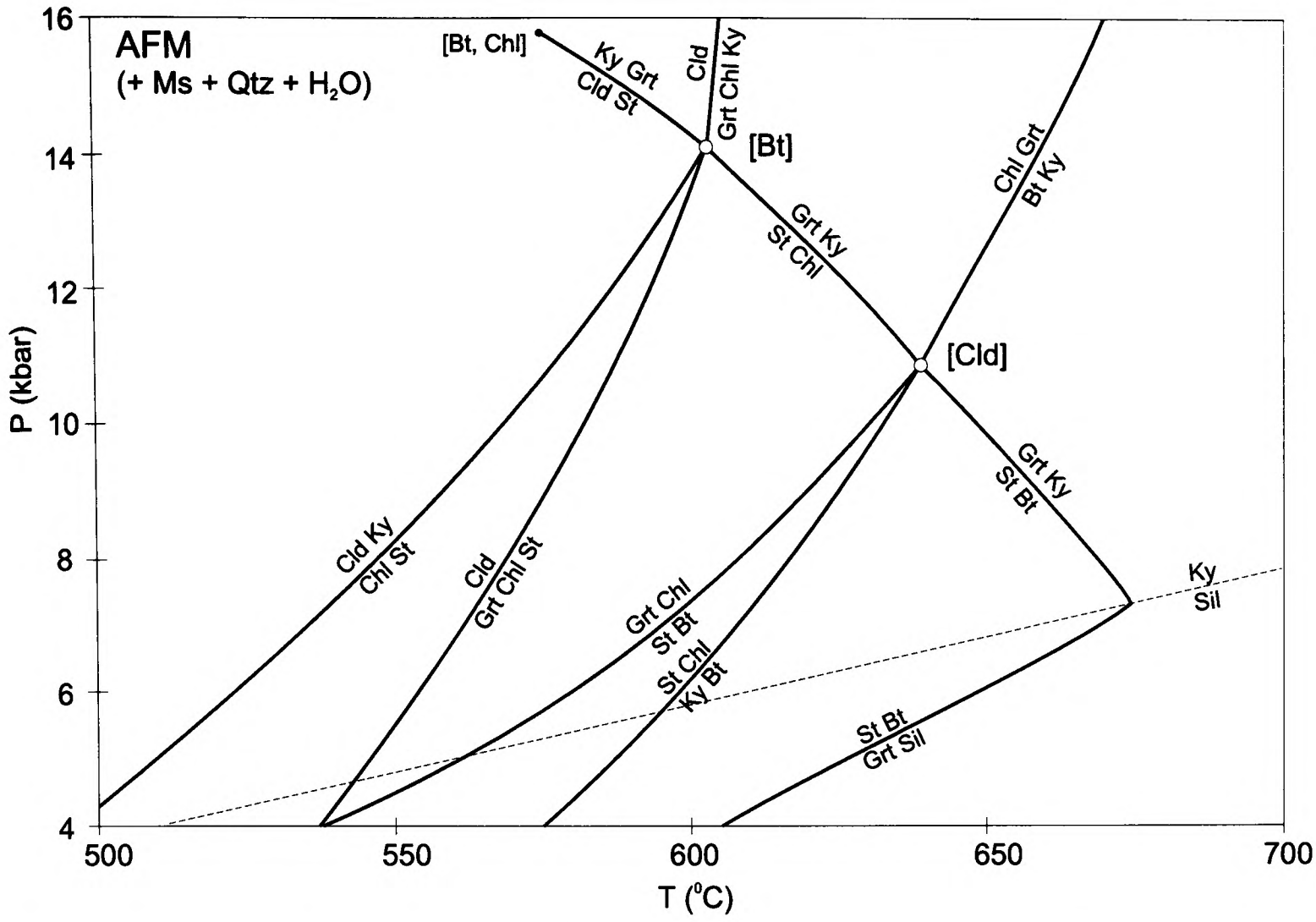


Figure 5.1.A P-T projection for the system KFMASH (+ Ms + Qtz + H_2O) calculated using THERMOCALC v2.7 and the dataset of Holland & Powell (1998). Phases in excess are not labelled.

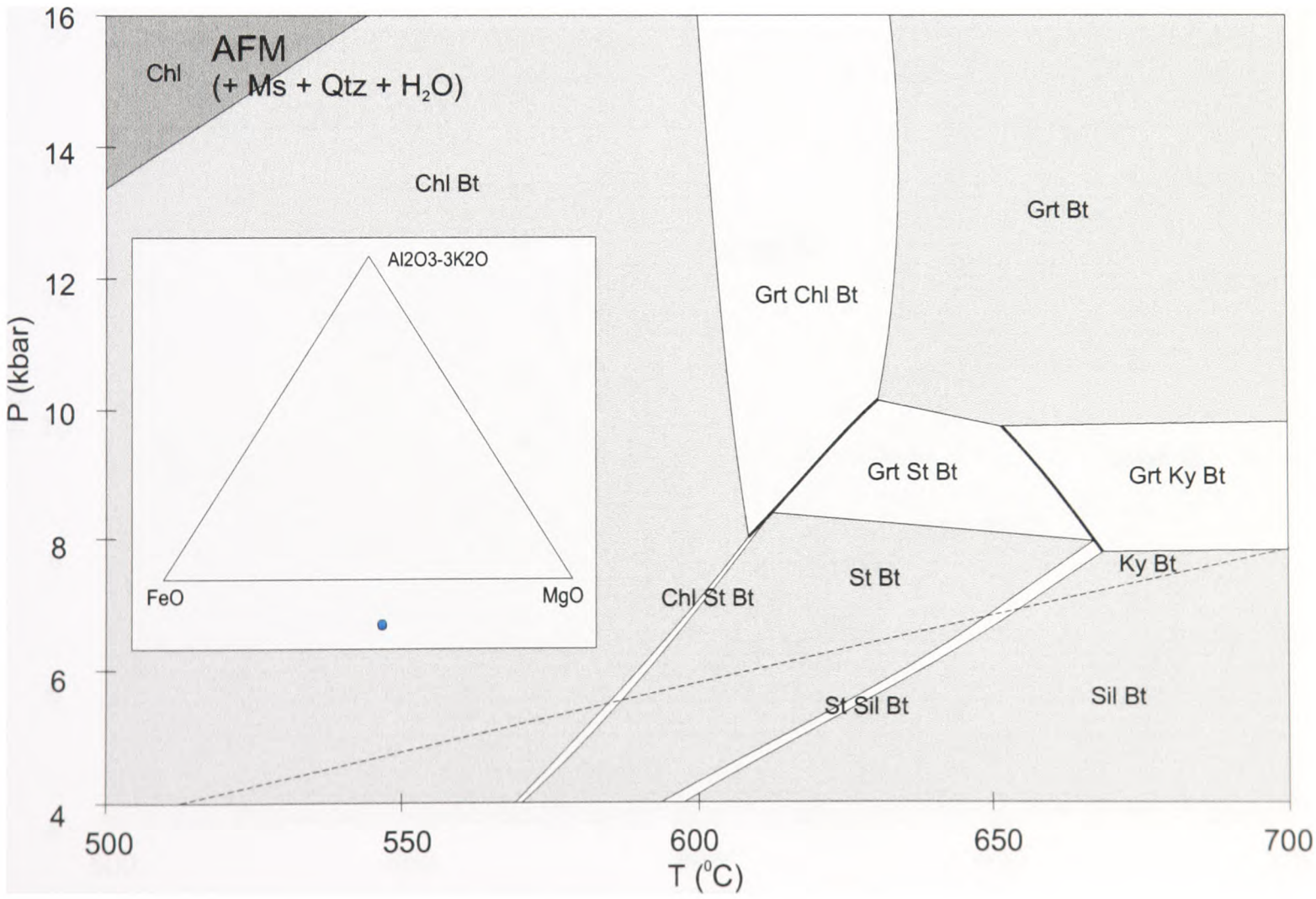


Figure 5.1.B P-T pseudosection in KFMASH (+ Ms + Qtz + H_2O) for a sub-aluminous pelite (Z47) with bulk composition Al_2O_3 = 0.5877, FeO = 0.537, MgO = 0.6029, K_2O = 0.244, as indicated on the AFM projection. The bulk composition is given in **moles**, and the Al_2O_3 content has been corrected for plagioclase.

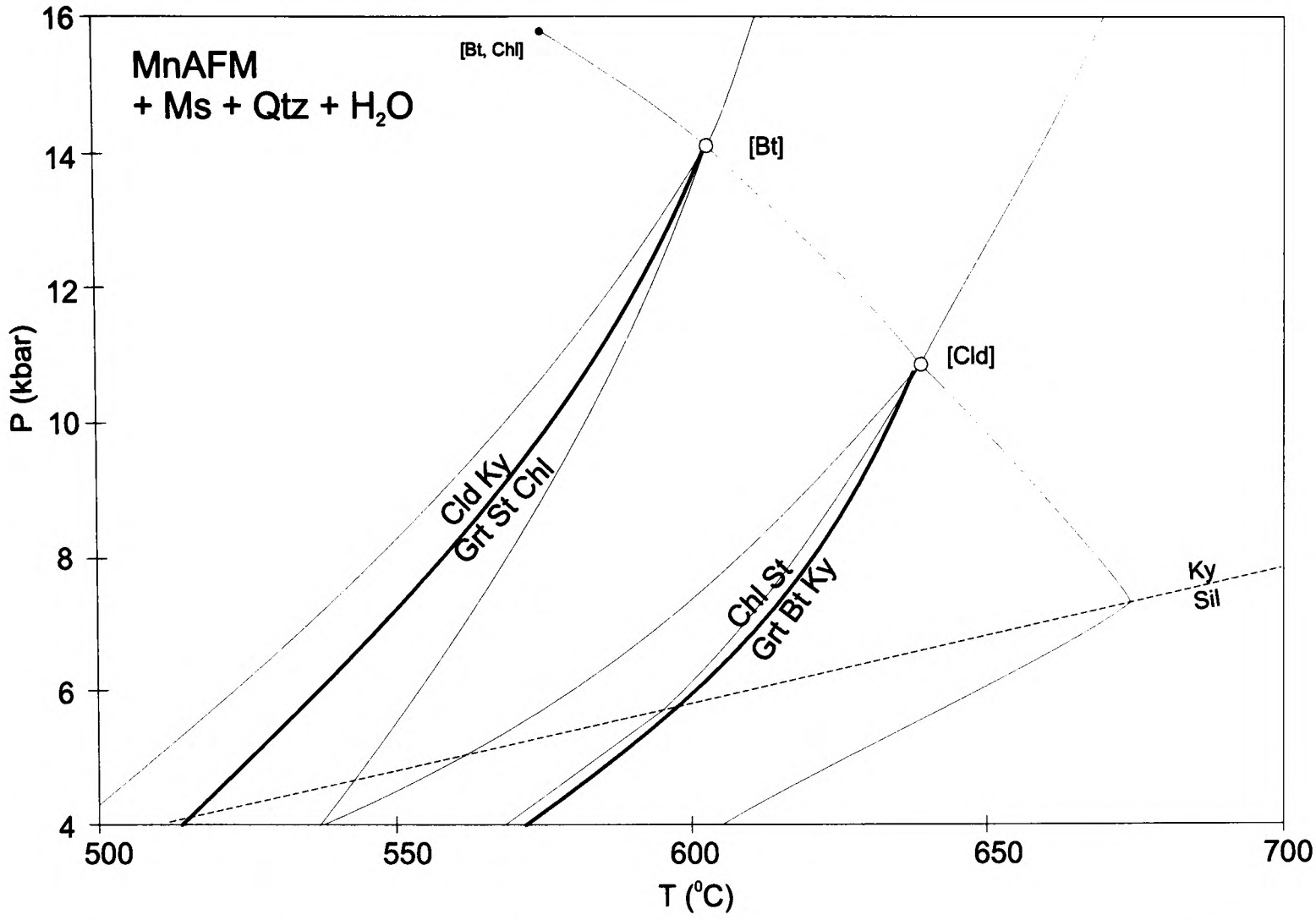


Figure 5.2.A P-T projection for MnKFMASH (+ Ms + Qtz + H_2O) showing KFMASH subsystem. Phases in excess not labelled.

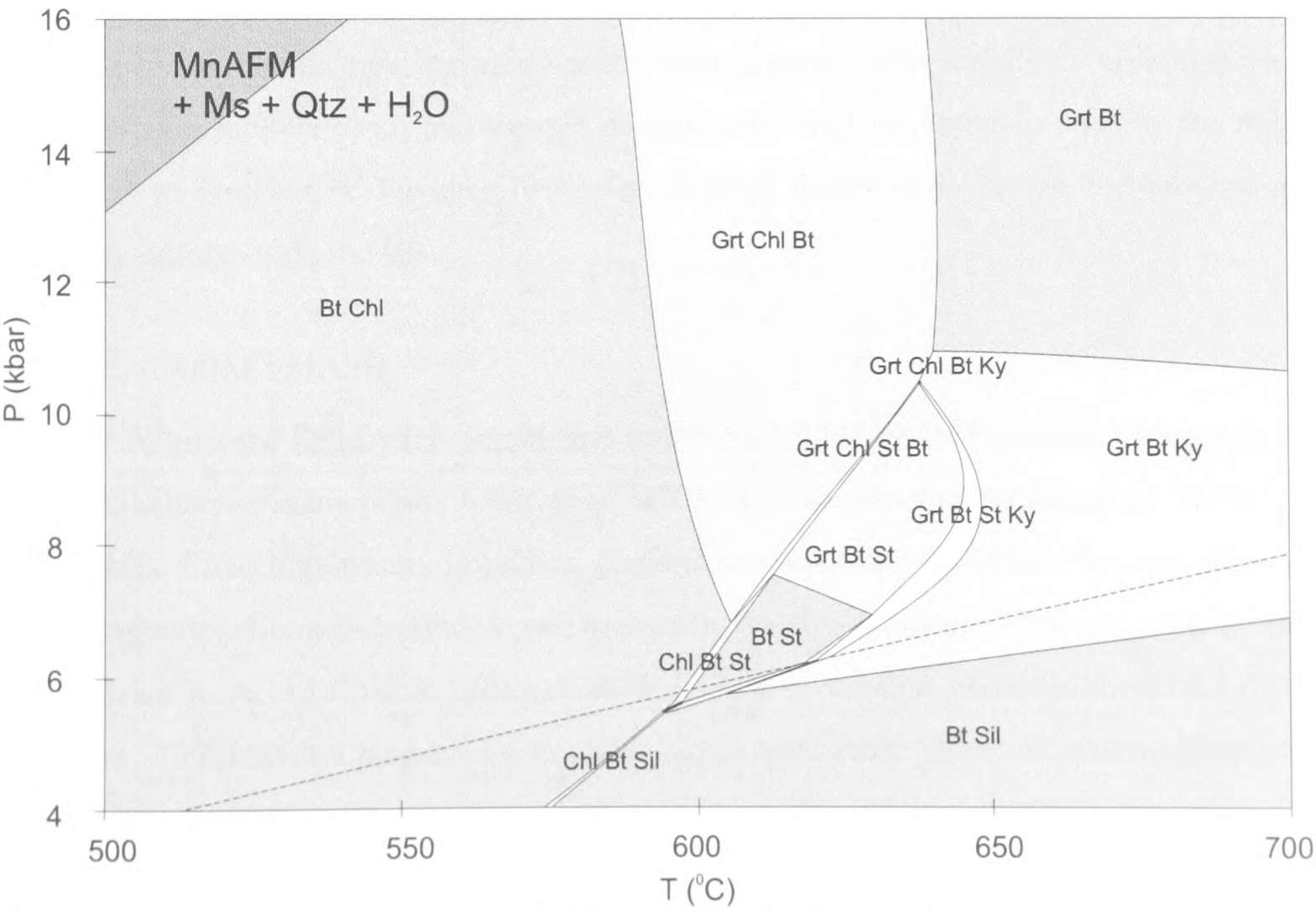


Figure 5.2.B P-T pseudosection in MnKFMASH (+ Ms + Qtz + H_2O) calculated for Z47 bulk composition with 0.0046 moles MnO added.

5.2.2.2. MnKFMASH

Studies have shown that Mn has a strong effect on pelite phase relations, in particular causing the stabilisation of garnet to higher and lower pressures and temperatures than those predicted by the KFMASH system (Droop & Harte, 1995; Mahar *et al.*, 1997). The stabilisation of garnet increases the number of assemblages that would have a lower variance in the KFMASH system, in keeping with naturally occurring assemblages. Figures 5.2.A. & B. are a P-T projection and pseudosection respectively, calculated using the same bulk composition as for Figures 5.1.A. & B., but adding the MnO content of the rock. It can be seen that the addition of MnO increases the stability field of garnet, and increases the width of 4-phase MnKFMASH fields, as expected. The KFMASH grid is also shown to illustrate how the petrogenetic grid for a chemical system must be related to the grids for subsystems; here the MnKFMASH *univariant* lines (Bt) and (Cld) emanate from the KFMASH *invariant* points [Bt] and [Cld].

In order to calculate MnKFMASH petrogenetic grids, and further into CNMnKFMASH, it was necessary to modify the existing datafiles for the Holland & Powell (1998) dataset that are provided with the program THERMOCALC. This comprised the incorporation of Mn into the garnet, chlorite, biotite, staurolite and chloritoid mixing models, which was a lengthy and complicated process in view of the complexity of the datafiles needed to describe the new thermodynamic mixing models. The activity-composition and bulk composition models used, and sample datafile are listed in Appendix A, but the reader is referred to Holland & Powell (1998) for detailed descriptions of the formulation of the activity-composition models.

5.2.2.3. CNMnKFMASH

Whilst the KFMASH system, and more so the MnKFMASH system adequately model the behaviour of many pelitic rocks, they still do not reproduce many important natural phase equilibria. Most importantly in pelites, plagioclase cannot be modelled. Nor can phases such as paragonite, clinozoisite/epidote and margarite, which although of lesser importance may be significant in Al- or Ca-rich pelites. CaO is known to stabilise garnet to lower temperatures (Mahar, 1997) whilst plagioclase is stable as an additional phase. Furthermore, grossular-anorthite equilibria are extremely important in thermobarometric equilibria, and so the ability to model a more complete pelite system is of paramount importance. These additional components MnO, CaO and Na_2O have been incorporated into the Holland and Powell (1998)

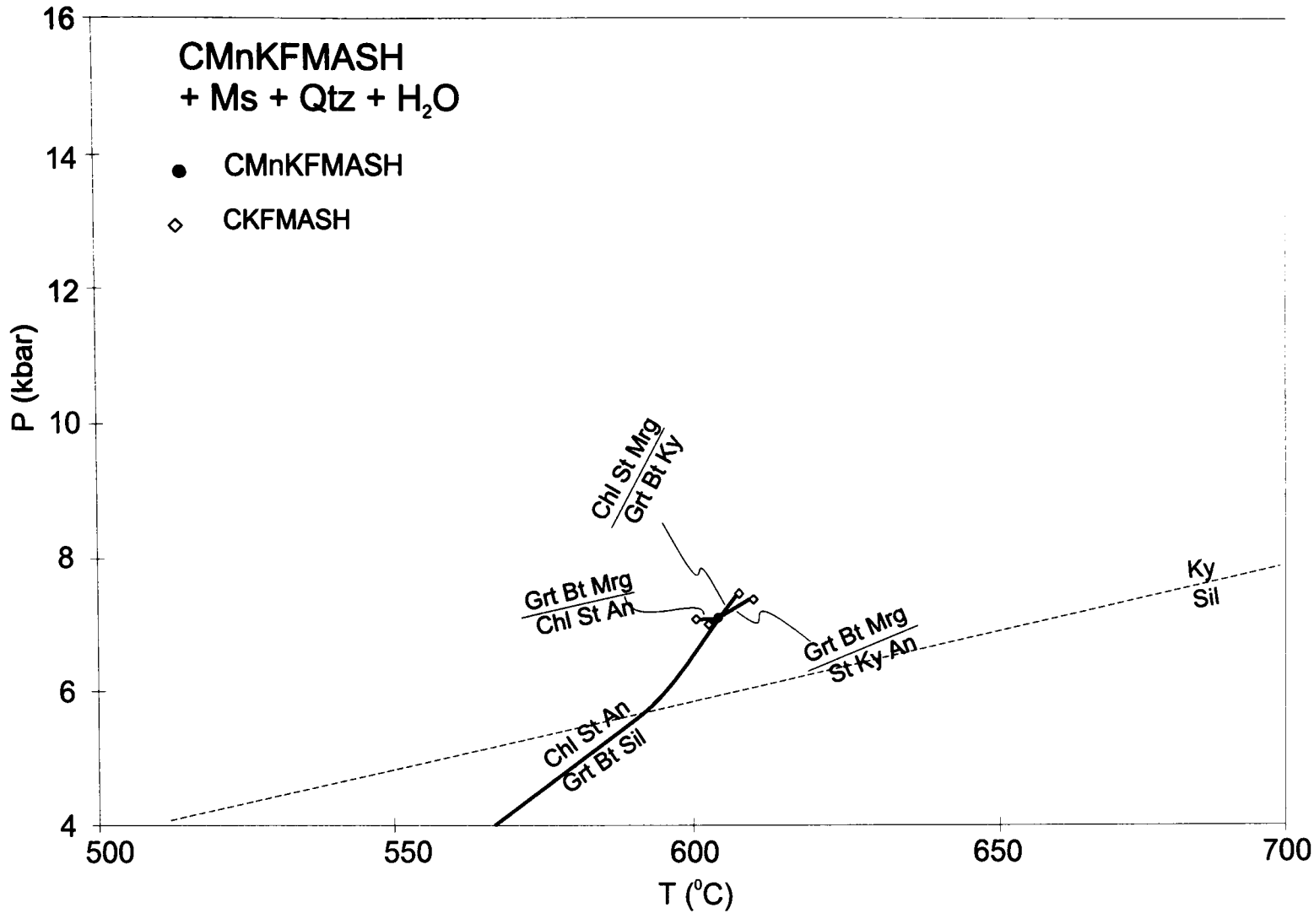


Figure 5.3.A P-T projection for the CMnKFMASH system (+ Ms + Qtz + H_2O). One invariant point is seen, [czo], and the univariant reactions terminate at CKFMASH invariant points.

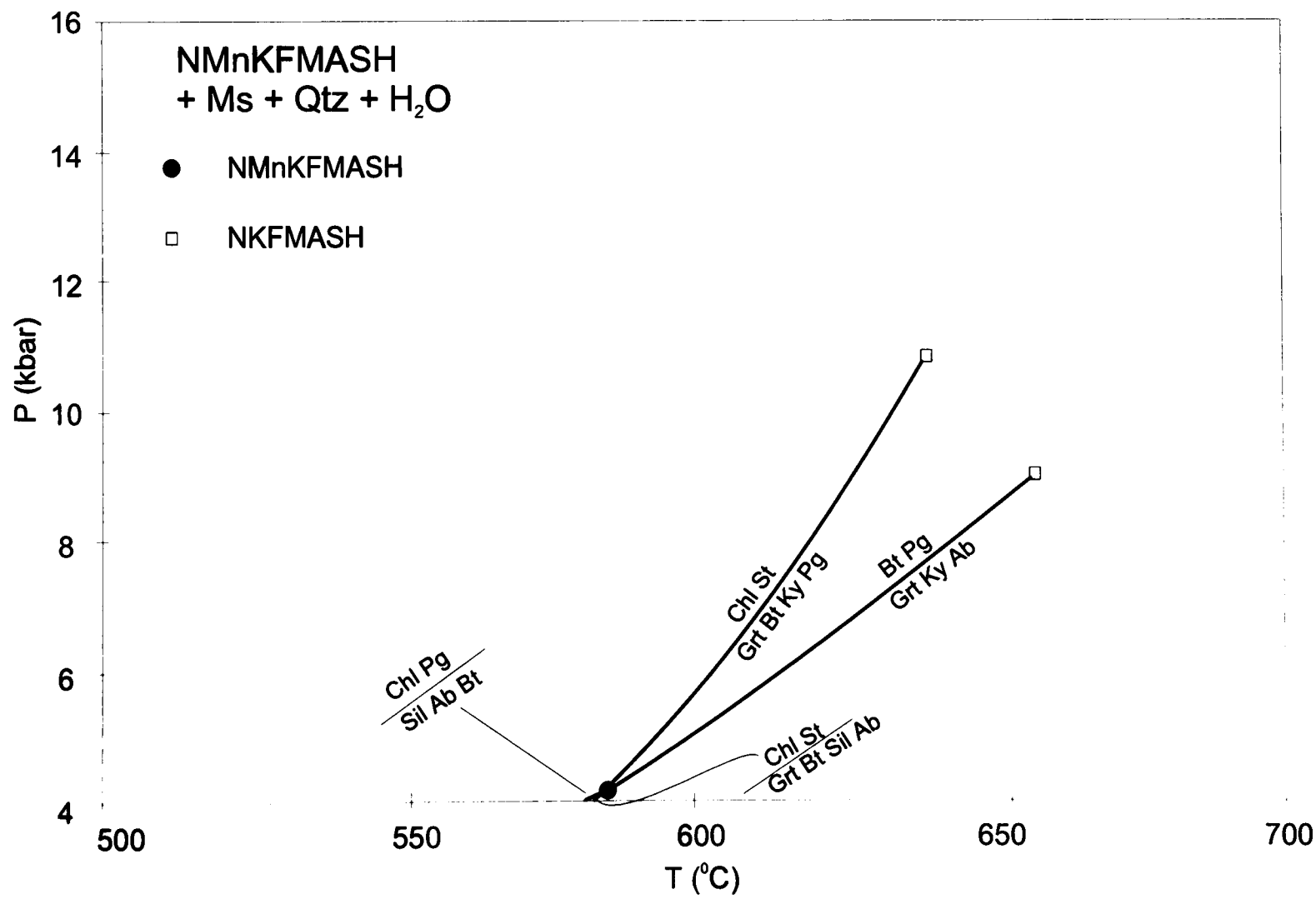


Figure 5.3.B P-T projection for the NMnKFMASH system (+ Ms + Qtz + H_2O). As for the CMnKFMASH grid one [Czo] invariant point is calculated. The univariants (Ab) and (Chl) terminate at the NKFMASH [Ab] and [Chl] invariant points respectively.

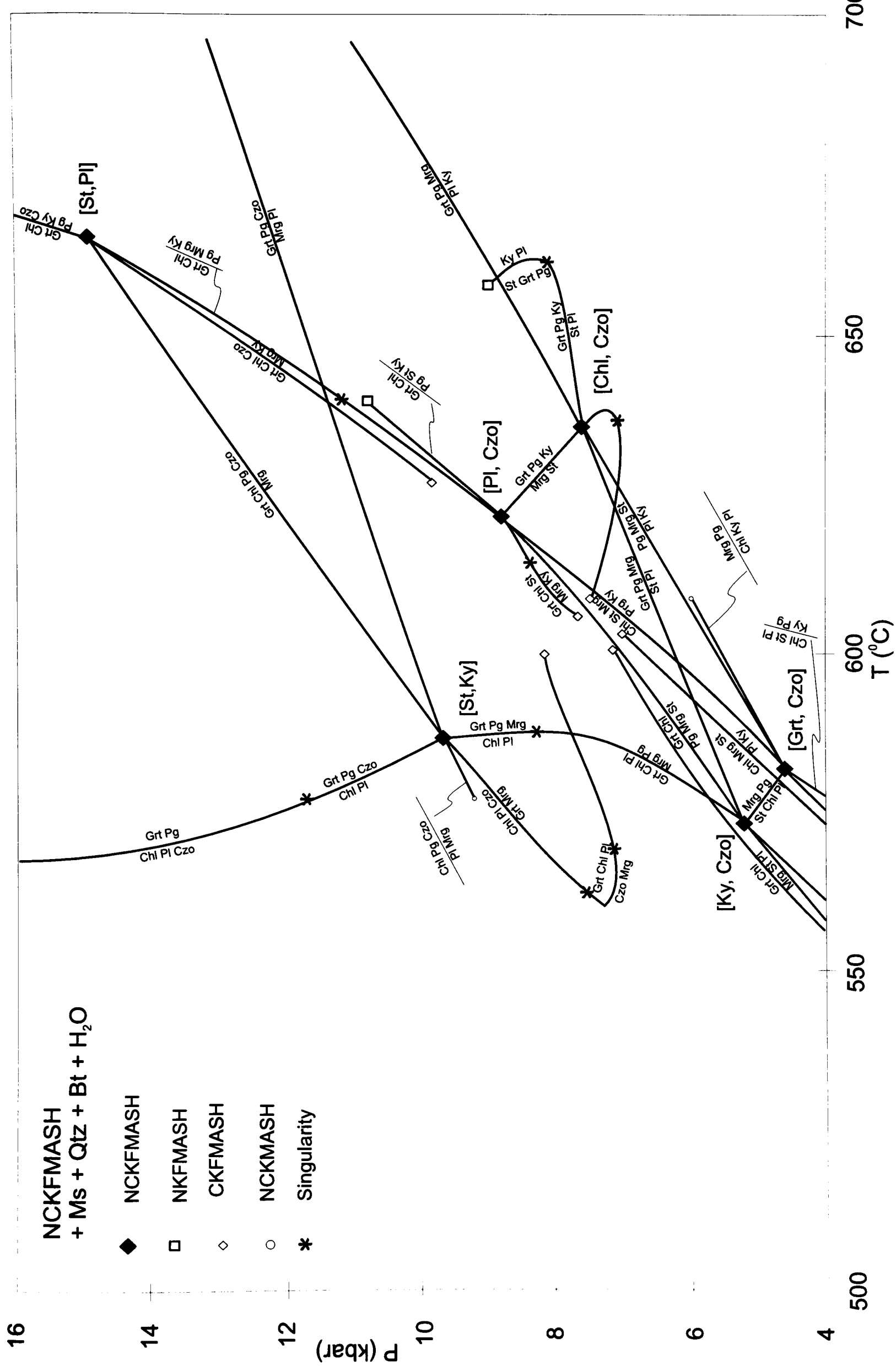


Figure 5.4. P-T projection for the system NCKFMASH (+ Bt + Ms + Qtz + H_2O). NKFMASH, CKFMASH and NCKMASH invariant points are shown where NCKFMASH univariants terminate at them. All equlibria are calculated using the C1 (sodic) plagioclase mixing model.

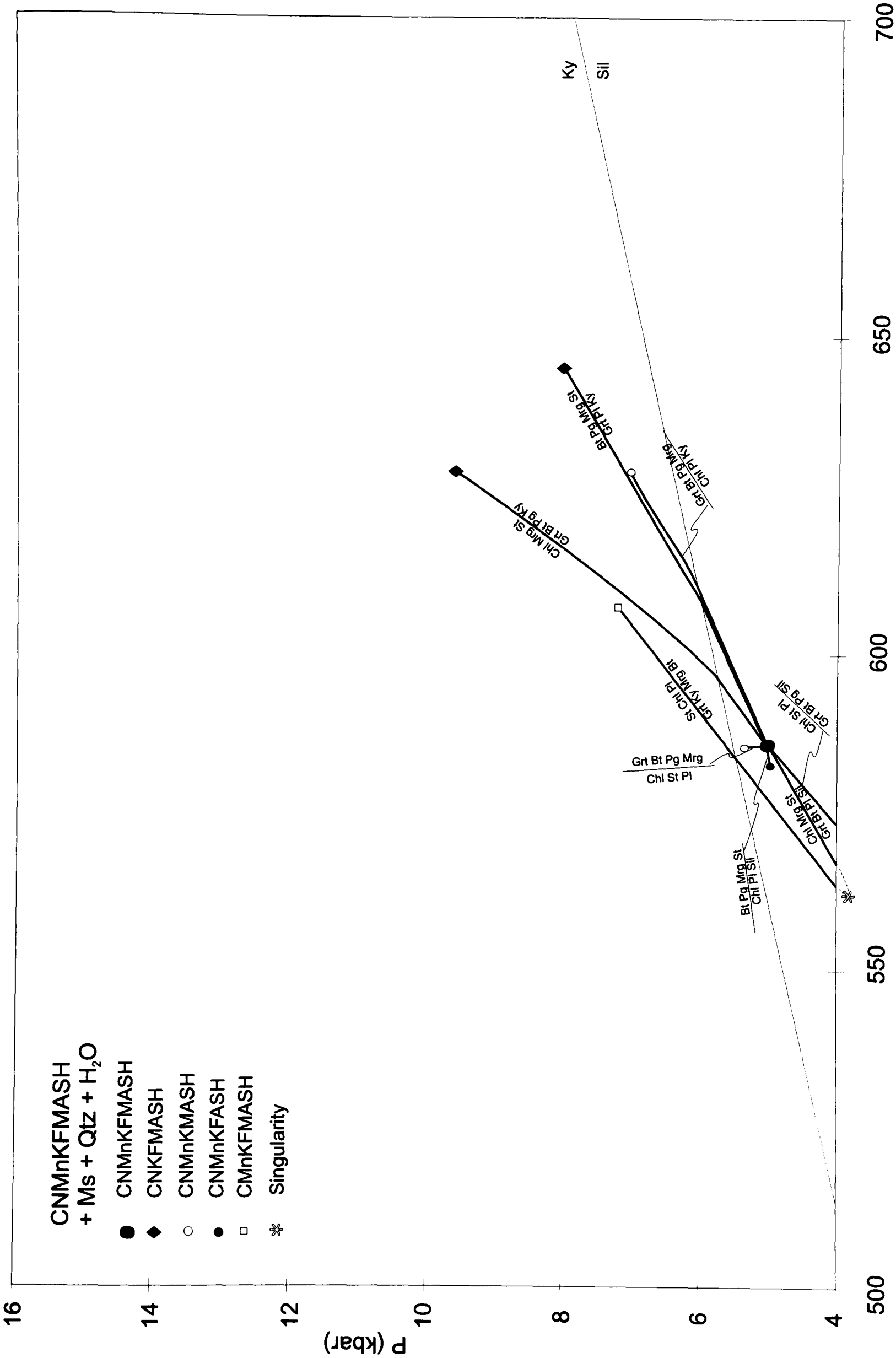


Figure 5.5. P-T projection for the system CNMnKFMASH (+ Ms + Qtz + H_2O). Subsystem invariant points as for Figure 5.4. All equilibria are calculated for $C\bar{1}$ (sodic) plagioclase.

datafiles as described above, allowing phase diagram calculations in the full CNMnKFMASH system.

As for the MnKFMASH grid, to construct the CNMnKFMASH grid it was necessary to first construct subsystems grids. Figures 5.3.A. & B. and 5.4. are CMnKFMASH, NMnKFMASH and CNKFMASH P-T projections respectively, included to illustrate some of the features of the CNMnKFMASH grid, shown in Figure 5.5. Two features not previously encountered are worth explaining. In the Holland & Powell (1998) dataset, plagioclase non-ideal mixing is modelled in terms of two separate phases, C1 and I1, using a Darken's Quadratic Formalism (DQF) approach (Holland & Powell 1992). At a given temperature, the C1 phase represents the low albite structure and I1 the body-centred anorthite structure.; at 600 ^{0}C the transition is about X_{An} ~ 0.45 (Worley & Powell, 1998). For the CNMnKFMASH grid, all equilibria calculated fell within the C1 stability field. *Singularities* occur along plagioclase + margarite- and plagioclase + paragonite-bearing equilibria, and represent compositional coplanarities which occur in response to the CaAl = NaSi substitution occurring to different extents in plagioclase and white mica (Worley & Powell, 1998). This causes a phase, or phases, to switch sides in a reaction.

In the CNMnKFMASH system, ten phases coexist along each univariant equilibrium. As this is many more than is commonly observed in natural assemblages, it illustrates that petrogenetic grids on their own are not particularly useful in the interpretation of P-T evolution, and the stability fields of higher variance assemblages need to be calculated by using pseudosections for particular bulk compositions. This provides a more realistic starting point for the interpretation of the evolution of Suru Valley rocks.

5.3. P-T pseudosections for Suru Valley rocks

5.3.1. Sample selection

Six samples were chosen for phase diagram construction, to represent different bulk compositions and geographical locations within the study area. The sample locations are shown in Figure 5.12.; L429, Z47, Z49 and Z70 are from near the closure of the Donara nappe, Z37 is from the Tapshah nappe along the Shansin nala, and Z18 is from the edge of the Suru Dome near Tongul. The compositions range from subaluminous to peraluminous and are chosen because their mineralogies nearly all represent the peak assemblage (Samples Z49 and Z18 contain chlorite which is interpreted to be retrograde, a feature which may well be of significant importance , as is shown in later sections). Furthermore, their mineralogy is simple

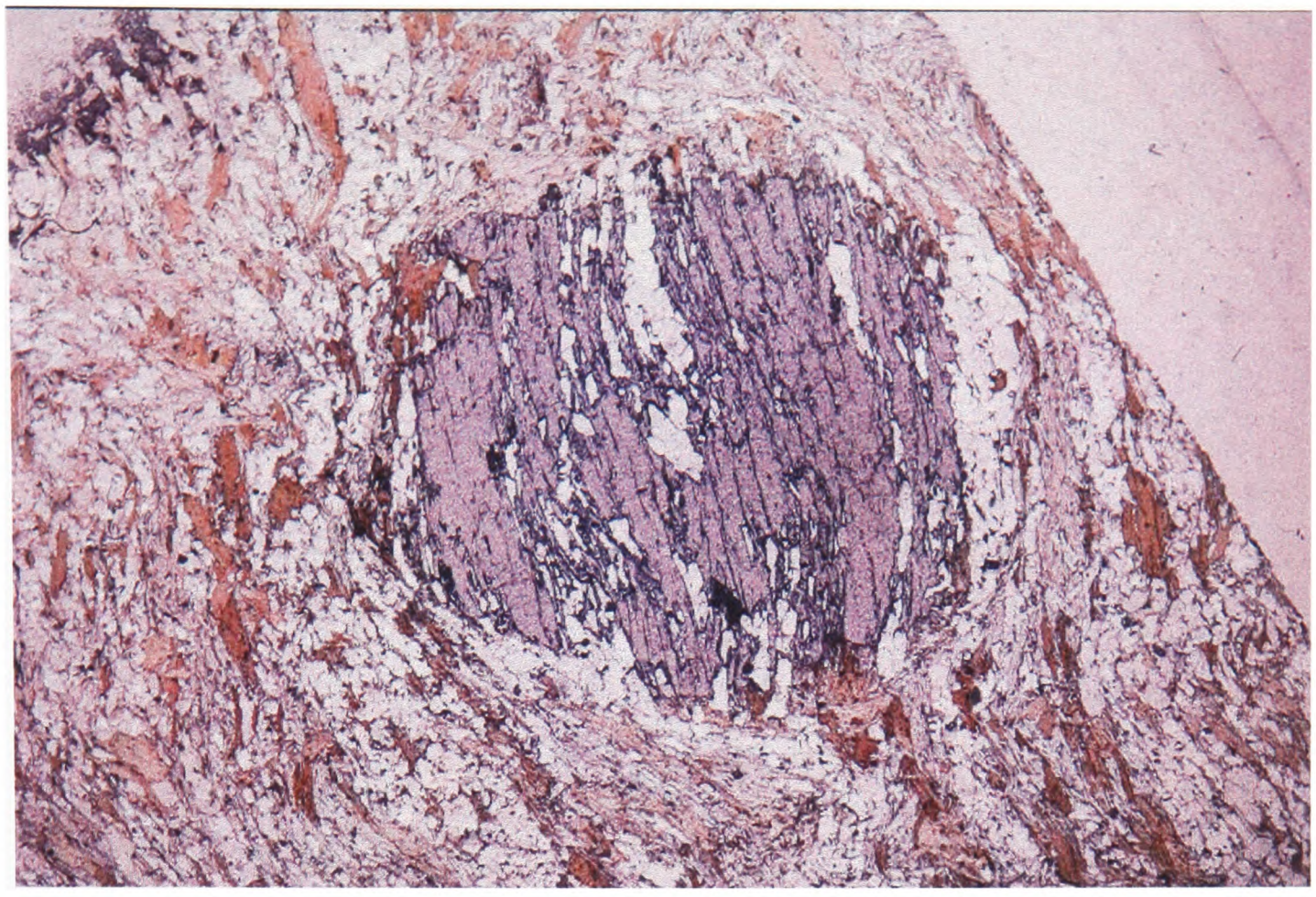


Figure 5.6.A. Sample L429 illustrating garnet microprobe traverse. Traverse has 28 points at 200 um spacing Garnet approximately 6mm in diameter.

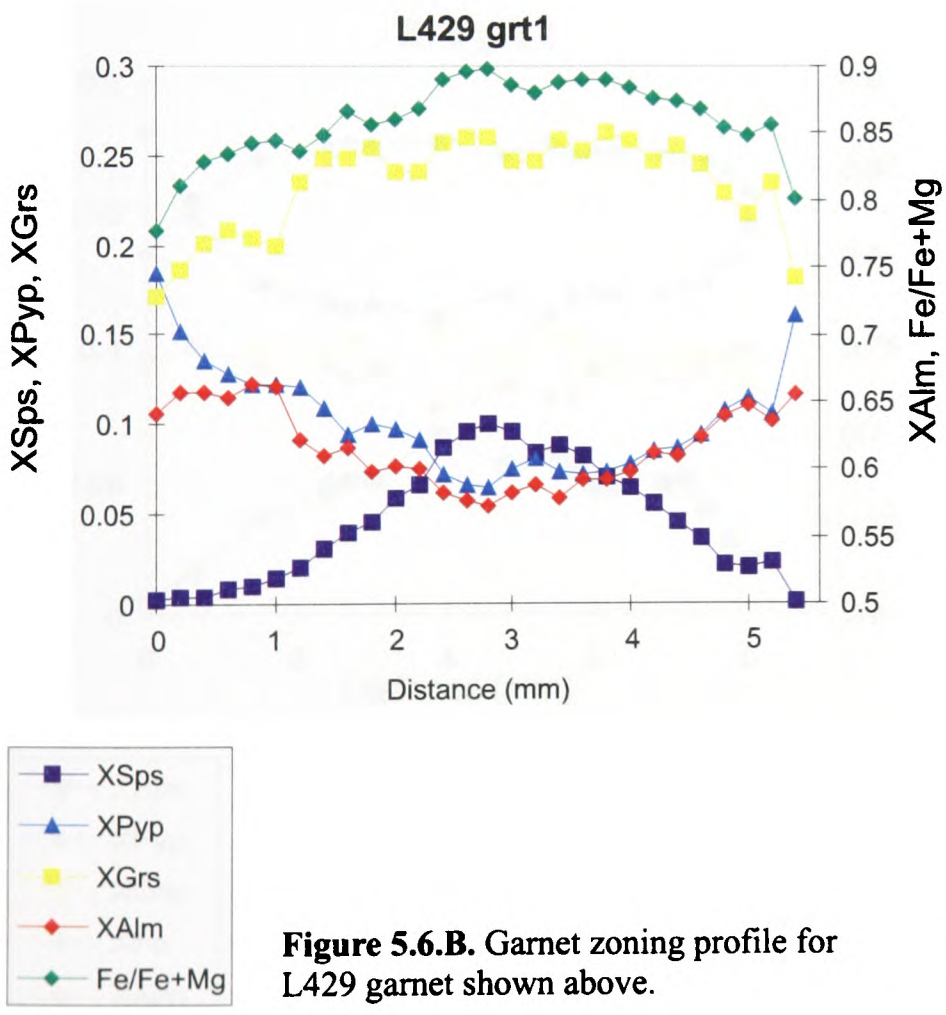


Figure 5.6.B. Garnet zoning profile for L429 garnet shown above.

Increment	dXSps	dXGrs	dXAlm
1	-0.0134	-0.0031	0.0104
2	-0.0211	-0.0156	0.0168
3	-0.007	-0.0009	0.0026
4	-0.0141	0.0143	-0.004
5	-0.0246	-0.0195	0.0241
6	-0.0054	-0.0354	0.0393
7	-0.0071	0.0088	-0.0081
8	-0.0058	-0.03787	-0.0118

Table 5.6.1. Increments of monitor parameters used in Gibbs method calculations

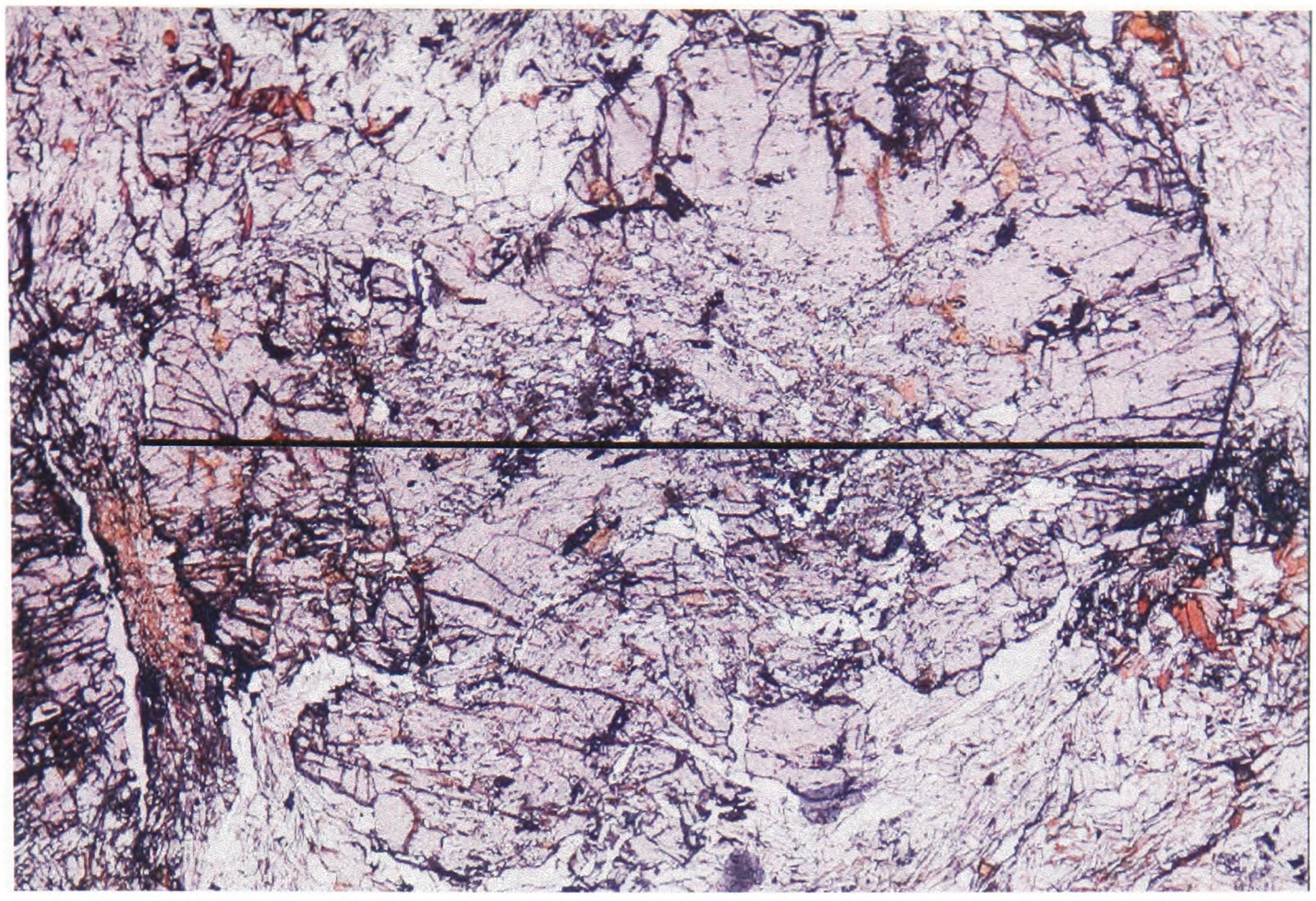


Figure 5.7.A. Sample Z70 illustrating garnet microprobe traverse. Garnet traverse approximately 9 mm long, with a sample spacing of 300 um.

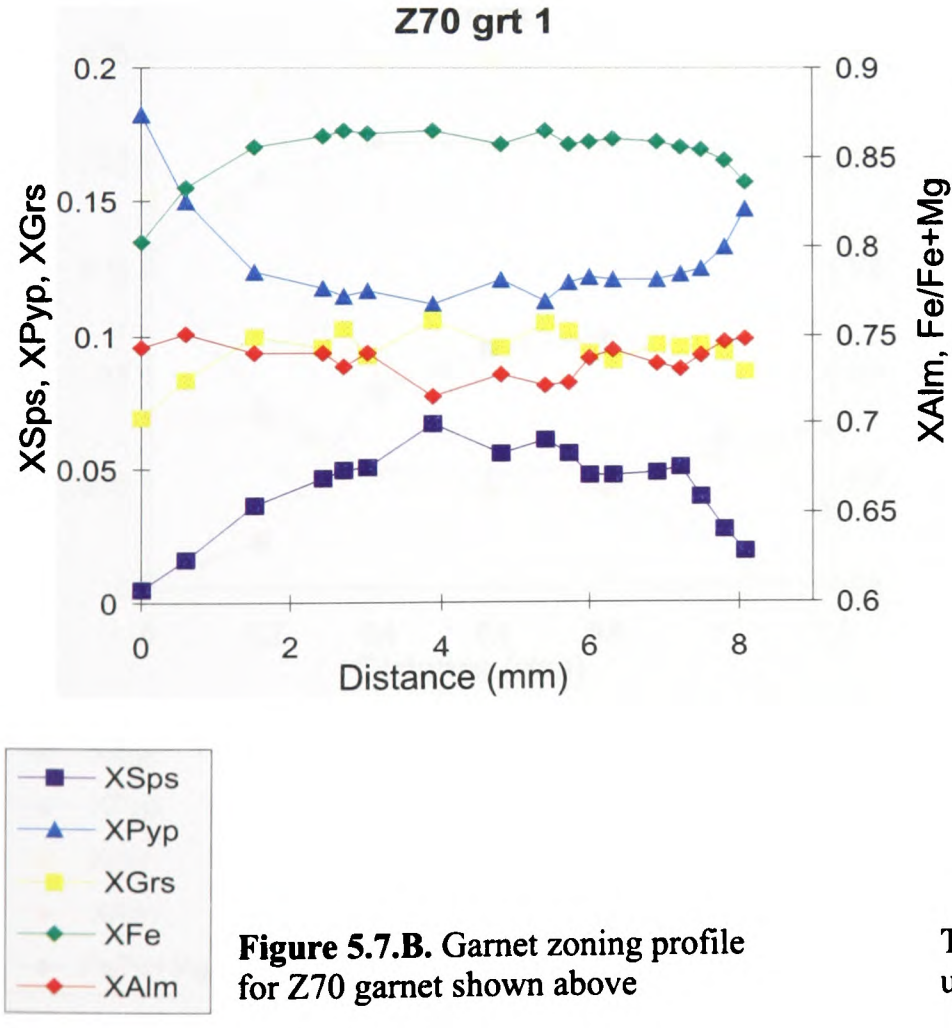


Figure 5.7.B. Garnet zoning profile for Z70 garnet shown above

Increment	dXSps	dXGrs	dXAlm
1	-0.0167	-0.0038	0.0232
2	-0.003	-0.0067	0.0068
3	-0.003	0.0039	0.0008
4	-0.0199	-0.0165	0.0106
5	-0.0118	-0.0133	-0.0077

Table 5.7.1. Increments of monitor parameters used in Gibbs method calculations

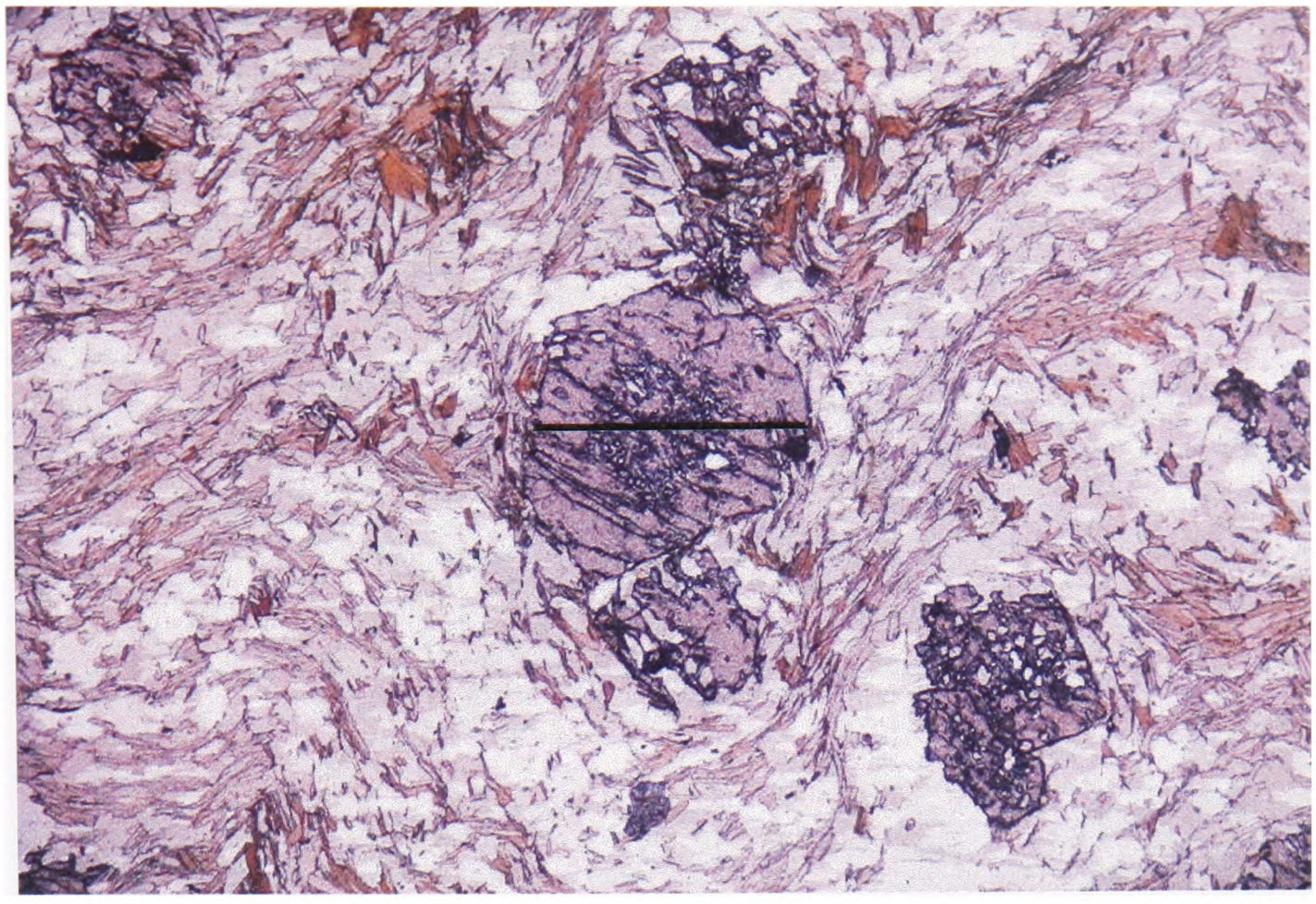


Figure 5.8.A. Sample Z47 illustrating garnet microprobe traverse. Garnet approximately 1.2 mm in diameter, with sample spacing of 200 um.

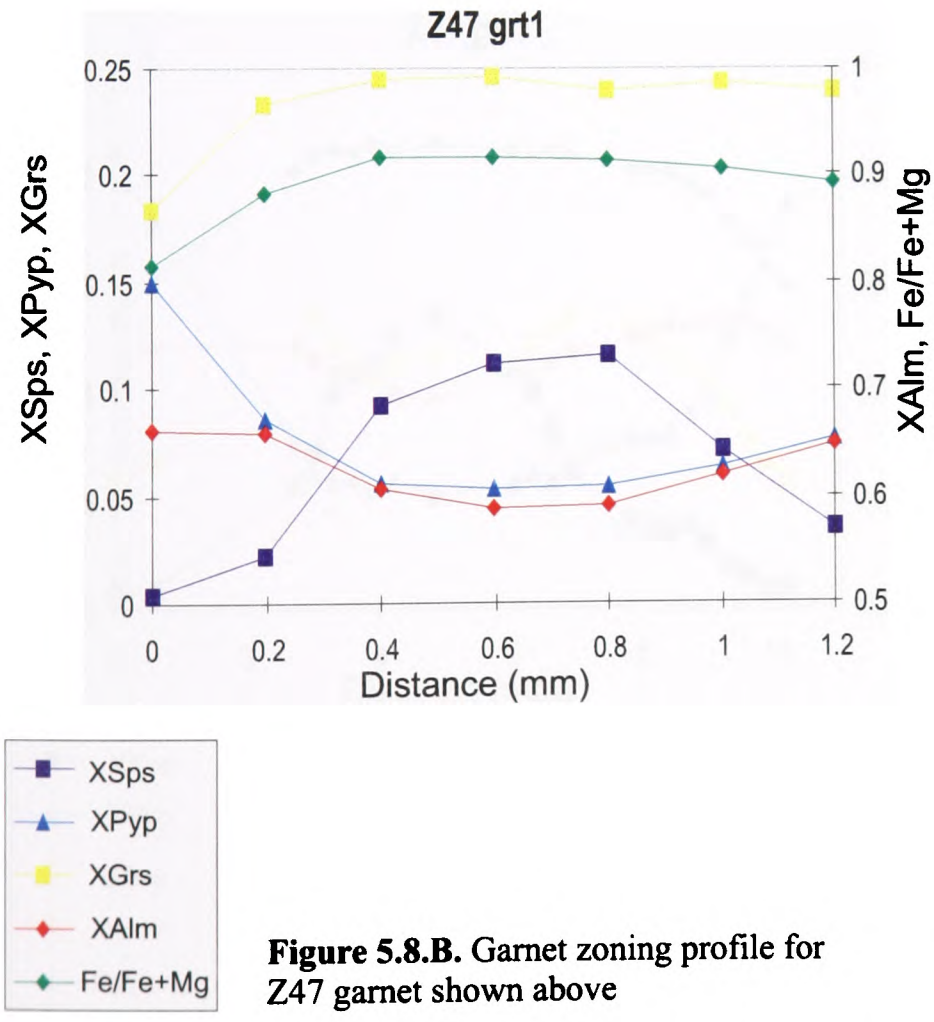


Figure 5.8.B. Garnet zoning profile for Z47 garnet shown above

Increment	dXSps	dXGrs	dXAlm
1	-0.0035	0.0067	-0.0012
2	-0.0204	-0.0011	0.0184
3	-0.0693	-0.0117	0.0505
4	-0.0183	-0.0498	0.0043

Table 5.8.1. Increments of monitor parameters used in Gibbs method calculations

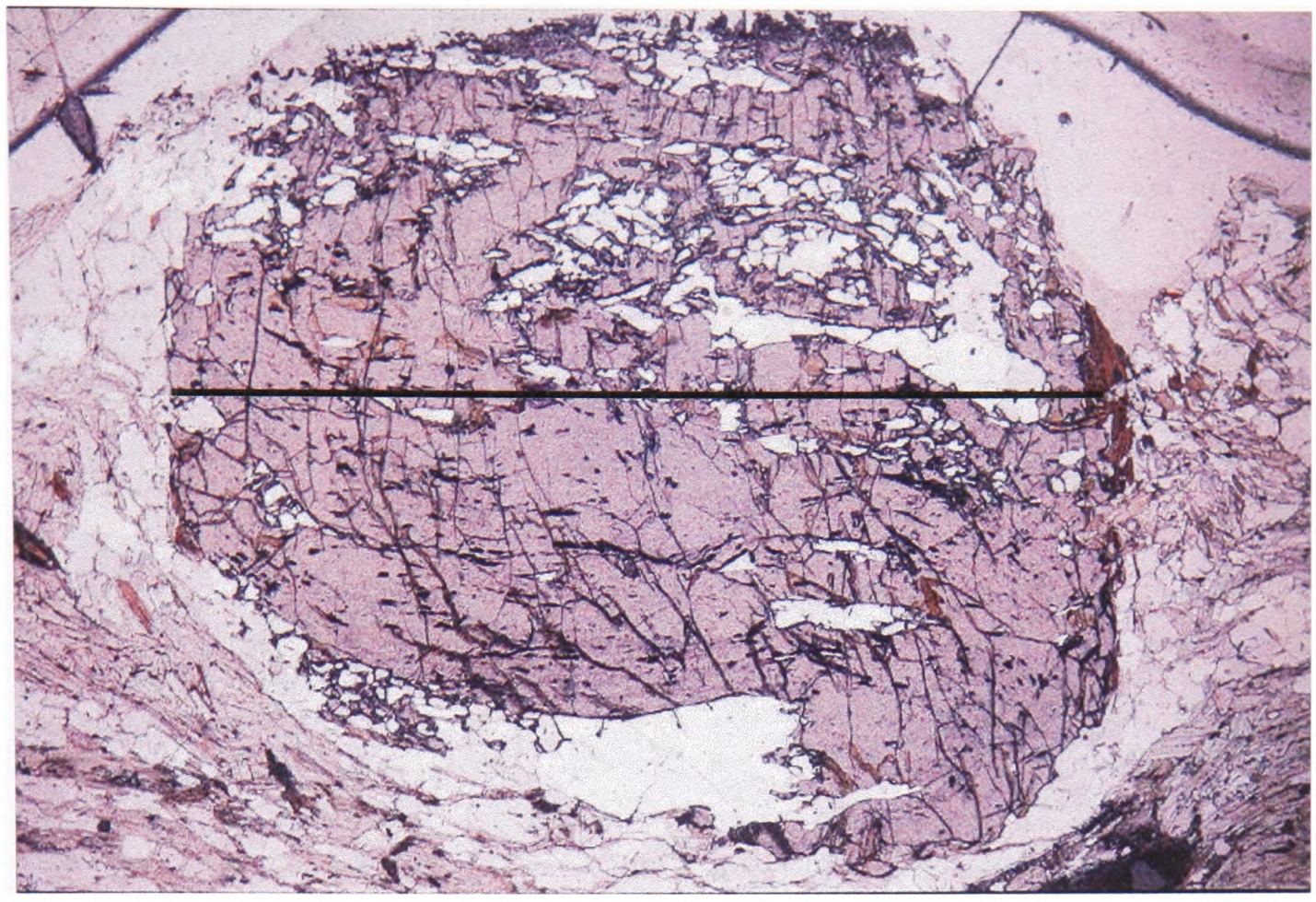


Figure 5.9.A. Sample Z37 illustrating garnet microprobe traverse. Garnet approximately 10 mm in diameter, with a sample spacing of 300 um.

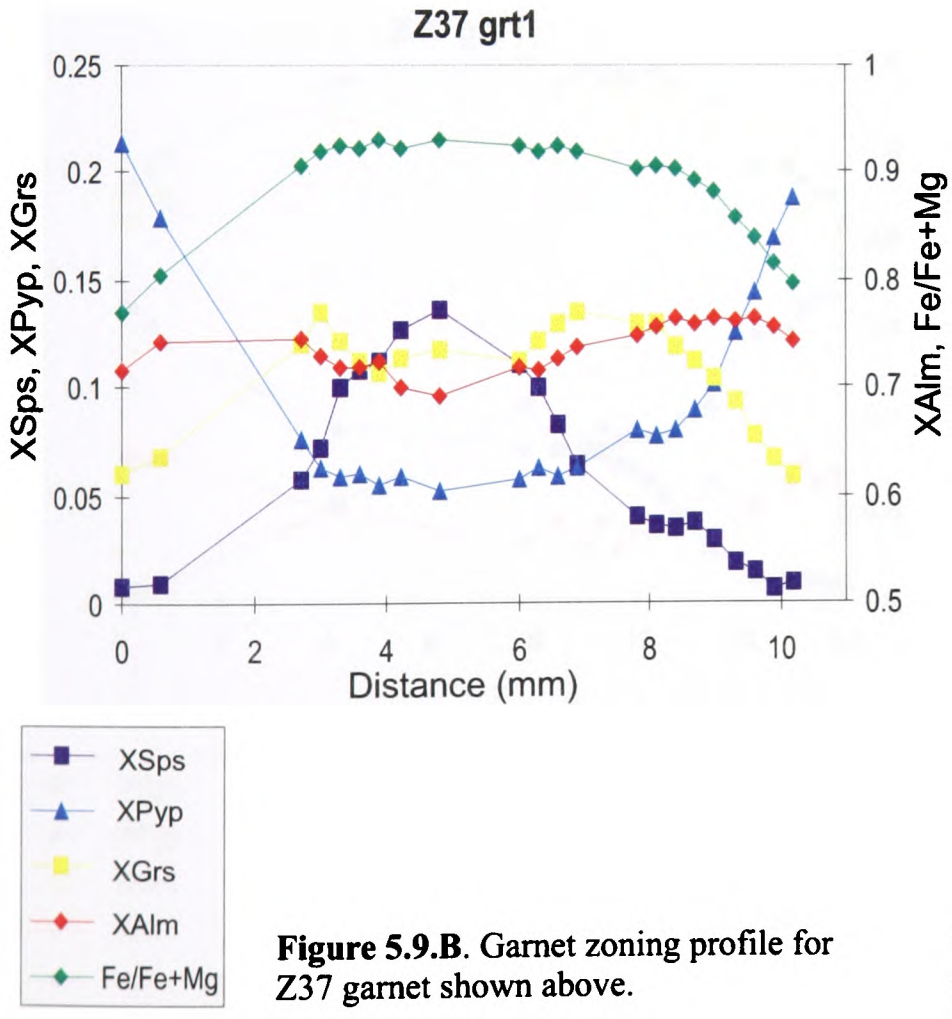


Figure 5.9.B. Garnet zoning profile for Z37 garnet shown above.

Increment	dXSps	dXGrs	dXAlm
1	-0.0243	-0.0058	0.0246
2	-0.0467	0.0224	0.0191
3	-0.025	0.0043	0.0122
4	-0.0019	-0.0185	0.0105
5	-0.0306	-0.0451	-0.006
6	0.0014	-0.0083	-0.0118

Table 5.9.1. Increments of monitor parameters used in Gibbs method calculations

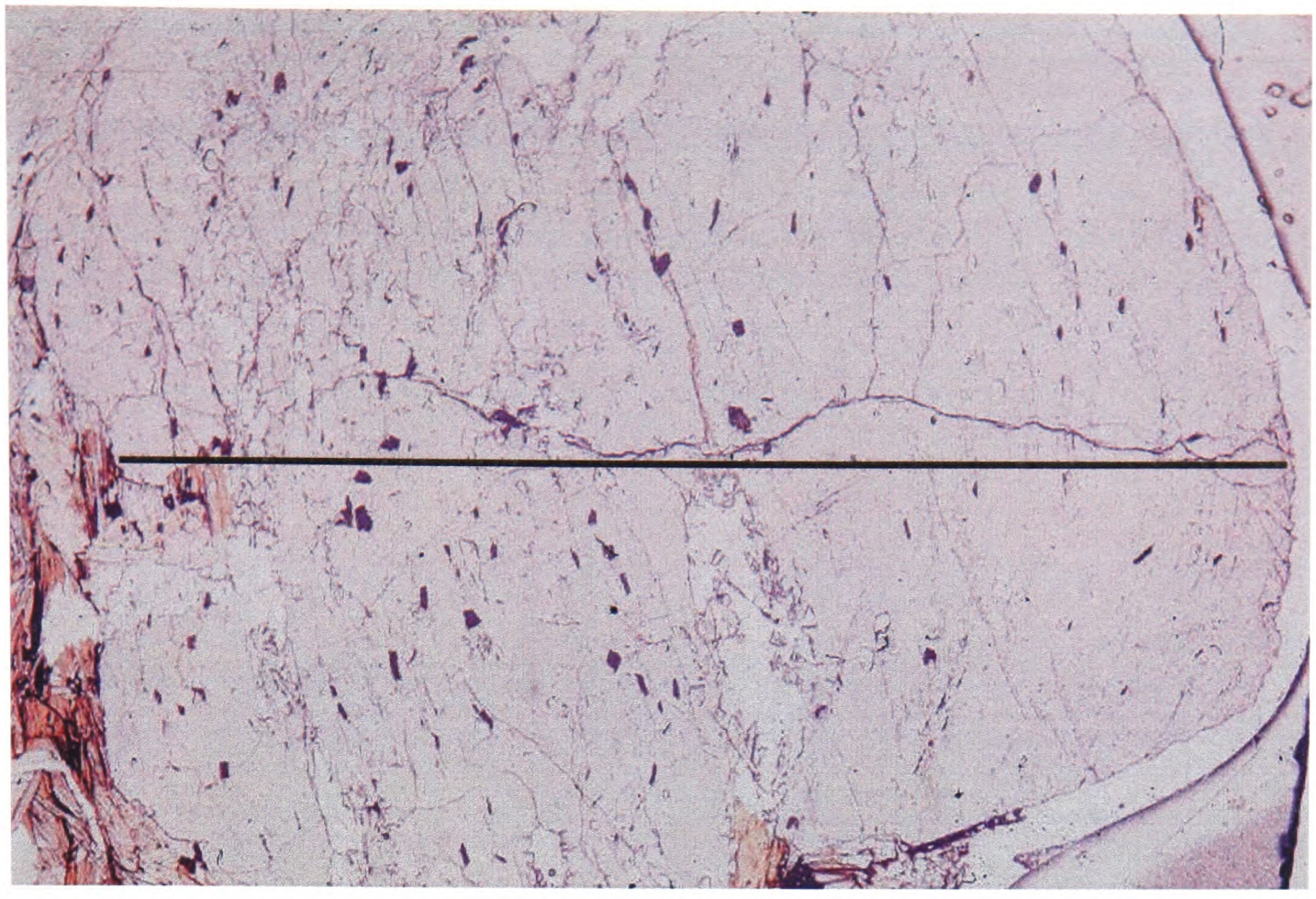


Figure 5.10.A. Sample Z49 illustrating garnet microprobe traverse. Garnet traverse 14 mm long, with a sample spacing of 300 um.

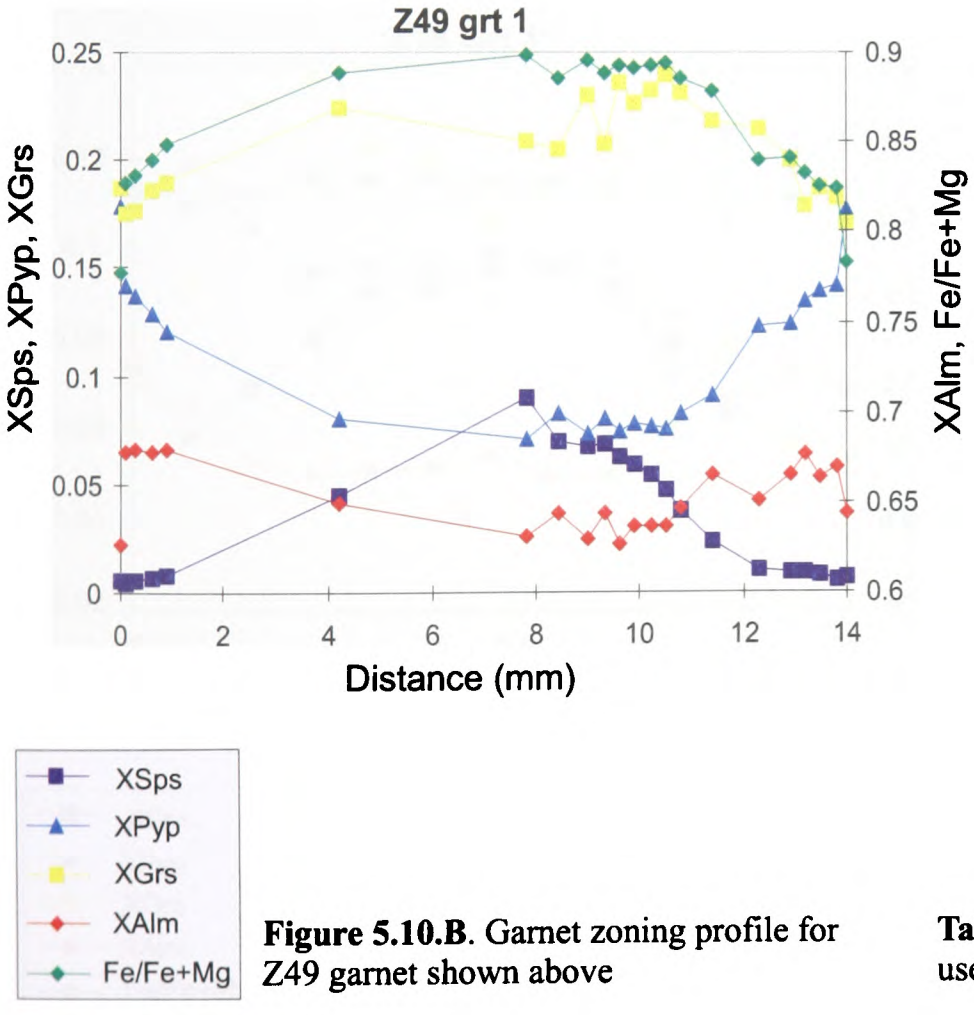


Figure 5.10.B. Garnet zoning profile for Z49 garnet shown above

Increment	dXSps	dXGrs	dXAlm
1	-0.02	-0.0037	0.0121
2	-0.0069	0.0315	-0.017
3	-0.015	0.0036	0.0105
4	-0.0369	-0.025	0.0144
5	-0.0017	-0.0359	0.0255
6	-0.0007	0.0084	-0.0122
7	-0.0015	-0.0159	-0.0205

Table 5.10.1. Increments of monitor parameters used in Gibbs method calculations

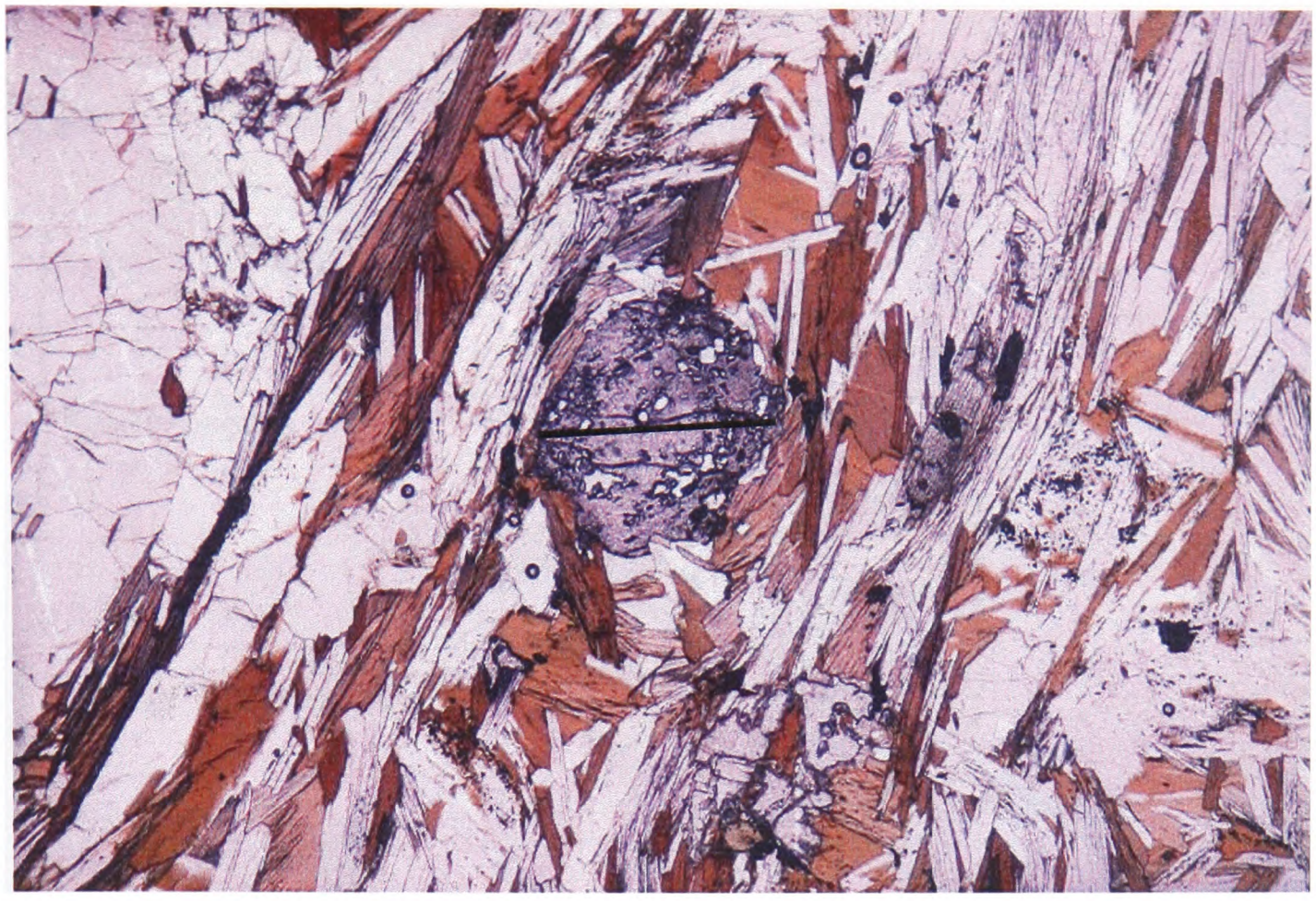


Figure 5.11.A. Sample Z18 illustrating garnet micrprobe traverse. Garnet traverse approximately 1mm in length, with a sample spacing of 65 um.

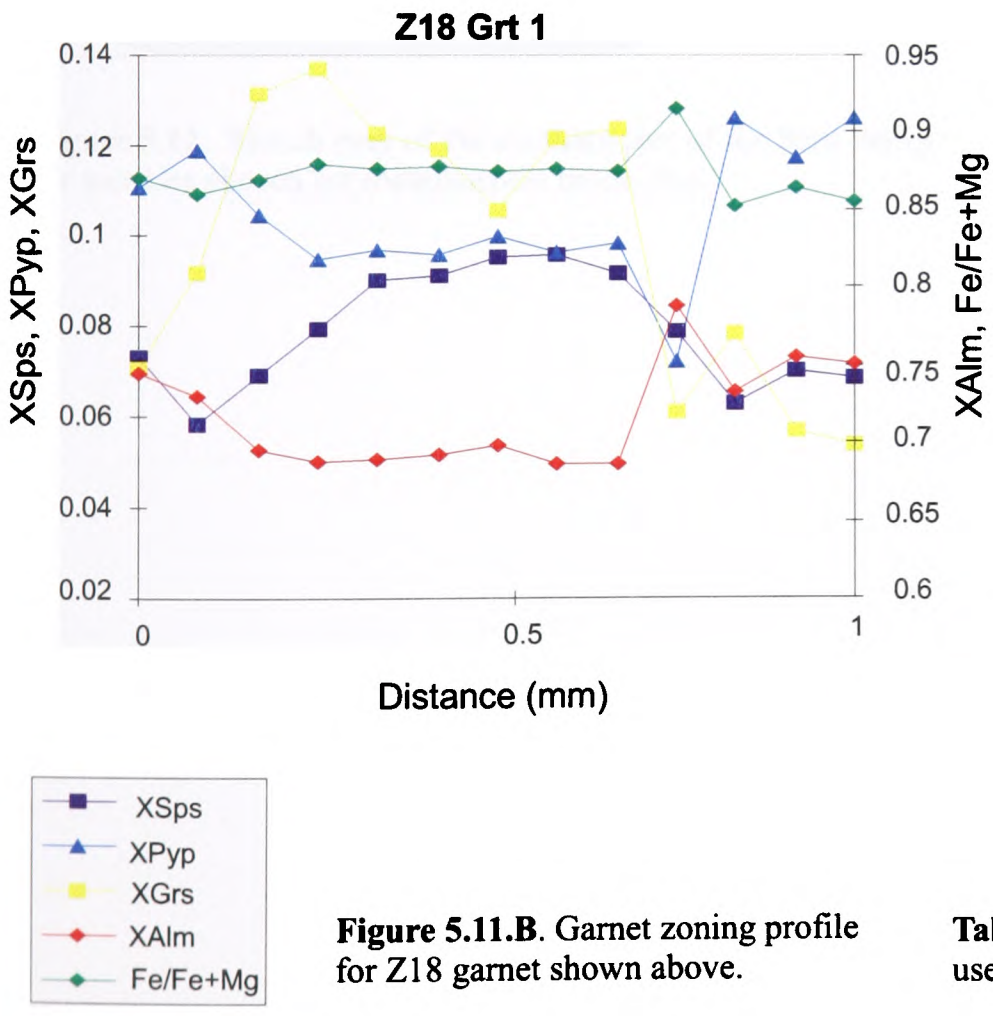


Figure 5.11.B. Garnet zoning profile for Z18 garnet shown above.

Increment	dXSps	dXGrs	dXAlm
1	-0.0006	-0.0158	0.013
2	-0.0039	0.0134	-0.0057
3	-0.001	0.0036	-0.0036
4	-0.0107	0.0143	-0.0013
5	-0.0106	-0.0039	0.0066
6	-0.0052	-0.0198	0.0178
7	-0.0052	-0.0198	0.0178
8	0.0144	-0.0208	0.0149

Table 5.11.1. Increments of monitor parameters used in Gibbs method calculations.

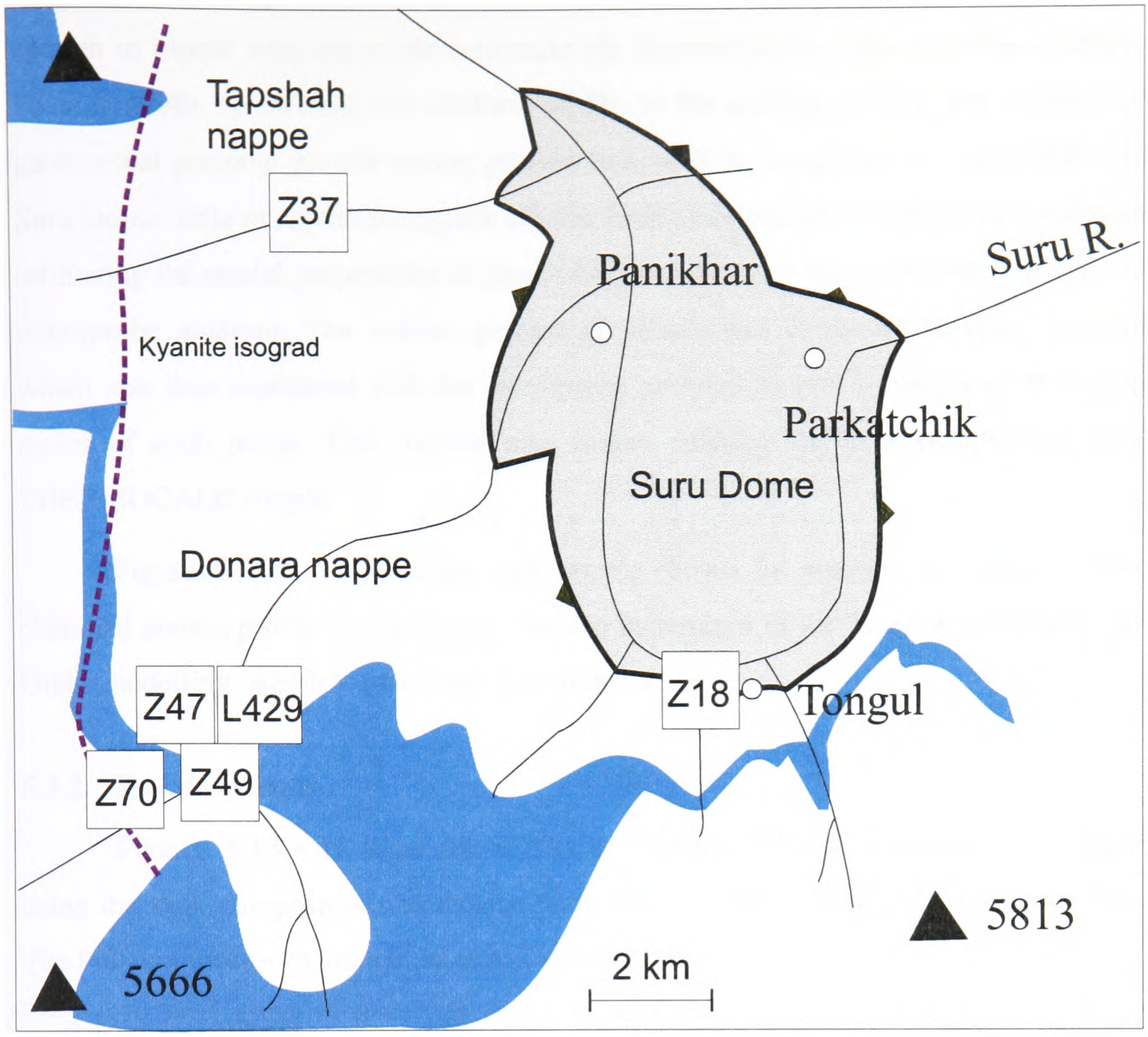


Figure 5.12. Sketch map of the southern part of the Suru valley study area showing the geographical location of the samples chosen for metamorphic modelling.

enough to model with the modifications to the thermodynamic data provided in Holland & Powell (1998), specifically the addition of Mn to the activity models. All samples contain garnets that preserve growth zoning profiles and, with the exception of sample Z18 from the Suru Dome, little or no rim retrograde effects. Bulk composition of samples was calculated by estimating the modal proportions of phases by point counting (see Appendix C), and electron microprobe analyses. The *volume* percent of phases was converted to *molar* proportions, which was then combined with the microprobe analyses to give estimates of the number of moles of each oxide. This method also makes entering the bulk composition data into THERMOCALC simple.

Figures 5.6.-5.11. show, for each sample chosen for analysis, the garnet probed, the chemical zoning profile of that garnet, and the increments of the monitor parameters used for Gibbs modelling, which is described in section 5.4.

5.3.2. Pseudosections

Figures 5.13.A-H show the results of CNMnKFMASH pseudosection calculations using the bulk compositions of the six Suru Valley samples illustrated in Figures 5.6.-5.11. The bulk compositions are tabulated in Table 5.2. below.

Oxide	L429	Z47	Z70	Z37	Z49	Z18
Al_2O_3	37.41	31.12	44.03	49.87	33.66	44.61
MgO	25.94	28.64	18.03	16.62	19.4	18.94
FeO	20.07	25.51	21.58	16.84	33.35	22.3
MnO*	0.11	0.21	0.12	0.18	0.23	0.18
K_2O	14.14	11.59	13.79	11.53	9.43	10.27
Na_2O	1.17	1.01	1.71	3.96	1.21	2.71
CaO	1.17	1.9	0.73	0.99	2.73	0.99

Table 5.2. Bulk compositions used for the calculation of pseudosections for Suru Valley rocks. The values given are in **moles** of oxides, normalised to 100%. * MnO bulk compositions were calculated in the way described in section 5.2.2.

5.3.2.1.THERMOCALC "modes"

Before describing the results of phase diagram calculations, it is worth clarifying the term "mode" as used in THERMOCALC and in phase diagrams presented in later sections.

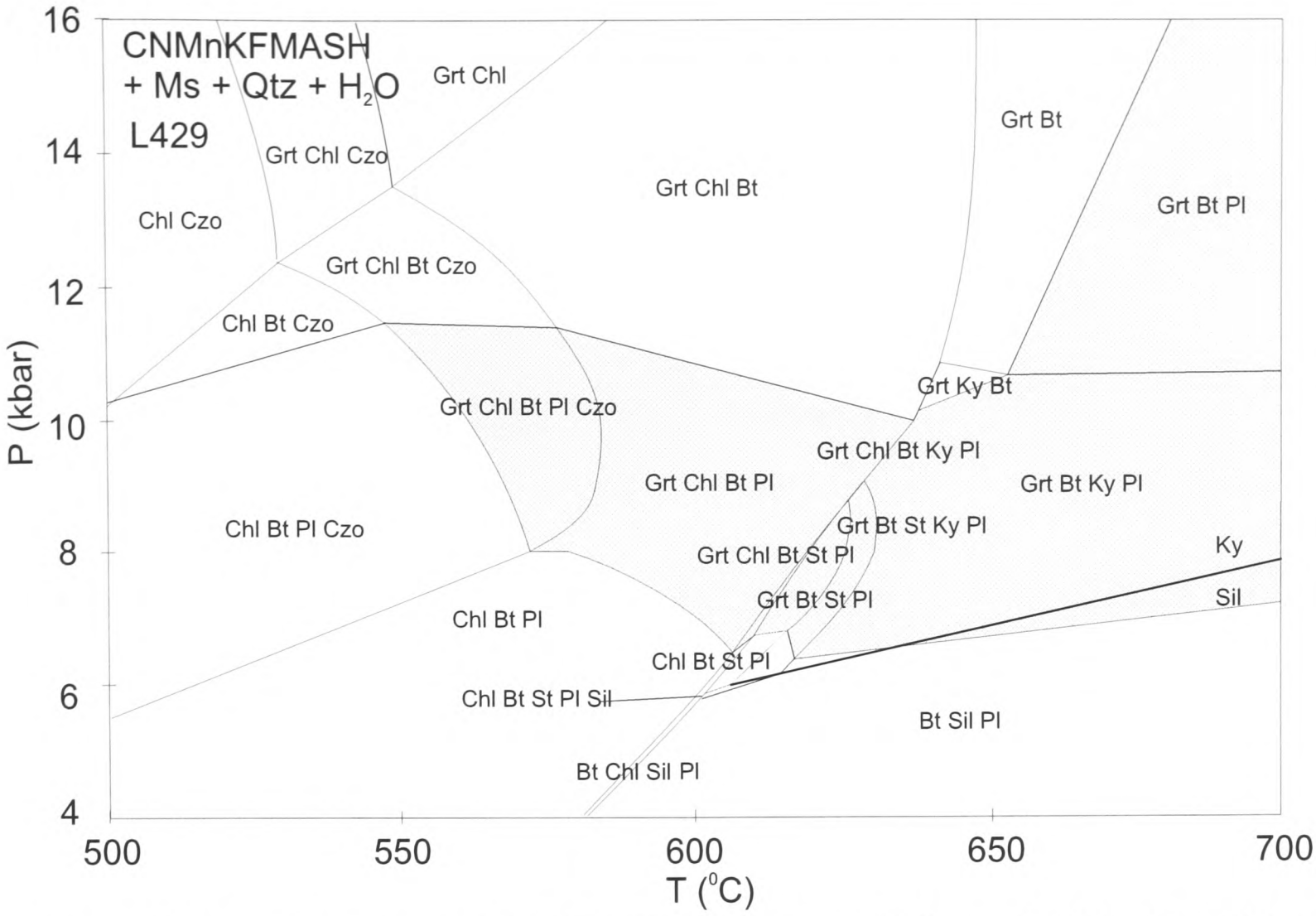


Figure 5.13.A. P-T pseudosection in CNMnKFMASH (+ Ms + Qtz + H_2O) for sample L429, calculated for **aH_2O = 1.0**. Shaded area delimits the extent of Grt + Pl stability.

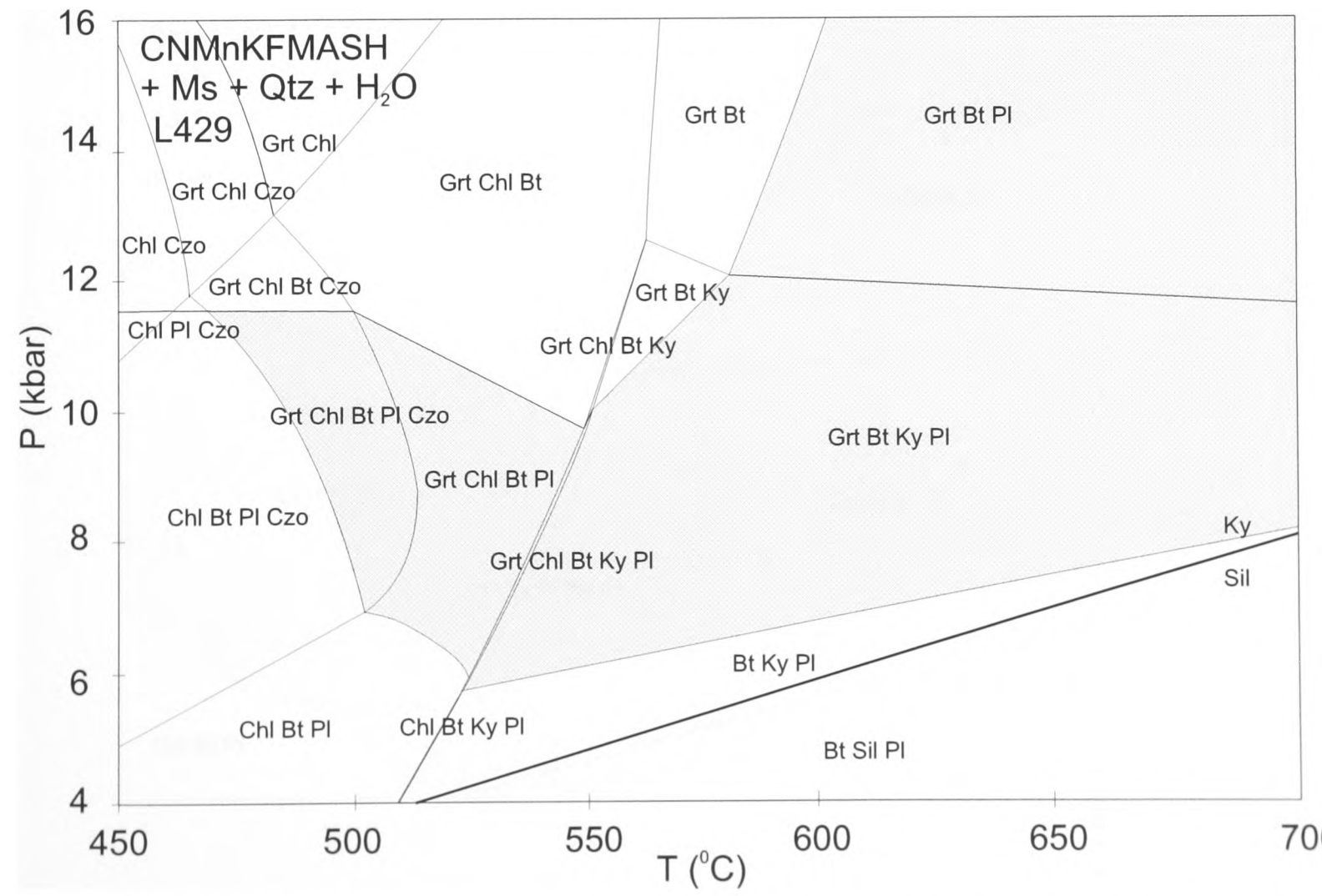


Figure 5.13.B. P-T pseudosection for CNMnKFMASH (+ Ms + Qtz + H_2O) for sample L429 ,calculated for **aH_2O = 0.5**, as estimated from average P-T calculations.

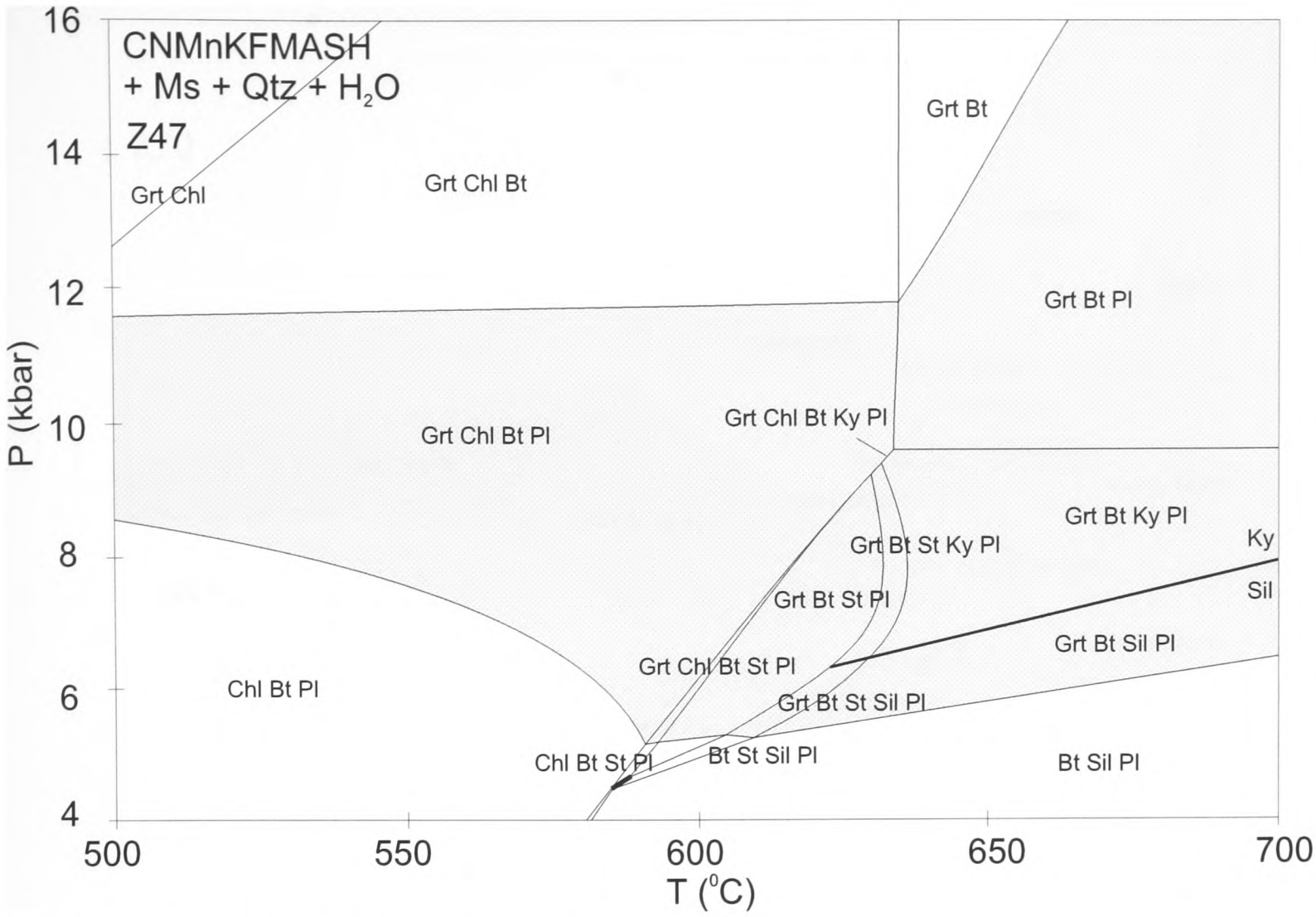


Figure 5.13.C. P-T pseudosection in CNMnKFMASH (+ Ms + Qtz + H_2O) for sample Z47, calculated for **aH_2O = 1.0**. Shaded area delimits the extent of Grt + Pl stability.

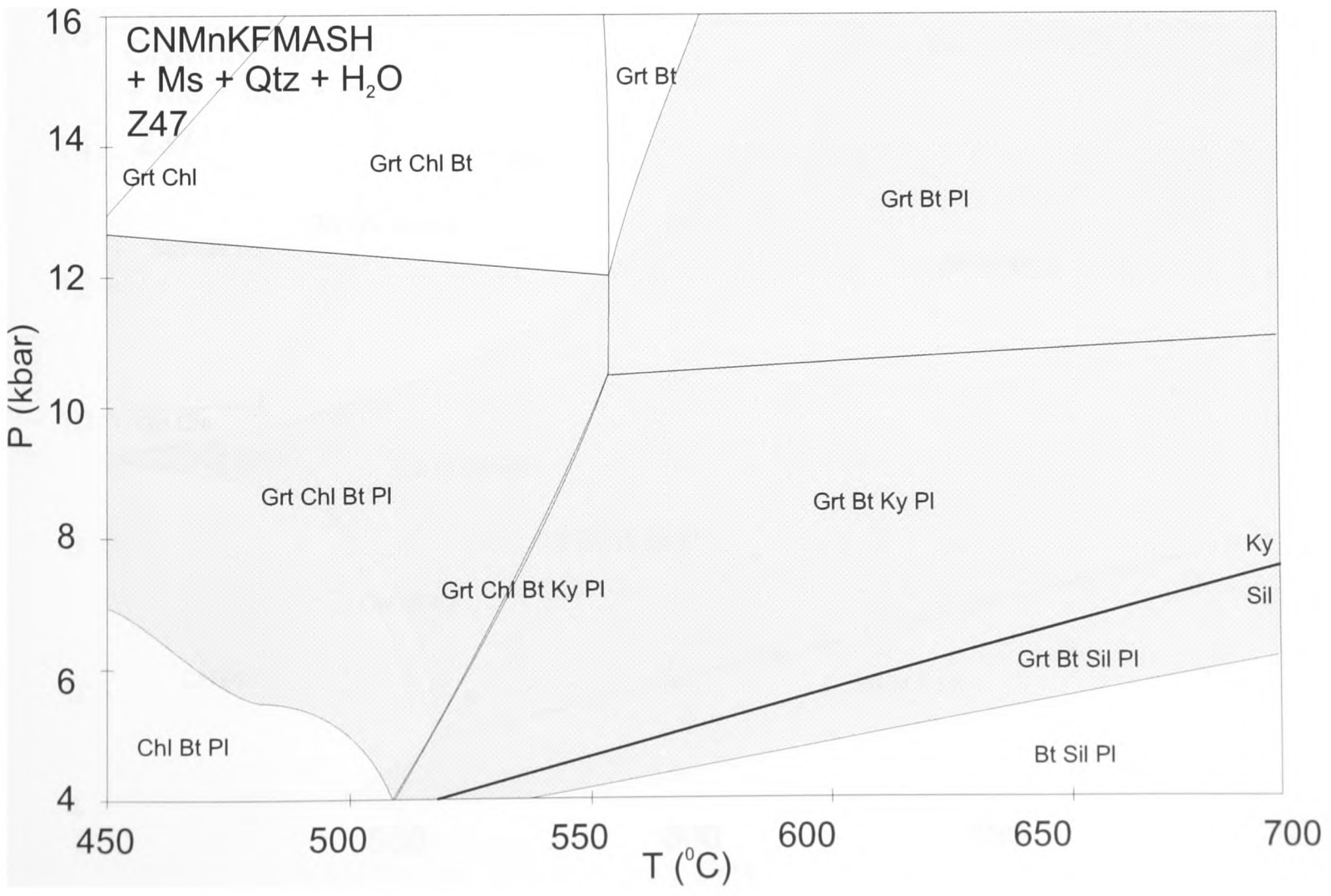


Figure 5.13.D. P-T pseudosection for CNMnKFMASH (+ Ms + Qtz + H_2O) for sample Z47 ,calculated for **aH_2O = 0.5**, as estimated from average P-T calculations.

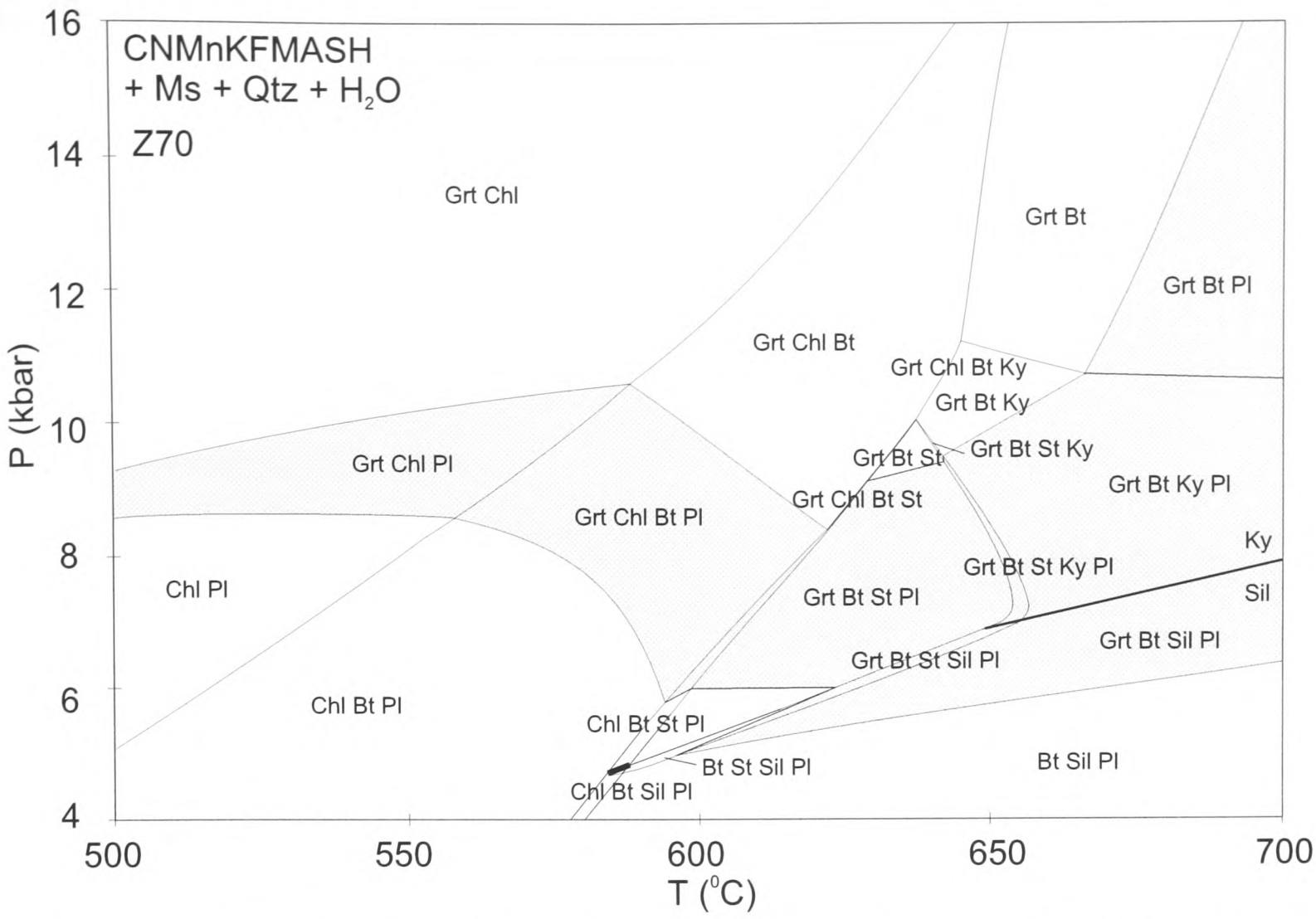


Figure 5.13.E. P-T pseudosection in CNMnKFMASH (+ Ms + Qtz + H_2O) for sample Z70, calculated for **aH_2O = 1.0**. Shaded area delimits the extent of Grt + Pl stability.

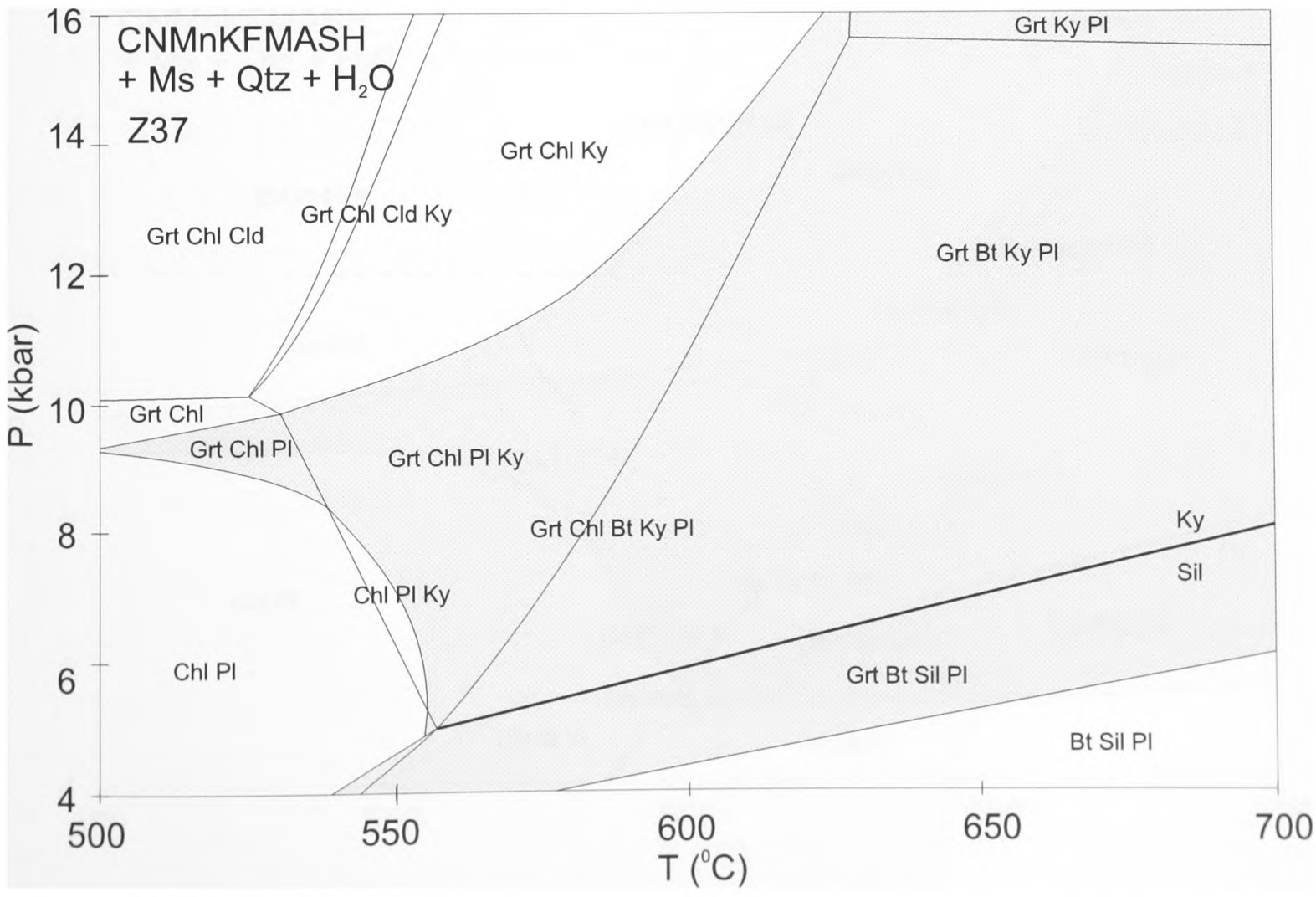


Figure 5.13.F. P-T pseudosection for CNMnKFMASH (+ Ms + Qtz + H_2O) for sample Z37 ,calculated for **aH_2O = 0.7**, as estimated from average P-T calculations.

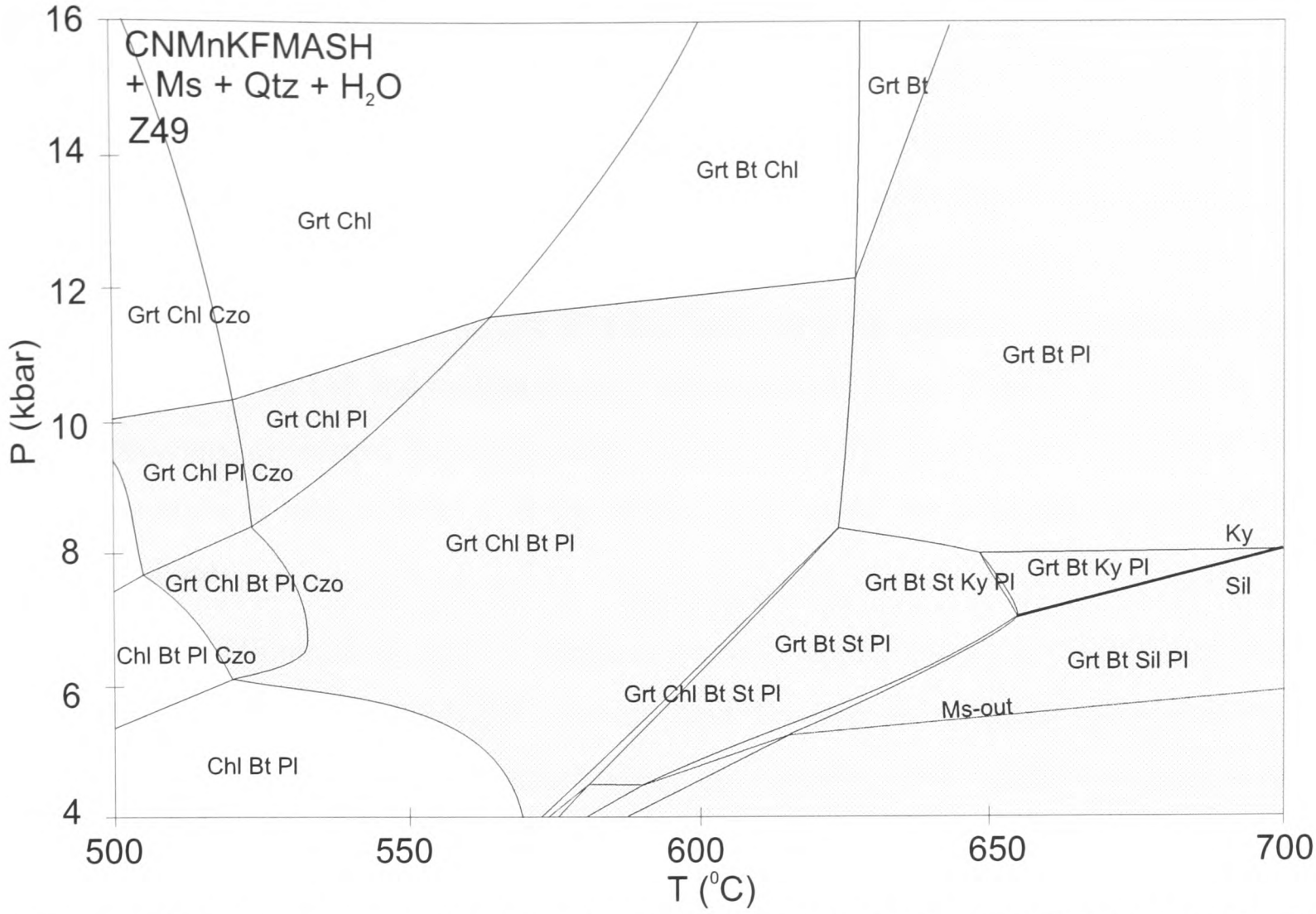


Figure 5.13.G. P-T pseudosection in CNMnKFMASH (+ Ms + Qtz + H_2O) for sample Z49, calculated for **aH_2O = 1.0**. Shaded area delimits the extent of Grt + Pl stability.

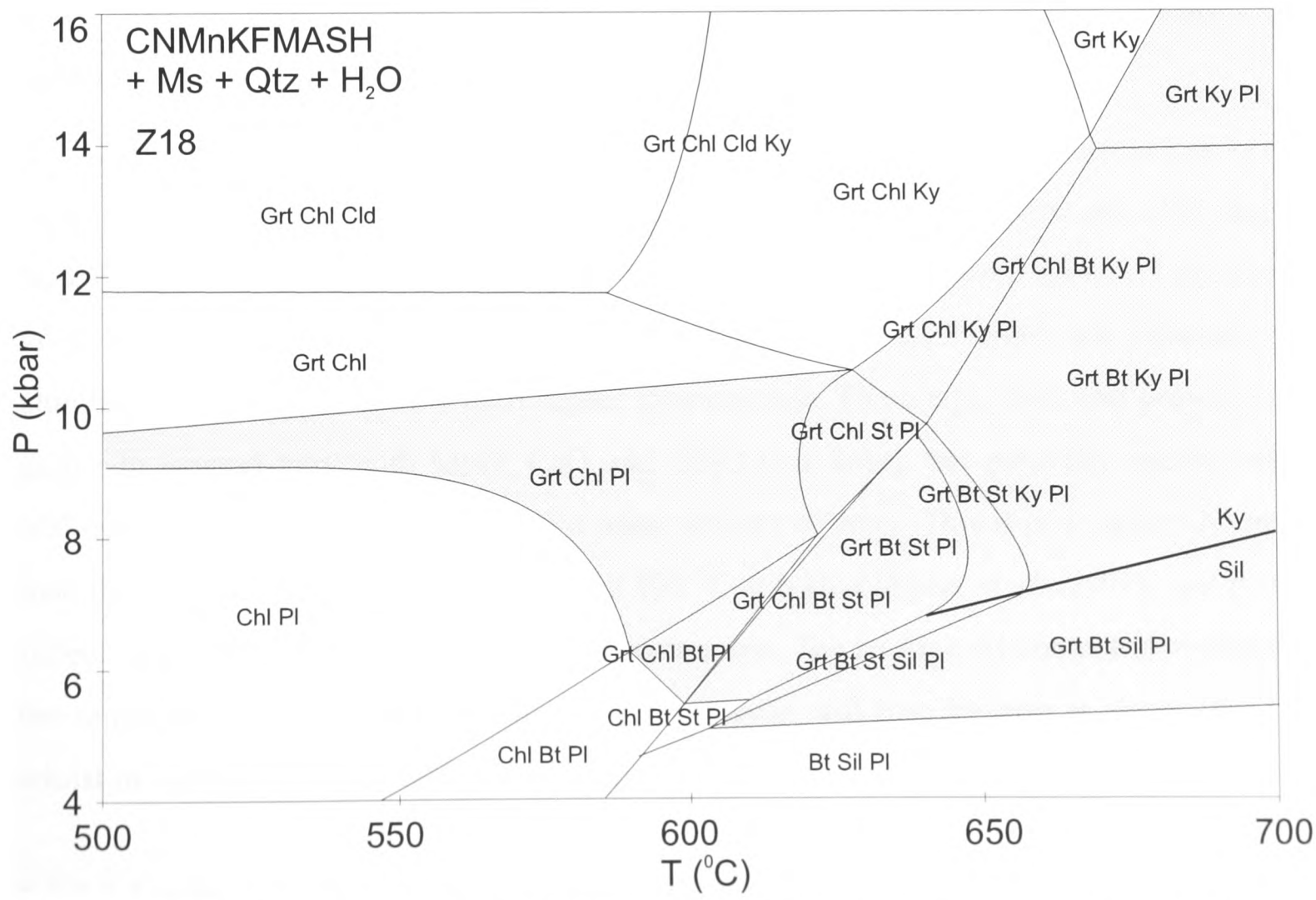


Figure 5.13.H. P-T pseudosection for CNMnKFMASH (+ Ms + Qtz + H_2O) for sample Z18 ,calculated for **aH_2O = 1.0**, as estimated from average P-T calculations.

As described in Stüwe & Powell (1995), the mode output value calculated by THERMOCALC is in mole percent normalised to one oxide. In order to compare these output values with volumetric mode proportions, which is the values obtained by point counting, they must be divided by the molar volume and multiplied by the number of *oxides* in the formula unit involved. Thus, to convert THERMOCALC modes of garnet to volumetric modes the value is divided by 115 and multiplied by 7 (see Appendix C and Table 5.1). In the presented pseudosections contoured for mode garnet (Figures 5.14.D-5.19.D.), the value for "mode" is the proportion of total number of moles of the oxides under consideration that are combined for that phase.

The addition of Mn and Ca stabilises garnet to higher and lower temperatures than for the MnKFMASH and KFMASH systems, and Ca and Na stabilise plagioclase-bearing assemblages. The dominant assemblages are quadri- and quinquivariant fields in CNMnKFMASH, with narrower staurolite-bearing trivariant assemblages at medium pressures and temperatures. Divariant fields, where seen, exist only over a few degrees and bars and so can be considered unimportant in the interpretation of the assemblages here, as nine phases coexisting in equilibrium are not seen. THERMOCALC calculates errors on all equilibria; for steep equilibria such as those including chlorite temperature is well constrained with errors in the range 5-10 ^{0}C, whereas shallow equilibria have large temperature errors associated with them for a particular specified pressure.

From the pseudosections, it can be seen that there are a number of similarities between samples, as well as systematic differences. For samples L429, Z47, Z70 and Z49 that have bulk compositions below the Grt-Chl tie-line on an AFM projection, garnet is predicted to grow in the assemblage Chl + Bt + Pl. Samples Z18 and Z37 which are relatively more aluminous do not grow biotite until higher temperatures. The temperature and pressure of the garnet-in isograd vary with MnO, CaO and aH_2O (see later), but generally occurs between 550-600 ^{0}C at 6 kbar for samples with a water activity of unity. This is at a higher temperature than the "classic" garnet isograd of around 500 ^{0}C at 6 kbar (Spear *et al.*, 1991), and probably reflects a relatively low MnO content of garnet cores. The relative Al content also determines the range of kyanite stability, in that Al-poorer rocks will lose kyanite at about 10-11 kbar whilst in sample Z37 it is stable until nearly 16 kbar.

5.3.2.2.Agreements between the calculated and the observed

The sub-aluminous pelite pseudosections for aH2O = 1.0 predict a sequence of mineral isograds that agree with the classic Barrow zones of NE Scotland, and for the range of

P-T conditions calculated for Suru Valley samples, i.e. 620-650 ^{0}C, 9.5-10.5 kbar, all predict the observed equilibrium assemblages. For most samples this is Grt + Bt + Pl + Ky, apart from sample Z70, where Grt + Bt + Ky is observed. The lack of plagioclase in sample Z70 means that a value for the pressure of equilibration could not be calculated; however, the pseudosection provides an extremely good constraint. From conventional thermobarometry a value of 640-650 ^{0}C for the peak temperature was calculated, which is consistent with the regional temperatures. It is also observed in thin section that staurolite is included at some garnet rims, but is not seen elsewhere in the matrix, implying that it ceased to be stable only shortly before the garnet ceased growing. From the pseudosection (Figure 5.13.E.), these constraints would predict a pressure of around 10 kbar, which is consistent with values from nearby samples. This illustrates the use of the pseudosection in predicting peak P-T conditions, and also serves as a check on the accuracy of the pseudosection.

5.3.2.3. The effect of aH_2O

The pseudosections described above have all been calculated using a water activity of unity which, in the absence of any other constraints, is a reasonable assumption to make for pelitic rocks. However, it is possible to make inferences about water activity from THERMOCALC in average P-T mode (see Chapter 4), and samples L429 and Z47 are believed to have equilibrated at around aH_2O = 0.5, and Z37 at aH_2O = 0.7. These pseudosections are compared with those at aH_2O = 1.0 for L429 and Z47, in Figures 5.13.B. & D. respectively, and is given for Z37 in Figure 5.13.F. The most striking feature of lowering aH_2O is to drastically lower the temperature of specific equilibria, most importantly the garnet-in isograd. This is to be expected, as most reactions have H_2O on the high temperature side, and will move to lower temperatures by obeying Le Chatelier's principle. Of greater interest is the predicted lack of staurolite in any of the samples with lowered aH_2O; for example, the trivariant field Grt + St + Bt + Ky + Pl is calculated to be metastable with respect to the field Grt + Chl + Bt + Ky + Pl in Z47, L429 and Z37. The experiments of Ganguly (1972) predict that lowering aH_2O from 1.0 to 0.5 will both decrease the size of the stability field of St + Mt + Qtz, and shift it to lower temperatures, which agrees well with this observation. The pseudosections calculated for aH_2O corresponding to that estimated from average P-T calculations predict both peak conditions and reaction history more accurately than those for aH_2O = 1.0 for the above samples, and these aH_2O values are used in all subsequent pseudosection calculations.

5.3.2.4. Discrepancies between the calculated and the observed.

It is worth drawing attention at this point to the limitations of the pseudosection in certain instances. In samples L429 and Z49, small clinozoisite crystals are preserved as inclusions within garnet porphyroblasts but are not present in the matrix. THERMOCALC does not predict Grt + Czo to be stable together at the calculated core composition (see Figures 5.20.A. & E.); garnet grows only with Chl + Bt + Pl. This discrepancy may arise through treating clinozoisite as a pure phase, i.e. a = 1.0, for the purpose of making calculations simpler. With more time and effort it may be possible to obtain information on the oxidation state of the samples, and therefore build a clinozoisite-epidote-pistacite solid solution into the model that incorporates Fe^{3+} Alternatively, it may be that clinozoisite is not reacting with the garnet (and explaining its presence as an inclusion mineral), and so will not be predicted to exist in stable equilibrium with it.

From Table 5.3 it can be seen that THERMOCALC makes good predictions for the peak assemblage mineralogy and composition for nearly all the samples modelled. Particular details are discussed in later sections. However, the predicted peak assemblage for sample Z49 is very different from the actual one. From average P-T calculations, Z49 is estimated to have equilibrated at 600 ± 11 ^{0}C, 8.4 ± 0.7 kbar (Table 4.3.), which lies in the predicted field Grt + Chl + Bt + Pl, and not the actual assemblage of Grt + Bt + Ky + Pl (Figure 5.13.G.). Conventional thermobarometry predicts temperatures of 640-650 ^{0}C and pressures of around 8 kbar (Table 4.4.), which is closer to the Grt + Bt + Ky + Pl field. From Table 5.3, however, it can be seen that even assuming these conditions calculated and measured modes and compositions do not correlate well. Two possibilities are the most likely causes for these discrepancies. Firstly, the bulk composition may have been incorrectly estimated, from incorrect assumptions when estimating the modes of phases. Secondly, the average P-T for Z49 of 600 ^{0}C and 8.4 kbar is likely to represent a degree of re-equilibration after peak conditions, as described in Chapter 4.

In all samples certain systematic discrepancies between the observed and predicted modes of phases are found. From Table 5.3. it can be seen that the calculated amount of garnet is always greater than the observed volumes, and that the calculated amount of muscovite is less than is observed. THERMOCALC also generally overestimates the volume of kyanite, and underestimates the amount of plagioclase. The most obvious explanation for this effect is that garnet fractionation is not being taken into account (see section 5.3.6.) and the system is being modelled entirely in equilibrium. If, as is the case in this situation, the garnet is not

allowed to fractionate system components such as Mn and Ca, it will be expected to grow faster than if it grew entirely in equilibrium with the original bulk rock composition. In the field Grt-Bt-Pl-Ky-(Ms-Qtz-H_2O), garnet and muscovite are predicted to grow at the expense of biotite, plagioclase and kyanite with increasing pressure. Therefore, if the amount of garnet is overestimated, the amount of muscovite will be underestimated, which is what is observed from the calculations.

5.3.2.5. Errors on phase boundaries

When considering phase diagrams in the context of interpreting natural assemblages it is important to have an appreciation of the magnitude of the errors involved. THERMOCALC calculates uncertainties on phase equilibria using standard deviations on enthalpies and activities in much the same way as it does for average P-T calculations (Appendix B). Equilibria with steep P-T slopes typically have uncertainties of 5-10 ^{0}C when temperature is calculated for a specific pressure, and around 1 kbar when pressure is calculated for a specific temperature. Flat phase boundaries such as the Grt-Bt-Ky-Pl garnet-in boundary are best calculated by specifying a temperature and calculating the pressure at that temperature, and have an uncertainty again of around 1 kbar.

Phase	Z47 Measured mode	Calculated mode 10.5 kbar 630 ^{0}C	Z70 Measured mode	Calculated mode 10 kbar 640 ^{0}C
Grt	16	31.6	14.3	32.2
Bt	60	46.4	28.6	26.8
Ms	24	16.8	54.3	39.4
Ky	2	3.4	1.43	1.7
Pl	4	1.8	-	-
	Composition	**Composition**	**Composition**	**Composition**
X_{Alm}	0.662	0.649	0.743	0.685
X_{Sps}	0.004	0.01	0.005	0.007
X_{Grs}	0.184	0.083	0.069	0.041
X_{An}	0.22	0.177	-	-
Phase	**L429 Measured mode**	**Calculated mode** 10 kbar 650 ^{0}C	**Z37 Measured mode**	**Calculated mode** 10 kbar 640 ^{0}C
Grt	9	15.9	9.6	20.2
Bt	49	54.3	17.8	29.7
Ms	41	26.7	42.9	28.3
Ky	1	3	8.8	15
Pl	2	2.3	8.4	6.8
	Composition	**Composition**	**Composition**	**Composition**
X_{Alm}	0.643	0.648	0.717	0.681
X_{Sps}	0.002	0.012	0.0087	0.016
X_{Grs}	0.171	0.0817	0.06	0.035
X_{An}	0.3	0.212	0.13	0.09
Phase	**Z18 Measured mode**	**Calculated mode** 9 kbar 640 ^{0}C	**Z49 Measured mode**	**Calculated mode** 7.8 kbar 630 ^{0}C
Grt	8.9	28.5	21.1	49.2
Bt	30.3	34	29.7	32.5
Ms	29	22	43.8	16.3
Ky	18.6	12	1.95	0.2
Pl	12	3.5	3.5	1.8
	Composition	**Composition**	**Composition**	**Composition**
X_{Alm}	0.731	0.708	0.678	0.723
X_{Sps}	0.059	0.0113	0.005	0.0076
X_{Grs}	0.092	0.035	0.0175	0.073
X_{An}	0.14	0.113	0.7	0.29

Table 5.3. THERMOCALC calculated modes and compositions for pseudosections, at average P-T of final rim equilibration. Measured modes are normalised to account for quartz, as this is not calculated by THERMOCALC. All modes given are **volume** percents, and the calculated modes have been converted from **molar** amounts using molar volumes.

5.3.3. Isopleths of garnet composition and mode

Whilst the pseudosections shown in Figures 5.13.A.-H. provide a useful framework in which to consider the P-T-X-M evolution of our samples, it is helpful to be able to visually compare changes in mineral composition with those measured, namely the garnet zoning profiles shown in Figures 5.6.-11. THERMOCALC can calculate isopleths of both mineral composition and mode for assemblages of any variance, and thus all P-T space of interest can

be contoured for variables of interest. In order to model garnet evolution as accurately as possible, each pseudosection has been contoured for isopleths of X_{Alm}, X_{Grs}, X_{Sps} and mode garnet, enabling us to see along what P-T paths garnet is expected to grow, and how its composition will change along those paths. These pseudosections are shown in Figures 5.14.-19.

The absolute values of the garnet composition isopleths vary with bulk composition, but the general orientation of them is similar in all the samples. Isopleths of X_{Alm} are steep and positive in Grt + Chl + Pl ± Bt fields, tending to become steeper and even negative when plagioclase is absent at higher pressures. X_{Alm} increases with increasing T before reaching a maximum between 550-600 ^{0}C in both chlorite-present and chlorite-absent fields, which is in agreement with the findings of Spear *et al.* (1991), and Vance & Mahar (1998). The slope of X_{Alm} isopleths flatten out to become sub horizontal and slightly negative in chlorite-absent fields, and are therefore relatively insensitive to changes in temperature. X_{Grs} decrease with increasing T and decreasing P, and isopleths are positive and less steep than those of X_{Alm} in Grt + Chl + Pl ± Bt bearing fields at lower pressures, but steepen up as pressure increases, finally becoming steep and negative when plagioclase is used up at high pressures. As with X_{Alm}, X_{Grs} isopleths become sub-horizontal after chlorite reacts out, and double back on themselves at around 7-8 kbar in certain samples. Thus, they are only really pressure-sensitive in chlorite-absent fields. X_{Sps} also decreases with increasing T and P, and are curved in Grt + Chl + Pl ± Bt bearing fields. Due to the very strong partitioning of Mn into garnet relative to chlorite and biotite, isopleths of X_{Sps} are almost exactly parallel to garnet growth isopleths, which is also in agreement with Spear *et al.* (1991).

For all isopleths there is a slight step as the assemblage changes at medium temperatures to Grt + Chl + Bt + St +Pl. This predicts that garnet should be resorbed slightly, and the isopleths of composition reverse briefly, which can be correlated with the KFMASH staurolite-in isograd

$$Grt + Chl = St + Bt + H_2O$$

which predicts that garnet will be used up. In the CNMnKFMASH system this is represented by a field rather than a line, albeit only a few degrees in width. For samples in which staurolite is not predicted, i.e. those in which aH_2O is less than unity, the assemblage Grt + Chl + Bt + Ky + Pl occurs instead, and this causes a similar step in isopleths. The garnet zoning profiles for samples L429, Z37, Z70 and Z49 which have a sufficient number of

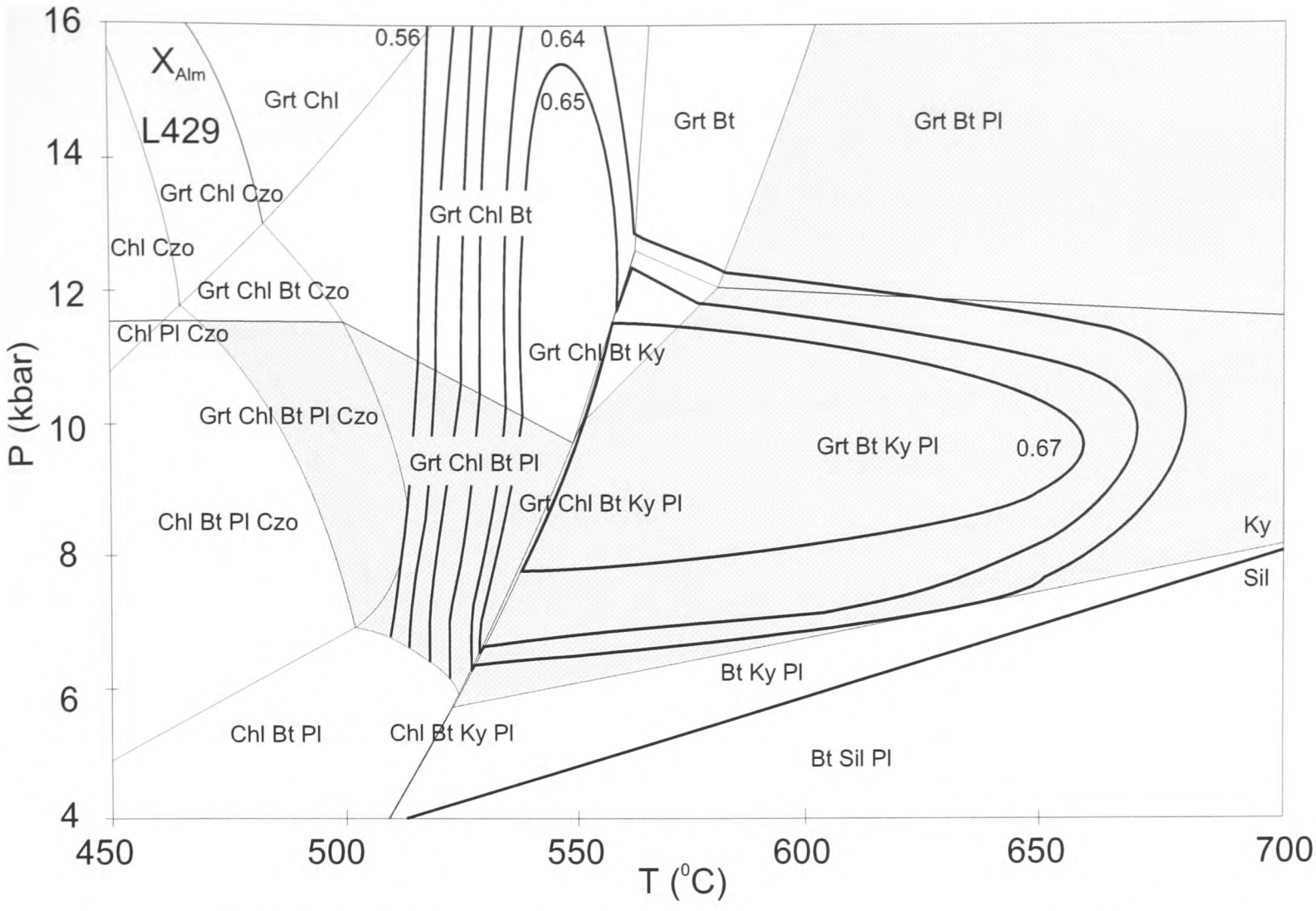


Figure 5.14.A. CNMnKFMASH (+ Ms + Qtz + H2O) pseudosection for sample L429 illustrating isopleths of X_{Alm} in garnet. $aH_2O = 0.5$.

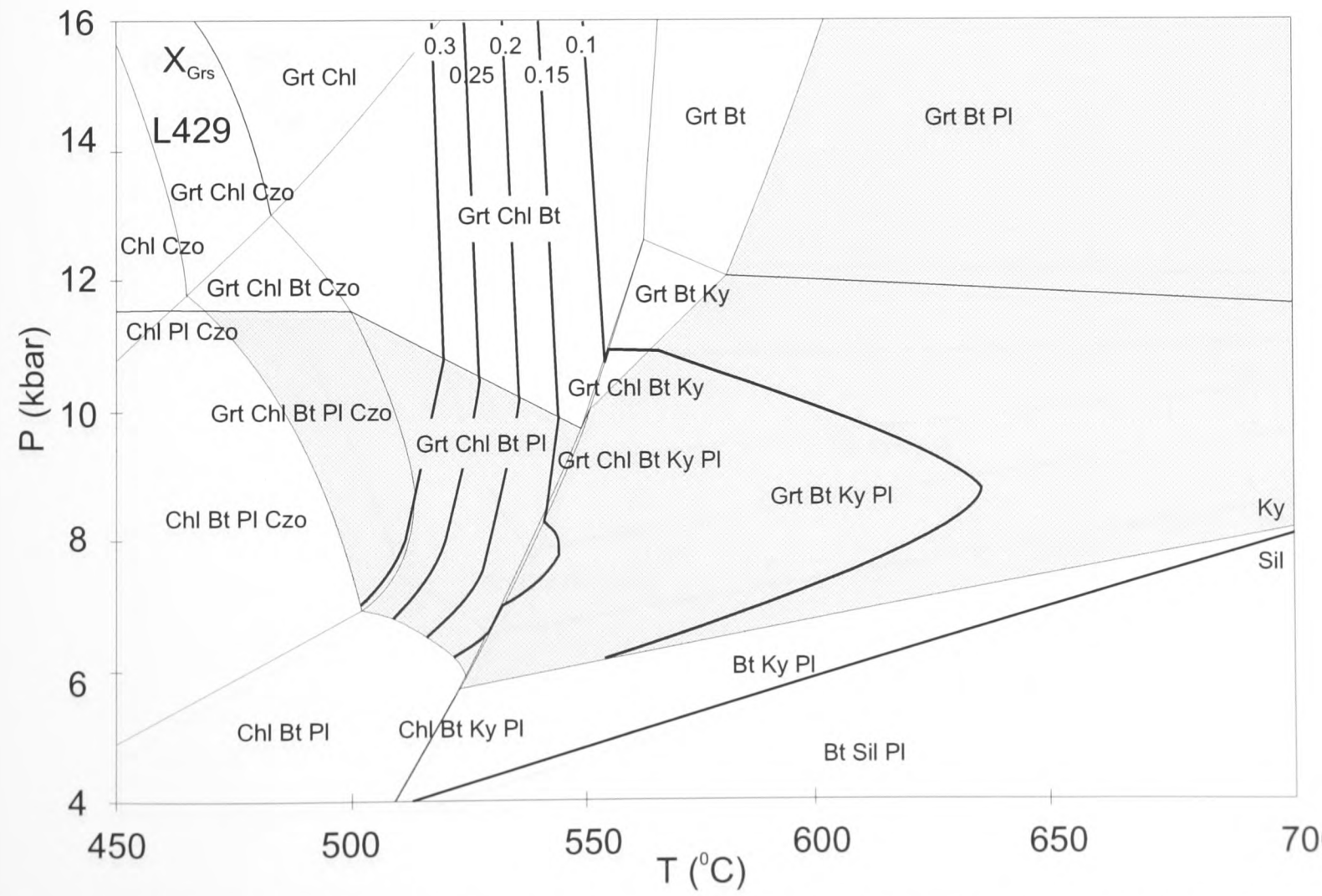


Figure 5.14.B. CNMnKFMASH (+ Ms + Qtz + H2O) pseudosection for sample L429 illustrating isopleths of X_{Grs} in garnet. $aH_2O = 0.5$.

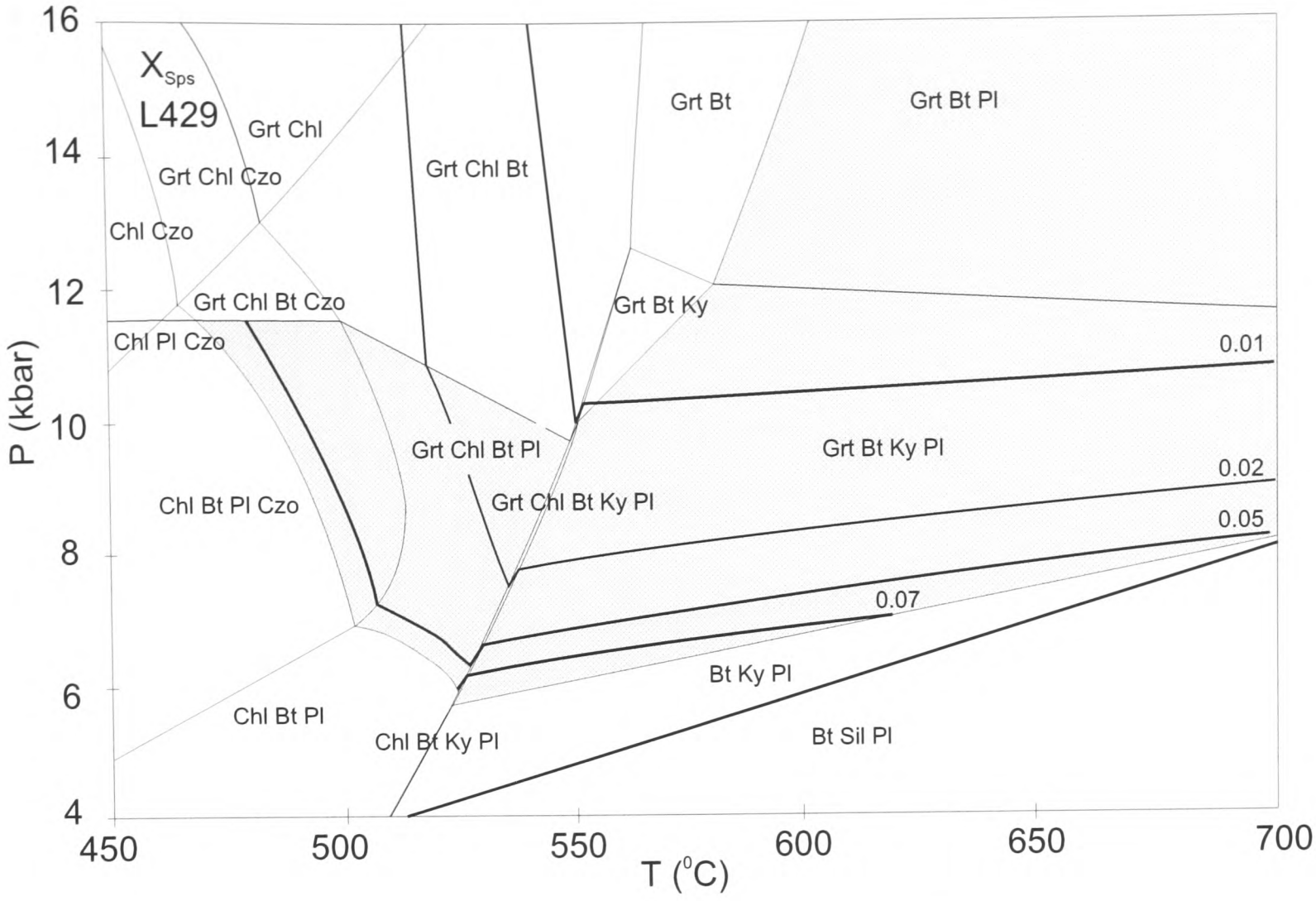


Figure 5.14.C. CNMnKFMASH (+ Ms + Qtz + H2O) pseudosection for sample L429 illustrating isopleths of X_{Sps} in garnet. $aH_2O = 0.5$.

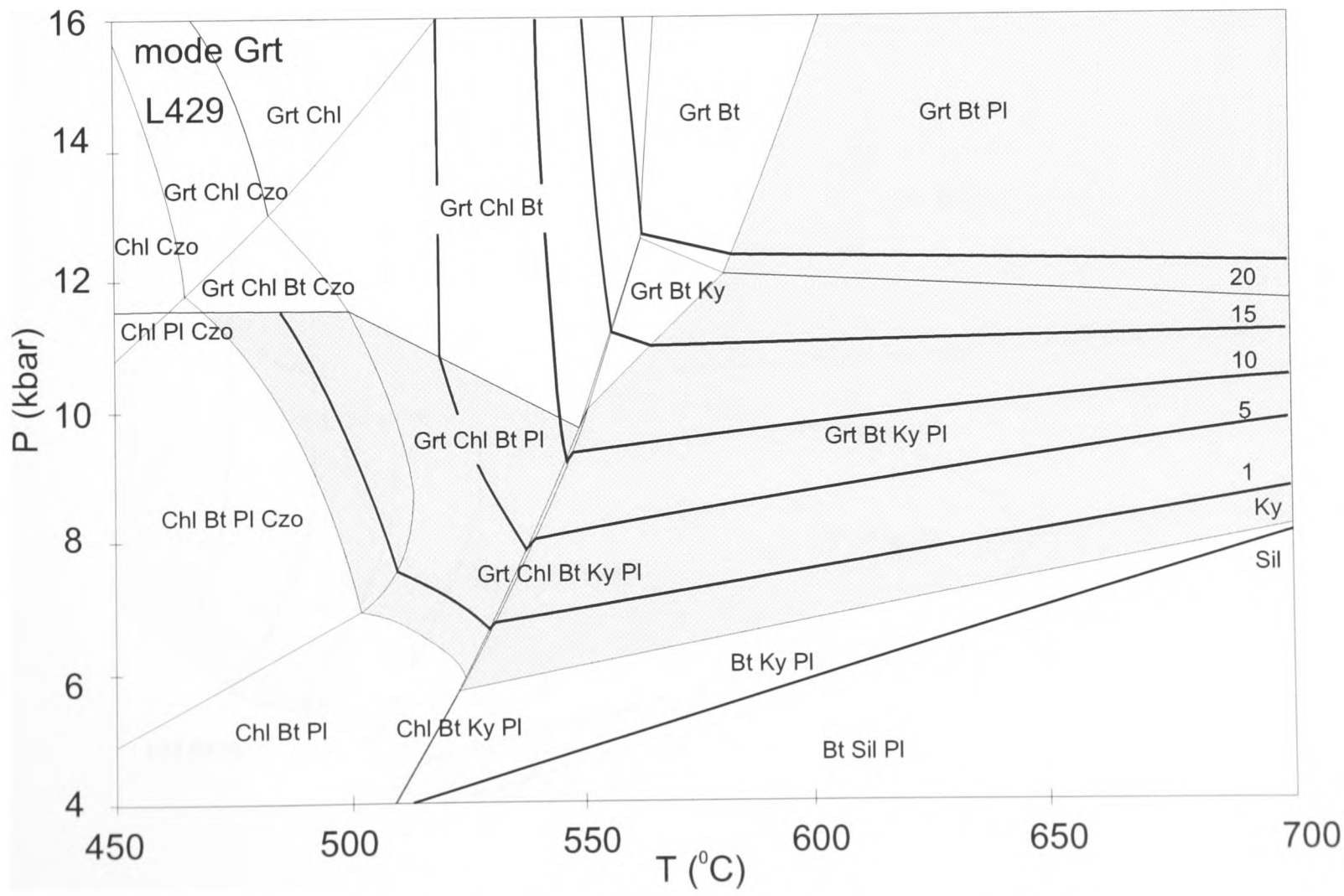


Figure 5.14.D. CNMnKFMASH (+ Ms + Qtz + H2O) pseudosection for sample L429 illustrating isopleths of modal percent garnet. Note that the values are **molar oxide** percents, and that the figure is relative to only the other AFM phases, as THERMOCALC does not calculate moles of quartz and water. See Table 5.3 for recalculated molar percents. $aH_2O = 0.5$.

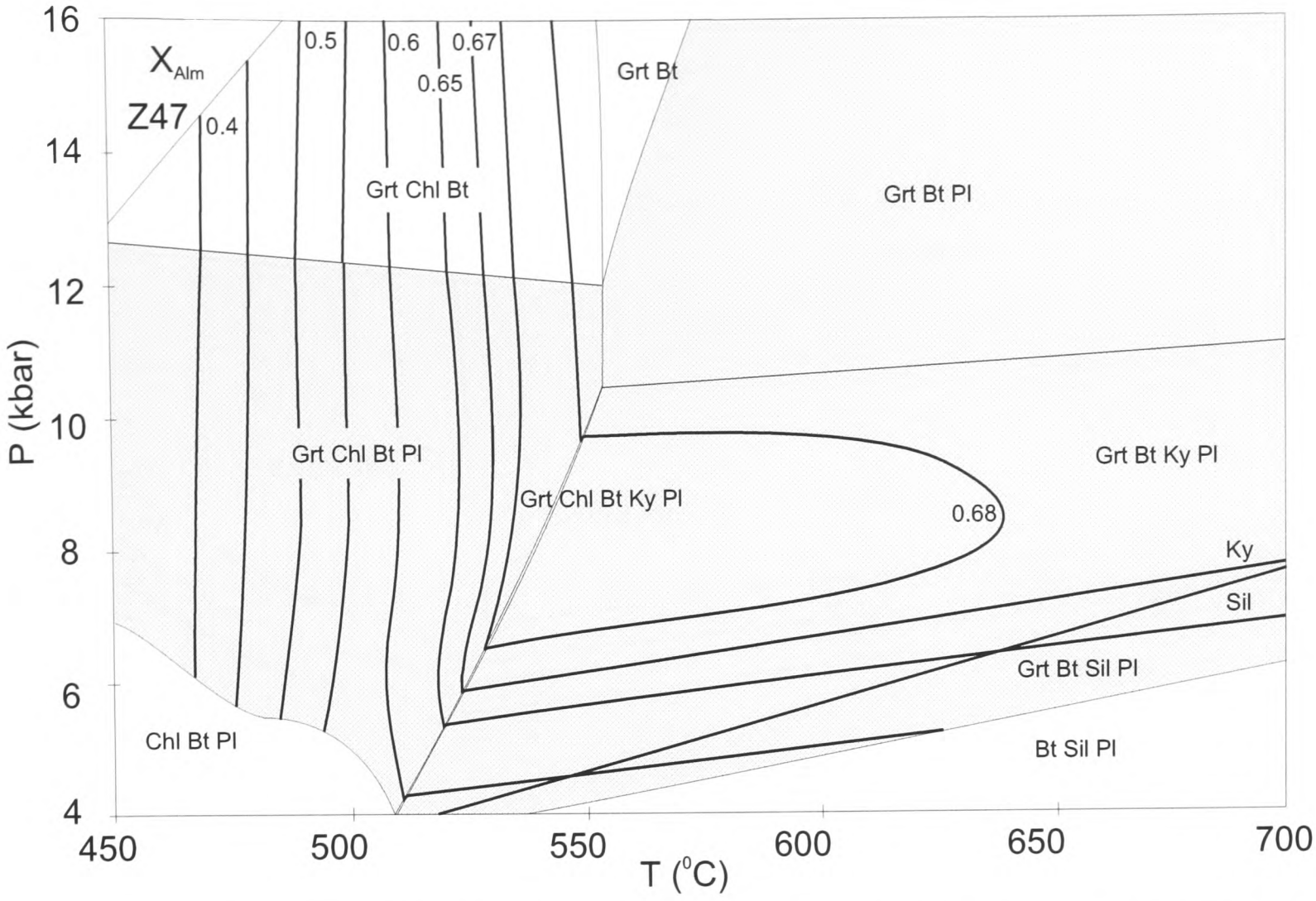


Figure 5.15.A. CNMnKFMASH (+ Ms + Qtz + H2O) pseudosection for sample Z47 illustrating isopleths of X_{Alm} in garnet. $aH_2O = 0.5$.

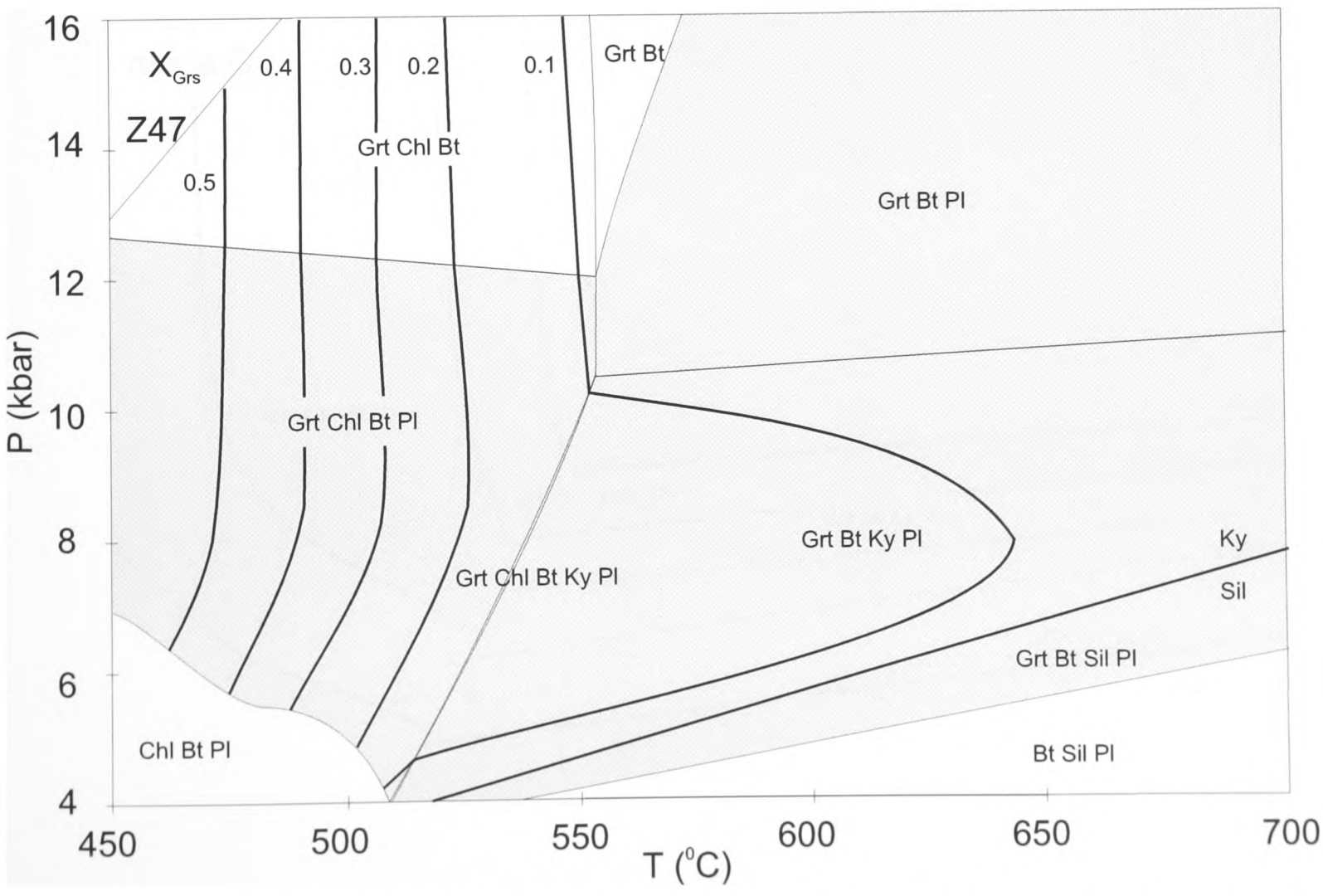


Figure 5.15.B. CNMnKFMASH (+ Ms + Qtz + H2O) pseudosection for sample Z47 illustrating isopleths of X_{Grs} in garnet. $aH_2O = 0.5$.

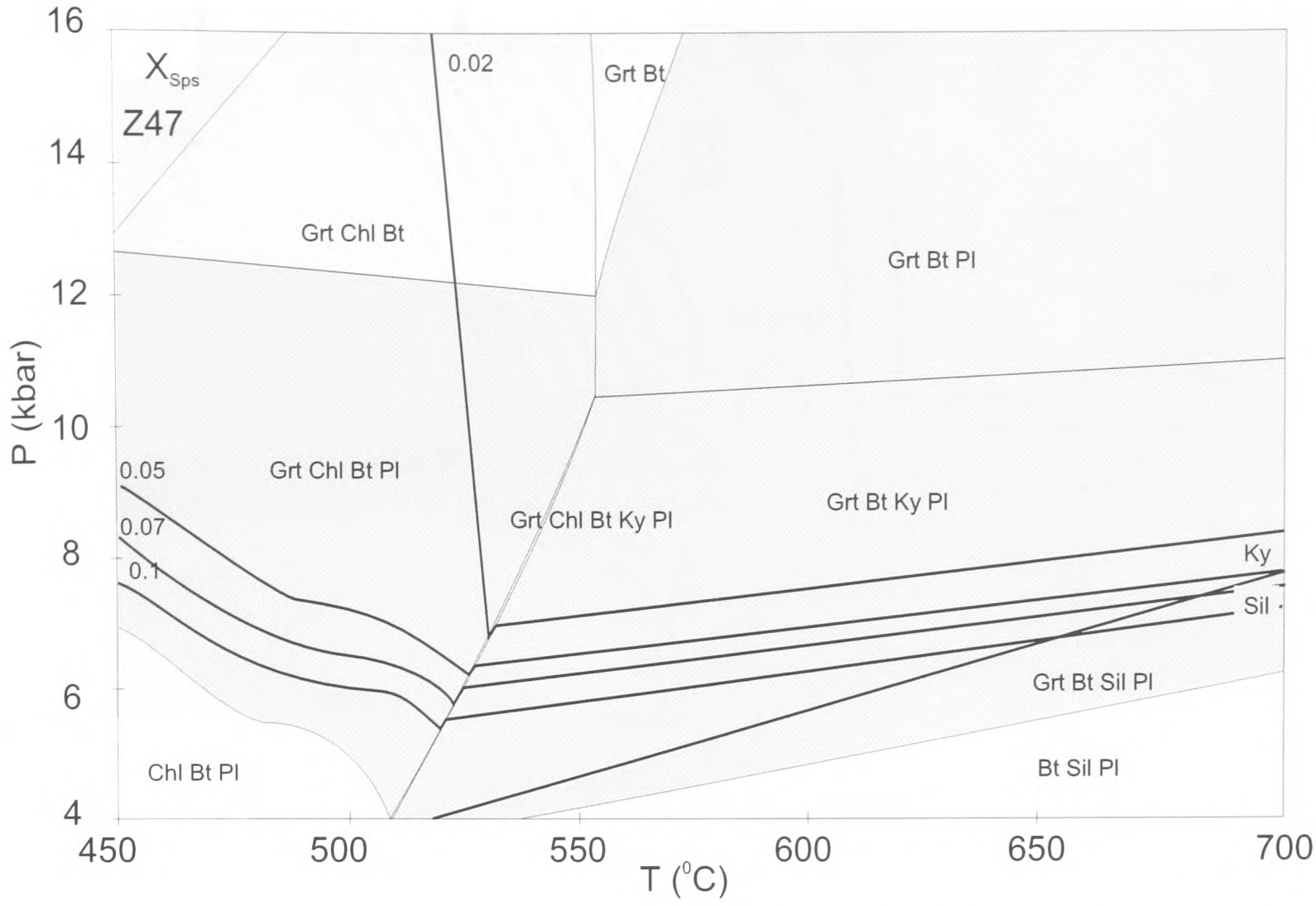


Figure 5.15.C. CNMnKFMASH (+ Ms + Qtz + H2O) pseudosection for sample Z47 illustrating isopleths of X_{Sps} in garnet. $aH_2O = 0.5$.

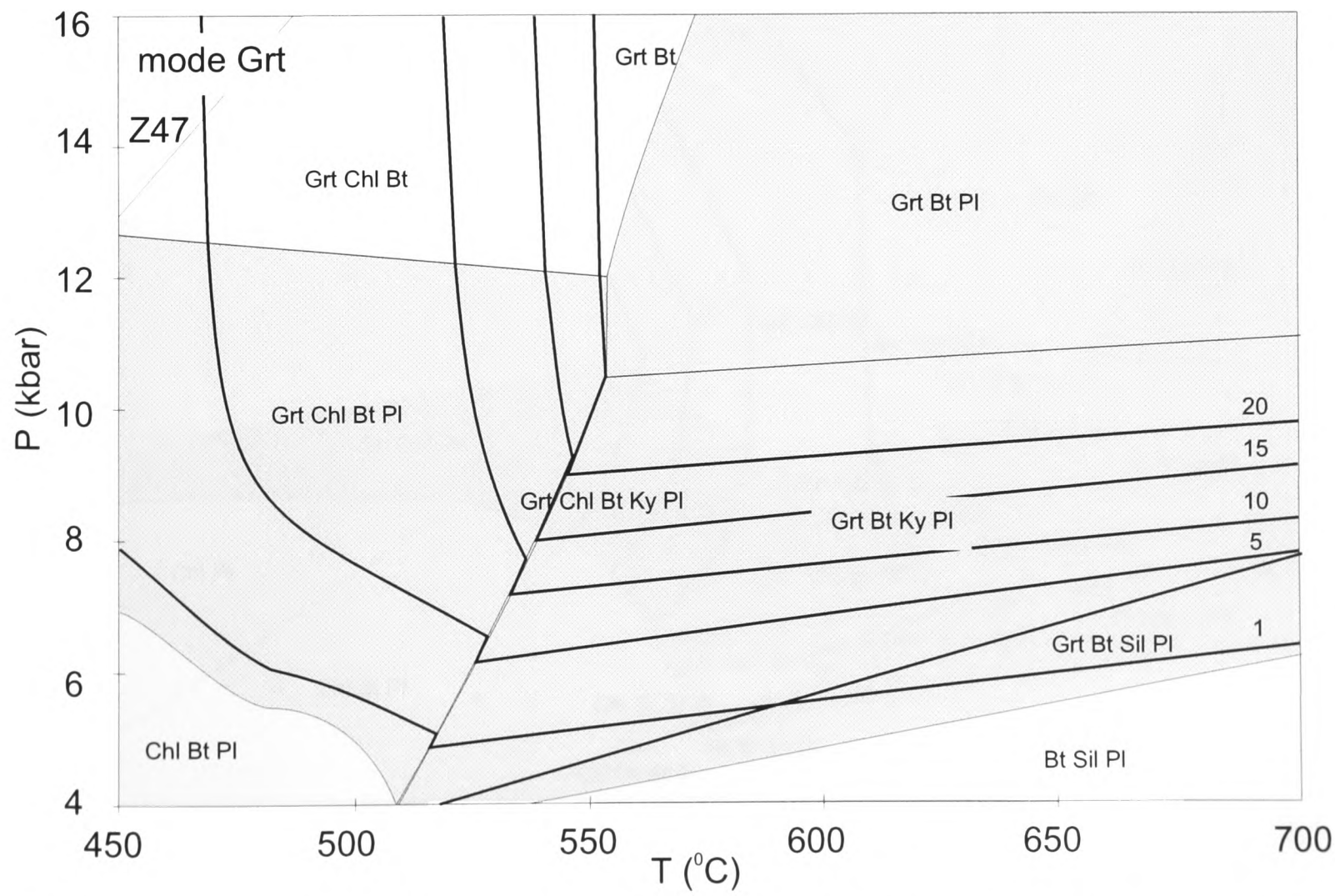


Figure 5.15.D.. CNMnKFMASH (+ Ms + Qtz + H2O) pseudosection for sample Z47 illustrating isopleths of modal percent garnet. Note that the values are **molar oxide** percents, and that the figure is relative to only the other AFM phases, as THERMOCALC does not calculate moles of quartz and water. See Table 5.3 for recalculated molar percents. $aH_2O = 0.5$.

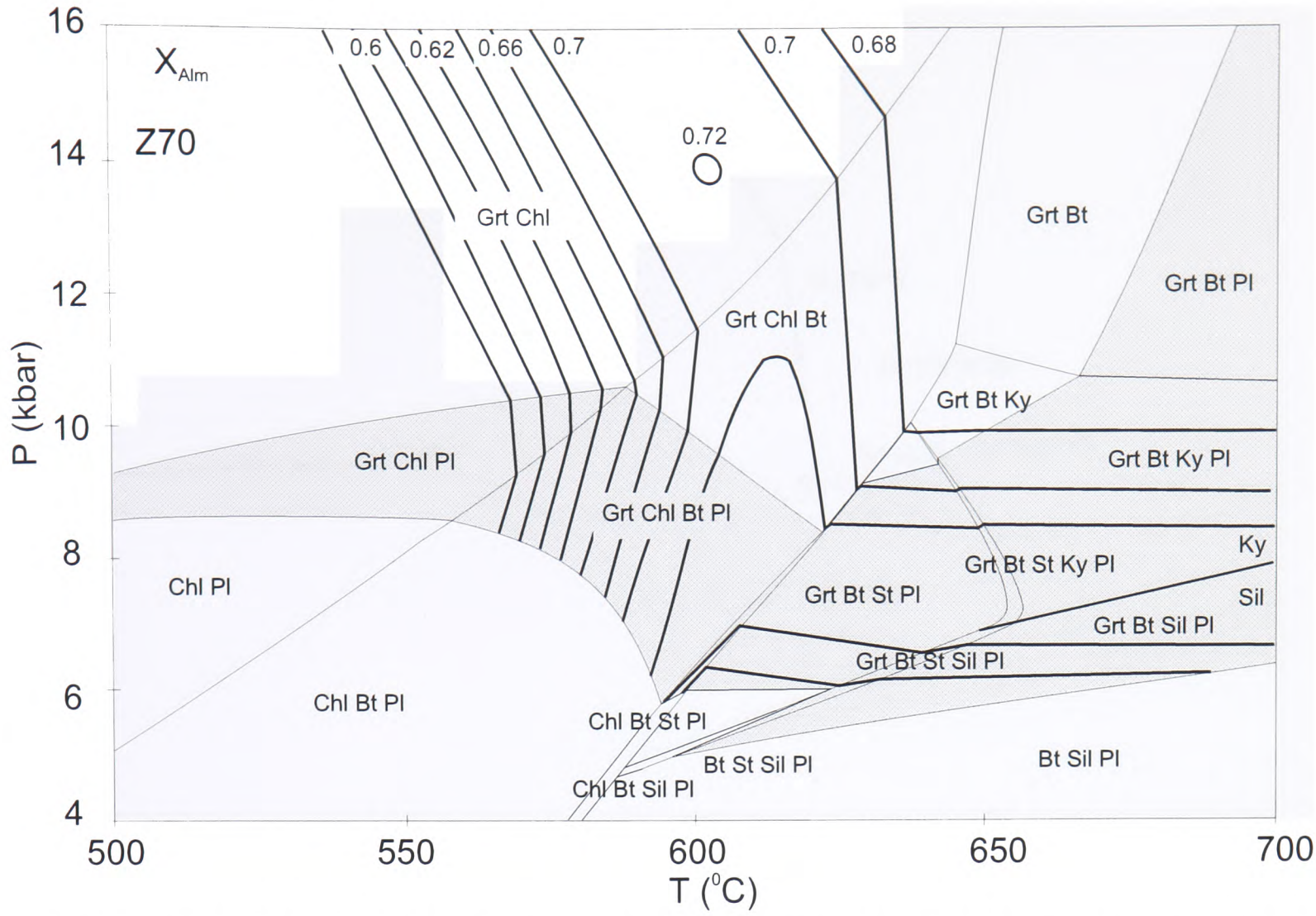


Figure 5.16.A. CNMnKFMASH (+ Ms + Qtz + H2O) pseudosection for sample Z70 illustrating isopleths of X_{Alm} in garnet. $aH_2O = 1.0$.

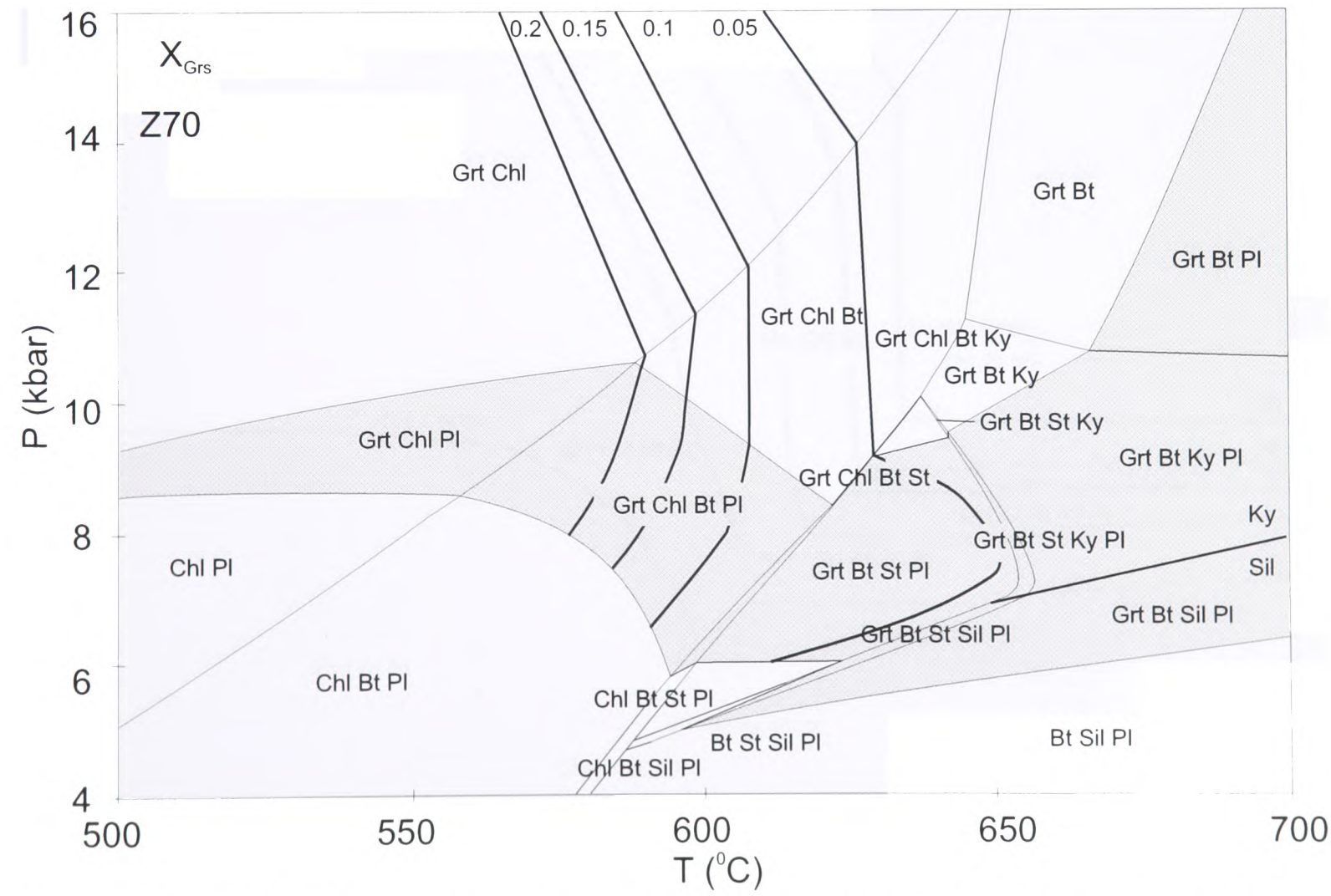


Figure 5.16.B. CNMnKFMASH (+ Ms + Qtz + H2O) pseudosection for sample Z70 illustrating isopleths of X_{Grs} in garnet. $aH_2O = 1.0$.

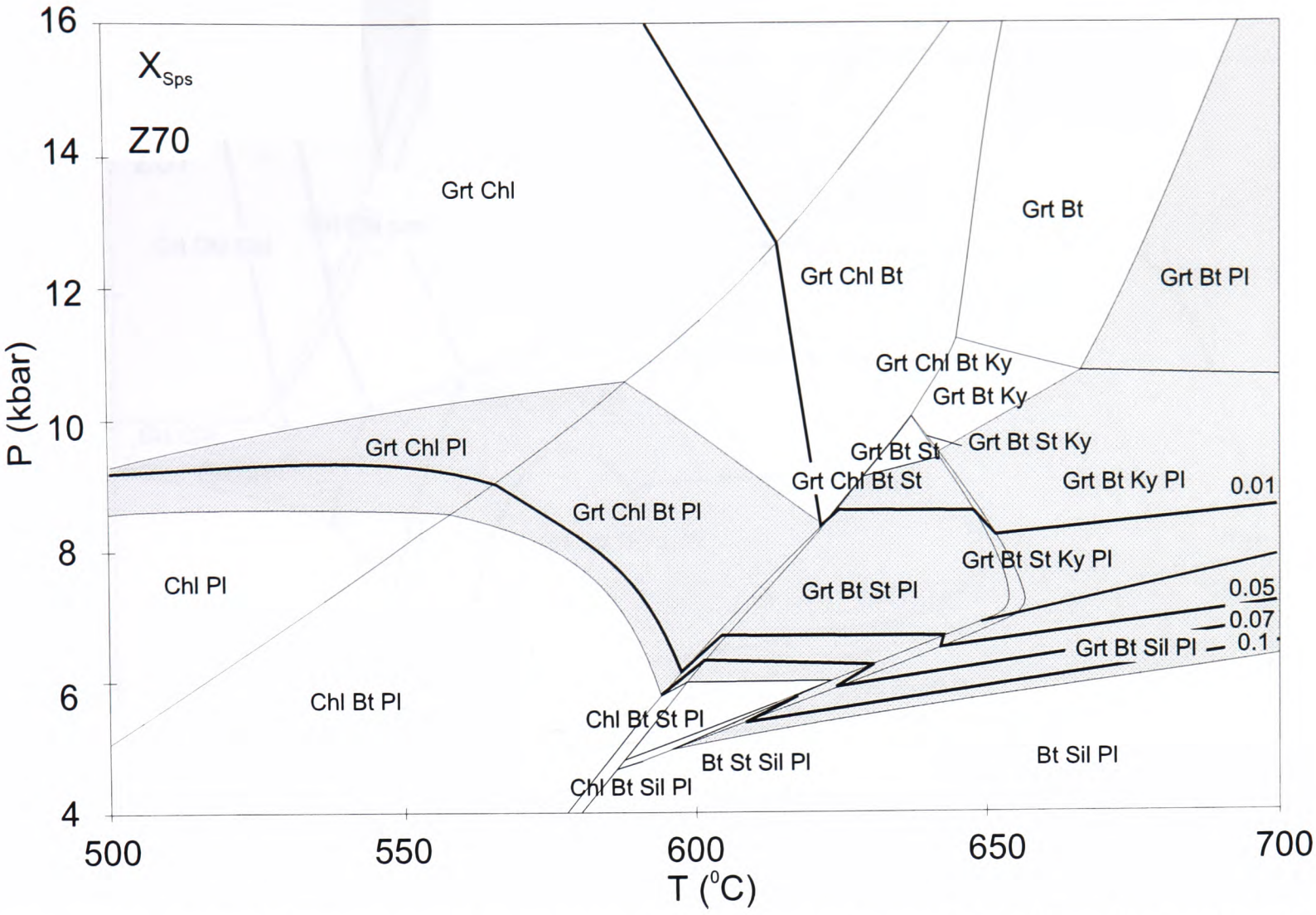


Figure 5.16.C. CNMnKFMASH (+ Ms + Qtz + H2O) pseudosection for sample Z70 illustrating isopleths of X_{Sps} in garnet. $aH_2O = 1.0$.

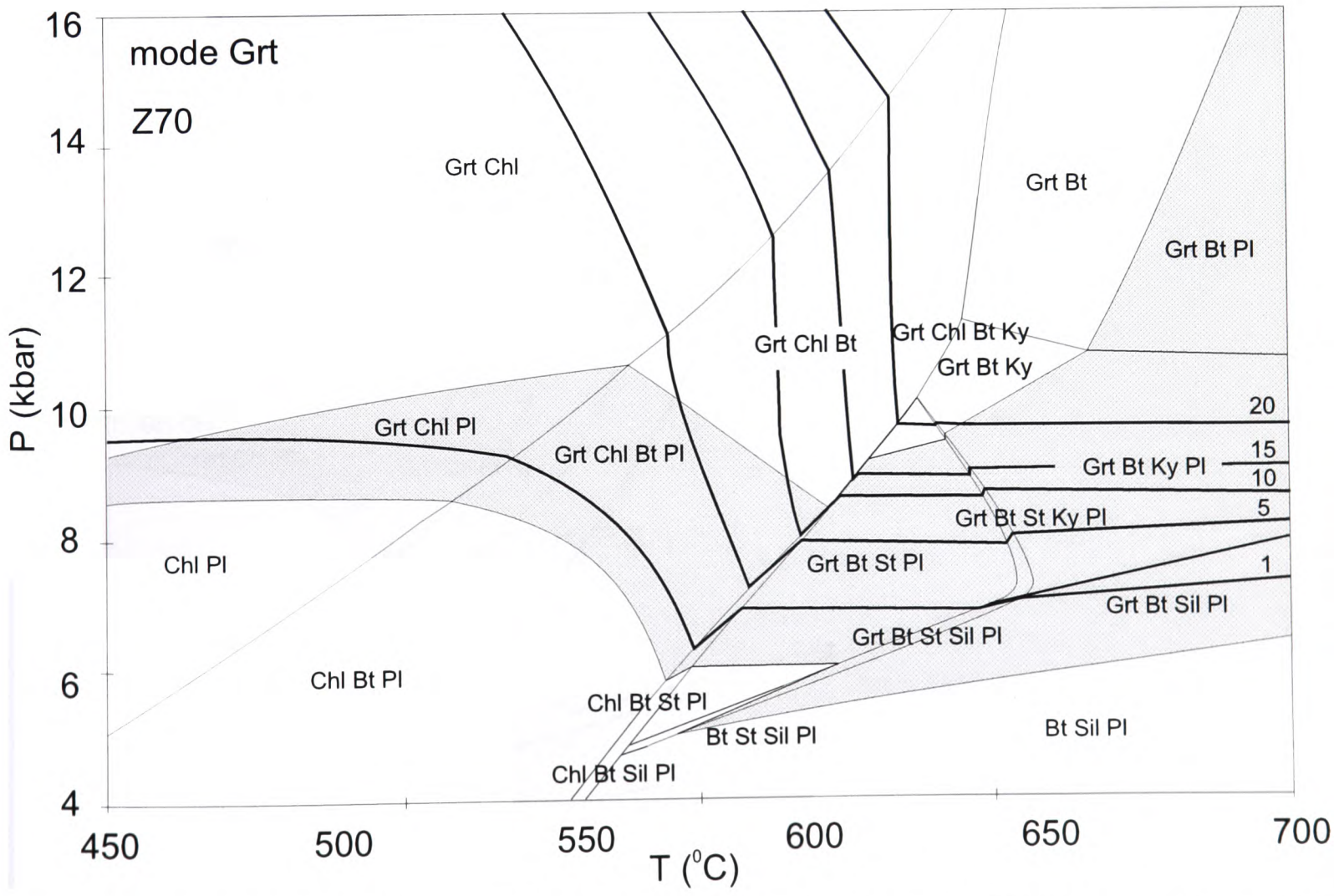


Figure 5.16.D. CNMnKFMASH (+ Ms + Qtz + H2O) pseudosection for sample Z70 illustrating isopleths of modal percent garnet. Note that the values are **molar oxide** percents, and that the figure is relative to only the other AFM phases, as THERMOCALC does not calculate moles of quartz and water. See Table 5.3 for recalculated molar percents. $aH_2O = 1.0$.

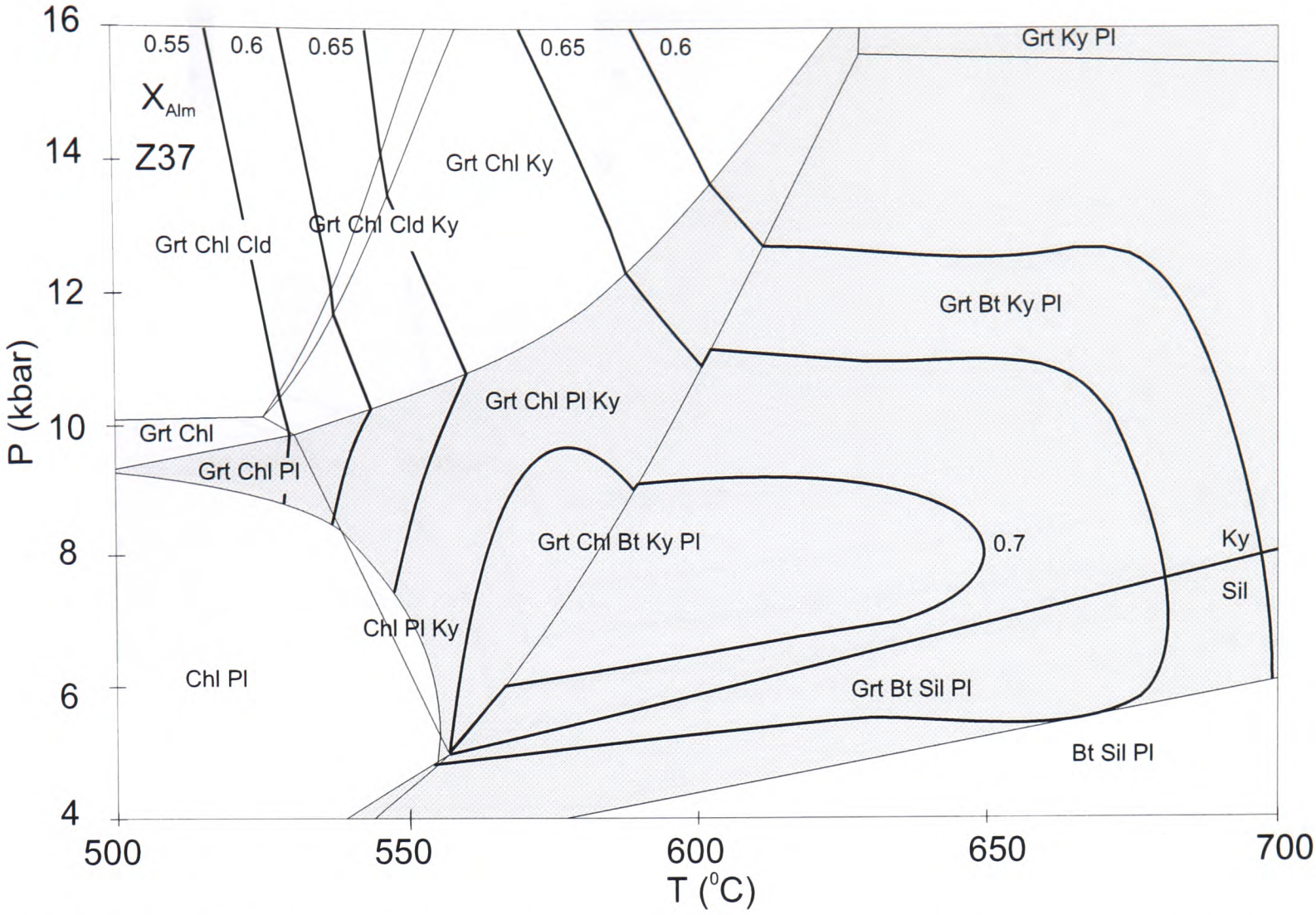


Figure 5.17.A. CNMnKFMASH (+ Ms + Qtz + H2O) pseudosection for sample Z37 illustrating isopleths of X_{Alm} in garnet. $aH_2O = 0.7$.

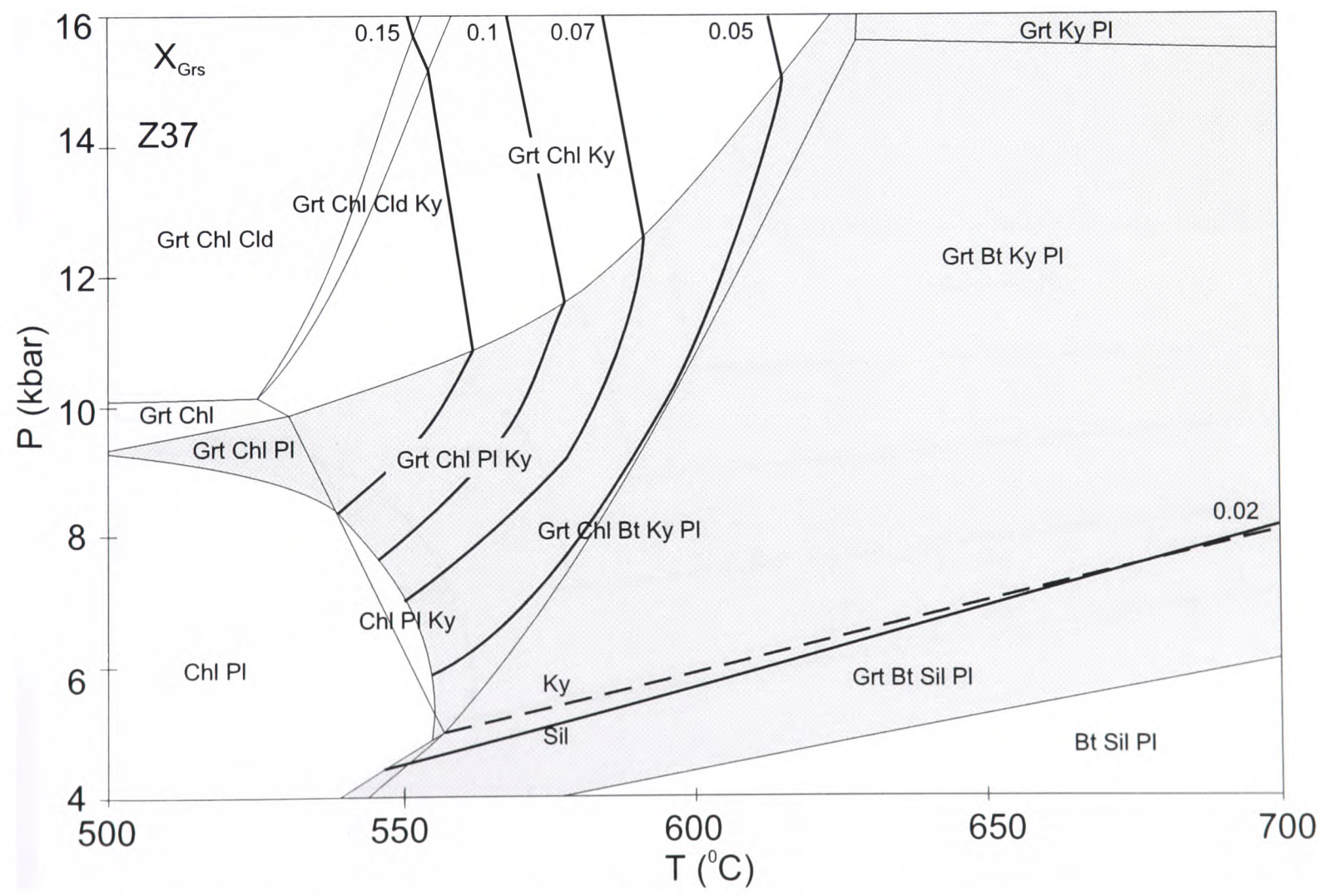


Figure 5.17.B. CNMnKFMASH (+ Ms + Qtz + H2O) pseudosection for sample Z37 illustrating isopleths of X_{Grs} in garnet. $aH_2O = 0.7$.

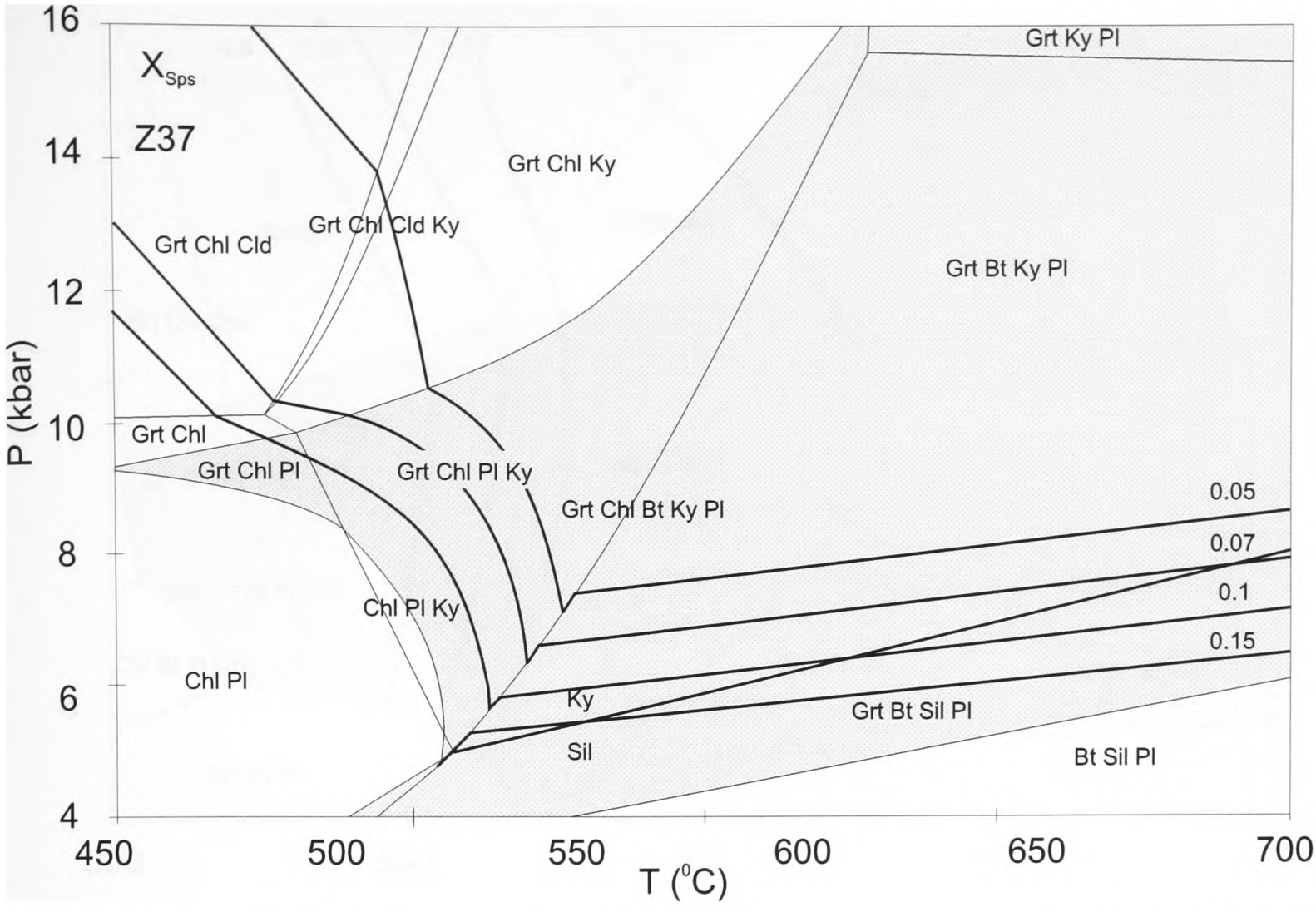


Figure 5.17.C. CNMnKFMASH (+ Ms + Qtz + H2O) pseudosection for sample Z37 illustrating isopleths of X_{Sps} in garnet. $aH_2O = 0.7$.

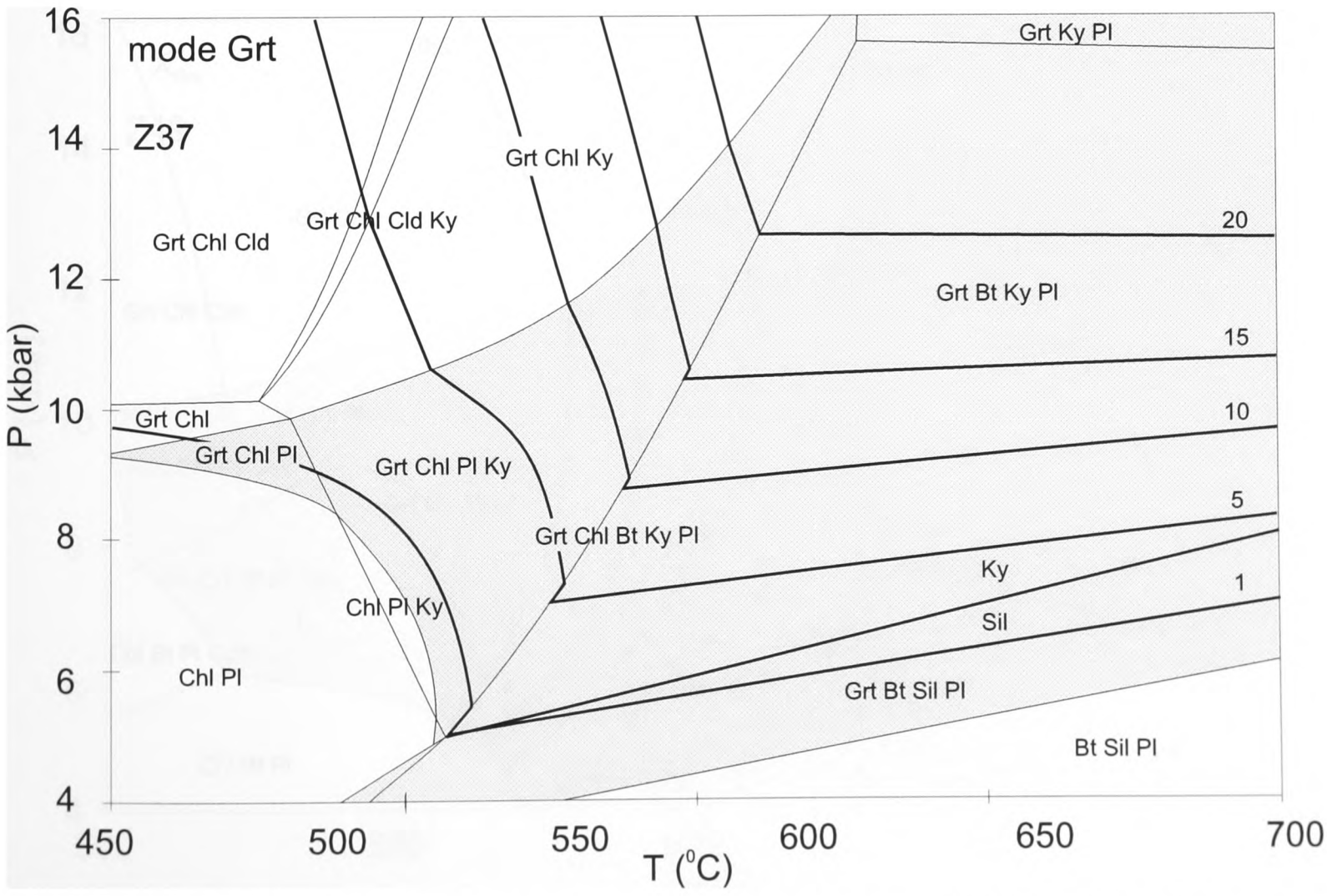


Figure 5.17.D. CNMnKFMASH (+ Ms + Qtz + H2O) pseudosection for sample Z37 illustrating isopleths of modal percent garnet. Note that the values are **molar oxide** percents, and that the figure is relative to only the other AFM phases, as THERMOCALC does not calculate moles of quartz and water. See Table 5.3 for recalculated molar percents. $aH_2O = 0.7$.

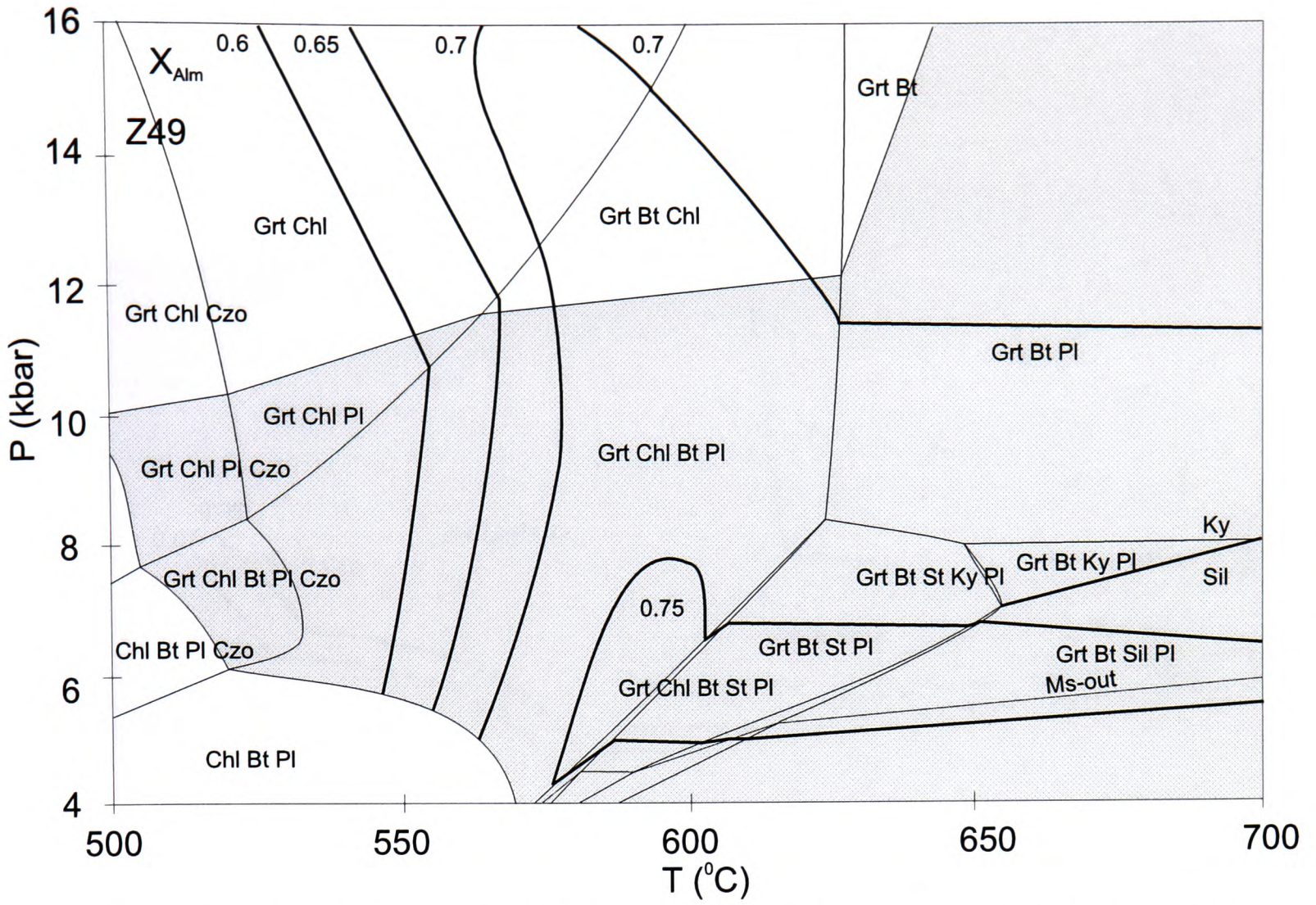


Figure 5.18.A. CNMnKFMASH (+ Ms + Qtz + H2O) pseudosection for sample Z49 illustrating isopleths of X_{Alm} in garnet. $aH_2O = 1.0$.

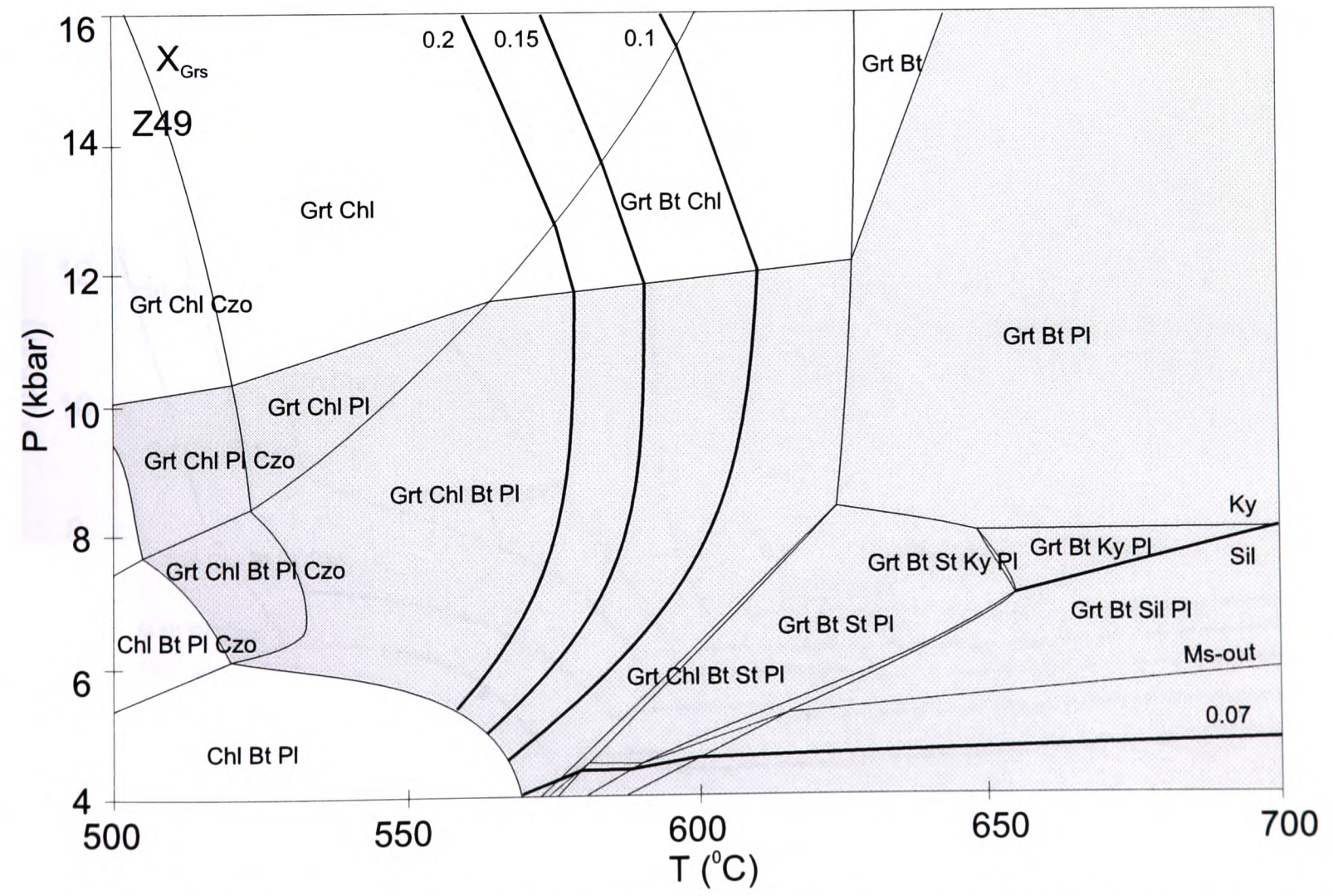


Figure 5.18.B. CNMnKFMASH (+ Ms + Qtz + H2O) pseudosection for sample Z49 illustrating isopleths of X_{Grs} in garnet. $aH_2O = 1.0$.

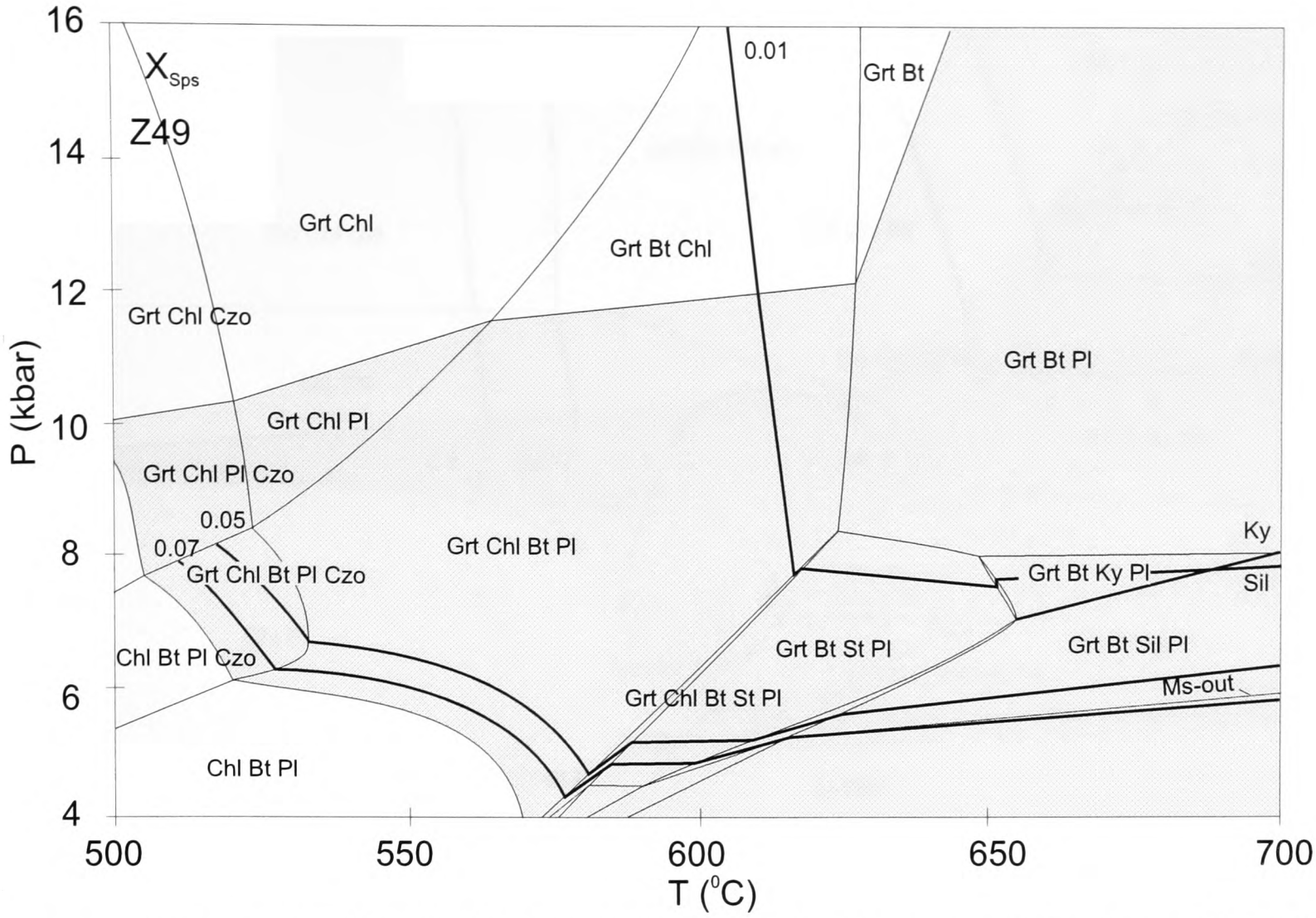


Figure 5.18.C. CNMnKFMASH (+ Ms + Qtz + H2O) pseudosection for sample Z49 illustrating isopleths of X_{Sps} in garnet. $aH_2O = 1.0$.

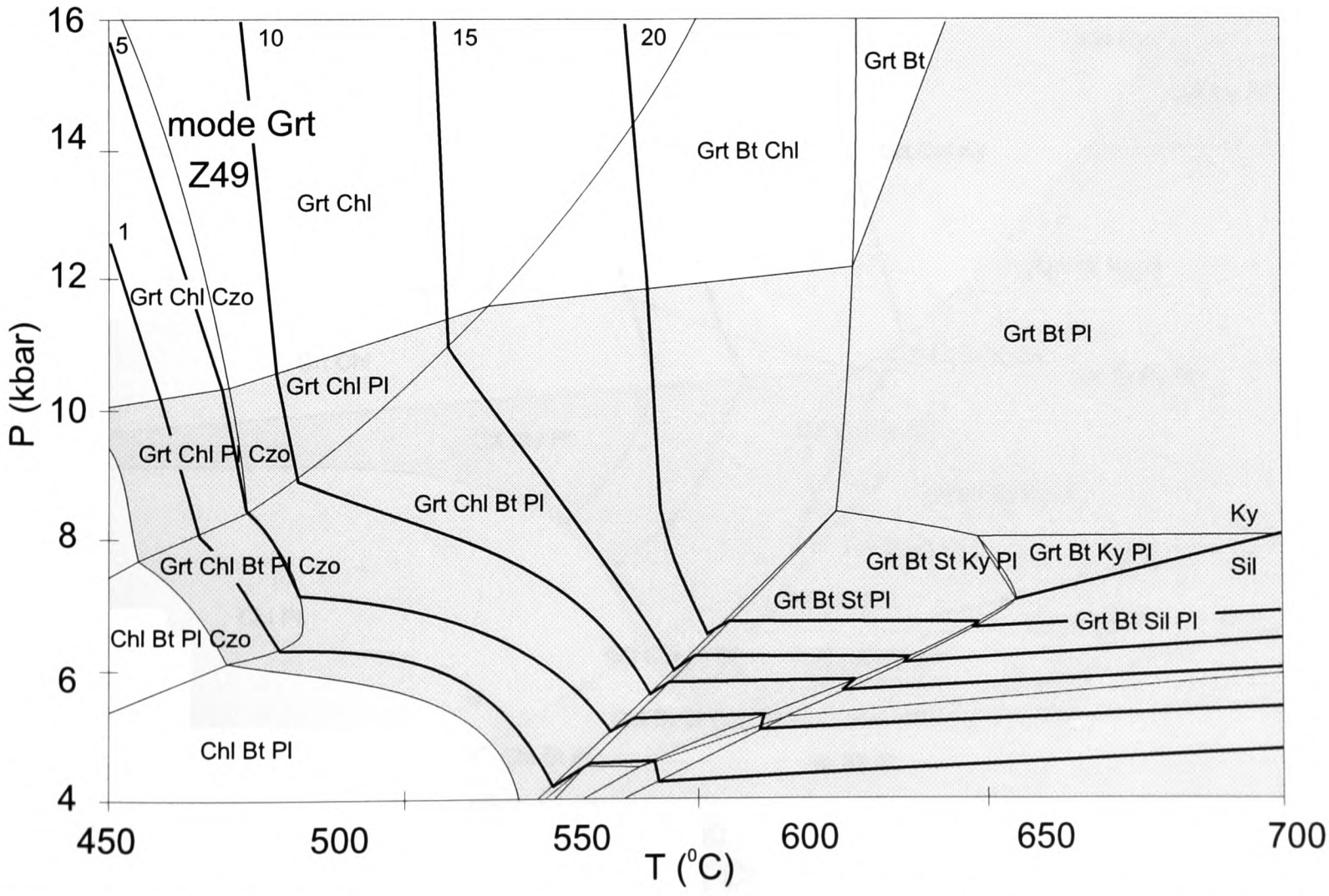


Figure 5.18.D. CNMnKFMASH (+ ms + qtz + H2O) pseudosection for sample Z49 illustrating isopleths of modal percent garnet. Note that the values are **molar oxide** percents, and that the figure is relative to only the other AFM phases, as THERMOCALC does not calculate moles of quartz and water. See Table 5.3 for recalculated molar percents. $aH_2O = 1.0$.

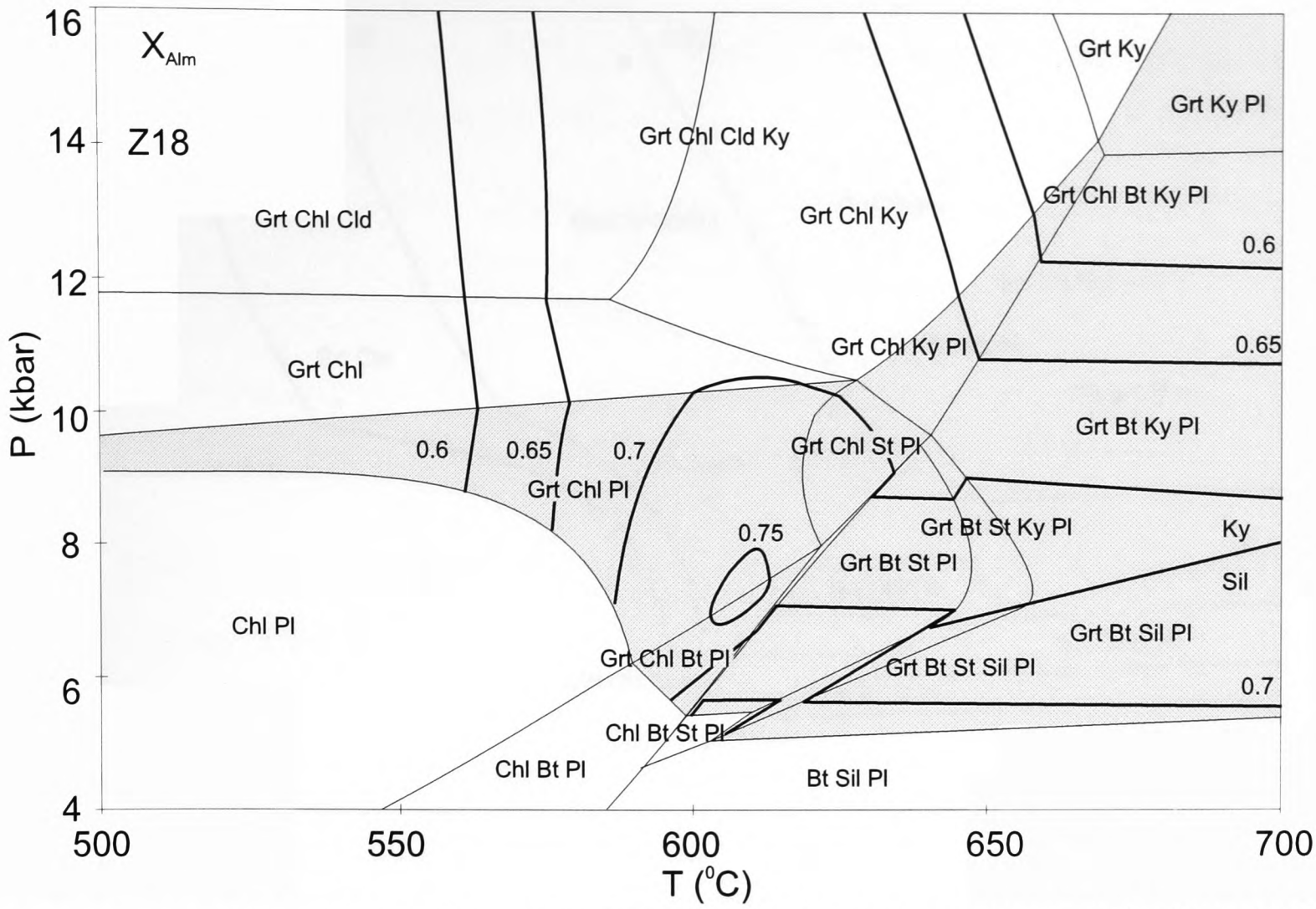


Figure 5.19.A. CNMnKFMASH (+ Ms + Qtz + H2O) pseudosection for sample Z18 illustrating isopleths of X_{Alm} in garnet. $aH_2O = 1.0$.

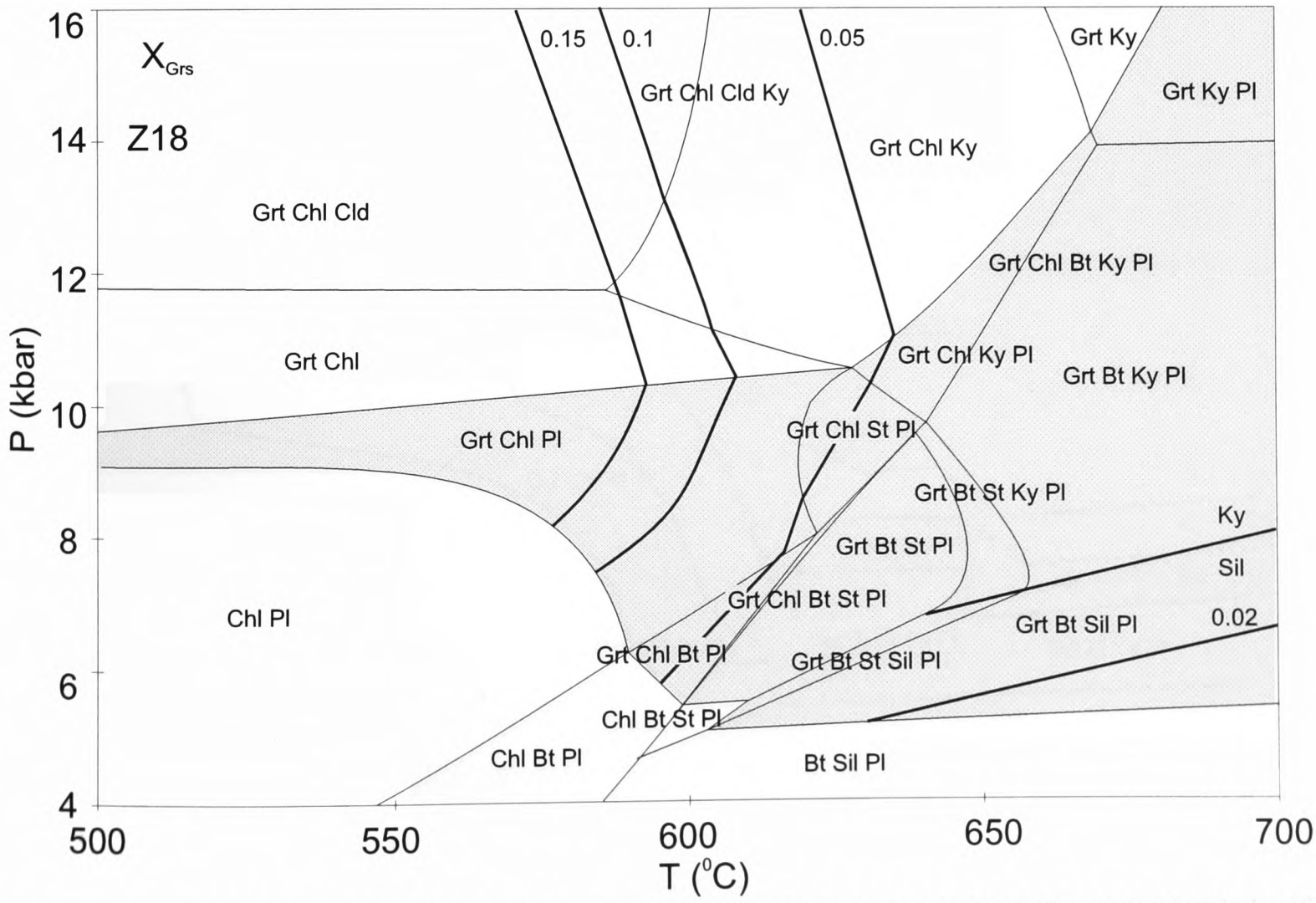


Figure 5.19.B. CNMnKFMASH (+ Ms + Qtz + H2O) pseudosection for sample Z18 illustrating isopleths of X_{Grs} in garnet. $aH_2O = 1.0$.

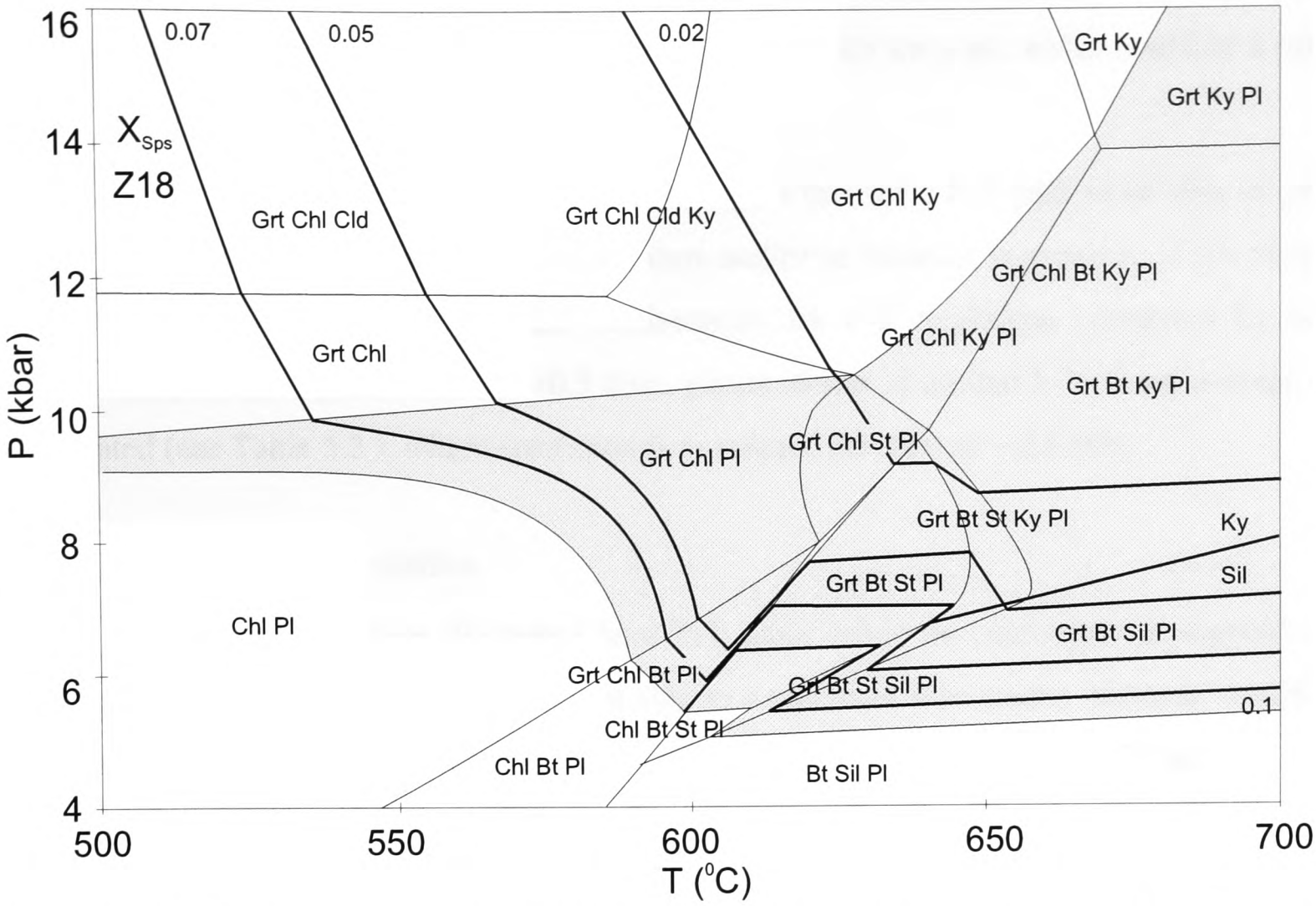


Figure 5.19.C. CNMnKFMASH (+ Ms + Qtz + H2O) pseudosection for sample Z18 illustrating isopleths of X_{Sps} in garnet. $aH_2O = 1.0$.

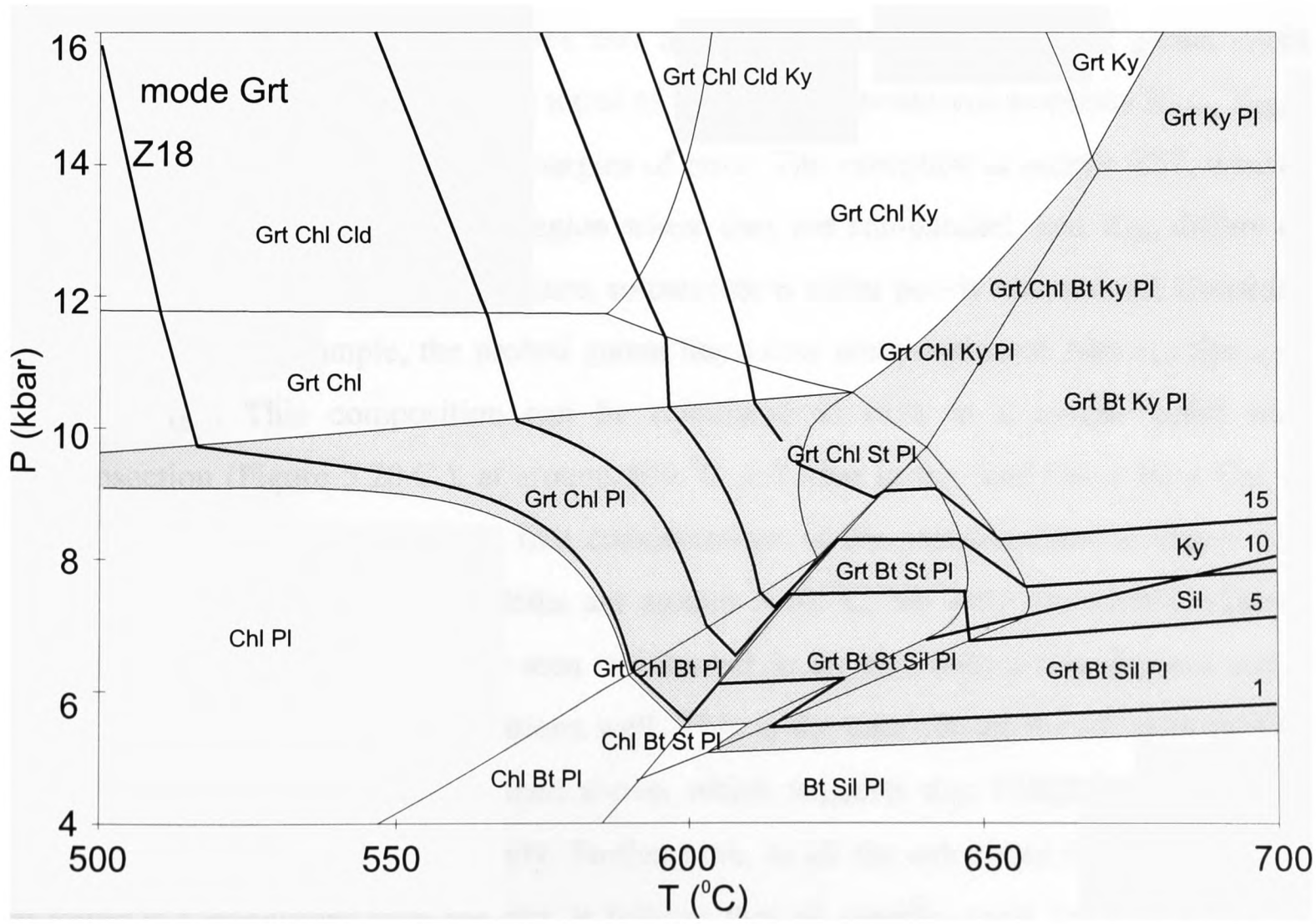


Figure 5.19.D. CNMnKFMASH (+ Ms + Qtz + H2O) pseudosection for sample Z18 illustrating isopleths of modal percent garnet. Note that the values are **molar oxide** percents, and that the figure is relative to only the other AFM phases, as THERMOCALC does not calculate moles of quartz and water. See Table 5.3 for recalculated molar percents. $aH_2O = 1.0$.

analyses all show a slight step in the X_{Sps} profile shortly after the core, which could be a result of the above equilibria acting on the assemblage.

From the plots of mode garnet, it can be seen that for a P-T path to be able to grow garnet it must involve an increase in temperature and/or an increase in pressure, if we assume it starts to grow at the garnet isograd. Furthermore, for P-T conditions calculated for Suru Valley samples i.e. 620-650 ^{0}C, 9.5-10.5 kbar, garnet modes of around 5-20 % on average are calculated (see Table 5.3.), which corresponds to volume percents of ~ 15-30%.

5.3.4. Garnet core calculation

The previous section illustrated how P-T space could be contoured for isopleths of mineral composition in order for us to be able to understand how zoned minerals would be expected to change in composition as pressure and temperature change. Using the same rationale it is possible to calculate isopleths for the exact measured garnet core composition, which should ideally meet at a point which is the P-T at which garnet first grew. By plotting the average P-T of final garnet rim equilibration it is possible to obtain a start and an end point for the P-T path along which garnet grew. This is plotted for Suru Valley samples in Figures 5.20.A.-F.

From the plots, it can be seen that the P-T positions of calculated garnet cores is extremely successful if considered in terms of the three compositional isopleths X_{Alm}, X_{Grs} and X_{Sps} meeting at a point, within the margins of error. The exception is sample Z37, where the X_{Alm} and X_{Sps} isopleths meet in a region where they are sub-parallel, and X_{Grs} differs quite significantly in temperature and pressure, so pressure is rather poorly constrained. Considering sample Z70 as an example, the probed garnet has a core composition of Alm $_{71.6}$ Sps $_{6.7}$ Pyp $_{11.2}$ Grs $_{10.6}$. This composition can be calculated to exist at a unique point on the pseudosection (Figure 5.20.C.), at around 590 ^{0}C, 6.7 kbar in the field Grt + Bt + Chl + Pl, which is what was expected from first considerations of the pseudosection in Figure 5.13.E The errors on the calculated isopleths are around 5-10 ^{0}C, but only the median values are illustrated for clarity; they can be seen to intersect in an area only a few degrees and bars across, constraining the P-T conditions well. This is the case for all the samples modelled, with the exception of Z37 mentioned above, which suggests that THERMOCALC models garnet core compositions realistically. Furthermore, as all the calculated core conditions plot at lower P-T conditions than the rim, it follows that all samples must have followed a P-T path involving both burial and heating. This is elaborated further in later sections.

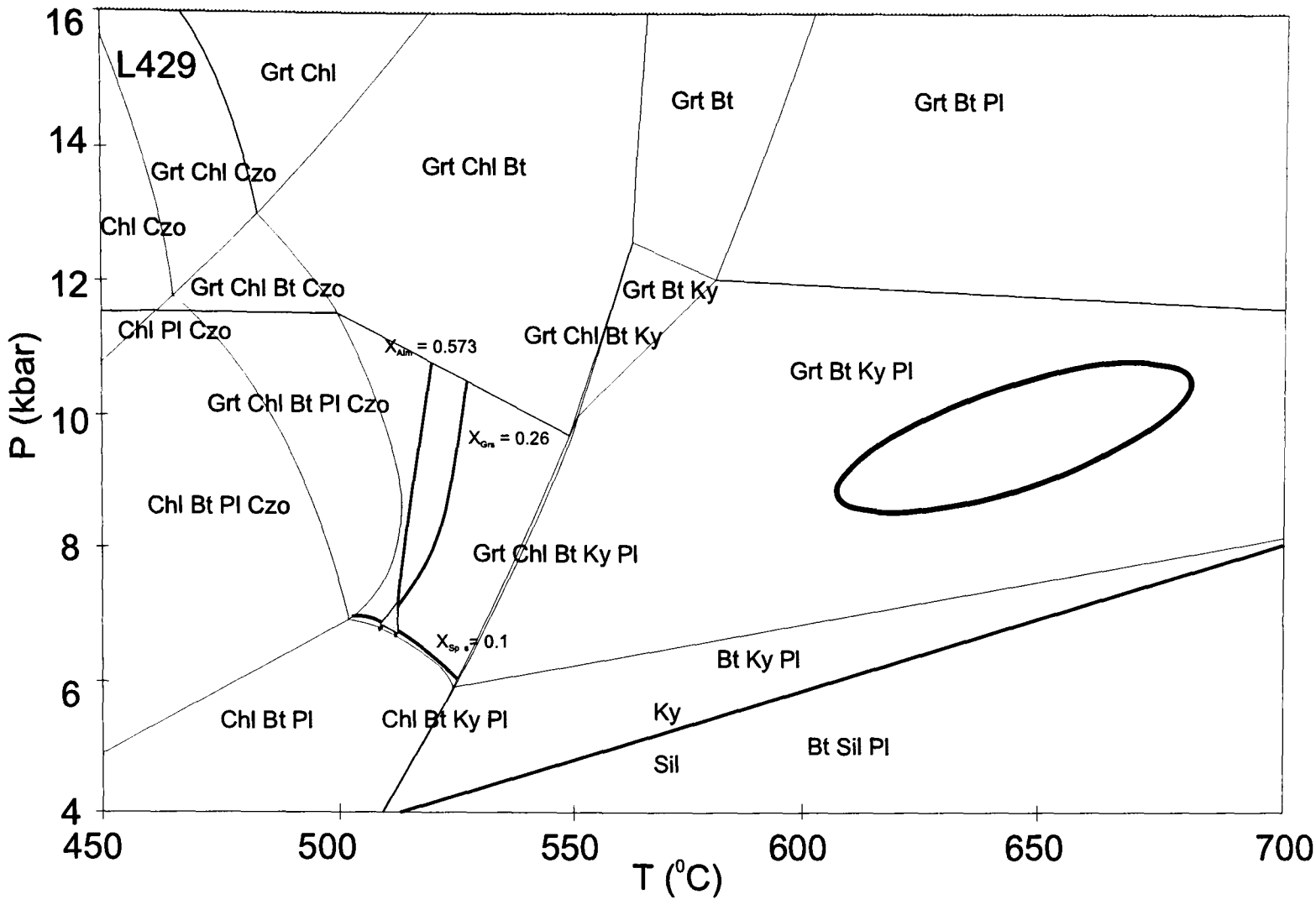


Figure 5.20.A. CNMnKFMASH pseudosection for sample L429 illustrating garnet core isopleths and the error ellipse for the THERMOCALC calculated average rim P-T. Errors on isopleths around 5-10 °C.

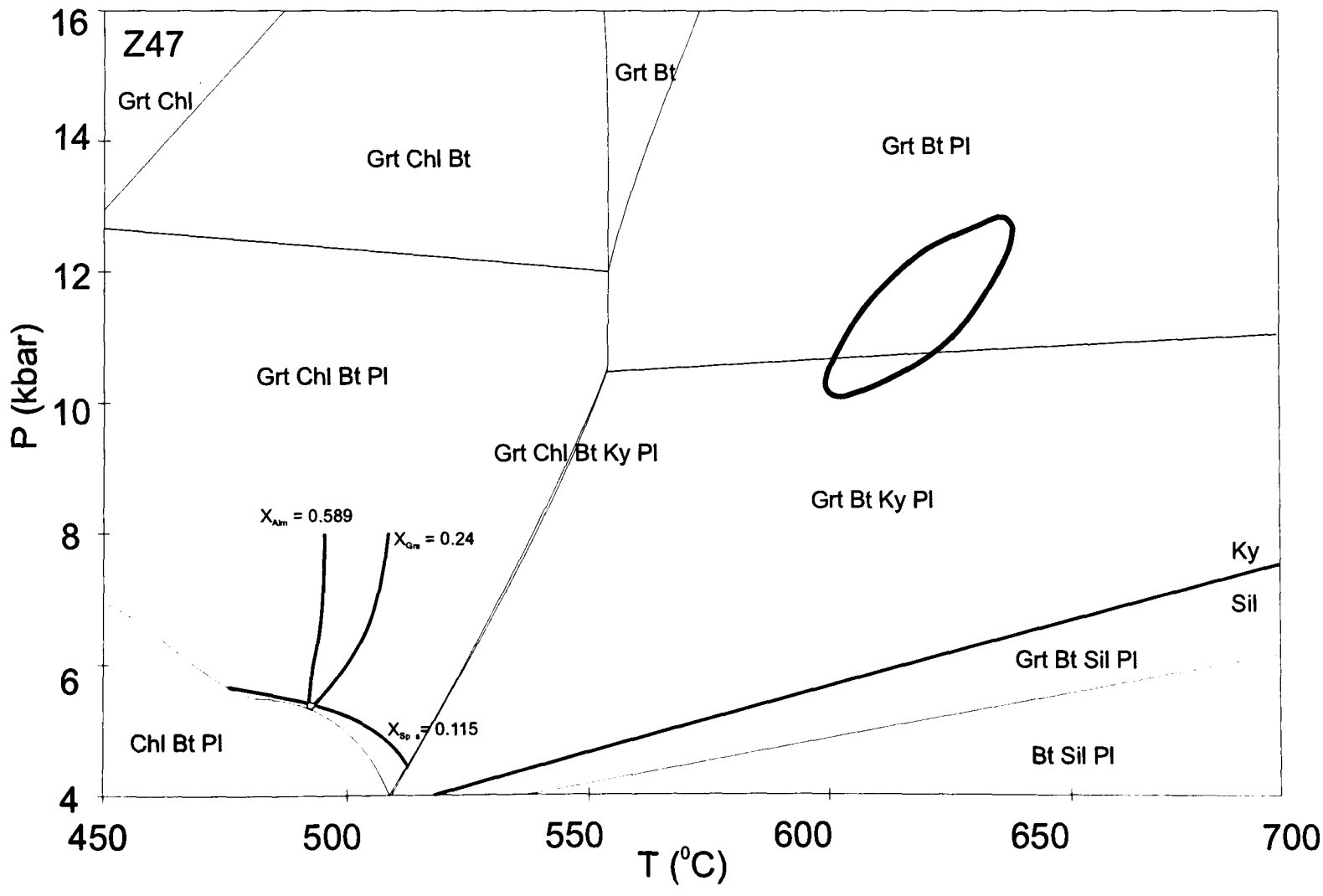


Figure 5.20.B. CNMnKFMASH pseudosection for sample Z47 illustrating garnet core isopleths and the error ellipse for the THERMOCALC calculated average rim P-T. Errors on isopleths around 5-10 °C.

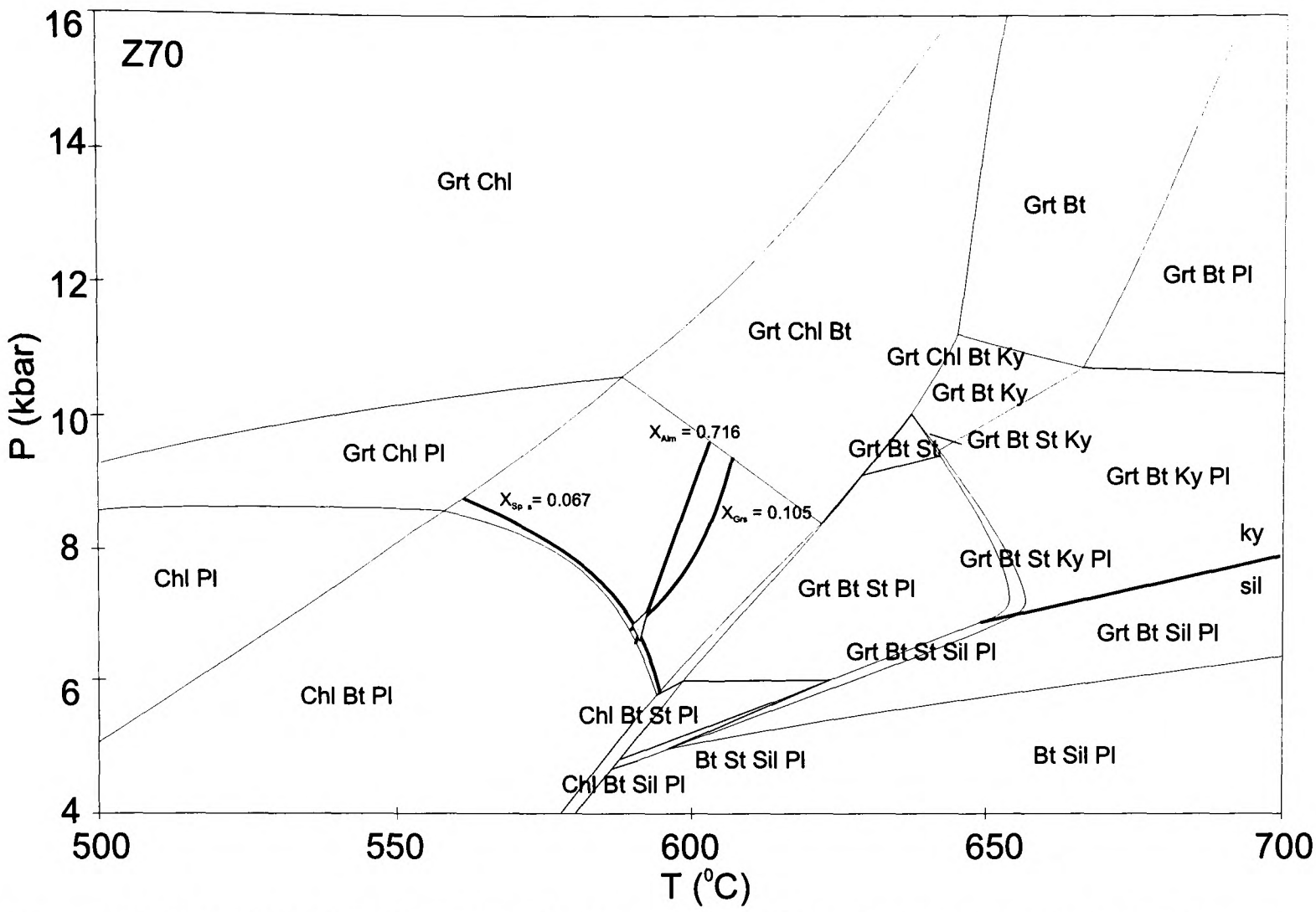


Figure 5.20.C. CNMnKFMASH pseudosection for sample Z70 illustrating garnet core isopleths. Errors on isopleths around 5-10 °C. For Z70 there is no THERMOCALC average P-T due to the lack of plagioclase in the assemblage. Conventional thermometry gives a peak T of 640-650 °C, and a P of around 9.5-10.5 kbar is estimated from surrounding samples and the pseudosection.

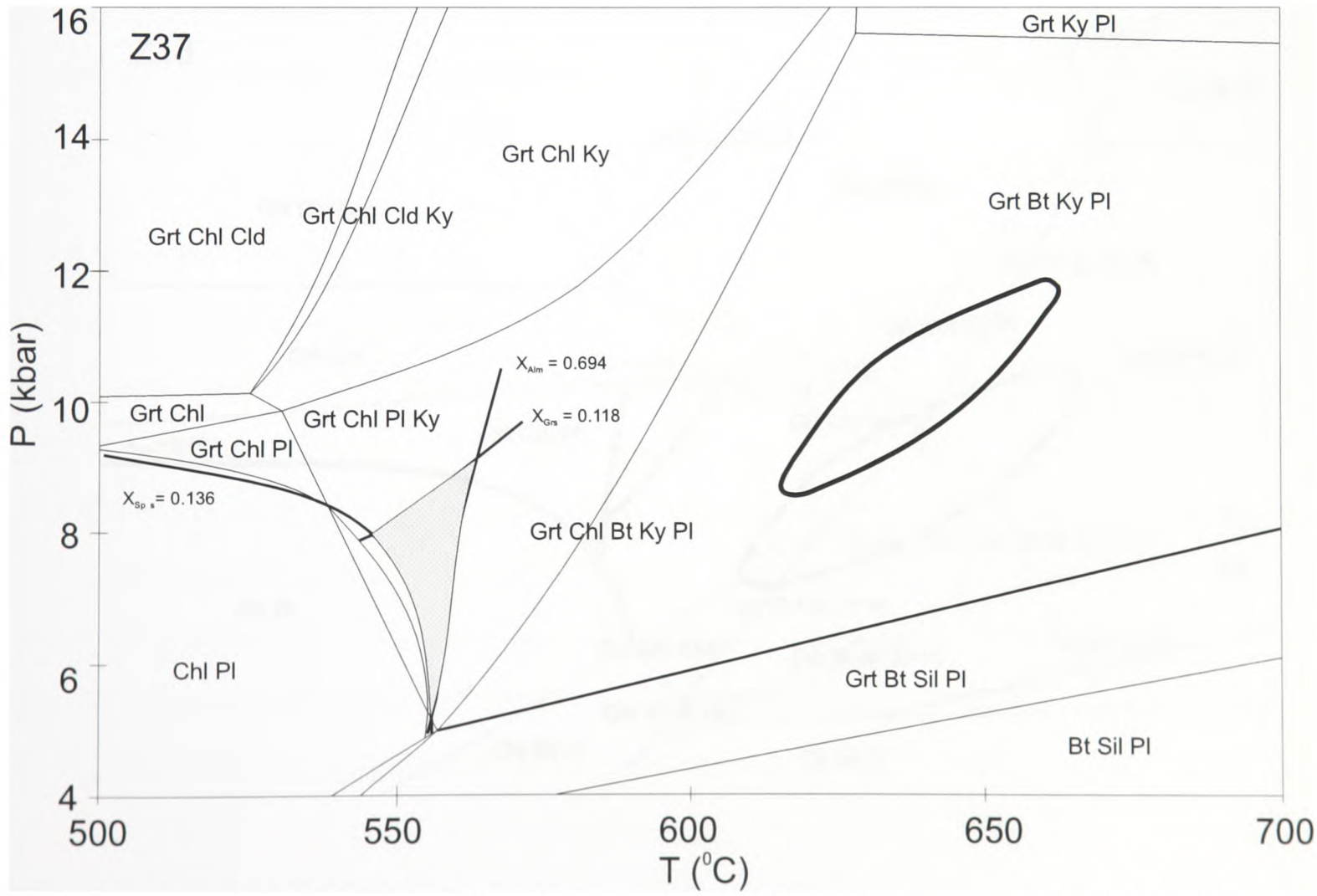


Figure 5.20.D. CNMnKFMASH pseudosection for sample Z37 illustrating garnet core isopleths and the error ellipse for the THERMOCALC calculated average rim P-T. Errors on isopleths around 5-10 °C.

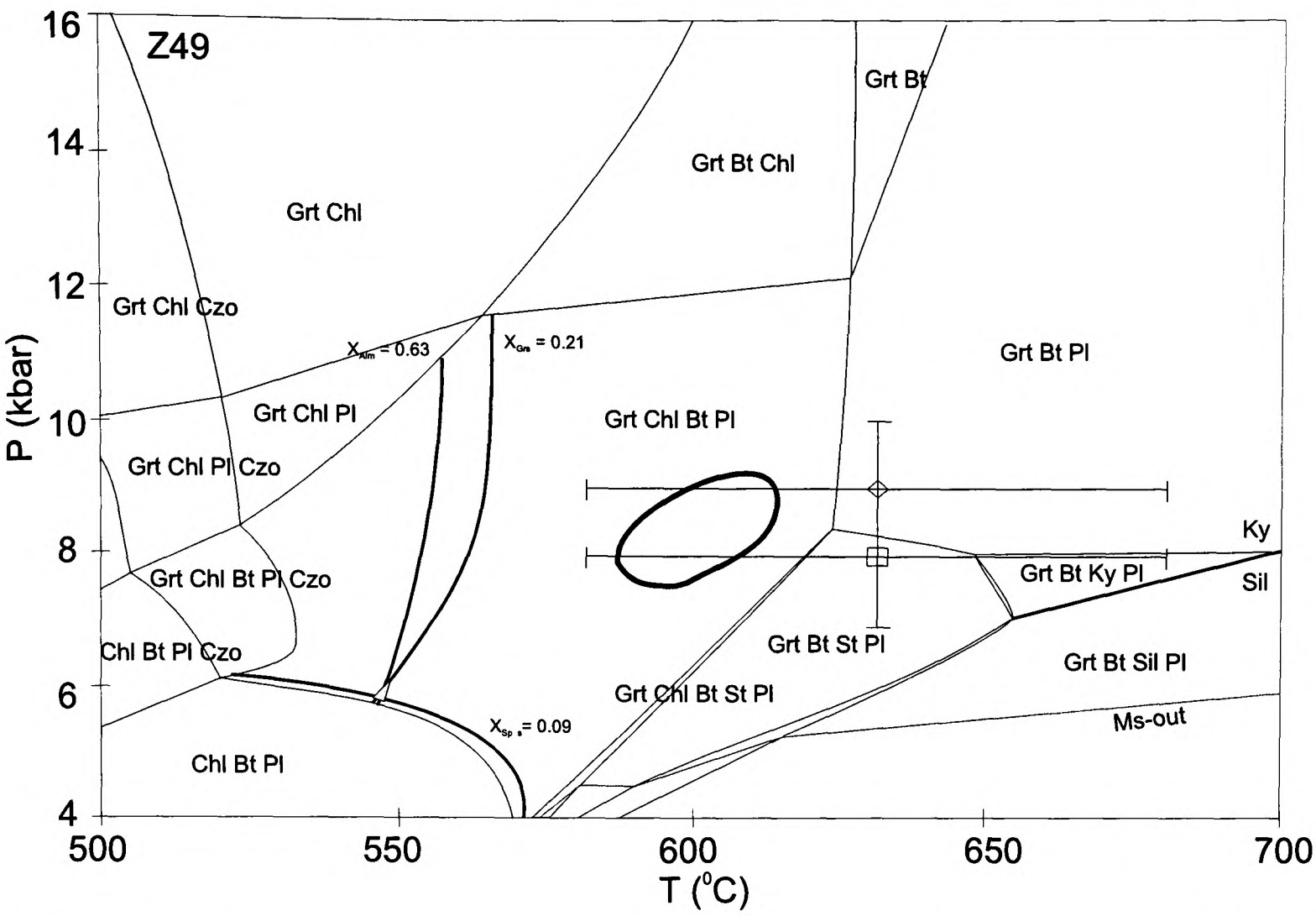


Figure 5.20.E. CNMnKFMASH pseudosection for sample Z49 illustrating garnet core isopleths. Errors on isopleths around 5-10 °C. THERMOCALC average P-T error ellipse is shown, as are the results of garnet-biotite thermometry and GPMB-Mg (circle) and GASP (square) barometry, with error bars of ± 50 °C and ± 1 kbar.

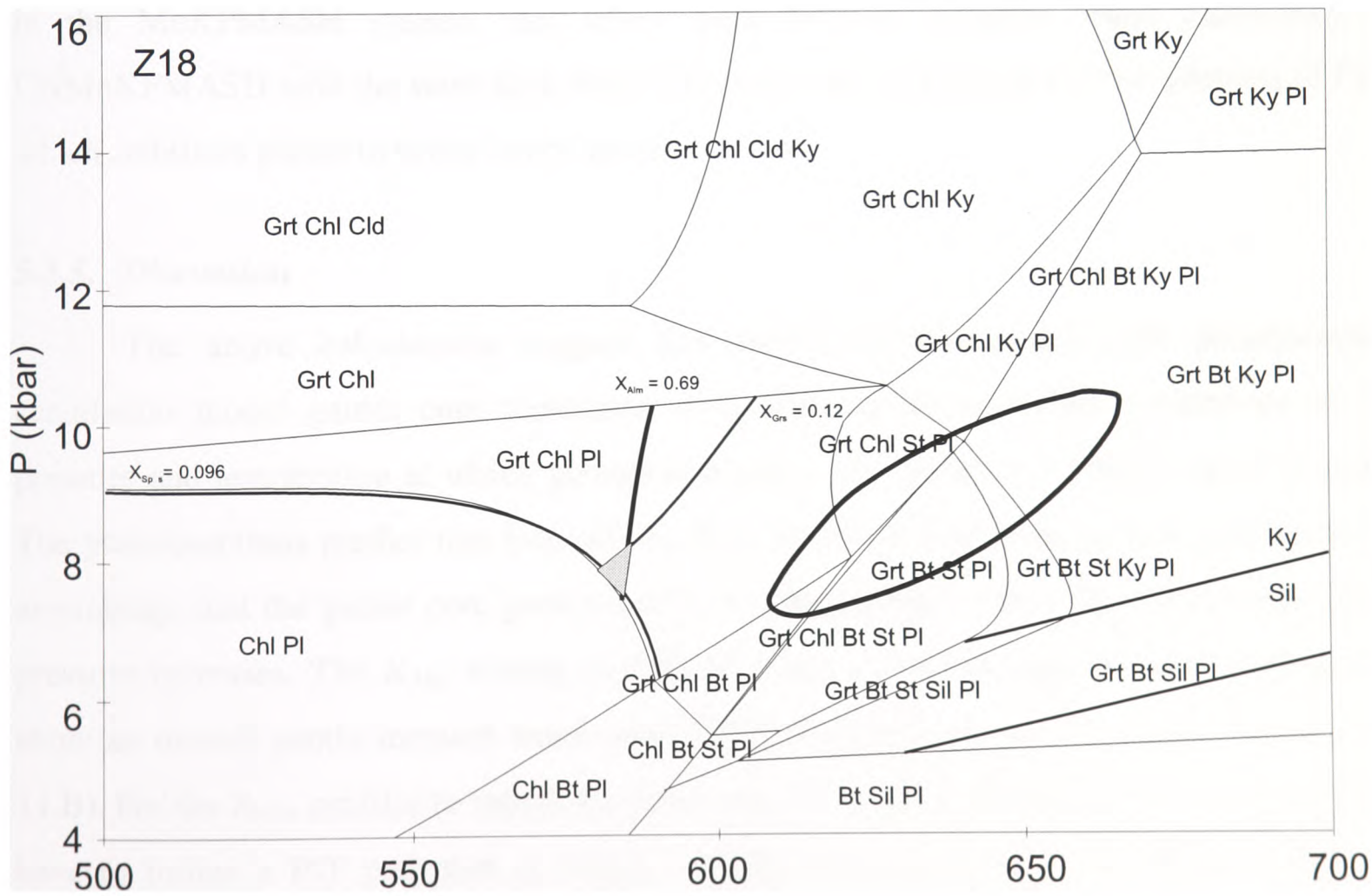


Figure 5.20.F. CNMnKFMASH pseudosection for sample Z18 illustrating garnet core isopleths and the error ellipse for the THERMOCALC calculated average rim P-T. Errors on isopleths around 5-10 °C.

Although THERMOCALC appears to model compositional contours well, there are slight discrepancies in the core assemblages calculated for samples L429 and Z49, as discussed in section 5.3.2.2. From Figures 5.20.A. & E., the core isopleths can be seen to meet in the field Grt + Bt + Chl + Pl and not in Grt + Bt + Chl + Pl + Czo, even though clinozoisite is observed throughout the cores of both these garnets.

For sample Z49 (Figure 5.20.E.) the results of conventional thermobarometry, (the garnet-biotite exchange thermometer and GPMB-Mg and GASP barometers) are plotted in addition to the THERMOCALC average P-T to illustrate that a calculated value for rim conditions may fall within the Grt-Bt-Pl-Ky stability field.

A further point to note from Figure 5.20. is that the calculated garnet core isopleths do not coincide exactly with the garnet-in isograd, although they are close. Vance & Mahar (1998) noted that their calculated core spessartine value occurred where the calculated volume of garnet was equal to 1 modal %, and attributed this to resorption and regrowth of garnet at the isograd as a result of changing the effective bulk composition due to the first appearance of garnet. This effect is not so noticeable here due to the way in which the bulk rock MnO is estimated (see earlier), although X_{Sps} does not always parallel the Grt = 0 isopleth. However, if bulk rock MnO is estimated by calculating the value of X_{Sps} in garnet at the Grt = 0 isopleth in the MnKFMASH system, this effect does become apparent when calculating in CNMnKFMASH with the same bulk MnO. However, this is attributed to the addition of CaO which stabilises garnet to lower temperatures.

5.3.5. Discussion

The above calculations suggest that bulk composition data and pseudosection calculation model garnet core conditions well. This allows confident predictions of the pressure and temperature at which garnets first grew, and therefore a start to our P-T paths. The pseudosections predict that isopleths of X_{Alm} in garnet will be steep and positive in the assemblage that the garnet core grew in, with X_{Grs} being shallower at first, steepening up as pressure increases. The X_{Alm} zoning profiles from the garnets themselves vary slightly, but show an overall gentle increase from core to rim, flattening out at near rims (Figures 5.6.-11.B). For the X_{Alm} profiles to satisfy the constraints of the pseudosections, the samples would have to follow a P-T path that is slightly shallower than the garnet isopleths at first, i.e. increasing reasonably steeply in pressure and temperature, before flattening out near the end (Figure 5.22.A.). X_{Grs} profiles are slightly more irregular, especially L429 and Z49 that contain clinozoisite inclusions, and may represent local disequilibrium with Ca in places (see

Chapter 3). In general, however, X_{Grs} is flat in the core of garnets before dropping off towards the rim. This is also consistent with a P-T path as described above. Samples Z37 and Z49 show a consistent slight increase in X_{Grs} before decreasing again, but this could be accommodated by a similar P-T path that is slightly steeper than the slope of the isopleths. Sample Z18 is from the Suru Dome, and shows rather different compositional zoning patterns to the overlying nappe rocks, which suggests a different P-T path. XAlm is much flatter in the core region, even showing a slight decrease from the core towards the rim on the left-hand side of the garnet (Figure 5.11.B.), implying a much steeper P-T path during the growth of the core before flattening out towards the rim (Figure 5.22.B.). This steep path would also explain the increase in X_{Grs} in the core region followed by the steep decrease towards the rim.

From Table 5.3. a number of systematic differences between the calculated and measured modes and compositions become apparent. X_{Alm} values are in reasonable agreement, although calculations tend to underestimate the values slightly, as for X_{Grs} values. Although the calculations predict a decrease in X_{Sps} in the manner observed, the calculations tend to overestimate the amount of spessartine at the garnet rim e.g. for L429 a "rim" value of X_{Sps} = 0.012 is predicted, whereas the actual value is 0.002. The exception is sample Z18 which shows an upturn in the X_{Sps} profile, which suggests a degree of re-equilibration. The calculated amounts and compositions of plagioclase, where appropriate, are also systematically different, in that THERMOCALC nearly always underestimates the molar amounts of the phase, and X_{An}.

The reason for these discrepancies, which are much larger than those for the core calculations, is likely to be largely a result of garnet fractionation, as discussed in Vance & Mahar (1998), and Spear *et al.* (1991). The effect of garnet fractionation will be to change the effective bulk composition of the rock as garnet grows, which will have the most noticeable effect on X_{Sps}, as MnO fractionates so strongly into garnet. In the case of plagioclase, as it is the only other calcium-bearing phase, the amount of calcium in garnet will affect the amount in plagioclase. THERMOCALC predicts a decrease in X_{An} and modal amount of plagioclase from garnet core to rim, as expected in pelites (Spear *et al.*, 1991), so possibly either the predicted core amount and composition of plagioclase is underestimated.

Thus, it is only really reasonable to consider the garnet core region in terms of modelling using the "equilibrium" bulk composition obtained from point counting and microprobe data, and it may be dangerous to extrapolate to outer regions of the garnet. It would be possible to construct pseudosections calculated every few degrees and changing the

bulk composition each time, but, as pointed out in Vance & Mahar (1998), this would be an unreasonably time-consuming process

5.3.6. "Garnet fractionation" pseudosections

Although it is impractical to model garnet fractionation realistically using the THERMOCALC-generated phase diagram approach, it is possible to consider the end-member effect of complete garnet fractionation, whereby pseudosections are calculated for a bulk composition with garnet completely removed. The removal of garnet from the bulk composition will have the effect of increasing bulk X_{Mg} and the Al_2O_3/FeO+MgO ratio, and decreasing the bulk MnO and CaO. The calculated pseudosections are shown in Figures 5.21.A.-F., and the modes and compositions tabulated in Table 5.4.

The effect of decreasing the amount of MnO is to shift the garnet-in isograd to higher temperatures and pressures. Decreasing CaO has a similar effect, and also restricts the range of Grt + Pl bearing fields, most notable in sample Z70, which has a low bulk CaO without the removal of garnet. Increasing the Al_2O_3/FeO+MgO ratio stabilises kyanite to higher pressures, and also increases the range of staurolite-bearing trivariant assemblages. The consequences of changing the bulk composition in this way does not appear to affect all the samples in the same way. For each sample the amount of garnet predicted is less than that for the equilibrium model at peak conditions, as is to be expected, and the volumes generally correlate better with the observed values. Accordingly, the amount of muscovite calculated increases, and is also closer to measured values. Samples Z47, Z37 and Z18 predict more garnet than is observed, whilst Z70, L429 and Z49 predict less. A similar trend is observed with the calculated values of X_{Sps} at peak conditions, in that Z47, Z37 and Z18 are predicted higher values for X_{Sps} than is observed and Z70, L429 and Z49 are predicted lower. There does not appear to be any systematic reason to account for this other than that the removal of garnet from the bulk composition has a greater effect on Z70, L429 and Z49. Generally, however, the fractionated bulk compositions predict a volume of garnet that is closer to the measured value.

The isopleths of garnet rim compositions are also plotted on Figures 5.21.A-F as a final consistency check. If the garnet rim grew in complete equilibrium with the matrix, one would expect the rim compositions to lie at the garnet-in phase boundary as calculated here for a rock with no garnet. It is clear from these pseudosections that this is nearly always not the case. This may arise as a result of two possible reasons. Firstly, the errors on both the isopleths and the phase boundaries in the relevant phase field (namely Grt-Bt-Ky-Pl-Ms-Qtz-H_2O) are in the region of 1-1.3 kbar. Within these margins of error, the phase boundaries and

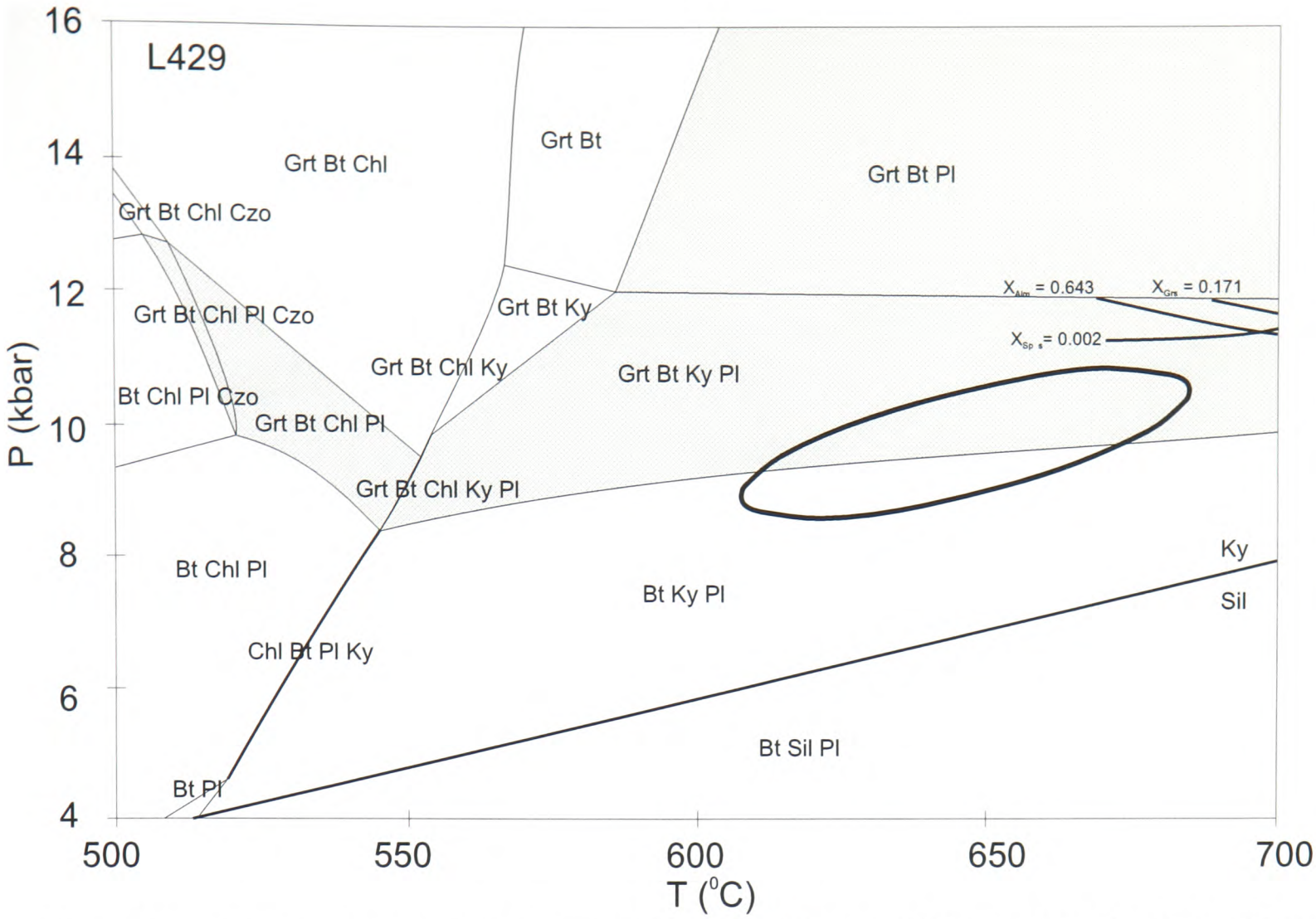


Figure 5.21.A. P-T pseudosection in CNMnKFMASH (+ Ms + Qtz + H_2O) for sample L429, calculated for a bulk composition without garnet in order to model garnet fractionation. Peak average P-T error ellipse is also plotted.

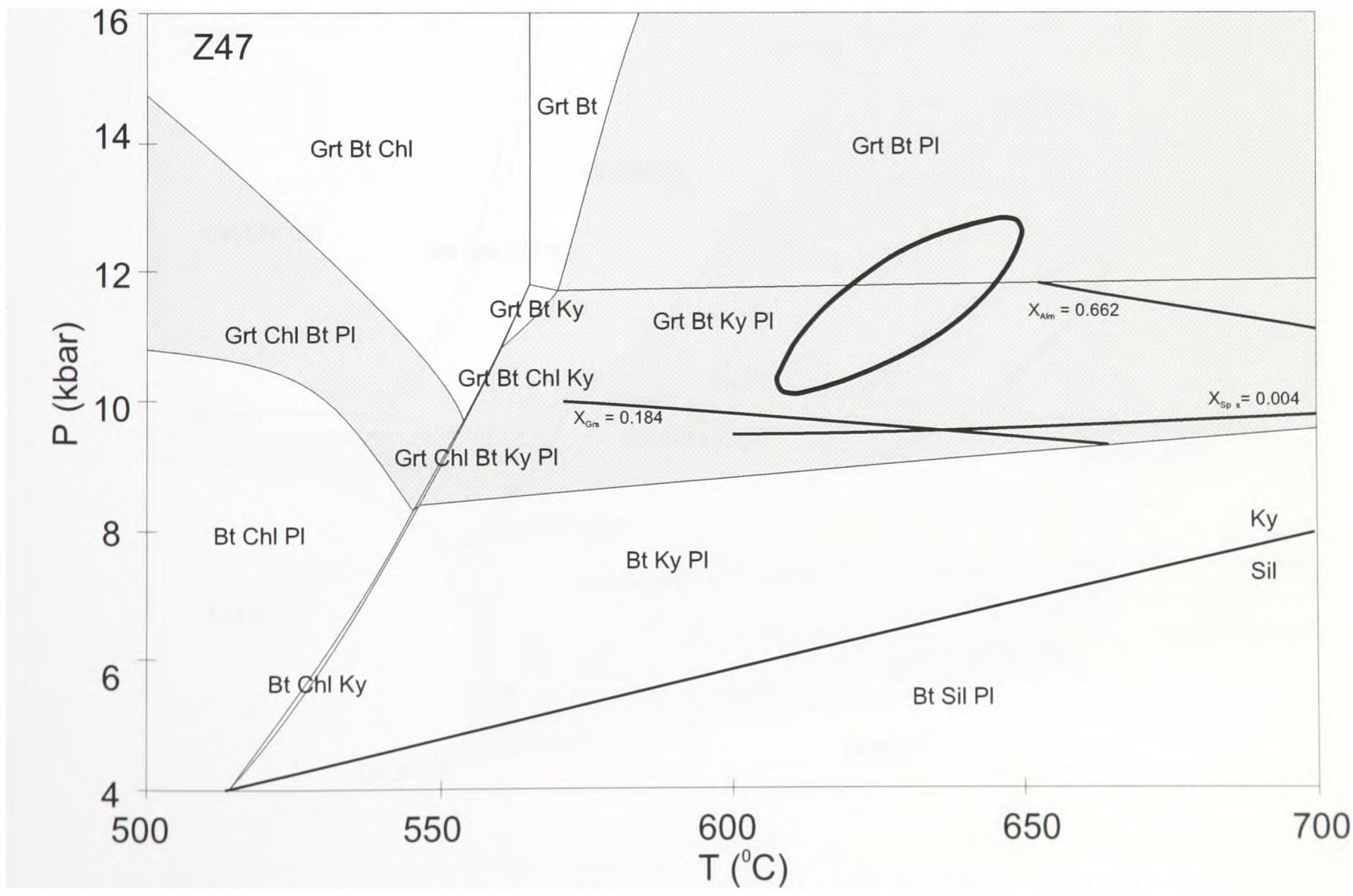


Figure 5.21.B. P-T pseudosection in CNMnKFMASH (+ Ms + Qtz + H_2O) for sample Z47, calculated for a bulk composition without garnet in order to model garnet fractionation. Peak average P-T error ellipse is also plotted.

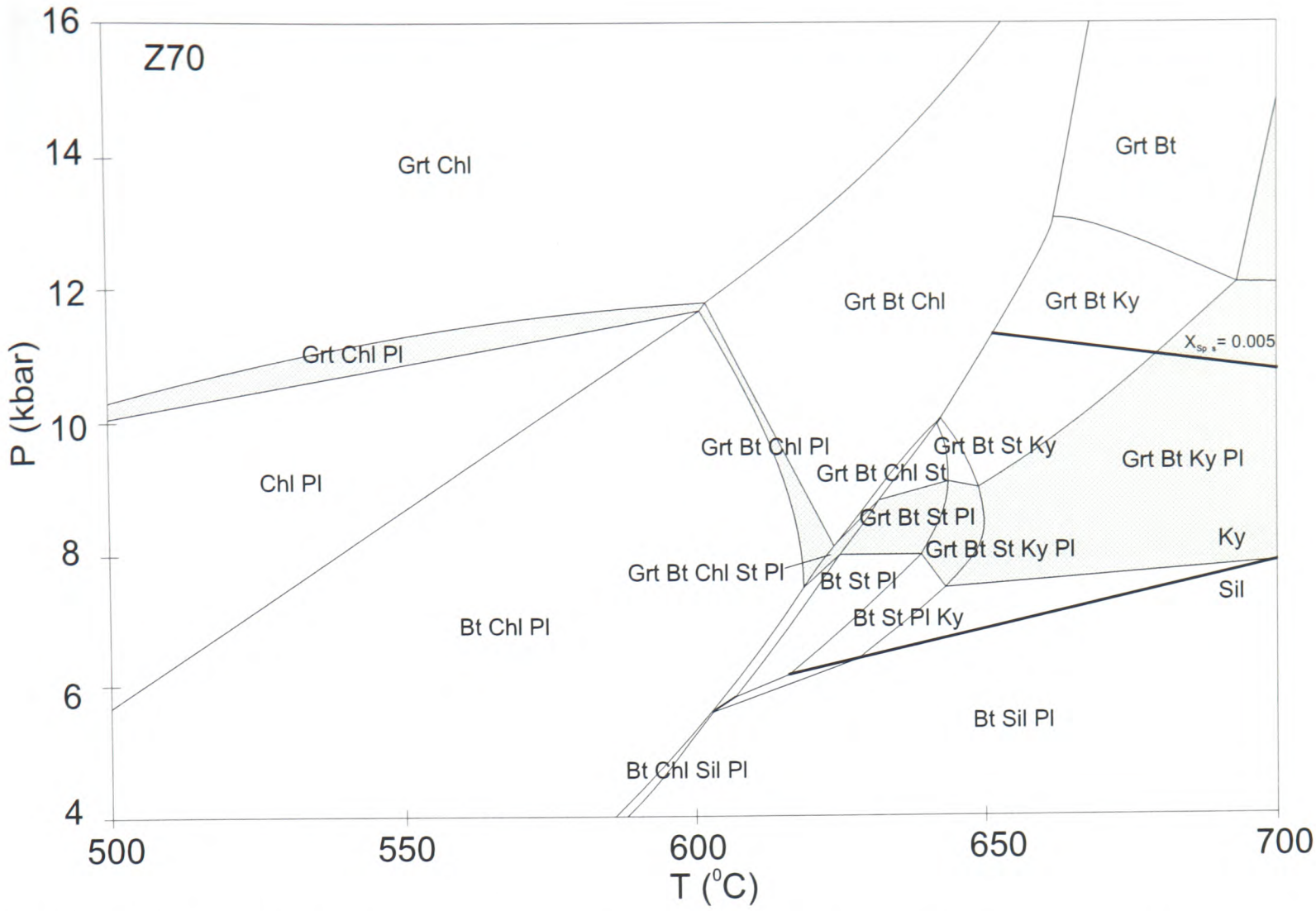


Figure 5.21.C. P-T pseudosection in CNMnKFMASH (+ Ms + Qtz + H_2O) for sample Z70, calculated for a bulk composition without garnet in order to model garnet fractionation.

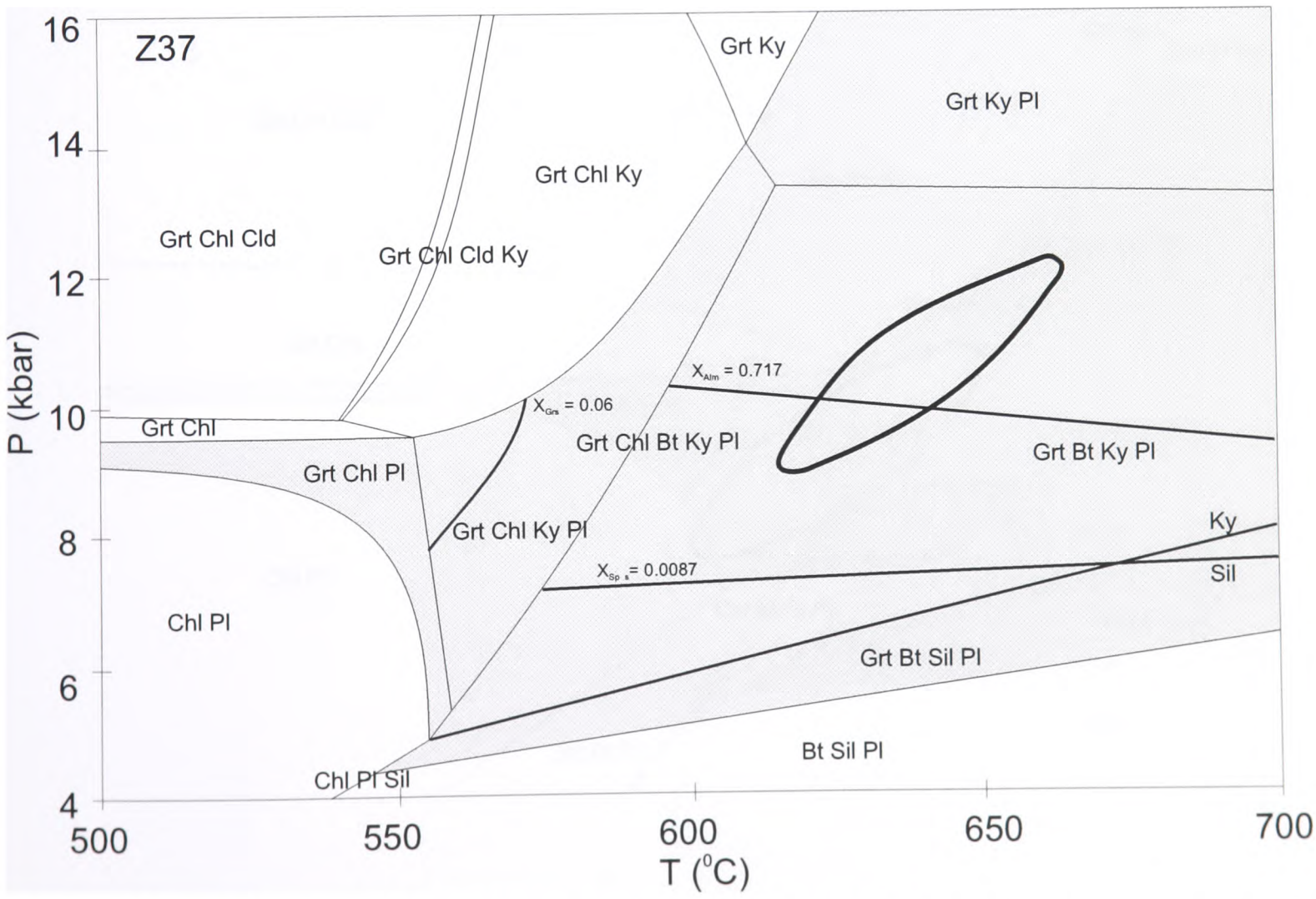


Figure 5.21.D. P-T pseudosection in CNMnKFMASH (+ Ms + Qtz + H_2O) for sample Z37, calculated for a bulk composition without garnet in order to model garnet fractionation. Peak average P-T error ellipse is also plotted.

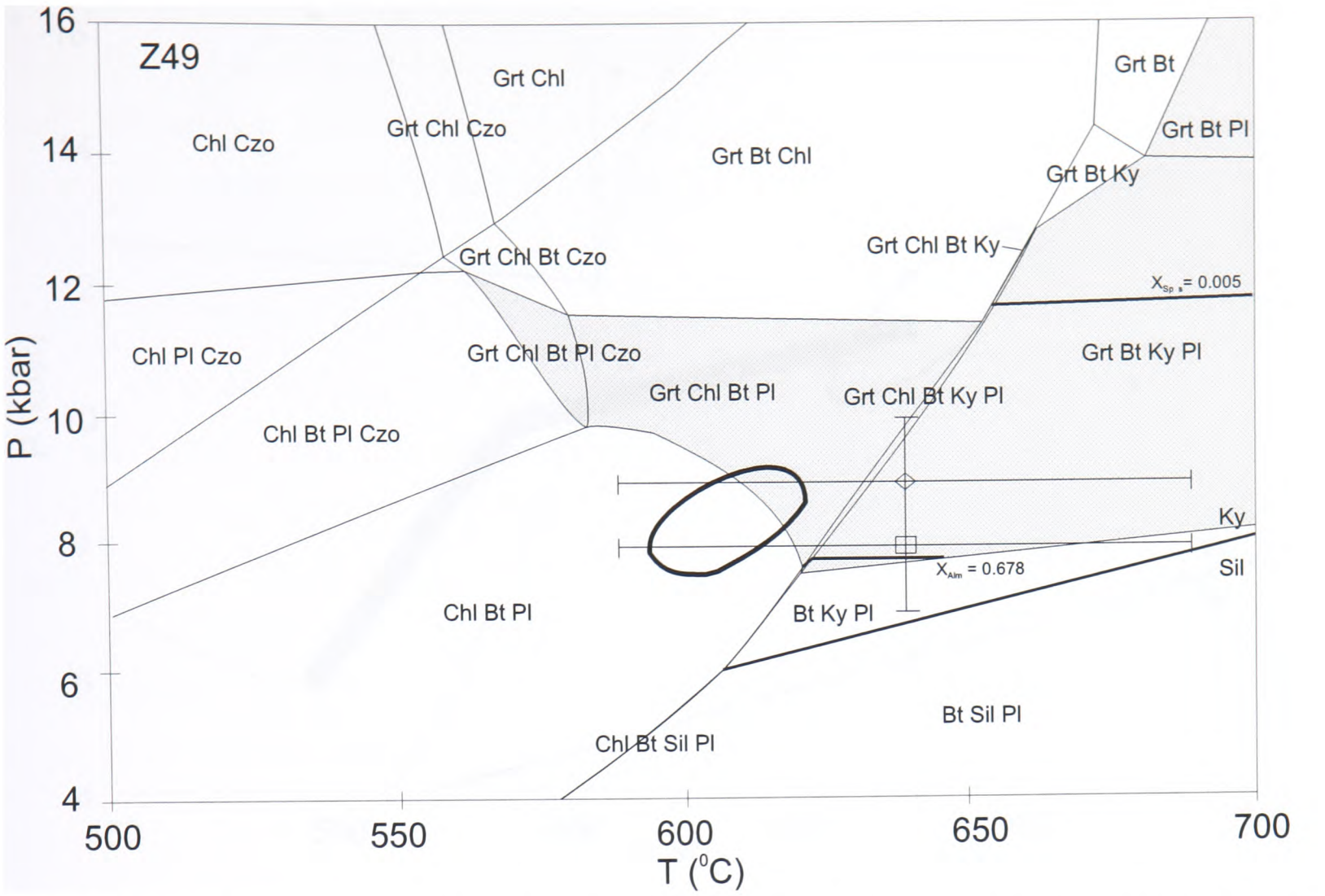


Figure 5.21.E. P-T pseudosection in CNMnKFMASH (+ Ms + Qtz + H_2O) for sample Z49, calculated for a bulk composition without garnet in order to model garnet fractionation. Results of garnet-biotite thermometry, and GASP (square) and GPMB-MG (circle) barometry are also shown, with error bars of ± 50 °C and ± 1 kbar.

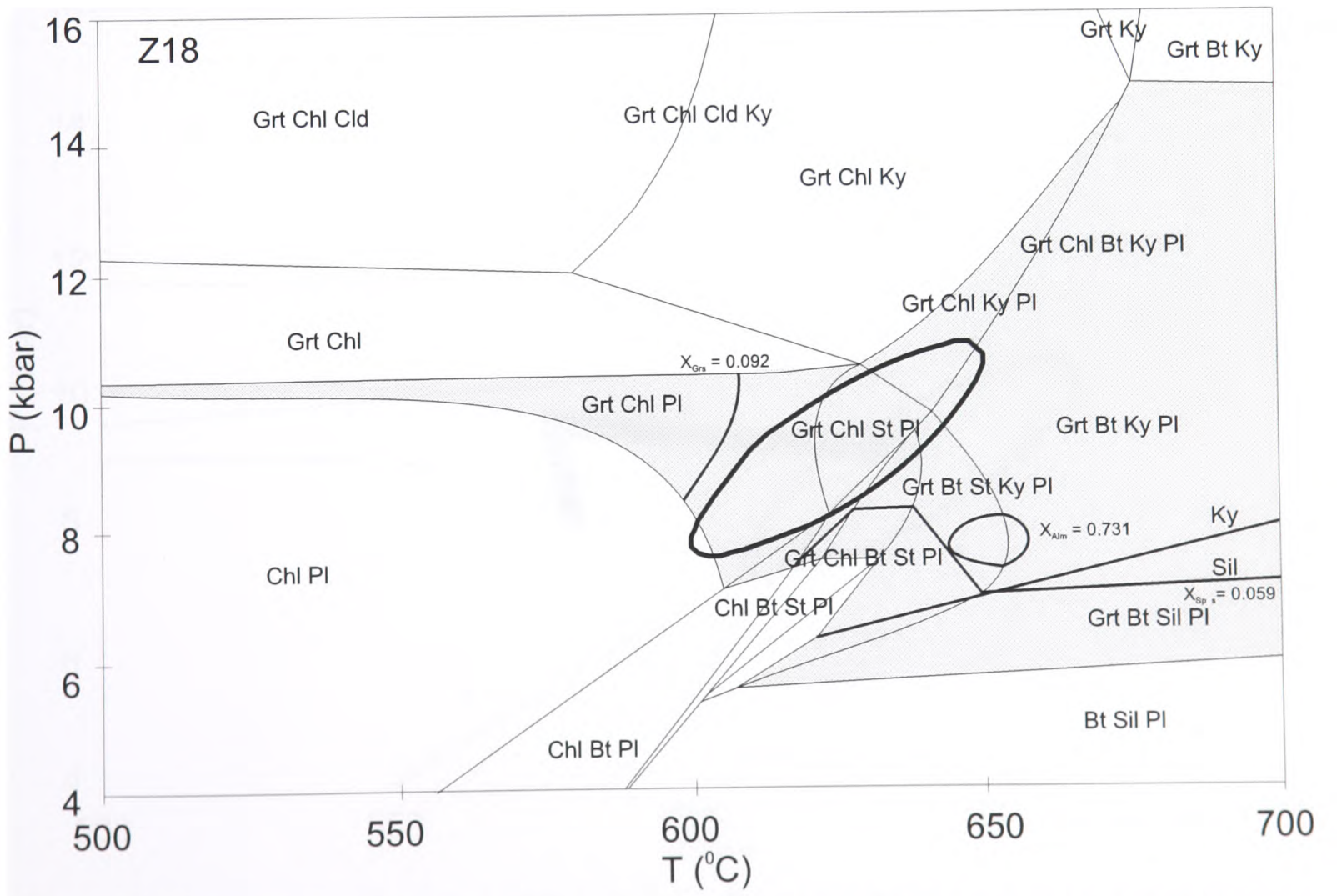


Figure 5.21.F. P-T pseudosection in CNMnKFMASH (+ Ms + Qtz + H_2O) for sample Z18, calculated for a bulk composition without garnet in order to model garnet fractionation. Peak average P-T error ellipse is also plotted.

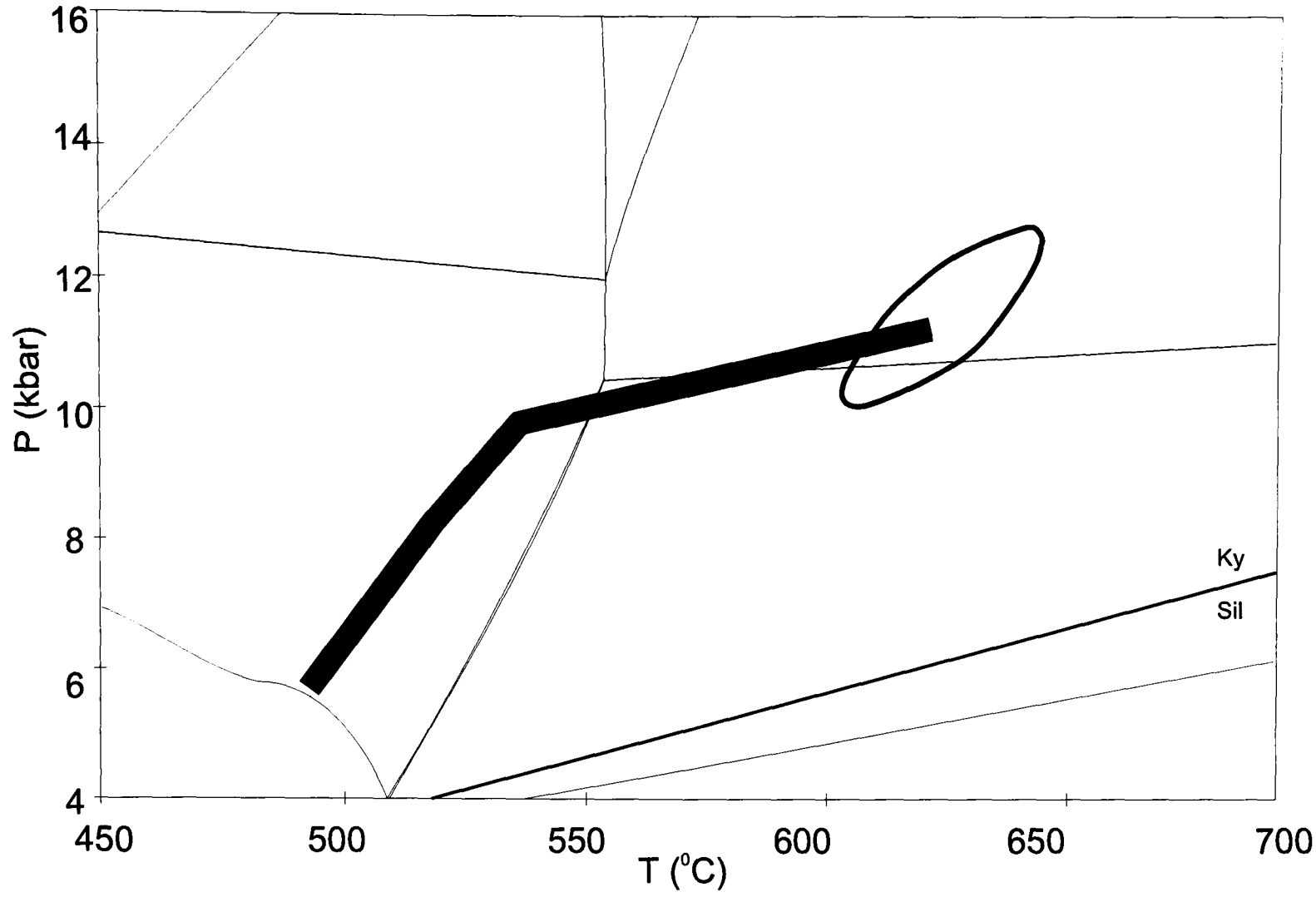


Figure 5.22.A. Schematic P-T path derived from the isopleths of compositional mole fractions in garnet for sample Z47, but applicable to L429, Z70.

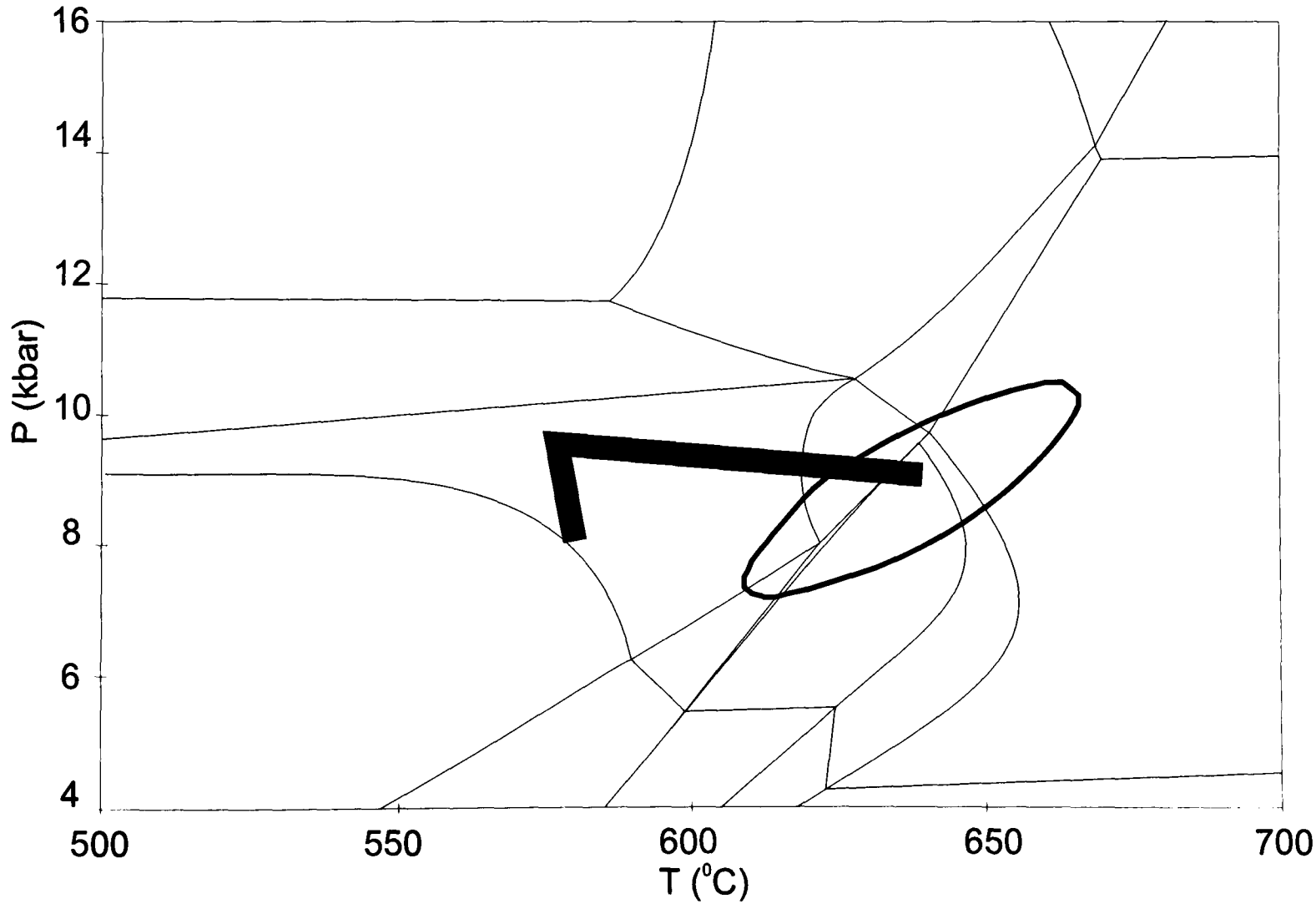


Figure 5.22.B. Schematic P-T path derived from the isopleths of compositional mole fractions in garnet for sample Z18.

isopleths for certain samples could coincide. Secondly, the problem may be a case of incorrect bulk composition estimation when considering the removal of garnet. The garnet-in boundaries are very sensitive to small changes in MnO and CaO, and a crude estimate of a "fractionated" bulk composition such as this is likely to differ from the "real" fractionated bulk composition.

From this somewhat crude attempt to observe the effects of garnet fractionation it can be seen that the "real" situation is quite difficult to model in this way, and that the two endmembers of complete equilibrium growth and complete fractionation have different relevance to different samples. While this is not exactly surprising, the results, and the comparison between the two sets, show that THERMOCALC modelling using an "equilibrium" bulk composition can predict phase relations and compositions for garnet cores adequately, but that fractionation is an important factor as garnet growth continues.

Phase	Z47 Measured mode	Calculated mode 11.5 kbar 630 ^{0}C	Z70 Measured mode	Calculated mode 10 kbar 640 ^{0}C
Grt	16	19.5	14.3	10.6
Bt	60	56.6	28.6	38.2
Ms	24	21.5	54.3	47.3
Ky	2	1.1	1.43	3.9
Pl	4	1.3	-	-
	Composition	**Composition**	**Composition**	**Composition**
X_{Alm}	0.662	0.685	0.743	0.705
X_{Sps}	0.004	0.001	0.005	0.0083
X_{Grs}	0.184	0.0089	0.069	0.0089
X_{An}	0.22	0.015	-	-
Phase	**L429 Measured mode**	**Calculated mode** 10 kbar 650 ^{0}C	**Z37 Measured mode**	**Calculated mode** 10 kbar 640 ^{0}C
Grt	9	2.1	9.6	14.7
Bt	49	63.9	17.8	26.5
Ms	41	28.4	42.9	41.9
Ky	1	3.7	8.8	10.5
Pl	2	1.9	8.4	6.5
	Composition	**Composition**	**Composition**	**Composition**
X_{Alm}	0.643	0.69	0.717	0.712
X_{Sps}	0.002	0.0084	0.0087	0.004
X_{Grs}	0.171	0.037	0.06	0.015
X_{An}	0.3	0.095	0.13	0.04
Phase	**Z18 Measured mode**	**Calculated mode** 9 kbar 640 ^{0}C	**Z49 Measured mode**	**Calculated mode** 8 kbar 600 ^{0}C
Grt	8.9	16.1	21.1	4.4
Bt	30.3	41.7	29.7	70.9
Ms	29	23.8	43.8	10.6
Ky	18.6	14.6	1.95	11.7
Pl	12	3.8	3.5	2.4
	Composition	**Composition**	**Composition**	**Composition**
X_{Alm}	0.731	0.714	0.678	0.681
X_{Sps}	0.059	0.013	0.005	0.025
X_{Grs}	0.092	0.025	0.0175	0.081
X_{An}	0.14	0.082	0.7	0.23

Table 5.4. THERMOCALC calculated modes and compositions for pseudosections calculated for garnet fractionation i.e. garnet is removed from the bulk composition. All modes are volume percents.

5.4. Gibbs method modelling

5.4.1. Introduction

The above sections describe how P-T pseudosections may be constructed and used to interpret the P-T evolution of metamorphic rocks. The results show that the technique is generally successful, and that garnet core composition and at least the early part of the P-T evolution can be well constrained. What THERMOCALC cannot do, however, is directly

calculate P-T paths from garnet zoning compositional data, and it cannot explicitly model garnet fractionation. In order to be able to do this, the approach of Spear (1982), Spear & Selverstone (1983) is taken, that is, using the Gibbs method. This approach utilises a thermodynamic dataset of much the same kind as used by THERMOCALC to calculate changes in thermodynamic variables of interest, in this case pressure, temperature, compositional terms of solid solutions, and molar volumes. The computer program GIBBS v.5.0 is used, along with a slightly modified thermodynamic dataset (Spear, pers. com.) that incorporates Mn into biotite and chlorite in the existing Spear & Cheney dataset. Program GIBBS also has the ability to account for garnet fractionation, which is extremely useful when considering accurate P-T evolution. The mixing models used are described in Appendix A, but the main differences between these and those used in the THERMOCALC calculations is that most of the phases incorporate ideal mixing models, with the exception of garnet and plagioclase.

5.4.2. Rationale and results

The approach taken for utilising Gibbs method calculations is to use the phase diagrams calculated with THERMOCALC as a framework within which to base these calculations. As the dataset used contains only entropy and volume data for the phases, only differential calculations can be performed; this does allow us to calculate a P-T path from the compositional data from the core of a garnet to the rim. As described in Section 5.2.1.1., Duhem's theorem states that once a bulk composition is specified, the variance of a system of any number of components, phases or chemical reactions will be 2 for a closed system. Thus, if the phase rule variance is 2 or more, any two specified thermodynamic variables will allow the calculation of all the others. The variables used are X_{Sps} and X_{Grs} in garnet, as these provide good constraints on temperature and pressure respectively. X_{Alm} is also sensitive to temperature changes, but does not change as systematically as X_{Sps}.

As THERMOCALC appears to models garnet core compositions consistently, a forward modelling approach is taken. Thus, the compositions and modes of phases at the pressure and temperature of garnet core growth are used as the starting point (Table 5.5.), and the increments of garnet growth tabulated in Tables 5.6.-11.1. Garnet is assumed to fractionate, as is water which is also allowed to leave the system. The increments of ΔX_{Sps} and ΔX_{Grs} are all taken from the left-hand side of the garnet-zoning profiles shown in Figures 5.6.-11.B, apart from samples Z49 and Z37 where the right-hand side of the profile is more complete, and reflect any significant changes in the slope of the zoning profile. Where the P-T

paths encounter a change in assemblage according to the THERMOCALC phase diagrams, the assemblage is changed in the Gibbs calculations, and recalculated for a new assemblage. The volumes of new phases added are also derived from the phase diagram calculations, and are shown in brackets in Table 5.5.

The P-T paths calculated from the Gibbs method calculations are shown in Figures 5.23.A.-F., and the calculated modes, compositions and final P-T's tabulated in Table 5.5. It can be seen that while some of the P-T paths appear to be consistent with the THERMOCALC-predicted paths, others are not. As the P-T path for each sample differs slightly, each will be discussed in turn. For sample L429 (Figure 5.23.A.) a number of P-T paths were calculated to illustrate the effect of the relative proportions of plagioclase and clinozoisite on predicted paths (Menard & Spear, 1993). In general, for a given amount of plagioclase at the beginning of garnet growth, the more clinozoisite present, the shallower the P-T path will be. The value of 4% plagioclase is closest to that predicted by THERMOCALC, and a starting guess of 0.5 % clinozoisite results in it all being used up by the garnet rim, which correlates with petrographic observation. The calculated P-T path for these starting guesses decreases in pressure slightly with a temperature increase at first, before increasing in pressure isothermally, finally following a gentle P-T increase to a final value of 616 ^{0}C, 9.2 kbar. This final value falls within the error ellipse of the THERMOCALC average P-T of 645 ± 31 ^{0}C, 9.7 ± 0.9 kbar. The overall path is one of heating of about 100 ^{0}C and a pressure increase of around 2.2 kbars.

The effect of the ratio of plagioclase to clinozoisite on the calculated P-T path is also apparent for sample Z49 (Figure 5.23.E.), and like L429 the X_{Grs} profile is quite irregular, leading to sharp kinks in the P-T path. As L429 and Z49 are from similar localities to Z47 and Z70 which do not show these kinks (Figures 5.23.B. & C respectively), it is suggested that the kinks are more a result of local Ca disequilibrium in garnets relating to clinozoisite inclusions rather than real variations in the P-T paths. The path of sample Z49 shows an overall increase in pressure and temperature that is steeper than that of L429, but which ends at 573 ^{0}C, 7.7 kbar, which is outside the P-T error ellipse calculated by THERMOCALC, although it is on course to intersect it.

The P-T path for sample Z47 predicts that for increments 1,2 and 3 in the assemblage Grt + Chl + Bt + Pl + Ms + Qtz + H_2O, pressure and temperature increase moderately until chlorite is removed and kyanite added, when for increment 4 temperature increases further and pressure increases at a lesser rate. This is in keeping with the path one might expect from

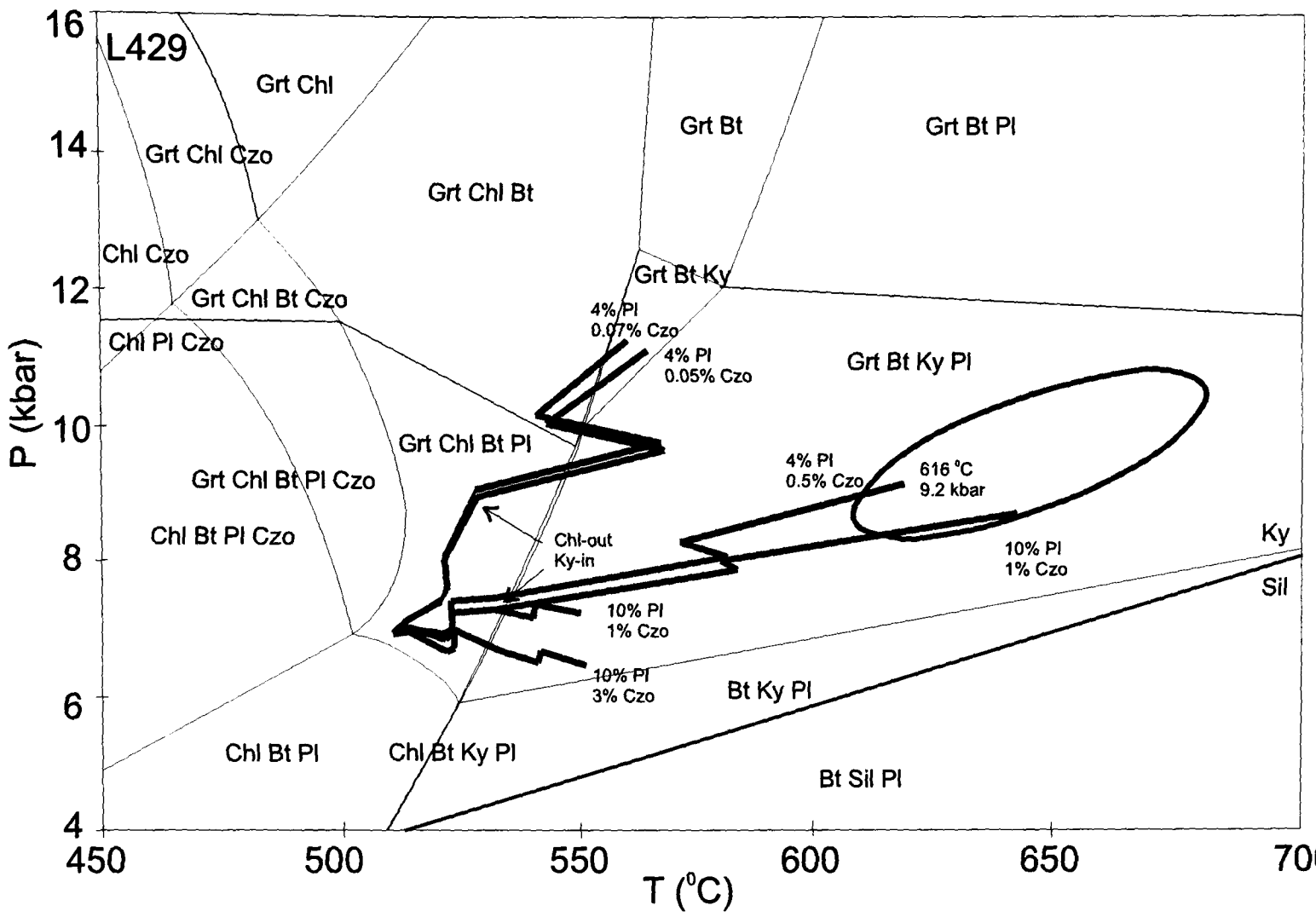


Figure 5.23.A. P-T paths from garnet zoning profiles for sample L429, calculated using program GIBBS. The starting point and rim peak error ellipse are calculated using THERMOCALC. Different P-T paths are shown to illustrate the effect of varying the amount of plagioclase and clinozoisite in the starting guesses. The values of 4% plagioclase and 0.5% clinozoisite are the closest to those predicted by THERMOCALC, and from observations.

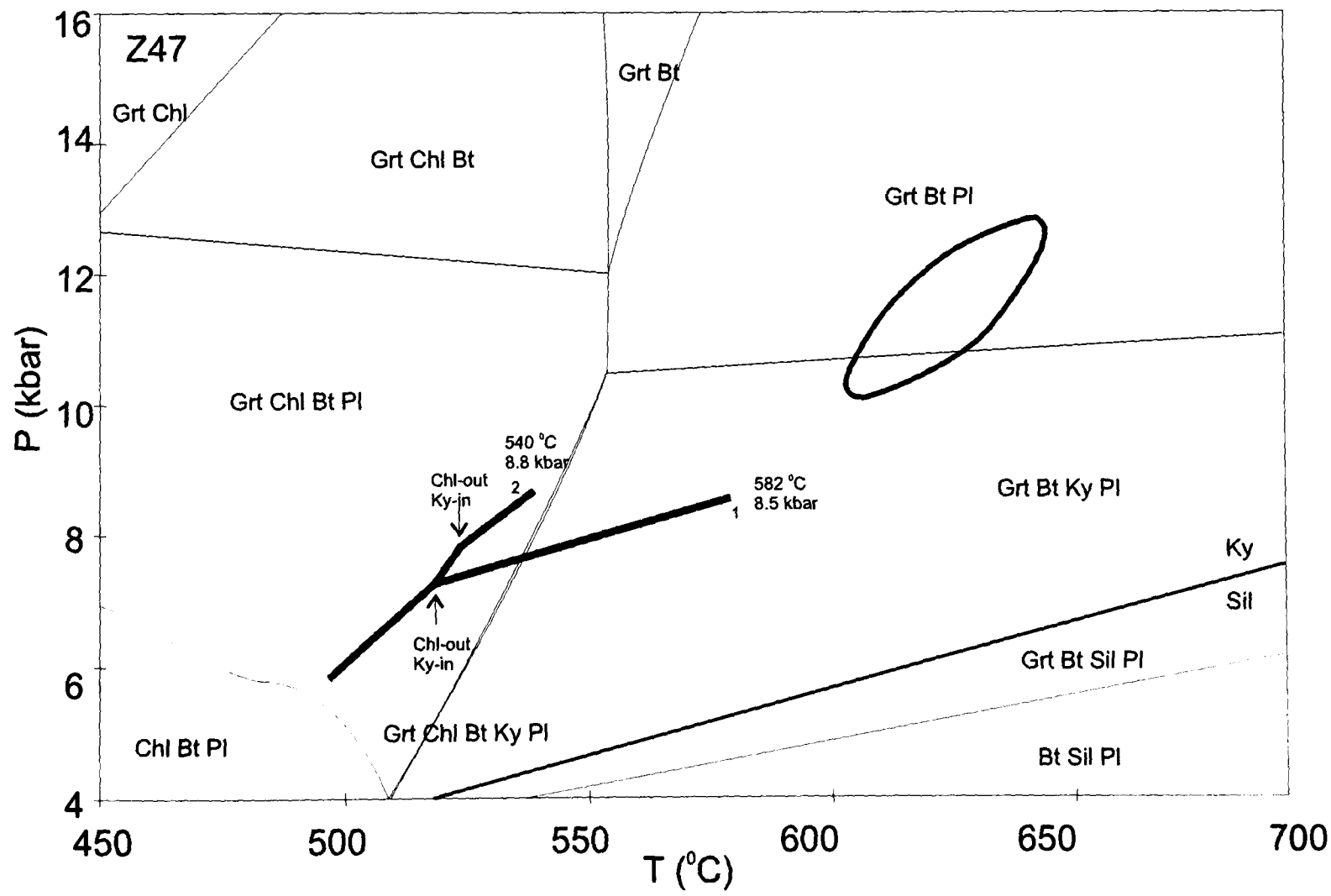


Figure 5.23.B. P-T paths from garnet zoning profiles for sample Z47, calculated using program GIBBS. The starting point and rim peak error ellipse are calculated using THERMOCALC. Different P-T paths are shown to illustrate the difference between removing chlorite half way through increment 4, and at the beginning of it

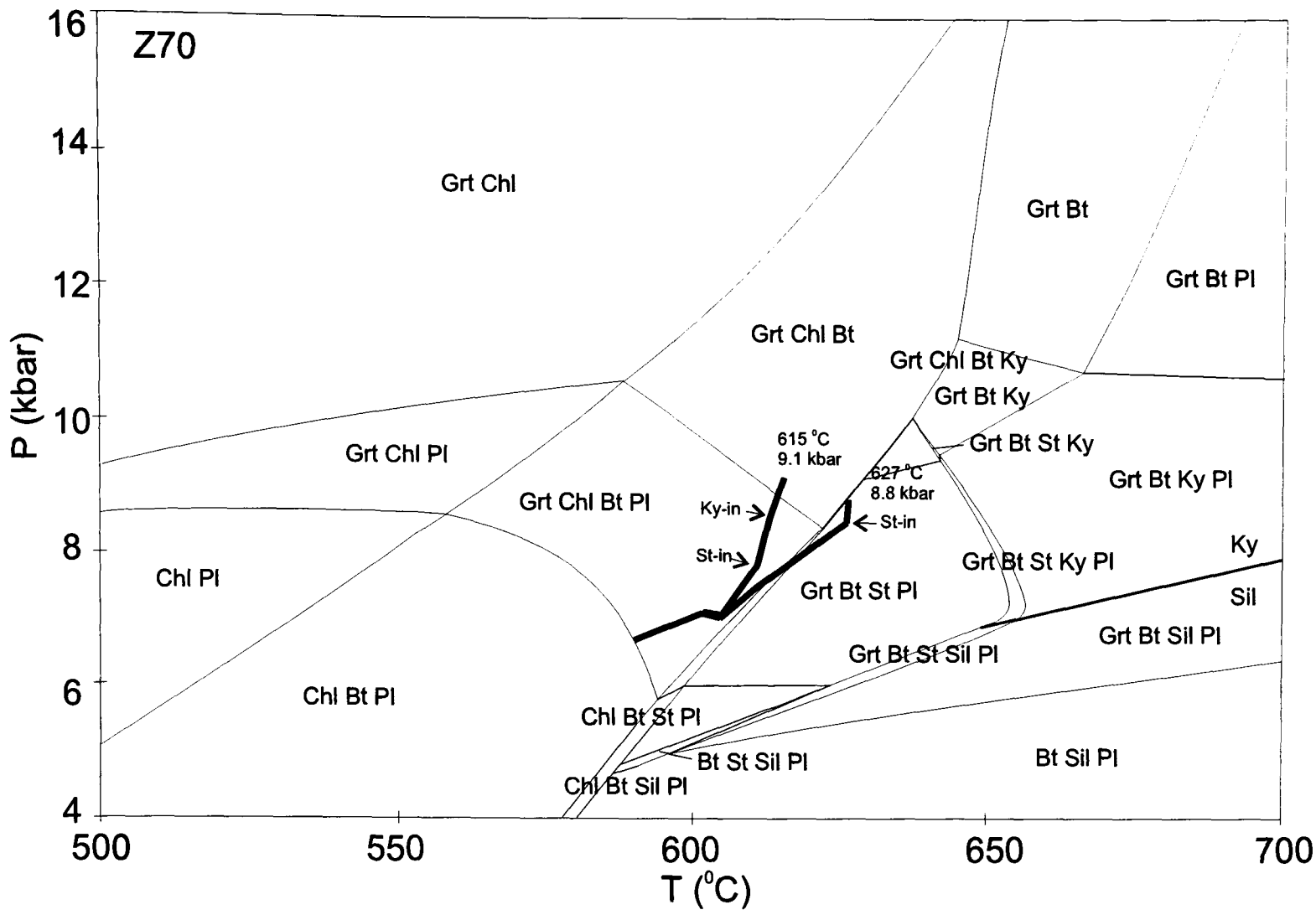


Figure 5.23.C. P-T paths from garnet zoning profiles for sample Z70, calculated using program GIBBS. The starting point is calculated using THERMOCALC, and the peak P-T is estimated at 640-650 °C and 9.5-10.5 kbar. The two different P-T paths are a result of adding staurolite after different increments. P-T path 2 correlates best with the pseudosection and the peak P-T.

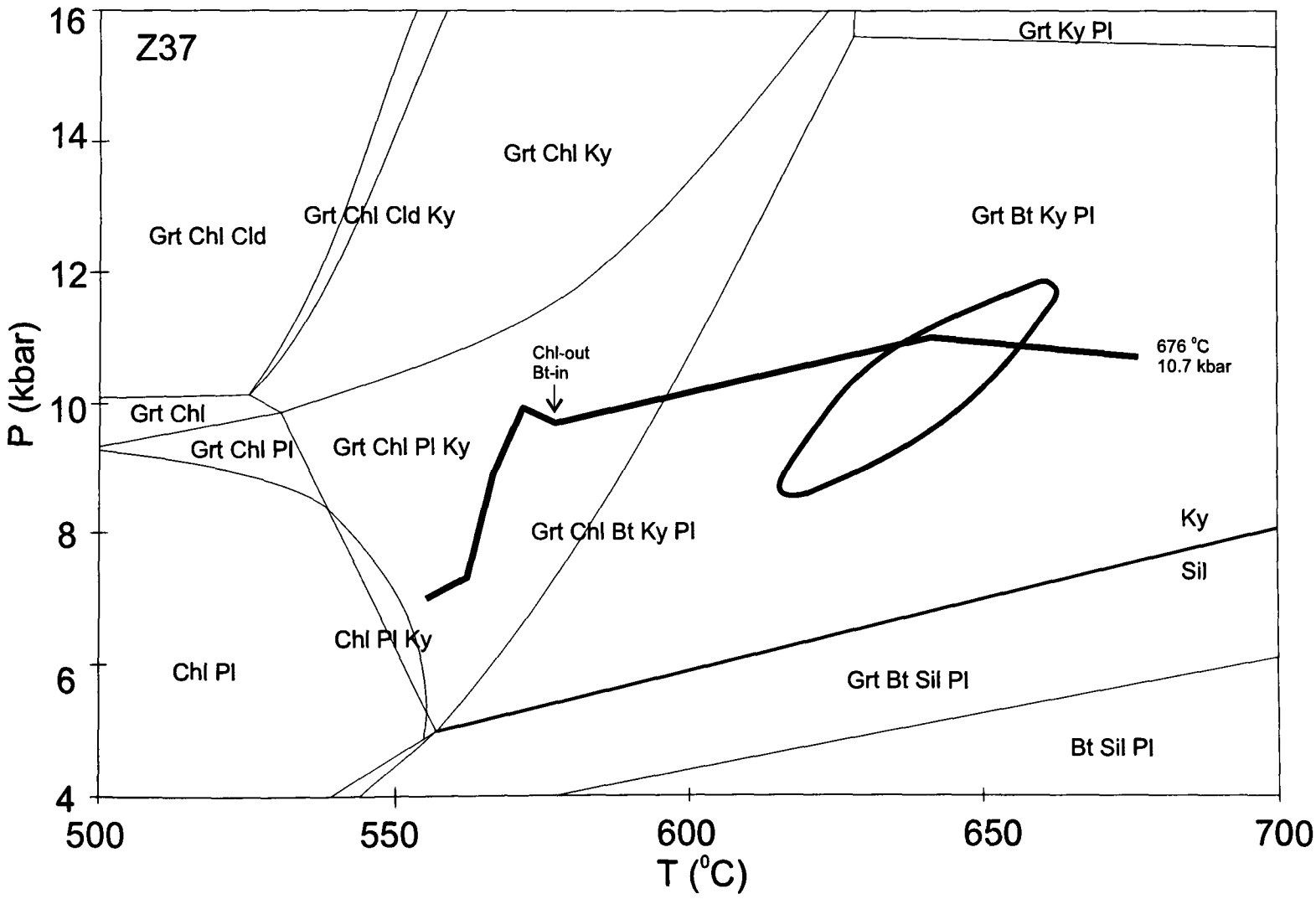


Figure 5.23.D. P-T path from garnet zoning profiles for sample Z37, calculated using program GIBBS. The starting point and peak P-T error ellipse are calculated using THERMOCALC.

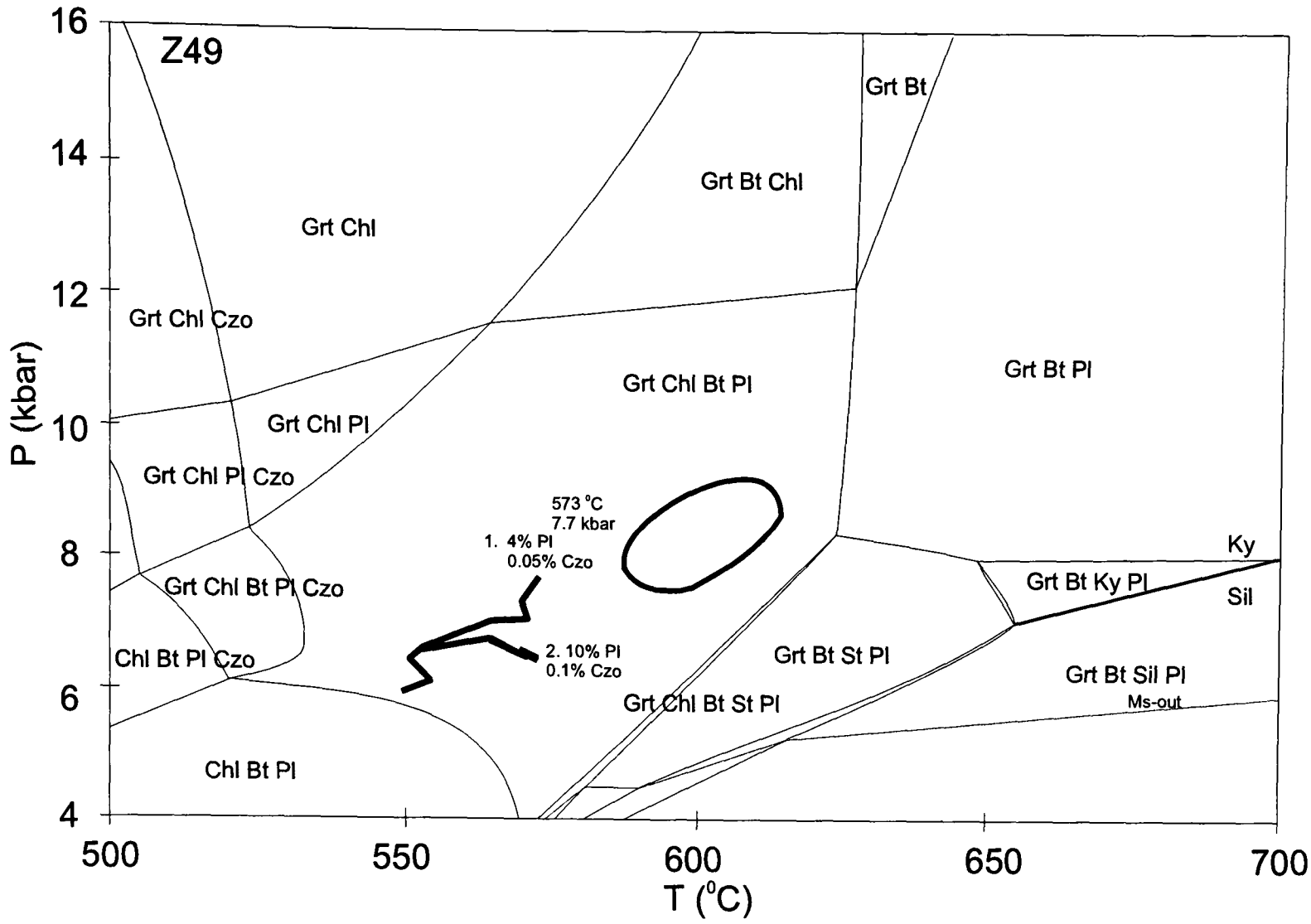


Figure 5.23.E. P-T paths from garnet zoning profiles for sample Z49, calculated using program GIBBS. The starting point and rim peak error ellipse are calculated using THERMOCALC. Different P-T paths are shown to illustrate the effect of varying the amount of plagioclase and clinozoisite in the starting guesses. The values of 4% plagioclase and 0.5% clinozoisite are the closest to those predicted by THERMOCALC, and from observations.

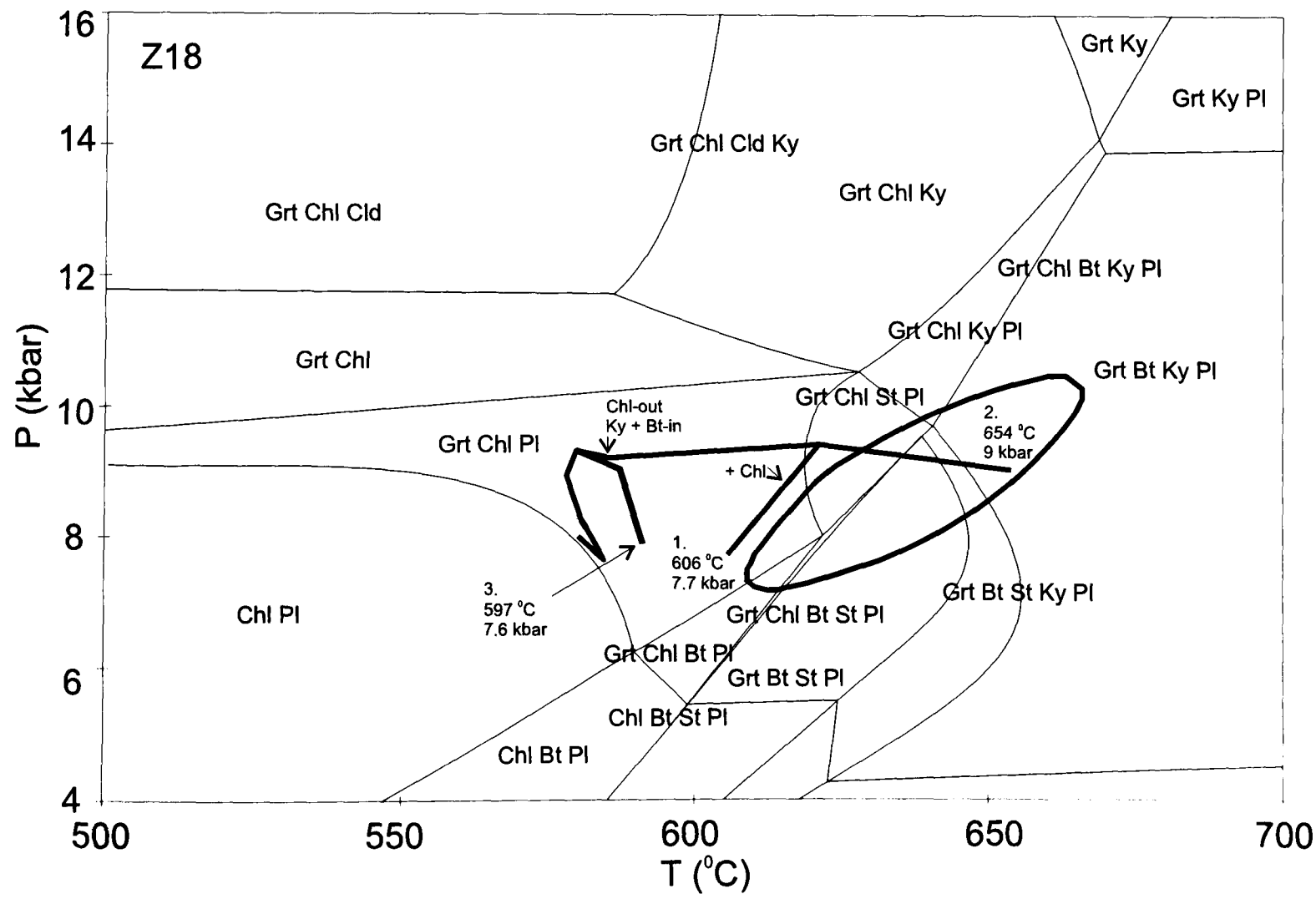


Figure 5.23.F. P-T paths from garnet zoning profiles for sample Z18, calculated using program GIBBS. The starting point and peak P-T error ellipse are calculated using THERMOCALC. The different P-T paths were calculated as follows: 1) Chl removed, Ky + Bt added after 6.5 increments, Chl added for increment 7; 2) As before except no Chl added on last increment; 3) All increments calculated for the assemblage Grt + Chl + Pl (+ Ms + Qtz + H_2O).

THERMOCALC -calculated isopleths. However, the path stops at 582 ^{0}C, 8.5 kbar, which is well short of the THERMOCALC calculated peak P-T error ellipse of 629 ±17 ^{0}C, 11.4 ± 1.1 kbar, although again the path is roughly in line with intersecting the ellipse. Another path is shown, whereby chlorite is retained in the assemblage until half way through increment 4 before kyanite is added, but this falls even shorter.

The path for Z70 is slightly more complex, as staurolite-bearing fields are involved, but the path calculated for staurolite entering the assemblage at the last increment calculates a path of moderately increasing pressure and temperature, similar to that of Z47, before increasing more steeply in pressure towards the end. This results in final conditions of 627 ^{0}C, 8.8 kbar, which is reasonable in light of the calculated 640 ^{0}C temperature and estimated 9.5-10.5 kbar pressure. The path does not quite reach kyanite-bearing fields according to the THERMOCALC pseudosection, but in light of the number of possible fields the path could pass through, GIBBS models the path adequately.

Sample Z37 records a calculated P-T path that increases quite steeply in pressure for the first 3 increments in the assemblage Grt + Ky + Chl + Pl + Ms + Qtz + H_2O, before shallowing out for increment 4. The removal of chlorite and the addition of biotite for the final two increments result in an overall path of temperature increase of about 100 ^{0}C, but pressure increase of only around 1 kbar, finishing at 676 ^{0}C, 10.7 kbar. This path both passes through the THERMOCALC peak P-T error ellipse, and conform to the path predicted from pseudosection isopleth calculations.

For sample Z18, three different paths were calculated to compare the effects of varying the assemblage that the garnet grew in. Path 3 (Figure 5.23.F.) is calculated entirely in the assemblage Grt + Chl + Pl + Ms + Qtz + H_2O, and increases steeply in pressure with a slight temperature decrease, before decreasing in pressure again with a slight temperature increase. This does not correlate well with the predicted rim and near-rim THERMOCALC peak P-T estimates. Paths 1 & 2 fit the P-T data but are somewhat contrived in that kyanite and biotite are added to the assemblage, and chlorite is removed, well before the phase diagram predicts that they should be stable. Path 1 adds chlorite for the last increment, which predicts a retrograde path to 606 ^{0}C, 7.7 kbar. Path 2 keeps the assemblage Grt + Bt + Ky + Pl + Ms + Qtz + H2O and finishes at 654 ^{0}C. 9 kbar. The THERMOCALC value for the P-T calculated using the garnet rim (and not the near-rim as was used in Chapter 4) is 633 ± 23 ^{0}C, 8.4 ± 1.2 kbar, which is in good agreement, and not that different from the near rim "peak". Thus the results for Z18 are somewhat contradictory, with the calculated path agreeing with both the

THERMOCALC calculated isopleths and peak P-T, but not the pseudosection. Z18 was collected from the Suru Dome, which is tectonically deeper than the Donara nappe, yet the average P-T results record a lower pressure. This is what would be predicted, as Suru Dome rocks record (to a greater or lesser degree) the effects of the M2 decompression event, which is most evident at Shafat to the east (Searle *et al.*, 1999). Thus, the P-T path calculated is in contradiction with tectonic models proposed for the Suru valley and other parts of the Zanskar Himalaya. Furthermore, isopleths of mode garnet calculated using THERMOCALC predict that garnet should not grow along a trajectory of uplift and cooling, but should instead be resorbed, which is in contradiction with growth path 1. In summary, the results for sample Z18 are treated with caution, and are not believed to represent actual P-T trajectories.

Table 5.5. Volume and composition data used in program GIBBS P-T path calculations. Garnet and water are assumed to fractionate. Numbers in brackets indicate amount of a phase added during the calculations. Numbers in brackets and italics in second volume column are actual measured volumes of phases.

L429 Start: 512^{0}C 7000 bars	Volume % of phase	Component	Mole fraction	**L429** End: 616^{0}C 9191 bars	Volume % of phase	Component	Mole fraction
Quartz	34	Quartz	1.0	Quartz	33.6 *(45)*	Quartz	1.0
H2O	0	H2O	1.0	H2O	0	H2O	1.0
Muscovite	18	Mg-celadonite	0.1	Muscovite	18.7 *(22)*	Mg-celadonite	0.129
		Fe-celadonite	0.1			Fe-celadonite	0.099
		Muscovite	0.8			Muscovite	0.772
Plagioclase	4	Albite	0.7	Plagioclase	3.7 *(1)*	Albite	0.747
		Anorthite	0.3			Anorthite	0.2528
Garnet	0	Pyrope	0.067	Garnet	3 *(5)*	Pyrope	0.1225
		Almandine	0.573			Almandine	0.7052
		Spessartine	0.1			Spessartine	0.0015
		Grossular	0.26			Grossular	0.1708
Biotite	29	Phlogopite	0.573	Biotite	28.2 *(26)*	Phlogopite	0.594
		Annite	0.425			Annite	0.406
		Mn-biotite	0.002			Mn-biotite	0.0001
Chlorite	8	Chlorite	0.6	Chlorite	0 *(0)*	Chlorite	-
		Daphnite	0.395			Daphnite	-
		Mn-chlorite	0.005			Mn-chlorite	-
Kyanite	0 (4.7)	Kyanite	1.0	Kyanite	4.7 *(0.5)*	Kyanite	1.0
Clinozoisite	0.5	Clinozoisite	0.9	Clinozoisite	-0.0084 *(0)*	Clinozoisite	0.1547
		Pistacite	0.1			Pistacite	0.8453

ZA7 Start: 500^{0}C 6000 bars	Volume % of phase	Component	Mole fraction	**ZA7** End: 582^{0}C 8515 bars	Volume % of phase	Component	Mole fraction
Quartz	40	Quartz	1.0	Quartz	39.6 *(47)*	Quartz	1.0
H2O	0	H2O	1.0	H2O	0	H2O	1.0
Muscovite	11.5	Mg-celadonite	0.036	Muscovite	12.1 *(12)*	Mg-celadonite	0.05
		Fe-celadonite	0.117			Fe-celadonite	0.132
		Muscovite	0.847			Muscovite	0.8176
Plagioclase	3	Albite	0.455	Plagioclase	2.1 *(2)*	Albite	0.7466
		Anorthite	0.545			Anorthite	0.2534
Garnet	0	Pyrope	0.0558	Garnet	1.49 *(8)*	Pyrope	0.0914
		Almandine	0.589			Almandine	0.7208
		Spessartine	0.1158			Spessartine	0.0043
		Grossular	0.2394			Grossular	0.1835
Biotite	33.6	Phlogopite	0.5176	Biotite	33 *(30)*	Phlogopite	0.5344
		Annite	0.48			Annite	0.4654
		Mn-biotite	0.0024			Mn-biotite	0.0001
Chlorite	11.6	Chlorite	0.5791	Chlorite	0 *(0.5)*	Chlorite	-
		Daphnite	0.414			Daphnite	-
		Mn-chlorite	0.0069			Mn-chlorite	-
Kyanite	0 (5)	Kyanite	1.0	Kyanite	4.9 *(1)*	Kyanite	1.0

Z70 Start: 590^{0}C 6700 bars	Volume % of phase	Component	Mole fraction	**Z70** End: 626^{0}C 8815 bars	Volume % of phase	Component	Mole fraction
Quartz	21	Quartz	1.0	Quartz	19.9 *(30)*	Quartz	1.0
H2O	0	H2O	1.0	H2O	0	H2O	1.0
Muscovite	36	Mg-celadonite	0.056	Muscovite	37.4 *(38)*	Mg-celadonite	0.0745
		Fe-celadonite	0.144			Fe-celadonite	0.1127
		Muscovite	0.8			Muscovite	0.8128
Plagioclase	4	Albite	0.757	Plagioclase	0.37 *(0)*	Albite	0.8871
		Anorthite	0.243			Anorthite	0.1129
Garnet	0	Pyrope	0.111	Garnet	10 *(10)*	Pyrope	0.1995
		Almandine	0.716			Almandine	0.7271
		Spessartine	0.067			Spessartine	0.0048
		Grossular	0.105			Grossular	0.0686
Biotite	19.6	Phlogopite	0.4697	Biotite	17.9 *(20)*	Phlogopite	0.6065
		Annite	0.529			Annite	0.3934
		Mn-biotite	0.0013			Mn-biotite	0.0001
Chlorite	19.9	Chlorite	0.47	Chlorite	8.2 *(0.5)*	Chlorite	0.6162
		Daphnite	0.496			Daphnite	0.3823
		Mn-chlorite	0.0034			Mn-chlorite	0.0015
Staurolite	0 (5)	Mg-staurolite	0.199	Staurolite	3 *(0.5)*	Mg-staurolite	0.1914
		Fe-staurolite	0.8			Fe-staurolite	0.8083
		Mn-staurolite	0.001	*(Kyanite)*	*(1)*	Mn-staurolite	0.0003

Z37 Start: 555^{0}C 6000 bars	Volume % of phase	Component	Mole fraction	**Z37** End: 676^{0}C 10650 bars	Volume % of phase	Component	Mole fraction
Quartz	50	Quartz	1.0	Quartz	49 *(52.2)*	Quartz	1.0
H2O	0	H2O	1.0	H2O	0	H2O	1.0
Muscovite	27	Mg-celadonite	0.028	Muscovite	26.8 *(22.4)*	Mg-celadonite	0.0745
		Fe-celadonite	0.11			Fe-celadonite	0.1127
		Muscovite	0.862			Muscovite	0.8128
Plagioclase	3	Albite	0.808	Plagioclase	2.7 *(4.4)*	Albite	0.88
		Anorthite	0.192			Anorthite	0.12
Garnet	0	Pyrope	0.052	Garnet	3 *(5)*	Pyrope	0.1901
		Almandine	0.694			Almandine	0.7426
		Spessartine	0.136			Spessartine	0.0089
		Grossular	0.118			Grossular	0.0584
Biotite	0 (20)	Phlogopite	0.6	Biotite	19.8 *(9.3)*	Phlogopite	0.6065
		Annite	0.499			Annite	0.3934
		Mn-biotite	0.001			Mn-biotite	0.0001
Chlorite	20	Chlorite	0.539	Chlorite	0 *(0.5)*	Chlorite	-
		Daphnite	0.455			Daphnite	-
		Mn-chlorite	0.006			Mn-chlorite	-
Kyanite	0	Kyanite	1.0	Kyanite	0.5 *(4.6)*	Kyanite	1.0

Z49 Start: 550^{0}C 6000 bars	Volume % of phase	Component	Mole fraction	**Z49** End: 573^{0}C 7711 bars	Volume % of phase	Component	Mole fraction
Quartz	43	Quartz	1.0	Quartz	36.5 *(46.6)*	Quartz	1.0
H2O	0	H2O	1.0	H2O	0	H2O	1.0
Muscovite	14	Mg-celadonite	0.035	Muscovite	14.6 *(22.4)*	Mg-celadonite	0.0398
		Fe-celadonite	0.196			Fe-celadonite	0.2033
		Muscovite	0.769			Muscovite	0.7569
Plagioclase	4	Albite	0.4	Plagioclase	1.8 *(1.8)*	Albite	0.7553
		Anorthite	0.6			Anorthite	0.2447
Garnet	0	Pyrope	0.0709	Garnet	3.8 *(10.8)*	Pyrope	0.095
		Almandine	0.6314			Almandine	0.7271
		Spessartine	0.0895			Spessartine	0.0068
		Grossular	0.2081			Grossular	0.1711
Biotite	15	Phlogopite	0.368	Biotite	14.3 *(15.2)*	Phlogopite	0.3976
		Annite	0.608			Annite	0.6022
		Mn-biotite	0.003			Mn-biotite	0.0002
Chlorite	22	Chlorite	0.384	Chlorite	19.2 *(2.2)*	Chlorite	-
		Daphnite	0.608			Daphnite	-
		Mn-chlorite	0.008			Mn-chlorite	-
Clinozoisite	0.05	Clinozoisite	0.9	Clinozoisite	0.0243 *(0)*	Clinozoisite	0.2854
		Pistacite	0.1			Pistacite	0.7146
				(Kyanite)	*(1)*		

Z18 Start: 580^{0}C 8000 bars	Volume % of phase	Component	Mole fraction	Z18 End: 606^{0}C 7724 bars	Volume % of phase	Component	Mole fraction
Quartz	26	Quartz	1.0	Quartz	26.1 *(23)*	Quartz	1.0
H2O	0	H2O	1.0	H2O	0	H2O	1.0
Muscovite	34	Mg-celadonite	0.042	Muscovite	30.1 *(20.4)*	Mg-celadonite	0.046
		Fe-celadonite	0.148			Fe-celadonite	0.1477
		Muscovite	0.81			Muscovite	0.806
Plagioclase	4	Albite	0.707	Plagioclase	3.6 *(8.4)*	Albite	0.7514
		Anorthite	0.293			Anorthite	0.2486
Garnet	0	Pyrope	0.096	Garnet	2 *(6.2)*	Pyrope	0.0828
		Almandine	0.686			Almandine	0.7654
		Spessartine	0.096			Spessartine	0.0732
		Grossular	0.122			Grossular	0.0732
Biotite	0 (20)	Phlogopite	0.599	Biotite	24.2 *(21.2)*	Phlogopite	0.576
		Annite	0.4			Annite	0.4231
		Mn-biotite	0.199			Mn-biotite	0.0014
Chlorite	36 (5)	Chlorite	0.483	Chlorite	3 *(3.3)*	Chlorite	-
		Daphnite	0.51			Daphnite	-
		Mn-chlorite	0.007			Mn-chlorite	-
Kyanite	0 (3)	Kyanite	1.0	Kyanite	4.7 *(13.2)*	Kyanite	1.0

The volumes and compositions of phases calculated by program GIBBS are in reasonable agreement with the measured values (see also Appendix C for modal values). For sample L429, GIBBS predicts that 3% by volume of garnet will have grown in comparison to the measured value of 5%, with a rim composition $Alm_{0.705}Pyp_{0.123}Sps_{0.0015}Grs_{0.171}$ compared to the actual $Alm_{0.643}Pyp_{0.184}Sps_{0.002}Grs_{0.171}$. X_{Sps} and X_{Grs} are specified monitors so they will be accurate, but almandine and pyrope compositions agree reasonably well. Program GIBBS overestimates the amount of Fe in garnet for each sample modelled. This may be a result of the mixing models used for chlorite and biotite, as they were considered only in terms of ternary Fe-Mg-Mn mixing in order to incorporate Mn, and did not allow for (Fe,Mg)Si = AlAl substitutions. The THERMOCALC mixing models are more sophisticated and incorporate both sets of substitutions which may explain why they consistently predict a lower X_{Alm} than program GIBBS. The modelling also predicts volumes and compositions of other phases such as biotite, muscovite and plagioclase that are in reasonable agreement with actual values. It is worth reiterating that the starting values used in the Gibbs modelling are themselves derived from THERMOCALC, so it is a good consistency check if the final calculated volumes and compositions correlate well with measured values. One phase where this is not the case is kyanite, where the amount added part-way through the calculations is overestimated from phase diagram calculations, such as L429 and Z47, or underestimated such as Z37 and Z18. The amounts of kyanite calculated by THERMOCALC in the phase diagram calculations do, however, agree well with the amount of kyanite measured from point counting, so the discrepancy may well be due again to the lack of Al in biotite and chlorite mixing models. The overestimation of the amount of kyanite may also explain why the amount of garnet is underestimated in many samples such as Z47, and why the P-T path falls short of the calculated rim conditions. As for the THERMOCALC phase diagrams, kyanite and biotite are used up to grow garnet in the field Grt-Bt-Pl-Ky, and so if GIBBS does not use up as much kyanite as one would expect then less garnet will grow. Increasing the amount of garnet grown would also have the effect of extending the P-T paths of samples such as Z47 closer to the peak rim conditions, as calculated by THERMOCALC.

5.4.2.1. Discrepancies between Gibbs modelling and THERMOCALC modelling

The Gibbs P-T paths differ from the THERMOCALC-predicted paths for a number of possible reasons. Firstly, the thermodynamic datasets used are different, which will lead to slight differences in the phase equilibria. Secondly, the THERMOCALC phase diagrams and isopleths are calculated assuming equilibrium growth models, in contrast to program GIBBS

which accounts for a fractionating garnet phase. Crude modelling with THERMOCALC shows the effect of shifting the bulk composition on phase boundaries, and so assumptions about the assemblage in which garnet is growing in may differ slightly when modelling using GIBBS. Furthermore, phase boundaries calculated using THERMOCALC, for most H_2O-producing equilibria at least, have typical errors of around 5-10 ^{0}C and 1 kbar. If we consider that one increment of garnet growth, as chosen from the zoning profile for modelling, may ultimately span a temperature interval of 50-100 ^{0}C (albeit usually much less than this), then not all of the garnet compositional increments may be modelled in the correct assemblage. This highlights the pitfalls of this type of modelling, and the fact that many previous attempts may be oversimplified.

A major difference between the Gibbs calculations and the THERMOCALC ones is that all Gibbs modelling was performed with $aH_2O = 1.0$. Although this is believed not to be the case for certain samples, namely L429, Z47 and Z37, attempts to model P-T paths using water activity less than unity meet with little success. For example, modelling sample Z47 with an H_2O-CO_2 mixed fluid predicts a P-T path that goes to high temperatures and pressures after increment 3, and the CO_2 component of the fluid becomes negative. A similar situation arises for all samples when P_{H2O} is allowed to vary independently of P_{rock}, whereby very high temperatures and pressures are predicted, and the predicted fluid pressure differs significantly from the rock pressure. This suggests that aH_2O is evolving over P-T space, which seems reasonable, but that it is actually quite difficult to model accurately, as the P-T values calculated are unrealistic. As GIBBS does not model different fluid compositions well for these samples, they are all modelled for a fixed fluid of composition $aH_2O = 1.0$. This simplification may well result in some of the discrepancies between the calculated P-T paths and the actual final calculated P-T's.

In summary, calculated P-T paths from Gibbs modelling using the program GIBBS predict that the garnets from all the samples grew along a path of both heating and compression. Samples L429, Z47, Z70 and Z49 followed paths with overall moderate P-T slopes, whilst Z37 and Z18 followed paths that were steep at first before shallowing out. The tectonic implications of this are discussed in the next chapter.

5.5. Conclusions

P-T pseudosections in the system CNMnKFMASH are calculated for six samples of varying bulk composition and location from the Suru Valley The most important factors

controlling garnet stability are bulk MnO and CaO (Mahar, 1997), whilst relative Al_2O_3 content determines the stability of aluminous phases such as staurolite and kyanite. Water activity also exerts a strong control on phase equilibria in that decreasing aH_2O shifts equilibria that produce H_2O to lower temperatures. The most obvious and important result of this is that samples calculated for low aH_2O are predicted to grow garnet earlier than those with a water activity of unity. Decreased aH_2O also restricts the stability of staurolite-bearing assemblages.

Pseudosections constructed using THERMOCALC model pelite evolution well, in that for all samples bar one, the assemblage predicted at the average peak P-T matches the actual assemblage. The compositions of phases predicted also correlate well, although THERMOCALC predicts that clinozoisite is not a stable phase at garnet core growth, which contrasts with petrological observations, and the amount of garnet predicted to grow is systematically overestimated. This believed to result from modelling garnet as being entirely in equilibrium with the bulk rock composition, which is known not to be the case. These pseudosections are contoured for isopleths of garnet composition and mode. This allows accurate prediction of the assemblage and P-T conditions when garnet first grew, which gives a starting point to the P-T path for each sample. The contours of garnet compositional isopleths imply that garnets grew along a path of heating and burial, which is consistent with calculated garnet growth isopleths. Samples L429, Z47, Z70 and Z49 followed paths that were moderately steep at first before shallowing out, whilst Z37 and Z18 followed paths that were steeper at first before shallowing out. Whilst THERMOCALC predicts garnet core compositions well, it is less accurate at predicting garnet rim values, although still reasonable. This is attributed to garnet fractionation, which is very difficult to model accurately using THERMOCALC. Endmember calculations for bulk compositions without garnet suggest that the "real" situation lies closer to the fractionated bulk composition, in terms of predicting the modal amount of garnet..

Gibbs method calculations are employed, using the program GIBBS, to calculate P-T paths from garnet compositional zoning. The core assemblage data and phase diagrams calculated using THERMOCALC are used as a framework on which to base the Gibbs calculations. Gibbs modelling of P-T paths meets with a reasonable degree of success in that consistent P-T slopes for samples from similar localities are calculated, and the predicted volumes and compositions of phases correlate well with the measured values. Samples L429, Z47, Z70 and Z49 followed paths with overall moderate P-T slopes, whilst Z37 followed a path that was steeper at first before shallowing out, although it must be noted that not all the

P-T paths finish in the peak P-T error ellipse as calculated by THERMOCALC. The P-T path calculated for sample Z18 does not agree with the calculated pseudosection or calculated P-T conditions, and is believed to result from re-equilibration that appears difficult to model. The discrepancies between THERMOCALC modelling and GIBBS modelling is attributed mainly to differences in the activity-composition models used, and the treatment of water activities used.

In summary, phase diagram modelling can prove extremely useful in predicting the sequence of assemblages that should be observed in a rock as it evolves through pressure-temperature space. It is generally successful at predicting the conditions of garnet growth, and the assemblage in which garnet grew, but care must be taken in interpreting P-T paths from garnet zoning, as the phase diagram approach cannot as yet account for garnet fractionation. However, even if an accurate P-T path cannot be confidently ascertained, THERMOCALC can be used to fix a start and end point for garnet growth with a good degree of confidence, which is in itself an important tool for interpreting the tectonic evolution of a rock.

Gibbs modelling can be combined with phase diagram modelling to aid in constraining P-T paths, as it has the ability to account for garnet fractionation. However, for rocks in which complex phase equilibria are predicted, or re-equilibration due to multiple metamorphic events has occurred, P-T path calculation becomes extremely difficult.

Chapter 6



Prayer flags and Leh gompa at sunset.

6. Synthesis

6.1 Introduction

This chapter summarises the conclusions drawn from chapters 2 to 5 in an attempt to present a tectonometamorphic model consistent with structural and petrographic observations, thermobarometry and metamorphic modelling. It also combines data from other sources that document the absolute timing of events in the Suru valley, and this data is used to constrain the P-T-t evolution of the study area. The validity of metamorphic modelling as a means of interpreting tectonic processes is also discussed.

6.2 Tectonometamorphic evolution of the HHC in the Suru valley area

6.2.1 Pre-collisional history (>54 Ma)

Figure 6.1.A.

The lithologies mapped in the Suru valley comprise pelites/semi-pelites/calc-pelites, psammites, marbles, amphibolites and granitoids which are correlated with the Upper-Palaeozoic-Mesozoic sediments of the Zanskar shelf and Permian igneous bodies. The most distinctive marker horizon mapped is a marble unit 170-500 m thick, associated with 20-100 m thick amphibolite units. The marbles can be correlated with unmetamorphosed Triassic limestones from Kashmir and Zanskar and the amphibolites with the Permian Panjal Trap basic volcanics (Honegger, 1982; this study). The granitoid bodies at Sankoo and Parkatchik are strongly deformed and infolded with the surrounding metasediments, and the Sankoo granite has been dated at 268 ± 5 Ma from monazite U-Pb ages (Noble *et al.*, in prep.). Field evidence suggests that intrusion of the Sankoo granite preceded the intrusion of subordinate basic units (Chapter 2), which agrees with the findings of Spring *et al.* (1993). They used zircon U-Pb ages to date the crystallisation of a rift-related alkali granite from SE Zanskar at 284 ± 1 Ma, whose intrusion predates the eruption of the Panjal Trap volcanics by some 10 Ma.

The recognition that the metamorphic rocks in the Suru valley represent the metamorphosed equivalents of the Tethyan shelf sediments to the north and east is useful in that it confirms a purely Himalayan age for metamorphism and deformation. Conventional U-Pb and SHRIMP dating of metamorphic and magmatic zircons from elsewhere along the High Himalaya suggest that some of the protolith for the HHC included Proterozoic Indian

basement rocks (e.g. Zeitler *et al.* 1993; Parrish & Hodges, 1996). In SE Zanskar and NW Lahoul there is U-Pb monazite evidence for a magmatic and possible metamorphic event at ca. 500 Ma (Pognante *et al.*, 1990; Walker, 1998) which has been overprinted to an uncertain extent by the Himalayan event. A crude palinspastic reconstruction of the metamorphic rocks of the Suru valley is shown in Figure 6.1.A. and Figure 2.21.

6.2.2 Post-collision and burial history (40-35 Ma)

Figure 6.1.B.

After the collision of India and Asia at around 54 Ma (Searle *et al.*, 1987, 1997), rocks of the Suru valley underwent burial and Barrovian metamorphism that reached kyanite grade in the deepest parts of the area. Crustal thickening was achieved by isoclinal folding and thrusting towards the SW, and the styles of deformation are observed to change with depth. Crustal thickening was achieved in the Tethyan shelf sediments of the Zanskar Himalaya by SW-verging tight to isoclinal folding and thrusting. Searle (1986) observed thrust-bound stacks of isoclinally folded limestones in the Zanskar Himalaya forming cliffs hundreds to thousands of metres high. In the HHC of the Suru valley this early phase of deformation (D_1) is preserved at low grades where overturned bedding-cleavage (S_0/S_1) relationships are observed near Sankoo (Chapter 2). Evidence of this early phase of deformation has also been inferred from folded inclusion trails within garnets and intrafolial isoclinal folds at higher grades (Chapters 2 & 3).

Searle et al. (1992) noted that peak $^{40}Ar/^{39}Ar$ hornblende ages from the Suru valley decrease with structural depth, from Sankoo to the Suru Dome, suggesting that metamorphism progressed from NE to SW. This could result from overthrusting of the Tethyan Himalaya along a large fault, which has been suggested to be a precursor to the Zanskar Shear Zone (e.g. Hodges *et al.*, 1996; Walker, 1998). Vance & Harris (1999) used Sm-Nd techniques to date garnets from the deeper levels of the Suru valley (from near Panikhar and Shafat), and were able to distinguish core and rim ages of garnet growth. Their results implied that garnets were growing before 33 Ma and stopped growing after 28 Ma. The results also suggested some diachroneity in garnet growth. Although it is difficult to tell from their location map which sample was collected from the greatest structural depths, their pseudosections predicted that the garnet with the youngest Sm-Nd core age would also have grown slightly later, and that less garnet would be expected to grow. This is most likely a feature of the influence of bulk rock composition on the stability of garnet, as has been shown in Chapter 5. Such a bulk composition effect may have consequences for interpreting the age of garnet growth,

especially if samples from different structural depths are being compared. Metamorphic modelling (Chapter 5) shows that garnets in samples from the Donara and Tapshah nappes started growing at conditions of 500-580 ^{0}C and 6-7 kbar, which corresponds to a minimum depth of around 21 km if a lithostatic gradient of 0.285 kbar/km is assumed. As little is known about the deformation state of the rocks in the Suru valley at this time, a layer-cake geometry is assumed for the isograds.

6.2.3 Post-collision and burial history (35-25Ma)

Figure 6.1.C.

This stage is defined by the time interval over which garnets are believed to have grown, as dated by Vance & Harris (1999). As garnets preserve information pertaining to timing, microstructure, absolute thermobarometry and metamorphic modelling, this stage is well constrained in terms of the tectonic evolution of the Suru valley. Peak metamorphic conditions obtained from THERMOCALC average P-T calculations and conventional thermobarometry are on average 9.5-10.5 kbar and 620-650 ^{0}C in the Donara and Tapshah nappes, although certain samples record pressures in excess of 11 kbar (Figure 6.2.A.). Samples from close to the garnet-in isograd near Sankoo preserve peak conditions of around 5 kbar and 400-500 ^{0}C. These pressures and temperatures represent the maximum M1 Barrovian conditions experienced in the Suru valley at differing depths, and record maximum depths of burial of up to 40 km. THERMOCALC phase diagram construction and Gibbs method modelling suggest that Suru valley garnets grew whilst undergoing further burial of 8-17 km and heating of 50-130 ^{0}C along paths with a moderate slope in P-T space. The data of Vance & Harris (1999) suggest that garnets grew within a period of 5 Ma.

At this time, kilometre scale SW-vergent recumbent folds (nappes) developed (D_2), interlocking in a complex three-dimensional pattern and occasionally separated by ductile shear zones. They formed in a ductile fashion due to non-coaxial simple shear at depth as a result of continued SW-directed folding and thrusting. Searle (1986) and Searle *et al.* (1997) propose that thrusting and folding in the overlying Tethyan sediments of the Zanskar Himalaya was also continuing at this time. Petrographic analysis (Chapter 3) implies that D_2 nappe formation was synchronous with, and was in places outlasted by M1 metamorphism, as defined by the growth of garnet, staurolite and kyanite porphyroblasts. This resulted in progressive deformation of the isograds as the nappes developed, although the isograds are *not* folded entirely around the fold hinges. This is also evident from field mapping, where isograds have been observed to cut the marble/amphibolite units, but have been folded by the nappes.

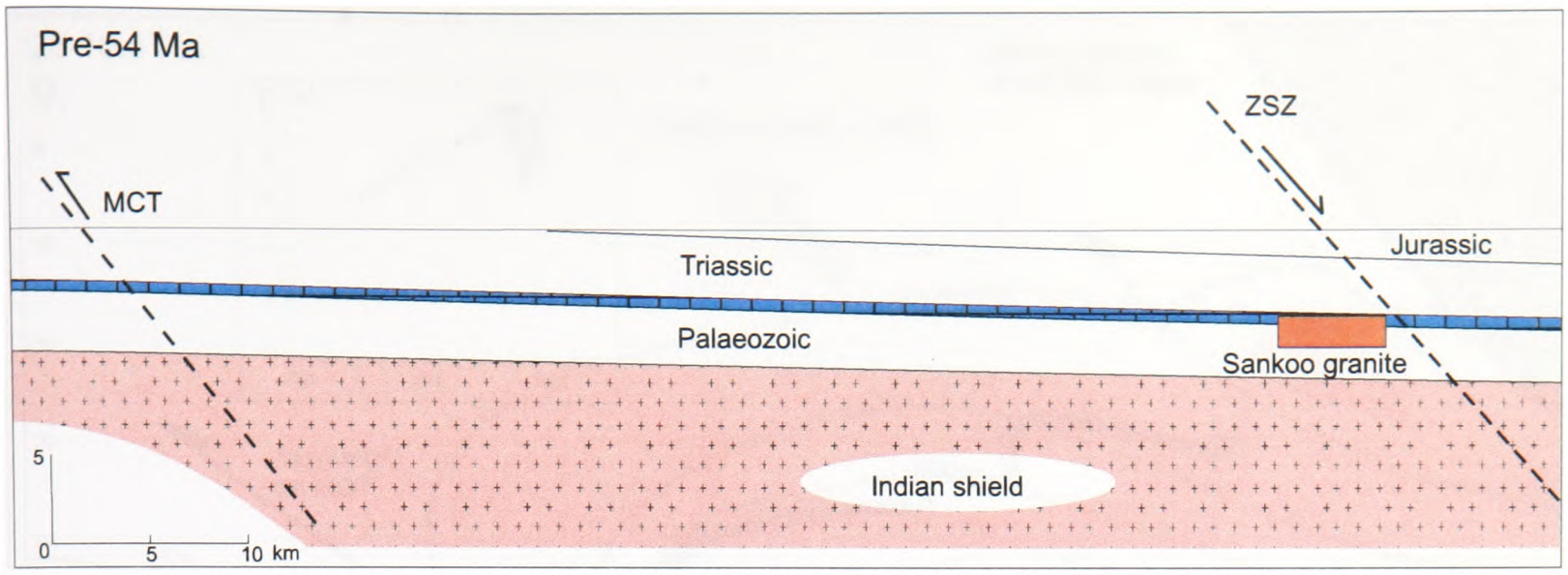


Figure 6.1.A. Palinspastic reconstruction of the Suru valley area of the High Himalaya prior to India-Asia collision. The Permian Panjal Traps and overlying Triassic limestones are shown as a marker horizon. The assumed position of the Permian Sankoo granite is also shown.

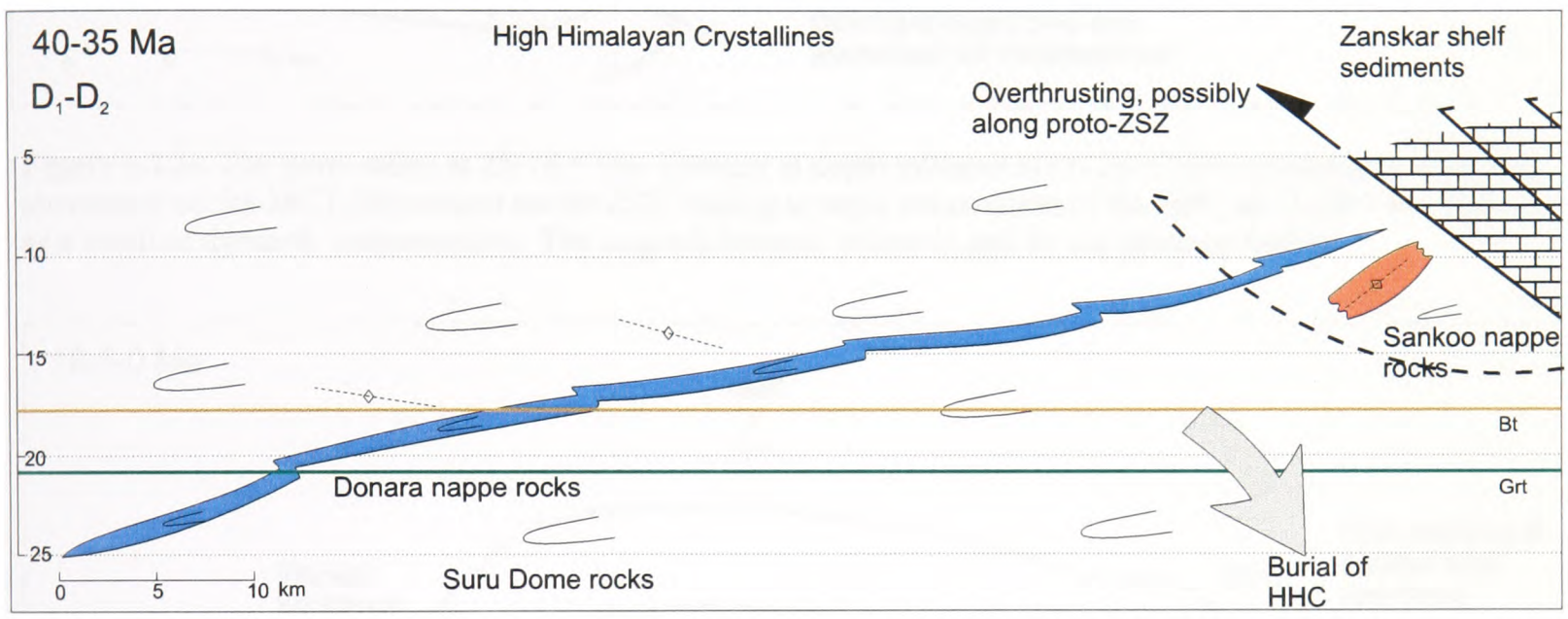


Figure 6.1.B. The Suru valley 15-20 Ma after collision. Crustal thickening by inferred isoclinal folding (small-scale, schematic in diagram) results in M1 Barrovian metamorphism. Garnet is beginning to grow at Suru Dome/ Donara nappe levels.

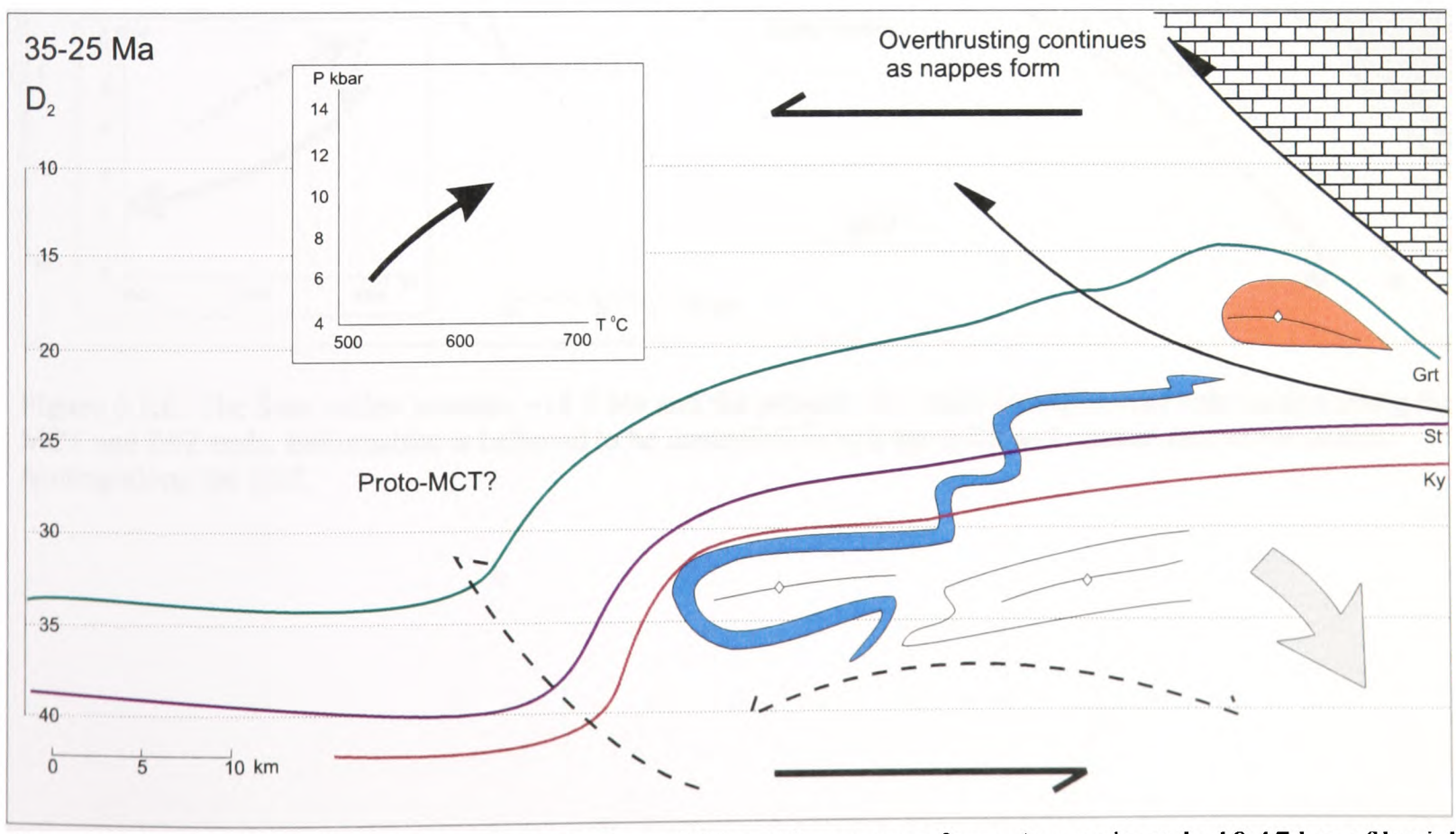


Figure 6.1.C. Burial and heating continues as large SW-verging nappes form. Approximately 10-17 km of burial is recorded during this time.

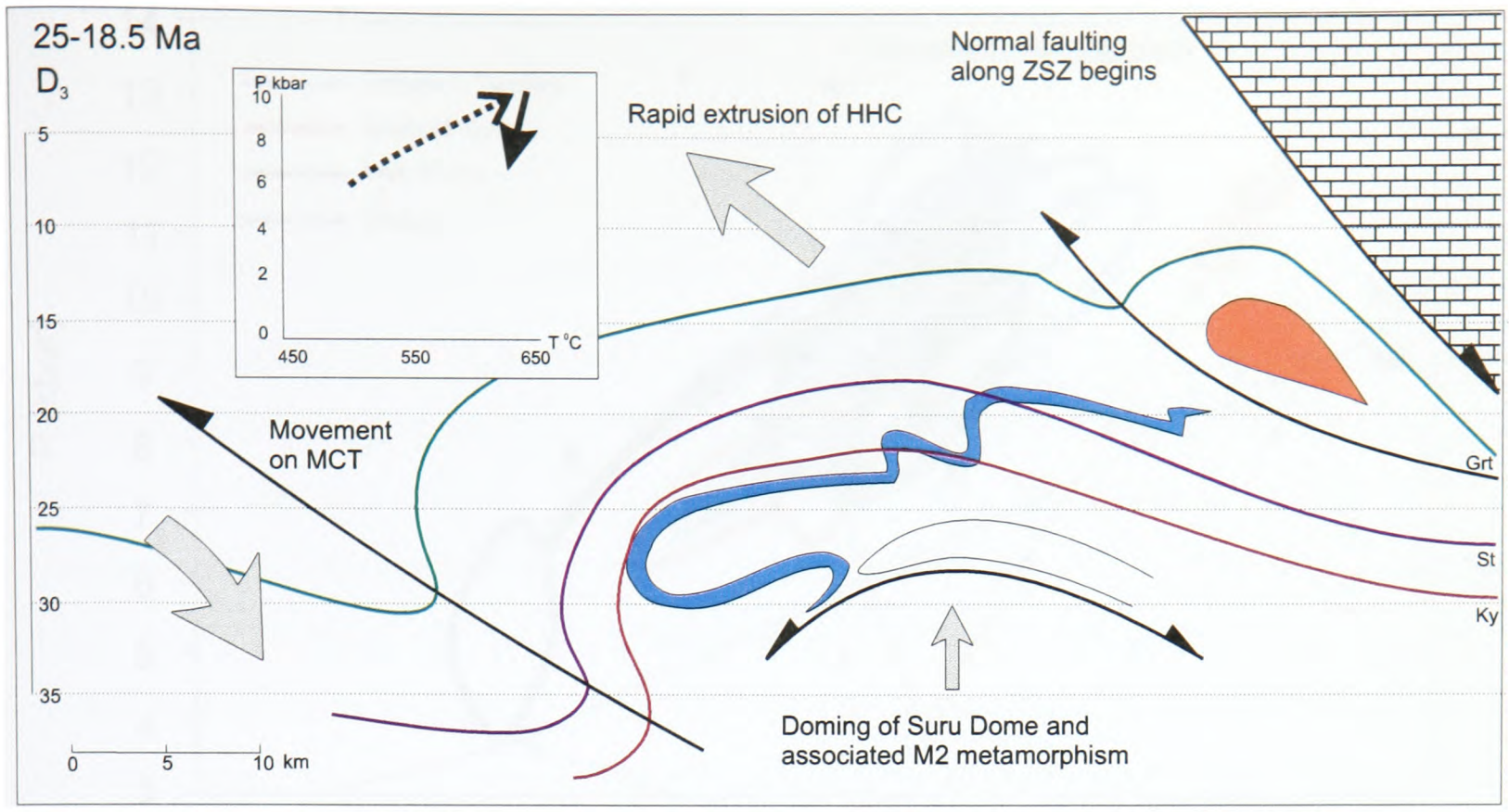


Figure 6.1.D. The Suru valley at 25-18.5 Ma. Doming at depth initiated at (?) 23-22 Ma, presumably related to movement on the MCT. Movement on the ZSZ leading to rapid exhumation of the HHC at 21-18.5 Ma follows as a result of dynamic compensation. The isograds become frozen in and do not advance further.

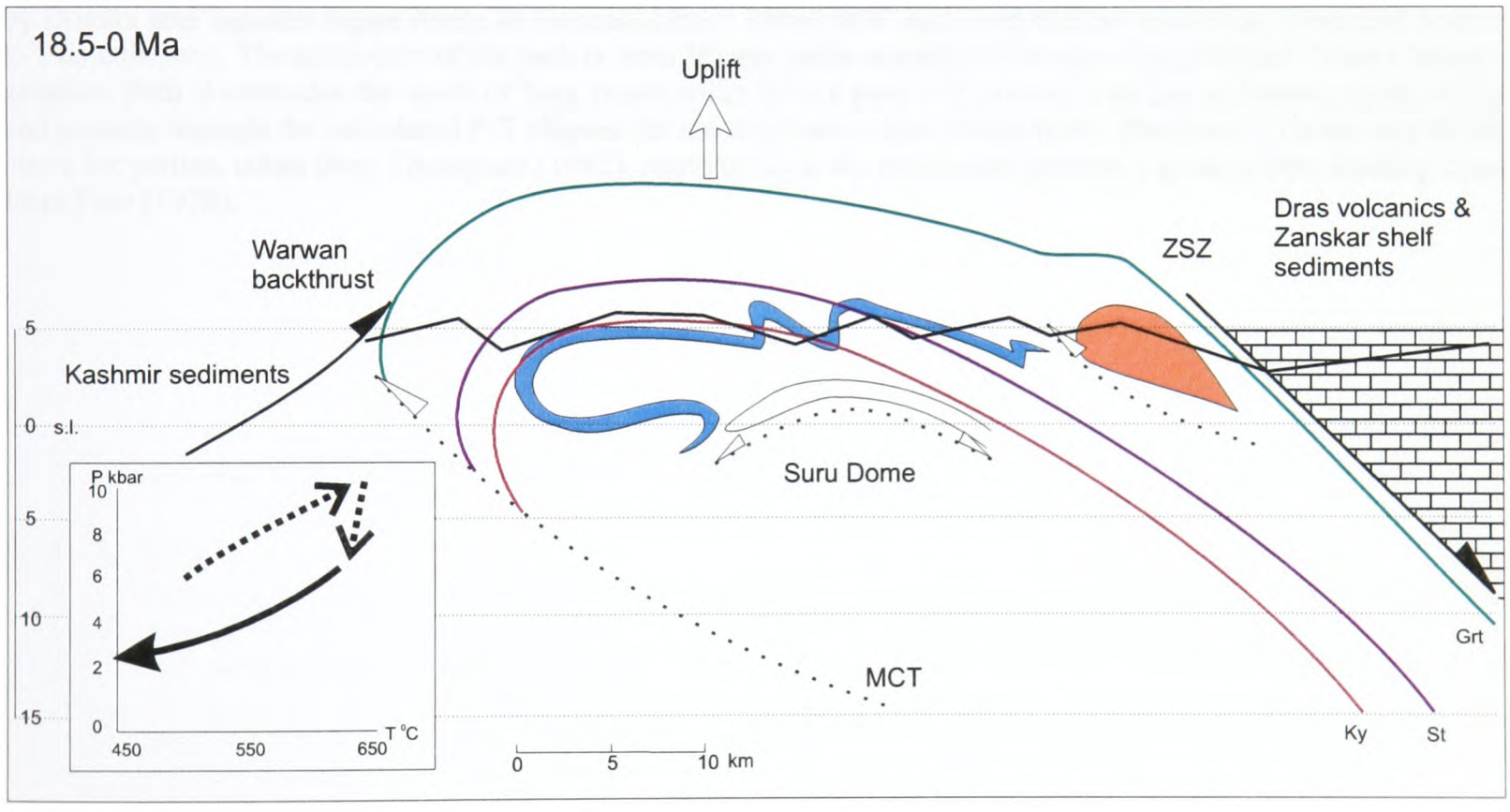


Figure 6.1.E. The Suru valley between ~18.5 Ma and the present. The most rapid phase of exhumation along the MCT and ZSZ ends. Exhumation is believed to be controlled mostly by uplift and erosion and brittle normal faulting along the ZSZ.

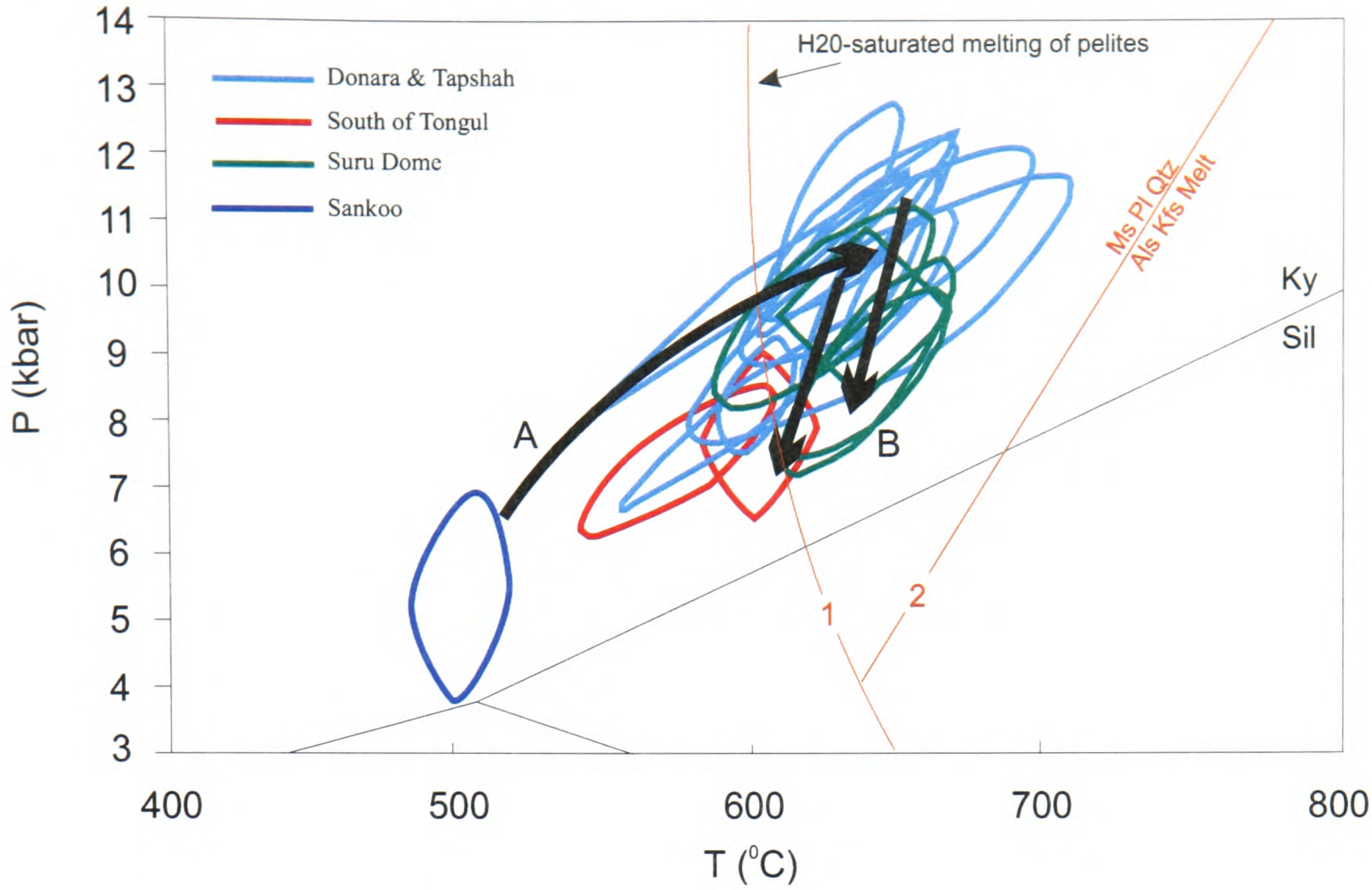


Figure 6.2. P-T diagram showing the general P-T evolution of the Suru valley. Path A describes the paths followed by Donara and Tapshah nappe rocks, as estimated from THERMOCALC and GIBBS modelling combined with peak P-T calculations. The uplift part of the path is from Waters (pers. comm) and using re-equilibrated Donara nappe samples. Path B estimates the uplift of Suru Dome rocks from a peak P-T greater than that of Donara nappe rocks and passing through the calculated P-T ellipses for the shallowest Suru Dome rocks. Reaction (1) is the wet melting curve for pelites, taken from Thompson (1982), reaction (2) is the muscovite-present, vapour-absent melting curve from Peto (1976).

Walker (1998) described a similar relationship, whereby M1 isograds became progressively folded around the Phojal-Kallath megafold. This close spatial association of deformation and metamorphism is not unusual, as deformation may facilitate mineral growth and metamorphism may change the deformability of a rock (e.g. Brodie & Rutter, 1985).

The metamorphic and structural evolution described in the above sections bears a strong similarity to that proposed by Vannay & Hodges (1996) for the Kali Gandaki Valley of Nepal. They describe an Eo-Himalayan (M1) Barrovian metamorphic event that involved burial to up to 35 km depth as a result of folding and thrusting in the Tibetan Tethys zone and subsequently the HHC (or Greater Himalayan Sequence). A $^{40}Ar/^{39}Ar$ hornblende age of ca. 37 Ma indicates Late Eocene metamorphism, with peak conditions of 9.4 kbar and 610 ^{0}C in the MCT zone. This was followed by Neo-Himalayan re-equilibration (M2) of samples at higher structural levels at 6.5 kbar and 540 ^{0}C, resulting from rapid exhumation in the Miocene along the MCT and the Annapurna Detachment, a branch of the STD, which they interpret as a reactivation of the thrust that buried the Greater Himalayan Sequence. Coleman and Hodges (1998) suggested that $^{40}Ar/^{39}Ar$ ages of 27-30 Ma preserved in the footwall of the STD in Nepal represent an M1 Eo-Himalayan event. Walker (1998) dated metamorphic monazites from the HHC of SE Zanskar and Lahoul that give U-Pb ages of 30 and 32 Ma. The chronological data presented in the above sections demonstrate that M1 Barrovian metamorphism was underway throughout the Himalaya by 30-35 Ma.

6.2.4 Doming and rapid extrusion (25-18.5 Ma)

Figure 6.1.D.

Subsequent to M1 metamorphism and SW-directed deformation in the Suru valley the manner in which deformation of the HHC was accommodated changed fairly rapidly. Stephenson (1997) interpreted this change as resulting from the concentration of non-coaxial strain along the base of the HHC leading to a zone of extremely high strain that became the ductile shear zone that is the MCT. Movement on the MCT may have initiated doming at deep levels in the HHC and uplift centred on these domes, such as the Suru Dome and the Chisoti Dome in the Kishtwar Himalaya. In the Suru valley this D_3 doming event is defined by a new S_3 foliation in and around the Suru Dome, and a crenulation of the S_2 foliation further away from the Dome, such as that seen in the Donara nappe. In the field this S_3 foliation occurs as an S-C shear fabric cross-cutting the S_2 foliation. Mineral lineations around the Suru Dome also suggest that attenuation occurred as the overlying nappes slid off the top. This process caused further doming of the M1 isograds in the Suru valley. Gapais *et al.* (1992) and

Stephenson (1997) attribute the formation of the domes to coaxial flow with a component of vertical uplift as non-coaxial flow is concentrated along the margins of the extruding HHC on the MCT and ZSZ.

Although the synchroneity of the MCT and ZSZ have been well documented (e.g. Burchfiel & Royden, 1985; Burchfiel *et al.*, 1992; Hodges *et al.*, 1992; Hodges *et al.*, 1996), it is possible that early movement on the MCT and subsequent doming and uplift preceded this by 1-2 Ma. Movement on the ZSZ could then have been triggered in response to gravitational collapse of the overthickened High Himalayan topographic high (Burchfiel *et al.*, 1992). It has also been suggested (e.g. Swapp & Hollister, 1991) that the onset of anatexis at depth may have caused rheological changes that triggered movement on the ZSZ. The initiation of movement on the MCT and ZSZ systems are generally bracketed at 20-23 Ma throughout the Himalaya. Hubbard & Harrison (1989) obtained a hornblende $^{40}Ar/^{39}Ar$ age of 20.9 ± 0.2 Ma from the MCT zone of eastern Nepal, which they interpreted as a deformation age. Hodges *et al.* (1992) dated leucogranites and sillimanite-grade metamorphic rocks from U-Pb and $^{40}Ar/^{39}Ar$ systematics from the Rongbuk Valley of Nepal. Their results implied movement on the STD between 19-22 Ma that was contemporaneous with metamorphism resulting from crustal thickening at deeper structural levels. Hodges *et al.* (1996) used U-Pb techniques to date zircons from leucogranites from the Annapurna range of Nepal and used these to constrain movement on the MCT and STD. They noted that movement on the MCT initiated at or before 22.5 Ma and may have ended only recently, and that rapid alternations between shortening and extension acted as a way of dynamically compensating the extruding High Himalayas.

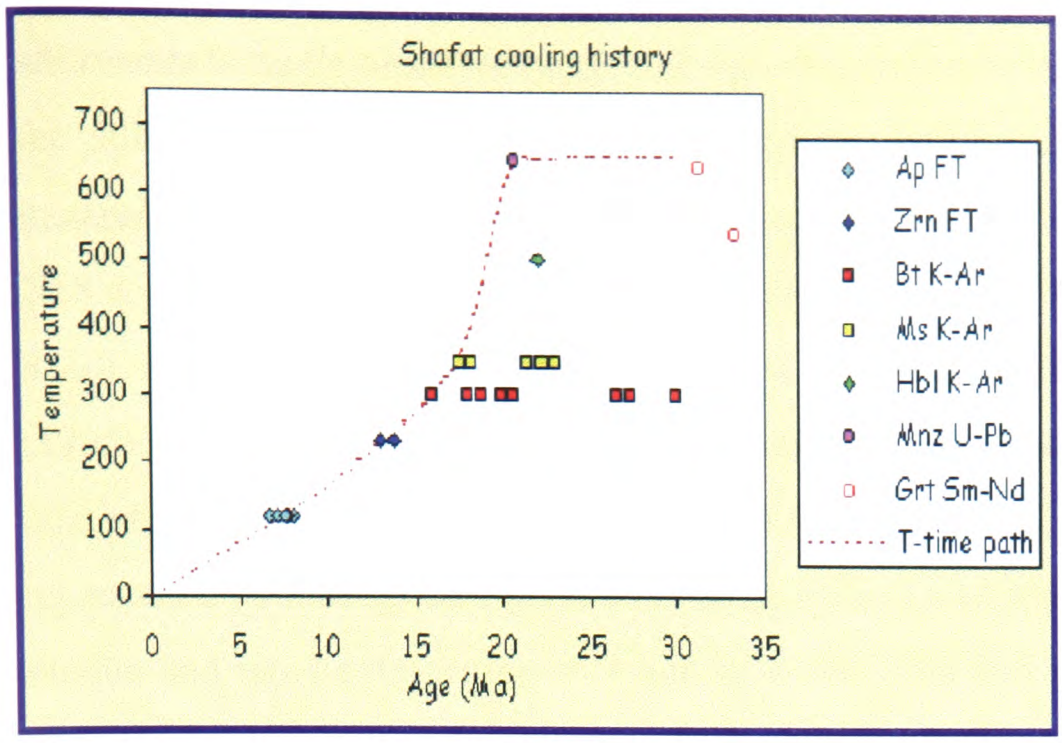
Intimately associated with movement on the MCT and ZSZ is a high-temperature M2 "Neo-Himalayan" metamorphic event that ultimately resulted in crustal anatexis throughout most of the Himalaya (e.g. Searle & Fryer, 1986). At Shafat, further east along the Suru valley, Noble & Searle (1995) obtained a U-Pb monazite age of 20.8 ± 0.3 Ma from a leucogranite believed to result from crustal anatexis. Walker (1998) dated the intrusion of the Gumburanjon leucogranite in SE Zanskar at 21-22 Ma. Samples from the Shafat area record conditions of up to 700 ^{0}C and 7 kbar, which are believed to represent peak M2 conditions (Searle *et al.*, 1992). In the area studied in this thesis the effects of this M2 metamorphism are subordinate to the early M1 event, but still noticeable. Coleman & Hodges (1998) presented data that demonstrated that M1 $^{40}Ar/^{39}Ar$ ages of 27-30 Ma were preserved in the hanging wall of the STD while U-Pb monazite ages recorded the 22 Ma M2 metamorphism in the

footwall. These two examples illustrate that the areas in which the two separate metamorphic events are preserved is crucial to our interpretation of them.

As well as developing a new fabric, samples from the Suru Dome typically record metamorphic conditions of 8.7-9.7 kbar and 630-640 ^{0}C, which are lower pressures than those recorded by rocks from the Donara nappe even though the Suru Dome is at deeper structural levels. Certain samples from the Donara nappe record conditions of 7.2-8.4 kbar and 570-600 ^{0}C (Chapter 4), which are again lower than the maximum recorded. In the core of the Zanskar Himalaya M2 conditions of 4.5-7 kbar and 650 -770 ^{0}C are recorded (Stephenson, 1997; Searle *et al.*, 1999). These conditions are believed to represent a degree of re-equilibration of these samples as they followed an uplift trajectory (Figure 6.2.A.). Similar conditions have been described by Vannay & Hodges (1996) from Nepal.

There is still disagreement over the causal mechanisms for high temperature, low pressure M2 metamorphism. Harris and Massey (1994) and Vance & Harris (1999) favoured vapour-absent melting as a result of rapid exhumation on the ZSZ. From Figure 6.2.A. it can be seen that for rocks hotter than those in the study area, such as in Central Zanskar, rapid decompression could carry rocks across the muscovite-present, vapour-absent melting curve. *In situ* migmatisation has been observed within the core of the HHC in Central Zanskar (Searle & Fryer, 1986; Searle & Rex, 1989; Stephenson, 1997) and is closely correlated spatially with the sillimanite + muscovite and sillimanite + K-feldspar isograds. Noble & Searle (1995) showed that U-Pb monazite ages of migmatitic leucosomes from the Umasi-la in the centre of the HHC are synchronous with higher level leucogranites from Shafat in the Suru valley. This suggests that anatexis is indeed the end result of metamorphism. Hodges & Silverberg (1988) calculated P-T paths for samples from the Garhwal Himalaya that imply Miocene burial and heating of rocks that had already been partially uplifted and cooled. They proposed that heat from leucogranites, possibly generated deeper in the slab, could have provided some of the heat for M2 metamorphism. From the P-T trajectories calculated in this study, and from samples closer to Shafat (Vance & Mahar, 1998; Vance & Harris, 1999), no evidence of renewed burial is found.

Figure 6.3.A. is taken from work carried out by Waters (pers. comm.) which uses a conductive thermal model to constrain the temperature-time and pressure-temperature trajectories of samples from Shafat. Petrographic constraints from the Shafat region include the observations that garnets have been seen to break down to kyanite, biotite and plagioclase (Searle *et al.*, 1992), i.e. in the kyanite stability field. This, combined with the fact that late



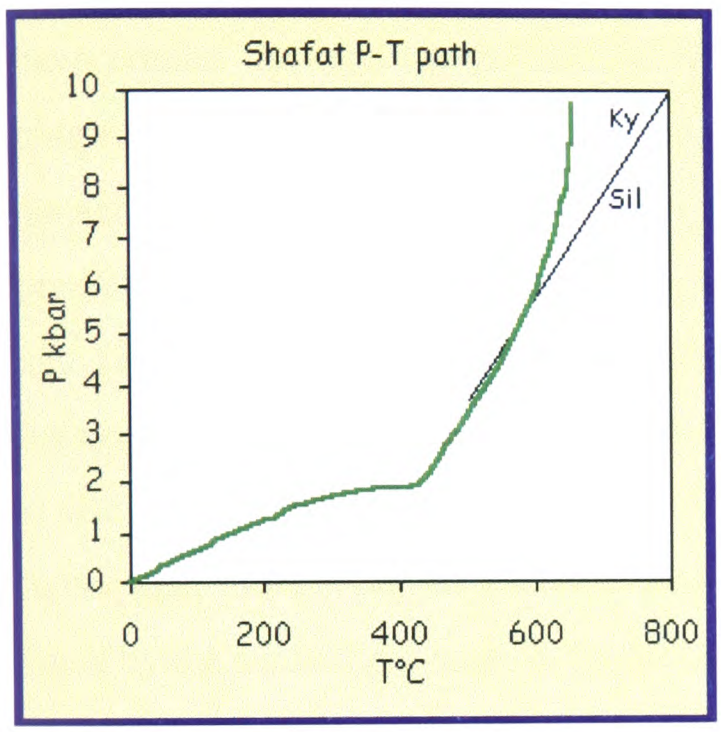
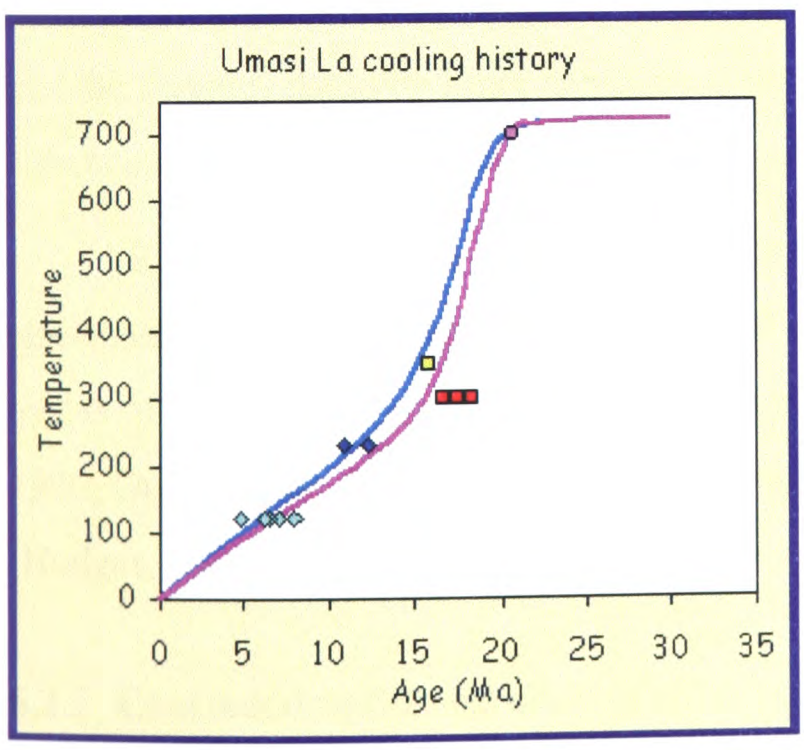


Figure 6.3.A. Temperature-time (above) and pressure-temperature (left) plots of the cooling and uplift trajectories of samples from Shafat, taken from Waters (pers. Comm.) The T-t data are constrained from a U-Pb monazite age for leucogranite generation (Noble & Searle, 1995), then K-Ar hornblende, muscovite and biotite cooling ages, and finally apatite and zircon fission track ages. See text for more details. The data are best modelled (curve) by a 3-stage exhumation process involving erosion at 0.68 mm/yr from 30-21 Ma, rapid exhumation on the ZSZ at 9 mm/yr from 21-18.5 Ma and finally slower erosion-controlled exhumation at 0.4 mm/yr from 18.5-0 Ma.



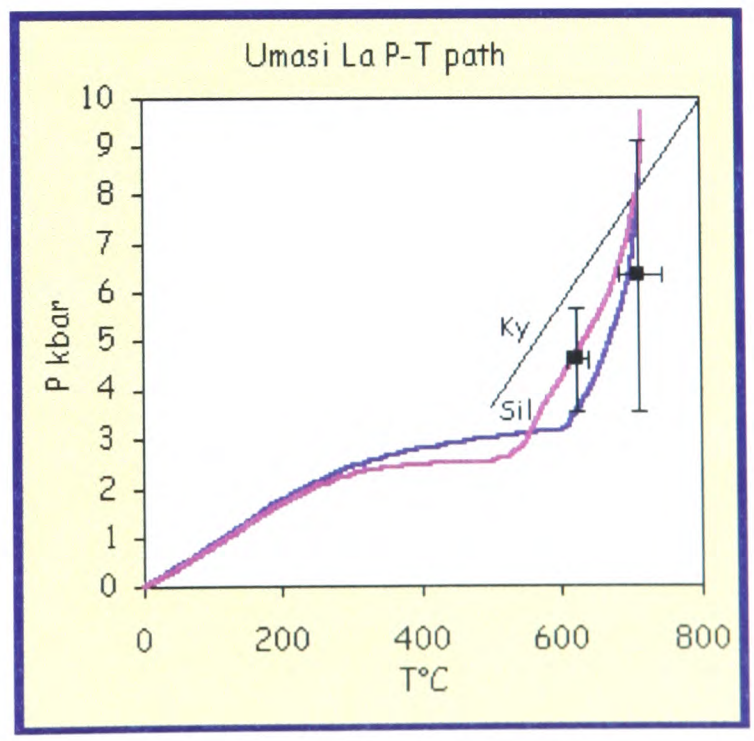


Figure 6.3.B. Temperature-time (left) and pressure-temperature (right) plots of the cooling and uplift trajectories of samples from the Umasi-la in Central Zanskar. Symbols as for Figure 6.3.A. The data is best modelled by a 3-stage model as above, plus cooling along the MCT below (red line).

sillimanite is rarely observed suggested that the uplift path did not cross very far, if at all, into the sillimanite stability field. Temperature-time constraints were obtained from the peak metamorphic garnet Sm-Nd ages of Vance & Harris (1996) (open circles), crustal melting at 20.8 ± 0.3 Ma (solid circle) (Noble & Searle, 1995), then mica cooling ages (squares) from Searle *et al.* (1992). The apatite and zircon fission track ages are taken from Kumar *et al.* (1995). The models fit the data best with a three-stage exhumation process involving relatively slow erosion at 0.68 mm/yr from the M1 peak at 30 Ma to the thermal maximum represented by leucogranite generation at 20.8 Ma. Thereafter, the rocks cooled quickly due to sudden and rapid exhumation at 9 mm/yr on the ZSZ and MCT from 20.8-18.5 Ma. This is documented by muscovite argon cooling ages of 17 Ma, which means that the rocks must have cooled through around 350 ^{0}C by this time, and it is reasonable to assume that the temperature evolution must have lagged slightly behind the exhumation. This was followed by slower, erosion-controlled uplift at 0.4 mm/yr from 18.5 Ma to the present day. The model predicts that some 18-25 km of overburden was removed from the Shafat region between 21 and 18.5 Ma. Walker (1998) calculated a similar uplift trajectory, with maximum extension between 23-20 Ma for the ZSZ in the vicinity of the Gumburanjon leucogranite. Figure 6.3.B. is also by Waters (pers. comm.) for the Umasi -la region of central Zanskar. Here the rocks are hotter than those from the Shafat region, but show a similar uplift and cooling path, and are fitted by the same three-stage exhumation history. Inger (1998) obtained Rb-Sr ages of around 25 Ma from muscovites close to the ZSZ in the Suru valley, which he interpreted as deformation ages, implying that the ZSZ was active as early as 25 Ma ago. These ages are earlier than those inferred from the model of Waters above; this most likely reflects the fact that the samples dated by Inger are taken from very close to the ZSZ and so will experience its effects earlier than those samples from deeper levels.

Exhumation of the HHC by simultaneous movement on the MCT and ZSZ (STD elsewhere in the Himalaya) is envisaged as extrusion of a ductile wedge from depth as a means of dynamic compensation of the orogenic belt (e.g. Searle & Rex, 1989; Hodges *et al.*, 1996; Grujic *et al.*, 1996), and that movement on the MCT and ZSZ are fundamentally linked (Hodges, 1998).

6.2.5 Continued uplift and erosion (18.5-0 Ma)

Figure 6.1.E.

This part of the uplift and cooling path is constrained by biotite $^{40}Ar/^{39}Ar$ cooling ages (~300 ^{0}C closure temperature) and apatite and zircon fission track dates. These data give a

relatively slow exhumation rate of 0.4 mm.yr^{-1}. From Figures 6.3.A&B it may be seen that this simple interpretation of mica cooling ages is complicated by the fact that the micas contain excess argon. However, it is reasonable to assume that, for samples from a restricted area, the youngest apparent age for each mineral probably reflects the time of cooling through its blocking temperature (Searle *et al.*, 1992). Samples from Sankoo record biotite cooling ages of around 19 Ma, whilst those from Parkatchik are slightly later at 17-15.5 Ma (Searle *et al.*, 1992), which is to be expected as the rocks are deeper in the slab. Inger (1998) dated a biotite Rb-Sr age of 16.2 Ma from Sankoo, which he interpreted as the age of cooling through 350 ^{0}C and a biotite Rb-Sr age of 12.8 ± 0.3 Ma from near Panikhar.

Movement on the MCT to the south is believed to have ended by 15 Ma (Stephenson, 1997), and by around 20 Ma in SE Zanskar (Walker, 1998), although Harrison *et al.* (1997) dated monazites inclusions in garnets from the MCT zone that give ages of 6-8 Ma, implying that it may still have been active at this time. It is believed that the exhumation of the Suru valley subsequent to ca. 18.5 Ma was controlled primarily by erosion-controlled uplift, with brittle extensional faulting along the ZSZ also a possible factor. The suggestion that the MCT, and the STD have been active since the Miocene is lent support by the observation that throughout large parts of the Himalaya they are marked by pronounced geomorphological features. In Bhutan and Nepal there is a pronounced contrast in topography between the HHC and the Tibetan-Tethys zone across the STD (e.g. Searle *et al.*, 1997; Edwards & Harrison, 1997), and the MCT zone is often marked by a break in slope.

A late-stage backthrust places sediments of the Kashmir basin over rocks of the HHC SW of the Donara nappe (Honegger, 1982; Searle *et al.*, 1992), but the exact timing of movement on this fault is not known. Backthrusting in the Indus Suture Zone and the North Zanskar shelf was also taking place during this time interval (Searle, 1983, 1986).

6.3 Tectonic implications

The data presented in this thesis, and synthesised in the model above, document the post-collisional burial and metamorphism of the Suru valley, and its subsequent exhumation from deep crustal levels. Metamorphic modelling and Sm-Nd dating of garnets (Vance & Harris, 1999) show that rocks had reached conditions suitable to grow garnets (500-580 ^{0}C, 6-7 kbar) by 33-31 Ma and that peak metamorphic conditions had been attained by 25 Ma ago. If the timing of India-Asia collision is taken to be 50-54 Ma (Searle *et al.*, 1987, 1997) then the timescale of 20-30 Ma to reach peak metamorphic conditions is in agreement with typical

conductive thermal models for overthrusting (e.g. England & Thompson, 1984). P-T trajectories calculated for garnet-bearing samples from the Donara and Tapshah nappes generally show paths of moderate P-T slope, and not those of nearly isothermal pressure increase followed by nearly isobaric heating as proposed by Vance & Mahar (1998), and as has been modelled using one-dimensional models assuming instantaneous overthrusting. One possibility to explain this is that the modelling is fundamentally inaccurate, and this is discussed in the next section. A more constructive approach is to consider the paths in terms of representing actual tectonic conditions. Garnets are predicted to begin growing at depths of 6-7 kbar, which corresponds to depths of 21-25 km if a lithostatic gradient of 0.285 kbar/km is assumed; in other words, we have no way of knowing the P-T path of the first 20 kilometres of burial. Furthermore, garnets are shown to be growing as crustal thickening by nappe formation in the Suru valley occurs. Although thrusting and thickening is believed to have still been occurring in the overlying Tethyan shelf sediments at this time (Searle, 1986; Searle *et al.*, 1997), nappe formation can be considered at the largest scale as homogenous thickening rather than purely simple overthrusting. This would lead to pressure increasing more slowly relative to temperature than a simple overthrusting scenario. Hodges *et al.* (1988) noted that the high concentration of radiogenic isotopes in High Himalayan samples imply heat production rates of up to three times greater than average heat production rates in the Earth's crust, and that this would influence the thermal structure of the HHC. Although their study concerned the central Himalayas, a factor such as this could possibly influence P-T trajectories in the way described above.

High temperatures persisted in the Suru valley until at least 20.8 Ma, when melting is believed to have occurred around Shafat. Although the time taken to reach peak metamorphic conditions (35-25 Ma) is in general agreement with the thermal models mentioned above, the maintaining of high temperatures until ca. 20 Ma is longer than would be predicted by a simple overthrusting model where thrusting occurred only along the India-Asia suture zone at 50-54 Ma, as pointed out by Vance & Harris (1999). If high temperatures are to persist for 10-15 Ma then some mechanism is needed to maintain them. Searle *et al.* (1987, 1997) described later break-back thrusting in the Tethyan Himalaya subsequent to initial collision that could have reloaded the pile, and this study shows that folding and thrusting continued until at least 35 Ma ago.

6.4 The validity of metamorphic modelling

The results of a large amount of metamorphic modelling have been presented in this thesis, with the ultimate aim of determining the prograde metamorphic evolution of suitable garnet-bearing samples. The results of the modelling have been integrated with field mapping, petrographic and microstructural analysis and thermobarometric analysis to construct a model for the tectonothermal evolution for the HHC of the Suru valley region. However, it is worth pointing out the extent to which the P-T trajectories and phase equilibria that have been calculated can be relied upon to represent "real" tectonometamorphic processes. The program THERMOCALC has been used to build phase diagrams for specific rock bulk compositions, or "pseudosections", and these have been shown to consistently predict the conditions of growth of garnet cores and rims. It also models the peak metamorphic assemblage of samples satisfactorily. What it cannot do, however, is model the fractionation of garnet during growth, which leads to discrepancies between predicted and observed amounts of phases and their compositions. Program GIBBS has the ability to account for garnet fractionation, and is used in conjunction with THERMOCALC-generated pseudosections to calculate P-T paths from garnet compositional zoning data. Thus, a start point and an end point for Gibbs modelling is specified by THERMOCALC, and also changes in the mineral assemblage along a P-T path.

The use of two different calculation methods allows comparison between the two and enables checks on the consistency of each others' results to be made. The chemical system that is chosen for the modelling of samples is crucial, as the stability of phases can be very sensitive to small changes in different system components. For example, it has been shown that garnet stability is extremely sensitive to changes in CaO and MnO in THERMOCALC-generated pseudosections, and that the slopes and lengths of P-T paths are very sensitive to the relative amounts of plagioclase and clinozoisite when using GIBBS. Furthermore, the inability of THERMOCALC to account for garnet fractionation will affect the pseudosection that is being used as a template for Gibbs modelling. The water activity of a sample is hard to estimate, and may change due to internal or external factors (buffering or fluid influx) during metamorphism. The important point to make is that the use of one calculation method on its own may not highlight discrepancies that only become apparent after modelling with the other.

In summary, in order to obtain reliable and consistent P-T paths from metamorphic rocks, both integrative and differential calculation techniques should be used. This allows checks on the consistency of each method, and exploits the features that each method

performs best. Furthermore, if these techniques are used to constrain the tectonic evolution of an area, then as much knowledge as possible must be obtained on the area in order to evaluate the validity of calculated P-T paths. This includes the correlation of regional deformation with microstructures, the introduction of structural time-markers into the evolution of mineral assemblages, and the absolute pressure-temperature conditions recorded by the mineral assemblages. Information from mineral inclusions preserved in porphyroblasts would provide additional extremely useful constraints.

6.5 Further work

This study presents an integrated field mapping, microstructural, thermobarometric and metamorphic modelling approach to the elucidation of the prograde metamorphic evolution of the High Himalayan Crystallines around the Suru valley. Whilst detailed mapping and thermobarometry have been performed throughout the Himalaya, metamorphic modelling as a tool for constraining the tectonic evolution of other parts of the Himalaya, and indeed other orogens has not been widely used. With respect to the detailed consideration of the modelling itself, a number of developments would greatly assist in the application of the techniques described in this thesis. Although it may prove too complex, the incorporation of fractional crystallisation calculations into the software of THERMOCALC would prove extremely useful in P-T path determination. This could also allow the consideration of fluids which are allowed to leave the system. In light of the conclusions reached in the previous section, it would also be useful to perform Gibbs method calculations using the same thermodynamic dataset used in the THERMOCALC calculations. It would be useful if the program allowed the specification and manipulation of activity-composition relationships in a manner as simple as that of THERMOCALC datafiles. Use of exactly the same datafile in both calculation methods would then allow greater confidence when comparing the two.

The modelling in this study was confined to rocks of a pelitic composition. It would be informative to attempt modelling on rocks of different bulk compositions such as amphibolites and compare the results with those obtained from pelites. This may constrain the P-T evolution of the area further.

Ultimately, it is the rates and magnitudes of tectonic processes that we wish to quantify. Detailed constraints on the still-active Himalayan orogen may be extremely helpful in solving problems encountered in older collision belts.

References

ATHERTON, M.P. (1968) The variation in garnet, biotite and chlorite composition in medium grade pelitic rocks from the Dalradian, Scotland, with particular reference to zonation in garnet. *Contributions to Mineralogy and Petrology* **18**, pp.347-371.

BAKER, J. & HOLLAND, T.J.B. (1996) Experimental reversals of chlorite compositions in divariant MgO + Al2O3 + SiO2 + H2O assemblages. *American Mineralogist* **81**, pp.676-684.

BARROW, G. (1893) On an intrusion of muscovite-biotite gneiss in the southeastern Highlands of Scotland, and its accompanying metamorphism. *Quarterly Journal of the Geological Society of London* **49**, pp.330-358.

BARROW, G. (1912) On the geology of lower Dee-side and the southern Highland Border. *Proceeds of the Geological Association* **23**, pp. 274-290.

BERMAN, R.G. (1988) Internally consistent thermodynamic data for minerals in the system Na2O-K2O-CaO-MgO-FeO-Fe2O3-Al2O3-SiO2-TiO2-H2O-CO2. *Journal of Petrology* **29**, pp.445-522.

BERMAN, R.G. (1990) Mixing properties of Ca-Mg-Fe-Mn garnets. *American Mineralogist* **75**, pp.238-377.

BHATTACHARYA, L., MOHANTY, L., MAJI, A., SEN, S.K., & RAITH, M. (1992) Non-ideal mixing in the phlogopite-annite binary: constraints from experimental data on Mg-Fe partitioning and a reformulation of the biotite-garnet geothermometer. *Contributions to Mineralogy and Petrology* **111**, pp.87-98.

BRODIE, K.H. & RUTTER, E.H. (1985) On the relationship between deformation and metamorphism, with special reference to the behaviour of basic rocks. *In;* Metamorphic reactions; kinetics, textures, and deformation, Thompson, A.B. & Rubie, D.C. (eds) *Advances in Physical Geochemistry* **4**, 138-179.

BRUNEL, M. & KIENAST, J-R. (1986) Étude pétro-structurale des chevauchements ductiles himalayens sur la transversale de l'Evereste -Makalu (Népal oriental). *Canadian Journal of Earth Sciences* **23**, pp.1117-1137.

BURCHFIEL, B.C. & ROYDEN, L.H. (1985) North-South extension within the convergent Himalayan region. *Geology* **13**, pp.679-682.

BURCHFIEL, B.C., CHEN, Z., HODGES, K.V., LIU, Y., ROYDEN, L.H., DENG, C. & XU, J. (1992) The South Tibetan Detachment System, Himalayan Orogen: Extension Contemporaneous With and Parallel to Shortening in a Collisional Mountain Belt. *Geological Society of America Special Paper* **269**, pp.41.

BURG, J.-P., BRUNEL, M., GAPIAS, D., CHEN, G.M. & LIU, G.H. (1984) Deformation of leucogranites of the crystalline Main Central Sheet in southern Tibet (China). *Journal of Structural Geology* **6**, pp.535-542.

BURTON, J. (1995) Petrogenesis of garnet migmatites and garnet granitoids, with reference to Namaqualand, South Africa and the Western Himalaya. Unpublished Ph.D. thesis, University of Oxford.

CHERNOFF, C.B., & CARLSON, W.D. (1997) Disequilibrium for Ca during growth of pelitic garnet. *Journal of Metamorphic Geology* **15**, pp.421-438.

CIRCONE, S. & NAVROTSKY, A. (1992) Substitution of Al in phlogopite: High temperature solution calorimetry, heat capacities, and thermodynamic properties of the phlogopite-eastonite join. *American Mineralogist* **77**, pp.1191-1205.

COPELAND, P., HARRISON, T.M., KIDD. W.S., RONGHAU, X. & YUQUAN, Z. (1987) Rapid early Miocene acceleration of uplift in the Gangdese belt, Xizang (southern Tibet), and its bearing on accommodation mechanisms of the India-Asia collision. *Earth and Planetary Sciences Letters* **86**, pp.240-252.

CORFIELD, R.I. (1998) Origin and emplacement of the Spontang ophiolite and crustal shortening processes in the Ladakh-Zanskar Himalaya, NW India. Unpublished D.Phil. thesis, University of Oxford.

CRAWFORD, M.L., KRAUS, D.W. & HOLLISTER, L.S. (1979) Petrologic and fluid inclusion study of calc-silicate rocks, Prince Rupert, British Columbia. *American Journal of Science* **9**, pp.1135-1159.

DASGUPTA, S., SENGUPTA, P., GUHA, D. & FUKUOKA, M. (1991) A refined garnet-biotite Fe-Mg exchange geothermometer and its application in amphibolites and granulites. *Contributions to Mineralogy and Petrology* **109**, pp.130-137.

DEER, W.A., HOWIE, R.A., & ZUSSMAN, J. (1982) Orthosilicates. Longman.

DEMPSTER, T.J. (1985) Garnet zoning and metamorphism of the Barrovian Type Area, Scotland. *Contributions to Mineralogy and Petrology* **89**, pp.30-38.

DIETRICH, V. & GANSSER, A. (1981) The leucogranites of the Bhutan Himalaya (crustal anatexis versus mantle melting)., *Schweizerische mineralogisch u. petrographisch Mittelungen*, Vol.**61**, pp.177-202.

DEWEY, J,F., CANDE, S. & PITMAN, S.C. (1989) Tectonic Evolution of the India/Eurasia collision zone. *Eclogae Geologicae Helvetiae* **82**, pp.717-37.

DRANSFIELD, M.W. (1994) Extensional exhumation of high-grade metamorphic rocks in western Norway and the Zanskar Himalaya. Unpublished D.Phil. thesis, Oxford University.

DROOP, G.T.R. & BUCHER-NURMINEN, K. (1984) Reaction Textures and Metamorphic Evolution of Sapphirine-bearing Granulites from the Gruf Complex, Italian Central Alps. *Journal of Petrology* **25**, pp.766-803.

DROOP, G.T.R. & HARTE, B. (1995) The effect of Mn on the Phase Relations of Medium-Grade Pelites: Constraints from Natural Assemblages on Petrogenetic Grid Topology. *Journal of Petrology* **36**, pp.1549-1578.

EDWARDS, M.A. & HARRISON, T.M. (1997) When did the roof collapse? Late Miocene north-south extension in the High Himalaya revealed by Th-Pb monazite dating of the Khula Kangri granite. *Geology* **25**, pp.543-546.

ENGLAND, P.C. & RICHARDSON, S.W. (1977) The influence of erosion on upon the mineral facies of rocks from different metamorphic environments. *Journal of the Geological Society of London* **134**, pp.201-213.

ENGLAND, P.C. & THOMPSON, A.B. (1984) Pressure-temperature-time paths of regional metamorphism, Part I: Heat transfer during the evolution of regions of thickened continental crust. *Journal of Petrology* **25**, pp.894-298.

ENGLAND, P.C., LE FORT, P., MOLNAR, P., & PECHER, A. (1992) Heat sources for Tertiary Metamorphism and Anatexis in the Annapurna-Manaslu Region, Central Nepal. *Journal of Geophysical Research* **97**, pp.2107-2128.

ENGLAND, P.C. & MOLNAR, P. (1993) The interpretation of inverted metamorphic isograds using simple physical calculations. *Tectonics* **12**, pp.145-157.

ERNST, W.G. (1973) Blueschist metamorphism and P-T regimes in active subduction zones. *Tectonophysics* **17**, pp.255-272.

ERNST, W.G. (1976) Petrologic Phase Equilibria. *W.H. Freeman, San Francisco.*

ESKOLA, P. (1914) On the petrology of the Orijärvi region in southwestern Finland. *Bull Commission Geol Finland* **40:277.**

ESKOLA, P. (1915) On the relation between the chemical and mineralogical composition in the metamorphic rocks of the Orijärvi region. *Bull. Commission Geol. Finland* **44** pp. 109-145.

EUGSTER, H.P., ALBEE, A.L., BENCE, A.E., THOMPSON, J.B.Jr, & WALDBAUM, D.R. (1972) The Two-Phase Region and Excess Mixing Properties of Paragonite-Muscovite Crystalline Solutions. *Journal of Petrology* **13**, pp.141-179.

FERRY, J.M. & SPEAR, F.S. (1978) Experimental Calibration of the Partitioning of Fe and Mg between Biotite and Garnet. *Contributions to Mineralogy and Petrology* **66**, pp.113-117.

FROST, B.R. & CHACKO, T. (1989) The granulite uncertainty principle: Limitations on thermobarometry in granulites. *Journal of Geology* **97**, pp.435-450.

FUCHS, G. (1979) On the geology of western Zanskar. *Jahrbuch der Geologischen Bundesanstalt Wien* **125**, pp.1-50.

GAETANI, M. & GARZANTI, E. (1991) Multicyclic History of the Northern India Continental Margin (Northwestern Himalaya). *American Association of Petroleum* Geologists **75**, pp.1427-1446.

GANGULY, J. (1972) Staurolite stability and related parageneses: Theory, experiments and applications. *Journal of Petrology* **13**, pp.335-365.

GANGULY, J. & SAXENA, S.K. (1984) Mixing properties of aluminosilicate garnets: constraints from natural and experimental data, and application to geothermobarometry. *American Mineralogist* **69**, pp.88-97.

GANSSER, A. (1964) Geology of the Himalaya. Wiley Interscience.

GAPAIS, A., PECHER, A., GILBERT, E. & BALLEVRE, M. (1992) Synconvergence spreading of the Higher Himalaya Crystalline in Ladakh. *Tectonics* **11**, pp.1045-1056.

GHENT, E.D., & STOUT, M.Z. (1981) Geobarometry and Geothermometry of Plagioclase-Biotite-Garnet-Muscovite Assemblages. *Contributions to Mineralogy and Petrology* **76,** pp.17-92.

GRUJIC, D., CASEY, M., DAVIDSON, C., HOLLISTER, L.S., KUNDIG, R., PAVLIS, T., & SCHMID, S. (1996) Ductile extrusion of the Higher Himalayan Crystalline in Bhutan: evidence from quartz microfabrics. *Tectonophysics* **260**. Pp.21-43.

GUIDOTTI, C.V. (1984) Micas in metamorphic rocks. *In Reviews in Mineralogy* **13***: Micas.* S.W. Bailey ed., pp.357-456.

GUIDOTTI, C.V. & SASSI, F.P. (1976) Muscovite as a petrogenic indicator mineral in pelitic schists. In: Neues Jahrbuch fur Mineralogie, pp.97-142. E. Schweizerbart'sche Verlagsbuchhandlung. Stuttgart, Federal Republic of Germany.

GUIDOTTI, C.V., CHENEY, J.T. & GUGGENHEIM, S. (1977) Distribution of titanium between coexisting muscovite and biotite in pelitic schists from northwestern Maine. *American Mineralogist* **62**, pp.438-448.

GUIDOTTI, C.V., SASSI, F.P., SASSI, R. & GLENCOE, J.G. (1994) The effects of ferromagnesian components on the paragonite-muscovite solvus; a semi-quantitative analysis based on chemical data for natural paragonite-muscovite pairs. *Journal of Metamorphic Geology* **12**, pp.779-788.

HACKLER, R.T. & WOOD, B.J. (1989) Experimental determination of Fe and Mg exchange between garnet and olivine and estimation of Fe-Mg mixing properties in garnet. *American Mineralogist* **74**, pp.994-999.

HARLEY, S.L. (1989) The origins of granulites: a metamorphic perspective. *Geological Magazine* **126**, pp.215-247.

HARRIS, N.B.W. & MASSEY, J. (1994) Decompression and anatexis of Himalayan metapelites. *Tectonics* **13**, pp.1537-1546.

HARRISON, T.M., RYERSON, F.J., LE FORT, P., YIN, A., LOVERA, O.M. & CATLOS, E.J. (1997) A Late Miocene-Pliocene origin for the Central Himalayan inverted metamorphism. *Earth and Planetary Science Letters* **146**, pp.E1-E7.

HERREN E. (1987) Zanskar Shear Zone: Northeast-Southwest extension within the Higher Himalayas (Ladakh, India), *Geology*, Vol.**15**, pp.409-413.

HIRN, A. (1988) Features of the crust-mantle structure of the Himalayas-Tibet: a comparison with seismic traverses of Alpine, Pyrenean and Variscan orogenic belts. *Philosophical Transactions of the Royal Society of London* **A326,** pp.17.32.

HIRN, A., LEPINE, J.-L., JOBERT, G., SAPIN, M., WITTLINGER, G., XIN, X.-Z., YUAN, G.-E., JING, W.-X., WEN, T.-J., BAI, X.-S., PANDEY, M.R. & TATER, J.M. (1984a) Crustal structure and variability of the Himalayan border of Tibet. *Nature* **307**, pp.23-25.

HODGES, K.V. (1998) The thermodynamics of Himalayan orogenesis. *In;* What Drives Metamorphism and Metamorphic Reactions, Treloar, P.J. & O'Brien, P.J. (eds) *Geological Society of London Special Publication* **138**, 7-22.

HODGES, K.V. & SPEAR, F.S. (1982) Geothermometry, geobarometry and the Al2SiO5 triple point at Metamorphism. Moosilauke, New Hampshire. *American Mineralogist* **67**, pp.1118-1134.

HODGES, K.V. & ROYDEN, L. (1984) Geologic thermobarometry of retrograded metamorphic rocks: an indication of the uplift trajectory of a portion of the Northern Scandinavian Caledonides. *Journal of Geophysical Research* **89**, pp.7077-7090.

HODGES, K.V. & MCKENNA, L.W. (1987) Realistic propagation of uncertainties in geologic thermobarometry. *American Mineralogist* **72**, pp. 671-680.

HODGES, K., HUBBARD, M.S., & SILVERBERG, D.S. (1988) Metamorphic constraints on the thermal evolution of the central Himalayan orogen. *Philosophical Transactions of the Royal Society of London* **A326**, pp.257-280.

HODGES, K.V. & SILVERBERG, D.S. (1988) Thermal evolution of the Greater Himalaya, Garhwal, India. *Tectonics* **7**, pp.583-600.

HODGES, K.V, PARRISH, R., HOUSH, T., LUX, D., BURCHFIEL, B.C., ROYDEN, L., & CHEN, Z. (1992) Simultaneous Miocene extension and shortening in the Himalayan orogen. *Science* **258**, pp.1466-70.

HODGES, K.V., BURCHFIEL, B.C., ROYDEN, L.H., CHEN, Z. & LIU, Y. (1993) The metamorphic signature of contemporaneous extension and shortening in the central Himalayan orogen: data from the Nyalam transect, southern Tibet. *Journal of Metamorphic Geology* **11**, pp.721-737.

HODGES, K.V., PARRISH, R.R., SEARLE, M.P. (1996) Tectonic evolution of the central Annapurna Range, Nepalese Himalayas. *Tectonics* **15**, pp.1264-1291.

HODGES, K., BOWRING, S., DAVIDEK, K., HAWKINS, D., & KROL, M. (1998) Evidence for rapid displacement on Himalayan normal faults and the importance of tectonic denudation in the evolution of mountain ranges. *Geology* **26**, pp.483-486.

HOLDAWAY, M.J. & LEE, S.M. (1977) Fe-Mg cordierite stability in high-grade pelitic rocks based on experimental, theoretical, and natural observations. *Contributions to Mineralogy and Petrology* **63**, pp.175-198.

HOLDAWAY, M.J. & MUKHOPADHYAY, B. (1993) of the stability relations of andalusite; thermochemical data and phase diagram for the aluminum silicates. *American Mineralogist* **78**, pp.298-315.

HOLLAND, T.J.B. & RICHARDSON, S.W. (1979) Amphibole Zonation in Metabasites as a Guide to the Evolution of Metamorphic Conditions. *Contributions to Mineralogy and Petrology* **70**, pp.143-148.

HOLLAND, T.J.B. & POWELL, R. (1985) An internally consistent thermodynamic dataset with uncertainties and correlations: 2. Data and results. *Journal of Metamorphic Geology* **3**, pp.343-370.

HOLLAND, T.J.B. & POWELL, R. (1990) An enlarged and internally consistent thermodynamic dataset with uncertainties and correlations: the system K2O-Na2O-CaO-MgO-MnO-FeO-Fe2O3-Al2O3-TiO2-SiO2-C-H2-O2. *Journal of Metamorphic Geology* **8**, pp.89-124.

HOLLAND, T.J.B. & POWELL, R (1992) Plagioclase feldspars: Activity-composition relations based on Darken's quadratic formalism and Landau theory. *American Mineralogist* **77**, pp.53-61.

HOLLAND, T.J.B. & POWELL, R. (1996) Thermodynamics of order-disorder in minerals: I. Symmetric formalism applied to minerals of fixed composition. *American Mineralogist* **81**, pp.1413-1424.

HOLLAND, T.J.B. & POWELL, R. (1996) Thermodynamics of order-disorder in minerals: II. Symmetric formalism applied to solid solutions. *American Mineralogist* **81**, pp.1425-1437.

HOLLAND, T.J.B. & POWELL, R. (1998) An internally consistent thermodynamic dataset for phases of petrological interest. *Journal of Metamorphic Geology* **16**, pp.309-343.

HOLLISTER, L.S. (1966) Garnet zoning: An interpretation based on the Rayleigh fractionation model. *Science* **154**, pp.1647-1651.

HOLLISTER, L.S. (1982) Metamorphic evidence for rapid (1-2mm/yr) uplift of a portion of the Central Gneiss Complex, Coast Mountains, B.C. *Canadian Mineralogist* **20**, pp.319-332.

HONEGGER, K. (1983) Struktur und Metamorphose des Zaskar/Kristallins, Suru Ladakh. Unpublished Ph.D. thesis, E.T.H. Zurich.

HONEGGER, K., DIETRICH, V., FRANK, W., GANSSER, A., THÖNI, M., & TROMMSDORFF, V. (1982) Magmatism and metamorphism in the Ladakh Himalayas (the Indus-Tsangpo suture zone). *Earth and Planetary Science Letters* **60**, pp.253-292.

HUBBARD, M.S (1989) Thermobarometric constraints on the thermal history of the Main Central Thrust zone and Tibetan Slab, eastern Nepal. *Journal of Metamorphic Geology* **7**, pp.19-30.

HUBBARD, M.S. (1996) Ductile Shear as a Cause of Inverted Metamorphism: Example from the Nepal Himalaya. *Journal of Geology* **104**, pp.493-499.

HUBBARD, M.S. & HARRISON. T.M. (1989) 40Ar/39Ar age constraints on deformation and metamorphism in the Main Central Thrust zone and Tibetan Slab, eastern Nepal Himalaya. *Tectonics* **8**, pp.865-880.

INGER, S. (1998) Timing of an extensional detachment during convergent orogeny: New Rb-Sr geochronological data from the Zanskar shear zone, northwest Himalaya. *Geology* **26**, pp.223-226.

INGER, S & HARRIS, N.B.W. (1992) Tectonothermal evolution of the High Himalayan Crystalline Sequence, Langtang Valley, northern Nepal. *Journal of Metamorphic Geology* **10**, pp.439-452.

INDARES, A. & MARTIGNOLE, J. (1984)Evolution of P-T conditions during a high-grade metamorphic event in the Maniwaki area (Grenville Provinces). *Canadian Journal of Earth Sciences* **21**, pp.853-863.

JAIN, A.K. & MANICKAVASAGAM, R.M. (1993) Inverted metamorphism in the intracontinental ductile shear zone during Himalayan collision tectonics. *Geology* **21**, pp.407-410.

JAUPART, C. & PROVOST, A. (1985) Heat focussing, granite genesis and inverted metamorphic gradients in continental collision zones. *Earth and Planetary Science Letters* **73**, pp.385-397.

KOHN, M.J. & SPEAR, F.S. (1991) Error propagation for barometers II: Application to rocks. *American Mineralogist* **76**, pp.138-147.

KRETZ, R. (1973) Kinetics of the crystallisation of garnet at two localities near Yellowknife. *Canadian Mineralogist* **12**, pp.1-20.

KUMAR, A., NAND, L. JAIN, A.K. & SORKHABI, R.B. (1995) Late Cenozoic-Quaternary Thermo-Tectonic History of Higher Himalayan Crystalline (HHC) in Kishtwar-Padar-Zanskar region, NW Himalaya: Evidence from fission track ages. *Journal of the Geological Society of India* **45**, pp.375-391.

KÜNDIG, R. (1989) Domal structures and high-grade metamorphism in the Higher Himalayan Crystalline, Zanskar Region, northwest Himalaya, India. *Journal of Metamorphic Geology* **7**, pp.43-55.

LE FORT, P. (1975) Himalayas; the collided range. Present knowledge of the continental arc. *American Journal of Science*, Vol.**275**, pp.1-44.

LE FORT, P. (1981) Manaslu leucogranites: A collision signature of the Himalaya, a model for its genesis and emplacement., *Journal of Geophysical Research*, Vol.**86**, pp.10545-68.

LE FORT, P., DEBON, F., PÊCHER, A., SONET, J. & VIDAL, P. (1986) The 500 Ma magmatic event in Alpine southern Asia, a thermal episode at Gondwana scale. *Sciences de la Terre,* **Memoire 47**, pp.191-209.

LOOMIS, T.P. (1975) Reaction of Zoning of Garnet. *Contributions to Mineralogy and Petrology* **52**, pp.411-423.

MACFARLANE, A. (1995) An evaluation of the inverted metamorphic gradient at Langtang National Park, Central Nepal Himalaya. *Journal of Metamorphic Geology* **13**, pp.595-612.

MAHAR, E.M. (1997) The effect of Mn, Ca, Na on mineral stability in pelites. Unpublished Ph.D thesis, University of Cambridge.

MAHAR, E.M., BAKER, J.M., POWELL, R., HOLLAND, T.J.B., & HOWELL, N. (1997) The effect of Mn on mineral stability in metapelites. *Journal of Metamorphic Geology* **15**, pp.223-238.

MENARD, T. & SPEAR, F.S. (1993) Metamorphism of Calcic Pelitic Schists, Strafford Dome, Vermont: Compositional Zoning and Reaction History. *Journal of Petrology* **34**, pp.977-1005.

METCALFE, R.P. (1990) A Thermotectonic evolution for the Main Central Thrust and Higher Himalaya, Western Garhwal, India. Unpublished Ph.D. thesis, Leicester University.

METCALFE, R.P. (1993) Pressure, temperature and time constraints on metamorphism across the Main Central Thrust zone and High Himalayan Slab in the Garhwal Himalaya. *In*: Himalayan Tectonics, Treloar, P.J, Searle, M.P. (eds), *Geological Society of London Special Publication* **74**, 485-509.

MIYASHIRO, A. (1961) Evolution of mountain belts. *Journal of Petrology* **2**, pp. 277-311.

MOLNAR, P. (1988) A review of the geophysical constraints on the deep structure of the Tibetan Plateau, the Himalaya and the Karakorum, and their tectonic implications. *Philosophical Transactions of the Royal Society of London* **A326**, pp.33-88.

MOLNAR, P. & TAPPONNIER, P. (1975) Cenozoic Tectonics of Asia: Effects of a Continental Collision. *Science* **189**, pp.419-426.

NAJMAN, Y., PRINGLE, M.S., JOHNSON, M.R.W., ROBERTSON, A.H.F., WIJBRANS, J. & OLIVER, G.J.H. (1997) $^{40}Ar/^{39}Ar$ dating of detrital micas in early Himalayan foredeep sediments, northern India: Implications for early Himalayan tectonics and exhumation history. *(Abstract) 12th Himalaya-Karakorum-Tibet Workshop, Rome.*

NEWTON, R.C., CHARLU, T.V. & KLEPPA, O.J. (1980) Thermochamistry of the high structural state plagioclases. *Geochimica et Cosmochimica Acta* **44**, pp.933-941.

NOBLE, S.R. & SEARLE, M.P. (1995) Age of crustal melting and leucogranite formation from U-Pb zircon and monazite dating in western Himalaya, Zanskar, India. *Geology* **23**, pp.1135-1138.

NOBLE, S.R, SEARLE, M.P. & WALKER, C.B. (1999) Age and tectonic significance of Permian granites, Zanskar, NW India (in prep.)

PARRISH, R.R. & HODGES, K.V. (1996) Isotopic constraints on the age and provenance of the Lesser and Greater Himalaya sequences, Nepalese Himalaya. *Geological Society of America Bulletin* **108**, pp.904-911.

PASSCHIER, C.W. & TROUW, R.A.J, (1996) Microtectonics. Springer-Verlag, Berlin.

PATRIAT, P. & ACHACHE, J. (1984) India-Eurasia collision chronology and its implications for crustal shortening and driving mechanisms of plates. *Nature* **311**, pp.615-621.

PÊCHER, A. (1978) Deformations et metamorphisme associes a une zone du cisaillement: Exemple du grand chevauchement central Himalayan (MCT). (D.Sc. thesis): Grenoble, France, Grenoble University,

PÊCHER, A. (1989) The metamorphism in the central Himalaya. *Journal of Metamorphic Geology* **7**, pp.31-41.

PERCHUK, L.L. & LAVRENT'EVA (1983) Experimental investigation of exchange equilibria in the system cordierite-garnet-biotite.; 3. In: Kinetics and equilibrium in mineral reactions, Saxena, S.K. (ed). *Advances in Physical Geochemistry*, pp.199-239.

PETO, P. (1976) An experimental investigation of melting reactions involving muscovite and paragonite in the silica-saturated portion of the system K_2O-Na_2O-Al_2O_3-SiO_2-H_2O to 15 kbar total pressure. *Programmes in experimental petrology*, NERC 3rd report, London, pp.41-45.

PETTERSON, M.G. (1984) The structure, petrology and geochemistry of the Kohistan batholith, Gilgit, NW Pakistan. Unpublished PhD thesis, University of Leicester.

POGNANTE, U., CATELLI, D, BENNA, P., GENOVESE, G., OBERLI, F., MEIER, M., & TONARINI, S. (1990) The crystalline units of the High Himalayas in the Lahul-Zanskar region (northwest India): metamorphic-tectonic history and geochronology of the collided and imbricated Indian plate. *Geological Magazine* **127**, pp.101-116.

POGNANTE, U. & BENNA, P. (1993) metamorphic zonation, migmatisation and leucogranites along the Everest transect of Eastern Nepal and Tibet: record of an exhumation history. In: Himalayan Tectonics, Treloar, P.J., & Searle, M.P. (eds). *Geological Society of London Special Publication* **74**, 323-340.

POWELL, R. (1987) Darken's quadratic formalism and the thermodynamics of minerals. *American Mineralogist* **72**, pp.1-11.

POWELL, R. & HOLLAND, T.J.B. (1985) An internally consistent thermodynamic dataset with uncertainties and worked examples and correlations: 1. Methods and a worked example. *Journal of Metamorphic Geology* **3**, pp. 327-342.

POWELL, R. & HOLLAND, T.J.B. (1988) An internally consistent dataset with uncertainties and correlations: 3. Applications to geobarometry, worked examples and a computer program. *Journal of Metamorphic Geology* **6**, pp.173-204.

POWELL, R. & HOLLAND, T.J.B (1990) Calculated mineral equilibria in the pelite system, KFMASH (K2O-FeO-MgO-Al2O3-SiO2-H2O). *American Mineralogist* **75**, pp.367-380.

POWELL, R. & HOLLAND, T.J.B (1993) On the formulation of simple mixing models for complex phases. *American Mineralogist* **78**, pp.1174-1180.

POWELL, R. & HOLLAND, T.J.B. (1994) Optimal geothermometry and geobarometry. *American Mineralogist Vol.* **79**, pp. 120-133.

POWELL, R., HOLLAND, T.J.B., & WORLEY, B. (1998) Calculating phase diagrams involving solid solutions via non-linear equations, with examples using THERMOCALC. *Journal of Metamorphic Geology* **16**, pp.577-588.

PRICE, N.J. & COSGROVE, J.W. (1990) The analysis of geological structures. Cambridge University Press.

RAMSAY, J.G. (1981) Tectonics of the Helvetic Nappes. *Thrust and Nappe Tectonics*, The Geological Society of London, pp.293-?

ST-ONGE, M.R. (1987) Zoned Poikiloblastic Garnets: P-T Paths and Syn-Metamorphic Uplift through 30km of Structural Depth, Wopmay Orogen, Canada. *Journal of Petrology* **28**, pp.1-21.

SCHÄRER, U., XU, R.H. & ALLEGRE, C.J. (1984) U-Pb geochemistry of Gangdese (Trans-Himalayan) plutonism in the Lhasa-Xigase region, Tibet. *Earth and Planetary Science Letters* **69**, pp.311-320.

SEARLE, M.P. (1983) Stratigraphy, structure and evolution of the Tibetan Tethys zone in Zanskar and the Indus suture zone in the Ladakh Himalaya. *Transactions of the Royal Society, Edinburgh, Earth Sciences* **73**, pp.203-217.

SEARLE, M.P. (1986) Structural evolution and sequence of thrusting in the High Himalayan, Tibetan-Tethys and Indus Suture Zones of Zanskar and Ladakh, western Himalaya. *Journal of Structural Geology*, Vol.**8**, pp.923-936.

SEARLE, M.P. (1991) Geology and Tectonics of the Karakorum Mountains. John Wiley & Sons, Chichester.

SEARLE, M.P. & FRYER, B.J. (1986) Garnet, tourmaline and muscovite-bearing leucogranites, gneisses and migmatites of the Higher Himalayas from Zanskar, Kulu, Lahoul and Kashmir. *Collision Tectonics*, ed. M.P. Coward & A.C. Ries, Geological Society Special Publication **19**, pp.185-201.

SEARLE, M.P., WINDLEY, B.F., COWARD, M.P., COOPER, D.J.W., REX, A.J., TINGDONG, L., XUCHANG, X., JAN, M.Q., THAKUR, V. & KUMAR, S. (1987) The closing of Tethys and the tectonics of the Himalayas. *Bulletin of the Geological Society of America* **98**, pp.678-701.

SEARLE, M.P., COOPER, D.J.W., & REX, A.J. (1988) Collision tectonics of the Ladakh-Zanskar Himalaya. *Philosophical Transactions of the Royal Society of London* **A326**, pp.117-150.

SEARLE, M.P. & REX, A.J. (1989) Thermal model for the Zanskar Himalaya. *Journal of Metamorphic Geology* **7**, pp.127-134.

SEARLE, M.P., WATERS, D.J., REX, D.C., & WILSON, R.N. (1992) Pressure, temperature and time constraints on Himalayan metamorphism from eastern Kashmir and western Zanskar. *Journal of the Geological Society, London* **149**, pp.753-773.

SEARLE, M.P., CORFIELD, R.I., STEPHENSON, B.,& McCARRON, J. (1997) Structure of the North Indian continental margin in the Ladakh-Zanskar Himalayas: implications for the timing of obduction of the Spontang ophiolite, India-Asia collision and deformation events in the Himalaya. *Geological Magazine* **134**, pp.297-316.

SEARLE, M.P., PARRISH, R.R., HODGES, K.V., HURFORD, A., AYRES, M.W. & WHITEHOUSE, M.J. (1997) Shisha Pangma Leucogranite, South Tibetan Himalaya: Field Relations, Geochemistry, Age, Origin and Emplacement. *Journal of Geology* **105**, pp.295-317.

SEARLE, M.P., WATERS, D.J., DRANSFIELD, M.W., STEPHENSON, B.J., WALKER, C.B., WALKER, J.D., & REX, D.C. (1999) Thermal and mechanical models for the structural and metamorphic evolution of the Zanskar High Himalaya . In: Continental Tectonics, MacNiocaill, C., & Ryan, P. (eds). *Geological Society of London Special Publication* **164**, pp.139-156.

SELVERSTONE, J., SPEAR, F.S., FRANZ, G, & MORTEANI, G. (1984) High-Pressure Metamorphism in the SW Tauern Window, Austria: P-T paths from Hornblende-Kyanite-Staurolite Schists. *Journal of Petrology* **25**, pp.501-531.

SPEAR, F.S. (1988) The Gibbs method and Duhem's theorem: The quantitative relationships among P, T, chemical potential, phase composition and reaction progress in igneous and metamorphic systems. *Contributions to Mineralogy and Petrology* **99**, pp.249-256.

SPEAR, F.S. (1993) Metamorphic Phase Equilibria and Pressure-Temperature-Time Paths. Mineralogical Society of America Monograph.

SPEAR, F.S. & SELVERSTONE, J. (1983) Quantitative P-T paths from Zoned Minerals: Theory and Tectonic Applications. *Contributions to Mineralogy and Petrology* **83**, pp.348-357.

SPEAR, F.S. & CHENEY, J.T. (1989) A petrogenetic grid for pelitic schists in the system K_2O-FeO-MgO-Al_2O_3-SiO_2-H_2O. *Contributions to Mineralogy and Petrology* **101**, pp.149-164.

SPEAR, F.S. & MENARD, T. (1989) Program GIBBS: A FORTRAN Program for Gibbs Method Calculations, version 4.0.

SPEAR, F.S., KOHN, M.J., FLORENCE, F.P., & MENARD, T. (1991) A model for garnet and plagioclase growth in pelitic schists: implications for thermobarometry and P-T path determinations. *Journal of Metamorphic Geology* **8**, pp.683-696.

SPRING, L., BUSSY, F., VANNAY, J.-C., HUON, S. & COSCA, M.A. (1993) Early Permian granitic dykes of alkaline affinity in the Indian High Himalaya of Upper Lahul and SE Zanskar: geochemical characterization and geotectonic implications, *Himalayan Tectonics*, ed. Treloar, P.J. & Searle, M.P. Vol. Geological Society Special Publication, pp, 251-264

STÄUBLI, A. (1989) Polyphase metamorphism and the development of the Main Central Thrust. *Journal of Metamorphic Geology* **7**, pp.73-93.

STEPHENSON, B.J. (1997) The tectonic and metamorphic evolution of the Main Central Thrust zone and High Himalaya around the Kishtwar and Kulu windows, northwest India. Unpublished D.Phil. thesis, Oxford University.

STÜWE, K. & POWELL, R. (1995) PT paths from modal proportions: application to the Koralm Complex, Eastern Alps. *Contributions to Mineralogy and Petrology* **114**, pp.83-93.

SWAPP, S.M. & HOLLISTER, L.S. (1991) Inverted metamorphism within the Tibetan Slab of Bhutan: Evidence for a tectonically transported heat-source. *Canadian Mineralogist* **29**, pp.1019-1041.

THOMPSON, A.B (1976) Mineral reactions in pelitic rocks: I. Prediction of P-T-X(Fe-Mg) phase relations. *American Journal of Science* **276**, pp.401-424.

THOMPSON, A.B (1976) Mineral reactions in pelitic rocks: II. Calculation of some P-T-X(Fe-Mg) phase relations. *American Journal of Science* **276**, pp.425-454.

THOMPSON, A.B (1982) Dehydration melting of pelitic rocks and the generation of H_2O-undersaturated granitic liquids. *American Journal of Science* **282**, pp.1567-1595.

THOMPSON, A.B., TRACY, R.J., LYTTLE, P.T. & THOMPSON, J.B. Jr. (1977) Prograde reaction histories deduced from compositional zonation and mineral inclusions in garnet from the Gassetts Schist, Vermont. *American Journal of Science* **277**, pp.1152-1167.

THOMPSON, J.B. Jr. (1957) The graphical analysis of mineral assemblages in pelitic schists. *American Mineralogist* **42**, pp.842-858.

TRACY, R.J. (1982) Compositional zoning and inclusions in metamorphic minerals. *In: Characterization of metamorphism through mineral equilibria; Reviews in Mineralogy* **10**, J.M. Ferry (ed.), pp.335-394.

TRACY, R.J., ROBINSON, P. & THOMPSON, A.B. (1976) Garnet composition and zoning in the determination of temperatures and pressures of metamorphism, central Massachusetts. *American Mineralogist* **61**, pp.762-775.

TRCZIENSKI, W.R. Jr. (1977) Garnet zoning-product of a continuous reaction. *Canadian Mineralogist* **15**, pp.250-256.

TURNER, F.J. (1981) Metamorphic Petrology, 2nd edition. McGraw-Hill, New York.

VANCE, D. & MAHAR, E.M. (1998) Pressure-temperature paths from P-T pseudosections and zoned garnets: potential pitfalls, and examples from the Zanskar Himalaya, NW India. *Contributions to Mineralogy and Petrology* **132**, pp.225-245.

VANCE, D. & HARRIS, N. (1999) Timing of prograde metamorphism in the Zanskar Himalaya. *Geology* **27**, pp.395-398.

VANNAY, J-C. & HODGES, K.V. (1996) Tectonometamorphic evolution of the Himalayan metamorphic core between the Annapurna and Dhaulagiri, central Nepal. *Journal of Metamorphic Geology* **14**, pp.635-656.

VANNAY, J-C. & GRASEMANN, B. (1998) Inverted metamorphism in the High Himalaya of Himachal Pradesh (NW India): phase equilibria versus thermobarometry. *Schweizerische mineralogisch u. petrographisch Mittelungen*, Vol.**78**, pp.107-132.

WALKER, J.D. (1998) The structural and metamorphic evolution of the High Himalayan Slab in SE Zanskar and NW Lahaul. Unpublished D.Phil. thesis, University of Oxford.

WATERS, D.J. , SEARLE, M.P., DRANSFIELD, M.W., REX, D.C. & STEPHENSON, B.J. (1996) Metamorphic profiles across the High Himalayas in western Zanskar, India. (Poster) 12th Himalayan-Karakorum-Tibet Workshop, Flagstaff.

WORLEY, B. & POWELL, R. (1998) Singularities in NCKFMASH (Na2O-CaO-FeO-MgO-Al2O3-SiO2-H2O). *Journal of Metamorphic Geology* **16,** pp.169-188.

ZEITLER, P.K., CHAMBERLAIN, C.P. & SMITH, H.A. (1993) Synchronous anatexis, metamorphism and denudation at Nanga Parbat (Pakistan Himalaya). *Geology* **21**, pp. 347-350.

A.1 Mixing models used in THERMOCALC

A.1.1 Mixing models for solutions used in phase diagram calculations

Unless otherwise stated, all the mineral activity-composition relations used in THERMOCALC calculations are taken from Holland & Powell (1998). For all of the phases involving solid solutions, ideal mixing on sites activities are used, but with a non-ideal contribution added. From Powell & Holland (1993); for any endmember, a, of a complex phase, the activity coefficient can be expressed as:

$$RT\ln\gamma_a = -\sum_i\sum_{j>i} (p_i^0 - p_i)(p_j^0 - p_j)W_{ij}$$

in which p_k is the *proportion* of endmember *k* in the phase, p_k^0 is the value of p_k in pure a, and W_{ij} is the macroscopic interaction parameter for the ij binary. The summations are over an independent set of endmembers chosen to represent the composition of the phase. The values of W used were those which best fitted the experimental data (Holland & Powell, 1998). In this study, Mn endmembers were incorporated into the activity-composition models provided with THERMOCALC v2.7, and the interaction parameters (W) of Mn with the other system components that it mixes with were set to zero, in the absence of any experimental data to suggest otherwise. The mixing models given are for the CNMnKFMASH system.

Garnet. Garnets are considered in terms of a quaternary Fe-Mg-Ca-Mn regular solution. From Vance & Holland (1993), a value of W_{CaMg} = 33 kJ.mol^{-1} was used to describe the significant Ca-Mg non-ideality in garnets. A small W_{FeMg} = 2.5 kJ.mol^{-1} was also incorporated.

Garnet variables: $(Fe,Mg,Ca,Mn)_3Al_2Si_3O_{12}$

x = Fe/Fe+Mg+Ca+Mn

ca = Ca/Fe+Mg+Ca+Mn

mn = Mn/Fe+Mg+Ca+Mn

endmembers: pyrope (Prp) $Mg_3Al_2Si_3O_{12}$

$a_{prp} = (1\text{-}x\text{-}ca\text{-}mn)^3$

$p_{pyp} = (1\text{-}p_{alm}\text{-}p_{grs}\text{-}p_{sps})$

$RT\ln\gamma_{prp} = W_{FeMg}x(x+ca+mn) + W_{CaMg}ca(x+ca+mn)$

almandine (Alm) $Fe_3Al_2Si_3O_{12}$

$a_{alm} = x^3$

$p_{alm} = x$

$RT\ln\gamma_{alm} = W_{FeMg}(1\text{-}x\text{-}ca\text{-}mn)(1\text{-}x) + W_{CaMg}ca(1\text{-}x\text{-}ca\text{-}mn)$

grossular (Grs) $Ca_3Al_2Si_3O_{12}$

$a_{grs} = ca^3$

$p_{grs} = ca$

$RT\ln\gamma_{grs} = W_{FeMg}(1\text{-}x\text{-}ca\text{-}mn)(x) - W_{CaMg}(1\text{-}ca)(1\text{-}x\text{-}ca\text{-}mn)$

spessartine (Sps) $Mn_3Al_2Si_3O_{12}$

$a_{sps} = mn^3$

$p_{sps} = mn$

$RT\ln\gamma_{sps} = W_{FeMg}(1\text{-}x\text{-}ca\text{-}mn)(x) - W_{CaMg}(1\text{-}ca)(1\text{-}x\text{-}ca\text{-}mn)$

Biotite. The incorporation of Mn into the Holland & Powell (1998) disordered mixing model for biotite proved rather cumbersome to code for THERMOCALC, and so the disordered model used in the older dataset (see Powell *et al.*, 1998) was used. Al is assumed to mix with Fe and Mg on two (M2) octahedral sites, and Al with Si on two (T2) tetrahedral sites. A term $W_{phleast}$ = 10 kJ.mol^{-1} is included to account for Al-Mg ordering on M2, after Circone & Navrotsky (1992).

Biotite variables: $K(Fe,Mg,Mn)(Fe,Mg,Mn,Al)_2Si_2(Si,Al)_2O_{10}(OH)_2$

x = Fe/Fe+Mg+Mn

mn = Mn/Fe+Mg+Mn

$y = 2X_{Al,M2} = Al^{oct}$

endmembers:

phlogopite (Phl) $KMg[Mg_2]Si_2[SiAl]O_{10}(OH)_2$

$a_{phl} = ¼\ (1\text{-}x\text{-}mn)^3(2\text{-}y)^2(1+y)(1\text{-}y)$ $(y = 0)$

$p_{phl} = (1\text{-}p_{ann}\text{-}p_{mnbt}\text{-}p_{east})$

$RT\ln\gamma_{phl} = W_{phl.east}(y)(x\text{-}mn)(3\text{-}y)(3y)$

annite (Ann) $KFe[Fe_2]Si_2[SiAl]O_{10}(OH)_2$

$a_{ann} = ¼\ (x)^3(2\text{-}y)^2(1+y)(1\text{-}y)$ $(y = 0)$

$p_{ann} = 1/3\ x(3\text{-}y)$

$RT\ln\gamma_{ann} = W_{phl.east}\ (\text{-}y)\text{-}[(x\text{-}mn)(3\text{-}y)](\text{-}3y)$

mnbiotite (Mnbt) $KMn[Mn_2]Si_2[SiAl]O_{10}(OH)_2$

$a_{mnbt} = ¼\ (mn)^3(2\text{-}y)^2(1+y)(1\text{-}y)$ $(y = 0)$

$p_{mnbt} = 1/3\ mn(3\text{-}y)$

$RT\ln\gamma_{mnbt} = W_{phl.east}\ \text{-}(\text{-}y)[\text{-}(x\text{-}mn)(3\text{-}y)](\text{-}3y)$

eastonite (East) $KMg[MgAl]Si_2[Al_2]O_{10}(OH)_2$

$a_{east} = ¼\ (1\text{-}x)^2y(1+y)(1\text{-}y)$ $(y = 1)$

$p_{east} = y$

$RT\ln\gamma_{east} = W_{phl.east}\ (1\text{-}y)[\text{-}(x\text{-}mn)(3\text{-}y)](\text{-}3y)$

Chlorite. The mixing model for chlorite given in Holland & Powell (1998) accounts for the need for ordering around the clinochlore composition in magnesian chlorites, after Baker & Holland (1996), and utilises the order-disorder models of Holland & Powell (1996*b*). In magnesian chlorites, Al mixes with Mg on the M1 and M4 sites, and with Si on two T2 sites, but orders preferentially onto the M4 site at lower temperatures. A new endmember, Al-free chlorite (afchl)is introduced, and the endmembers Al-free chlorite, amesite and clinochlore are assumed to mix according to a ternary regular solution. Daphnite is considered as a fully Fe-Al ordered independent endmember. Mixing parameters with values $W_{af.cl}$ = 18 kJ.mol^{-1}, $W_{af.da}$ = 14.5 kJ.mol^{-1}, $W_{am.da}$ = 13.5 kJ.mol^{-1}, $W_{af.am}$ = 20 kJ.mol^{-1} and $W_{cl.am}$ = 18 kJ.mol^{-1} are used. The Fe-endmember W values are from Holland (pers. comm.)

Chlorite variables: $(Fe,Mg,Mn)_4(Fe,Mg,Mn,Al)_2Si_2(Si,Al)_2O_{10}(OH)_8$

x = Fe/Fe+Mg+Mn

mn = Mn/Fe+Mg+Mn

$y = X_{Al,T2}$

$N = X_{(Al,M4-XAl,M1)}/2$

endmembers: Al-free chlorite (Afchl) $[Mg_4][Mg][Mg]Si_2[Si_2]O_{10}(OH)_8$

$a_{afchl} = (1-x-mn)^6(1-y+N)(1-y-N)(1-y)^2$ (y = 0)

$p_{afchl} = 1-y-N$

$RT\ln\gamma_{afchl} = W_{af.cl/5}(y-N)[10N-(2x-2mn)(3-y)] + W_{af.da/5}(y+N)[2x(3-y)] + W_{af.am}(y+N)(y-N) - W_{cl.am/5}(y-N)[10N-(2x-2mn)] - W_{am.da/5}(y+N)[2x(3-y)]$

clinochlore (Clin) $[Mg_4][Mg][Al]Si_2[SiAl]O_{10}(OH)_8$

$a_{clin} = 4\,(1-x-mn)^5(1-y-N)(y+N)(1-y)$ (y = 0.5)

$p_{clin} = (1-p_{afchl}-pd_{aph}-p_{mnchl}-p_{ames})$

$RT\ln\gamma_{clin} = W_{af.cl/5}(1-y-N)[(5-10N)+(2x-2mn)(3-y)] - W_{af.da/5}(1-y-N)[2x(3-y)] - W_{af.am}(1-y-N)(y-N) + W_{cl.am/5}(y-N)[(5-10N)-(2x-2mn)(3-y)]-W_{am.da/5}(y-N)[2x(3-y)]$

daphnite (Daph) $[Fe_4][Fe][Al]Si_2[SiAl]O_{10}(OH)_8$

$a_{daph} = 4\,x^5(1-y+N)(y+N)(1-y)y$ (y = 0.5)

$p_{daph} = 2/5\,x(3-y)$

$RT\ln\gamma_{daph} = W_{af.da/5}(1-y-N)[5-2x(3-y)] -W_{af.cl/5}(1-y-N)[10N-(2x-2mn)(3-y)]- W_{af.am}(1-y-N)(y-N) - W_{cl.am/5}(y-N)[10N-(2x-2mn)(3-y)]+W_{am.da/5}(y-N)[5-2x(3-y)]$

mn-chlorite (Mnchl) $[Mn_4][Mn][Al]Si_2[SiAl]O_{10}(OH)_8$

$a_{mnchl} = mn^5(1-y-N)(y+N)(1-y)y$ (y = 0.5)

$p_{mnchl} = 2/5\,mn(3-y)$

$RT\ln\gamma_{mnchl} = -W_{af.da/5}(1-y-N)[2x(3-y)] -W_{af.cl/5}(1-y-N)[10N-(2x-2mn)(3-y)]- W_{af.am}(1-y-N)(y-N) - W_{cl.am/5}[(y-N)][10N-(2x-2mn)(3-y)]-W_{am.da/5}(y-N)[2x(3-y)]$

amesite (Ames) $[Mg_4][Al][Al]Si_2[Al_2]O_{10}(OH)_8$

$a_{ames} = 4\,(1-x-mn)^4(y-N)(y+N)y^2$ (y = 1)

$p_{ames} = (y-N)$

$$RT\ln\gamma_{ames} = W_{af.am}(1\text{-}y\text{-}N)(1\text{-}y\text{-}N) + W_{cl.am/5}(1\text{-}y\text{-}N)[10N\text{-}(2x\text{-}2mn)(3\text{-}y)] + W_{am.da/5}(1\text{-}y\text{-}N)[2x(3\text{-}y)] - W_{af.da/5}(1\text{-}y\text{-}N)[2x(3\text{-}y)] - W_{af.cl/5}(1\text{-}y\text{-}N)[10N\text{-}(2x\text{-}2mn)(3\text{-}y)]$$

Muscovite-Phengite. The phengite mixing model used in Holland & Powell (1998) assumes octahedral (Mg,Fe)-Al ordering such that each (Mg,Fe) entering the dioctahedral sheet has Al as its nearest neighbours. This approximates to a situation where Al and (Mg,Fe) can only mix on one M2 site (M2A), so that each M2A is surrounded by three M2B, and vice-versa. Energetically, phengitic micas were found to be approximately ideal for the mixing models used below (i.e. $W_{mu.cel} = 0$). When Na is considered in the mica system, non-ideal mixing of Na and K on the A site must be accounted for. This is modelled by a regular solution of the K-endmembers with a fictive paragonite endmember. The regular solution parameters are taken as $W_{mu.pa} = 12 + 0.4P$, $W_{pa.cel} = 14 + 0.2P$ and $W_{pa.fcel} = 14 + 0.2P$, and the DQF Gibbs energy increment for the fictive paragonite endmember $I_{pa} = 1.42 + 0.4P$, after Eugster *et al.* (1972) and Guidotti *et al.* (1994).

Muscovite variables: $(K,Na)_(Fe,Mg,Al)_2Si_2(SiAl)_2O_{10}(OH)_2$

$x = Fe/Fe+Mg$

$y = X_{Al,M2}$

$z = Na/Na+K$

endmembers:

muscovite (Ms) $K_[Al_2]Si_2[SiAl]O_{10}(OH)_2$

$a_{ms} = (1\text{-}z)y^2(2\text{-}y)$ $(y = 1)$

$p_{ms} = (1\text{-}p_{cel}\text{-}p_{fcel}\text{-}p_{pa})$

$RT\ln\gamma_{ms} = W_{ms.pg}\, z(1\text{-}y+z) - W_{cel.pg}\, z(1\text{-}y)(1\text{-}x) - W_{fcel.pg}\, zx\,(1\text{-}y)$

celadonite (Cel) $K_[Mg_2]Si_2[SiSi]O_{10}(OH)_2$

$a_{cel} = ¼\,(1\text{-}z)(1\text{-}x)(1\text{-}y)(2\text{-}y)^2$ $(y = 0)$

$p_{cel} = (1\text{-}x)(1\text{-}y)$

$RT\ln\gamma_{cel} = W_{cel.pg}\, z[1+(1\text{-}y)(1\text{-}x)] - W_{fcel.pg}\, xz(1\text{-}y) - W_{ms.pg}\, z(y\text{-}z)$

ferroceladonite (Fcel) $K_[Fe_2]Si_2[SiSi])O_{10}(OH)_2$

$a_{fcel} = ¼\,(1\text{-}z)x(1\text{-}y)(2\text{-}y)^2$ $(y = 0)$

$p_{fcel} = x(1\text{-}y)$

$RT\ln\gamma_{fcel} = W_{fcel.pg}\, z[1+x(1\text{-}y)] - W_{ms.pg}\, z(y\text{-}z) - W_{cel.pg}\, z(1\text{-}x)(1\text{-}y)$

paragonite (Pg) $Na_[Al_2]Si_2[SiAl]O_{10}(OH)_2$

$a_{pg} = zy^2(2\text{-}y)$ $(y = 1)$

$p_{pg} = z$

$RT\ln\gamma_{pg} = W_{ms.pg}(1\text{-}z)(y\text{-}z) - W_{cel.pg}\,(1\text{-}z)(1\text{-}y)(1\text{-}x) - W_{fcel.pg}\,(1\text{-}z)x(1\text{-}y)$

DQF: $I_{pa} = 1.42 + 0.4P$

White micas. Paragonite and margarite were coded after Vance & Holland (1993) and Worley & Powell (1998). They modelled non-ideal mixing on the A site using the DQF approach, as for muscovite. For paragonite, the Gibbs energies of the fictive endmembers muscovite and margarite were incremented by 14 kJ.mol^{-1} and 27-0.016T kJ.mol^{-1} respectively. In margarite, a fictive paragonite component has a Gibbs energy increment of 10 kJ.mol^{-1}.

Paragonite variables: $(K,Ca,Na)_Al_2Si_2(Si,Al)O_{10}(OH)_2$

$k = K/K+Na+Ca$

$c = Ca/K+Na+Ca$

endmembers: paragonite (Pg) $Na_[Al_2]Si_2[SiAl]O_{10}(OH)_2$

$a_{pg} = (1-k-c)(1-c)(1+c)$

$p_{pg} = (1-p_{ms}-p_{mrg})$

margarite (Mrg) $Ca_[Al_2]Si_2[SiAl]O_{10}(OH)_2$

$a_{mrg} = ¼\ c(1+c)^2$

$p_{mrg} = c$

$RT\ln\gamma_{mrg} = I_{mrg.pg}$

muscovite (Ms) $K_[Al_2]Si_2[SiAl]O_{10}(OH)_2$

$a_{ms} = k(1-c)(1+c)$

$p_{ms} = k$

$RT\ln\gamma_{ms} = I_{ms.pg}$

Margarite variables: $(Ca,Na)_ Al_2Si_2(Si,Al)O_{10}(OH)_2$

c= Ca/Ca+Na

endmembers margarite (Mrg) $Ca_[Al_2]Si_2[SiAl]O_{10}(OH)_2$

$a_{mrg} = ¼\ c(1+c)^2$

$p_{mrg} = (1-p_{pg})$

paragonite (Pg) $Na_[Al_2]Si_2[SiAl]O_{10}(OH)_2$

$a_{pg} = (1+c)(1-c)^2$

$p_{pg} = (1-c)$

$RT\ln\gamma_{pg} = I_{pa.mrg}$

Plagioclase. Plagioclase is modelled after Holland & Powell (1992), who used Darken's Quadratic Formalism (DQF) to treat the solution in terms of two separate regions, C1 and I1, each of which can be approximated by a simple regular solution. The C1 region represents the sodic, low albite structure for a given temperature, and I1 the calcic, body-centred anorthite structure. For the C1 phase, a Gibbs energy increment of the fictive anorthite component in albite of 6.01-0.0035T kJ.mol^{-1} was used. For the I1 phase, a value of $W_{an.ab}$ = 9.8 kJ.mol-1

for the regular solution parameter was used, and a Gibbs energy increment of 1.38-0.0039T kJ.mol^{-1} for the fictive albite component.

C1 plagioclase variables: $(Ca,Na)Si_2(Al,Si)_2O_8$

c = Ca/Ca+Na

endmembers: albite (Ab) $Na[AlSi_3]O_8$

$a_{ab} = (1-c)$

$p_{ab} = (1-p_{an})$

anorthite (An) $Ca[Al_2Si_2]O_8$

$a_{an} = c$

$p_{an} = c$

$RT\ln\gamma an = I_{an.ab}$

I1 plagioclase variables: $(Ca,Na)Si_2(Al,Si)_2O_8$

c = Ca/Ca+Na

endmembers: anorthite (An) $Ca[Al_2Si_2]O_8$

$a_{an} = c$

$p_{an} = (1-p_{ab})$

$RT\ln\gamma_{an} = W_{an.ab}(1-c)^2$

albite (Ab) $Na[AlSi_3]O_8$

$a_{ab} = (1-c)$

$p_{ab} = (1-c)$

$RT\ln\gamma_{ab} = W_{ab.an}c^2$ DQF: $RT\ln\gamma_{ab} = I_{ab.an}$

Staurolite. Staurolite was modelled assuming ternary Fe-Mg-Mn mixing, with W_{FeMg} = -4 kJ.mol^{-1}.

Staurolite variables: $(Fe,Mg,Mn)_4Al_{18}Si_{7.5}O_{48}H_4$

x = Fe/Fe+Mg+Mn

mn = Mn/Fe+Mg+Mn

endmembers: staurolite (St) $[Fe_4]Al_{18}Si_{7.5}O_{48}H_4$

$a_{st} = x^4$

$p_{st} = x$

$RT\ln\gamma_{st} = W_{FeMg}\,(1-x-mn)(1-x)$

magnesiostaurolite (Mst) $[Mg_4]Al_{18}Si_{7.5}O_{48}H_4$

$a_{mst} = (1-x-mn)^4$

$p_{mst} = (1-p_{st}-p_{mnst})$

$RT\ln\gamma_{mst} = W_{FeMg}\,x(x+mn)$

Mn-staurolite (Mn-st) $[Mn_4]Al_{18}Si_{7.5}O_{48}H_4$

$a_{mnst} = mn^4$

$p_{mnst} = mn$

$$RT\ln\gamma_{mnst} = W_{FeMg}\, x(1\text{-}mn)$$

Chloritoid. Chloritoid is modelled as a simple Fe-Mg-Mn ternary in the same way as staurolite, with $W_{Fe.Mg} = 1.0$ kJ.mol^{-1}.

Chloritoid variables: $(Fe,Mg,Mn)Al_2SiO_5(OH)_2$

x = Fe/Fe+Mg+Mn

mn = Mn/Fe+Mg+Mn

endmembers:

Mg-chloritoid (Mcld) $MgAl_2SiO_5(OH)_2$

$a_{mcld} = (1\text{-}x\text{-}mn)$

$p_{mcld} = (1\text{-}p_{fcld}\text{-}p_{mncld})$

$RT\ln\gamma_{mcld} = W_{Fe.Mg}\, x(x+mn)$

Fe-chloritoid (Fcld) $FeAl_2SiO_5(OH)_2$

$a_{fcld} = x$

$p_{fcld} = x$

$RT\ln\gamma_{fcld} = W_{Fe.Mg}\, (1\text{-}x)(1\text{-}x\text{-}mn)$

Mn-chloritoid (Mncld) $FeAl_2SiO_5(OH)_2$

$a_{mncld} = mn$

$p_{mncld} = mn$

$RT\ln\gamma_{mncld} = W_{Fe.Mg}\, x(1\text{-}mn)$

Other phases.

Kyanite/Sillimanite	(Ky/Sil) Al_2SiO_5	$a_{ky} = 1$
Quartz	(Qtz) SiO_2	$a_{qtz} = 1$
Clinozoisite	(Czo) $Ca_2Al_2O.AlOH(Si_2O_7)(SiO_4)$	$a_{czo} = 1$
H_2O	(H_2O)	a_{H2O} = user specified

A.1.2 Mixing models used in AX

AX is a program which takes mineral analyses in the form of either oxide weight percent or as cations per formula unit and calculates the activities of the mineral endmembers useful for thermodynamic computations. Errors are propagated from the probe data to the final activities. This is used when THERMOCALC is used in average P-T mode to perform thermobarometric calculations. The program was written by Tim Holland, and the version used is the 1998 update. This uses essentially the same mixing models as described above and in Holland & Powell (1998), with a few minor differences that are described here.

Garnets are described using a 2-site mixing model, with regular solution gammas of:

$W_{py.alm}$=2.5 kJ.mol^{-1}, $W_{gr.py}$=41.4 - 0.0188T kJ.mol^{-1}, $W_{py.andr}$=73 kJ.mol^{-1}, $W_{alm.andr}$=60 kJ.mol^{-1}, $W_{sps.andr}$=60 kJ.mol^{-1}. **Biotites** use the model described in Holland & Powell (1998) i.e. an ordered Al-Mg model, and not the disordered model described above. Neither biotite or chlorite include Mn, but as concentrations of MnO are very low in the high-grade samples of the Suru valley, this is not seen as an important difference. **Staurolites** use a simple Fe-Mg ideal mixing model. **Clinozoisites** are modelled after Holland & Powell (1998), where they are treated as a ternary solution of clinozoisite, Fe-epidote and epidote, with Fe^{3+} ordering onto the M3 site.

A.1.3 Sample data file used for THERMOCALC phase diagram construction

This illustrates the structure of a THERMOCALC datafile used for phase diagram construction in the CNMnKFMASH system and coded using the phases and activity models detailed above. Everything after a % on a line is ignored by the program. Note that many of the mineral abbreviations read by THERMOCALC (e.g. "g") differ from those used elsewhere in the text (e.g. "Grt"). For more details on datafile construction see the web site of Roger Powell at:

http://www.rubens.unimelb.edu.au/~rpowell/THERMOCALC/THERMOCALC.html.

```
g 4
  py    1  1    1 3 -1 1 -1 2 -1 3 3 % a_pyp
   gamma 2  2.5 0 0 1 1    1 2   0 1 1 1 1   0 3 1 1 1 2 1 3 1 % W(FeMg)
            33 0 0 1 1    1 2   0 1 1 2 1   0 3 1 1 1 2 1 3 1 % W(CaMg)
  alm   1  1    0 1 1 1 3 % a_alm
   bulk  1  1    0 1 1 1
   gamma 2  2.5 0 0 1 1    1 2   1 3 -1 1 -1 2 -1 3 1   1 1 -1 1 1 % W(FeMg)
            33 0 0 1 1    1 2   0 1 1 2 1    1 3 -1 1 -1 2 -1 3 1 % W(CaMg)

  gr    1  1    0 1 1 2 3 % a_grs
   bulk  1  1    0 1 1 2
   gamma 2  2.5 0 0 1 1    -1 2   0 1 1 1 1   1 3 -1 1 -1 2 -1 3 1 % W(FeMg)
            33 0 0 1 1    1 2   1 1 -1 2 1    1 3 -1 1 -1 2 -1 3 1 % W(CaMg)
  spss  1 1   0 1 1 3 3 % a_sps
   bulk  1  1    0 1 1 3
   gamma 2   2.5 0 0 1 1    -1 2   0 1 1 1 1   1 3 -1 1 -1 2 -1 3 1 % W(FeMg)
             33 0 0 1 1    -1 2   0 1 1 2 1    1 3 -1 1 -1 2 -1 3 1 % W(CaMg)
  x(g) 0.6
  ca(g) 0.1
  mn(g) 0.2

bi 4
   phl  0.25 4    1 2 -1 1 -1 2 3    2 1 -1 3 2    1 1 1 3 1    1 1 -1 3 1 % a_phl
        gamma 1
           3.33  0  0 2 % Wphleast/3
             1 1 1   0 1 1 3 1
             2 1 2   0 2 1 1 -1 2 1   3 1 -1 3 1
               1 1   0 1 3 3 1
   ann  0.25 4    0 1 1 1 3    2 1 -1 3 2    1 1 1 3 1    1 1 -1 3 1 % a_ann
        bulk 0.3333 2   0 1 1 1    3 1 -1 3
        gamma 1
          3.33  0  0 2 %Wphleast/3
          1 -1 1    0 1 1 3 1
          3 -1 2    0 2 1 1 -1 2 1   3 1 -1 3 1
             1 1    3 1 0 1 1
             -1 1   0 1 3 3 1
```

```
 mnbi  0.25 4    0 1 1 2 3    2 1 -1 3 2    1 1 1 3 1    1 1 -1 3 1 % a_mnbt
       bulk 0.3333 2   0 1 1 2    3 1 -1 3
       gamma 1
        3.33 0 0 2 %Wphleast/3
            1 -1 1    0 1 1 3 1
            3 -1 2    0 2 1 1 -1 2 1   3 1 -1 3 1
               1 1    3 1 0 1 1
              -1 1    0 1 3 3 1
  east  0.25 4    1 2 -1 1 -1 2 2    0 1 1 3 1    1 1 1 3 2    2 1 -1 3 1 % a_east
        bulk 1 1    0 1 1 3
        gamma 1
        3.33 0 0 2 %Wphleast/3
             1 1 1    1 1 -1 3 1
            3 -1 2    0 2 1 1 -1 2 1   3 1 -1 3 1
               1 1    3 1 0 1 1
              -1 1    0 1 3 3 1
 f(bi) 0.4
 mn(bi) 0.05
 y(bi) 0.3

chl 5
   afchl  1   4    1 2 -1 1 -1 3 6      1 2 -1 2 1 4 1      1 2 -1 2 -1 4 1     1 1 -1 2 2 % a_afchl
      bulk 1 1     1 2 -1 2 -1 4
      gamma 6
      3.6 0 0 2  % W(af-cl)/5
        1  1 1   0 2 1 2 1 4 1
        2 -1 2   0 2 2 1 -2 3 1      3 1 -1 2 1
           1 1   0 1 10 4 1
      2.9 0 0 2    % W(af-da)/5
        1  1 1   0 2 1 2 1 4 1
        1  1 2   0 1 2 1 1      3 1 -1 2 1
      20 0 0 1   % W(af-am)
        1  1 2   0 2 1 2 1 4 1   0 2 1 2 -1 4 1
      3.6 0 0 2  % W(cl-am)/5
        1 -1 1   0 2 1 2 -1 4 1
        2 -1 2   0 2 2 1 -2 3 1      3 1 -1 2 1
           1 1   0 1 10 4 1
      0.1 0 0 2  % W(cl-da)/25
        1 -1 2   0 1 2 1 1      3 1 -1 2 1
        2 -1 2   0 2 2 1 -2 3 1      3 1 -1 2 1
           1 1   0 1 10 4 1
      2.7 0 0 2  % W(am-da)/5
        1 -1 1   0 2 1 2 -1 4 1
        1  1 2   0 1 2 1 1      3 1 -1 2 1

clin  4    5    1 2 -1 1 -1 3 5   1 2 -1 2 1 4 1   0 2 1 2 1 4 1    1 1 -1 2 1   0 1 1 2 1 % a_clin
      gamma 6
      3.6 0 0 2  % W(af-cl)/5
        1  1 1   1 2 -1 2 -1 4 1
        2  1 2   0 2 2 1 -2 3 1      3 1 -1 2 1
           1 1   5 1 -10 4 1
```

```
  2.9 0 0 2    % W(af-da)/5
    1 -1 1   1 2 -1 2 -1 4 1
    1  1 2   0 1 2 1 1      3 1 -1 2 1
  20 0 0 1   % W(af-am)
    1 -1 2   1 2 -1 2 -1 4 1   0 2 1 2 -1 4 1
  3.6 0 0 2  % W(cl-am)/5
    1  1 1   0 2 1 2 -1 3 1
    2  1 2   0 2 2 1 -2 3 1      3 1 -1 2 1
       1 1   5 1 -10 4 1
  0.1 0 0 2  % W(cl-da)/25
    1  1 2   0 1 2 1 1      3 1 -1 2 1
    2  1 2   0 2 2 1 -2 3 1      3 1 -1 2 1
       1 1   5 1 -10 4 1
  2.7 0 0 2  % W(am-da)/5
    1 -1 1   0 2 1 2 -1 4 1
    1  1 2   0 1 2 1 1      3 1 -1 2 1

daph  4   5    0 1 1 1 5    1 2 -1 2 1 4 1   0 2 1 2 1 4 1   1 1 -1 2 1   0 1 1 2 1 % a_daph
    bulk 2/5 2   0 1 1 1   3 1 -1 2
    gamma 6
    3.6 0 0 2  % W(af-cl)/5
      1 -1 1   1 2 -1 2 -1 4 1
      2 -1 2   0 2 2 1 -2 3 1      3 1 -1 2 1
         1 1   0 1 10 4 1
    2.9 0 0 2    % W(af-da)/5
      1  1 1   1 2 -1 2 -1 4 1
      2  1 2   0 1 -2 1 1      3 1 -1 2 1
         1 1   5 1 0 1 1
    20 0 0 1   % W(af-am)
      1 -1 2   1 2 -1 2 -1 4 1   0 2 1 2 -1 4 1
    3.6 0 0 2  % W(cl-am)/5
      1 -1 1   0 2 1 2 -1 4 1
      2 -1 2   0 2 2 1 -2 3 1      3 1 -1 2 1
         1 1   0 1 10 4 1
    0.1 0 0 2  % W(cl-da)/25
      2 -1 2   0 2 2 1 -2 3 1      3 1 -1 2 1
         1 1   0 1 10 4 1
      2  1 2   0 1 -2 1 1      3 1 -1 2 1
         1 1   5 1 0 1 1
    2.7 0 0 2  % W(am-da)/5
      1  1 1   0 2 1 2 -1 4 1
      2  1 2   0 1 -2 1 1      3 1 -1 2 1
         1 1   5 1 0 1 1
ames  1   4    1 2 -1 1 -1 3 4      0 2 1 2 -1 4 1      0 2 1 2 1 4 1   0 1 1 2 2 % a_ames
    bulk 1 1   0 2 1 2 -1 4
    gamma 6
    3.6 0 0 2  % W(af-cl)/5
      1 -1 1   1 2 -1 2 -1 4 1
      2 -1 2   0 2 2 1 -2 3 1      3 1 -1 2 1
         1 1   0 1 10 4 1
    2.9 0 0 2    % W(af-da)/5
```

```
  1 -1 1   1 2 -1 2 -1 4 1
  1  1 2   0 1 2 1 1     3 1 -1 2 1
 20 0 0 1   % W(af-am)
  1  1 2   1 2 -1 2 1 4 1   1 2 -1 2 -1 4 1
 3.6 0 0 2  % W(cl-am)/5
  1  1 1   1 2 -1 2 1 4 1
  2 -1 2   0 2 2 1 -2 3 1     3 1 -1 2 1
     1 1   0 1 10 4 1
 0.1 0 0 2  % W(cl-da)/25
  1 -1 2   0 1 2 1 1     3 1 -1 2 1
  2  1 2   0 2 2 1 -2 3 1     3 1 -1 2 1
     1 1   0 1 10 4 1
 2.7 0 0 2  % W(am-da)/5
  1  1 1   1 2 -1 2 1 4 1
  1  1 2   0 1 2 1 1     3 1 -1 2 1

mnchl 4  5   0 1 1 3 5     1 2 -1 2 1 4 1    0 2 1 2 1 4 1    1 1 -1 2 1    0 1 1 2 1 % a_mnchl
      bulk  2/5 2   0 1 1 3    3 1 -1 2
      gamma 6
      2.7 0 0 2  % W(am-da)/5
        1 -1 1   0 2 1 2 -1 4 1
        1  1 2   0 1 2 1 1     3 1 -1 2 1
      0.1 0 0 2  % W(cl-da)/25
        1 -1 2   0 1 2 1 1     3 1 -1 2 1
        2 -1 2   0 2 2 1 -2 3 1     3 1 -1 2 1
           1 1   0 1 10 4 1
       3.6 0 0 2  % W(cl-am)/5
         1 -1 1   1 2 1 2 -1 4 1
         2 -1 2   0 2 -2 1 -2 3 1     3 1 -1 2 1
            1 1   0 1 10 4 1
       3.6 0 0 2  % W(cl-af)/5
         1 -1 1   1 2 -1 2 -1 4 1
         2 -1 2   0 2 2 1 -2 3 1     3 1 -1 2 1
            1 1   0 1 10 4 1
        2.9  0 0 2  % W(af-da)/5
         1 -1 1   1 2 -1 2 -1 4 1
         1  1 2   0 1 2 1 1     3 1 -1 2 1
        20  0 0 1  % W(af-am)
         1 -1 2   1 2 -1 2 -1 4 1    0 2 1 2 -1 4 1
     x(chl) 0.1
     y(chl) 0.5
     mn(chl) 0.01
     N(chl) 0.4

mu 4
   mu   1  3     0 1 1 2 2   2 1 -1 2 1   1 1 -1 3 1 % a_ms
     gamma  3
      12.0 0 0.4  1   % W(pa-mu)
       1   1 2   1 2 -1 2 1 3 1     0 1 1 3 1
      14.0 0 0.2  1   % W(cel-pa)
       1  -1 3   1 1 -1 2 1     1 1 -1 1 1   0 1 1 3 1
```

```
  14.0 0 0.2  1   % W(fcel-pa)
   1  -1  3    1  1 -1  2  1     0  1  1  1  1    0  1  1  3  1

cel   1/4  4     1  1 -1  1  1   1  1 -1  2  1   2  1 -1  2  2   1  1 -1  3  1  % a_cel
  gamma   3
   12.0 0 0.4  1   % W(pa-mu)
    1  -1  2    0  2  1  2 -1  3  1     0  1  1  3  1
   14.0 0 0.2  2   % W(cel-pa)
    2  -1  2    1  1 -1  2  1    1  1 -1  1  1
       1  1     1  0
    1   1  1    0  1  1  3  1
   14.0 0 0.2  1   % W(fcel-pa)
    1  -1  3    1  1 -1  2  1    0  1  1  1  1    0  1  1  3  1
   bulk  1 2      1  1 -1  1      1  1 -1  2

fcel   1/4  4     0  1  1  1  1   1  1 -1  2  1   2  1 -1  2  2   1  1 -1  3  1  % a_fcel
   gamma   3
    12.0 0 0.4  1   % W(pa-mu)
     1  -1  2    0  2  1  2 -1  3  1     0  1  1  3  1
    14.0 0 0.2  1   % W(cel-pa)
     1  -1  3    1  1 -1  2  1     1  1 -1  1  1    0  1  1  3  1
    14.0 0 0.2  2   % W(fcel-pa)
     2  -1  2    1  1 -1  2  1     0  1  1  1  1
        1  1     1  0
     1   1  1    0  1  1  3  1
    bulk  1 2      0  1  1  1      1  1 -1  2

   pa   1   3      0  1  1  2  2   2  1 -1  2  1   0  1  1  3  1  % a_pg
     gamma   3
      12.0 0 0.4  1   % W(pa-mu)
       1   1  2    0  2  1  2 -1  3  1     1  1 -1  3  1
      14.0 0 0.2  1   % W(cel-pa)
       1   1  3    1  1 -1  2  1     1  1 -1  1  1    1  1 -1  3  1
      14.0 0 0.2  1   % W(fcel-pa)
       1   1  3    1  1 -1  2  1     0  1  1  1  1    1  1 -1  3  1
      DQF         1.42 0 0.4
      bulk  1 1      0  1  1  3
  x(mu) 0.7
  y(mu) 0.8
  z(mu) 0.05

pa  3
   pa  1   3      1  2 -1  1 -1  2  1     1  1 -1  2  1     1  1  1  2  1  % a_pg
   ma  0.25  2    0  1  1  2  1     1  1  1  2  2
       bulk     1  1    0  1  1  2
                DQF    27  -0.016  0
   mu   1   3     0  1  1  1  1     1  1 -1  2  1    1  1  1  2  1  % a_ms
       bulk     1  1    0  1  1  1
                DQF    14  0  0
     k(pa)  0.4
     c(pa)  0.1
```

```
ma  2
    ma   0.25  2      0 1 1 1 1     1 1 1 1 2 % a_mrg
    pa   1  2          1 1 1 1 1     1 1 -1  1 2 % a_pg
        bulk   1  1    1 1 -1  1
            DQF  10 0 0
   c(ma)  0.8

st 3
  mst      1   1     1 2 -1  1 -1  2  4  % a_mst
    gamma  1   -4.0 0 0   1  1     1  2    0  1  1  1  1    0  2  1  1  1  2  1  % W(FeMg)
  fst      1   1     0  1  1  1  4  % a_fst
    bulk   1   1     0  1  1  1
    gamma  1   -4.0 0 0 1  1     1  2    1  2 -1  1  -1  2  1    1  1  -1  1  1  % W(FeMg)
 mnst          1   1     0  1  1  2  4  % a_mnst
    bulk   1   1     0  1  1  2
    gamma  1   -4.0 0 0   1  1     -1  2    0  1  1  2  1    0  2  1  1  1  2  1    % W(FeMg)
  x(st)  0.8
  mn(st)  0.01

ctd 3
  mctd     1   1     1 2 -1  1 -1  2  1  % a_mcld
    gamma  1   1.0 0 0   1  1     1  2    0  1  1  1  1    0  2  1  1  1  2  1  % W(FeMg)
 fctd      1   1     0  1  1  1  1  % a_fcld
    bulk   1   1     0  1  1  1
    gamma  1   1.0 0 0   1  1     1  2    1  2 -1  1 -1  2  1    1  1  -1  1  1  % W(FeMg)
  mnctd    1   1     0  1  1  2  1  % a_mncld
    bulk   1   1     0  1  1  2
    gamma  1   1.0 0 0   1  1     -1  2    0  1  1  2  1    0  2  1  1  1  2  1          % W(FeMg)
  x(ctd)  0.8
  mn(ctd)  0.01

C1pl   2
  ab  1  1     1  1 -1  1  1  % a_ab
  an  1  1     0  1  1  1  1  % a_an
    bulk  1  1   0  1  1  1
    DQF   6.01  -0.0035  0
  Ca(plg)  0.12

I1pl 2
  an  1  1     0  1  1  1  1  % a_an
    gamma   1  9.8 0 0    1  1    1  1     1  1 -1  1  2  % W_an.ab
    bulk    1  1   0  1  1  1
ab  1  1     1  1 -1  1  1  % a_ab
    gamma   1  9.8 0 0    1  1    1  1     0  1  1  1  2  % W_ab.an
    DQF     1.38  -0.0039  0
Ca(plg)  0.6

q ky sill  H2O
```

A.2 Mixing models used with program GIBBS

The thermodynamic dataset used with program GIBBS was a modified version of the tutorial file provided with GIBBS v.5.0 (Spear, pers. comm.). In general the activity-composition models utilised were simpler than those in Holland & Powell (1998), and assumed ideal mixing. The chemical formulae of the minerals modelled are given in the above section and are not repeated here.

Biotite, chlorite and staurolite assumed ideal, single-site ternary Fe- Mg-Mn mixing. **Muscovite** was modelled in terms of ideal Fe-Mg-Al mixing with endmembers Ms, Mg-celadonite, Fe-celadonite. **Garnet** was modelled according to a single-site Fe-Mg-Ca-Mn quaternary mixing model, with the non-ideal parameters of Hodges & Spear (1982). This assumes that only Ca-Mg interactions in garnet are significantly non-ideal and assigns a value of $W_{Ca.Mg}$ = 41.4 kJ.mol^{-1}. **Plagioclase** was modelled using the Al-avoidance model of Newton *et al.* (1980). **Clinozoisite** was modelled as a clinozoisite-pistacite binary with ideal mixing.

B.1 Basic thermodynamic principles

The following section briefly states some of the most important conditions required to satisfy heterogeneous equilibrium, or equilibria between assemblages of phases, and how they are used in calculations of geological interest. Unless otherwise stated, all equations are taken from Spear (1993).

The general form of a stoichiometric relation among phase components of a heterogeneous system is:

$$\mathbf{0 = {}^{m}\sum_{j=1}\nu_j M_j} \qquad \mathbf{(B.1)}$$

where M_j is the chemical symbol of the different phase components and ν_j is the stoichiometric coefficient of the phase components in the reaction and the summation is over all m phase components in the reaction. Any relation of the form (B.1) can also be written for the chemical potentials of the phase components:

$$\mathbf{0 = {}^{m}\sum_{j=1}\nu_j \mu_j} \qquad \mathbf{(B.2)}$$

For each chemical potential of each phase component it can also be written:

$$\mathbf{\mu_j = \mu_j^0 + RT\ln a_j} \qquad \mathbf{(B.3)}$$

which separates the chemical potential into its standard state part and its "real", or activity part. Substituting an equation of the form (B.3) for each chemical potential into equation (B.2):

$$\mathbf{0 = {}^{m}\sum_{j=1}\nu_j\mu^0_j + {}^{m}\sum_{j=1}\nu_j RT\ln a_j = {}^{m}\sum_{j=1}\nu_j\mu^0_j + RT\ln(a_j)^{\nu j} = {}^{m}\sum_{j=1}\nu_j\mu^0_j + RT\ln {}^{m}\prod_{j=1}(a_j)^{\nu j}} \qquad \mathbf{(B.4)}$$

or $$\mathbf{0 = \Delta\mu^0 + RT\ln K_{eq}} \qquad \mathbf{(B.5)}$$

where $$\mathbf{K_{eq} = {}^{m}\prod_{j=1}(a_j)^{\nu j}} \qquad \mathbf{(B.6)}$$

From the definition of chemical potential:

$$\mathbf{\Delta\mu^0 \equiv \Delta\underline{G}^0 = \Delta\underline{H}^0 - T\Delta\underline{S}^0} \qquad \mathbf{(B.7)}$$

where the Gibbs free energy, enthalpy and entropy are *molar* quantities, equation (B.5) can be written:

$$\mathbf{0 = \underline{\Delta}G^0\ \Delta\underline{H}^0 - T\Delta\underline{S}^0 + RT\ln Keq} \qquad \mathbf{(B.8)}$$

which is valid for ΔH^0 and ΔS^0 calculated at the temperature and pressure of interest. If we wish to reference the calculations for thermodynamic data tabulated at standard state, i.e. 298 ^{0}K (25 ^{0}C) and 1 bar, it is necessary to include the extrapolations of ΔH and ΔS up to pressure and temperature:

$$0 = \Delta G^0 = \Delta H(298,1) + {}_{298}{}^{T}\!\int \Delta Cp\, dT + {}_{1}{}^{P}\!\int \Delta V\, dP - T\left(\Delta S(298,1) + {}_{298}{}^{T}\!\int \Delta Cp/T\, dT\right) + RT\ln K_{eq} \qquad \textbf{(B.9)}$$

This is the fundamental equation describing the pressure and temperature dependence of the equilibrium constant, and it is the equation that forms the basis of all calculations on mineral equilibria as a function of these variables. At equilibrium the free energy must be zero. There are two general methods of applying equation (B.9) to metamorphic petrology, both of which are utilised in this thesis. The first is to perform calculations using two or more equilibria of the form of (B.9) and solve simultaneously for parameters such as pressure and temperature. The second involves calculations that utilise a set of equations of the form of equation (B.9) that completely define the phase equilibria of the system. These types of calculations permit simultaneous calculation of the compositions of all minerals in an equilibrium assemblage at any values of P and T. If mass balance equations are used in conjunction with equation (B.9) then it is possible to ascertain both the *intensive* variables P, T and X (mineral composition) and the *extensive* variables (mineral abundance)

B.1.1 Applications to thermobarometry

It is possible to simplify equation (B.9) by performing the integrals to calculate the values of ΔH, ΔS, ΔV and ΔC_P at the pressures and temperatures of interest. C_P and V are functions of T and P. The heat capacity integral

$$_{298}\int^{T}\Delta C_P dT \qquad \textbf{(B.10)}$$

is done at 1 bar, and the volume integral

$$_{1}\int^{P}\Delta V dP \qquad \textbf{(B.11)}$$

is done at the temperature of interest. The enthalpy and entropy at any temperature are calculated from the heat capacity integrations:

$$H(T,1) = H(298,1) + {}_{298}\int^{T}\Delta C_P dT \qquad \textbf{(B.12)}$$

$$S(T,1) = S(298,1) + {}_{298}\int^{T}\Delta C_P/T dT \qquad \textbf{(B.13)}$$

Substituting into (B.9):

$$\Delta G = 0 = \Delta H^0 - T\Delta S^0 + \int \Delta V dP + RT\ln K_{eq} \qquad \textbf{(B.14)}$$

Correcting for pressure:

$$H(T,P) = H(T,1) + {}_{1}\int^{P}(V - V\alpha T)dP \qquad \textbf{(B.15)}$$

$$S(T,1) = S(T,1) + {}_1\int^P V\alpha dP \quad \textbf{(B.16)}$$

where α is the thermal expansivity. This enables us to write:

$$\Delta G(P,T,X) = 0 = \Delta H(T,P) - T\Delta S(T,P) + RT\ln Keq \quad \textbf{(B.17)}$$

which describes the free energy calculated at P and T of interest.

A useful form of this employs the temperature and pressure derivatives of the free energy to obtain:

$$\Delta G = 0 = -\Delta S(T,P)dT + \Delta V(T,P)dP + (RT\ln K_{eq})dT + (RT\ln K_{eq})dP \quad \textbf{(B.18)}$$

In ideal solutions, K_{eq} is independent of T and P, so (B.18) reduces to:

$$\Delta G = 0 = (-\Delta S(T,P) + R\ln K_{eq})dT + \Delta V(T,P)dP \quad \textbf{(B.19)}$$

and rearranging:

$$(\partial P/\partial T)_{\ln Keq} = (-R\ln K_{eq} + \Delta S(T,P))/\Delta V(T,P) = \Delta H(T,P,X)/T\Delta V(T,P,X) \quad \textbf{(B.20)}$$

$$(\partial \ln K_{eq}/\partial T)_P = (-R\ln K_{eq} + \Delta S(T,P)/RT) = \Delta H(T,P,X)/RT^2 \quad \textbf{(B.21)}$$

$$(\partial \ln K_{eq}/\partial P)_T = -\Delta V(T,P)/RT \quad \textbf{(B.22)}$$

These equations describe the effect of the thermodynamic quantities ΔS, ΔV and ΔH on the temperature and pressure dependence of the equilibrium constant. Reactions with large values of ΔS and small values of ΔV (such as dehydration reactions or cation exchange reactions) will have steep contours of K_{eq} on a P-T diagram. Reactions with large enthalpies and entropies of reaction will show strong temperature dependence of K_{eq}, and reactions with large ΔV will show strong pressure dependence.

The basic method of thermobarometry is to use values of ΔH, ΔS, ΔC_P and ΔV that are known from experimental calibrations or thermodynamic tables. The equilibrium constant K_{eq} can be measured by determining the compositions of coexisting minerals using an electron microprobe

B.1.2 Uncertainties in thermobarometry

When considering the uncertainties on any thermodynamic calculation, it is important to distinguish between two main types of error, namely *systematic* errors and *random* errors. Systematic errors include errors in the experimental calibration of mineral reactions, errors in ΔH, ΔS, ΔV and ΔC_P of reaction, and uncertainty in activity-composition relationships. Random errors include analytical imprecision in electron microprobe analysis, uncertainty of electron microprobe standard compositions and correction factors, "geological uncertainty" arising from compositional heterogeneities in minerals and not least errors made by the petrologist when assessing the degree to which coexisting minerals are in equilibrium. Errors of geological uncertainty and assumptions by the petrologist are impossible to quantify. In

this thesis, errors on calculated P-T points are only given for THERMOCALC-calculated average P-T's, the derivation of which is shown in the next section. For conventional thermometers and barometers studies such as Hodges & McKenna (1987) and Kohn & Spear (1991) attempt to constrain the magnitudes of the uncertainties on calculated equilibria. For example, Hodges & McKenna (1987) consider the most important sources of uncertainty to be analytical imprecision and systematic errors associated with experimental calibration techniques. They obtain estimates of the values of statistical errors by propagating uncertainties through the formula:

$$\sigma^2_x = (\partial X/\partial z_1)^2\sigma^2_{z1} + (\partial X/\partial z_2)^2\sigma^2_{z2} + \ldots\ldots + 2\sum_{i=1}^{n}\sum_{j=1}^{n} \rho_{zizj}\, \partial X/\partial z_i\, \partial X/\partial z_j\, \sigma^{1/2}_{zi}\sigma^{1/2}_{zj}$$

and a Monte Carlo propagation. Their estimates of analytical uncertainties are in the region of $\pm$ 45 ^{0}C and $\pm$ 0.1 kbar. Total uncertainties on absolute P-T conditions obtained by combining these values with their estimates for calibration uncertainties are of the order of $\pm$ 150 ^{0}C and $\pm$ 4 kbar for 2σ errors. Kohn and Spear (1991) predict uncertainties of a similar and often larger magnitude. It is important to point out, however, that if P-T's are calculated with the same set of thermobarometers then calibration errors will cancel and the overall uncertainties will be smaller.

B.2 Calculations using THERMOCALC

THERMOCALC is a computer program that calculates mineral equilibria from a self-consistent dataset of thermodynamic data. The rationale behind the development of the dataset and computer program is described in detail in Holland & Powell (1985, 1990, 1998) and Powell & Holland (1985, 1988) but is explained briefly here. The rationale is, that any equilibrium reaction may be calculated as long as a database of thermodynamic data is used that possesses reliable data for all phases in that reaction. The principle problem with such a thermodynamic database is that calorimetrically-determined enthalpies of formation (ΔH_f) of mineral endmembers are often not precise enough for calculation purposes. This arises through the derivation of enthalpies where a small difference is taken between several large numbers. Further problems arise through the fact that, although entropies may be precisely measured, they may require incremental addition to account for substitution or positional disorder. Powell & Holland (1985, and references thereafter) assume that for each experimentally determined reaction the only unknown is ΔH_f , and so the enthalpy of reaction for a P-T curve to pass through the end of an experimentally-reversed bracket is:

$$\Delta H = T\Delta S - P(\Delta V + \Delta(\alpha V)(T - 298) - \Delta(\beta V)P/2) - {}_{298}^{T}\int \Delta Cp\, dT + T\,{}_{298}^{T}\int \Delta Cp/T\, dT - \sum r_i RT\ln f_i - RT\ln K \quad \textbf{(B.23)}$$

which can be obtained by rearranging (B.9) and including terms for thermal expansions (α) and isobaric compressibilities (β). P and T are the conditions at the end of the experimental bracket and r_i are the reaction coefficients of the fluid species H_2O and CO_2. The experimentally determined P-T reversals bracket the enthalpy of reaction, brackets on the high temperature side giving an upper bound on the enthalpy of reaction, brackets on the low temperature side giving a lower bound. These enthalpy brackets are converted to one enthalpy bracket representing this reaction (see Holland & Powell, 1990), and this is included in a weighted least-squares analysis. This permits calculation of uncertainties on, and correlations between, the enthalpies of formation for all phases in the dataset. This in turn enables error propagation through the calculations to determine the uncertainties in any phase equilibrium calculations performed using the dataset.

B.2.1 Uncertainties in calculations

In the application of the dataset to phase diagram generation, the covariance matrix for the enthalpies of formation provides the uncertainties which must be propagated through the calculations. When it is applied to real rocks, the uncertainties introduced by imprecisely known a-X relationships and analytical uncertainties are comparable with those from enthalpies alone.

There are two different uncertainty calculations which are relevant; *overall* uncertainties, and *comparison* uncertainties for each result in a set of results. If we consider a particular barometer, we can consider systematic sources of uncertainty, and random sources. Systematic uncertainties include uncertainties in thermodynamic data and a-X relationships. Random uncertainties include mineral analysis uncertainty (probe errors, petrological errors) and mineral chemistry uncertainty (zoning etc.). Systematic uncertainties give rise to *correlation* between calculated pressures. If the calculation of absolute pressures is desired, overall uncertainties should be calculated; if relative pressures, or pressure differences are required, comparison uncertainties are more valid.

The uncertainty in ΔH for a reaction whose reaction coefficients are in a row vector $\mathbf{r}$, and the covariance matrix of the enthalpies of formation of the end-members in the reaction $\mathbf{h}$, is $\mathbf{V_h}$, **is:**

$$\sigma^2_{\Delta H} = (\, d\Delta H/dh) V_h (\, d\Delta H/dh)^T = r V_h r^T. \qquad \textbf{(B.24)}$$

Thus the uncertainty in the enthalpy of reaction can be calculated from the reaction coefficients and the ΔH of the end-members, e.g. for the reaction jd + q = ab

$$\sigma^2_{\Delta H} = r V_h r^T. = \sigma^2_{jd} + \sigma^2_q + \sigma^2_{ab} - 2\sigma_{ab\text{-}q} - 2\sigma_{jd\text{-}ab} + 2\sigma_{jd\text{-}q} \qquad \textbf{(B.25)}$$

The uncertainty in lnK for a reaction, with reaction coefficient r_i whose activities a_i, are uncorrelated but involve uncertainties σ_{ai} is given by:

$$\sigma^2_{\ln K} = \sum_1^n (d\ln K/da_i)^2 \sigma_{ai}^2 = \sum_1^n (r_i/a_i)^2 \sigma^2_{ai} \qquad \textbf{(B.26)}$$

THERMOCALC provides default uncertainties on activities, using a scheme that can be summarized as:

for $a' \geq t/\sigma_s$ $\qquad\qquad$ $\sigma_a = n\, a(1\text{-}a')2\sigma_s$

for $a' < t/\sigma_s$ $\qquad\qquad$ $\sigma_a = n\, a\, t/a'$

It is assumed for these uncertainty calculations that

$a = a'^n$, where a' is a normalised activity on an effective one-site solid solution involving n sites. There are two adjustable parameters, σ_s and t, with σs controlling the default uncertainties at large a' and t controlling them at small a'.

Uncertainties an calculated pressures and temperatures can be calculated from:

$$\sigma^2_P = (\partial P/\partial \Delta H)^2 \sigma^2_{\Delta H} + (\partial P/\partial \ln K)^2 \qquad \textbf{(B.27)}$$

$$\sigma^2_T = (\partial T/\partial \Delta H)^2 \sigma^2_{\Delta H} + (\partial T/\partial \ln K)^2 \sigma^2_{\ln K} \qquad \textbf{(B.28)}$$

This simple form of error propagation equation is sufficient here, as ΔH and lnK are uncorrelated. In more complicated calculations, e.g. those that have more than one reaction with end-members in common, the more general equation $\mathbf{V_y = J V_x J^T}$ **for** $\mathbf{y = f(x)}$ is required. As soon as two reactions involve any of the same endmembers the lnK and ΔH

values are correlated. For most geobarometers, the uncertainty on the lnK term is much greater than that from the ΔH term.

In the calculation of the PT of intersections, the requirement is the vector, $[P\ T]^T$ and the corresponding covariance matrix. This can be performed using any two of the reactions involved in the intersection. The covariance matrix is:

$$\mathbf{V_{PT}} = \begin{pmatrix} \sigma^2_P & \sigma^P_T \\ \sigma^P_T & \sigma^2_T \end{pmatrix} = \mathbf{JVJ^T}$$

where

$$\mathbf{J} = \begin{pmatrix} \partial P/\partial \Delta \mathbf{H} & \partial P/\partial \mathbf{lnK} \\ \partial T/\partial \Delta \mathbf{H} & \partial T/\partial \mathbf{lnK} \end{pmatrix} \qquad \mathbf{V} = \begin{pmatrix} \mathbf{V}_{\Delta H} & 0 \\ 0 & \mathbf{V}_{lnK} \end{pmatrix}$$

where ΔH is the vector of the two enthalpies of reaction and lnK is the vector of the two lnK. VΔH and VlnK will not be diagonal if the two reactions used to calculate the positions of the intersections have end-members in common. Even where **V** is strictly diagonal, as in the case of two crossing reactions which share no phases in common, the resulting $\mathbf{V_{PT}}$ is not diagonal and so P and T are always correlated. The covariance matrix can be represented by an uncertainty ellipse which is the two-dimensional equivalent of the ± on a value. The ellipse is related to the uncertainty box by a correlation coefficient, ρ. For zero correlation the ellipse is tangential to the box at T = T' and P = P' (P and T of intersection). At complete correlation, ρ = 1, the ellipse becomes a slope across the box from corner to corner through P'T'. This is illustrated in Figure B.1.

B.2.2 Calculating average P-T's using THERMOCALC

There are two main ways that equation (B.9) is used with the dataset. First, phase diagram calculations involve determining the variation of phase relationships with P, T and fluid composition. It is difficult to portray the uncertainties in the positions of lines on such diagrams because of the important correlations between the positions of the lines. However, the covariance matrix for intersections of reactions, when portrayed as an uncertainty ellipse, is most useful in average PT calculations. In contrast, when calculating equilibrium P-T's, it is of no interest to calculate the positions of reactions involving end-members of the minerals in a rock, it being presumed that all the reactions intersect ideally at a point; the activities of the end-members only being relevant at this point. The approach of THERMOCALC is to combine the information from all the reactions which can be written between the end-members in the minerals in a rock. Most of these reactions are linear combinations of other

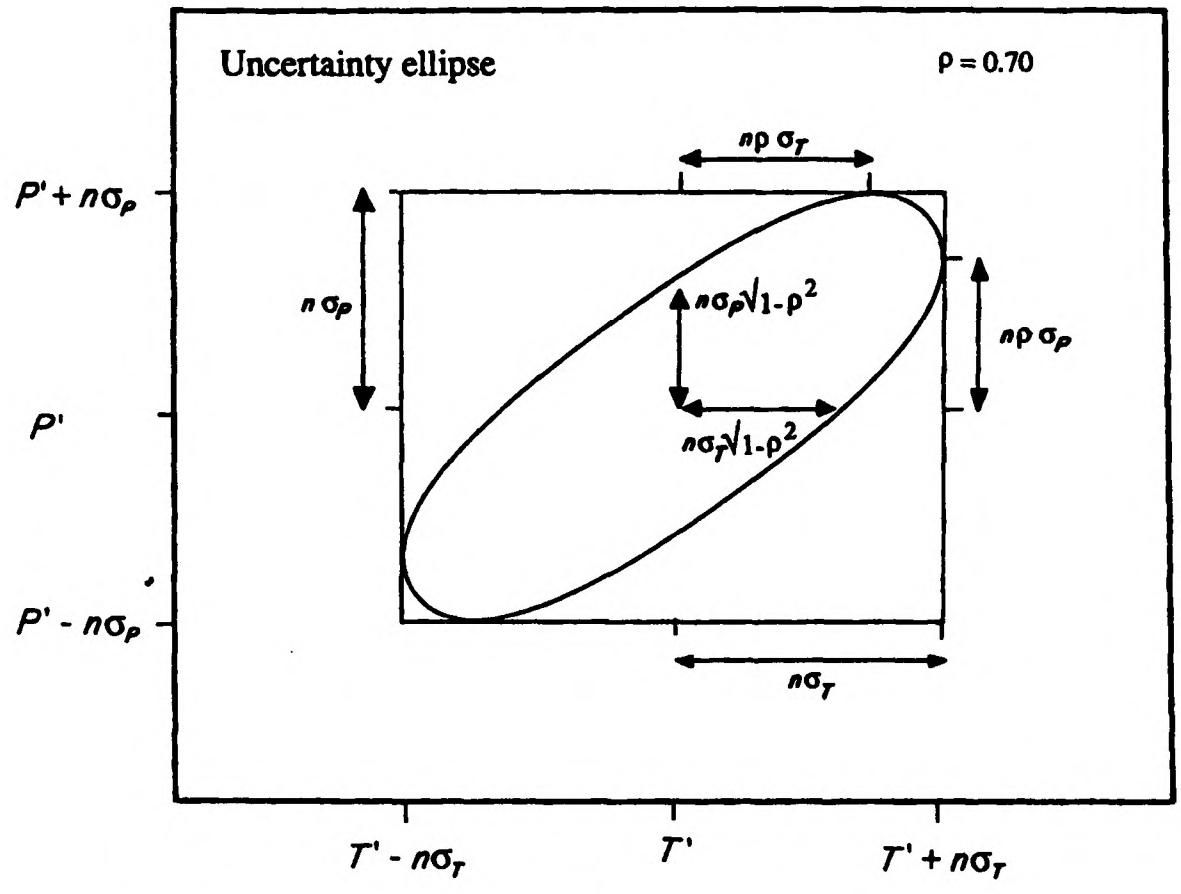


Figure B.1. Geometry of the error ellipse described in the text. From Powell & Holland (1988).

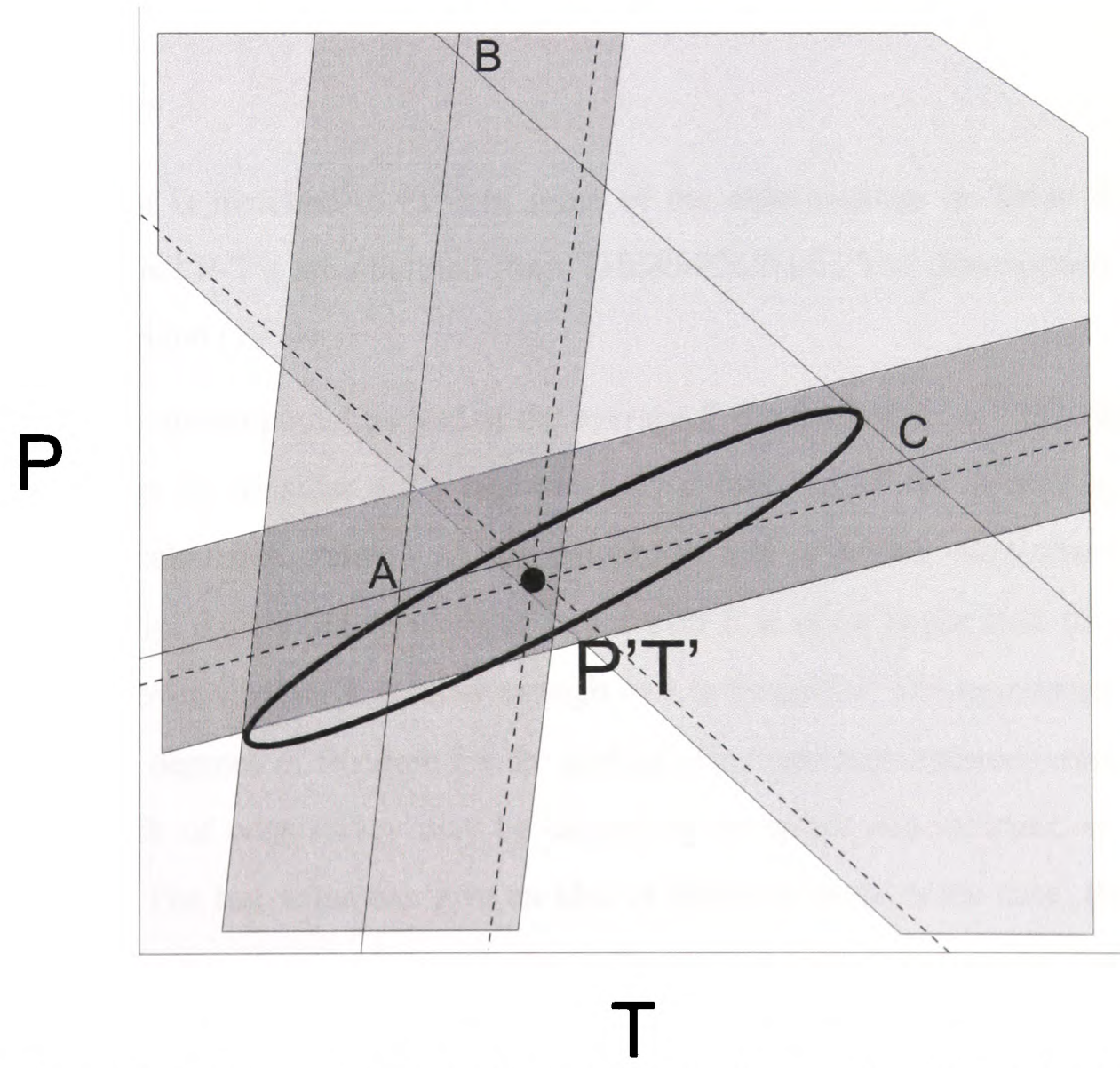


Figure B.2. P-T uncertainty ellipse as described in the text. The optimal P-T calculated by THERMOCALC lies in the consistent region where all three uncertainty bands overlap. The correlated uncertainties in reactions 1, 2 and 3 cause the the optimal P-T to lie outside the triangle ABC and have a highly flattened uncertainty ellipse. After Powell & Holland (1994).

reactions, for an m end-member, n component system, there are ${}^{m}C_{n+1}$ total reactions, of which only m-n are independent. It is these independent reactions which are used.

An uncertainty for the P-T obtained for two reactions can be obtained as an ellipse that is tangential to, and within, the polygon of intersection of the uncertainty bands of these reactions. If a third reaction is added, whose uncertainty bands overlap with those of the first two, there should exist, in a statistical sense, a unique P and T which will lie within the uncertainty interval of all three reactions. It is not sufficient to simply average the P-T points, as they are in general highly correlated (Figure B.2.).

THERMOCALC employs the least squares method to obtain the optimal P-T from an independent set of reactions, including uncertainties and correlations on the activities and enthalpies of formation of the end-members. Essentially this process varies the positions of the reactions, in proportion to their uncertainties and correlations, so that they all intersect *at* one point; the **average P-T**. The reactions with the smallest uncertainty are displaced the least and have a controlling influence on the average P-T. Furthermore, the displacements in any one reaction cannot be made independently of the other reactions because they are all correlated through the shared end-members

B.2.2.1 Diagnostics

This section is included to explain some of the abbreviations in Table 4.3. and to describe how optimal P-T's are obtained from THERMOCALC. The descriptions are taken from Powell & Holland (1994).

Diagnostics are outputted as part of the average P-T calculations in THERMOCALC. The important ones to consider are : σ_{fit}, which is a measure of the scatter in residuals (observed minus calculated values) of the enthalpies and activities normalized by their uncertainties. Ideally, σ_{fit} should be close to 1; however it is often larger than this, and a χ^2 test is used to discover whether it is close enough to 1 to be useful. The maximum allowable σ_{fit} depends on the degrees of freedom for the problem (independent reactions minus number of unknowns). Lack of consistency may be caused by an errant end-member, or a general scatter in the data. The **hat** value can give an idea of which of these is the case; they give an indication of how far a particular datum lies from the centre of the data spread. They can have values of between 0 and 1; the larger the value, the more influence the end-member is having on the final result. Another measure of outlying tendency is the activity residual, Δa_k, the difference between the measured activity and the calculated activity required for all the

activity to intersect at the average PT. These are normalized to the uncertainty on the measured activity and denoted by **e***, defined by $\Delta a_k/\sigma_{ak}$. Large values of e* indicate that the corresponding activities are not being well fitted. The σ_{fit} column produced by THERMOCALC is the σ_{fit} that would result from doubling the uncertainties on each end-member. If an end-member is influential in the calculation, then the uncertainties on average PT increase on doubling the uncertainty of that end-member, because the influential end-member controls the calculation less. In average PT calculations it is best to delete single outliers in turn until the χ^2 test is passed. In cases where there is a general scatter it may be best to enlarge all the activity uncertainties and recalculate.

B.2.3 Calculating P-T projections and pseudosections using THERMOCALC

Although the thermodynamic principles used in all calculation methods have been outlined above, the calculation of phase diagrams using THERMOCALC is outlined briefly here, for reference to Chapter 5 and also in contrast to the average P-T method described above. The methodology is from Powell *et al.* (1998).

THERMOCALC is essentially built around a non-linear equation solver, and this approach is suited to calculating equilibria of a specified variance. This makes calculation of P-T projections and compatibility diagrams straightforward. For example, to calculate the invariant point [Bt] in the KFMASH system (Figure 5.1.A.), the system Cld-St-Chl-Grt-Ky-Ms-Qtz-H_2O must be considered. In general, for an *n*-component model system, if phase *k* involves e_k endmembers, then it involves e_k-*1* compositional variables. For *p* phases in the equilibrium there will be ${}^{p}\sum_{k=1}\ e_k \equiv s$ endmembers of phases, and ${}^{p}\sum_{k=1}\ (e_k\text{-}1) = s\text{-}n$ composition variables. The number of reactions between the endmembers that make up an independent set is the number of endmembers minus the number of components, *s-n*. The number of things that must be set to solve for s-n unknowns is simply the number of degrees of freedom of the equilibria. There is a non-linear equation for each reaction in the independent set of the form $0 = \Delta G_k^0 + RT\ln K_k$. Whereas ΔG_k^0 is a function of only P and T, K_k is in general a function of P, T and composition. For the invariant point [Bt], there is a set of nine independent reactions:

(1) 72Mcld + 11Pyp + 3Ames = 8Mst + 17Clin

(2) 8Mst + 17Clin + 6Ky = 84Mcld + 1Pyp

(3) 10Mst + 19Clin + 3Qtz = 96Mcld + 13Pyp

(4) 39Mcld + 4Pyp = 4Mst + 7Clin + $3H_2O$

(5) 8Fst + 17Daph + 6Ky = 84Fcld + 11Alm

(6) 10Fst + 19Daph +3Qtz = 96Fcld + 13Alm

(7) 39Fcld + 4Alm = 4Fst + 7Daph + $3H_2O$

(8) 8Mst + 14Clin + 3Cel = 72Mcld + 11Pyp + 3Ms

(9) 8Fst + 14Daph + 3Fcel = 72Fcld + 11Alm + 3Ms

using the abbreviations in Appendix A.1. The equilibrium relationship for the first equation is:

$$0 = \Delta G_1^0 + RT\ln((a_{mst}^{st})^8(a_{clin}^{chl})^{17}/(a_{mcld}^{cld})^{72}(a_{pyp}^{grt})^{11}(a_{ames}^{chl})^3)$$

The activities shown in Appendix A.1 would then be inserted here, but these are not shown for obvious reasons of complexity; however, these nine equations are in nine unknowns, P,T, x_{st}, x_{cld}, x_{grt}, x_{chl}, y_{chl}, x_{mu} and y_{ms} (remember these are in the KFMASH system and are therefore simpler than the complete CNMnKFMASH activities in Appendix A.1), and can be solved for. To calculate a divariant equilibrium would lead to seven equilibrium relationships in nine unknowns, and so two variables must be fixed, and so on.

To calculate pseudosections, to each equation of the form $0 = \Delta G^0 + RT\ln K$ must be added a set of equations derived from mass balance constraints. For the specified bulk composition that is being used for the calculation, these additional equations relate the mole proportion of each component in the bulk composition with the sum of the calculated mineral compositions multiplied by their modal proportions. This means that the bulk composition has to be able to be made up of an assemblage of the phases of interest. From Duhem's' theorem (Chapter 5), if two things are specified, the number of equations equals the number of unknowns regardless of the number of phases involved.

The mass balance constraints that are needed involve combinations of the composition and mode variables. For example, in the above equilibria, for the amount of MgO :

$$\begin{aligned}\mathrm{MgO} = {} & p_{chl}\{c_{MgO,clin}x_{clin.chl} + c_{MgO.ames}x_{ames\cdot chl} + c_{MgO.daph}x_{daph.chl}\} \\ & + p_{bt}\{c_{MgO.phl}x_{phl.bt} + c_{MgO.east}x_{east.bt} + c_{MgO.ann}x_{ann.bt}\} \\ & + p_{grt}\{c_{MgO.pyp}x_{pyp.grt} + c_{MgO.alm}x_{alm.grt}\} \\ & + p_{st}\{c_{MgO.mst}x_{mst.st} + c_{MgO.fst}x_{fst.st}\} \\ & + p_{cld}\{c_{MgO.mcld}x_{mcld.cld} + c_{MgO.fcld}x_{fcld.cld}\} \\ & + p_{ms}\{c_{MgO.ms}x_{ms.ms} + c_{MgO.cel}x_{cel.ms} + c_{MgO.fcel}x_{fcel.ms}\}\end{aligned}$$

The proportions of endmembers in terms of compositional variables is shown in Appendix 1.A. In the above example, p_{bt} is the modal proportion of biotite in the equilibrium, $x_{phl.bt}$ is the proportion of the endmember phlogopite in the biotite, and $c_{MgO.phl}$ is the number of MgO in the formula of phlogopite.

Finally, THERMOCALC has the ability to determine the relative stabilities of a set of possible assemblages at a given P-T for a particular bulk composition by performing Gibbs energy minimisation calculations. Using Duhem's theorem and setting the two unknowns to be P and T, the program loops through all the divariant and specified higher equilibria in the system and determines the Gibbs energy of each of these. This is a useful tool when attempting to construct pseudosections in complex systems such as CNMnKFMASH, where there are many variables.

B.3 Calculations using GIBBS

The approach taken by THERMOCALC is to solve the integrated forms of the equilibrium thermodynamic equations as described above. This method is best suited for the study of the phase relations of rocks and *absolute* values of P, T, X and M. The Gibbs method, however, calculates the *changes* in P, T, X and M by solving the differential forms of the thermodynamic equations. These are derived briefly here.

The total derivative of the equilibrium condition:

$$\mathbf{0 = {}^{m}\sum_{j=1}\nu_j\mu_j} \qquad \mathbf{(B.2)}$$

begins by appreciating that the chemical potential (μ_j) of each phase component is a function of T, P and every independent mole fraction X_i. The partial derivatives of μ_j with respect to T and P are the partial molar entropy $\underline{S}$ and volume, $\underline{V}$ respectively:

$$\mathbf{(\partial\mu_j/\partial T)_{P,X} = -\underline{S}_j} \qquad \mathbf{(B.29)}$$

$$\mathbf{(\partial\mu_j/\partial P)_{T,X} = \underline{V}_j} \qquad \mathbf{(B.30)}$$

To obtain the total derivative of μ_j with respect to mineral composition (X) it is necessary to recognise that the chemical potential of component j in phase k is a function of every independent component in k. Choosing the standard state μ_j as the pure component at the P and T of interest:

$$\mathbf{\mu_j(T,P,X) = \mu_j^0(T,P) + \alpha RTlna_j = \mu_j^0(T,P) + \alpha_j RTlnX_j + \alpha_j RTln\gamma} \qquad \mathbf{(B.31)}$$

where a_j is the activity of component j in the phase, X_j is the mole fraction, α_j is the site multiplicity and γ_j is the activity coefficient. The term $RT\ln X_j$ is a function of only X_j whereas the term $\alpha_j RT\ln\gamma_j$ is a function of all the X_i in the phase. Therefore:

$$(\partial\mu_j/\partial X_j)_{T,P,Xi\neq j} = RT\alpha_j/X_j + RT\alpha_j/\gamma_j(\partial\gamma_j/\partial X_j)_{T,P,Xi\neq j} \quad \textbf{(B.32)}$$

and

$$(\partial\mu_j/\partial X_i)_{T,P,X1\neq i} = RT\alpha_j/\gamma_j(\partial\gamma_j/\partial X_i)_{T,P,X1\neq i} \quad \textbf{(B.33)}$$

The total derivative of μ_j with respect to T, P and X is then:

$$d\mu_j = S_j dT + V_j dP + (RT\alpha_j/X_j)dX_j + [^{npct}\textstyle\sum_{i=1} RT\alpha_j/\gamma_j\,(\partial\gamma_j/\partial X_i)_{T,P,X1\neq i}]dX_i \quad \textbf{(B.34)}$$

where the subscript j refers to the component whose chemical potential is being differentiated and the subscript i refers to all components in the system. The summation is over all phase components (npct) in the system. Each phase component in equation (B.2) has a total derivative similar to to equation (B.34). Multiplying each total derivative by the respective stoichiometric coefficient results in:

$$0 = -\Delta S(T,P,X)dT + \Delta V(T,P,X)dP + {}^{m}\textstyle\sum_{j=1}\nu_j(RT\alpha_j/X_j)dX_j +$$

$${}^{m}\textstyle\sum_{j=1}\nu_j[^{npct}\sum_{i=1} RT\alpha_j/\gamma_j\,(\partial\gamma_j/\partial X_i)_{T,P,X1\neq i}]dX_i \quad \textbf{(B.35)}$$

This result is essentially a Gibbs-Duhem equation of the form $0 = \underline{S}dT - \underline{V}dP + \sum X_j d\mu_j$ as is more commonly written in the literature (e.g Spear & Selverstone, 1983).

The total differential of the stoichiometric constraint

$$1 = {}^{npck}\textstyle\sum_{j=1} X_j^k$$

which is only a function of mineral composition, is:

$$0 = {}^{npck}\textstyle\sum_{j=1} dX_j^k \quad \textbf{(B.36)}$$

where X_j^k is the mole fraction of phase component j in phase k and npc^k is the number of phase components in phase k.

The total differential of the mass balance constraint

$$m_i = {}^{nph}\textstyle\sum_{k=1} M^k\ {}^{npck}\sum_{j=1} n_{i,j}^k\ X_j^k$$

is, for a closed system where $dm_i = 0$, (change in the number of moles of each system component:

$$0 = {}^{nph}\textstyle\sum_{k=1} M^k\ {}^{npck}\sum_{j=1} n_{i,j}^k\ dX_j^k + {}^{nph}\sum_{k=1} dMk\ {}^{npck}\sum_{j=1} n_{i,j}^k\ X_j^k \quad \textbf{(B.37)}$$

where n_i^k is the number of moles of system component i in one mole of phase k, M^k is the number of moles of phase k in the rock and X_j^k is the mole fraction of phase component i in phase k, as above.

The Gibbs method as utilised in program GIBBS calculates solutions to the total differentials of the above equations (B35), (B.36) and (B37). In order to use these equations for the solution of a problem it is necessary to specify initial values of P, T, X and M for the assemblage i.e. we must know the equilibrium values at the start which will serve as reference conditions. The approach taken in this thesis was to use equilibrium conditions calculated by THERMOCALC as our Gibbs method reference conditions, which was then used to calculate changes on P and T from the starting values.

C Modal analyses

Modal analysis was performed on a number of samples in order to get a representative measurement of the volume percents of all the major phases. The volumes of each phase were converted to moles and combined with compositional data obtained from the electron microprobe to obtain bulk compositions for each sample. For example, if a rock contains the aluminium-bearing phases Bt + Ms + Grt + Pl + Ky, the total bulk molar aluminium is calculated from: moles $_{Bt}$ * cations $_{Al\ in\ Bt}$ + moles $_{Ms}$ * cations $_{Al\ in\ Ms}$ + moles $_{Grt}$ * cations $_{Al\ in\ Grt}$ + moles $_{Pl}$ * cations $_{Al\ in\ Pl}$ + moles $_{Ky}$ * cations $_{Al\ in\ Ky}$. This figure is then divided by 2 to get the bulk moles Al_2O_3, which is simple to use in THERMOCALC. The measured volumes of each phase are also used to compare with the volumes of phases calculated by THERMOCALC.

The modal analyses were obtained using a mechanical stage attached to a petrological microscope. The stage was set up to have a grid interval of 0.4 mm, and 500 points were measured on thin sections and probe slides of suitable samples. All samples chosen for analysis contain garnet, porphyroblasts of which are by definition larger than the matrix phases. In order to maintain statistical consistency, large porphyroblasts were not included in the point counting, and only the proportions of matrix phases measured. The overall proportion of porphyroblasts was then estimated from the whole section and hand specimens.

Phase	Molar volume	Volume %						Moles					
		L429	**Z47**	**Z70**	**Z37**	**Z49**	**Z18**	**L429**	**Z47**	**Z70**	**Z37**	**Z49**	**Z18**
Qtz	23	45	47	30	52.2	46.6	26.8	1.96	2.043	1.3	2.27	2.03	1.165
Grt	115	5	8	10	5	10.8	6.2	0.04	0.069	0.087	0.043	0.094	0.054
Bt	150	26	30	20	9.3	15.2	21.2	0.17	0.2	0.133	0.062	0.1	0.141
Ms	141	22	12	38	22.4	22.4	20.4	0.16	0.085	0.269	0.159	0.159	0.145
Pl	100	1	2	0	4.4	1.8	8.4	0.01	0.02	0	0.044	0.018	0.084
Ky	44	0.5	1	1	4.6	1	13.2	0.01	0.023	0.023	0.1	0.023	0.3
Chl	215		0.5		0.57	2.2	3.8		0.002		0.003	0.01	0.018
St	447			0.5						0.002			

Table C.1. Tabulated results of point counting listing mineral volume percents and moles. Molar volumes used are taken from the dataset of Holland & Powell (1998), and the mineral endmember volume data are averaged to give a figure for the phase as a whole depending on the composition e.g. the garnet molar volume is weighted towards the value for almandine. Molar volumes in J.bar $^{-1}$ *10.

D. Electron microprobe analyses

	Z2	Z2	Z2	Z2	Z2	Z4	Z4	Z9	Z9
Min	Grt	Bt	Chl	Hbl	Pl	Grt	Bt	Grt	Bt
	avrim	av	av	av	av1	av rim	av agrt	rim	a grt
SiO2	38.35	36.76	28.30	48.31	58.03	38.02	36.5	37.33	33.36
TiO2	0.08	2.92	0.25	0.18	0.02	0.04	2.5	-	2.72
Al2O3	21.40	16.06	17.64	12.60	25.93	21.24	16.06	20.45	16.67
Fe2O3	0.24	-	-	4.29	0.2	0.23	-	-	-
FeO	28.14	18.39	23.44	14.55	-	27.88	19.84	32.29	32.56
MnO	0.35	0.03	0.09	0.08	-	0.48	0.07	1.25	0.18
MgO	3.34	11.71	16.01	8.75	0.02	2.07	10.61	0.35	1.53
CaO	8.96	0.02	0.09	11.46	8.18	10.49	0.01	8.52	-
Na2O	-	0.17	0.04	1.09	6.82	0	0.12	-	0.08
K2O	-	8.69	0.46	0.84	0.15	0	8.97	-	9.31
Total	100.87	94.76	86.33	97.65	99.35	100.46	94.69	100.19	96.42
Oxygens	12	11	14	23	8	12	11	12	11
Si	3	2.791	2.998	6.536	2.613	3.002	2.798	3.012	2.699
Ti	0.005	0.167	0.02	0.02	0.001	0.002	0.144	-	0.165
Al	1.974	1.437	2.203	2.216	1.376	1.977	1.452	1.945	1.59
Fe3+	0.014	-	-	0.482	0.007	0.013	-	0.031	-
Fe2+	1.842	1.168	2.077	1.815	-	1.841	1.272	2.148	2.203
Mn	0.023	0.002	0.008	0.01	-	0.032	0.005	0.085	0.012
Mg	0.389	1.325	2.528	1.945	0.001	0.244	1.212	0.042	0.184
Ca	0.752	0.002	0.01	1.832	0.395	0.888	0.001	0.737	-
Na	-	0.025	0.008	0.315	0.595	0	0.018	-	0.013
K	-	0.842	0.062	0.16	0.009	0	0.878	-	0.962
Sum	8	7.758	9.915	15.332	4.995	8	7.78	8	7.828

Sample	Z10	Z10	Z10	Z10	Z25	Z25	Z25	Z25	Z28	Z28	Z28	Z28
Min	Grt	Bt	Ms	Pl	Grt	Bt	Ms	Pl	Grt	Bt	Ms	Pl
	avrim	adj grt	adj grt	adj ms	rim	av agrt	av agrt	av	avrim	av	av	av
SiO2	38.32	35.03	46.10	48.96	37.67	36.00	46.08	64.78	38.11	35.79	46.11	64.31
TiO2	0.09	2.29	0.30	-	0.08	2.42	0.85	0.02	0.11	1.77	0.73	0.02
Al2O3	21.15	18.56	34.81	29.05	21.22	19.21	34.93	22.14	21.15	18.27	33.29	22.39
Fe2O3	-	-	-	-	-	-	-	0.14	0.2	-	-	0.08
FeO	31.90	20.57	1.48	-	35.69	19.04	1.03	-	32.02	19.44	1.77	-
MnO	0.11	0.01	-	-	0.55	0.04	-	0.02	2.21	0.24	0.01	-
MgO	2.17	8.39	0.68	-	3.41	9.6	0.74	0.02	3.54	10.16	1.09	0.03
CaO	7.3	0.11	-	11.07	2.14	0.03	-	3.22	3.98	0.03	-	3.77
Na2O	-	0.20	0.48	3.07	-	0.26	0.9	9.68	-	0.1	0.38	9.3
K2O	-	9.00	10.73	0.7	-	8.44	9.64	0.11	-	9.34	10.62	0.15
Total	101.05	94.17	94.59	92.85	100.77	95.05	94.18	100.14	101.32	95.15	94.02	100.05
Oxygens	12	11	11	8	12	11	11	8	12	11	11	8
Si	3.025	2.712	3.096	2.38	3	2.721	3.087	2.85	3.005	2.729	3.122	2.834
Ti	0.005	0.133	0.015	-	0.005	0.138	0.043	0.001	0.007	0.102	0.037	0.001
Al	1.968	1.694	2.756	1.665	1.992	1.712	2.759	1.148	1.966	1.642	2.657	1.163
Fe3+	-	-	-	-	-	-	-	0.005	0.012	-	-	0.003
Fe2+	2.106	1.332	0.083	-	2.377	1.203	0.058	-	2.111	1.24	0.1	-
Mn	0.007	0.001	-	-	0.037	0.003	-	0.001	0.148	0.016	0.001	-
Mg	0.255	0.968	0.068	-	0.405	1.081	0.074	0.001	0.416	1.155	0.11	0.002
Ca	0.616	0.009	-	0.577	0.183	0.002	-	0.152	0.337	0.002	-	0.178
Na	-	0.03	0.063	0.289	-	0.038	0.117	0.826	-	0.015	0.05	0.795
K	-	0.89	0.920	0.043	-	0.815	0.825	0.006	-	0.91	0.918	0.008
Sum	7.985	7.768	7.002	4.954	7.999	7.712	6.962	4.989	8	7.81	6.996	4.984

Sample	Z37	Z37	Z37	Z37	Z42	Z42	Z42	Z42	Z43	Z43	Z43	Z43
Min	Grt	Bt	Ms	Pl	Grt	Bt	Hbl	Pl	Grt	Bt	Ms	Pl
	rim	adj grt	adj grt	adj grt	rim	adj grt	adj grt	av	rim	adj grt	adj grt	
SiO2	37.27	36.31	45.61	63.85	37.99	35.77	42.39	62.12	38.17	36.41	48.09	59.54
TiO2	0.03	1.44	0.64	-	0.11	2.65	0.85	-	0.11	2.60	0.43	0.02
Al2O3	21.44	19.29	34.25	21.53	20.95	15.88	14.67	22.6	21.37	18.89	33.24	25.01
Fe2O3	0.60	0.16	-	-	0.15	1.13	4.71	0.14	-	-	1.58	-
FeO	32.78	16.26	1.10	-	28.85	19.32	13.26	-	31.56	19.32	0.61	-
MnO	0.32	0.08	0.02	-	0.85	-	0.18	-	0.24	-	-	-
MgO	4.96	11.58	1.02	-	2.42	10.82	8.88	0.03	1.75	9.01	1.48	-
CaO	2.07	0.04	0.01	2.95	8.98	0.09	11.12	6.64	8.25	-	-	7.24
Na2O	-	0.26	1.66	9.91	-	0.22	1.52	8.13	-	0.20	0.22	6.89
K2O	-	7.93	7.92	0.09	-	8.45	0.81	-	-	9.67	9.47	0.49
Total	99.47	93.35	92.24	98.33	100.3	94.33	98.39	99.67	101.46	96.11	95.13	99.18
Oxygens	12	11	11	8	12	11	23	8	12	11	11	8
Si	2.972	2.748	3.099	2.86	3.01	2.754	6.262	2.77	3.006	2.742	3.18	2.629
Ti	0.002	0.082	0.033	-	0.007	0.153	0.094	-	0.007	0.147	0.021	0.001
Al	2.016	1.721	2.744	1.137	1.957	1.441	2.555	1.188	1.984	1.677	2.591	1.371
Fe3+	0.036	0.009	-	-	0.009	0.065	0.524	0.005	-	-	0.079	-
Fe2+	2.186	1.029	0.063	-	1.912	1.244	1.638	-	2.079	1.217	0.034	-
Mn	0.022	0.005	0.001	-	0.057	-	0.023	-	0.016	-	-	-
Mg	0.589	1.306	0.103	-	0.286	1.242	1.955	0.002	0.205	1.011	0.146	-
Ca	0.177	0.003	0.001	0.142	0.763	0.007	1.76	0.317	0.697	-	-	0.361
Na	-	0.038	0.219	0.861	-	0.033	0.435	0.704	-	0.029	0.028	0.621
K	-	0.766	0.687	0.005	-	0.831	0.153	-	-	0.930	0.80	0.028
Sum	8	7.708	6.949	5.004	8	7.771	15.399	4.986	7.995	7.752	6.878	5.010

Sample	Z46	Z46	Z46	Z46	Z47	Z47	Z47	Z47	Z49	Z49	Z49	Z49	Z49
Min	Grt	Bt	Ms	Pl	Grt	Bt	Ms	Pl	Grt	Chl	Bt	Ms	Pl
	av rim	avagrt	avagrt	av	rim	a grt	a grt	av	av rim	av	av	av	av
SiO2	38.39	35.96	48.00	61.91	38.07	36.4	47.2	62.38	37.89	24.7	36.59	45.47	50.35
TiO2	-	3.28	1.20	0.07	0.02	1.55	0.69	-	0.05	0.08	1.39	0.57	0.01
Al2O3	21.47	18.19	32.63	23.83	21	19.13	33.64	23.04	21.43	22.43	18.61	33.25	30.14
Fe2O3	-	-	-	0.27	0.39	0.97	-	0.11	0.64	0.25	-	-	0.09
FeO	30.28	22.14	2.24	-	30.09	15.51	1.52	-	28.99	18.78	15.11	1.74	-
MnO	0.92	0.15	0.03	0.01	-	-	-	-	0.28	0.18	0.09	0.02	0.01
MgO	2.00	7.26	1.35	0.06	3.98	12.84	1.51	-	4.65	18.58	12.7	1.13	0.03
CaO	7.84	0.03	-	5.40	6.52	0.01	0.01	4.97	6.08	0.02	0.01	-	12.83
Na2O	-	0.12	0.25	8.25	-	0.26	0.88	8.84	-	0.02	0.27	0.95	3.9
K2O	-	9.25	10.43	0.23	-	9.04	9.69	0.11	-	0.05	8.56	9.23	0.09
Total	100.91	96.39	96.14	100.03	100.08	95.73	95.15	99.45	100.02	85.08	93.34	92.37	97.45
Oxygens	12	11	11	8	12	11	11	8	12	14	11	11	8
Si	3.026	2.737	3.175	2.746	3.009	2.702	3.137	2.779	2.983	2.598	2.765	3.115	2.345
Ti	-	0.188	0.06	0.002	0.001	0.087	0.034	-	0.003	0.006	0.079	0.029	-
Al	1.995	1.632	2.544	1.246	1.957	1.674	2.636	1.21	1.989	2.782	1.658	2.685	1.655
Fe3+	-	-	-	0.009	0.023	0.054	-	0.004	0.038	0.02	-	-	0.003
Fe2+	1.996	1.409	0.124	-	1.989	0.963	0.084	-	1.909	1.652	0.955	0.1	-
Mn	0.061	0.01	0.002	-	-	-	-	-	0.019	0.016	0.006	0.001	-
Mg	0.235	0.823	0.133	0.004	0.469	1.42	0.15	-	0.546	2.913	1.43	0.115	0.002
Ca	0.663	0.002	-	0.257	0.553	0.001	0.001	0.237	0.513	0.002	0.001	-	0.64
Na	-	0.018	0.032	0.709	-	0.037	0.113	0.764	-	0.004	0.04	0.126	0.352
K	-	0.899	0.881	0.013	-	0.857	0.822	0.006	-	0.007	0.826	0.808	0.005
Sum	7.976	7.718	6.95	4.986	8	7.795	6.978	4.999	8	10	7.76	6.98	5.004

Sample	Z50	Z50	Z50	Z50	Z51	Z51	Z51	Z51	Z51	Z56	Z56	Z56	Z56
Min	Grt	Bt	Ms	Pl	Grt	Bt	Ms	Pl	Hbl	Grt	Bt	Ms	Pl
	av rim	av	av	adjgrt	av rim	av	av	av		av rim	av	av	a grt
SiO2	38.03	36.34	46.34	57.31	38.48	37.24	46.13	60.41	43.04	39.12	37.09	46.56	58.53
TiO2	-	1.42	0.52	-	-	1.9	0.64	-	0.46	0.06	1.91	0.51	-
Al2O3	21.24	18.62	33.39	26.1	21.42	18.15	33.4	24.43	16.1	21.65	18.81	33.87	25.61
Fe2O3	1.22	0.1	-	0.18	0.75	-	-	-	4.48	-	-	-	0.04
FeO	28.66	16.14	1.5	-	29.47	15.48	1.44	-	12.17	28.49	13.82	1.02	-
MnO	0.31	0.03	0.02	-	0.49	0.07	0.02	-	0.05	0.13	0.04	0.01	-
MgO	3.95	12.43	1.25	-	4.33	12.54	1.17	-	9.31	6.12	12.96	1.24	-
CaO	7.38	0.02	0.01	8.41	6.5	0.04	-	7.08	10.36	5.51	0.01	-	7.91
Na2O	-	0.18	0.77	6.89	-	0.12	1.07	7.32	1.62	-	0.27	0.67	7.07
K2O	-	9	9.88	0.12	-	9.58	9.92	0.07	0.52	-	9.41	10.14	0.10
Total	100.8	94.29	93.69	99.01	101.45	95.13	93.8	99.31	98.11	101.09	94.33	94.03	99.26
Oxygens	12	11	11	8	12	11	11	8	23	12	11	11	8
Si	2.982	2.741	3.133	2.594	2.995	2.779	3.12	2.704	6.289	3.017	2.766	3.13	2.634
Ti	-	0.081	0.026	-	-	0.107	0.033	-	0.051	0.003	0.107	0.026	-
Al	1.964	1.656	2.661	1.393	1.966	1.597	2.663	1.289	2.774	1.969	1.654	2.685	1.359
Fe3+	0.072	0.006	-	0.006	0.044	-	-	-	0.493	-	-	-	0.001
Fe2+	1.88	1.018	0.085	-	1.918	0.966	0.081	-	1.487	1.838	0.862	0.057	-
Mn	0.021	0.002	0.001	-	0.032	0.004	0.001	-	0.006	0.008	0.003	0.001	-
Mg	0.462	1.397	0.126	-	0.502	1.395	0.118	-	2.027	0.703	1.44	0.124	-
Ca	0.621	0.002	0.001	0.408	0.543	0.003	-	0.34	1.622	0.456	0.001	-	0.381
Na	-	0.026	0.101	0.605	-	0.017	0.14	0.635	0.459	-	0.039	0.087	0.617
K	-	0.867	0.853	0.007	-	0.913	0.857	0.004	0.097	-	0.896	0.871	0.006
Sum	8	7.795	6.987	5.012	8	7.781	7.014	4.971	15.305	7.995	7.768	6.981	4.998

Sample	Z64	Z64	Z64	Z64	Z64	Z66	Z66	Z66	Z66	Z69	Z69
Min	Grt	Bt	Ms	Pl	Czo	Grt	Bt	Ms	Pl	Grt	Bt
	av rim	av	av	avhiAn	av	rim	av	av	av	av rim	av
SiO2	38.14	36.36	46.45	56.54	38.62	37.28	34.83	46.96	55.23	37.96	36.9
TiO2	0.11	2.34	0.70	-	0.09	0.12	3.12	0.52	-	0.08	1.45
Al2O3	21.38	16.92	31.65	26.61	31.55	21.35	17.81	34.97	27.75	21.02	18.52
Fe2O3	2.06	-	-	0.04	0.70	0.63	-	1.60	0.08	1.04	-
FeO	26.30	15.63	1.55	-	1.18	30.93	20.71	0.62	-	29.61	15.79
MnO	0.60	0.02	-	-	0.04	0.34	0.01	0.01	-	1.64	-
MgO	4.15	12.14	1.62	-	0.08	1.73	8.11	0.92	-	4.56	12.16
CaO	8.59	0.03	-	9.01	24.27	8.06	0.02	0.01	9.82	4.73	0.01
Na2O	0.04	0.13	0.35	6.50	-	-	0.11	0.26	5.80	-	0.3
K2O	0.07	9.07	10.56	0.11	-	-	9.32	8.62	0.19	-	8.8
Total	101.44	92.65	92.89	98.81	96.55	100.45	94.05	94.50	98.87	100.65	93.94
Oxygens	12	11	11	8	12.5	12	11	11	8	12	11
Si	2.961	2.791	3.179	2.567	2.996	2.971	2.711	3.112	2.512	2.989	2.781
Ti	0.006	0.135	0.036	-	0.005	0.007	0.183	0.026	-	0.005	0.082
Al	1.957	1.531	2.554	1.424	2.886	2.006	1.634	2.732	1.488	1.951	1.645
Fe3+	0.12	-	-	0.02	0.041	0.038	-	0.08	0.003	0.062	-
Fe2+	1.708	1.003	0.089	-	0.077	2.061	1.348	0.034	-	1.95	0.995
Mn	0.039	0.001	-	-	0.003	0.023	0.001	0.001	-	0.109	-
Mg	0.48	1.389	0.165	-	0.009	0.205	0.941	0.091	-	0.535	1.366
Ca	0.715	0.002	-	0.438	2.019	0.689	0.002	0.001	0.479	0.399	0.001
Na	0.006	0.019	0.046	0.572	-	-	0.017	0.033	0.512	-	0.044
K	0.007	0.889	0.923	0.006	-	-	0.926	0.729	0.011	-	0.847
Sum	8	7.762	6.993	5.01	8.036	8	7.761	6.838	5.004	8	7.76

Sample	Z70	Z70	Z71	Z71	Z71	Z71	Z71	Z71
Min	Grt	Bt	Grt	Bt	Ms	Pl	St	Hbl
	rim	adj grt	rim	adj grt	adj grt	av	nr grt	rim
SiO2	37.79	36.36	38.34	36.54	47.19	57.17	28.12	41.57
TiO2	-	1.66	0.21	1.27	0.37	0.01	0.23	-
Al2O3	20.95	19.36	21.2	18.03	32.08	26.48	52.08	16.31
Fe2O3	0.79	-	0.05	0	-	0.21	-	4.18
FeO	32.9	16.11	30.72	16.36	2.92	-	13.85	15.61
MnO	2.11	0.04	1.64	0	-	-	0.19	-
MgO	3.07	11.88	4.28	12.24	1.28	-	2.3	7.48
CaO	3.65	-	4.7	0.01	-	9.27	-	9.63
Na2O	-	0.26	-	0.24	0.85	6.14	-	1.45
K2O	-	9.57	-	9.21	9.68	0.08	-	0.37
Total	101.26	95.25	101.15	93.91	94.38	99.36	96.77	96.6
Oxygens	12	11	12	11	11	8	46	23
Si	2.997	2.72	3.006	2.773	3.184	2.579	7.894	6.255
Ti	-	0.093	0.012	0.072	0.019	-	0.049	-
Al	1.959	1.708	1.96	1.613	2.552	1.408	17.236	2.893
Fe3+	0.047	-	0.003	0	-	0.007	-	0.474
Fe2+	2.182	1.008	2.015	1.039	0.165	-	3.252	1.964
Mn	0.142	0.003	0.109	0	-	-	0.045	-
Mg	0.363	1.325	0.5	1.385	0.129	-	0.963	1.677
Ca	0.31	-	0.395	0.001	-	0.448	-	1.553
Na	-	0.038	-	0.035	0.111	0.537	-	0.423
K	-	0.914	-	0.893	0.834	0.005	-	0.071
Sum	8	7.809	8	7.811	6.994	4.984	29.44	15.31

Sample	Z73	Z73	Z73	Z73	Z73	Z73	Z78	Z78	Z81	Z81	Z81	Z81
Min	Grt	Bt	Chl	Ms	Pl	Czo	Grt	Bt	Grt	Bt	Ms	Pl
	rim	av agrt	av	av agrt	av agrt		av rim	av	avrim	agrt	agrt	a grt
SiO2	38.08	36.11	25.20	47.19	59.17	38.42	37.35	34.87	37.85	36.65	48.02	69.15
TiO2	-	1.83	0.07	0.63	-	-	-	1.96	0.03	1.93	0.45	-
Al2O3	21.37	17.83	21.78	32.81	25.66	27.98	19.96	16.05	20.96	16.78	31.17	19.21
Fe2O3	0.99	-	0.45	-	0.06	6.65	3.21	-	0.42	-	2.55	-
FeO	28.85	18.96	24.15	1.04	-	0.06	19.92	32.78	29.49	19.41	0.57	-
MnO	0.48	0.08	0.09	0.01	-	0.04	5.17	-	3.61	-	-	-
MgO	3.40	10.97	16.18	1.61	-	0.10	0.05	0.63	1.65	10.73	1.72	-
CaO	7.91	-	-	-	7.58	22.80	15.15	-	7.18	0.11	-	0.26
Na2O	-	0.12	-	0.68	7.21	-	-	0.03	-	0.13	0.52	11.66
K2O	-	9.22	-	10.01	0.12	-	-	9.66	-	8.62	8.76	0.1
Total	101.09	95.12	87.93	93.99	99.80	96.07	100.81	96.00	100.38	94.38	93.77	100.38
Oxygens	12	11	14	11	8	12.5	12	11	12	11	11	8
Si	2.984	2.744	2.634	3.171	2.645	3.030	2.969	2.828	3.005	2.802	3.224	3.008
Ti	-	0.105	0.006	0.032	-	-	-	0.12	0.002	0.111	0.023	-
Al	1.974	1.597	2.684	2.60	1.352	2.601	1.87	1.535	1.962	1.513	2.467	0.985
Fe3+	0.058	-	0.035	-	0.002	0.394	0.192	-	0.025	-	0.129	-
Fe2+	1.891	1.205	2.111	0.058	-	0.004	1.324	2.224	1.958	1.241	0.032	-
Mn	0.032	0.005	0.008	0.001	-	0.003	0.348	-	0.243	-	-	-
Mg	0.397	1.242	2.523	0.161	-	0.012	0.006	0.076	0.195	1.223	0.172	-
Ca	0.665	-	-	-	0.363	1.928	1.291	-	0.611	0.009	-	0.012
Na	-	0.018	-	0.089	0.625	-	-	0.005	-	0.019	0.068	0.983
K	-	0.895	-	0.859	0.007	-	-	1.001	-	0.842	0.751	0.006
Sum	8	7.809	10.001	6.971	4.994	7.972	8	7.887	8	7.76	6.865	4.994

Sample	Z83	Z83	Z18	Z18	Z18	Z18	Z33	Z33	Z33	Z33
Min	Grt	Bt	Grt	Bt	Ms	Pl	Grt	Bt	Ms	Pl
	av rim	av	nr rim	av	av	av	rim	av	av agrt	av
SiO2	37.61	36.19	37.85	35.32	45.92	63.44	37.96	35.69	45.73	56.84
TiO2	-	2.55	-	2.26	0.74	-	0	2.3	0.39	0.02
Al2O3	20.86	16.41	22.11	18.2	35.63	21.92	21.71	18.76	34.67	26.45
Fe2O3	0.75	-	0.35	-	-	0.04	0	-	-	0.18
FeO	28.18	22.22	34.32	19.02	1.04	-	31.51	16.85	1.45	-
MnO	5.14	0.13	1.08	0.03	0.04	-	0.23	0.1	0.03	0.01
MgO	1.35	8.62	4.18	9.61	0.66	0.02	4.06	10.85	0.75	0.02
CaO	7.16	0.05	1.87	-	-	3.31	4.62	-	0.02	9.14
Na2O	-	0.1	-	0.21	1.45	9.84	0	0.17	0.72	6.39
K2O	-	9.44	-	9.39	9.17	0.09	0	9.82	10.53	0.14
Total	101.06	95.73	101.76	94.05	94.66	98.66	100.09	94.55	94.3	99.19
Oxygens	12	11	12	11	11	8	12	11	11	8
Si	2.998	2.785	2.968	2.723	3.059	2.837	3	2.711	3.083	2.572
Ti	-	0.148	0	0.131	0.037	-	-	0.131	0.02	0.001
Al	1.96	1.489	2.044	1.654	2.798	1.156	2.022	1.68	2.756	1.411
Fe3+	0.045	-	0.02	-	-	0.001	-	-	-	0.006
Fe2+	1.878	1.43	2.251	1.226	0.058	-	2.082	1.071	0.082	-
Mn	0.347	0.009	0.072	0.002	0.002	-	0.015	0.006	0.002	-
Mg	0.161	0.988	0.488	1.104	0.066	0.001	0.478	1.228	0.075	0.001
Ca	0.612	0.004	0.157	-	-	0.159	0.392	-	0.001	0.443
Na	-	0.015	-	0.031	0.187	0.853	-	0.025	0.094	0.561
K	-	0.928	-	0.925	0.78	0.005	-	0.953	0.907	0.008
Sum	8	7.795	8	7.797	6.988	5.013	7.989	7.806	7.02	5.003

Sample	Z34	Z34	Z34	Z58	Z58	Z58	Z58	Z58	Z59	Z59	Z59	Z59
Min	Grt	Bt	Pl	Grt	Bt	Ms	Pl	St	Grt	Bt	Ms	Pl
	av rim	av	av agrt	nr rim	av	av	av	av rim	rim	adj grt	adj grt	av rim
SiO2	38.3	36.04	59.32	38.21	33.72	46.36	65.18	27.57	37.78	35.31	46.04	64.46
TiO2	-	1.83	0.04	-	1.88	0.65	-	0.73	-	2.63	0.63	-
Al2O3	21.45	18.66	24.57	21.84	19.32	34.17	20.81	52.69	21.07	18.16	35.42	21.19
Fe2O3	0.73	-	0.22	0.2	3.37	-	0.02	-	0.28	-	-	0.08
FeO	27.58	17.22	-	34.43	17.17	1.05	-	13.74	31.22	21.88	1.44	-
MnO	0.46	0.12	0.01	0.67	0.09	0.04	-	0.2	4.78	0.15	0.02	-
MgO	2.96	10.91	0.04	4.82	10.41	0.87	0.02	1.75	1.93	7.88	0.58	0.01
CaO	9.74	-	7.1	1.55	0.01	-	2.55	0.01	4.43	0.02	-	3.22
Na2O	-	0.16	7.64	-	0.3	1.45	10.12	0.01	-	0.09	0.82	9.78
K2O	-	9.28	0.12	-	7.51	8.99	0.11	0.03	-	9.21	10.23	0.15
Total	101.22	94.23	99.06	101.72	93.78	93.59	98.81	96.73	101.49	95.34	95.19	98.89
Oxygens	12	11	8	12	11	11	8	46	12	11	11	8
Si	2.991	2.74	2.673	2.988	2.589	3.119	2.9	7.746	3.004	2.719	3.068	2.873
Ti	-	0.105	0.001	-	0.109	0.033	-	0.154	-	0.152	0.032	-
Al	1.975	1.673	1.305	2.013	1.749	2.711	1.091	17.453	1.975	1.649	2.783	1.113
Fe3+	0.043	-	0.008	0.011	0.195	-	0.001	-	0.017	-	-	0.003
Fe2+	1.801	1.095	-	2.252	1.102	0.059	-	3.229	2.076	1.409	0.08	-
Mn	0.03	0.008	-	0.044	0.006	0.002	-	0.048	0.322	0.01	0.001	-
Mg	0.344	1.236	0.003	0.562	1.191	0.087	0.001	0.733	0.229	0.904	0.058	0.001
Ca	0.816	-	0.343	0.13	0.001	-	0.122	0.003	0.378	0.002	-	0.154
Na	-	0.024	0.667	-	0.045	0.189	0.873	0.005	-	0.013	0.106	0.845
K	-	0.901	0.007	-	0.736	0.773	0.006	0.011	-	0.906	0.871	0.009
Sum	8	7.781	5.007	8	7.722	6.973	4.994	29.381	8	7.764	6.998	4.996

Table D.1. Mineral analyses used in thermobarometric calculations.
Abbreviations: "a", "adj" = adjacent to; "av" = average; "nr" = near.